Symposium on critical and strategic materials proceedings, November 13-14, 2015, Victoria, British Columbia

Edited by G.J. Simandl and M. Neetz

Pacific Section Geological Association of Canada

Ressources naturelles Canada

Natural Resources Canada

Ministry of Energy and Mines, British Columbia Geological Survey
Paper 2015-3

British Columbia Geological Survey
Ministry of Energy and Mines
www.em.gov.bc.ca/geology

Symposium on critical and strategic materials proceedings, November 13-14, 2015, Victoria, British Columbia

Edited by G.J. Simandl and M. Neetz

Co-sponsored by the British Columbia Geological Survey, Natural Resources Canada (Geological Survey of Canada), and the Pacific Section of the Geological Association of Canada

Ministry of Energy and Mines
British Columbia Geological Survey
Paper 2015-3

Ministry of Energy and Mines
Mines and Mineral Resources Division
British Columbia Geological Survey

Recommended citation format for individual papers:

Rukhlov, A.S., Bell, K., and Amelin, Y., 2015. Carbonatites, isotopes and evolution of the subcontinental mantle: An overview. In: Simandl, G.J. and Neetz, M., (Eds.), Symposium on Strategic and Critical Materials Proceedings, November 13-14, 2015, Victoria, British Columbia, British Columbia Ministry of Energy and Mines, British Columbia Geological Survey Paper 2015-3, pp. 39-64.

Front Cover: Rhythmic, metre-scale magmatic layering of kakortokite (a medium- to coarse-grained nepheline syenite) in the southern part of the Ilímaussaq alkaline complex, South Greenland. Sharp-based basal black layers of predominantly arfvedsonite grade upward to red layers rich in eudialyte, which are overlain by relatively thick white layers rich in nepheline and alkali-feldspar. Body of water in lower left is Kangerdlkuarssuk Fjord. See Friis, H., 2015. Primary and secondary mineralogy of the Ilímaussaq alkaline complex, South Greenland. This volume. **Photo by Henrik Friis.**

Back Cover: Sill-like body of calcite-carbonatite, Howard Creek, British Columbia. See Rukhlov, A.S., Bell, K., and Amelin, Y., 2015. Carbonatites, isotopes, and evolution of the subcontinental mantle: An overview. This volume. **Photo by Alexei Rukhlov.**

This publication is available, free of charge from the British Columbia Geological Survey website:
http://www.empr.gov.bc.ca/Mining/Geoscience/PublicationsCatalogue/Papers/Pages/2015-3.aspx

British Columbia Cataloguing in Publication Data

Main entry under title:

Geological Paper: - 1974 -

Issuing body varies

Vols. for 1978-1996 issued in series: Paper / British Columbia. Ministry of Energy, Mines and Petroleum Resources; vols. for 1997 - 1998, Paper / British Columbia. Ministry of Employment and Investment; vols. for 1999-2004, Paper / British Columbia. Ministry of Energy and Mines; vols. for 2005-2009, Paper / British Columbia. Ministry of Energy, Mines and Petroleum Resources; vols. for 2010, Paper / British Columbia. Ministry of Forests, Mines and Lands; vols. for 2011, Paper / British Columbia. Ministry of Energy and Mines; vols. for 2012- , Paper / British Columbia. Ministry of Energy, Mines and Natural Gas; vols. for 2015- , Paper / British Columbia. Ministry of Energy and Mines.

Includes Bibliographical references.

ISSN 0381-243X=Geological Paper

1. Geology - British Columbia - Periodicals. 2. Mines and mineral resources - British Columbia - Periodicals. 3. Geology - Fieldwork - Periodicals. 4. Geology, Economic - British Columbia - Periodicals. 5. British Columbia. Geological Survey Branch - Periodicals. I. British Columbia. Geological Division. II. British Columbia. Geological Survey Branch. III. British Columbia. Geological Survey Branch. IV. British Columbia. Dept. of Mines and Petroleum Resources. V. British Columbia. Ministry of Energy, Mines and Petroleum Resources. VI. British Columbia. Ministry of Employment and Investment. VII. British Columbia Ministry of Energy and Mines. VIII. Series: Paper (British Columbia. Ministry of Energy, Mines and Petroleum Resources). IX. Series: Paper (British Columbia. Ministry of Employment and Investment). X. Series: Paper (British Columbia Ministry of Energy and Mines). XI. Series: Paper (British Columbia Ministry of Energy, Mines and Petroleum Resources). XII. Series: Paper (British Columbia Ministry of Forests, Mines and Lands). XIII. Series: Paper (British Columbia Ministry of Energy and Mines). XIV. Series: Paper (British Columbia Ministry of Energy, Mines and Natural Gas). XV. Series: Paper (British Columbia Ministry of Energy and Mines).

QE187.46 622.1'09711 C76-083084-3 (Rev.)

Victoria
British Columbia
Canada

November 2015

Preface

Symposium on Strategic and Critical Materials

The demand for strategic and critical materials has grown rapidly in recent years, as ever more technologically advanced devices and industrial processes make use of their unique properties. This volume contains extended abstracts of papers presented at the Critical and Strategic Materials Symposium held in Victoria, British Columbia, November 13-14, 2015. The Symposium coincides with the end of the 'Specialty Metals Project', a five-year collaborative effort between the British Columbia Geological Survey, the Geological Survey of Canada, and several academic and industry partners. 'Specialty metals', also known as 'rare metals' are uncommon, nonferrous metals used in quantities of typically less than 150,000 tonnes/year or derived from geographically restricted areas. The Specialty Metals Project ran from 2010 to 2015 and was supported by the fourth iteration of the Targeted Geoscience Initiative Program (TGI-4). The International Workshop on the Geology of Rare Metals, held in Victoria in 2010, launched the TGI-4 Specialty Metals Project and brought together an international group of research scientists and industry professionals. Interest in specialty metals was peaking in 2010 owing to their growing global demand, high value, declining exports from China, and the ongoing challenges of finding new deposits. These factors created a window of opportunity for Canada to establish itself as a world leader in specialty metal exploration and, potentially, exploitation given the favourable geology in parts of Canada. The two main components of the TGI-4 Specialty Metals Project included: 1) a review of specialty metal ore deposits and their mineral economics in Canada; and 2) the development of techniques to guide exploration towards ore-grade zones.

The Critical and Strategic Materials Symposium is an opportunity to once again bring together an international group of researchers and industry professionals to examine the latest results of the TGI-4 Specialty Metals Project and discuss materials of high economic or trade importance (hence 'critical') and those of importance to a nation's security (hence 'strategic'). Studies of these critical and strategic materials will form the basis of a new project supported by the fifth iteration of the Targeted Geoscience Initiative Program (TGI-5). This volume is a record of the Symposium proceedings with papers on a variety of topics including: the uses, markets, and resources for select critical materials; carbonatites and related mineralization; peralkaline intrusion-related mineralization; rare earth elements, graphite, recent developments in exploration and analytical methods, and regional geological studies.

Staff of the British Columbia Geological Survey lead by Dr. George Simandl organized the Symposium. The Survey team consisted of Melanie Mitchell, Dr. Mao Mao, Carlee Akam, and Michaela Neetz. The Symposium was co-sponsored by the Pacific Section of the Geological Association of Canada (GAC-PAC) and the Geological Survey of Canada (GSC), part of Natural Resources Canada (NRCan). We appreciate the support of both organizations and especially the encouragement of Mike Villeneuve during the early stages of Symposium development.

We acknowledge with thanks the many authors of the contributions who laboured under editorial pressure to submit their contributions in a timely manner. All contributions were peer reviewed, and we appreciate the efforts of several anonymous reviewers as well as Carlee Akam, (BCGS, Victoria, BC), John Carter (Bureau Veritas Mineral Laboratories, Australia), John Goode, (J.R. Goode and Associates, Toronto, ON), Todd Hoefen (United States Geological Survey, Denver, CO), Ray Lett, (Consulting Geochemist and British Columbia Geological Survey, Emeritus, Victoria, BC), Duncan A.R. Mackay (De Beers, Yellowknife, NWT), Suzanne Paradis (Geological Survey of Canada, Sidney, BC), Doug Rumble III (Geophysical Laboratory of the Carnegie Institution, Washington, DC), Andreas Stracke (Institute of Mineralogy at the University of Münster, Germany), Mike Thomas (Geological Survey of Canada, Ottawa, ON), and Anthony Williams-Jones (Department of Earth and Planetary Sciences, McGill University, Montreal).

We thank George Owsiacki of Total Earth Science Services for layout and desktop publishing.

Stephen M. Rowins
Chief Geologist and Executive Director
British Columbia Geological Survey
Victoria, November 2015

Table of Contents

Exploration and analytical methods

Regional

Which materials are ‘critical’ and ‘strategic’

George J. Simandl[1, 2, a], Carlee Akam[1], and Suzanne Paradis[3]

[1] British Columbia Geological Survey, Ministry of Energy and Mines, Victoria, BC, V8W 9N3
[2] School of Earth and Ocean Sciences, University of Victoria, Victoria, BC, V8P 5C2
[3] Geological Survey of Canada, Pacific Division, Sidney, BC, V8L 4B2
[a] corresponding author: george.simandl@gov.bc.ca

Recommended citation: Simandl, G.J., Akam, C., and Paradis, S., 2015. Which materials are ‘critical’ and ‘strategic’. In: Simandl, G.J. and Neetz, M., (Eds.), Symposium on Strategic and Critical Materials Proceedings, November 13-14, 2015, Victoria, British Columbia. British Columbia Ministry of Energy and Mines, British Columbia Geological Survey Paper 2015-3, pp. 1-4.

1. Introduction

Raw materials are essential to the global economy and for maintaining and improving our quality of life. Recent years have witnessed a rapid growth in the use and demand for metals or industrial minerals used in high-technology products. Availability of these materials at competitive prices is essential for advances in high-technology products, clean-energy technology, and commercializing new inventions. Most demand and supply analyses emphasize technical, economic, environmental, and social parameters, and technologic breakthroughs. ‘Criticality analysis’ does the same, but focuses on identifying and evaluating the risks and impacts of supply disruptions on the economy, national security, implementing green energy programs, or other initiatives, depending on the interests of the organization that commissions the study. Metals that are commonly perceived as ‘critical’ or ‘strategic’ are rare earth elements (REE), tantalum (Ta), niobium (Nb), lithium (Li), beryllium (Be), gallium (Ga), germanium (Ge), indium (In), zirconia, and graphite.

For many materials (e.g., limestone, silica sand, iron) reserves, resources, and producing mines are abundant and widely distributed. For these materials, future supply is not at risk and can be crudely assessed by using the ratios of (global reserve/yearly production) and (global resource/yearly production). For other materials (e.g., heavy rare earth elements [HREE], Nb, antimony [Sb]) the assessment is more complex. Factors such as authoritarian regimes, monopoly- or oligopoly-type market conditions, political instability, and potential or existing regional conflicts can threaten reliable supply, and analyses must account for these risks. Furthermore, some high-technology metals are derived as a by-product of base-metal extraction (e.g., Ga, Ge, In). Supply of these metals is tied directly to production levels of related base metals. Their level of production cannot be easily increased independently of the main base-metal co-product without a major increase in their price.

According to the Webster’s New Collegiate Dictionary (1975), the distinction between ‘critical’ (“indispensable for the weathering, solution, or overcoming of a crisis”) and ‘strategic’ (“required for the conduct of war <materials> or necessary to or important in the initiation, conduct, or completion of strategic plan”) may be seen as subtle or non-existent. These definitions are more or less in line with current European use (e.g., European Commission, 2011 and 2014a), where ‘critical’ materials are considered to be of high economic or trade importance, whereas ‘strategic’ materials are those essential to a country’s defence. In North America, Ishee et al. (2013), defined a mineral as ‘critical’ if it is essential to a vital sector of the US economy and a mineral as ‘strategic’ if it is “important to the Nation’s economy, particularly for defense issues; doesn’t have many replacements; and primarily comes from foreign countries”. However, the same publication (Ishee et al., 2013), acknowledges that US government-wide definitions do not exist. Similar to government publications, the distinction between the terms ‘critical’ and ‘strategic’ is largely lost in scientific and technical publications, trade journals, and newspapers.

Herein we summarize lists of critical and strategic materials prepared by the European Commission (EC), the US Department of Defense (DoD), and the US Department of Energy (DoE), emphasizing that lists of critical and strategic materials differ, based on whether the criticality analyses is being applied to the general economy (EC), the military (DoD), or clean-air technologies (DoE), and that these lists change through time due to technological breakthroughs, political pressures and instabilities, and depletion of resources. We underline that the designation of a material as ‘critical’ or ‘strategic’ depends on the subject and focus of study; therefore, if the terms ‘critical’ and ‘strategic’ are used, they should be clearly defined in an early portion of the publication and should not be applied out of context.

2. Case studies

2.1. ‘Critical’ raw materials from the economic point of view: the European Commission

With a long mining history, most major near-surface deposits in Europe have been mined out. Some deposits in densely populated areas are undeveloped due to strict environmental regulations. Therefore, discovery, permitting, and development of new mines in Central and Western Europe appear more

difficult relative to other parts of the world. Securing reliable access to raw materials at competitive prices is an ongoing concern for most industrialized European countries (e.g., United Kingdom and Germany) and is reflected in several studies (e.g., Erdman et al., 2011; British Geological Survey, 2012; European Commission 2011, 2014a, b).

The European Commission released its first report on critical raw materials for the EU in 2011, updating it in 2014 (European Commission, 2011, 2014a, b), with plans to produce revised versions every three years. The methodology used in both studies is identical. Economic importance was determined by assessing the proportion of each material associated with industrial mega-sectors at an EU level. These proportions were then combined with the mega-sectors' gross value added to the EU's gross domestic product (GDP). The total was then scaled according to the total EU GDP to define an overall economic importance for the material. To quantify the supply risk, the European Commission relied on the World Governance Indicator (WGI). The WGI includes factors such as voice and accountability, political stability and absence of violence, government effectiveness, regulatory quality, rule of law, and control of corruption (European Commission, 2014a). Both iterations identified critical metals in terms of two key factors: 1) importance to the economy of the European Union; and 2) an estimate of the level of risk associated with supply of each material under consideration.

The 2011 study identified 14 materials as critical from a starting list of 41 non-energy, non-food materials. This list included cobalt (Co), fluorspar, graphite, magnesium (Mg), platinum group elements (PGE), REE (yttrium [Y], scandium [Sc], lanthanum [La], cerium [Ce], praseodymium [Pr], neodymium [Nd], samarium [Sm], europium [Eu], gadolinium [Gd], terbium [Tb], dysprosium [Dy], holmium [Ho], erbium [Er], thulium [Tm], ytterbium [Yb], and lutetium [Lu]), tungsten (W), Ta, Sb, Be, Ga, Ge, In, and Nb (European Commission, 2011).

The 2014 study started with a list of 54 materials and identified 19 as critical (Fig. 1). The extended list included 7 new abiotic materials and 4 biotic materials, including coking coal. For the purpose of this document, biotic materials are omitted. In addition to this expansion, the REE were subdivided into 'heavy' and 'light' categories (European Commission, 2014a). The current list of critical inorganic materials specific to the European community includes: borates, chromium (Cr), fluorspar, magnesite, natural graphite, phosphate rock, heavy REE, light REE, silicon metal, Sb, Be, Co, Ga, Ge, In, Mg, Nb, PGE, and W (European Commission, 2014a). Tantalum and Sc were downgraded to non-critical in the 2014 study.

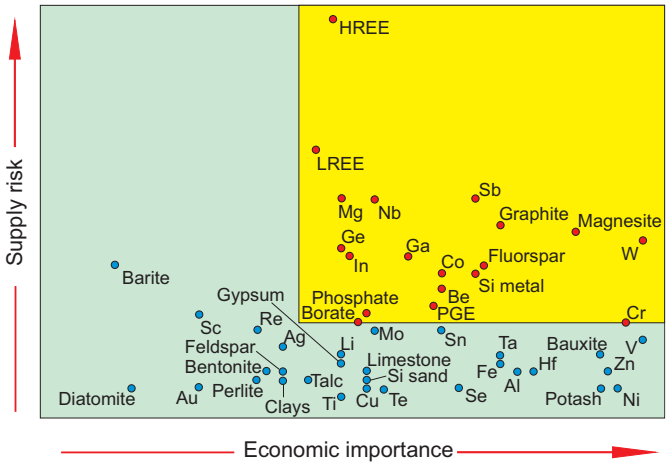

Fig. 1. Critical inorganic materials for the European Union. Criticality field in yellow, individual critical materials as red dots. Modified from European Commission (2014a). HREE–heavy rare earth elements, LREE–light rare earth elements, Mg–magnesium, Ge–germanium, In–indium, Nb–niobium, Ga–gallium, PGE–platinum group elements, Co–cobalt, Be–beryllium, Sb–antimony, Si–silicon, W–tungsten, Cr–chromium, Sc–scandium, Au–gold, Re–rhenium, Ag–silver, Li–lithium, Ti–titanium, Cu–copper, Mo–molybdenum, Te–tellurium, Sn–tin, Se–selenium, Ta–tantalum, Fe–iron, Al–aluminum, Hf–hafnium, Zn–zinc, Ni–nickel, V–vanadium.

2.2. Critical and strategic materials from the military point of view: US Department of Defense

A study commissioned by the US Department of Defense (US DoD) considered the stockpile requirements and availability of 76 materials (US Department of Defense, 2013). It identified 23 materials that would exhibit 'shortfalls' during a hypothetical 4-year time interval consisting of one year of all out conflict involving the USA followed by three years of recovery (starting in 2015 and lasting until the end of 2018). Referred to as 'critical and strategic', the materials determined to be in shortfall are tin (Sn), aluminum oxide fused (Al_2O_3), bismuth (Bi), manganese (Mn), silicon carbide (SiC), fluorspar (acid grade), Sb, W, Ta, Ge, Be, Cr, Dy, Er, Ga, Tb, Tm, Y, Sc, and four proprietary materials including three types of carbon fibers and a rare earth oxide (Fig. 2).

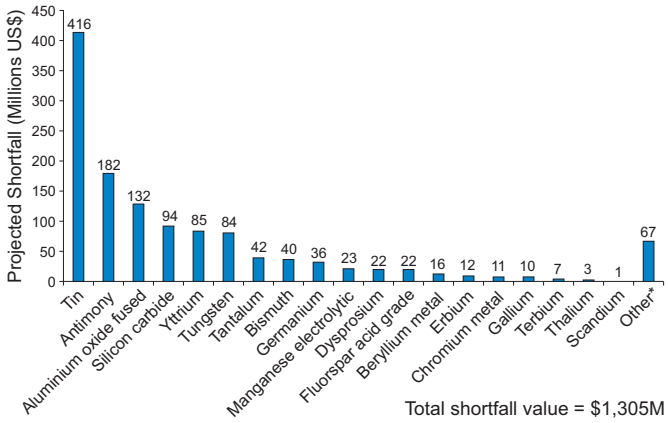

Fig. 2. Projected (2015-2018) shortfalls for 23 critical and strategic materials identified by US Department of Defense. Other* includes three types of carbon fiber and a rare earth oxide (details were not disclosed for proprietary reasons). All shortfall values in 2012 US dollars. After US Department of Defense (2013).

2.3. Critical materials from the clean energy point of view: US Department of Energy

A report prepared by the US Department of Energy Office of Policy and International Affairs (US Department of Energy, 2011) highlighted the importance of 16 elements needed to develop clean technologies (e.g., wind turbines, electric vehicles, photovoltaic thin films, and energy-efficient lighting), and light REE (especially La and Ce) as catalysts to produce gasoline. The criticality of these materials was assessed for the periods 2011 to 2015 and 2015 to 2025. Both assessments were based on: 1) the importance to clean energy; and 2) the level of supply risk. In the assessment for 2015 to 2025 (Fig. 3), Nd, Dy, Eu, Y, and Tb were considered critical, Li and tellurium [Te]) were considered near-critical, and Ce, La, Sm, Pr, Mn, Co, In, Ga, and nickel non-critical. In the earlier assessment period, Li was judged as non-critical, whereas Ce, La, Te, and In were classified as near-critical. Dy, Eu, Nd, Tb, and Y remained on the critical list during both assessment periods.

3. Summary

Table 1 summarizes the results of four criticality studies released since 2011. The document released by the European Commission (2011) lists all REE plus 13 other materials. The European Commission (2014) identified 5 industrial minerals, REE (excluding Sc), PGE and 10 other metals, and coking coal as critical. The list of strategic and critical materials prepared for the US Department of Defense (2013) reported 23 materials as strategic and critical, including SiC, fused Al_2O_3, fluorspar, 7 REE (one of them not shown on Table 1), 10 metals, and 3

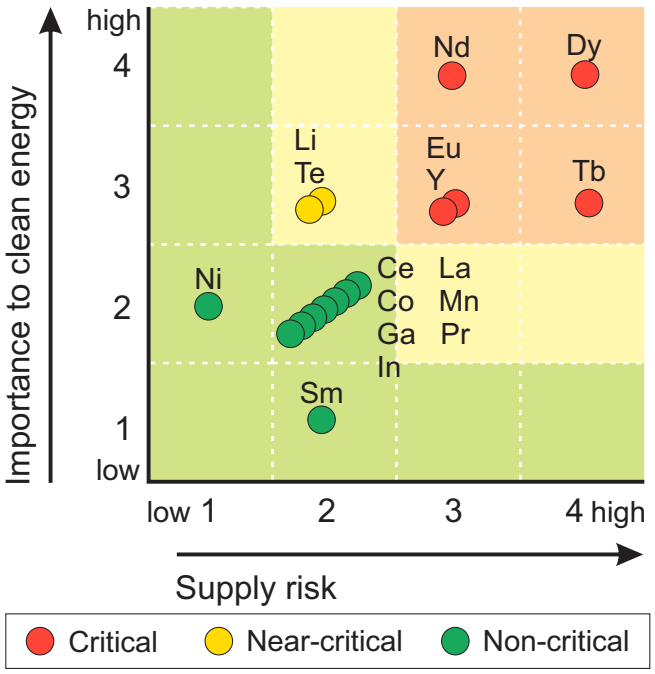

Fig. 3. US Department of Energy criticality matrix of 16 elements for 2015-2025, based on importance to clean energy and supply risk. Modified from US Department of Energy (2011).

Table 1. Results of four criticality studies discussed in the paper. Abbreviations: EU Com–European Commission, US DoD–US Department of Defense, US DoE–US Department of Energy. US DoE divided results into critical and near-critical; near-critical materials are shown by unfilled circles.

Material	EU Com 2011	EU Com 2014	US DoD 2013	US DoE 2011
Al_2O_3			●	
Be	●	●	●	
Bi			●	
Borates		●		
Ce	●	●		
Co	●	●		
Cr		●	●	
Dy	●	●	●	●
Er	●	●	●	
Eu	●	●		●
Fluorspar	●	●	●	
Ga	●	●	●	
Gd	●	●		
Ge	●	●	●	
Graphite	●	●		
Ho	●	●		
In	●	●		
La	●	●		
Li				○
Lu	●	●		
Magnesite		●		
Mg	●	●		
Mn			●	
Nb	●	●		
Nd	●	●		●
PGE	●	●		
Phosphate		●		
Pr	●	●		
Sb	●	●	●	
Sc	●		●	
Si		●		
SiC			●	
Sm	●	●		
Sn			●	
Ta	●		●	
Tb	●	●	●	●
Te				○
Tm	●	●	●	
W	●	●	●	
Y	●	●	●	●
Yb	●	●		

types of carbon fiber (not shown in Table 1). The report of the US Department of Energy (2011) found 5 REE (Nd, Dy, Eu, Y, and Tb) to be critical and 2 metals (Li and Te) to be near-critical for the period of 2015 to 2025 (Fig. 3; Table 1). Thirteen materials are common to at least three of the studies and only three elements (Dy, Tb, and Y) are common to all four studies.

4. Conclusion

Lack of consistency in use of the terms 'critical' and 'strategic' leads to misunderstandings, miscommunications, and potentially misrepresentations. Which materials are considered critical depends to a large extent on the priorities and objectives of the organization or country that commissions the study. Therefore, if the terms 'critical' and 'strategic' are used, they should be clearly defined and should not be applied out of context. The lists of critical and strategic materials produced by the European Commission (2011 and 2014), the US Department of Defense (2013), and the US Department of Energy (2011) differ significantly and illustrate this point. The longest list of critical materials comes from the European Commission (2014), which considered risks to overall economy, and was broad in focus. The shortest list comes from the highly focused study of the US Department of Energy, which considered only the supply risks for materials essential to develop clean air technologies. Lists of critical materials change with time because of breakthroughs in technology, political instabilities in major producing countries, environmental pressures, and discovery, development, or exhaustion of resources.

Acknowledgments

Review by Michaela Neetz of the British Columbia Geological Survey greatly improved the clarity of the manuscript.

References cited

British Geological Survey, 2012. Risk list 2012- An update to supply risk index for elements or element groups that are of economic value. <http://www.bgs.ac.uk/mineralsuk/statistics/risklist.html> Accessed July 15, 2015.

Erdman, L., Behrendt, S., and Feil, M., 2011. Kritische Rohstoffe für Deutschland. Final report, Commissioned by KfW Bankengruppe, Berlin, 134p. <https://www.izt.de/fileadmin/downloads/pdf/54416.pdf> Accessed August 15, 2015.

European Commission, 2011. Critical raw materials for the EU, 85p. <http://ec.europa.eu/enterprise/policies/raw-materials/files/docs/report-b_en.pdf> Accessed July 15, 2015.

European Commission, 2014a. Report on critical raw materials for the EU, 41p. <http://ec.europa.eu/enterprise/policies/raw-materials/files/docs/crm-report-on-critical-raw-materials_en.pdf> Accessed July 15, 2015.

European Commission, 2014b. Annexes to the report on critical raw materials for the EU, 38p. <http://ec.europa.eu/enterprise/policies/raw-materials/files/docs/crm-annexes_en.pdf> Accessed July 15, 2015.

Ishee, J., Alpern, E., and Demas, A., 2013. Going critical: being strategic with our mineral resources. U.S. Department of the Interior, U.S. Geological Survey. <http://www.usgs.gov/blogs/features/usgs_top_story/going-critical-being-strategic-with-our-mineral-resources/> Accessed July 22, 2015.

US Department of Defense, 2013. Strategic and critical materials 2013 report on stockpile requirements. Office of the Under Secretary of Defense for Acquisition, Technology and Logistics, 189p. <http://mineralsmakelife.org/assets/images/content/resources/Strategic_and_Critical_Materials_2013_Report_on_Stockpile_Requirements.pdf> Accessed July 15, 2015.

US Department of Energy, 2011. Critical Materials Strategy. Office of Policy and International Affairs, 190p.

Webster's New Collegiate Dictionary, 1975. Webster's New Collegiate Dictionary. Thomas Allen & Son Limited, Toronto, 1536p.

Rare earth elements: Global market overview

J.S. Dickson[1, a]

[1] Industrial Minerals, 8 Bouverie Street, London, UK, EC4Y 8AX
[a] corresponding author: james.dickson@indmin.com

Recommended citation: Dickson, J.S., 2015. Rare earth elements: Global market overview. In: Simandl, G.J. and Neetz, M., (Eds.), Symposium on Strategic and Critical Materials Proceedings, November 13-14, 2015, Victoria, British Columbia. British Columbia Ministry of Energy and Mines, British Columbia Geological Survey Paper 2015-3, pp. 5-11.

1. Introduction

Rare earth elements (REE), as defined by the International Union of Pure and Applied Chemistry (IUPAC), include yttrium (Y), scandium (Sc), and the lanthanides, comprising lanthanum (La), cerium (Ce), praseodymium (Pr), neodymium (Nd), promethium (Pm), samarium (Sm), europium (Eu), gadolinium (Gd), terbium (Tb), dysprosium (Dy), holmium (Ho), erbium (Er), thulium (Tm), ytterbium (Yb), and lutetium (Lu). In the scientific community, subdivisions into light (LREE) and heavy (HREE) categories are based on electron configuration. In this context, LREE include La, Ce, Pr, Nd, Pm, Sm, Eu, and Gd and HREE include Y, Tb, Dy, Ho, Er, Tm, Yb, and Lu (Connelly et al., 2005). Industry commonly refers to LREE as lanthanides from La to Sm, and HREE as lanthanides from Eu to Lu, plus Y (Simandl, 2014). World mine production of rare earth oxides (REO) for 2014 is estimated at approximately 117,000 tonnes, including Y_2O_3, which accounts for 7000 tonnes of the total (Gambogi, 2015a, b). In 2014, the main producing countries for REE less Y were China, with 86% of worldwide production (Gambogi, 2015a), the United States, India, Australia, Russia, and Thailand (Fig. 1).

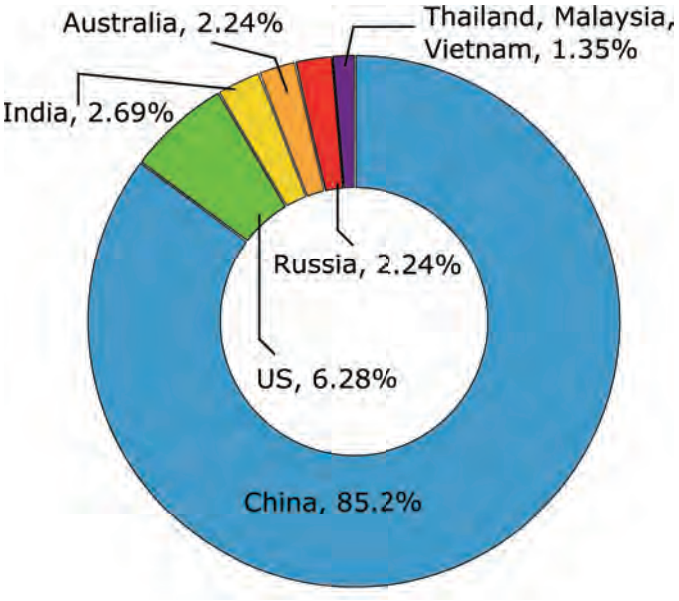

Fig. 1. Proportion of REE, less Y, contributed by producing countries in 2015 (Gambogi, 2015a).

The United States historically dominated production. However, its position declined throughout the late 1990s and 2000s (Xie, 2014; Simandl, 2014). China reached the peak of its dominance in 2007, when it produced just under 97% of the world's REE less Y output (Hedrick, 2008).

2. Many metals, many uses, many deposit types

REE are used in permanent magnets, catalytic converters, polishing powders, fluorescent and arc lighting, lighter flints, lantern mantles, and data storage devices (Royal Society of Chemistry, 2015; Humphries, 2012; Haque et al., 2014) and are well known for their importance in the high-technology industries (Xie et al., 2014). REE have distinct uses and are not easily substituted. The most common REE in the Earth's crust, cerium, is roughly as abundant as copper, at 0.006% by composition, while the equilibrium mass of the least common REE, natural Pm in the Earth crust is equal to 560 g (Belli et al., 2007).

Exploration companies are examining carbonatites, peralkaline igneous rocks, pegmatites, monazite ± apatite veins, ion adsorption clays, placers, and some deep-ocean sediments as potential sources of REE (Kanawaza and Kamitani, 2006; Koschinsky et al., 2010). Currently, most LREE are extracted from carbonatite-related deposits and most HREE are derived from REE-bearing ion adsorption clays (Wall, 2014; Simandl, 2014).

Assuming favourable market conditions in the future, REE could be derived as a by-product of phosphate fertilizer production (Dickson, 2015c), uranium ore (Barkley et al., 1986) and alumina red mud processing (Ochsenkuhn-Petropulu et al., 1996), and exploitation of Olympic Dam subtype iron-oxide copper gold (IOCG) deposits (Simandl, 2014). Recycling is a potential future source of REE (Haque et al., 2014; Torrisi, 2014a).

Ion adsorption clays rich in REE are found in southern China (Kanawaza and Kamitani, 2006; Papangelakis and Moldoveanu, 2014), and in Madagascar (Desharnais et al., 2014). Small quantities of REE are also derived from placer deposits and the Lovozero peralkaline intrusion-related deposit (Simandl, 2014; Wall, 2014).

China accounts for 44% of the world's REE resources (Fig. 2; Gambogi, 2015a). China's dominance of the REE industry

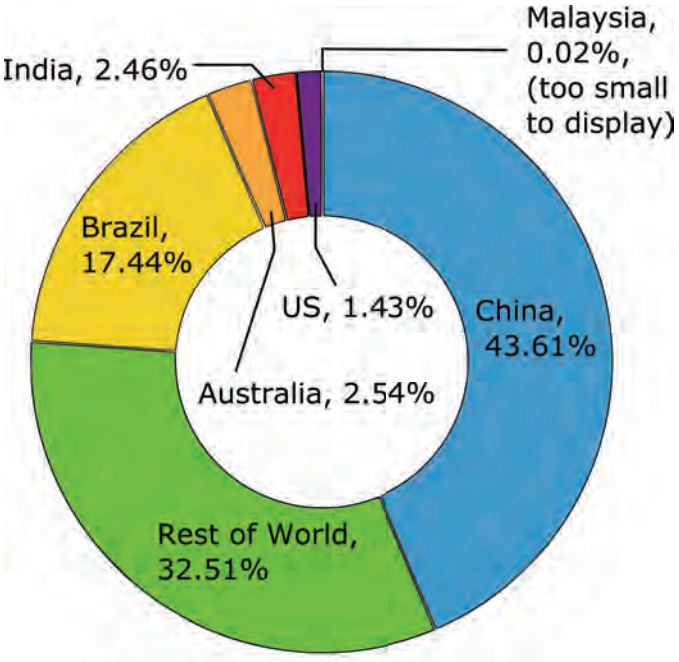

Fig. 2. Global distribution of REE resources in 2014, excluding Y (Gambogi, 2015a).

was initiated by the country's low production and labour costs and lax environmental regulations (Broad, 2010; Folger, 2011).

3. Boom and bust

In 2010, a territorial dispute regarding the Japan-administered, China-claimed Senkaku Islands boiled over after a Chinese trawler collided with a Japanese Coast Guard vessel in Senkaku Island waters. This resulted in China temporarily banning REE exports to Japan (Agence France-Presse, 2010). Between 2006 and 2012, the Chinese government also emplaced stricter export quotas on REE (Morrison and Tang, 2012). These actions precipitated a spike in REE prices, and the shares of associated companies (Dickson and Syrett, 2015). The average price of Ce_2O_3 increased by 2400% (from US$6/kg to US$149.5/kg) from June 2010 to August 2011. The price of Nd_2O_3 increased by 991% (from US$33/kg to US$360/kg) and the price of Dy_2O_3 increased by 700% (from US$300/kg to US$2400/kg) during the same period (Torrisi, 2014a). High prices led to mine openings in the US and Australia by Molycorp Inc. and Lynas Corp.

During this period of high prices, REE users switched to less expensive, more reliably sourced substitutes, and the search for alternative materials accelerated (Elmquist, 2011; Loh et al., 2015; Reddall and Gordon, 2012; Miller and Zheng, 2015). Cerium, in particular, was replaced by other polishing powder materials, or was recycled (Elmquist, 2011; Loh et al., 2015) and REE oversupply ensued. In 2014, the World Trade Organization passed a ruling requiring China to suspend REE quotas, removing another barrier to oversupply (Associated Press, 2015; Haque et al., 2014), contributed to further by illegal mining in the country.

The pricing corrections that followed the spike, as oversupply took hold and demand dissipated, were as severe as the steep increases leading to 2011. In some cases, prices fell back by 98% (Industrial Minerals, 2015). While intermittent rallies have occurred since 2011, the downward trend in pricing has continued into 2015 (Industrial Minerals, 2015). Recent REE oxide prices from the Industrial Minerals Pricing Database may be viewed in Table 1.

4. Investor interest

Investor interest in REE remains substantial after the correction and many projects being planned in 2010 remain active. Over 50 deposits are in advanced stages of development (Technology Metals Research, 2015). Examples of active REE projects include Mountain Pass, Bear Lodge, Bokan Mountain, Round Top, Ngulla, Browns Range, Kvanefjeld and Ashram.

The REE industry remains highly fluid and is prone to disruption by technological advancement, which is less common in more established markets. As a highly complex set of chemical products with distinct uses and markets, project viability assessment is more complex for REE than for many other materials. Some of the parameters critical to understanding economic viability are: proprietary or licensed processing technologies; the relative proportion of each rare earth in a deposit and thus projected rare earth basket prices; overall grade; and mineralogy (Bogner, 2014; Hatch, 2010).

5. Lanthanum and Cerium oversupply

Lanthanum (used in polishing powders and catalysts) and

Table 1. Industrial Minerals Prices Database: Prices for selected REO as of 27 August, 2015. Minimum grade 99%, free on board China, in US$/kg bulk (Industrial Minerals, 2015).

Industrial Minerals REE prices	Low	High
Cerium oxide, min 99%, FOB, China, $/kg, Bulk	2	2.5
Dysprosium oxide, min 99%, FOB, China, $/kg, Bulk	235	250
Europium oxide, min 99%, FOB, China, $/kg, Bulk	200	225
Lanthanum oxide, min 99%, FOB, China, $/kg, Bulk	2.1	2.5
Neodymium oxide, min 99%, FOB, China, $/kg, Bulk	41	46
Praseodymium oxide, min 99%, FOB, China, $/kg, Bulk	57	62
Samarium oxide, min 99%, FOB, China, $/kg, Bulk	2.1	3.1

Ce (used primarily in alloys) are both in oversupply (Kennedy, 2014; Mackowski, 2014). Many junior explorers seek to remove the two elements from the processing chain to minimize processing costs (Dickson, 2015d). They are considering stockpiling the material once in production, in anticipation of improved markets. However, in the medium term Ce and La are likely to remain in oversupply.

6. Processing technologies

Recognizing the technological and financial hurdles represented by on-site processing, junior companies are increasingly looking towards established REE processors and specialist chemical companies for joint venture and offtake opportunities (e.g., Rare Earth Salts, 2014; Tantalus Rare Earths, 2015). A number of innovative processing technologies are promoted by junior research and mining companies (for a review of processing methods, see Verbaan et al., 2015).

7. The case for development

HREE market conditions are more positive than LREE market conditions. Both of the West's new mines, Lynas's Mount Weld in Australia and Molycorp's Mountain Pass in California, are carbonatite-hosted deposits. These deposits have a high proportion of the LREE compared to HREE (Fig. 3), and have supplemented strong supply of LREE from Northern and Western China.

HREE are supplied almost exclusively by southern China and remain in tight supply. Most deposits have a LREE bias and therefore HREE continue to command better prices (Table 1).

Additionally, with venture capital flowing into batteries and high-technology companies, interest in REE permanent magnets

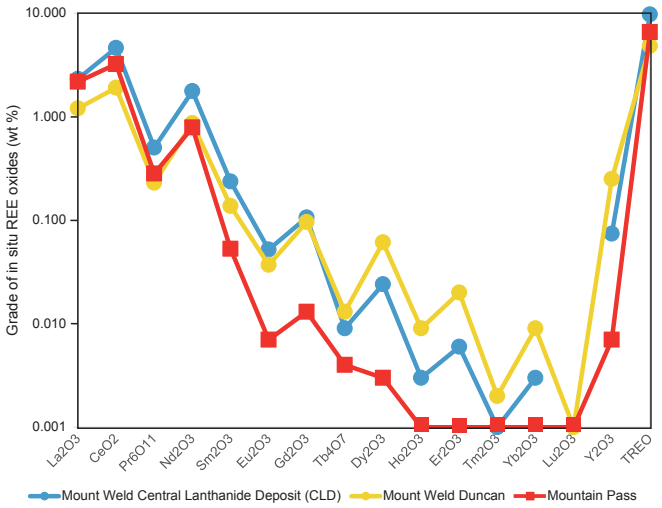

Fig. 3. The grade of in situ REO at Lynas's Mount Weld Duncan and Lanthanide deposits, and Molycorp's Mountain Pass mine, revealing the compositional bias of the two mines towards light REO. From Technology Metals Research (2015). Some REO register only trace concentrations, hence the cluster of data points at the base of the chart. Only Lu at Mountain Pass is below the detection limit.

(mostly Nd-iron-boron (NdFeB) magnets; Fraden, 2010; Torrisi, 2014b) has resulted in the promotion of exploration projects based on Nd and Pr concentrations (Dickson, 2015a). The proportion of REE consumed in the magnet sector is rising, as is the proportion of value derived from Nd and other magnet metals (Fig. 4) Nd demand is also expected to rise (Fig. 5).

The optimism for magnet demand is tempered by reports that, despite expanding magnet industry consumption of REE, including Nd, stockpiled material is difficult to sell (Syrett, 2015). Dysprosium, used in NdFeB magnets to prevent denaturing at high temperatures, could potentially be substituted by lower-priced Ce co-doped with cobalt (Pathak et al., 2015). In percentage terms, the value of Dy consumed is likely to fall against other REE used in magnets (Fig. 6).

Europium, one of the higher-priced REE, also has the potential to recede as alternative products and processes emerge. Previously used in cathode ray tube (CRT) television sets before the appearance of modern plasma and liquid crystal display (LCD) screens, today Eu finds use in fluorescent bulbs and strip-lights to increase the warmth of the light emitted. The emergence of even more energy efficient light emitting diodes (LEDs) could see prices fall in the medium term, although supply tightening may offset this effect (Dickson, 2015e).

8. Recent developments in China

Toward the end of the 2000s, China began to plan and implement a policy of consolidation to dampen the environmentally damaging effects of REE production in China (Folger, 2011), simplify regulation of the sector (Rubenstein, 2015; Sylvester, 2015), and conserve a non-renewable natural resource (Morrison and Tang, 2012). By the end of the consolidation, the only companies permitted to mine REE in China, including via their subsidiaries, will be: China Northern Rare Earth Group High-Tech Co. Ltd. (formerly Baotou Steel Rare Earth Group High-Tech Co. Ltd.); China Minmetals Corp.; Aluminum Corp. of China (Chalco, via its subsidiary China Rare Earth Holdings); Ganzhou Qiandong Rare Earth Group; Guangdong Rising Nonferrous Metals Group Co. Ltd.; and Xiamen Tungsten Co. Ltd. (Torrisi, 2014b). China Northern is by far the largest of the planned groups, accounting for 57% of Chinese production quotas alone (Dickson, 2015b). However, its Baotou, Inner Mongolia production base contains mainly LREE (Sylvester, 2015), minimizing potential returns.

The Chinese government also hopes that consolidation, stronger local government regulations, and the elimination of illegal mining and smuggling will reduce REE oversupply (Jacobsen, 2014).

The shift towards resource taxes, mining quota, and consolidation may help the Chinese government to exert further control over the industry, possibly making it more opaque while changing little (e.g., data may become scarce owing to centralization and professionalization of the industry production quota could become an export quota equivalent Dickson and Syrett, 2015; Wallace, 2015).

The World Trade Organization's October 2014 decision,

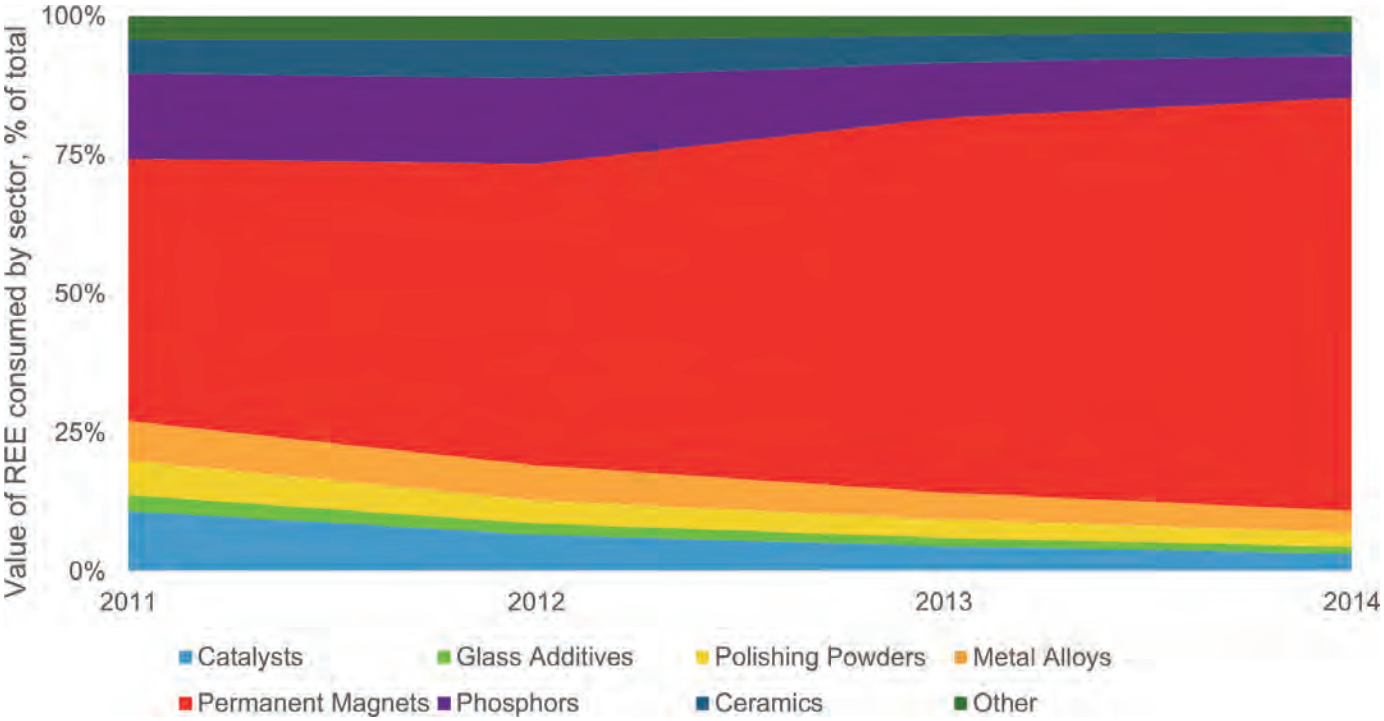

Fig. 4. The proportional value of REO consumed by various industries from 2011-2014 (Industrial Minerals Company of Australia, 2015). The permanent magnet sector is, proportionally, increasing in importance on a total consumption value basis.

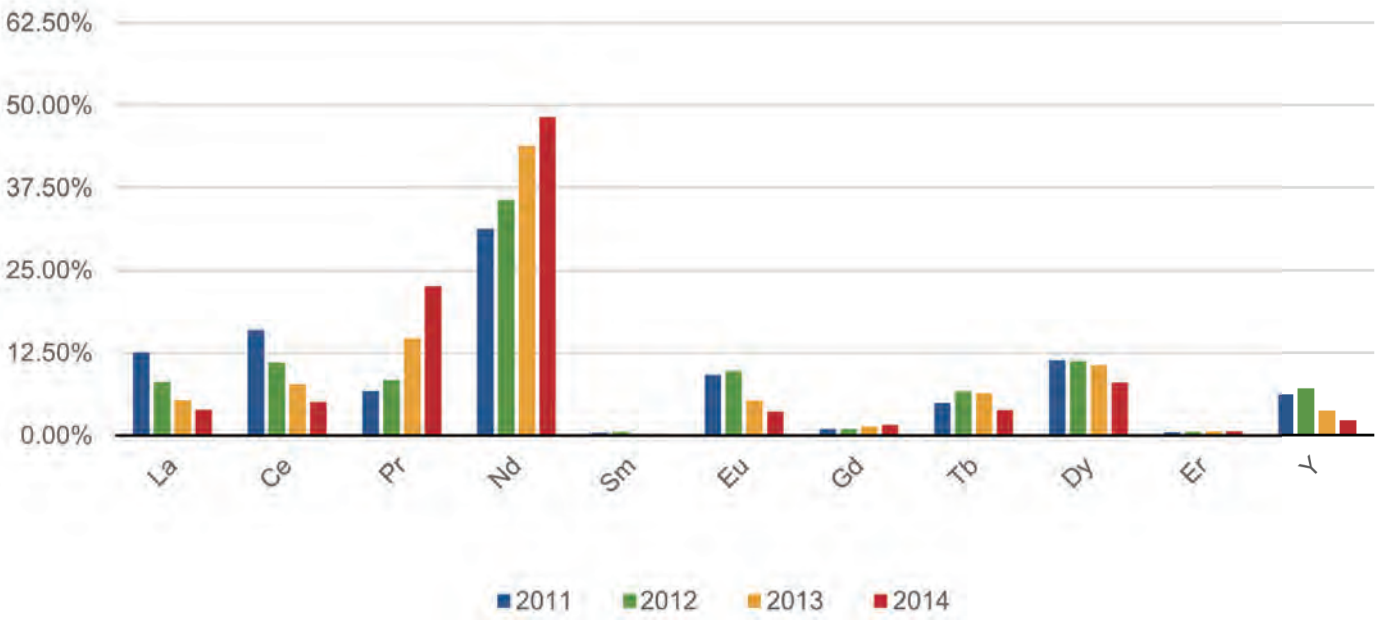

Fig. 5. The relative consumption value of each REO compared to the total industry consumption value from 2011-2014 (Industrial Minerals Company of Australia, 2015). The proportion of value in the Nd and Pr markets is expected to increase, primarily at the expense of La, Ce, and Eu.

which demanded that China remove its export taxes on REE resulted in a policy shift from export quota and taxes to production quota and resource taxes (Li, 2015a). On May 1, 2015, the resource tax rate for LREE was pegged at 11.5% in Inner Mongolia, 9.5% in Sichuan province, and 7.5% in Shandong province. Middle-heavy REE resource taxes were set at 27% (Li, 2015a).

China has started to encourage value addition in its domestic REE industry. This policy resulted in a US$157 million-equivalent grant to the Baotou region's REE industry in the summer of 2015 (Li, 2015b) and a similar subsidy of US$72 million to Ganzhou province shortly afterwards (Dickson

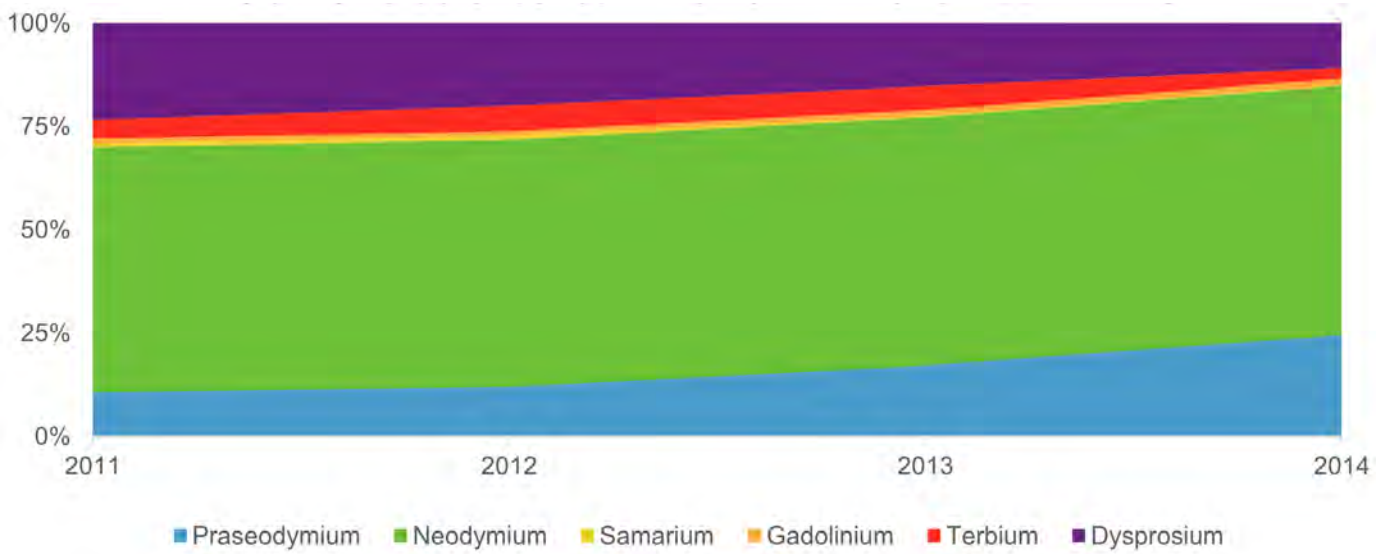

Fig. 6. Relative value of consumption of magnet-utilised REO only from 2011-2014 (Industrial Minerals Company of Australia, 2015). Nd and Pr are set to increase in relative consumption value among all REE used in magnets.

and Li, 2015) to develop high-technology, high-return REE products.

9. Western woes

In the West, the REE industry is equally unstable. Lynas's debts stood at A$650.8m at the end of 2014 (Lynas, 2015), but the business is starting to generate cash flow (Sydney Morning Herald, 2015). In contrast, Molycorp filed for bankruptcy protection in late June 2015 (Dickson, 2015f) after voluntarily deferring a number of interest payments on its loans (Lazenby, 2015). It has declared total liabilities of US$1.7bn (Miller and Zheng, 2015).

Acknowledgments

Suggestions and edits by Carlee Akam (British Columbia Geological Survey) greatly improved the content and clarity of this document.

References cited

Agence France-Presse, 2010. China blocked exports of rare earth metals to Japan, traders claim. The Daily Telegraph. <http://www.telegraph.co.uk/finance/china-business/8022484/China-blocked-exports-of-rare-earth-metals-to-Japan-traders-claim.html> Accessed August 18, 2015.

Associated Press, 2015. China scraps quotas on rare earths after WTO complaint. The Guardian. < http://www.theguardian.com/world/2015/jan/05/china-scraps-quotas-rare-earth-wto-complaint> Accessed September 3, 2015.

Barkley, D. J., Blanchette, M., Cassidy, R. M., and Elchuk, S., 1986. Dynamic chromatographic systems for the determination of rare earths and thorium in samples from uranium ore refining processes. Analytical chemistry, 58, 2222-2226.

Belli, P., Bernabei, R., Cappella, F., et al., 2007. Search for α decay of natural Europium. Nuclear Physics A, 789, 15–29.

Bogner, S., 2014. The Knock-Out Criteria for Rare Earth Element Deposits: Cutting the Wheat from the Chaff. Rockstone Research Ltd. <www.rockstone-research.com/images/PDF/Commerce1en.pdf> Accessed September 3, 2015.

Broad, W.J., 2010. Mining the Seafloor for Rare Earth Minerals. The New York Times. <www.nytimes.com/2010/11/09/science/09seafloor.html> Accessed September 3, 2015.

Connelly, N.G., Damhus, T., Hartshorn, R.M., and Hutton, A.T., 2005. Nomenclature of Inorganic Chemistry UPAC Recommendations 2005. The Royal Society of Chemistry, Cambridge. <http://web.archive.org/web/20080527204340/http:/www.iupac.org/publications/books/rbook/Red_Book_2005.pdf> Accessed August 12, 2015.

Desharnais, G., Camus, Y., Bisaillon, C., 2014. NI 43-101 Technical Report: Resources for the Tantalus Rare Earth Ionic Clay Project, Northern Madagascar. SGS Canada Inc. < http://www.tre-ag.com/~/media/Files/T/Tantalus-Rare-Earths/Attachments/pdf/SGS-Competent-Persons-Report-December-2014.pdf> Accessed September 3, 2015.

Dickson, J.S., 2015a. Tanatalus CEO: rare earths projects should be assessed by magnet potential. Industrial Minerals. <www.indmin.com/Article/3427048/Tantalus-CEO-rare-earths-projects-should-be-assessed-by-magnet-potential.html> Accessed September 5, 2015.

Dickson, J.S., 2015b. Industrial Minerals. China to produce 105,000 tonnes rare earths in 2015. <http://www.indmin.com/Article/3454088/China-to-produce-105000-tonnes-rare-earths-in-2015.html> Accessed August 18, 2015.

Dickson, J.S., 2015c. EuroChem reveals phosphate expansion plans at Kovdor and beyond. Industrial Minerals. <http://www.indmin.com/Article/3455925/EuroChem-reveals-phosphate-expansion-plans-at-Kovdor-and-beyond.html> Accessed August 13, 2015.

Dickson, J.S., 2015d. IM Rare Earths News in Brief 18 – 25 May. Industrial Minerals. <http://www.indmin.com/Article/3456752/IM-Rare-Earths-News-in-Brief-1825-May.html> Accessed August 13, 2015.

Dickson, J.S., 2015e. Greenland Minerals and Energy aims to rival rare earths suppliers to Europe by 2019. Industrial Minerals. <http://www.indmin.com/Article/3457662/Greenland-Minerals-and-Energy-aims-to-rival-rare-earths-suppliers-to-Europe-by-2019.html> Accessed August 14, 2015.

Dickson, J.S., 2015f. Molycorp files voluntarily for Chapter 11 bankruptcy protection, delisting to follow. Industrial Minerals. <http://www.indmin.com/Article/3465583/Molycorp-files-

voluntarily-for-Chapter-11-bankruptcy-protection-delisting-to-follow.html> Accessed September 5, 2015.

Dickson, J.S., and Li, A., 2015. IM Rare Earths News in Brief 4 – 10 August. Industrial Minerals. <http://www.indmin.com/Article/3478631/IM-Rare-Earths-News-in-Brief-410-August.html> Accessed August 18, 2015.

Dickson, J.S., and Syrett, L., 2015. PDAC 2015: Rare earths forgotten in a lithium and graphite focused EV and high-tech world. Industrial Minerals. < http://www.indmin.com/Article/3432631/PDAC-2015-Rare-earths-forgotten-in-a-lithium-and-graphite-focused-EV-and-high-tech-world.html> Accessed August 13, 2015.

Elmquist, S., 2011. Rare Earths Fall as Toyota Develops Alternatives. Bloomberg. <http://www.bloomberg.com/news/articles/2011-09-28/rare-earths-fall-as-toyota-develops-alternatives-commodities> Accessed August 15, 2015.

Folger, T., 2011. Rare Earth Elements: The Secret Ingredients of Everything. National Geographic. <www.ngm.nationalgeographic.com/2011/06/rare-earth-elements/folger-text> Accessed September 4, 2015.

Fraden, J., 2010. Handbook of modern sensors: physics, designs, and applications. Springer Science & Business Media, Berlin. pp. 72-73. <http://folk.ntnu.no/andberge/Sensors.pdf> Accessed September 5, 2015.

Gambogi, J., 2015a. Rare Earths. U.S. Geological Survey, Mineral Commodity Summaries, pp. 128-129. <http://minerals.usgs.gov/minerals/pubs/commodity/rare_earths/mcs-2015-raree.pdf> Accessed August 12, 2015.

Gambogi, J., 2015b, Yttrium. U.S. Geological Survey, Mineral Commodity Summaries, pp. 182-183. <http://minerals.usgs.gov/minerals/pubs/commodity/rare_earths/mcs-2015-yttri.pdf> Accessed August 12, 2015.

Haque, N., Hughes, A., Lim, S., and Vernon, C., 2014. Rare earth elements: Overview of mining, mineralogy, uses, sustainability and environmental impact. Resources, 3, 614-635.

Hatch, G., 2010. Comparative Value Metrics For 13 Advanced Rare Earth Projects. Technology Metals Research LLC. <www.techmetalsresearch.com/2010/11/comparative-value-metrics-for-13-advanced-rare-earth-projects> Accessed September 4, 2015.

Hedrick, J. B., 2008. Rare Earths. U.S. Geological Survey, Mineral Commodity Summaries. pp. 134-135. < http://minerals.usgs.gov/minerals/pubs/commodity/rare_earths/mcs-2008-raree.pdf> Accessed September 2, 2015.

Humphries, M., 2012. Rare earth elements: the global supply chain. Congressional Research Service, 7-5700. < https://fas.org/sgp/crs/natsec/R41347.pdf> Accessed September 5, 2015.

Industrial Minerals, 2015. Industrial Minerals Pricing Database. <http://www.indmin.com/PricingDatabase.html> Accessed September 2, 2015.

Industrial Minerals Company of Australia Pty Ltd. (IMCOA), 2015. March 2015 Quarterly company report. Provided by Peak Resources Ltd. and Bell Pottinger Ltd.

Jacobsen, J., 2014. Analysts: Chinese consolidation of rare earths sector to have limited impact on global market. North Square Blue Oak Ltd. <www.nsbo.com/news/Chinese%20consolidation%20of%20rare%20earths%20sector%20to%20have%20limited%20impact%20on%20global%20market.pdf> Accessed September 4, 2015.

Kanazawa, Y., and Kamitani, M., 2006. Rare earth minerals and resources in the world. Journal of Alloys and Compounds, 408, 1339-1343.

Kennedy, J., 2014. Molycorp and the Pandora Production Principle. Seeking Alpha. <www.seekingalpha.com/article/1988221-molycorp-and-the-pandora-production-principle> Accessed September 3, 2015.

Koschinsky, A., Hein, J., Schmidt, K., Alexander, B., and Bau, M., 2010. Rare and valuable metals for high-tech applications found in marine ferromanganese nodules and crusts: relationships to genetic endmembers. Toward the Sustainable Development of Marine Minerals: Geological, Technological, and Economic Aspects. Proceedings of the 39th Underwater Mining Institute Conference. <http://137.227.239.65/reports/reprints/Koschinsky_UMI2010.pdf> Accessed September 5, 2015.

Lazenby, H., 2015. Molycorp defers second interest payment in 2 weeks. Creamer Media's Mining Weekly. <www.miningweekly.com/article/molycorp-defers-second-interest-payment-in-2-weeks-2015-06-15> Accessed September 5, 2015.

Li, A., 2015a. China confirms rare earth resource tax rates. Industrial Minerals <http://www.indmin.com/Article/3450559/China-confirms-rare-earth-resource-tax-rates.html> Accessed September 5, 2015.

Li, A., 2015b. Chinese government gives Baotou Rmb 1bn to upgrade rare earths industry. Industrial Minerals. <http://www.indmin.com/Article/3462035/RareEarths-LatestNews/Chinese-government-gives-Baotou-Rmb-1bn-to-upgrade-rare-earths-industry.html> Accessed August 14, 2015.

Loh, T., Darie, T., and Casey, S., 2015. How a Bet on Rare Earths Flopped as Scarcity Was a Mirage. Bloomberg. < http://www.bloomberg.com/news/articles/2015-06-28/how-a-bet-on-rare-earths-flopped-as-scarcity-was-a-mirage> Accessed September 3, 2015.

Lynas, 2015. Lynas half year results and finaning agreement. Lynas Corp. <https://www.lynascorp.com/Announcements/2015/Lynas%20Half%20Year%20Results%20And%20Financing%20Agreement%20-%2013%20March%202015.pdf>.

Mackowski, S., 2014. The future of the non-Chinese rare earth market. InvestorIntel. <www.investorintel.com/technology-metals-intel/mackowski-future-non-chinese-rare-earth-market> Accessed September 3, 2015.

Miller, J., and Zheng A., 2015. Molycorp Files for Bankruptcy Protection. The Wall Street Journal. <http://www.wsj.com/articles/SB10907564710791284872504581069270334872848> Accessed August 18, 2015.

Morrison, W.M., Tang, R., 2012. China's Rare Earth Industry and Export Regime. Economic and Trade Implications for the United States. Congressional Research Service. <https://www.fas.org/sgp/crs/row/R42510.pdf> Accessed September 4, 2015.

Ochsenkuhn-Petropulu, M., Lyberopulu, T., Ochsenkuhn, K. M., and Parissakis, G., 1996. Recovery of lanthanides and yttrium from red mud by selective leaching. Analytica Chimica Acta, 319(1), 249-254.

Papangelakis, V.G., and Moldoveanu, G., 2014. Recovery of Rare Earth Elements From Clay Minerals. Proceedings of ERES2014: 1st European Rare Earth Resources Conference. <http://www.eurare.eu/docs/eres2014/fifthSession/VladimirosPapangelakis.pdf> Accessed September 4, 2015.

Pathak, A.K., Khan, M., Gschneidner, K.A., McCallum, R.W., Zhou, L., Sun, K., Dennis, K.W., Zhou, C., Pinkerton, F.E., Kramer, M.J., Pecharsky, V.K., 2015. Cerium: An Unlikely Replacement of Dysprosium in High Performance Nd–Fe–B Permanent Magnets. Advanced Materials 27(16), 2663-2667.

Reddall, B. and Gordon, J., 2012. Analysis: Search for rare earth substitutes gathers pace. Reuters. <www.reuters.com/article/2012/06/22/us-rareearths-alternatives-idUSBRE85L0YB20120622> Accessed September 3, 2015.

Royal Society of Chemistry, 2015. Periodic Table. Royal Society of Chemistry. <http://www.rsc.org/periodic-table> Accessed August 13, 2015.

Rubenstein, A., 2015. China To Consolidate Rare Earth Industry Through Mergers. Law 360. <www.law360.com/articles/656429/china-to-consolidate-rare-earth-industry-through-mergers> Accessed September 4, 2015.

Simandl, G.J., 2014. Geology and market-dependent significance of rare earth element resources. Mineralium Deposita, 49, 889-904.

Sydney Morning Herald, 2015. Rare earths miner Lynas Corp achieves positive cash flow in March, shares up. Sydney Morning Herald. <www.smh.com.au/business/mining-and-resources/rare-earths-miner-lynas-corp-achieves-positive-cash-flow-in-march-shares-up-20150424-1mscis.html> Accessed September 5, 2015.

Sylvester, B., 2015. Gareth Hatch: New REE Export Rules Inside China Level the International Playing Field. The Au Report. <http://www.theaureport.com/pub/na/gareth-hatch-new-ree-export-rules-inside-china-level-the-international-playing-field> Accessed August 18, 2015.

Syrett, L., 2015. Summer torpor hits industrial minerals early. Industrial Minerals. < http://www.indmin.com/Article/3472939/Summer-torpor-hits-industrial-minerals-early.html> Accessed August 13, 2015.

Tantalus Rare Earths, 2015. Tantalus Signs Supply Contract with ThyssenKrupp. Tantalus Rare Earths AG. < http://irpages2.equitystory.com/cgi-bin/show.ssp?companyName=meldeverlinkung&language=English&id=999&newsID=1479349&companyDirectoryName=tantalusrareearths> Accessed September 4, 2015.

Technology Metals Research, 2015. TMR Advanced Rare-Earth Projects Index. Technology Metals Research LLC. <http://www.techmetalsresearch.com/metrics-indices/tmr-advanced-rare-earth-projects-index> Accessed August 15, 2015.

Torrisi, A., 2014a. Rare earths recycling and recovery: the two sides of the industry. Industrial Minerals, no. 566, 39-43.

Torrisi, A., 2014b. China to raise rare earths tax and complete industry consolidation. Industrial Minerals<http://www.indmin.com/Article/3413742/China-to-raise-rare-earths-tax-and-complete-industry-consolidation.html> Accessed August 18, 2015.

Verbaan, N., Bradley, K., Brown, J., and Mackie, S., 2015. A review of hydrometallurgical flowsheets considered in current REE projects. In: Simandl, G.J. and Neetz, M., (Eds.), Symposium on Strategic and Critical Materials Proceedings, November 13-14, 2015, Victoria, British Columbia. British Columbia Ministry of Energy and Mines, British Columbia Geological Survey Paper 2015-3, pp. 147-162.

Wall, F., 2014. Rare earth elements. In: Gunn, G. (ed.), Critical Metals Handbook, John Wiley and Sons Ltd., Hoboken, pp. 312-339.

Wallace, R., 2015. Lynas survival a 50-50 proposition, says rare earths expert. The Australian. <www.theaustralian.com.au/business/mining-energy/lynas-survival-a-50-50-proposition-says-rare-earths-expert/story-e6frg9df-1227177694904> Accessed September 5, 2015.

Xie, F., Zhang, T. A., Dreisinger, D., and Doyle, F. 2014. A critical review on solvent extraction of rare earths from aqueous solutions. Minerals Engineering, 56, 10-28.

Niobium and tantalum: Geology, markets, and supply chains

D.A.R. Mackay[1, 2, a] and G.J. Simandl [2, 3]

[1] De Beers Group of Companies, Yellowknife, NT, X1A 1P8
[2] School of Earth and Ocean Sciences, University of Victoria, Victoria, BC, V8P 5C2
[3] British Columbia Geological Survey, Ministry of Energy and Mines, Victoria, BC, V8W 9N3
[a] corresponding author: duncan.mackay87@gmail.com

Recommended citation: Mackay, D.A.R. and Simandl, G.J., 2015. Niobium and tantalum: Geology, markets, and supply chains. In: Simandl, G.J. and Neetz, M., (Eds.), Symposium on Strategic and Critical Materials Proceedings, November 13-14, 2015, Victoria, British Columbia. British Columbia Ministry of Energy and Mines, British Columbia Geological Survey Paper 2015-3, pp. 13-22.

1. Introduction

Until 2014, niobium (Nb) and tantalum (Ta) were on the critical metals list of the European Union (European Commission, 2011; 2014). Both Ta and Nb have high levels of supply chain risk and even temporary disruptions in supply could be difficult to cope with. The Ta market is subject to influx of 'conflict' columbite-tantalite concentrate, or 'Coltan,' into the supply chain, displacing production in Australia and Canada. The growing consumer appetite for goods made of ethically sourced or 'conflict-free' minerals and metals has put pressure on manufacturers of components for consumer electronics, such as smart phones, laptop computers, computer hard drives, digital cameras, GPS navigation systems, and airbag triggers to stop using Ta from 'conflict' areas. Other uses of Ta include medical implants, super alloys used in jet turbine and rocket nozzle production, corrosion prevention in chemical and nuclear plants, as a sputtering target, and in optical lenses (Tantalum-Niobium International Study Center, 2015a, b). These applications make Ta economically and strategically important to industrialised countries (European Commission, 2011, 2014; Brown et al., 2012; Papp, 2012).

Niobium (Nb) is primarily used in high-strength low-alloy (HSLA) steel used extensively in the oil and gas and automotive industries. Niobium is also a major component in vacuum-grade alloys used in rocket components and other aeronautic applications (Tantalum-Niobium International Study Center, 2015a, c). Demand for Nb is increasing due to greater use of Nb in steel making in China, India, and Russia (Roskill, 2013b; Mackay and Simandl, 2014). Because most primary Nb production is restricted to a single country (Brazil), security of supply is considered at risk (European Commission, 2014). New sources of supply may be developed to diversify geographic location of supply for strategic reasons (Mackay and Simandl, 2014). Herein we summarize the geology, market, and supply chains of Niobium and Tantalum metals.

2. Geology of tantalum- and niobium-bearing deposits

This section considers the geology of pegmatite-related Ta deposits, peraluminous granite-related Ta ±Nb deposits, carbonatite-related Nb deposits, and peralkaline complex-hosted Nb-Ta-REE deposits. In near-surface environments, these primary deposits are commonly enriched by weathering and are also a source of placer deposits.

2.1. Pegmatite-related Ta deposits

Pegmatites are coarse-grained (most crystals >1 cm) igneous intrusive rocks found in a variety of tectonic and metamorphic settings. They form small (usually less than a metre thick and tens to hundreds of metres long) sills, dikes, and irregular pods and lenses (Jahns, 1955; Varlamoff, 1972; Černý, 1975, 1982). Exceptionally large pegmatite bodies (e.g. Greenbushes, Wodgina, and Tanco) can be tens of metres in thickness and extend along strike for kilometres. The main rock forming minerals in pegmatites are potassium feldspar, albite, and quartz ±muscovite and/or biotite (Černý, 1991a). Accessory mineralogy is occurrence specific with hundreds of exotic minerals in highly fractionated pegmatites (Černý, 1991a). Complete reviews of pegmatite mineralogy are provided by Černý and Ercit (1985), Černý (1991a), and Černý and Ercit (2005).

Pegmatites have been the subject of numerous detailed studies and genetic reviews (Ginsberg, 1984; Černý, 1982, 1991a, b; Černý and Ercit, 2005; and references therein). Of the five pegmatite classes based on geological environment and geochemistry (abyssal, muscovite, muscovite-rare-element, rare-element, and miarolitic; Černý and Ercit, 2005), the rare-element class is the most important for Ta exploration.

Pegmatites can also be classified into three petrogenetic families (Černý, 1991a; Černý and Ercit, 2005): 1) the LCT family (enriched in Li, Cs, and Ta); 2) the NYF family (enriched in Nb, Y, and F); and 3) the relatively rare mixed NYF+LCT family with overlapping mineralogical or chemical characteristics of the two previously mentioned families (Černý, 1991a; Černý and Ercit, 2005).

The LCT family shows petrogenetic affinity to peraluminous and metaluminous S-type rare-element enriched granites (Černý, 1991a, b; Černý and Ercit, 2005; Martin, 2007). These pegmatites mainly occur in orogenic settings and are associated

with crustal shortening (Moloshag, 1974; Anhaeusser, 1976; Černý, 1982; Trueman and Černý, 1982; Möller and Morteani, 1983). Rare-element content (specifically Li, Cs, Be, Ta, and Nb), Ta:Nb ratio, and degree of albitization increase with distance from the source intrusion (Trueman and Černý, 1982; Černý, 1991b). LCT pegmatites are characterised by the presence of muscovite, garnet, tourmaline, and aluminosilicates (Černý and Ercit, 2005). Common Ta-bearing minerals are columbite-tantalite, microlite, wodginite, and euxenite (Hatcher and Bolitho, 1982; Trueman and Černý, 1982; Černý, 1991a; Hatcher and Clynick, 1990). Pegmatites hosting Ta deposits that have been exploited in the past (e.g. Wodgina and Greenbushes, Australia; Tanco, Canada; and Kenticha, Ethiopia) typically belong to the LCT family.

Pegmatites belonging to the NYF family are found mainly in continental anorogenic settings and show affinity to the fractionated portions of metaluminous A- and I-type granites (Černý, 1991a; Černý and Ercit, 2005). Pegmatitic phases of peralkaline and carbonatite complexes share many characteristics with NYF pegmatites (Martin and De Vito, 2005; Martin, 2007), and have the potential to be mineralized in Nb, REE, and other rare-elements (e.g. Strange Lake, Canada).

2.2. Peraluminous granite-related Ta ±Nb deposits

Rare-element-enriched peraluminous granites (Al_2O_3/($CaO+Na_2O+K_2O$)>1; Shand, 1927; Clarke, 1981) can be enriched in Ta and Nb and are found in post-orogenic and orogenic tectonic settings (Pitcher, 1983, 1993; Barbarin, 1990; Lin et al., 1995; Linnen and Cuney, 2005). These granites are small vertically zones intrusions covering surface areas from 0.25 km^2 (Beauvoir granite; Raimbault et al., 1995) to about 2 km^2 (Orlovka; Reyf et al., 2000). Like pegmatites, mineralization is associated with increasing degree of fractionation (Černý and Meintzer, 1985; Breaks et al., 2003). Some occurrences have stockscheider and/or greisenized cupola containing quartz, muscovite, lepidolite, topaz, and commonly tourmaline, fluorite, wolframite, and cassiterite with accessory beryl or Ta- and Nb-bearing minerals (Černý and Meintzer, 1988; Johan and Johan, 1994; Lin et al., 1995; Linnen and Cuney, 2005). Characteristic rock forming minerals in rare-element-enriched granites include quartz, plagioclase, alkali feldspar, and accessory minerals such as biotite, muscovite, garnet, cordierite, staurolite, aluminosilicates, mullite, topaz, tourmaline, spinel, and corundum (Clarke, 1981). The Yichun granite in China (Lin et al., 1995; Papp, 2012), the Beauvoir granite in France (Raimbault et al., 1995), and the Orlovka granite in Russia (Seltmann et al., 2010) are examples of current or former Ta producers.

2.3. Carbonatite-related Nb deposits

Carbonatites are defined as igneous rocks containing more than 50% modal carbonate minerals and no more than 20 wt.% SiO_2 and are commonly subdivided by proportion of CaO, MgO, and $FeO+Fe_2O_3+MnO$ (Le Maitre, 2002). More elaborate classifications involving mineralogical and genetic concepts were developed by Woolley (2003), Mitchell (2005), and Woolley and Kjarsgaard (2008); these are not typically used by the exploration industry. Most carbonatites are found in extensional intracratonic tectonic settings and less commonly at cratonic margins (Woolley and Kjarsgaard, 2008). A few rare occurrences are found in oceanic settings. They form sills, dikes, plugs, or zoned complexes such as at St. Honoré (Thivierge et al., 1983; Lafleur and Ayad, 2012). Some carbonatites (specifically those found on cratonic margins) are complexly deformed (e.g. Upper Fir; Chong et al., 2012). Rarely, they form extrusive and pyroclastic aprons.

The composition of carbonate minerals in carbonatite complexes can range from calcite through dolomite to magnesite, siderite, and ankerite (Woolley, 2003; Mitchell, 2005; Woolley and Kjarsgaard, 2008). Carbonatites are commonly enriched in incompatible elements (Sr, Ba, Nb, REEs, and especially LREE) and are the main sources and exploration targets for Nb and LREEs (Mariano, 1989a, b; Richardson and Birkett, 1995; Birkett and Simandl, 1999). They may also host economic concentrations of U, Th, Ba, P, Zr, F, V, Fe, and possibly Ta. Many carbonatite complexes, such as St. Honoré, Canada, and Araxá, Brazil, are spatially associated with nepheline syenites or other alkaline silicate igneous rocks (Thivierge et al., 1983; Woolley, 2003; Mitchell, 2005; Woolley and Kjarsgaard, 2008; Lafleur and Ayad, 2012). Lunate, semi-circular, or concentric rock units are formed by successive phases of igneous intrusion, and common in carbonatite (Mitchell, 2005; Woolley and Kjarsgaard, 2008). Late stage carbothermal fluids may form a central brecciated REE-, Sr- and Ba-rich plug (Mitchell, 2005; Woolley and Kjarsgaard, 2008).

Alkali-rich hydrothermal fluids from carbonatite intrusions commonly produce envelopes of sodic or potassic alteration, or fenitization (Heinrich, 1985; Le Bas, 2008). The degree of fenitization decreases with distance from the carbonatite. Fenites can be macroscopically indistinguishable from alkaline igneous silicate rocks, intensely altered host rocks, and mildly brecciated or fractured rocks with veinlets of K, Na, and/or Fe minerals. Recognition of the fenitization zones increases the size of the carbonatite exploration target (Mackay and Simandl, 2014).

2.4. Peralkaline complex-hosted Nb-Ta-REE deposits

Peralkaline igneous rocks have an alumina saturation index (K_2O+Na_2O)/Al_2O_3>1 (Shand, 1927) and are commonly found in extensional anorogenic continental tectonic settings (Pitcher, 1983, 1993; Barbarin, 1990). All peralkaline intrusions are enriched in high field strength elements (HFSE), especially agpaitic intrusions with complex Zr–Ti–REE silicates such as eudialyte, mosandrite, and rinkite (Gerasimovskii, 1956; Sørensen, 1960, 1968). They are also characterized by sodic phases such as aegirine, reibeckite, arfvedsonite, and albite. Agpaitic intrusions can be broadly subdivided into two categories: 1) layered intrusions, which display rhythmic or microrhythmic layering (e.g., Nechalacho, Canada; Lovozero, Russia; and Ilímaussaq, Greenland); 2) intrusions characterized

by HFSE enrichment in pegmatitic/stockscheider related cupola(s) or nearby NYF affinity pegmatite/aplite dikes (e.g. Strange Lake, Canada; Miller, 1986; Richardson and Birkett, 1995; Salvi and Williams-Jones, 1990; Martin, 2007; Sheard et al., 2012). Detailed description of these different styles of intrusion are beyond the scope of this paper (see detailed examples in Mackay and Simandl, 2014 and references therein).

2.5. Tantalum and niobium ore minerals

The most common Nb and Ta ore minerals are pyrochlore supergroup minerals, columbite-tantalite series minerals, struvereite, loparite, and euxenite. Mineral chemistry for the columbite-tantalite series (the main ore minerals for Ta) can be plotted on a Mn/(Mn+Fe) and Ta/(Ta+Nb) quadrilaterals (Fig. 1). Columbite from carbonatites have specific chemistry; they are Nb-rich, with Mn/(Mn+Fe) ≤0.25 and Ta/(Ta+Nb) ≤0.20 (Fig. 1; Mackay and Simandl, 2015). Columbite from peralkaline complexes plot along the $FeNb_2O_6$–$MnNb_2O_6$ join of the quadrilateral with Mn/(Mn+Fe) ≤0.65 and Ta/(Ta+Nb) ≤0.15. Columbite-tantalite series minerals from LCT pegmatites and peraluminous granites are not well constrained and slightly overlap with columbite-(Fe) from carbonatites. Minerals from carbonatites, peralkaline complexes, peraluminous granites, and LCT pegmatites display a slight compositional overlap.

Pyrochlore supergroup minerals from carbonatites occupy the pyrochlore field and extend slightly into the betafite and microlite fields (>35% Nb, <65% Ti, and <45% Ta) when plotted on a Nb-Ti-Ta ternary discrimination diagram (Fig. 2; Mackay and Simandl, 2015). A narrow zone parallel to the Nb-Ti join (>40% Nb, <60% Ti, and <10% Ta) defines the mineral chemistry of pyrochlore from peralkaline complexes. Pyrochlore supergroup minerals from LCT pegmatites occupy the microlite field (<90% Nb, ≤40% Ti, and >15% Ta). Pyrochlore from peraluminous granites display microlite chemistry following the Nb-Ta join, extending slightly into the pyrochlore field (<65% Nb, <10% Ti, and >35% Ta). Figures 1 and 2 illustrate how pyrochlore supergroup and tantalite-columbite series concentrates produced from carbonatites and peralkaline complexes have low Ta content relative to concentrates produced from LCT pegmatites and peraluminous granite. These figures, in conjunction with the current Ta and Nb concentrate pricing practices (see below), indicate that carbonatites and peralkaline complexes are unlikely to become sources of Ta in the foreseeable future.

3. Grade and tonnage of Ta and Nb deposits

The tonnage and grade of Ta and Nb deposits varies significantly (Fig. 3). The level of confidence for resource and reserve estimates from many deposits in South America and Africa is less than for well-defined deposits in North America and Australia. Information from many deposits in China and Russia are lacking and these deposits are not included in Figure 3.

Overall, the highest Ta_2O_5 grades (Fig. 3a) correspond to LCT pegmatites (e.g., Tanco; Wodgina; and Morrua), substantially higher (e.g., Tanco 0.2160% Ta_2O_5) than rare element-enriched peraluminous granites (e.g., Orlovka, 0.0147% Ta_2O_5; Beauvoir, 0.0120% Ta_2O_5) or carbonatite-hosted deposits (e.g., Upper Fir, 0.0191% Ta_2O_5). All the deposits, including pegmatites, can be further enriched by weathering (e.g., Greenbushes or Volta Grande). These high-grade deposits generally have relatively low tonnage compared to peralkaline deposits. Peralkaline complexes have the largest resource in terms of total tonnage (e.g. Ghurayyah, and the Aires prospect, Motzfeldt). These peralkaline complexes are in early to moderate stages of exploration; none produce Ta. The highest Nb_2O_5 grades and tonnages (Fig. 3b) correspond to weathering-enriched carbonatite complexes (e.g. Araxá, Catalão I and II, and Seis Lagos) followed by hard rock carbonatite-related deposits (e.g., Aley and St. Honoré). Peralkaline-related deposits also represent significant tonnage and Nb_2O_5 content (e.g., Lovozero and Nechalacho).

4. Markets and sources

4.1. Tantalum market

Since 1999, a substantial portion (~22%) of the Ta supply chain includes concentrate sourced in politically unstable regions of West Africa (Papp, 2015a). Central and East Africa accounts for ~64% of Ta production. Introduction of coltan and inexpensive artisanally mined concentrates have undercut prices and resulted in several major past producers (e.g., Wodgina, Australia) being placed on care and maintenance (Tantalum-Niobium International Study Center, 2015a). Production is currently suspended at the Kenticha mine (Ethiopia) during renovations and expansions (Tantalum Niobium International Study Center, 2015a; Elenilto Mining, 2015; Papp, 2015a).

Capacitor-grade powders accounted for 25% of Ta shipments to worldwide processors during 2009-2013, down from 40% during 2001-2008 (Tantalum-Niobium International Study Center, 2015a). In 2013, Ta-chemicals accounted for 15% of Ta production, 2% in Ta-carbide, 11% in Ta-ingot, 22% in mill products, and 21% in metallurgical powders and scrap.

Waste and scrap recycling accounted for 48% of United States Ta imports in 2014, while primary production accounted for the remaining 52% (Papp, 2015a). Up to 79% of primary Ta production is from mining, with 21% from Sn slags (Tantalum-Niobium International Study Center, 2015a). Historically, Sn slags have accounted for up to 40% of global Ta production (Schwartz et al., 1995). Cassiterite placer deposits in Thailand and Malaysia were mined for their Sn content while Ta_2O_5 derived from columbite-tantalite and Ta-Nb rutile (strüverite) was also recovered from these deposits (Hassan, 1994; Schwartz et al., 1995).

World production of Ta from mining (excluding production from Ta contained in Sn slags) for 2014 was roughly 1157 tonnes of metal content (Fig. 4; Papp, 2015a). World Ta production began to increasing in 1999. During the 1990s and early 2000s, the price of Ta_2O_5 concentrate was relatively stable, under US$100/kg. By the year 2000, an increase in demand and perceived shortfall and instability in supply caused spot prices

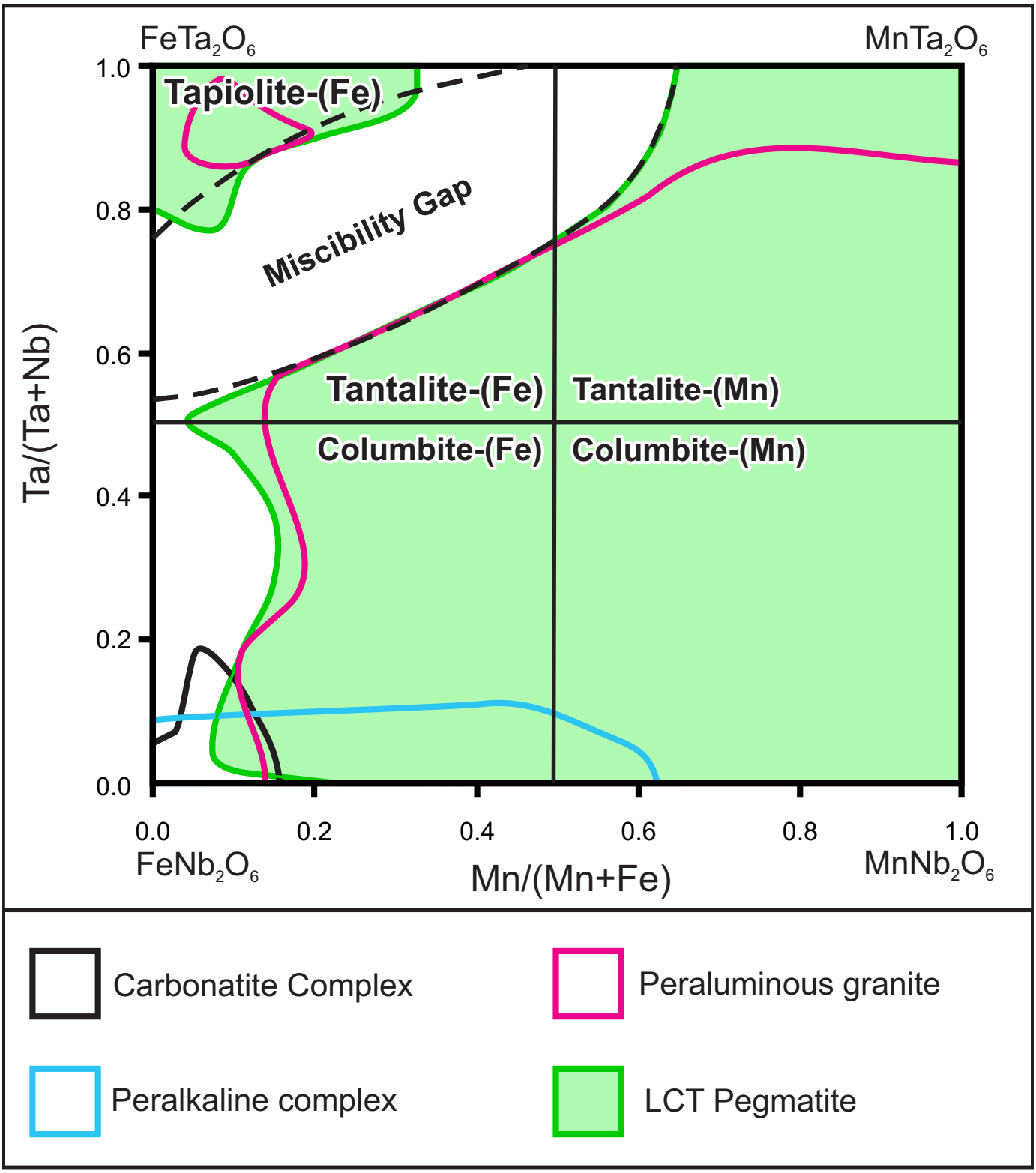

Fig. 1. Composition of columbite-tantalite series minerals in carbonatites, peralkaline complexes, LCT pegmatites, and peraluminous granites. Modified from Mackay and Simandl (2015). Classification according to Černý and Ercit (1985, 1989).

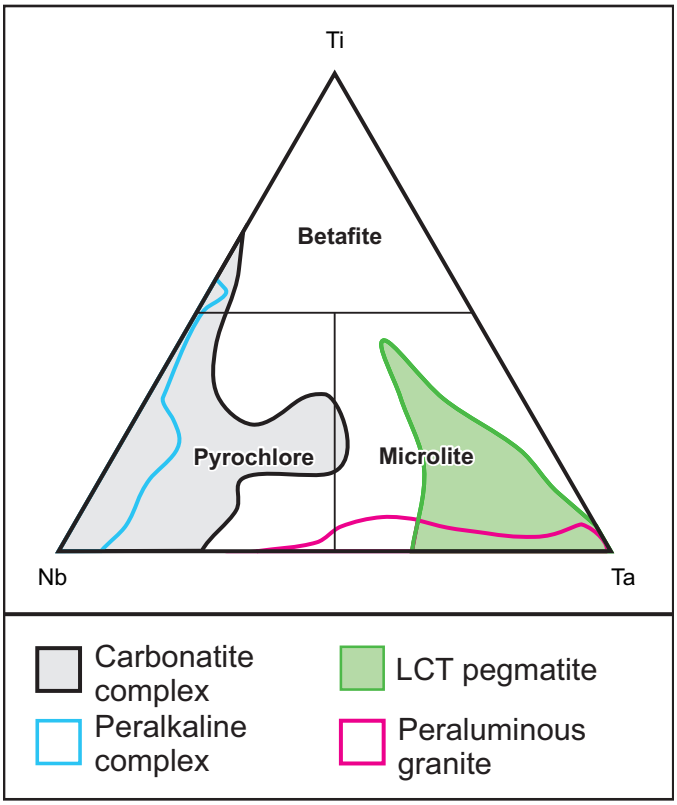

Fig. 2. Compositional fields for pyrochlore supergroup minerals from carbonatites, peralkaline complexes, LCT pegmatites, and peraluminous granites. Modified from Mackay and Simandl (2015). Nomenclature of Atencio et al. 2010.

to spike to US$647/kg of contained Ta_2O_5 (Simandl, 2002). In response, production increased in the dominant supplier nation, Australia (Mackay and Simandl, 2014). Tantalum pentoxide prices had dropped and stabilized under US$120/kg by 2002. Prices again began to rise in 2010, peaking in 2011 at $275/kg and falling slightly to $242/kg in 2014 (Papp, 2015a). Higher Ta_2O_5 concentrate prices may be related to shortages of conflict-free concentrate, the high economic importance of Ta, and high supply risk (European Commission, 2011). Tantalum was recently removed from the critical metals list of the European Union. The supply risk for Ta remains elevated relative to other economically significant metals such as Cu or Fe (European Commission, 2014).

4.2. Tantalum sources

Lithium-cesium-tantalum (LCT) pegmatites and related weathered crusts, rare-element-enriched granites, and placer deposits account for most Ta production (Mackay and Simandl, 2014). Well known examples of LCT pegmatites that are, or were, historically mined for Ta include Greenbushes and Wodgina, Australia; Tanco, Canada; Ketcha, Ethiopia; and Marropino, Mozambique (Mackay and Simandl, 2014). Other historical sources of Ta ores include peraluminous granites (e.g. Yichun, China, and Orlovka, Russia) and artisanally mined placers located in Rwanda, Congo, Burundi, and as a by-product of Sn slag refining in Thailand and Malaysia (Simandl, 2002; Shaw and Goodenough, 2011; Papp, 2012; Pohl, 2012).

Currently, most Ta concentrates are produced artisanally from placer deposits in western and central Africa, the Mibra Mine, Volta Grande, and the Pitinga Mine (all in Brazil; ~8% of Ta production), and Marropino in Mozambique (Fig. 4). Tantalum production from Sn placer deposits in Thailand is not considered in Figure 4. The Pitinga deposit is hosted in a peralkaline unit within a predominantly peraluminous granite (Nardi et al., 2012; Horbe et al., 1991; Bastos Neto et al., 2009). The Yichun mine (China) is another well-known source of Ta, as well as Nb and Li (Lin et al., 1995; Papp, 2012), though production details are not reliably known (Mackay and Simandl, 2014). China accounts for ~5% of Ta production (Fig. 4; Papp, 2015a).

Infrastructure and permitting and, in some cases, mining and processing equipment are in place at most past-producing mines currently on care and maintenance. Favourable market conditions could see these mines reopen, giving them a head start and low starting cost advantage over grass roots Ta exploration projects. Pegmatites, rare-element-enriched peraluminous granites, their weathered equivalents, and placers remain the most favourable hosts for undiscovered economically significant Ta resources (Mackay and Simandl, 2014). Some carbonatite-hosted deposits are also promoted based on the recovery of Ta as a co-product of Nb, such as the Upper Fir (Chong et al., 2012) and Crevier (Duplessis and Girard, 2010) deposits in Canada.

4.3. Niobium market

The vast majority of primary Nb production, ~90%, comes from Brazil (Fig. 5). Any loss of Nb production in Brazil would drastically impact the economies of most modern industrialised nations. A few Nb deposits are on care and maintenance or have existing infrastructure and could be restarted quickly. Niobium co-production with other elements (such as REEs, Zr, and/or Y) from peralkaline complexes (e.g. Nechalacho and Strange Lake) is technically possible but unlikely under current REE market conditions.

In 2013, 88% of Nb was used to produce high-strength low-alloy (HSLA) steel (containing at most 0.1% Nb, commonly approximately 0.03% Nb) used extensively in high-pressure pipeline construction, offshore petroleum drilling platforms, and as major components in the automotive industry, with minor use of Nb in superconducting alloys (Roskill, 2013b; Tantalum-Niobium International Study Center, 2015). Only 4% of Nb was used in high-strength and corrosion resistant Nb-super alloys or vacuum-grade niobium alloys. These super alloys are essential for rocket and jet engine components used in the space and aviation industries (Papp, 2015b). The remaining Nb was used to produce Nb chemicals including catalysts (4%), pure Nb metal (3%), and as Nb alloys such as NbTi (1%) used in superconducting applications (Tantalum-Niobium International Study Center, 2015).

The price of ferroniobium (Fe-Nb alloy containing 65%

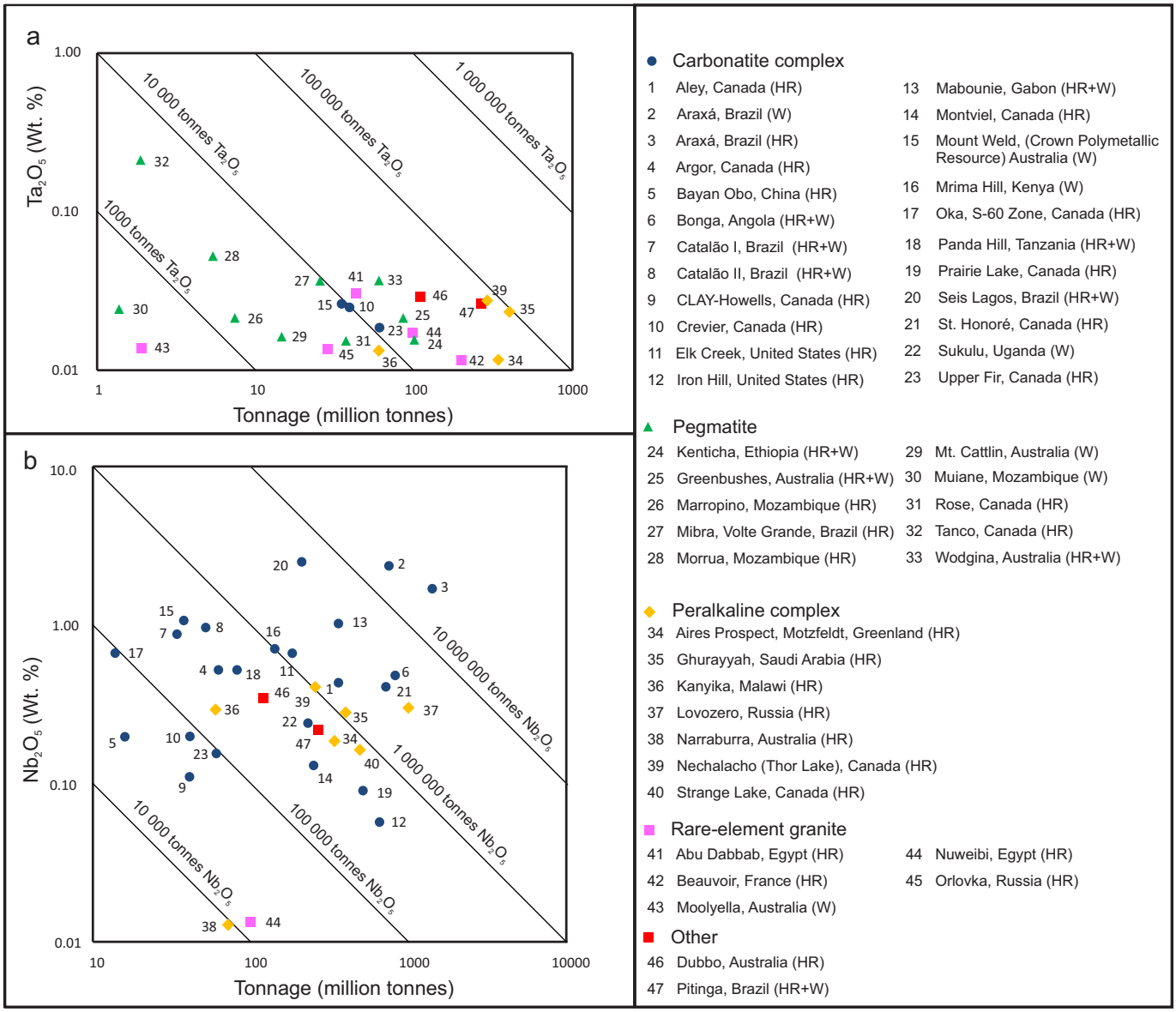

Fig. 3. Grades and tonnages of **a)** Ta and **b)** Nb deposits associated with carbonatite complexes, pegmatites, peralkaline complexes, and rare-element granites. Diagonal lines indicate tonnage of Ta_2O_5 and Nb_2O_5. Modified from Mackay and Simandl (2014). Grade and tonnage references are available in Mackay and Simandl (2014) and in updates based on Gippsland (2015a, b), Vallieres et al. (2013), Anglo American PLC (2015), and Pittuck et al. (2015). Abbreviations: (HR) hard rock ore, (W) weathered ore, (HR+W) hard rock and weathered ore combined.

Nb_2O_5) began to rise rapidly in 2006 (Mackay and Simandl, 2014). Higher prices since 2006 coincide with increased production, indicating a growing demand for Nb in HSLA steel worldwide. Prices peaked at 43,658 US$/tonne of ferroniobium in 2012 and fell slightly to 42,000 in 2014 (Papp, 2015b).

Mine production of Nb has increased rapidly over the last 15 years, from 18,323 tonnes of contained Nb in 1994 to 59000 tonnes in 2014, down slightly from 68,700 tonnes in 2013 (Fig. 5; Papp, 2015b). In 2013, about 20% of Nb was sourced from recycled material (Tantalum-Niobium International Study Center, 2015). Currently, steel production in the USA, Japan, South Korea, Brazil, and EU uses higher concentrations of Nb than China, India, and Russia (Roskill, 2013a). Demand for Nb will likely continue to rise until concentrations of Nb in Chinese, Indian, and Russian steel reach the same levels as those in the EU and United States.

4.4. Niobium sources

The main Nb producers in Brazil, the Araxá and Catalão I and II carbonatites, account for about 90% of Nb mine production. Outside of Brazil, the St. Honoré carbonatite (Canada) accounts for most of the remaining global Nb production (~8%), with a small portion (~2%) sourced from loparite concentrate from the Lovozero peralkaline complex (Russia; Papp, 2015b). Niobium is predominantly derived from weathering-enriched material associated with carbonatite complexes (e.g. Araxá and

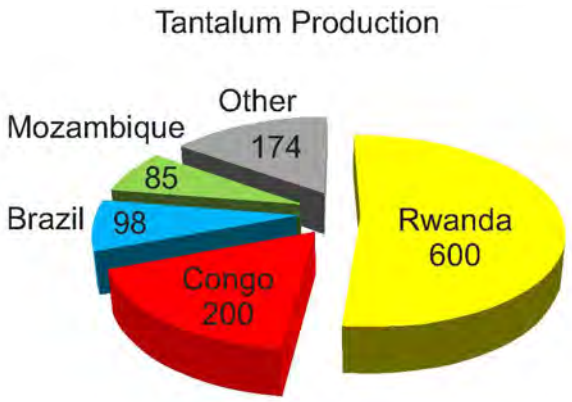

Fig. 4. World mine production (metric tonnes) of contained Ta metal (excluding Ta recovered as a by-product of Sn mining) by country in 2014. Values for Rwanda and Congo updated on May 14, 2015. "Other" includes China (60), Nigeria (60), Ethiopia (40), Burundi (14). Data from Papp (2015a).

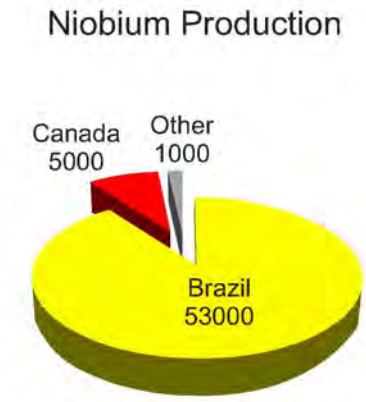

Fig. 5. World mine production of contained Nb metal by country from 2014. Data compiled from Papp (2015b).

Catalão I and II, Brazil; Mackay and Simandl, 2014). Niobium ore is rarely produced from unweathered carbonatite deposits (e.g. St. Honoré and historically Oka, Canada).

Future co-production of Nb with REEs is being considered at several carbonatite complexes such as St. Honoré (Ciuculescu et al., 2013), and Iron Hill, United States (Staatz et al., 1979; v. Gosen, 2009). Similarly, co-production of Nb with phosphate may increase economic viability at deposits such as Prairie Lake, Canada (Nuinsco Resources Ltd., 2014); Nkombway Hill, Zambia (v. Straaten, 2002); and Sukulu, Uganda (Karagambe-Kaliiza, 1989). There is potential for co-production of Nb with other metals (REEs, Y, and/or Zr) in peralkaline deposits such as Nechalacho, Canada (Ciuculescu et al., 2013); Strange Lake, Canada (Gowans et al., 2013); Kipawa, Canada (Saucier et al., 2013); Lovozero, Russia (Zaitsev et al., 1998); and Motzfeldt, Greenland.

4.5. Ta and Nb concentrate pricing considerations

The Nb and Ta markets are limited. Prices of Ta and Nb concentrates are set for each contract by negotiations between buyers and sellers. Tantalite concentrates are expected to contain more than 30% Ta_2O_5 (Tantalum-Niobium International Study Center, 2013a). Concentrates with a minimum content of 20% Ta_2O_5 may also be considered. The value of concentrate is based on Ta_2O_5 content; Nb_2O_5 is commonly ignored. The price for Nb concentrate with low Ta_2O_5 content is determined by summation of Nb_2O_5+Ta_2O_5 content and valuation is based on the price for Nb_2O_5. The higher value of Ta_2O_5 relative to $Nb_2O_5$is ignored (Tantalum-Niobium International Study Center, 2013a, b). When sold for production of ferroniobium Ta is ignored, as it cannot be removed. Additionally, some Ta and Nb concentrates may have non-negligible U and Th content. High concentrations of these elements require extra health and environmental precautions during mining, concentrate transportation, and processing (Tantalum-Niobium International Study Center, 2013a, b).

Multiple co-products are perceived to insulate a project from economic downturns as REE, Nb, Ta, and Zr are used in different products. However, complex metallurgy commonly results in high capital and plant operating costs (Mackay and Simandl, 2014). The potential for Nb recovery as a co-product of Zr and REE from peralkaline complexes is determined to a large extent by the mineralogy, mineral chemistry, texture, and particle size and is deposit specific as illustrated by Nechalacho (Ciuculescu et al., 2013), Kipawa (Saucier et al., 2013), and Lovozero (Zaitsev et al., 1998). Metallurgical aspects of Ta and Nb deposits are covered in detail by Shaw and Goodenough (2011) and Linnen et al. (2014).

5. Summary

Tantalum availability, in the short to medium term, may be affected by increasing resistance to use of conflict materials. Pegmatites, peraluminous granites, weathered crusts, and placers account for most primary Ta production. Slag refining of Sn placer deposits currently accounts for approximately 21% of Ta production; recycling accounts for 48% of the supply chain. Should the gap in Ta availability persist, large-scale mechanized mining of pegmatite-hosted Ta-bearing deposits, such as at Greenbushes and Wodgina (Australia), which are currently on care-and-maintenance, are likely to return into production. Niobium is high on the critical metals list of the European Commission critical metals report for the EU, largely because 90% of primary Nb production is geographically restricted to a single country (Brazil). Most of the balance (~8%) comes from the St. Honoré carbonatite (Canada). A small portion (~2%) of Nb production is from loparite concentrate from the Lovozero peralkaline complex (Russia).

Acknowledgments

This project was funded by the Targeted Geoscience Initiative 4 (TGI4), a Natural Resources Canada programme carried out under the auspices of the Geological Survey of Canada in collaboration with the British Columbia Geological Survey. Suggestions by David L. Trueman (consulting geologist) are greatly appreciated.

References cited

Anhaeusser, C.R., 1976. Archean metallogeney in Southern Africa. Economic Geology, 71, 16–45.

Anglo American PLC, 2015. Annual Report 2014. Anglo American PLC. London, UK. http://www.angloamerican.com/~/media/Files/A/Anglo-American-PLC-V2/report-builder-2014/annual-report/aa-ar14-interactive-final.pdf Accessed 11 September 2015

Atencio, D., Andrade, M. B., Christy, A. G., & Grieré, R. 2010. The Pyrochlore Supergroup of Minerals: Nomenclature. The Canadian Mineralogist, 48, 673-698.

Barbarin, B., 1990. Granitoids: Main petrogenetic classification in relation to origin and tectonic setting. Geological Journal, 25, 227–238.

Bastos Neto, A.C., Pereira, V.P., Ronchi, L.H., de Lima, E.F., and Frant, J.C., 2009. The world-class Sn, Nb, Ta, F (Y, REE, Li) deposit and the massive cryolite associated with the albite-enriched facies of Madeira a-type granite, Pitinga mining district, Amazonas State, Brazil. Canadian Mineralogist, 47, 1329–1357.

Birkett, T.C. and Simandl, G.J., 1999. Carbonatite-associated deposits. In: Simandl, G.J., Hora, Z.D., and Lefebure, D.V., (eds) Selected British Columbia mineral deposit profiles, vol. 3: industrial minerals and gemstones. British Columbia Ministry of Energy, Mines and Petroleum Resources, British Columbia Geological Survey, Open File 1999-10.

Breaks, F.W., Selway, J.B., and Tindle, A.G., 2003. Fertile peraluminous granites and related rare-element mineralisation in pegmatites, Superior Province, Northwest and Northeast Ontario: Operation Treasure Hunt. Ontario Geological Survey, Open File Report 6099.

Brown, T.J., Walters, A.S., Idoine, N.E., Shaw, R.A., Wrighton, C.E., and Bide, T., 2012. World mineral production 2006–10. British Geological Survey, Keyworth, 78 p.

Černý, P., 1975. Pegmatite studies. Centre for Precambrian Studies, University of Manitoba, Annual Report, Part 2, 92–102.

Černý, P., 1982. The Tanco pegmatite, southeastern Manitoba. American Mineralogist, 67, 183–183

Černý, P., 1991a. Rare-element granitic pegmatites part I anatomy and internal evolution of pegmatite deposits. Geoscience Canada, 18, 49–67.

Černý, P., 1991b. Rare-element granitic pegmatites part II regional to global environments and petrogenesis. Geoscience Canada, 18, 68–81.

Černý, P. and Ercit, T.S., 1985. Some recent advances in the mineralogy and geochemistry of Nb and Ta in rare-element granitic pegmatites. Bulletin of Mineralogy, 108, 499–532.

Černý, P. and Ercit, T.S., 1989. Mineralogy of niobium and tantalite: Crystal chemical relationships, paragenetic aspects and their economic implications. In: Möller, P., Černý, P., and Saupé, F. (eds) Lanthanides, Tantalum and Niobium. Springer-Verlag, Berlin, 27-79.

Černý, P. and Ercit, T.S., 2005. The classification of granitic pegmatites revisited. Canadian Mineralogist, 43, 2005–2026.

Černý, P. and Meintzer, R.E., 1988. Fertile granites in the Archean and Proterozoic fields of rare-element pegmatites, crustal environment, geochemistry and petrogenetic relationships. In: Taylor, R.P. and Strong, D.F., (eds) Recent advances in the geology of granite-related mineral deposits. Canadian Institute of Mining and Metallurgy, Special Volume, 39, 170-207.

Chong, A., Postolski, T., Mendoza, R.R., Lipiec, T., and Omidvar, B., 2012. Blue River tantalum-niobium project, (British Columbia, Canada). NI-43-101 Technical Report. Commerce Resource Corp. Vancouver, Canada, June 22, 2012. http://www.commerceresources.com/i/pdf/TechnicalReport-BlueRiverResourceUpdate.pdf. Accessed 11 Dec 2013.

Ciuculescu, T., Foo, B., Gowans, R., Hawton, K., Jacobs, C., and Spooner, J., 2013. Technical report disclosing the results of the feasibility study on the Nechalacho rare earth elements project. Toronto, Ontario, Canada, Avalon Rare Metals Inc. http://avalonraremetals.com/_resources/projects/may_2013_ni43_report.pdf. Accessed 11 Dec 2013.

Clarke, D.B., 1981. The mineralogy of peraluminous granites: a review. Canadian Mineralogist, 19, 1–17.

Duplessis, C. and Girard, R., 2010. Niobium and tantalum resource estimation update of the Crevier deposit-2010. MDN Inc. and Crevier Minerals Ind.

Elenilto Mining, 2015. Kenticha Tantalum Project. http://www.elenilto.com/projects/tantalum-niobium/ethiopia-bupo-kilkile/. Accessed 1 Sept 2015.

European Commission, 2011. Critical raw materials for the EU. http://ec.europa.eu/enterprise/policies/raw-materials/files/docs/report-b_en.pdf. Accessed 9 Dec 2013.

European Commission, 2014. Report on critical raw materials for the EU. http://ec.europa.eu/enterprise/policies/raw-materials/files/docs/crmreport-on-critical-raw-materials_en.pdf. Accessed 6 Jun 2014.

Gerasimovskii, V.I., 1956. Geochemistry and mineralogy of nepheline syenite intrusions. Geokhimya, 5, 494–511.

Ginsberg, A.I., 1984. The geological condition of the location and the formation of granitic pegmatites. Proceedings of the 27th International Geological Congress, 15, 245–260.

Gippsland Limited (2015a) Abu Dabbab Tantalum. http://www.gippslandltd.com/Projects/AbuDabbab.aspx. Accessed 11 Sept 2015

Gippsland Limited (2015b) Nuweibi–tantalum, niobium, feldspar. http://www.gippslandltd.com/Projects/Nuweibi.aspx. Accessed 11 Sept 2015

Gowans, R.M., Hutchison, I., Lewis, W.J., Shoemaker, Jr. S., Spooner, J., and Zalnieriunas, R.V., 2013. NI 43–101 technical report on the prefeasibility study for the Strange Lake property, Quebec, Canada. Quest Rare Metals Ltd. Toronto, Canada. http://www.questrareminerals.com/pdfs/Strange%20Lake%20PFS%20Results%2043-101.pdf. Accessed 13 Dec 2013

Hassan, W.F., 1994. Geochemistry and mineralogy of Ta-Nb rutile from Peninsular Malaysia. Journal of Southeast Asian Earth Science, 10, 11-23.

Hatcher, M.I. and Bolitho, B.C., 1982. The greenbushes pegmatite, South-West Western Australia. In: Černý, P., (ed) Granitic pegmatites in science and industry. Mineralogical Association of Canada Short Course, 513–525.

Hatcher, M.I. and Clynick, G., 1990. Greenbushes tin–tantalum–lithium deposit. In: Hughes, F.E., (ed) Geology of the mineral deposits of Australia and Papua New Guinea. The Australas Institute of Mining and Metallurgy, Parkville, pp 599–603.

Heinrich, E.W., 1985. Infinite variations on fenite theme. Indian Mineral, Sukheswala, volume 151–162.

Horbe, M.A., Horbe, A.C., Costi, H.T., and Teixeira, J.T., 1991. Geochemical characteristics of cryolite-tin-bearing granites from the Pitinga Mine, northwestern Brazil - A review. Journal of Geochemical Exploration, 40, 227–249.

Jahns, R.H., 1955. The study of pegmatites. Division of the Geological Sciences, California Institute of Technology, Pasadena, 106p.

Johan, V. and Johan, Z., 1994. Accessory minerals of the Cínovec (Zinnwald) granite cupola, Czech Republic. Mineralogy and Petrology, 51, 333–343.

Karagambe-Kaliiza, F.A., 1989. The Sukulu phosphate deposits, South-Eastern Uganda. In: Bell, K. (ed) Carbonatites genesis and evolution. Unwin Hyman, London, pp 184–186

Lafleur, P.J. and Ayad, M.A.B., 2012. NI 43–101 technical report to present the mineral resources of the rare earth elements zone Niobec mine. IAMGOLD Corporation, Toronto, Canada. 145 p. http://www.iamgold.com/files/REE%2043-101%20Technical%20Report%20March%202012.pdf. Accessed 12 Dec 2013.

Le Bas, M.J., 2008. Fenites associated with carbonatites. Canadian

Mineralogist, 46, 915–932.
Le Maitre, R.W., (ed) 2002. Igneous rocks: a classification and glossary of terms; recommendations of the International Union of Geological Sciences Subcommission on the systematics of igneous rocks. Cambridge University Press, Cambridge.
Lin, Y., Pollard, P.J., Hu, S., and Taylor, R.G., 1995. Geological and geochemical characteristics of the Yichun Ta–Nb–Li deposit, Jiangxi Province, south China. Economic Geology, 90, 577–585.
Linnen, R.L. and Cuney, M., 2005. Granite-related rare-element deposits and experimental constraints on Ta–Nb–W–Sn–Zr–Hf mineralization. In: Linnen, R.L. and Samson, I.M., (eds) Rare-element geochemistry and mineral deposits, short course notes, Geological Association of Canada, Special Publication, 17, 45–68.
Linnen, R.L., Trueman, D.L., and Burt, R., 2014. Tantalum and niobium. In: Gunn, G., (ed) Critical metals handbook, 1st edn. John Wiley and Sons, Ltd, West Sussex, pp 361–384.
Mackay, D.A.R. and Simandl, G.J., 2014. Geology, market and supply chain of niobium and tantalum–a review. Mineralium Deposita, 49, 1025-1047.
Mackay, D.A.R. and Simandl, G.J., 2015. Indicator minerals for specialty metal deposits. Geochemistry: Exploration, Environment, Analysis, doi:10.1144/geochem2014-289.
Mariano, A.N., 1989a. Nature of economic mineralization in carbonatites and related rocks. In: Bell K (ed) Carbonatites: genesis and evolution. Chapman and Hall, London, pp 149–176.
Mariano, A.N., 1989b. Economic geology of rare earth minerals. In: Lipman, B.R. and McKay, G.A., (eds) Geochemistry and mineralogy of rare earth elements. Reviews in Mineralogy, 21, 309–338.
Martin, R.F., 2007. The importance of tectonic setting in understanding granitic pegmatites. Granitic pegmatites: the State of the Art—International Symposium. May 2007, Porto, Portugal.
Martin, R.F. and De Vito, C., 2005. The patterns of enrichment in felsic pegmatites ultimately depend on tectonic setting. Canadian Mineralogist, 43, 2027–2048. Miles KR, Carroll D, Rowledge HP (1945) Tantalumand niobium: Perth, Department of Mines, Mineral Resources of Western Australia Bulletin 3, 150p
Miller, R.R., 1986. Geology of the Strange Lake alkalic complex and the associated Zr–Y–Nb–Be–REE mineralization. In: Current Research, Newfoundland Department of Mines and Energy, Mineral Development Division; Report 86–1, pp 11–19.
Mitchell, R.H., 2005. Carbonatites and carbonatites and carbonatites. The Canadian Mineralogist, 43, 2049–2068.
Möller, P. and Morteani, G., 1983. On the geochemical fractionation of rare earth elements during the formation of Ca-minerals and its application to problems of the genesis of ore deposits. In: Augusthitis, S.S. (ed) The significance of trace elements in solving petrogenetic problems and controversies. Theophrastus Publications, Athens, pp 747–791.
Moloshag, V.P., 1974. On the geochemistry of the rare elements in one of the rare-metal pegmatites shields of Siberia. Moscow University Geology Bulletin, 29, 87–89.
Nardi, L.V.S., Milton, L.L., Jarvis, K., Oliveira, L., Bastos Neto, A.C., and Fontana, E., 2012. REE, Y, Nb, U, and Th contents and tetrad effects in zircon from a magmatic-hydrothermal F-rich system of Sn-rare metal-cryolite mineralized granites from the Pitinga Mine, Amazonia, Brazil. Journal of South American Earth Science, 33, 34–42.
Nuinsco Resources Limited (2014) Prairie lake (Canada) project information. http://www.nuinsco.ca/projects/prairie-lake/. Accessed 14 Aug 2015
Papp, J.F., 2012. Niobium and tantalum (advanced release). In: U.S. Geological Survey 2011 Minerals Yearbook. http://minerals.usgs.gov/minerals/pubs/commodity/niobium/myb1-2011-niobi.pdf. Accessed 17 Jul 2013.
Papp, J.F., 2015a. Tantalum. In: U.S. Geological Survey, Mineral Commodity Summaries 2013, pp 162–163.
Papp, J.F., 2015b. Niobium (columbium). In: U.S. Geological Survey, Mineral Commodity Summaries 2013, pp 110–111.
Pitcher, W.S., 1983. Granite type and tectonic environment. In: Hsü, K.J., (ed) Mountain building processes. Academic Press, London.
Pitcher, W.S., 1993. The Nature and origin of granite. Blackie, London.
Pittuck, M.F., Parsons, B., Bair, D. 2015. NI 43-101 Technical Report Updated Mineral Resource Estimate Elk Creek Niobium Project, Nebraska. NioCorp Developments Ltd.
Pohl, W.L., 2012. Sample chapter: niobium and tantalum (updated December 18, 2012). In: Pohl WL (ed) Economic geology, principles and practice: metals, minerals, coal and hydrocarbons—an introduction to formation and sustainable exploitation of mineral deposits. Wiley-Blackwell, West Sussex, pp 261–265
Raimbault, L., Cuney, M., Azencott, C., Duthou, J.L., and Joron, J.L., 1995. Geochemical evidence for a multistage magmatic genesis of Ta, Sn, Li mineralization in the granite at Beauvoir, French Massif Central. Economic Geology, 90, 548–576.
Reyf, F.G., Seltmann, R., and Zaraisky, G.P., 2000. The role of magmatic processes in the formation of banded Li, F-enriched granites from the Orlovka tantalum deposit, Transbaikalia, Russia: Microthermometric evidence. Canadian Mineralogist, 38, 915–936.
Richardson, D.G. and Birkett, T.C., 1995. Peralkaline rock-associated rare metals. In: Eckstrand, O.R., Sinclair, W.D., and Thorpe, R.I. (eds) Geology of Canadian mineral deposits types, No. 8. Geological Survey of Canada, pp 523–540.
Roskill, 2013a. Tantalum: market outlook to 2016. http://www.roskill.com/reports/minor-and-light-metals/tantalum. Accessed 27 Jul 2013.
Roskill, 2013b. Niobium: market outlook to 2017, 12th edn. http://www.roskill.com/reports/steel-alloys/niobium/?searchterm=niobium. Accessed 27 Jul 2013.
Salvi, S. and Williams-Jones, A.E., 1990. The role of hydrothermal processes in the granite hosted Zr, Y, REE deposit at Strange Lake, Quebec/Labrador: Evidence from fluid inclusions. Geochimica et Cosmochimica Acta, 54, 2403–2418.
Saucier, G., Noreau, C., Casgrain, P., Côté, P., Larochelle, E., Bilodeau, M., Hayden, A., Poirier, E., Garon, M., Bertrand, V., Kissiova, M., Malloux, M., Rouger, M., Camus, Y., and Gagnon, G., 2013. NI-43-101 report-feasibility study for the Kipawa project Temiscamingue area, Québec, Canada. Matamec Explorations Inc., Montréal.
Schwartz, M.O., Rajah, S.S., Askury, A.K., Putthapiban, P., and Djaswadi, S., 1995. The Southeast Asian tin belt. Earth Science Review, 38, 95–293.
Seltmann, R., Soloviev, S., Shatov, V., Pirajno, F., Naumov, E., and Cherkasov, S., 2010. Metallogeny of Siberia: Tectonic, geologic and metallogenic settings of selected significant deposits. Australian Journal of Earth Science, 57, 655–706.
Shand, S.J., 1927. Eruptive rocks, 1st edition. Wiley, New York.
Shaw, R. and Goodenough, K., 2011. Niobium–tantalum. British Geological Survey, Keyworth.
Sheard, E.R., Williams-Jones, A.E., Heiligmann, M., Pederson, C., and Trueman, D.L., 2012. Controls on the concentration of zirconium, niobium, and the rare earth elements in the Thor Lake rare metal deposit, Northwest Territories, Canada. Economic Geology, 107, 81–104.
Simandl, G.J., 2002. Tantalum market and resources: an overview. In: Geological Field Work 2001. British Columbia Ministry of Energy and Mines, Geological Survey of British Columbia Paper 2002–1, pp 313–318.
Sørensen, H., 1960. On the agpaitic rocks. Rep 21st International Geological Congress, Norden 13, 319–327.
Sørensen, H., 1968. Rhythmic igneous layering in peralkaline intrusions. An essay review on Ilimaussaq (Greenland) and Lovozero (Kola, USSR). Lithos, 2, 261–283.

Staatz, M.H., Armbrustmacher, T.J., Olson, J.C., Brownfield, I.K., Brock, M.R., Lemons, J.F. Jr, Coppa, L.V., and Clingan, B.V., 1979. Principal thorium resources in the United States. US Geological Survey Circular, 805.

Tantalum-Niobium International Study Center, 2015a. Tantalum-Niobium Internation Study Center, Bulletin No. 160. http://tanb.org/webfm_send/326. Accessed 14 Aug 2015.

Tantalum-Niobium International Study Center, 2015b. Tantalum–raw materials and processing. http://tanb.org/tantalum. Accessed 14 Aug 2015.

Tantalum-Niobium International Study Center, 2015c. Niobium–raw materials and processing. http://tanb.org/niobium. Accessed 14 Aug 2015.

Thivierge, S., Roy, O.W., Chown, E.H., and Gauthier, A., 1983. Évolution du complexe alcalin de St. Honoré (Québec) Après sa Mise en Place. Mineralium Deposita, 18, 267–283.

Trueman, D.L. and Černý, P., 1982. Exploration for rare-element granitic pegmatites. In: Černý, P., (ed) Granitic pegmatites in science and industry. Mineral Association of Canada Short Course, Volume 8, Winnipeg, Canada, pp 463–493.

Van Gosen, B.S., 2009. The Iron Hill (Powderhorn) carbonatite complex, Gunnison County, Colorado: a potential source of several uncommon mineral resources. U.S. Geological Survey, Open-File Report 2009-1005.

van Straaten, P., 2002. Rocks for crops: Agrominerals of Sub-Saharan Africa. ICRAF, Nairobi.

Vallieres, D., Pelletier, P., Gaultier, P., Felatte, G., Tremblay, J.F., and Sirois, R. 2013. NI 43-101 Techincal Report, Update on Niobec Expansion, December 2013. IAMGOLD Corporation.

Varlamoff, N., 1972. Central and West African rare-metal granitic pegmatites, related aplites, quartz veins and mineral deposits. Mineralium Deposita, 7, 202–216.

Woolley, A.R., 2003. Igneous silicate rocks associated with carbonatites: their diversity, relative abundances and implications for carbonatite genesis. Periód Mineral, 72, 9–17.

Woolley, A.R. and Kjarsgaard, B.A., 2008. Paragenetic types of carbonatite as indicated by the diversity and relative abundances of associated silicate rocks: evidence from a global database. Canadian Mineralogist, 46, 741–752.

Zaitsev, A.N., Wall, F., and Le Bas, M.J., 1998. REE–Sr–Ba minerals from the Khibina carbonatites, Kola Peninsula, Russia: Their mineralogy, paragenesis and evolution. Mineralogical Magazine, 62, 225–250.

Indium, germanium and gallium in volcanic- and sediment-hosted base-metal sulphide deposits

Suzanne Paradis[1, a]

[1] Geological Survey of Canada, Pacific Division, Sidney, BC, V8L 4B2
[a] corresponding author: suzanne.paradis@canada.ca

Recommended citation: Paradis, S., 2015. Indium, germanium and gallium in volcanic- and sediment-hosted base-metal sulphide deposits. In: Simandl, G.J. and Neetz, M., (Eds.), Symposium on Strategic and Critical Materials Proceedings, November 13-14, 2015, Victoria, British Columbia. British Columbia Ministry of Energy and Mines, British Columbia Geological Survey Paper 2015-3, pp. 23-29.

1. Introduction

Indium (In), germanium (Ge), and gallium (Ga) have unique chemical and physical properties. This makes them critical for a wide variety of high technology, pharmaceutical, metallurgical and chemical industries. This extended abstract consists of three parts. The first part covers In, Ge, and Ga in terms of their physical and chemical properties, ore mineralogy and uses. The second part summarizes available information on global reserves and resources and production. The third part introduces major deposit-types from which In, Ge, and Ga are recovered, focusing on volcanic-hosted massive sulphide (VHMS) and sediment-hosted massive sulphide (SHMS) deposits. For the purpose of this paper, SHMS deposits include syngenetic or early diagenetic sedimentary exhalative (SEDEX), Mississippi Valley-type (MVT), and Kipushi-type deposits.

2. Physical and chemical properties, mineralogy and uses

2.1. Indium

Indium is a silvery white, soft (1.2 on the Mohs scale), malleable, and ductile post-transition metal. It is in period 5, group 13 of the Periodic Table, having an average atomic mass of 114.818. The melting point of In is 156.60°C, and its liquid density is 7.02 g/cm^3 at that temperature (Hammond, 2008). Indium is not oxidized in air at ambient temperatures (Schwarz-Schampera and Herzig, 2002). The addition of In generally increases strength, corrosion resistance, and hardness of metals and metal alloys. Indium has high plastic properties even at freezing temperatures (Hammond, 2008; Mercer, 2105).

Relative to other metallic elements, In is rare. The average continental crust contains about 0.05 ppm In; the average oceanic crust contains about 0.072 ppm In (Rudnick and Gao, 2003; Schwarz-Schampera, 2014). Of the 12 indium-bearing minerals that have been discovered, roquesite ($CuInS_2$) is the most important; it represents a trace component in ore-forming minerals (Schwarz-Schampera and Herzig, 2002).

Indium substitutes for elements with similar ionic radii in base-metal sulphides, especially those having tetrahedral coordination. High In concentrations can be detected in zinc and copper sulphides, of which sphalerite is the most important for global In production. Other carriers are chalcopyrite, stannite, tin-sulfosalts, tennantite, and cassiterite. Indium is incorporated into these minerals mainly as nano- and micro-scale mineral inclusions (e.g., roquesite inclusions in sphalerite, chalcopyrite, and other sulphides), solid solution through a diadochic replacement of zinc, and in the lattice of tetrahedral-coordinated sulphides. In sphalerite, In is frequently incorporated into the mineral structure via a simple coupled substitution $2Zn^{2+} \leftrightarrow Cu^{+} + In^{3+}$.

The principal industrial application of In is in In-Sn oxide (ITO) as a thin-film coating for electronic devices (Fig. 1a). It is also used in alloys and solders, electrical components and semiconductors, and intermetallic compounds (Polinares, 2012).

2.2. Germanium

Pure Ge is a hard (7.6 on the Mohs scale), lustrous, greyish white, brittle semi-metal (metalloid). It is an important semiconductor that has many useful applications in high-technology industry (Hammond, 2008; Berger, 2008). Germanium is located in period 4, group 14 of the Periodic Table, and has an average atomic mass of 72.64. The melting point of Ge is 938.25°C, and its liquid density at that temperature is 5.60 g/cm^3 (Hammond, 2008).

Germanium is more common in the Earth's crust than In. It has concentrations of about 2-2.4 ppm in continental crust and 1.5 ppm in oceanic crust (Taylor and McLennan, 1985; Ketris and Yudovich, 2009). Germanium is present in trace amounts in most rock types because of its siderophile, lithophile, chalcophile, and organophile natures. It does not occur as a native metal in nature. Approximately 30 minerals are known to contain Ge, and many are sulphides. Ge is a substituting element in zinc sulphide structures (e.g., up to 3000 ppm in sphalerite and wurtzite) and copper sulphides (e.g., up to 5000 ppm in enargite, tennantite, bornite, and chalcopyrite) (Höll et al., 2007; Melcher and Buchholz, 2014). Germanium is also present as a substituting element in silicates (e.g., up to 4000 ppm in willemite $ZnSiO_4$; up to 700 ppm in topaz), oxides (e.g., up to 7000 ppm in hematite), hydroxides (e.g., up to 5310 ppm in goethite), phosphates, arsenates, vanadates, tungstates, and sulphates (Höll et al., 2007; Melcher and Buchholz, 2014).

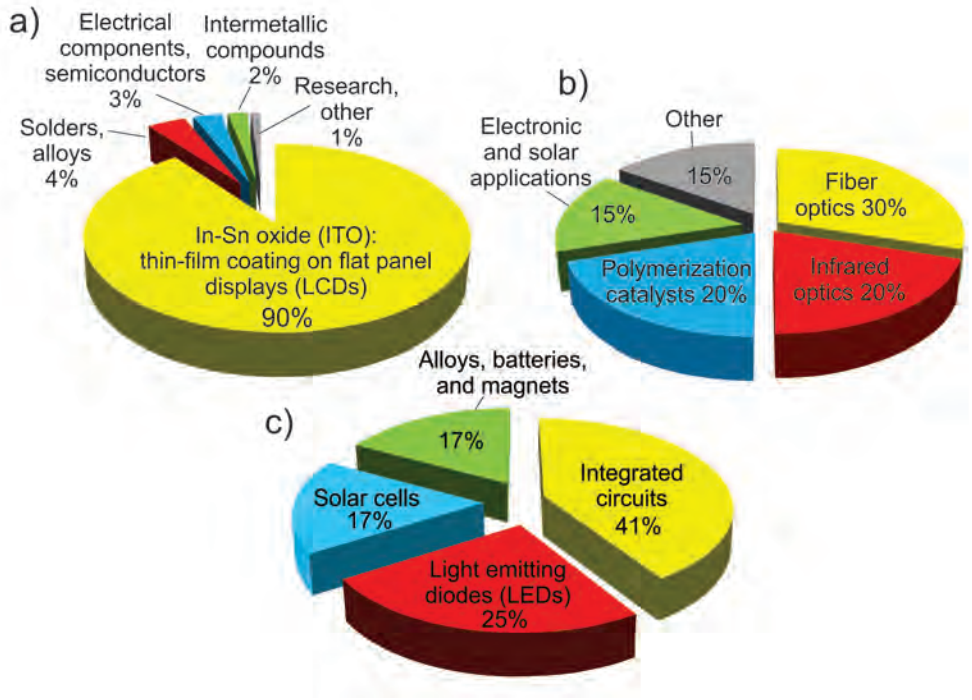

Fig. 1. a) The main end-uses of indium in 2014. Data from Polinares (2012). **b)** The main end-uses of germanium in 2014. Data from Guberman (2015). **c)** The main end-uses of gallium in 2014. Data from European Commission (2015).

Germanium is predominantly used in fiber optics, infrared optics, polymerization catalysts, electronic and solar applications, and other uses such as phosphors, metallurgy and chemotherapy (Fig. 1b; Guberman, 2015).

2.3. Gallium

Gallium is a soft, silvery blueish metal, located in period 4, group 13 of the Periodic Table, having an average atomic mass of 69.723 (Hammond, 2008). Solid gallium fractures conchoidally like glass, and exhibits an unusually large liquid range as it has a melting point of 30ºC and a boiling point of 2204ºC (Butcher and Brown, 2014). This provides the metal with an interesting property, that a solid piece of Ga will liquefy when placed in one's hand (Moskalyk, 2003). The liquid density of Ga at melting point temperature is 6.08 g/cm^3 (Hammond, 2008).

Elemental Ga does not occur in nature, but occurs as Ga(III) compounds that are mostly present in trace amounts in sphalerite and in bauxite (Butcher and Brown, 2014). Its abundance in the Earth's crust is approximately 19 ppm (Butcher and Brown, 2014).

Gallium can combine with a wide variety of elements to produce bromides, chlorides, hydrides, iodides, nitrides, oxides, selenides, sulphides, and tellurides (Handbook of Chemistry and Physics, 2015). Gallium arsenide (GaAs) and gallium nitride (GaN) are valuable compounds presently employed in advanced semiconductors for integrated circuits (ICs), light emitting diodes (LEDs), and solar cells. Other uses are in medical equipment such as alloys, batteries, and magnets (Fig. 1c; European Commission, 2015).

3. Resources, reserves and production

3.1. Indium

Indium is a by-product of smelting polymetallic base-metal ores, primarily zinc and to a lesser extent, tin and copper. In such ore concentrates, the In content is about 70 to 200 ppm, but may reach values of 800 ppm (Schwarz-Schampera, 2014). About 95% is produced as a by-product from zinc sulphide concentrates with elevated Cu contents at or above 2%. The rest (5%) is extracted from the residues of copper and tin treatment (Schwarz-Schampera, 2014; Werner et al., 2015).

Reliability of global In resource estimates is questionable as details relating to trace metal concentrations in sulphide deposits are not commonly reported by the mining industry. However, it can be estimated from Zn and Cu resources worldwide. By assuming Zn reserves of 250 Mt and 50 grams of In per tonne of Zn, Schwarz-Schampara (2014) projected global resources of 95,000 tonnes and reserves of 12,500 (Table 1). A similar estimate was calculated from global Cu resources.

Large mines with In-bearing ore are in production on all continents with the exception of Antarctica. Globally, zinc concentrates were the principal source of primary In, with world production of primary In estimated at 640 tonnes in 2011 (Tolcin, 2012).

Global In refinery production in 2014 was estimated at 819 tonnes (Fig. 2a; Tolcin, 2015). The largest producers of refined In are China (420 tonnes), South Korea (150 tonnes), Japan (72 tonnes), Canada (65 tonnes), France (48 tonnes), and Belgium (30 tonnes). Some of these countries, such as Belgium, do not have significant In-bearing ore deposits (Schwarz-Schampera, 2014).

Table 1. Calculated global resources and reserves of indium in tonnes. From Schwarz-Schampara (2014).

	Resources	Reserves
Zinc ores	95,000	12,500
Copper ores	30,000	6,300
Total	125,000	18,800

3.2. Germanium

Germanium is extracted mainly as a by-product of mining zinc sulphide-rich ores. It comes from sphalerite concentrates containing 50 to 3000 ppm Ge (Sinclair, 2014). Current production mostly comes from SHMS deposits in China (Huize, Jinding and Fankou), the United States (Red Dog SEDEX deposit, Alaska; and MVT deposits of the Elmwood-Gordonsville district, Tennessee) and the Democratic Republic of the Congo (Kipushi deposit). The overall Ge grades in these deposits range from 10 to 300 ppm, for total Ge resources of approximately 5400 tonnes (Bonnet et al., 2014; Melcher and Buchholz, 2014). Germanium is also extracted from coal ash in China, Russia, Ukraine, and possibly Uzbekistan (Melcher and Buchholz, 2014). Germanium content of coal ranges from 30 to 1043 ppm and can be enriched 5- to 10-fold in the ash (Frenzel et al., 2014).

Global Ge resource and reserve data are inconsistent because Ge concentrations in many deposits are not properly reported. Frenzel et al. (2014) estimated that the minimum amounts of recoverable Ge contained in proven reserves of zinc sulphide ores (at grades in excess of 100 ppm in sphalerite) and coals (in excess of 200 ppm), given current processing technologies, is at least 122,000 tonnes (~10,000 tonnes in zinc ores and ~112,000 tonnes in coal). Melcher and Buchholz (2014) published a compilation of combined reserves and resources for producing mines and exploration base-metal, lignite and coal projects around the world. The total combined reserves and resources are estimated at around 35,903 tonnes of Ge, with approximately 11,000 tonnes coming from the sulphide deposits and associated slags, and 25,000 tonnes coming from the Ge-rich coal and lignite deposits.

The world refinery production of Ge in 2014 was about 165 tonnes (this doesn't include data from the United States; Guberman, 2015), and most of it comes from China (Fig. 2b). In China, both zinc-smelter residues and coal are used. In Canada, another major supplier, production is from zinc ores only. The rest of the world's refinery production comes from Russia, the United States, Spain, India, Finland, and Australia (Mikolajczak, 2011; Melcher and Buchholz, 2014; Guberman, 2015). In addition to primary Ge production and refining, Ge is also recycled from scrap (infrared optics, fibre optics, electronic and solar electrical products, and polymerization catalysts) in China, Russia, Belgium, the United States, and other countries (Guberman, 2015).

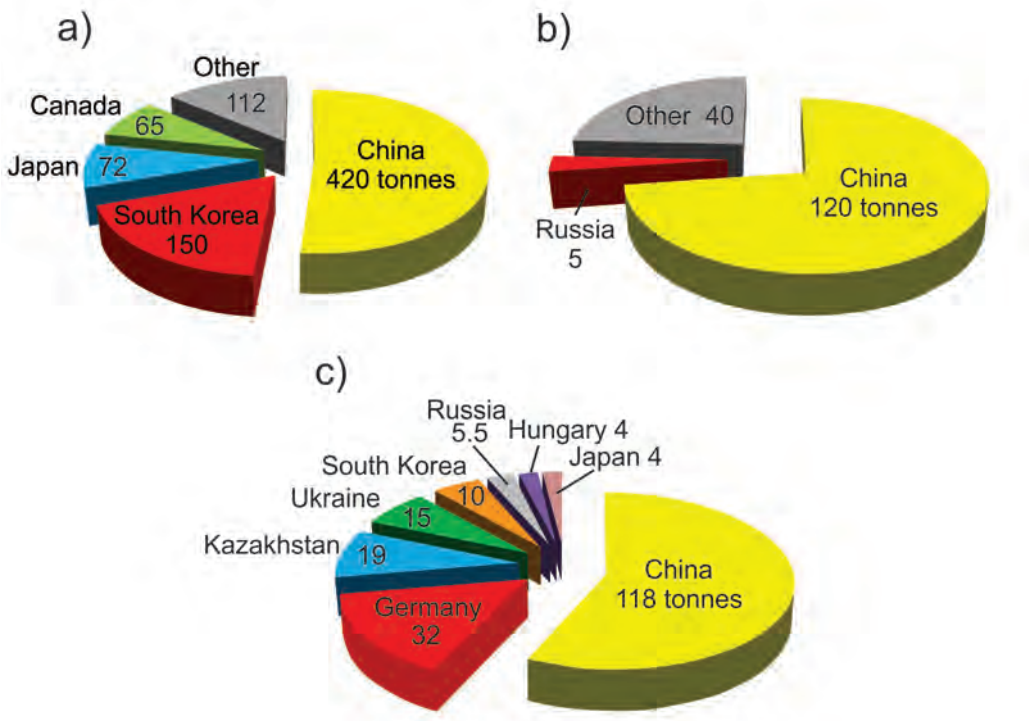

Fig. 2. a) Global indium refinery production in 2014 per country (data from Tolcin, 2015). **b)** Global germanium refinery production in 2014 per country (data from Guberman, 2015). **c)** Estimated world annual primary gallium production for 2010 per country (data from Roskill Information Services Ltd., 2011).

3.3. Gallium

Globally, most primary Ga is recovered as a by-product of bauxite and, locally, of zinc ore processing. Recovery rates are not in the public domain but are considered to be low. Therefore, an estimate of current global Ga reserves and resources comparable to In and Ge is difficult to make (Jaskula, 2015). However, because almost all Ga is extracted as by-product during beneficiation of bauxite, Ga reserves in bauxite deposits are estimated at 1.36 Mt and reported resources are probably in a 2.75 to 3.75 Mt range (Dittrich et al., 2011).

The world primary Ga production in 2014 was estimated at 440 tonnes (Jaskula, 2015; production data per country in 2014 are not available), more than double the figure of about 205 tonnes for 2010 (Fig. 2c; Roskill Information Services Ltd., 2011). China, Germany, Japan, and Ukraine were the leading producers in 2014; countries with lesser output were Hungary, South Korea, and Russia. Kazakhstan, reported as a leading producer in 2012, did not produce any primary Ga in 2013, and it is uncertain if it had production in 2015.

Refined Ga production for 2014 was estimated to be 170 tonnes (Jaskula, 2015). China, Japan, the United Kingdom, the United States, and possibly Slovakia were the principal producers of refined Ga. Gallium was recycled from scrap in Canada, Germany, Japan, the United Kingdom, and the United States.

4. Major indium-bearing deposit types with focus on volcanic- and sediment-hosted Zn-Pb deposits

Indium is reported from a variety of deposit types, including VHMS, SHMS, polymetallic epithermal vein-breccia-stockwork, porphyry Cu (+/-Zn-Pb), polymetallic vein (+/-Sn), vein-stockwork Sn-W, and skarn (Fig. 3). It is found primarily in Zn ores with a high Cu content, and in Sn ores. This section focuses on two of the main base-metal deposit types, VHMS and SHMS, that contribute to the bulk of identified In resources.

Examples of In-rich VHMS deposits are those of the Iberian Pyrite Belt in Spain and Portugal (e.g., Neves Corvo), Kidd Creek, Brunswick No.12 and Heath Steele deposits in Canada, and Gaiskoye deposit in Russia (Fig. 3).

In VHMS deposits, recoverable concentrations of In are commonly associated with significant amounts of Ag, Sn, Bi, Co, and Se, which can be important by-products. In many deposits, In exhibits a positive correlation with Zn, and Sn and, locally, with Cu. The presence of Bi, Co and In in a deposit typically indicates elevated formation temperatures. Most of the In is present in the crystal lattice of sphalerite and chalcopyrite, and other sulphides (Cook et al., 2009; 2011). Some of it can also occur as mineral inclusions, such as roquesite, which may be present as a trace component in sphalerite- and chalcopyrite-rich ores.

Indium contents in VHMS ores vary from 1 to 320 g/t (Werner et al., 2015), but can be higher in some deposits (e.g., Neves Corvo). At the Kidd Creek deposit, the zinc concentrate had an average of 270 ppm In (Pinto et al., 2014), and annual indium production was 50 tonnes of In metal before the closure of a smelter in Timmins, Ontario in 2010 (Schwarz-Schampera, 2014). Roquesite in massive chalcopyrite and chalcopyrite stringer ores is estimated to account for about 70% of the bulk In in the deposit; the remainder occurs as solid solution in massive sphalerite (Hannington et al., 1999). At the Brunswick No.12 deposit, In values were associated with sphalerite and chalcopyrite. The zinc concentrate contained concentrations of 400 ppm In and the copper concentrate had 200 ppm In (Werner, et al., 2015). At Neves Corvo, In is present as minor element in the structure of major minerals such as sphalerite, chalcopyrite, stannite group minerals, and tetrahedrite-tennantite group minerals. The highest In grades are observed in the zinc-rich ores at the Graça and Lombador orebodies and in the copper-zinc-rich ores of the Zambujal orebody (Pinto et al., 2013). Overall, in all orebodies of the Neves Corvo deposit, In grades vary between 20 to 1100 ppm and In, Cu, and Sn are positively correlated (Carvalho et al., 2014), especially in the bornite facies of massive cupriferous ores and stringer zones. This contrast with other In-bearing VHMS deposits where In and Zn are positively correlated.

In SHMS deposits of MVT and SEDEX types, In can be an important by-product of Zn-Pb (±Ag)-rich sulphides. However, SHMS deposits typically have lower In concentrations than VHMS deposits. Examples of SHMS deposits with high In content are Red Dog in the United States, Broken Hill and HYC in Australia, Rammelsberg in Germany, and Polaris in Canada. At the Rammelsberg SEDEX deposit, the highest In values were found in chalcopyrite replacement mineralization of bedded sphalerite ore, which had In values between 180 and 300 ppm (Schwarz-Schampera and Herzig, 2002). At the Polaris MVT deposit, In content was on average 100 ppm in the zinc concentrate (Pinto et al., 2014). Sphalerite from the Pine Point MVT deposit in Canada has variable In content (0 to 890 ppm; avg. 120 ppm), and sphalerite from the Robb Lake deposit in the northern Canadian Cordillera has similar In content of 0 to 750 ppm (avg. 167 ppm) (Paradis, unpublished data). However, sphalerite from other MVT deposits of the southern Canadian Cordillera has much lower In values (0 to 167 ppm; avg. 23.5 ppm). In all the Canadian MVT deposits, no positive correlation was observed between In and Zn, Fe, and Cu; instead, In seems to correlate with Sn, Ag, Ga, Ge, and Cd (Paradis, unpublished data).

5. Major germanium-bearing deposit types with focus on sediment-hosted Zn-Pb deposits

Germanium is widely distributed but recovered mainly from SHMS deposits (SEDEX, MVT, and Kipushi-type). The other main source of primary Ge production is the ash produced from lignite deposits. Germanium content of lignite ranges from 30 to >1000 ppm and can be enriched 5- to 10-fold in the ash (Frenzel et al., 2014). The Ge content in sulphide minerals (sphalerite and wurtzite) in SHMS deposits is between 0.1 and 1000 ppm Ge, and the average Ge content is in the order of 10s of ppm (Frenzel et al., 2014). During zinc smelting, Ge is enriched in the oxidic residues, typically by a factor of 10 compared to the

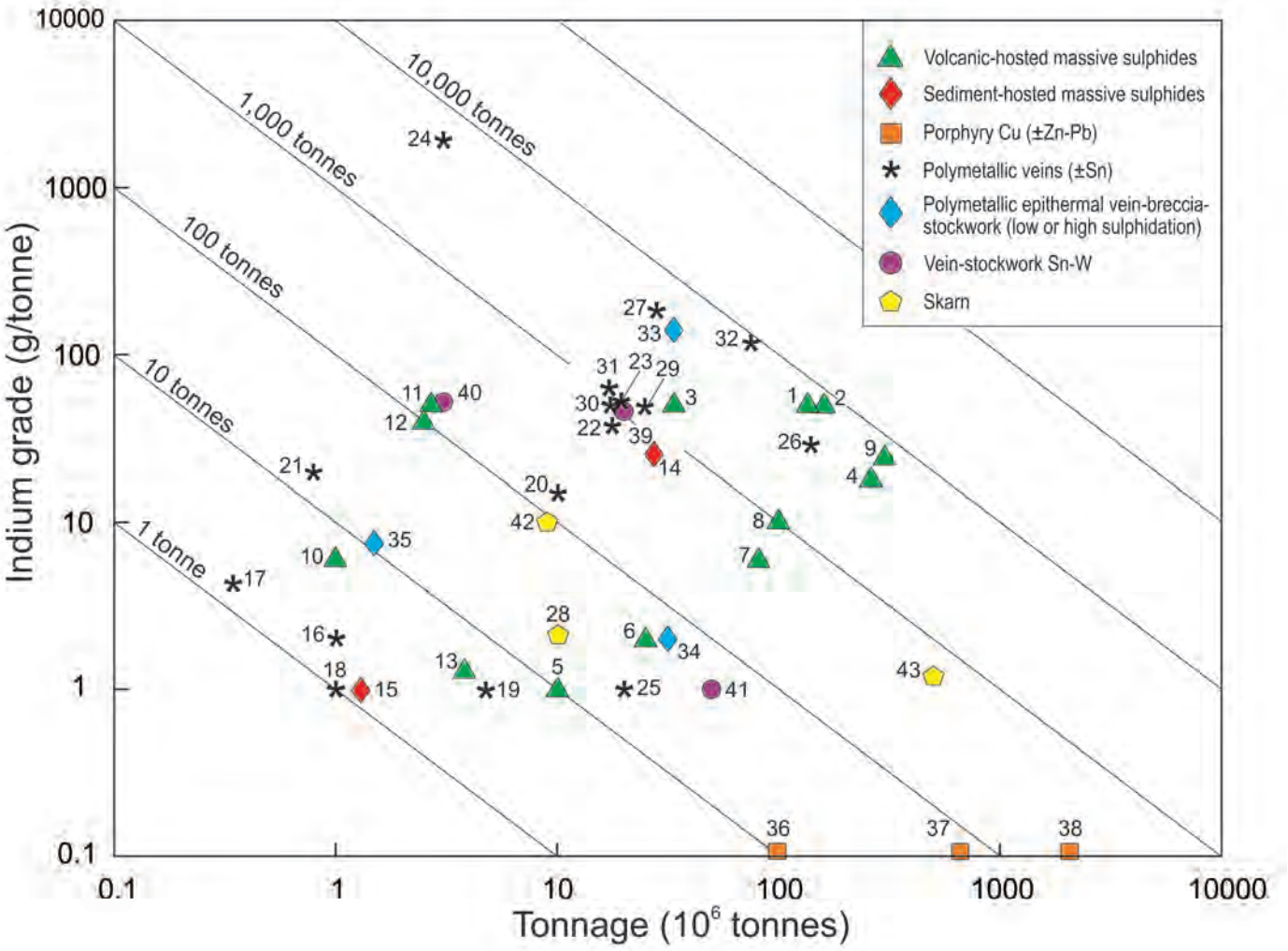

Fig. 3. Indium grade (g/tonne) versus tonnage (10^6 tonnes) for the main indium-bearing ore deposit types (modified from Schwarz-Schampera and Herzig, 2002). Deposit 1- Kidd Creek; 2- Brunswick No.12; 3 - Heath Steele; 4 - Neves-Corvo; 5 – Letneye; 6 – Komsomolskoye; 7 – Podolskoye; 8 – Sibaiskoye; 9 – Gaiskoye; 10 - Bakr-Tau; 11 - Maranda J; 12 - Lau Basin; 13 – TAG; 14 – Rammelsberg; 15 – Långban; 16 – Tosham; 17 – Omodani; 18 - W.Shropshire; 19 – Freiberg; 20 – Carguaicollu; 21 – Bolivar; 22 – Colquiri; 23 – Porco; 24 - Huari Huari; 25 -San Vicente; 26 – Potosi; 27 – Dulong; 28 – Morococha; 29 – Ashio; 30 – Akenobe; 31 – Ikuno; 32 – Dachang; 33 – Toyoha; 34 - Equity Silver; 35 – Kirki; 36 - Elacite/Asarel; 37 - Santa Rita; 38 – Bingham; 39 - Mount Pleasant; 40 - Baal Gammon; 41 – Cinovec; 42 – Ulsan; 43 - Cerro de Pasco.

original zinc concentrate (Dutrizac et al., 1996). In SEDEX, Ge content is typically 10-100 ppm, in MVT deposits, it is in the range of 100-1000 ppm, and in Kipushi-type deposits, Ge is 10-1000 ppm (Höll et al., 2007). Germanium can also be recovered from VHMS deposits, although they typically have low Ge concentrations (<100 ppm; e.g., Kuroko deposits, Japan).

Sphalerite in the Red Dog SEDEX deposit has an average Ge content of about 100 ppm (Kelley et al., 2004). The Trail smelter in Canada, which processes the zinc concentrates from Red Dog and Pend Oreille mines, produced about 40 tonnes of Ge in 2007 (Guberman, 2010). SEDEX deposits in China typically have much lower Ge content in sphalerite (<10 ppm; Ye et al., 2011). Indium concentrations in sphalerite from the sandstone-hosted Jinding deposit are slightly higher, with values ranging from 1.8 to 56.3 ppm (Ye et al., 2011).

Known MVT districts have higher Ge content in their zinc concentrates than SEDEX deposits, but values are variable. In MVT deposits, Ge is usually substituted into the sphalerite and wurtzite structures, and discrete Ge mineral inclusions are usually absent. Sphalerite at the Tres Marias MVT deposit in Mexico has on average 1000 ppm Ge (Melcher and Buchholz, 2014). The MVT deposits of the Tri-State district in the United States have 60 to 400 ppm Ge in sphalerite concentrates (Bonnet et al., 2014); those of the Appalachian Basin have much lower Ge values (avg. 10 ppm). MVT deposits of the Bleiberg district in Austria have on average 300 ppm Ge and produced a total of 126 tonnes of Ge. Sphalerite from the Huize MVT deposit in China has up to 354 ppm Ge, and sphalerite from the Niujiaotang MVT deposit has up to 546 ppm Ge (Bernstein, 1985; Höll et al., 2007, Ye et al., 2011). In Canada, the Pine Point MVT deposit has up to 600 ppm Ge (avg. 78 ppm; Paradis, unpublished data). Similar values are

obtained from sphalerite of the southern Canadian Cordillera MVT deposits (Paradis, unpublished data). In these deposits, Ge shows a positive correlation with Fe, and locally with Ga. Kipushi-type Cu-Zn-Pb-Ag-Ge deposits (Kipushi, Tsumeb and Kabwe) have some of the highest concentrations of Ge (up to 1.5%), and are host to several Ge-bearing minerals (e.g., briartite, reniérite, and germanite). Sphalerite in these deposits is not the main carrier of Ge as it contains <100 ppm Ge (Höll et al., 2007). Germanium is mostly carried by Ge minerals (germanite, reniérite, and briartite), stannoidite, enargite, and tennantite-tetrahedrite (Höll et al., 2007), which occur in Cu-rich and Zn-Cu-(Pb) mixed ores. It is interesting to note that Ge-rich ores may also be rich in Ga. At Kipushi in Democratic Republic of the Congo (DRC), the Cu-rich and Zn-Cu-(Pb) ores contain Ge- and Ga-rich ore masses that have up to 1.5% Ge and 2.5% Ga (Kampunzu et al., 2009). At Tsumeb, germanite (rare and replaced by reniérite at Kipushi) is the most abundant Ge-bearing phase. The Pb-Zn-Cu ore contains 0.6-1230 ppm Ge and 19-1130 ppm Ga (Kampunzu et al., 2009).

6. Major gallium-bearing deposit types with focus on sediment-hosted Zn-Pb deposits

Gallium is primarily recovered as a by-product from the industrial processes during the manufacture of aluminium metal upon treatment of bauxite, and processing of sphalerite in zinc sulphide ores. In bauxite, Ga occurs in concentrations of <10-160 ppm (avg. 50 ppm; Dittrich et al., 2011). Gallium concentrations in sphalerite of certain MVT deposits can reach values of 0.01 to 0.1%, greater than from most other types of deposits, but Ga content in these deposits is commonly erratic. As mentioned above, Ga can reach high concentrations in Kipushi-type deposits.

7. Relationship between In, Ge and Ga concentrations in sphalerite

Trace element content of sphalerite was suspected to indicate deposit-type for more than 75 years (Oftedahl, 1940). At least theoretically, the distinction can be made between the trace element signature of sphalerite in VHMS, SEDEX, MVT, skarns, and epithermal veins. Typically, In content is elevated in higher temperature systems, such as VHMS deposits, and Ga and Ge contents are higher in lower-temperature ores, such as MVT deposits (Cook et al., 2009).

8. Conclusions

Indium, Ge and Ga are minor and trace elements in a variety of mineral deposit types, but they can reach economic concentrations in base-metal deposits. Indium is typically more abundant in higher temperature base-metal deposits (i.e., VHMS), whereas Ge and Ga are more abundant in lower-temperature ore deposit-types (i.e., SEDEX and MVT). The presence or absence of these elements can, to a large extent, be correlated with ore deposit-type.

Indium, Ge and Ga are essential for a variety of high-technology applications such as integrated circuits, optoelectronic devices, fiber optics, thin-film coatings, and metal alloys, and the future demand for these metals will continue to increase. Exploration for base-metals has been highly cyclical in recent decades, but resurgence of global exploration for base-metal deposits will likely result in increased In, Ge, and Ga reserves. Assuming that the principle of supply and demand applies to In, Ga, and Ge, high demand for these elements may result in search and preferential development of base-metal deposits with economically recoverable concentrations of these elements.

Acknowledgments

Carlee Akam from the British Columbia Geological Survey helped with the compilation of statistical data. Review by Michaela Neetz of the British Columbia Geological Survey improved the clarity of the manuscript.

References cited

Berger, L.I., 2008. Handbook of Chemistry and Physics, 89th Edition. In: Lide, D.R., (Ed.), Boca Raton, United States, 2736 p.

Bernstein, L.R., 1985. Germanium geochemistry and mineralogy. Geochimica et Cosmochimica Acta, 49, 2409–2422.

Bonnet, J., Mosser-Ruck, R., André-Mayer, A.-S., Cauzid, J., and Bailly, L., 2014. Germanium distribution in sphalerite from North-East America MVT deposits: A multiscale study. Acta Geologica Sinica, 88 (supp. 2), 437-439.

Butcher, T., and Brown, T., 2014. Gallium. In: Gunn, G. (ed.), Critical Metals Handbook, John Wiley and Sons, Ltd., 150-176.

Carvalho, J.R.S., Relvas, J.M.R.S., Pinto, A.M.M., Marques, F., Rosai, C.J.P., Pacheco, N., and Fonseca, R., 2014. New insights on the metallogenesis of the Neves Corvo deposit: mineralogy and geochemistry of the zinc-rich Lombador orebody. Goldschmidt Abstracts, 2014, 353, 8-13 June, Sacramento, California.

Cook, N.J., Ciobanu, C.L., Pring, A., Skinner, W., Danyushevsky, L., Shimizu, M., Saini-Eidukat, B., Melcher, F., 2009. Trace and minor elements in sphalerite: a LA-ICP-MS study. Geochimica et Cosmochimica Acta 73, 4761–4791.

Cook, N.J., Ciobanu, C.L., and Williams, T., 2011. The mineralogy and mineral chemistry of indium in sulphide deposits and implications for mineral processing. Hydrometallurgy, 108, 226-228.

Dittrich, T.H., Seifert, T.H., and Gutzmer, J., 2011. Gallium in bauxite deposits. Mineralogical Magazine, 75(3), 765.

Dutrizac, J., Chen, T., and Longton, R., 1996. The mineralogical deportment of germanium in the Clarksville Electrolytic Zinc Plant of Savage Zinc Inc. Metallurgical and Materials Transactions B, 27, 567–576.

European Commission, 2015. Critical raw materials profiles. Report on critical raw materials for the EU, 202 p. http://ec.europa.eu/index_en.htm.

Frenzel, M., Ketris, M.P., and Gutzmer, J., 2014. On the geological availability of germanium. Mineralium Deposita, 49, 471-486.

Guberman, D.E., 2010. Germanium. U.S. Geological Survey 2008 Minerals Yearbook, 30.0-30.7. <http://minerals.usgs.gov/minerals/pubs/commodity/germanium/myb1-2007-germa.pdf>.

Guberman, D.E., 2015. Germanium. U.S. Geological Survey, Mineral Commodity Summaries. 64-65. http://minerals.usgs.gov/minerals/pubs/commodity/germanium/mcs-2015-germa.pdf.

Hammond, C.R., 2008. Handbook of Chemistry and Physics, 89th Edition. In: Lide, D.R., (Ed.), Boca Raton, United States, 2736 p.

Hannington, M.D., Bleeker, W., and Kjaersgaard, I., 1999. Sulfide mineralogy, geochemistry, and ore genesis of the Kidd Creek deposit: Part I North, Central, and South orebodies. Economic Geology, 10, 163-224.

Höll, R., Kling, M., and Schroll, E., 2007. Germanium: geochemistry, mineralogy, geology, and economics — a review. Ore Geology Reviews, 30, 145–180.

Jaskula, B.W., 2015. Gallium. U.S. Geological Survey, Mineral Commodity Summaries, 2015. United States Geological Survey, 58-59. http://minerals.usgs.gov/minerals/pubs/commodity/gallium/mcs-2015-galli.pdf accessed September, 25. 2015.

Kampunzu, A.B., Cailteux, J.L.H., Kamona, A.F., Intiomale, M.M., and Melcher, F., 2009. Sediment-hosted Zn–Pb–Cu deposits in the Central African Copperbelt. Ore Geology Reviews, 35, 263-297.

Kelley, K.D., Leach, D.L., Johnson, C.A., Clark, J.L., Fayek, M., Slack, J.F., Anderson, V.M., Ayuso, R.A., and Ridley, W.I., 2004. Textural, Compositional, and Sulfur Isotope Variations of Sulfide Minerals in the Red Dog Zn-Pb-Ag Deposits, Brooks Range, Alaska: Implications for Ore Formation. Economic Geology, 99, 1509-1532.

Ketris, M.P., and Yudovich, Y.E., 2009. Estimations of Clarkes for carbonaceous biolithes: World averages for trace element contents in black shales and coals. International Journal of Coal Geology, 78, 135–148.

Melcher, F., and Buchholz, O., 2014. Germanium. In: Gunn, G. (Ed.), Critical Metals Handbook, John Wiley and Sons, Ltd., 177-203.

Mercer, C.N., 2015. Indium—Bringing liquid-crystal displays into focus: U.S. Geological Survey Fact Sheet 2015-3012, 2 p., http://dx.doi.org/10.3133/fs20153012.

Mikolajczak, C., 2011. The economic linkage between zinc and germanium. International lead and zinc study group, Lisbon, Portugal, September 29, 2011, presentation, p. 24.

Moskalyk, R.R., 2003. Gallium: the backbone of the electronics industry. Minerals Engineering, 16, 921-929.

Oftedahl, I., 1940. Untersuchungen über die Nebenbestandteile von Erzmineralien norwegischer zinkblendführender Vorkommen. Skrift. Norsk Videnskabs Akademi Oslo, Mathematik-Naturvidenskab Kl 8, 1–103.

Pinto, A., Relvas, J.M.R.S., Carvalho, J.R.S., Pacheco, N., and Liu, Y., 2013. Mineralogy and distribution of indium and selenium metals within zinc-rich ore types of the Neves Corvo deposit, Portugal. GOLDSCHMIDT 2013, Florence, Italy.

Pinto, A., Relvas, J.M.R.S., Carvalho, J.R.S, Liu, Y., Pacheco, N., Pinto, F., and Fonseca, R., 2014. High-tech metals in the zinc-rich massive ores of the Neves Corvo deposit. Comunicações Geológicas (2014) 101, Especial II, 825-828. http://www.lneg.pt/iedt/unidades/16/paginas/26/30/185.

Polinares, 2012. Fact Sheet: Indium. POLINARES working paper n. 39, March 2012 http://www.polinares.eu/docs/d2-1/polinares_wp2_annex2_factsheet5_v1_10.pdf Accessed August 10, 2015.

Roskill (2011) Gallium: Global industry markets and outlook, 8th edition. Roskill Information Services Ltd., London, UK.

Rudnick, R.L., and Gao. S., 2003. Composition of the continental crust. In: Rudnick, R.L. (ed.), The Crust Vol. 3, Treatise on Geochemistry (eds. H.D. Holland and K.K. Turekian), Elsevier-Pergamon, Oxford, 64 p.

Schwarz-Schampera, U., and Herzig, P.M., 2002. Indium Geology, Mineralogy, and Economics. Springer, Heidelberg, 257p.

Schwarz-Schampera, U., 2014. Indium. In: Gunn, G. (ed.), Critical Metals Handbook, John Wiley and Sons, Ltd., 204-229.

Sinclair, W.D., 2014. Electronic metals (In, Ge and Ga): Present and future resources. Acta Geologica Sinica, 88 (supp. 2), 463-465.

Taylor, S.R., McLennan, S.M., 1985. The Continental Crust: Its Composition and Evolution. Blackwell Science, Oxford, 312 p.

Tolcin, A.C., 2012. Indium. U.S. Geological Survey, Mineral Commodity Summaries, January 2012. http://minerals.usgs.gov/minerals/pubs/commodity/indium/mcs-2012-indiu.pdf.

Tolcin, A.C., 2015. Indium. US geological Survey, Mineral Commodity Summaries, 2015. http://minerals.usgs.gov/minerals/pubs/commodity/indium/mcs-2015-indiu.pdf Accessed July 29, 2015.

Werner, T.T., Mudd, G.M., and Jowitt, S.M., 2015. Indium: key issues in assessing mineral resources and long-term supply from recycling. Applied Earth Science (Trans. Inst. Min. Metall. B). http://www.maneyonline.com/doi/abs/10.1179/1743275815Y.0000000007?journalCode=aes.

Ye, L., Cook, N.J., Ciobanu, C.L., Yuping, L., Qian, Z., Tiegeng, L., Wei, G., Yulong, Y., and Danyushevskiy, L., 2011. Trace and minor elements in sphalerite from base metal deposits in South China: A LA-ICPMS study. Ore Geology Reviews, 39 (4), 188–217.

Carbonatites and related exploration targets

George J. Simandl[1, 2, a]

[1] British Columbia Geological Survey, Ministry of Energy and Mines, Victoria, BC, V8W 9N3
[2] School of Earth and Ocean Sciences, University of Victoria, Victoria, BC, V8P 5C2
[a] corresponding author: george.simandl@gov.bc.ca

Recommended citation: Simandl, G.J., 2015. Carbonatites and related exploration targets. In: Simandl, G.J. and Neetz, M., (Eds.), Symposium on Strategic and Critical Materials Proceedings, November 13-14, 2015, Victoria, British Columbia. British Columbia Ministry of Energy and Mines, British Columbia Geological Survey Paper 2015-3, pp. 31-37.

1. Introduction

Mineralized carbonatite systems are multi-commodity, highly sought after, but poorly understood exploration targets (Mariano, 1989a, b; Pell, 1996; Birkett and Simandl, 1999). They are the main sources of niobium and rare earth elements (REE), which are considered critical metals for some key economic sectors (European Commission, 2014), and have become popular exploration targets for junior mining companies worldwide. Carbonatites also contribute to our understanding of the Earth's mantle (e.g., Bell and Tilton, 2001, 2002).

Herein, we discuss the definition and classification of carbonatites; summarize information pertinent for carbonatite exploration such as tectonic setting, shape, geophysical signature, associated rocks, alteration, and temporal distribution; and highlight the multi-commodity aspect of carbonatite-related exploration targets and mineral prospectivity.

2. Definition and classification

Carbonatites are defined by the International Union of Geological Sciences (IUGS) as igneous rocks containing more than 50% modal primary carbonates (Le Maitre, 2002). Depending on the predominant carbonate mineral, a carbonatite is referred to as a 'calcite carbonatite' (sövite), 'dolomite carbonatite' (beforsite) or 'ankerite carbonatite'. If more than one carbonate mineral is present, the carbonates are named in order of increasing modal concentrations, for example a 'calcite-dolomite carbonatite' is composed predominately of dolomite. If non-essential minerals (e.g., biotite) are present, this can be reflected in the name as 'biotite-calcite carbonatite'.

Where the modal classification cannot be applied, the IUGS chemical classification is used (Fig. 1). This classification subdivides carbonatites into calciocarbonatites, magnesiocarbonatites, and ferrocarbonatites. For calciocarbonatites, the ratio of CaO/(CaO+MgO+FeO $+Fe_2O_3$+MnO) is greater than 0.8. The remaining carbonatites are subdivided (based on wt.% ratios) into magnesiocarbonatite [MgO > (FeO+Fe_2O_3+MnO)] and ferrocarbonatite [MgO < (FeO+Fe_2O_3+MnO)] (Woolley and Kempe, 1989; Le Maitre, 2002). If the SiO_2 content of the rock exceeds 20%, the rock is referred to as silicocarbonatite.

When the IUGS chemical classification is used, care should be taken to ensure that magnetite and hematite-rich calciocarbonates or magnesiocarbonatites are not erroneously classified as ferrocarbonatites (Gittins and Harmer, 1997).

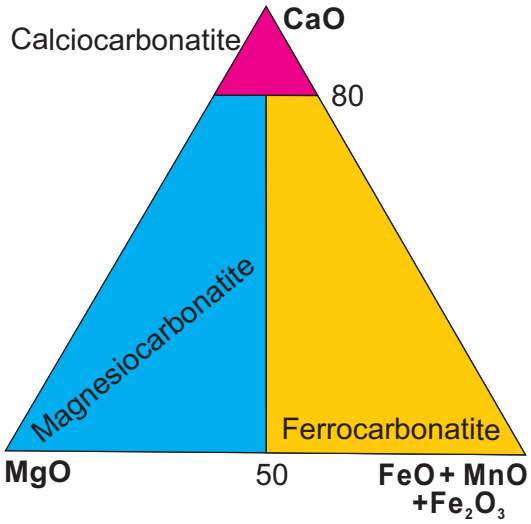

Fig. 1. IUGS classification of carbonatites (Le Maitre, 2002).

A refinement to the IUGS chemical classification based on molar proportions (Gittins and Harmer, 1997), introduced 'ferrugineous' carbonatites (Fig. 2). The boundary separating calciocarbonatites from magnesiocarbonatites and 'ferrugineous' carbonatites is set at 0.75, above which carbonatites contain more than 50% calcite on a molar basis. Although not universally accepted, Gittins and Harmer's classification is commonly used in studies of carbonatite-hosted ore deposits. A mineralogical-genetic classification of carbonatites was proposed by Mitchell (2005). His paper points to pitfalls of the IUGS classification and subdivides carbonatites into 'primary carbonatites' and 'carbothermal residua'. The introduction of the term 'carbothermal residua' is significant as it alerts mantle specialists to fundamental processes involved in the formation of many carbonatite-related deposits, and reduces rifts between camps of ore deposit geologists, petrologists, and mantle specialists. From the exploration perspective, the current IUGS classification is too restrictive.

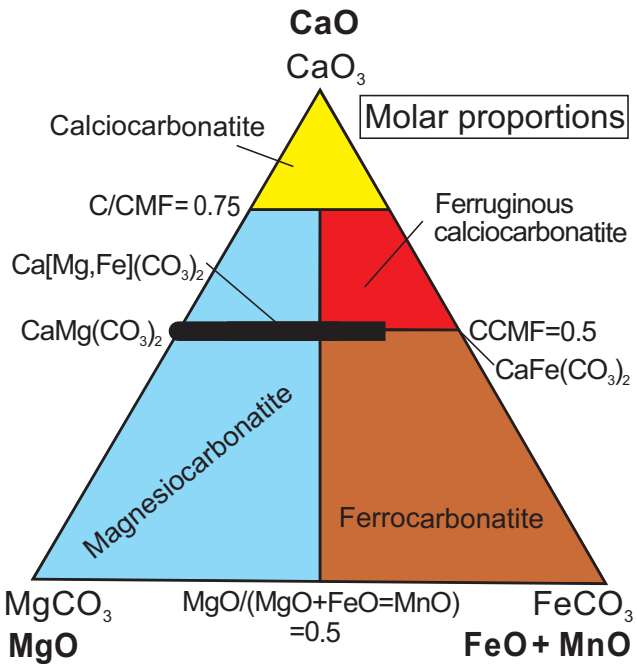

Fig. 2. Carbonatite classification according to Gittins and Harmer (1997).

3. Exploring for carbonatites: Where to look and what to look for

3.1. Tectonic setting, geometry, and geophysical signature

Most carbonatites are emplaced in continental extensional settings along large-scale, intra-plate fracture zones or rifts. Some are in orogenic belts. They may have been emplaced during post-orogenic extensional collapse or before a transition from rift to compressional tectonic regime. In rare cases, carbonatites are in oceanic environments (Woolley and Kjarsgaard, 2008a). Carbonatites are components of alkaline complexes, or occur as isolated pipes, sills, dikes, plugs, lava flows, and pyroclastic blankets. Where not severely deformed by post intrusive tectonic activity, many carbonatites display circular, ring, or crescent-shaped aeromagnetic and radiometric anomalies (Satterly, 1970; Thomas et al., 2011). Deformation, metamorphism, hydrothermal and supergene alteration may significantly change the shape or apparent shape of a carbonatite, the mineralogical, chemical, and textural characteristics of the ore and gangue minerals, and the shape and grade of the mineralized zone. Ore minerals stable in a surface environment may be concentrated by weathering.

3.2. Carbonatite-associated igneous rocks

Most intrusive carbonatite occurrences are spatially tied to one or more of seven intrusive silicate rock groups including melilitolites, ijolites, akali gabbros, feldspathoid syenites, syenites, kimberlites, and lamprophyres and/or their volcanic equivalents (Woolley and Kjarsgaard, 2008b). Peridotites and pyroxenites, commonly found near ijolites and melilitolites, are not considered as a distinct association because they are interpreted as cumulates (Woolley and Kjarsgaard, 2008a). Nevertheless, these rocks are important from the exploration point of view because they are most commonly observed in deeply eroded carbonatite complexes, providing indirect information about the depth of erosion and, by extension, about the mineralization potential of the complex (Frolov, 1970; Epshteyn and Kaban'kov, 1984). Phoscorites are "magnetite, olivine, apatite rocks usually associated with carbonatites" (Le Maitre, 2002). This definition is restrictive because olivine commonly retrogrades into pyroxene, amphibole, and serpentine. A much broader definition and classification of 'phoscorites' is anchored in Russian literature (e.g., Yegorov, 1993). Krasnova et al. (2004) proposed that phoscorite should be redefined as a "plutonic ultramafic rock comprising magnetite, apatite, and one of the silicates, forsterite, diopside, or phlogopite". According to Krasnova et al. (2004) most of the 21 phoscorite (sensu lato) occurrences that they were aware of are mineralized. If this broader definition were applied worldwide, the number of phoscorite occurrences would increase dramatically. For example, in British Columbia, the Aley carbonatite and several carbonatites in the Blue River area would be considered to contain phoscorite units.

In some cases, carbonatite represents only a small part of a carbonatite complex. Consequently, recognizing the spatial association of carbonatites to related intrusive silicate rocks and to phoscorite substantially increases the size of an exploration target (Fig. 3).

3.3. Alteration

A fenitization halo (typically desilicification with the addition of Fe^{3+}, Na, K, ± Ca, ± Al) surrounds carbonatites or carbonatite/alkaline complexes (Morogan, 1994; Smith, 2007; Le Bas, 2008; Williams-Jones and Palmer, 2002). Several generations of fenites may be present in the same complex and

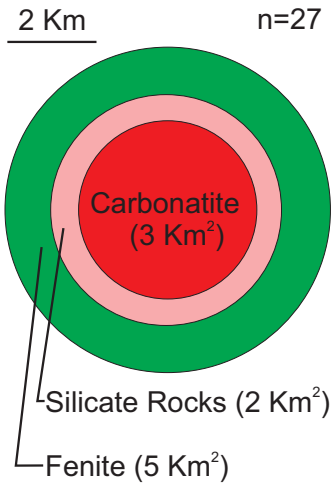

Fig. 3. The average surface area of carbonatites is approximately 3 km^2. In most cases the carbonatites are surrounded by alkali silicate rocks, which are in turn surrounded by a zone of fenitization. If a geologist recognizes the carbonatite, associated fenitized zone (~5 km^2), and associated silicate rocks (~2 km^2) the target area increases to 10 km^2. The surface areas of the 27 carbonatite complexes used to prepare this figure vary from 0.01 to 78.5 km^2.

may be genetically associated with the carbonatites and related alkaline igneous rocks. Depending on the size, orientation, and shape of the carbonatite intrusion, as well as the nature of the host rock, incorporating fenitization into the carbonatite model may more than double the surface area of an exploration target (Fig. 3). Fenitization may be manifested by the presence of Na- and K-amphiboles, aegerine-augite, wollastonite, nepheline, mesoperthite, antiperthite, pale brown mica, and albite. Intensity of fenitization may be used to vector towards a carbonatite (Simandl et al., 2013).

3.4. Temporal patterns: Can carbonatite ages be used to screen explorations targets?

Frequency plots of carbonatites with well-established ages indicate a general trend with the number of carbonatites decreasing with age (Fig. 4). The reasons for this trend are unclear (Veizer, 1992; Woolley and Kjarsgaard, 2008a). The frequency of mineralized carbonatite occurrences follows a similar pattern, except for the interval between 150 and 0 Ma. Relatively shallow erosional levels may explain this divergence, because most carbonatite-related mineralization is spatially related to intrusive carbonatite phases,whereas near-surface equivalents are commonly barren, unless subjected to supergene enrichment. In view of the broad temporal range of carbonatites, and the divergence within the 150 and 0 Ma interval, ages alone are of limited use in screening carbonatite exploration targets.

4. Carbonatite-related ore deposits

Carbonatites, carbonatite complexes (including carbonatite-related igneous rocks) and, in some cases, associated fenite zones and overlying regoliths (including zones of supergene enrichment) are favourable hosts of metallic and industrial minerals (Fig. 5). Reviews and compilations of carbonatite-related mineralization are provided by Deans (1966), Heinrich (1980), Mariano (1989a, b), Pell (1996), Richardson and Birkett (1996a, b), Birkett and Simandl (1999), Woolley and Kjarsgaard (2008a), Berger et al. (2009), Simandl (2014), and Mackay and Simandl (2014, 2015).

Carbonatite complexes and carbonatite-related deposits are currently the main sources, and represent large resources of light rare earth elements (e.g., Bayan Obo, China; Maoniuping, China; Mountain Pass, USA; Mount Weld, Australia) and niobium (e.g., Catalão, Brazil; Lueshe, South Africa; St. Honoré, Oka, and Aley, Canada) as summarized by Verwoerd (1986), Mariano (1989a, b), Berger et al. (2009), Simandl (2014), and Mackay and Simandl (2014). In terms of REE, the ore may consist of unweathered carbonatite rock such as at Mountain Pass, USA, (Castor, 2008) and St-Honoré, Canada, (Lafleur and Ayad, 2012) and/or overlying regolith such as at Mount Weld, Australia (Lynas Corp., 2015; Lottermoser, 1990). The REE mineralization tends to be concentrated in late carbonatite phases such as ferrocarbonatites or calcio-carbonatites, forming central breccia zones, ring dikes, or cone sheets. However, they can also be distal to the carbonatite (e.g., Bayan Obo, China, Smith et al., 2015). Similarly, Nb ore may be part of a carbonatite rock unit (e.g., St-Honoré, Canada, Tremblay et al., 2015), carbonatite-associated alkaline rocks (e.g., Crevier deposit, Canada, Solgadi et al., 2015), fenitized zones, and/or in overlying regolith (e.g., Catalão I, Brazil, Cordeiro et al., 2011; Araxá, Brazil, Issa Filho et al., 2015). Vermiculite and phlogopite deposits are predominantly hosted by mafic or ultramafic units of the carbonatite system (e.g., Northern pyroxenite at Palabora, South Africa, Heinrich, 1970; Fourie and De Jager, 1986), near the contacts of carbonatites with these rocks, or within mafic country rocks (e.g., Upper Fir carbonatite, Canada, Simandl et al., 2010). Most carbonatite-related apatite deposits currently in production, such as Tapira, Brazil (Capponi et al., 2009), Ipanema, Brazil (Born, 1986), and Catalão I, Brazil (Carvalho and Bressan, 1986), were enriched

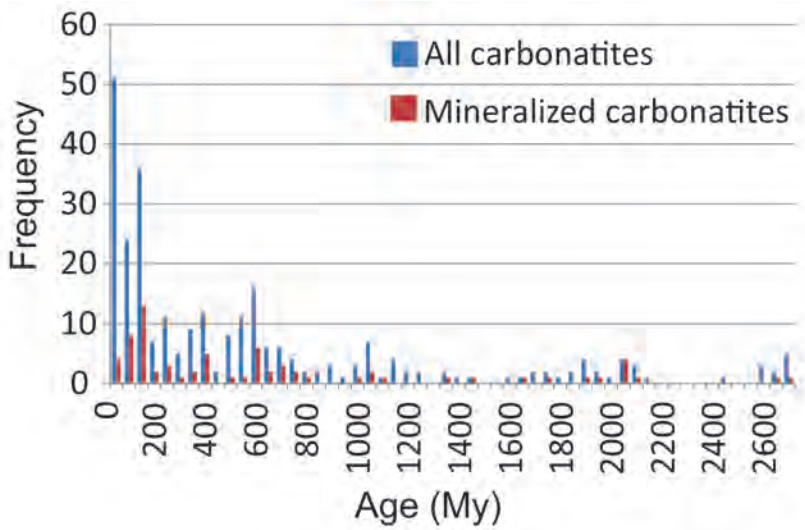

Fig. 4. The frequency of all known carbonatite occurrences with isotopic ages decreases with time. With the exception of carbonatites younger than 150 Ma, the frequency of mineralized carbonatite occurrences shows a similar decrease. Figure based on data from Woolley and Kjarsgaard (2008a), with minor updates.

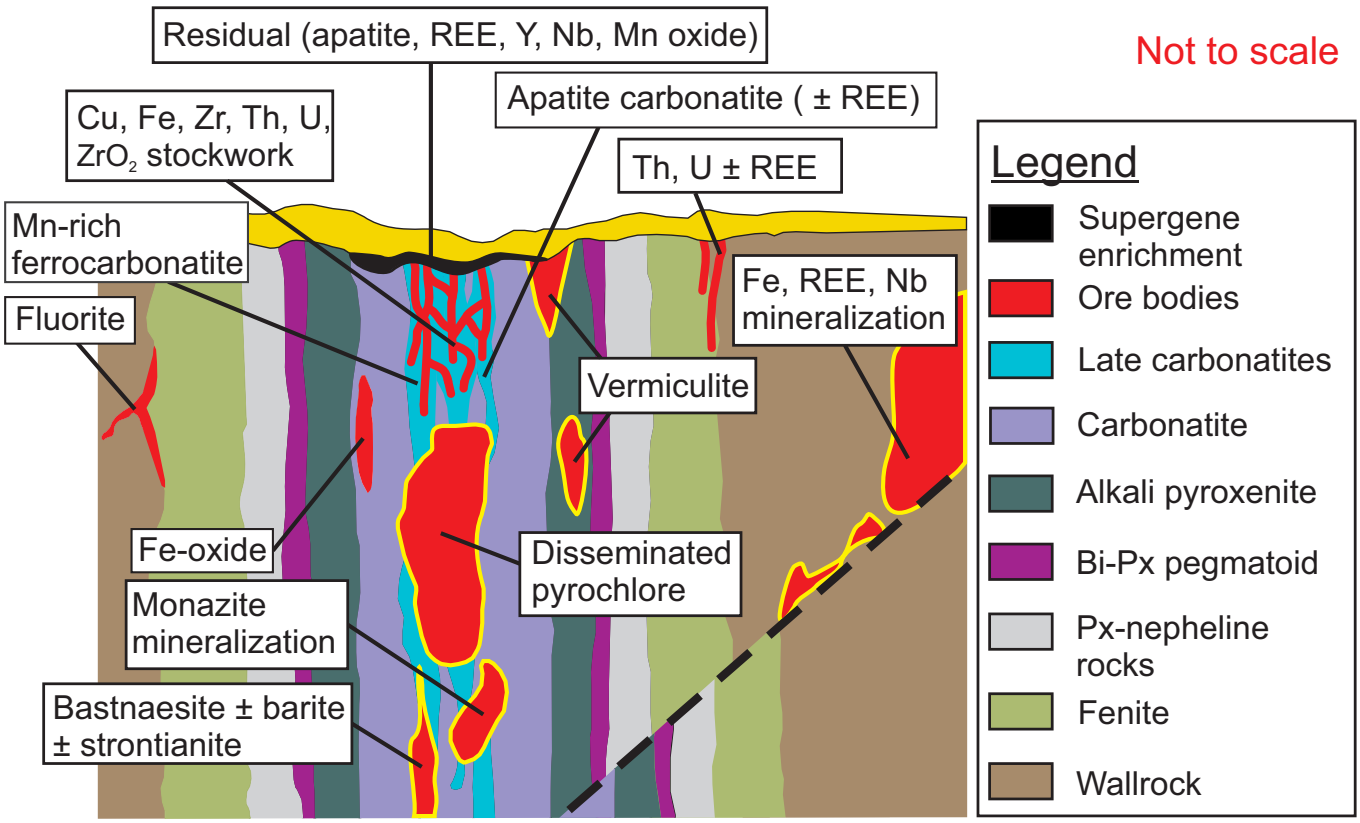

Fig. 5. Vertical section of a hypothetical carbonatite mineralizing system, modified from Laznicka (2004).

by weathering. Exceptions are Siilinjärvi mine, Finland (O'Brien et al., 2015) and Cajati mine, Brazil (Alves, 2008). Copper, uranium, thorium, and baddeleyite (natural zirconia) were produced for decades from the Palabora carbonatite in South Africa (Heinrich, 1970; Clarke, 1981), but baddeleyite is currently produced only from the Kovdor deposit in Russia (Dickson, 2015).

Other materials produced from carbonatite or related deposits are: iron (Kovdor, Russia, Dickson, 2015; Bayan Obo, China, Smith et al., 2015; Palabora, South Africa, Heinrich, 1970); fluorite (Mato Preto, Brazil; Okorusu, Namibia; Amba Dongar, India; Hagni, 1999); carbonates for lime and cement production (Tororo, Uganda and Xiluvo, Mozambique, van Straaten, 2002; Jacupiranga, Brazil, Alves, 2008); and sodalite for use as dimension, ornamental and semi-precious stone (Swartboosdrift, Namibia, Menge, 1986; Cerro Sapo, Bolivia, Schultz et al., 2004). Some carbonatites, such as Tapira, Brazil (Swanepoel, 2014) and Powder Horn, USA (Van Gosen and Lowers, 2007), represent large resources of titanium minerals, and are being evaluated for future development.

5. Successful exploration and development of carbonatite-related deposits: What are the odds?

As a rule of thumb, the exploration industry considers that less than one in 1,000 discoveries becomes a profitable mine (Marshall, 2012; Preston, 2015). According to the Ontario Mining Association (2015), the odds are even lower: "Only about one mineral exploration project in ten is taken to the drill stage, and one drill program in 1000 finds a viable mineral deposit".

Interpretation of data compiled by Woolley and Kjarsgaard (2008a) indicates that about 6% of known carbonatites host active mines, 3% hold historic mines, and 11% contain an established resource (Fig. 6). These numbers suggest that carbonatites have exceptional potential, and that a newly discovered carbonatite or carbonatite complex has a 9 out of 100 probability of hosting a mine.

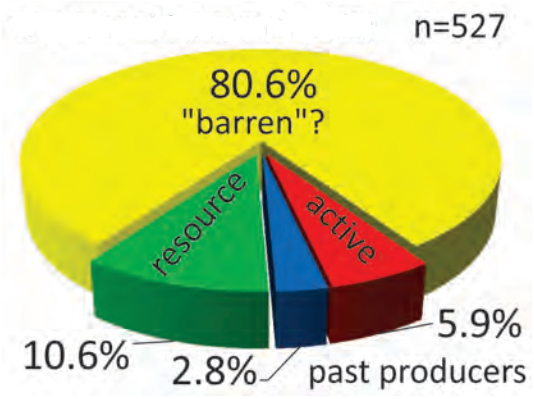

Fig. 6. Prospectivity of newly discovered carbonatite. Interpretation based on data from Woolley and Kjarsgaard (2008a).

6. Conclusion

Carbonatite-related deposits are significant sources of Nb, LREE, Fe, Cu, baddeleyite, vermiculite, phlogopite, fluorite, apatite, calcium carbonate, and sodalite, and have historically provided U, and Th. Given that 9 out of 100 carbonatites contain currently producing or historic mines, carbonatite mineralizing systems represent outstanding multi-commodity exploration targets. Identifying and incorporating carbonatite-related silicate igneous rocks and fenitites into carbonatite models results in increased size of exploration targets. Carbonatites range from Archean to Recent and hence age alone is not a valid prospectivity indicator, although within the same complex, the latest carbonatite pulses are commonly enriched in REE, and metasomatic overprinting may result in remobilization of these elements.

Acknowledgments

This project was supported by the Targeted Geoscience Initiative 4 (2010–2015), a Natural Resources Canada program. The Specialty Metal component of this program was carried out collaboratively between the Geological Survey of Canada and the British Columbia Geological Survey. Reviews by Pearce Luck, Carlee Akam, and Michaela Neetz, from the British Columbia Geological Survey,Victoria are greatly appreciated. Suggestions of Anthony E. William-Jones from McGill University, Montréal and Michaela Neetz from the British Columbia Geological Survey, Victoria greatly improved this manuscript.

References cited

Alves, P.R., 2008. The carbonatite-hosted apatite deposit of Jacupiranga, SE Brazil: styles of mineralization, ore characterization and association with mineral processing. MSc Thesis, Missouri University of Science and Technology, 140p. <http://scholarsmine.mst.edu/cgi/viewcontent.cgi?article=7722&context=masters_theses> Accessed August 6, 2015.

Bell, K., and Tilton, G.R., 2001. Nd, Pb and Sr isotopic compositions of east African carbonatites: evidence for mantle mixing and plume inhomogeneity. Journal of Petrology, 42, 1927–1945.

Bell, K., and Tilton, G.R., 2002. Probing the mantle: the story from carbonatites. American Geophysical Union, Eos Transactions, 83, 273, 276–277.

Berger, V.I., Snger, D.A., and Orris, G.J., 2009. Carbonatites of the world, explored deposits of Nb and REE – database and grade and tonnage models. U.S. Geological Survey Open-File Report 2009-1139, 17p. < http://pubs.usgs.gov/of/2009/1139/> Accessed August 4, 2015.

Birkett, T.C., and Simandl, G.J., 1999. Carbonatite associated deposits: magmatic, replacement and residual. In: Simandl, G.J., Hora, Z.D., and Lefebure, D.V. (Eds.), Selected British Columbia Mineral Deposit Profiles, Vol. 3: Industrial Minerals and Gemstones. British Columbia Ministry of Energy, Mines and Petroleum Resources, British Columbia, Geological Survey, Open File 1999-10. <http://www.empr.gov.bc.ca/Mining/Geoscience/MineralDepositProfiles/ListbyDepositGroup/Pages/NCarbonatites.aspx#n01> Accessed August 6, 2015.

Born, H., 1986. The Ipanema phosphate deposit, São Paulo, Brazil. In: Notholt, A.J.G., Sheldon, R.P., and Davidson, D.F., (Eds.), Phosphate Deposits of the World, Volume 2, Phosphate Rock Resource, Cambridge University Press, Cambridge, pp.116-119.

Capponi, L., Peroni, R.D.L., Grasso, C.B., and Fontes, S.B., 2009. Sampling protocol review of a phosphate ore mine to improve short term mine planning. In: Fourth World Conference on Sampling and Blending. The Southern African Institute of Mining and Metallurgy, Paper 40, pp. 65-72.

Carvalho, W.T., and Bressan, S.R., 1986. The phosphate deposit of Catalão I ultramafic alkaline complex, Goiás, Brazil. In: Notholt, A.J.G., Sheldon, R.P., and Davidson, D.F., (Eds.), Phosphate Deposits of the World, Volume 2, Phosphate Rock Resource, Cambridge University Press, Cambridge, pp.104-110.

Castor, S.B., 2008. The Mountain Pass rare-earth carbonatite and associated ultrapotassic rocks, California. The Canadian Mineralogist, 46, 779-806.

Clarke, G., 1981. The Palabora complex – triumph over low grade ores. Industrial Minerals, No. 169, 45-62.

Deans, T., 1966. Economic mineralogy of African carbonatites. In: Tuttle, O.F., and Gittins, J., (Eds.), Carbonatites, Wiley, New York, pp. 358-413.

Cordeiro, P.F.O., Brod, J.A., Palmieri, M., de Oliveira, C.G., Barbosa, E.S.R., Santos, R.V., Gaspar, J.C., and Assis, L.C., 2011. The Catalão I niobium deposit, central Brazil: Resources, geology and pyrochlore chemistry. Ore Geology Reviews, 41, 112-121.

Dickson, J.S., 2015. EuroChem reveals phosphate expansion plans at Kovdor and beyond. Industrial Minerals, May 2015. <http://www.indmin.com/Article/3455925/EuroChem-reveals-phosphate-expansion-plans-at-Kovdor-and-beyond.htm> Accessed August 5, 2015.

Epshteyn, Ye.M, and Kaban'kov, V.Ya., 1984. The depth of emplacement and mineral potential of ultramafic, ijolite, and carbonatite plutons. International Geology Review, 26, 1402-1415.

European Commission, 2014. Report on critical raw materials for the EU. <http://ec.europa.eu/enterprise/policies/raw-materials/files/docs/crm-report-on-critical-raw-materials_en.pdf> Accessed August 6, 2015.

Fourie, P.J., and De Jager, D.H., 1986. Phosphate in the Phalaborwa complex. In: Anhaeusser, C.R., and Maske, S., (Eds.), Mineral Deposits of Southern Africa, II, The Geological Society of South Africa, pp. 2239-2253.

Frolov, A.A., 1970. Vertical zonation in deposition of ore, as in ultrabasic-alkaline rocks and carbonatites: International Geology Review, v. 13, p. 685-695.

Gittins, J., and Harmer, R.E., 1997. What is ferrocarbonatite? A revised classification. Journal of African Earth Sciences, 25, 159-168.

Hagni, R.D., 1999. Mineralogy of beneficiation problems involving fluorspar concentrates from cabonatite-related fluorspar deposits. Mineralogy and Petrology, 67, 33-44.

Heinrich, E.W.M., 1970. The Palabora carbonatitic complex – a unique copper deposit. The Canadian Mineralogist, 10, 585-598.

Heinrich, E.W.M., 1980. The geology of carbonatites. Robert E. Kreiger Publishing Company, Huntington, New York, 585p.

Issa Filho, A., Riffel, B.F., and de Faria Sousa, C.A., 2015. Some aspects of the mineralogy of CBMM niobium deposit and mining and pyrochlore ore processing – Araxá, MG – Brazil. < http://www.cbmm.com.br/Repositorio/Media/site/internas/operations/minerologyaspectsniobiumdeposit.pdf>. Accessed: October 27, 2015.

Krasnova, N.I., Petrov, T.G., Balaganskaya, E.G., Garcia, D., Moutte, J., Zaitsev, A.N., and Wall, F., 2004. Introduction to phoscorites: occurrence, composition, nomenclature and petrogenesis. In: Wall, F., and Zaitsev, A.N., (Eds.), Phoscorites and Carbonatites from Mantle to Mine: the Key Example of the Kola Alkaline Province: The Mineralogical Society, London, pp. 1-36.

Lafleur, P.J., and Ayad, A.B., 2012. NI 43-101 technical report to present the mineral resources of the rare earth elements zone Niobec Mine – IAMGOLD Corporation. 145p. <www.sec.gov/Archives/edgar/data/1203464/000119312512119663/

d317389dex991.htm> Accessed August 4, 2015.
Laznicka, P., 2004. Total Metallogeny-Geosites. AMF, Adelaide, 740 p and poster.
Le Bas, M.J., 2008. Fenites associated with carbonatites. The Canadian Mineralogist, 46, 915-932.
Le Maitre, R.W., 2002. Igneous Rocks: A Classification and Glossary of Terms. Cambridge University Press, Cambridge, U.K., 236 p.
Lottermoser, B.G., 1990. Rare-earth element mineralisation within the Mt. Weld carbonatite laterite, Western Australia. Lithos, 24, 151-167.
Lynas Corp., 2015. Mount Weld mineral resource and ore reserve update 2015. <https://www.lynascorp.com/PublishingImages/Pages/Mt-Weld-Resources-and-Reserves/ASX%20Announcement%20-%20Ore%20Reserves%20and%20Resources%20FINAL%20051015.pdf>. Accessed October 27, 2015.
Mackay, D.A.R., and Simandl, G.J., 2014. Geology, market and supply chain of niobium and tantalum-a review. Mineralium Deposita, 49, 1025-1047.
Mackay, D.A.R. and Simandl, G.J., 2015. Niobium and tantalum: Geology, markets, and supply chains. In: Simandl, G.J. and Neetz, M., (Eds.), Symposium on Strategic and Critical Materials Proceedings, November 13-14, 2015, Victoria, British Columbia. British Columbia Ministry of Energy and Mines, British Columbia Geological Survey Paper 2015-3, pp. 13-22.
Mariano, A.N., 1989a. Economic geology of rare earth minerals. In: Lipman, B.R., McKay, G.A., (Eds.), Geochemistry and mineralogy of rare earth elements. Mineralogical Society of America, Chantilly, Reviews in mineralogy v. 21, pp. 303–337.
Mariano, A.N., 1989b. Nature of economic mineralization in carbonatites and related rocks. In: Bell, K., (Ed.), Carbonatites: genesis and evolution. Unwin Hyman, London, pp. 149–176.
Marshall, L., 2012. Hitting paydirt. Mines, Colorado School of Mines Magazine. <http://minesmagazine.com/6211/> Accessed August 5, 2015.
Menge, G.F.W., 1986. Sodalite carbonatite deposits of Swartbooisdrif, South West Africa/Namibia. In: Anhaeusser, C.R., and Maske, S. (Eds.), Mineral Deposits of Southern Africa, II. The Geological Society of South Africa, pp. 2261-2268.
Mitchell, R.H., 2005. Carbonatites and carbonatites and carbonatites. The Canadian Mineralogist, 43, 2049-2068.
Morogan, V., 1994. Ijolite versus carbonatite as sources of fenitization. Terra Nova, 6, 166-176.
O'Brien, H., Heilimo, E., and Heino, P., 2015. The Archean Siilinjärvi carbonatite complex. In: Maier, D.W., Lahtinen, R., and O'Brien, H., (Eds.), Mineral Deposits of Finland, Elsevier, pp. 327-343.
Ontario Mining Association, 2015. Mining 101. <http://www.oma.on.ca/en/ontariomining/Mining101.asp?hdnContent=> Accessed August 5, 2015.
Pell, J., 1996, Mineral deposits associated with carbonatites and related alkaline igneous rocks. In: Mitchell, R.H., (Ed.), Unsaturated alkaline rocks: Mineralogy, petrogenesis, and economic potential. Mineralogical Association of Canada, Short Course Series, v. 4, pp. 271-310.
Preston, G., 2015. Roundup takeaway 1: outsmart tough odds. Mining.com. <http://www.mining.com/web/roundup-takeaway-1-outsmart-tough-odds/> Accessed August 5, 2015.
Richardson, D.G., and Birkett, T.C., 1996a. Carbonatite associated deposits. In: Eckstrand, O.R., Sinclair, W.D., and Thorpe, R.I., (Eds.), Geology of Canada 8: Geology of Canadian deposit types. Geological Survey of Canada, pp. 541-558.
Richardson, D.G., and Birkett, T.C., 1996b. Residual carbonatite-associated deposits. In: Eckstrand, O.R., Sinclair, W.D., and Thorpe, R.I., (Eds.), Geology of Canada 8: Geology of Canadian mineral deposit types. Geological Survey of Canada, pp. 108-119.
Satterly, J., 1970. Aeromagnetic maps of carbonatite-alkalic complexes in Ontario. Ontario Department of Mines and Northern Affairs, Preliminary Map no. P452 (revised).
Schultz, F., Lehmann, B., Tawackoli, S., Rössling, R., Belyatsky, B., and Dulski, P., 2004. Carbonatite diversity in the Central Andes: the Ayopaya alkaline province, Bolivia. Contributions to Mineralogy and Petrology, 148, 391-408.
Simandl, G.J., 2014. Geology and market-dependent significance of rare earth element resources. Mineralium Deposita, 49, 889-904.
Simandl, G.J., Paradis, S., Simandl, L., and Dahrouge, J., 2010. Vermiculite in the Blue River Area, East-Central British Columbia, Canada. In: Geological Fieldwork 2009, British Columbia Ministry of Energy, Mines and Natural Gas, British Columbia Geological Survey Paper 2010-1, pp. 83-91.
Simandl, G.J., Reid, H.M., and Ferri, F., 2013. Geological setting of the Lonnie niobium deposit, British Columba, Canada. In: Geological Fieldwork 2012, British Columbia Ministry of Energy, Mines and Natural Gas, British Columbia Geological Survey Paper 2013-1, pp. 127-138.
Smith, M.P., 2007. Metasomatic silicate chemistry at the Bayan Obo Fe-REE-Nb deposit, Inner Mongolia, China: Contrasting chemistry and evolution of fenitizing and mineralizing fluids. Lithos, 93, 126-148.
Smith, M.P., Campbell, L.S., and Kynicky, J., 2015. A review of the genesis of the world class Bayan Obo Fe-REE-Nb deposits, Inner Mongolia, China: Multistage processes and outstanding questions. Ore Geology Reviews, 64, 459-476.
Solgadi, F., Groulier, P.-A., Moukhsil, A., Ohnenstetter, D., André-Mayer, A.-S., and Zeh, A., 2015. Nb-Ta-REE mineralization associated with the Crevier alkaline intrusion. In: Simandl, G.J. and Neetz, M., (Eds.), Symposium on Strategic and Critical Materials Proceedings, November 13-14, 2015, Victoria, British Columbia. British Columbia Ministry of Energy and Mines, British Columbia Geological Survey Paper 2015-3, pp. 69-74.
Swanepoel, E., 2014. Iluka in Brazil titanium deal with Vale. Creamer Media's Mining Weekly. <http://www.miningweekly.com/print-version/iluka-in-brazil-titanium-deal-with-vale-2014-06-04> Accessed August 6, 2015.
Thomas, M.D., Ford, K.L., and Keating, P., 2011. Exploration Geophysics for intrusion-hosted rare earth metals. Geological Survey of Canada, Open File 6828 (Poster). <http://ftp2.cits.rncan.gc.ca/pub/geott/ess_pubs/288/288092/of_6828.pdf> Accessed Oct. 30, 2015.
Tremblay, J., Bédard, L.P., and Matton, G., 2015. A petrographic study of Nb-bearing minerals at the Saint-Honoré niobium deposit. In: Simandl, G.J. and Neetz, M., (Eds.), Symposium on Strategic and Critical Materials Proceedings, November 13-14, 2015, Victoria, British Columbia. British Columbia Ministry of Energy and Mines, British Columbia Geological Survey Paper 2015-3, pp. 75-81.
Van Gosen, B., and Lowers, H., 2007. The Iron Hill (Powderhorn) carbonatite complex, Gunnison County, CO – a potential source of several uncommon mineral resources. Proceedings of 2007 SME Annual Meeting, Denver, Colorado, Society for Mining, Metallurgy, and Exploration, pp.298-305.
van Straaten, P., 2002. Rocks for Crops: Agrominerals of sub-Saharan Africa. ICRAF, Nairobi, Kenya, 338p.
Veizer, J.E.A., 1992. Temporal distribution of carbonatites. Geology, 20, 1147–1149.
Verwoerd, W.J., 1986. Mineral deposits associated with carbonatites and alkaline rocks. In: Anhaeusser, C.R., and Maske, S., (Eds.), Mineral Deposits of Southern Africa, II. The Geological Society of South Africa, pp. 2173-2191.
Williams-Jones, A.E., and Palmer, D.A.S., 2002. Fluid evolution of the Amba Dongar carbonatite complex, India. Chemical Geology, 185, 283-301.
Woolley, A.R., and Kempe, D.R.C., 1989. Carbonatites: nomenclature, average chemical compositions and element

distribution. In: Bell, K., (Ed.), Carbonatites: Genesis and Evolution. Unwin Hyman, London, pp. 1-14.
Woolley, A.R., and Kjarsgaard, A., 2008a. Carbonatite occurrences of the world: map and database. Geological Survey of Canada, Open File 5796, 22p.
Woolley, A.R., and Kjarsgaard, A., 2008b. Paragenetic types of carbonatite as indicated by the diversity and relative abundances of associated silicate rocks: evidence from a global database. The Canadian Mineralogist, 46, 741-752.
Yegorov, L.S., 1993. Phoscorites of the Maymecha-Kotuy ijolite-carbonatite association. International Geology Review, 35, 346-358.

Carbonatites, isotopes and evolution of the subcontinental mantle: An overview

Alexei S. Rukhlov[1, 2, a], Keith Bell[1], and Yuri Amelin[3, 4]

[1] Ottawa-Carleton Geoscience Centre, Department of Earth Sciences, Carleton University, Ottawa, ON, Canada, K1S 5B6
[2] Present address: British Columbia Geological Survey, 1810 Blanshard Street, Victoria, BC, Canada V8W 9N3
[3] Geological Survey of Canada, 601 Booth Street, Ottawa, ON, Canada, K1A 0E84
[4] Present address: Research School of Earth Sciences and Planetary Science Institute, The Australian National University, Canberra ACT0200, Australia
[a] corresponding author: alexei.rukhlov@gov.bc.ca

Recommended citation: Rukhlov, A.S., Bell, K., and Amelin, Y., 2015. Carbonatites, isotopes and evolution of the subcontinental mantle: An overview. In: Simandl, G.J. and Neetz, M., (Eds.), Symposium on Strategic and Critical Materials Proceedings, November 13-14, 2015, Victoria, British Columbia, British Columbia Ministry of Energy and Mines, British Columbia Geological Survey Paper 2015-3, pp. 39-64.

1. Introduction

Carbonatites, made up of at least 50% primary carbonates, are the products of low-degree partial melting of a carbonate-bearing mantle. Found on all continents, carbonatites are well suited for tracking the secular evolution of the sub-continental mantle because they span ages from 3.0 Ga to the present and because they are extremely enriched in Sr, Nd, and other REEs (Bell et al., 1982; Bell and Blenkinsop, 1987a; Nelson et al., 1988). Of more than 500 known carbonatite occurrences, only three are from oceanic islands (Cape Verdes, Canary Islands, and the Kerguelens; Woolley and Kjarsgaard, 2008). This raises questions about the role of continental lithosphere in carbonatite genesis. Are carbonatites formed by partial melting of metasomatized lithosphere? Or does the continental lithosphere simply act as an impermeable barrier trapping uprising volatiles from the asthenosphere below? Globally, the abundance of carbonatite occurrences appears to increase through time, and some parts of the Earth's crust (e.g., the Canadian Shield, the East European Craton, the Tanzanian Craton, and West Greenland) have witnessed repeated carbonatite magmatism over billions of years. This apparent increase in carbonatitic magmatism with time has been attributed either to an increasingly metasomatized mantle by volatiles from below (Woolley, 1989; Blichert-Toft et al., 1996; Woolley, 2003) or it may simply reflect a probable preservation bias (Veizer et al., 1992).

The origin of carbonatites remains controversial. Most carbonatites are spatially associated with much larger volumes of ultramafic and alkaline silicate rocks of similar age, implying petrogenetic relationships between the silica-undersaturated and alkaline silicate, and carbonate magmas. Although still debated, proposed models for the origin of carbonatitic melts include: 1) immiscible separation or fractional crystallization of parental carbonated silicate magmas; and 2) low-degree partial melting of carbonated mantle peridotite below 75 km (see reviews in Bell, 1989; Bell and Rukhlov, 2004). Arguments for origins within the lithosphere are partly based on the repeated intrusion of carbonatites into the same parts of the continental crust (e.g., the Canadian Shield, the East European Craton, the Tanzanian Craton, and West Greenland) over billions of years (Woolley, 1989; Larsen and Rex, 1992; Bailey and Woolley, 1995; Yang and Woolley, 2006; Woolley and Bailey, 2012). An in situ lithospheric source, however, is difficult to reconcile with the primitive isotopic signatures of noble gases (He, Ne, Ar, Kr, and Xe) and nitrogen found in some carbonatites from Brazil, Canada, and Russia, which indicate derivation from a relatively undegassed mantle (Sasada et al., 1997; Marty et al., 1998; Dauphas and Marty, 1999; Tolstikhin et al., 2002). The Sr, Nd, and Pb isotopic compositions of young (<200 Ma) carbonatites worldwide also cover the same range as those of oceanic island basalts (OIBs) involving high-$^{238}U/^{204}Pb$ or μ (HIMU), enriched mantle 1 and 2 (EM1 and EM2), and 'FOcus ZOne' (FOZO) mantle components (e.g., Bell and Simonetti, 1996; Bell and Tilton, 2001). Although several oceanic signatures are associated with carbonatites, it seems that depleted MORB mantle (DMM) played little, if any, role in generating carbonated melts. In many isotope ratio diagrams, particularly $^{87}Sr/^{86}Sr$ vs. $^{206}Pb/^{204}Pb$ and $^{143}Nd/^{144}Nd$ vs. $^{206}Pb/^{204}Pb$, the DMM signature is quite different to any of those involved with mixing, with the result that DMM is spatially isolated from them as well as the mixing patterns (Hoernle and Tilton, 1991; Bell and Simonetti, 1996; Bell and Tilton, 2001, 2002; Ignacio et al., 2006). For an overview of mantle components from oceanic settings, we refer the reader to Hofmann (2014). Isotopic signatures similar to OIBs suggest a sub-lithospheric source for carbonatitic melts and imply generation from mantle plumes or asthenospheric upwellings (e.g., Gerlach et al., 1988; Nelson et al., 1988; Simonetti et al., 1995; 1998; Marty et al., 1998; Dauphas and Marty, 1999; Bell, 2001; Bizzarro et al., 2002; Tolstikhin et al., 2002; Bell and Rukhlov, 2004; Kogarko et al., 2010). Plume-generated carbonatite magmatism is also consistent with the observation that many carbonatites are related to large igneous provinces (LIPs), characterized by high-volume, short-duration, intraplate magmatism including flood basalts

and feeder systems manifested by regional radiating mafic dike swarms (e.g., Ernst and Bell, 2010).

Carbonatites provide isotopic insights into mantle evolution not offered by other rocks because they contain extremely high amounts of Sr and Nd, which buffer Sr and Nd isotopic compositions from changes due to contamination, and the fact that they are widely distributed, and span 3 Ga of Earth history. Although some carbonatites have relatively high Hf contents (up to 71 ppm, or ~15 times greater than in continental crust), low values (~5 ppm) are more typical (e.g., Woolley and Kempe, 1989; Bizimis et al., 2003; Chakhmouradian, 2006). Previous studies show that initial Sr, Pb, Nd, and Hf isotope ratios in carbonatites and alkaline rocks from the Canadian and Baltic shields and Greenland trace the evolution of depleted subcontinental mantle over at least 3 Ga (Bell et al., 1982; Bell and Blenkinsop, 1987a; Nelson et al., 1988; Kwon et al., 1989; Tilton and Kwon, 1990; Kramm, 1993; Tilton and Bell, 1994; Rukhlov et al., 2001; Rukhlov and Bell, 2003; Bell and Rukhlov, 2004; Tappe et al., 2007, 2008; Kogarko et al., 2010; Tichomirowa et al., 2006, 2013). Initial $^{86}Sr/^{87}Sr$ and $^{206}Pb/^{204}Pb$ ratios suggest that this widespread, depleted reservoir formed ~3 Ga ago, assuming a reference reservoir of bulk silicate Earth (BSE; DePaolo and Wasserburg, 1976; Kwon et al., 1989). Most Archean carbonatites, however, have positive ε_{Nd} and ε_{Hf} values indicating that depleted mantle existed long before 3 Ga. These data are consistent with a depletion event, recorded in some of the oldest terrestrial materials, that must have taken place during the Hadean (>4 Ga; e.g., Amelin et al., 1999, 2000, 2011; Blichert-Toft and Arndt, 1999; Blichert-Toft et al., 2004; Harrison et al., 2005; Hoffmann et al., 2010; Kemp et al., 2010; Caro, 2011; Puchtel et al., 2013).

Here we re-examine mantle evolution using new Sr, Pb, Nd and Hf isotopic data from several carbonatite occurrences, mainly from the northern hemisphere, along with published global data (Fig. 1). This isotopic evidence lends support to a model in which carbonatite magmas are generated by plumes that originate from a widespread, relatively primitive source in the deep mantle.

2. Samples

Samples for this study were collected from 42 carbonatite complexes worldwide, spanning ages from 3.0 to 0.1 Ga. Most of the complexes are in the Baltic and Canadian shields (Fig. 1, Table 1). We performed whole-rock and mineral fraction analyses, using amphibole, ankerite, apatite, baddeleyite, calcite, dolomite, kimzeyite, siderite, and zircon. Rukhlov and Bell (2010) reported results from most of the samples for U-Th-Pb (apatite, calcite, dolomite, and whole-rock) and U-Pb (baddeleyite, kimzeyite, and zircon).

3. Methods

Rock crushing and mineral separation were carried out in the Department of Earth Sciences at Carleton University in Ottawa (for details, see Rukhlov and Bell, 2010). Fresh rock chips were pulverized in a stainless steel mill to obtain samples for whole-rock analyses. Following density and magnetic separation, pure fractions of mineral grains or fragments were hand-picked under a binocular microscope.

3.1. Rb-Sr, Sm-Nd and U-Th-Pb isotopic analyses

Sr, Nd and Pb isotopic compositions and Rb-Sr, Sm-Nd and U-Th-Pb isotope dilution analyses of carbonates, apatite and whole-rocks were performed in the Department of Earth Sciences at Carleton University. Samples spiked with mixed ^{87}Rb–^{84}Sr, ^{149}Sm–^{145}Nd, and ^{235}U–^{230}Th–^{205}Pb tracers were analyzed for Rb/Sr, Sm/Nd, Th/Pb, U/Pb and Pb isotopic composition using conventional chemical separation techniques. Both Finnigan MAT 261 and Finnigan Triton TI multi-collector thermal ionization mass spectrometers (TIMS) were used, operating in the static mode. Unspiked samples were analyzed for Sr and Nd isotopic compositions using conventional separation techniques. For details of the sample spiking, dissolution, chemical separation, mass spectrometry, and data reduction procedures the reader is referred to Rukhlov and Bell (2010) and Stoppa et al. (2014). The Sr and Nd isotopic ratios were normalized for instrumental mass fractionation relative to $^{88}Sr/^{86}Sr = 8.37500$ and $^{146}Nd/^{144}Nd = 0.7219$, respectively, using an exponential law. The $^{87}Sr/^{86}Sr$ ratios in samples are adjusted to the conventional value of 0.710245 for the NBS 987 standard. The $^{143}Nd/^{144}Nd$ ratios in samples are adjusted to the conventional value of 0.511850 in La Jolla standard. Repeated analysis of NBS 987 and La Jolla standards (over 6 years) yielded $^{87}Sr/^{86}Sr = 0.710283 \pm 0.000073$ and $^{143}Nd/^{144}Nd = 0.511855 \pm 0.000031$, respectively (errors given at the 2σ level). USGS reference material BCR-1 analyzed during this study yielded $^{87}Sr/^{86}Sr = 0.705030 \pm 0.000013$, $^{87}Rb/^{86}Sr = 0.4042 \pm 0.0030$, $^{143}Nd/^{144}Nd = 0.512635 \pm 0.000009$, and $^{147}Sm/^{144}Nd = 0.1384 \pm 0.0003$ (2σ errors, n = 1). The procedural blanks of <7.8 ng Sr, <0.15 ng Rb, <3.0 ng Nd, and <0.29 ng Sm (n = 20) are negligible.

Initial $^{87}Sr/^{86}Sr$ ratios and $\varepsilon_{Sr}(T)$ values were calculated using a decay constant of ^{87}Rb of 1.3968×10^{-11} a^{-1} (Rotenberg et al., 2012) and the bulk Earth values of DePaolo and Wasserburg (1976). Initial $^{143}Nd/^{144}Nd$ ratios and $\varepsilon_{Nd}(T)$ values were calculated using a decay constant of ^{147}Sm of 6.539×10^{-12} a^{-1} (Lugmair and Marti, 1978) and the chondritic uniform reservoir (CHUR; after Jacobsen and Wasserburg, 1980; Hamilton et al., 1983). Initial $^{206}Pb/^{204}Pb$ and $^{208}Pb/^{204}Pb$ ratios and $\gamma_{Pb}(T)$ values were calculated using decay constants of ^{238}U of 1.55125×10^{-10} a^{-1} (Jaffey et al., 1971) and ^{232}Th of 4.9475×10^{-11} a^{-1} (Le Roux and Glendenin, 1963) and the bulk silicate Earth (BSE) parameters of Allègre and Lewin (1989).

3.2. Lu-Hf isotopic analyses

Individual grains or fragments of large crystals of baddeleyite, kimzeyite and zircon were analyzed either by isotope dilution or laser ablation, multi-collector inductively coupled plasma mass spectrometer (MC-ICPMS). Using isotope dilution, U-Pb and Lu-Hf were analysed at the Geological Survey of Canada (GSC) in Ottawa. Details of dissolution and the U-Pb isotopic

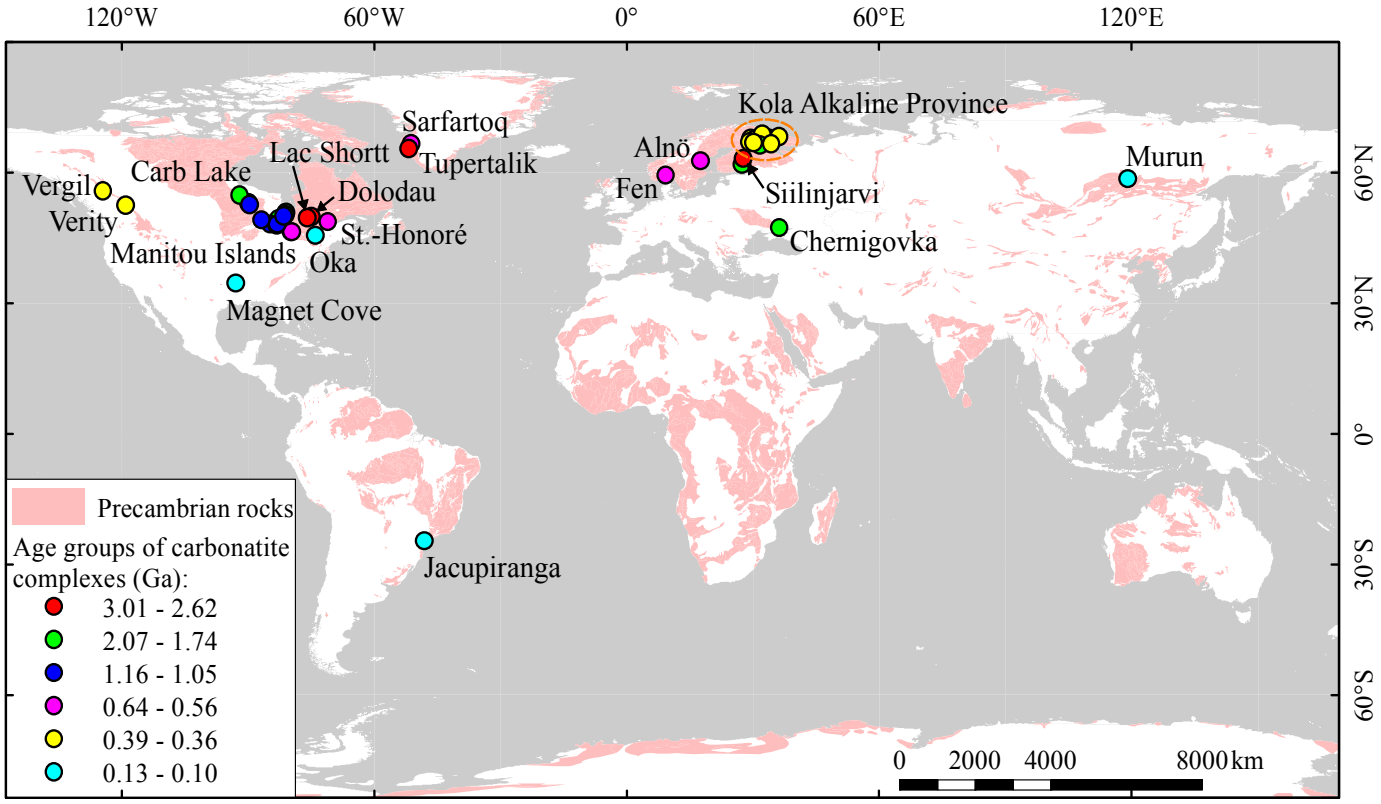

Fig. 1. Exposed Precambrian rocks (after Chorlton, 2007) and location of studied carbonatite complexes.

data can be found in Rukhlov and Bell (2010). The samples were spiked with a mixed ^{176}Lu–^{180}Hf tracer, and Lu and Hf were separated using a standard chemical separation procedure for Zr-bearing minerals modified at the GSC. Hafnium isotopic composition was measured using a Nu Plasma MC-ICPMS with DSN-100 desolvating nebulizer. Lutetium was analyzed on a single rhenium filament with graphite using a Finnigan Triton TI TIMS. The Hf isotopic ratios were normalized for instrumental mass fractionation relative to $^{179}Hf/^{177}Hf = 0.7325$ using an exponential law. The $^{176}Hf/^{177}Hf$ ratios in samples are adjusted to the conventional value of 0.28216 in JMC-475 standard. Repeated analysis (n = 43) of JMC-475 standard yielded $^{176}Hf/^{177}Hf = 0.282164 \pm 0.000019$, $^{178}Hf/^{177}Hf = 1.46723 \pm 0.00006$, and $^{180}Hf/^{177}Hf = 1.88629 \pm 0.00024$ (errors given at the 2σ level). The procedural blanks of <1.3 pg Hf and <0.04 pg Lu (n = 9) are negligible. Details of the Lu-Hf isotope dilution analytical procedures can be found in Amelin et al. (2011). For laser ablation MC-ICPMS analyses, zircon and baddeleyite grains were mounted into polished epoxy mounts and analyzed for Lu-Hf isotopic composition using an Excimer (193 nm) ArF laser ablation coupled with IsoProbe Micromass MC-ICPMS in the Geotop laboratory at the Université du Québec à Montréal (Geotop-UQAM). Zircon reference material 91500 analyzed during this study (n = 13) yielded mean values (±2σ) of $^{176}Hf/^{177}Hf = 0.282288 \pm 0.000052$, $^{178}Hf/^{177}Hf = 1.46775 \pm 0.00031$, $^{180}Hf/^{177}Hf = 1.88824 \pm 0.00103$, $^{176}Lu/^{177}Hf = 0.00033 \pm 0.00018$, and $^{176}Yb/^{177}Hf = 0.0112 \pm 0.0080$. Details of the Lu-Hf laser ablation protocol are outlined in Machado and Simonetti (2001).

Initial $^{176}Hf/^{177}Hf$ ratios and $\varepsilon_{Hf}(T)$ values were calculated using a decay constant of ^{176}Lu of 1.867×10^{-11} a^{-1} (Söderlund et al., 2004) and the chondritic uniform reservoir (CHUR) of Iizuka et al. (2015). Uncertainties (2σ) of $\varepsilon_{Hf}(T)$ values, propagated using the program of Ickert (2013), include errors associated with age, measured $^{167}Lu/^{177}Hf$ and $^{176}Hf/^{177}Hf$ ratios, decay constant, and CHUR parameters.

4. Results and discussion

Below we show new and published radiogenic isotope data from carbonatites in a series of isotope ratio diagrams that reflect the isotopic composition of mantle sources as a function of time. We also compare the data from the Kola Alkaline Province, Russia (ca. 380 Ma), one of the largest and among the best studied of alkaline provinces, with global carbonatites with ages of <200 Ma and oceanic mantle components (Table 2) in $\varepsilon_{Sr}(T)$ vs. $\varepsilon_{Nd}(T)$, $\varepsilon_{Sr}(T)$ vs. $\gamma_{Pb}(T)$, and $\gamma_{Pb}(T)$ vs. $\varepsilon_{Nd}(T)$ diagrams. Because isotope ratios are only strictly comparable for samples of the same age, we use epsilon and gamma values, which are the relative difference in parts per 10^4 (epsilon) and 10^2 (gamma) between a sample and a reference reservoir (i.e. CHUR, BSE) at a given time (e.g., Ickert, 2013), to compare the isotopic signatures for samples of different ages.

4.1. Sr isotopic evolution

Bell et al. (1982) reported initial $^{87}Sr/^{86}Sr$ ratios in 1.9 to 0.1 Ga carbonatite and syenitic complexes from the Canadian Shield

Table 1. Samples.

Sample	Rock	Fraction	Complex	Age (Ma)	Method	Longitude	Latitude	Location	Provided by	Age reference
MB-8cc	carbonatite	cc (2)	Murun	134	Rb-Sr, Sm-Nd, U-Th-Pb	119.067	58.400	Aldan Shield	A.N. Zaitsev	Makhotkin (1991)
AFR-BMA2	carbonatite	zr (core, rim)	Afrikanda	381	Lu-Hf (LA)	32.800	67.417	Baltic Shield	A.R. Chakhmouradian	Wu et al. (2013)
AFR-ZAZ1	carbonatite	zr	Afrikanda	381	Lu-Hf (LA)	32.800	67.417	Baltic Shield	A.R. Chakhmouradian	Wu et al. (2013)
SOK-1	phoscorite	cc	Sokli	380	Rb-Sr, Sm-Nd, U-Th-Pb	29.450	67.800	Baltic Shield	K. Bell	Rukhlov and Bell (2010)
SOK-Stg2	carbonatite	cc	Sokli	380	Rb-Sr, Sm-Nd, U-Th-Pb	29.450	67.800	Baltic Shield	K. Bell	Rukhlov and Bell (2010)
SOK-CoreIV	carbonatite	cc-ap	Sokli	380	Rb-Sr, Sm-Nd, U-Th-Pb	29.450	67.800	Baltic Shield	K. Bell	Rukhlov and Bell (2010)
SOK-IVmet	silicocarbonatite	ap, bd (3)	Sokli	380	ap Rb-Sr, Sm-Nd, U-Th-Pb; bd Lu-Hf (ID, 2 LA)	29.450	67.800	Baltic Shield	K. Bell	Rukhlov and Bell (2010)
SOK-Stg4	carbonatite	cc-ap	Sokli	380	Rb-Sr, Sm-Nd, U-Th-Pb	29.450	67.800	Baltic Shield	K. Bell	Rukhlov and Bell (2010)
SV-49/225	carbonatite	sid	Sallanlatvi	372	Rb-Sr, Sm-Nd, U-Th-Pb	29.167	66.950	Baltic Shield	A.N. Pilipiuk	Zaitsev et al. (2004)
SV-50/185	carbonatite	ank	Sallanlatvi	372	Rb-Sr, Sm-Nd, U-Th-Pb	29.167	66.950	Baltic Shield	A.N. Pilipiuk	Zaitsev et al. (2004)
SV-53/190	carbonatite	wr	Sallanlatvi	372	Rb-Sr, Sm-Nd, U-Th-Pb	29.167	66.950	Baltic Shield	A.N. Pilipiuk	Zaitsev et al. (2004)
SV-54/236	carbonatite	wr	Sallanlatvi	372	Rb-Sr, Sm-Nd, U-Th-Pb	29.167	66.950	Baltic Shield	A.N. Pilipiuk	Zaitsev et al. (2004)
SV-56/139.7	carbonatite	wr	Sallanlatvi	372	Rb-Sr, Sm-Nd, U-Th-Pb	29.167	66.950	Baltic Shield	A.N. Pilipiuk	Zaitsev et al. (2004)
N.64.18C	carbonatite	cc	Turiy Peninsula	377	Rb-Sr, Sm-Nd, U-Th-Pb	34.450	66.583	Baltic Shield	E.A. Spencer	Rukhlov and Bell (2010)
C.18.30	phoscorite	cc-ap (2), bd	Turiy Peninsula	377	cc-ap Rb-Sr, Sm-Nd, U-Th-Pb; bd Lu-Hf (ID)	34.450	66.583	Baltic Shield	E.A. Spencer	Rukhlov and Bell (2010)
C.23.300	carbonatite	cc	Turiy Peninsula	377	Rb-Sr, Sm-Nd, U-Th-Pb	34.450	66.583	Baltic Shield	E.A. Spencer	Rukhlov and Bell (2010)
C.XC.5	carbonatite	cc	Turiy Peninsula	377	Rb-Sr, Sm-Nd, U-Th-Pb	34.450	66.583	Baltic Shield	E.A. Spencer	Rukhlov and Bell (2010)
T-19/115	carbonatite	zr (3)	Turiy Peninsula	377	Lu-Hf (ID, 2 LA)	34.450	66.583	Baltic Shield	A.N. Pilipiuk	Rukhlov and Bell (2010)
HCK286/88.5	carbonatite	cc	Vuorijarvi	377	Rb-Sr, Sm-Nd, U-Th-Pb	30.117	66.800	Baltic Shield	A.N. Pilipiuk	Bayanova (2006)

Table 1. Continued.

Sample	Rock	Fraction	Complex	Age (Ma)	Method	Longitude	Latitude	Location	Provided by	Age reference
HCK228/67.5	carbonatite	cc, dol	Vuorijarvi	377	Rb-Sr, Sm-Nd, U-Th-Pb	30.117	66.800	Baltic Shield	A.N. Pilipiuk	Bayanova (2006)
HCK364/73.8	carbonatite	cc	Vuorijarvi	377	Rb-Sr, Sm-Nd, U-Th-Pb	30.117	66.800	Baltic Shield	A.N. Pilipiuk	Bayanova (2006)
KOV-105	carbonatite	cc-ap, bd	Kovdor	379	cc-ap Rb-Sr, Sm-Nd, U-Th-Pb; bd Lu-Hf (ID)	30.483	67.567	Baltic Shield	A.N. Zaitsev	Amelin and Zaitsev (2002)
KOV-127/85	carbonatite	zr	Kovdor	379	Lu-Hf (ID)	30.483	67.567	Baltic Shield	A.N. Zaitsev	Amelin and Zaitsev (2002)
KOV-783/141	carbonatite	ap, cc	Kovdor	379	Rb-Sr, Sm-Nd, U-Th-Pb	30.483	67.567	Baltic Shield	A.N. Zaitsev	Amelin and Zaitsev (2002)
KOV-9/626.7	carbonatite	cc	Kovdor	379	Rb-Sr, Sm-Nd, U-Th-Pb	30.483	67.567	Baltic Shield	A.N. Zaitsev	Amelin and Zaitsev (2002)
KOV-BDT	carbonatite	bd (2)	Kovdor	379	Lu-Hf (LA)	30.483	67.567	Baltic Shield	A.N. Zaitsev	Amelin and Zaitsev (2002)
KZ303/86	volcanic carbonatite	cc	Kontozero	380	Rb-Sr, Sm-Nd, U-Th-Pb	36.117	68.133	Baltic Shield	A.A. Arzamastsev	Arzamastsev and Belyatsky (2000)
KZ320/86	volcanic carbonatite	cc	Kontozero	380	Rb-Sr, Sm-Nd, U-Th-Pb	36.117	68.133	Baltic Shield	A.A. Arzamastsev	Arzamastsev and Belyatsky (2000)
W-440	calcite phonolite	cc	Kandalaksha	380	Rb-Sr, Sm-Nd, U-Th-Pb	32.338	67.098	Baltic Shield	A.S. Rukhlov	Claesson et al. (2000)
P1516	calcite nephelinite	cc	Pinozero	380	Rb-Sr, Sm-Nd, U-Th-Pb	32.499	67.316	Baltic Shield	A.S. Rukhlov	Claesson et al. (2000)
P-409A	alnöite	am	Kandalaksha	380	Rb-Sr, Sm-Nd, U-Th-Pb	32.446	67.124	Baltic Shield	A.S. Rukhlov	Claesson et al. (2000)
P-412	alnöite	wr	Kandalaksha	380	Rb-Sr, Sm-Nd, U-Th-Pb	32.446	67.123	Baltic Shield	A.S. Rukhlov	Claesson et al. (2000)
W-401	aillikite	am	Kandalaksha	380	Rb-Sr, Sm-Nd, U-Th-Pb	32.424	67.129	Baltic Shield	A.S. Rukhlov	Claesson et al. (2000)
W-513A	alnöite	am	Kandalaksha	380	Rb-Sr, Sm-Nd, U-Th-Pb	32.416	67.102	Baltic Shield	A.S. Rukhlov	Claesson et al. (2000)
SB333/581	carbonatite	wr	Sebljavr	378	Rb-Sr, Sm-Nd, U-Th-Pb	32.133	68.717	Baltic Shield	A.N. Pilipiuk	Bayanova (2006)
SB339/363	carbonatite	cc-ap	Sebljavr	378	Rb-Sr, Sm-Nd, U-Th-Pb	32.133	68.717	Baltic Shield	A.N. Pilipiuk	Bayanova (2006)
SB340/297	carbonatite	dol	Sebljavr	378	Rb-Sr, Sm-Nd, U-Th-Pb	32.133	68.717	Baltic Shield	A.N. Pilipiuk	Bayanova (2006)

Table 1. Continued.

Sample	Rock	Fraction	Complex	Age (Ma)	Method	Longitude	Latitude	Location	Provided by	Age reference
SB340/55	carbonatite	wr	Sebljavr	378	Rb-Sr, Sm-Nd, U-Th-Pb	32.133	68.717	Baltic Shield	A.N. Pilipiuk	Bayanova (2006)
SB340/94	carbonatite	cc, dol	Sebljavr	378	Rb-Sr, Sm-Nd, U-Th-Pb	32.133	68.717	Baltic Shield	A.N. Pilipiuk	Bayanova (2006)
931-4	calcite ijolite	wr	Kandaguba	386	Rb-Sr, Sm-Nd	32.145	67.100	Baltic Shield	A.N. Pilipiuk	Rukhlov and Bell (2010)
951-9	calcite ijolite	ap (2), cc (3), wr	Kandaguba	386	wr Rb-Sr, Sm-Nd; ap, cc Rb-Sr, Sm-Nd, U-Th-Pb	32.145	67.100	Baltic Shield	A.N. Pilipiuk	Rukhlov and Bell (2010)
KM-122	carbonatite	wr, cc, dol	Kandaguba	386	wr Rb-Sr, Sm-Nd; cc, dol Rb-Sr, Sm-Nd, U-Th-Pb	32.145	67.100	Baltic Shield	A.N. Pilipiuk	Rukhlov and Bell (2010)
KM-2/13	carbonatite	wr, cc	Kandaguba	386	wr Rb-Sr, Sm-Nd; cc Rb-Sr, Sm-Nd, U-Th-Pb	32.145	67.097	Baltic Shield	A.N. Pilipiuk	Rukhlov and Bell (2010)
KM-3/70.4	carbonatite	wr	Kandaguba	386	Rb-Sr, Sm-Nd	32.145	67.097	Baltic Shield	A.N. Pilipiuk	Rukhlov and Bell (2010)
KM-31	carbonatite	wr (2)	Kandaguba	386	Rb-Sr, Sm-Nd	32.145	67.097	Baltic Shield	A.N. Pilipiuk	Rukhlov and Bell (2010)
KM-74	zircon-apatite vein	ap, zr (4)	Kandaguba	386	ap Rb-Sr, Sm-Nd; zr Lu-Hf (ID, 3 LA)	32.145	67.097	Baltic Shield	A.N. Pilipiuk	Rukhlov and Bell (2010)
KM-78	carbonatite	ank, wr (2)	Kandaguba	386	wr Rb-Sr, Sm-Nd; ank Rb-Sr, Sm-Nd, U-Th-Pb	32.145	67.097	Baltic Shield	A.N. Pilipiuk	Rukhlov and Bell (2010)
KM-8	carbonatite	wr	Kandaguba	386	Rb-Sr, Sm-Nd	32.145	67.097	Baltic Shield	A.N. Pilipiuk	Rukhlov and Bell (2010)
KM-9	carbonatite	wr	Kandaguba	386	Rb-Sr, Sm-Nd	32.145	67.097	Baltic Shield	A.N. Pilipiuk	Rukhlov and Bell (2010)
FE1	carbonatite	dol-ap	Fen	578	Rb-Sr, Sm-Nd, U-Th-Pb	9.283	59.300	Baltic Shield	I. Hornig-Kjarsgaard	Dahlgren (1994)
FE2	carbonatite	cc	Fen	578	Rb-Sr, Sm-Nd, U-Th-Pb	9.283	59.300	Baltic Shield	I. Hornig-Kjarsgaard	Dahlgren (1994)
FE5	carbonatite	ap, cc	Fen	578	Rb-Sr, Sm-Nd, U-Th-Pb	9.283	59.300	Baltic Shield	I. Hornig-Kjarsgaard	Dahlgren (1994)
P2-003	carbonatite	cc (2)	Alnö	583	Rb-Sr, Sm-Nd, U-Th-Pb	17.500	62.500	Baltic Shield	J. Gittins	Rukhlov and Bell (2010)
P1-997	carbonatite	cc	Alnö	583	Rb-Sr, Sm-Nd, U-Th-Pb	17.500	62.500	Baltic Shield	J. Gittins	Rukhlov and Bell (2010)

Table 1. Continued.

Sample	Rock	Fraction	Complex	Age (Ma)	Method	Longitude	Latitude	Location	Provided by	Age reference
P2-036	carbonatite	ap (2), bd (4), cc (3), zr (2)	Alnö	583	ap, cc Rb-Sr, Sm-Nd, U-Th-Pb; bd Lu-Hf (ID, Hf, 2 LA); zr Lu-Hf (LA)	17.500	62.500	Baltic Shield	J. Gittins	Rukhlov and Bell (2010)
P2-037	carbonatite	ap, bd (2), cc (2)	Alnö	583	ap, cc Rb-Sr, Sm-Nd, U-Th-Pb; bd Lu-Hf (ID, LA)	17.500	62.500	Baltic Shield	J. Gittins	Rukhlov and Bell (2010)
H-1E	carbonatite	cc, zr (2)	Halpanen	1792	cc Rb-Sr, Sm-Nd, U-Th-Pb; zr Lu-Hf (ID, LA)	27.433	61.767	Baltic Shield	D.L. Konopelko	Rukhlov and Bell (2010)
H-1S	carbonatite	cc	Halpanen	1792	Rb-Sr, Sm-Nd, U-Th-Pb	27.433	61.767	Baltic Shield	D.L. Konopelko	Rukhlov and Bell (2010)
TSH146/96-107	carbonatite	ap (2), cc	Tiksheozero	1999	Rb-Sr, Sm-Nd, U-Th-Pb	31.667	66.283	Baltic Shield	N.A. Frantz	Corfu et al. (2011)
TSH154/210-220	carbonatite	cc, zr (3)	Tiksheozero	1999	cc Rb-Sr, Sm-Nd, U-Th-Pb; zr Lu-Hf (ID, 2 LA)	31.667	66.283	Baltic Shield	N.A. Frantz	Corfu et al. (2011)
TSH154-15/127.4	carbonatite	cc (2)	Tiksheozero	1999	Rb-Sr, Sm-Nd, U-Th-Pb	31.667	66.283	Baltic Shield	A.N. Pilipiuk	Corfu et al. (2011)
TSH158-25/248.2	carbonatite	cc	Tiksheozero	1999	Rb-Sr, Sm-Nd, U-Th-Pb	31.667	66.283	Baltic Shield	A.N. Pilipiuk	Corfu et al. (2011)
TSH169/142-152	carbonatite	ap (2), dol, zr (2)	Tiksheozero	1999	ap, dol Rb-Sr, Sm-Nd, U-Th-Pb; zr Lu-Hf (ID, LA)	31.667	66.283	Baltic Shield	N.A. Frantz	Corfu et al. (2011)
4-ALV	carbonatite	ap, cc, zr (2)	Chernigovka	2074	ap, cc Rb-Sr, Sm-Nd, U-Th-Pb; zr Lu-Hf (ID, Hf)	36.250	47.233	Ukrainian Shield	V.M. Zagnitko	Rukhlov and Bell (2010)
4-BEF	carbonatite	dol	Chernigovka	2074	Rb-Sr, Sm-Nd, U-Th-Pb	36.250	47.233	Ukrainian Shield	V.M. Zagnitko	Rukhlov and Bell (2010)
4-SOV	carbonatite	ap, cc, zr (2)	Chernigovka	2074	ap, cc Rb-Sr, Sm-Nd, U-Th-Pb; zr Lu-Hf (ID, Hf)	36.250	47.233	Ukrainian Shield	V.M. Zagnitko	Rukhlov and Bell (2010)
SIL101	carbonatite	ap, cc	Siilinjarvi	2617	Rb-Sr, Sm-Nd, U-Th-Pb	27.733	63.133	Baltic Shield	K. Bell	Rukhlov and Bell (2010)
SIL102	carbonatite	zr (4)	Siilinjarvi	2617	Lu-Hf (ID, 3 LA)	27.733	63.133	Baltic Shield	K. Bell	Rukhlov and Bell (2010)
SIL103	carbonatite	cc	Siilinjarvi	2617	Rb-Sr, Sm-Nd, U-Th-Pb	27.733	63.133	Baltic Shield	K. Bell	Rukhlov and Bell (2010)
SIL104	carbonatite	cc (2)	Siilinjarvi	2617	Rb-Sr, Sm-Nd, U-Th-Pb	27.733	63.133	Baltic Shield	K. Bell	Rukhlov and Bell (2010)

Table 1. Continued.

Sample	Rock	Fraction	Complex	Age (Ma)	Method	Longitude	Latitude	Location	Provided by	Age reference
SIL106	carbonatite	ap (2), cc (2)	Siilinjarvi	2617	Rb-Sr, Sm-Nd, U-Th-Pb	27.733	63.133	Baltic Shield	K. Bell	Rukhlov and Bell (2010)
SIL2	carbonatite	zr	Siilinjarvi	2617	Lu-Hf (ID)	27.733	63.133	Baltic Shield	K. Bell	Rukhlov and Bell (2010)
SIL2000	carbonatite	cc	Siilinjarvi	2617	Rb-Sr, Sm-Nd, U-Th-Pb	27.733	63.133	Baltic Shield	K. Bell	Rukhlov and Bell (2010)
ST2800	carbonatite	cc	Siilinjarvi	2617	Rb-Sr, Sm-Nd, U-Th-Pb	27.733	63.133	Baltic Shield	K. Bell	Rukhlov and Bell (2010)
MC-1	carbonatite	kz	Magnet Cove	95	Lu-Hf (ID)	-92.867	34.450	Gulf Coastal Plain	M. Howard	Baksi (1997)
MC-115	carbonatite	ap	Magnet Cove	95	Sr	-92.867	34.450	Gulf Coastal Plain	M. Howard	Baksi (1997)
CH-T2	carbonatite	ap	Oka	109	Sr	-74.000	45.500	St. Lawrence Platform	K. Bell	Wen et al. (1987)
J-14	carbonatite	ap, bd	Jacupiranga	131	ap Sr; bd Lu-Hf (ID)	-48.133	-24.700	Parana Basin	R.O.M.	Roden et al. (1985)
J-4	carbonatite	bd	Jacupiranga	131	Lu-Hf (ID)	-48.133	-24.700	Parana Basin	R.O.M.	Roden et al. (1985)
L4-242	carbonatite	ap, zr (4)	Vergil	352	ap Sr; zr Lu-Hf (ID, 3 LA)	-124.417	55.717	Canadian Cordillera	J. Pell	Pell (1994)
4-470	carbonatite	zr (4)	Verity	350	Lu-Hf (ID, 3 LA)	-119.150	52.400	Canadian Cordillera	J. Pell	Rukhlov and Bell (2010)
BI-101	carbonatite	ap	Burritt Island	568	Sr	-79.750	46.250	Canadian Shield	K. Bell	Rukhlov and Bell (2010)
C-6	carbonatite	zr (2)	Calder Island	568	Lu-Hf (ID, Hf)	-79.583	46.250	Canadian Shield	R.O.M.	Rukhlov and Bell (2010)
CI-100	carbonatite	ap	Calder Island	568	Sr	-79.583	46.250	Canadian Shield	K. Bell	Rukhlov and Bell (2010)
II-102	carbonatite	ap (2)	Iron Island	568	Sr	-79.750	46.250	Canadian Shield	R.O.M.	Rukhlov and Bell (2010)
NI-PYR	carbonatite	zr (2)	Newman Island	568	Lu-Hf (ID, Hf)	-79.583	46.250	Canadian Shield	R.O.M.	Rukhlov and Bell (2010)
R-4DYKE	carbonatite	zr	Rankin Island	568	Lu-Hf (ID)	-79.583	46.250	Canadian Shield	R.O.M.	Rukhlov and Bell (2010)
STH-104	carbonatite	ap, zr (4)	St. Honoré	571	ap Sr; zr Lu-Hf (LA)	-71.067	48.550	Canadian Shield	K. Bell	McCausland et al. (2009)
STH-105	carbonatite	zr	St. Honoré	571	Lu-Hf (ID)	-71.067	48.550	Canadian Shield	K. Bell	McCausland et al. (2009)
STH-18	carbonatite	zr	St. Honoré	571	Lu-Hf (ID)	-71.067	48.550	Canadian Shield	K. Bell	McCausland et al. (2009)

Table 1. Continued.

Sample	Rock	Fraction	Complex	Age (Ma)	Method	Longitude	Latitude	Location	Provided by	Age reference
SR-18-10	carbonatite	bd	Schryburt Lake	1083	Lu-Hf (ID)	-89.600	52.617	Canadian Shield	R.O.M.	Rukhlov and Bell (2010)
SR-18-9	carbonatite	bd	Schryburt Lake	1083	Lu-Hf (ID)	-89.600	52.617	Canadian Shield	R.O.M.	Rukhlov and Bell (2010)
LAC5	carbonatite	ap	Lackner Lake	1101	Sr	-83.167	47.750	Canadian Shield	K. Bell	Heaman and Machado (1992)
BB-35	silicocarbonatite	ap, bd	Big Beaver House	1093	ap Sr; bd Lu-Hf (ID)	-89.917	52.917	Canadian Shield	R.O.M.	Rukhlov and Bell (2010)
NL203A	carbonatite	ap, zr (2)	Nemegosenda Lake	1105	ap Sr; zr Lu-Hf (LA)	-83.083	48.000	Canadian Shield	K. Bell	Heaman and Machado (1992)
V22/2269.0	carbonatite	bd (7)	Valentine Township	1106	Lu-Hf (ID) - bomb versus hot-plate dissolution experiments	-81.500	50.000	Canadian Shield	R.O.M.	Rukhlov and Bell (2010)
V23/1410.3	carbonatite	bd	Valentine Township	1106	Lu-Hf (ID)	-81.500	50.000	Canadian Shield	R.O.M.	Rukhlov and Bell (2010)
H8/298.0	silicocarbonatite	cc, kz	Firesand River	1143	cc Sr; kz Lu-Hf (ID)	-84.667	48.000	Canadian Shield	R.O.M.	Rukhlov and Bell (2010)
DP-26F	silicocarbonatite	zr (2)	Prairie Lake	1164	Lu-Hf (ID, Hf)	-86.717	49.033	Canadian Shield	K. Bell	Rukhlov and Bell (2010)
P21A/64.8	phoscorite	ap, bd (2)	Prairie Lake	1164	ap Sr; bd Lu-Hf (ID, Hf)	-86.717	49.033	Canadian Shield	K. Bell	Rukhlov and Bell (2010)
A8/889.0	carbonatite	zr	Argor	1769	Lu-Hf (ID)	-81.017	50.750	Canadian Shield	R.O.M.	Rukhlov and Bell (2010)
AB3/792.3	carbonatite	ap, zr	Argor	1769	ap Sr; zr Lu-Hf (ID)	-81.017	50.750	Canadian Shield	R.O.M.	Rukhlov and Bell (2010)
3-53-82B	carbonatite	zr (2)	"Carb" Lake	1865	Lu-Hf (ID, Hf)	-92.000	54.800	Canadian Shield	R.O.M.	Rukhlov and Bell (2010)
H2/72.5	carbonatite	zr (2)	"Carb" Lake	1865	Lu-Hf (ID, Hf)	-92.000	54.800	Canadian Shield	R.O.M.	Rukhlov and Bell (2010)
H2-61	carbonatite	ap	"Carb" Lake	1865	Sr	-92.000	54.800	Canadian Shield	R.O.M.	Rukhlov and Bell (2010)
TP109-108/1720.8	carbonatite	bd (2)	Spanish River	1881	Lu-Hf (ID, Hf)	46.583	81.717	Canadian Shield	R.O.M.	Rukhlov and Bell (2010)
BO-200	carbonatite	zr	Borden	1882	Lu-Hf (LA)	-83.183	47.917	Canadian Shield	K. Bell	Rukhlov and Bell (2010)
BO-203	carbonatite	ap	Borden	1882	Sr	-83.183	47.917	Canadian Shield	K. Bell	Rukhlov and Bell (2010)

Table 1. Continued.

Sample	Rock	Fraction	Complex	Age (Ma)	Method	Longitude	Latitude	Location	Provided by	Age reference
BO-205	carbonatite	zr (3)	Borden	1882	Lu-Hf (ID, 2 LA)	-83.183	47.917	Canadian Shield	K. Bell	Rukhlov and Bell (2010)
G1A/590.0	carbonatite	zr	Goldray	1886	Lu-Hf (ID)	-81.167	50.217	Canadian Shield	R.O.M.	Rukhlov and Bell (2010)
G2/1201.4	carbonatite	ap	Goldray	1886	Sr	-81.167	50.217	Canadian Shield	R.O.M.	Rukhlov and Bell (2010)
CCM-26/195.85	carbonatite	ap, bd	Cargill Township	1897	ap Sr; bd Lu-Hf (ID)	-82.817	49.317	Canadian Shield	R.O.M.	Rukhlov and Bell (2010)
CCM-6/140.1	silicocarbonatite	zr	Cargill Township	1897	Lu-Hf (ID)	-82.817	49.317	Canadian Shield	R.O.M.	Rukhlov and Bell (2010)
DOD-77	carbonatite	ap, zr (5)	Dolodau Dike	2680	ap Sr; Lu-Hf (ID, 4 LA)	-75.000	49.767	Canadian Shield	K. Bell	Tilton and Bell (1994)
DOD-91	silicocarbonatite	zr (2)	Dolodau Dike	2680	Lu-Hf (ID, LA)	-75.000	49.767	Canadian Shield	K. Bell	Tilton and Bell (1994)
LSC65	carbonatite	ap, zr (2)	Lac Shortt	2691	ap Sr; zr Lu-Hf (ID, LA)	-75.883	49.583	Canadian Shield	K. Bell	Dion et al. (1995)
LSC7910	carbonatite	zr (2)	Lac Shortt	2691	Lu-Hf (ID, LA)	-75.883	49.583	Canadian Shield	K. Bell	Dion et al. (1995)
LSC7912	carbonatite	ap, zr (3)	Lac Shortt	2691	ap Sr; zr Lu-Hf (ID, 2 LA)	-75.883	49.583	Canadian Shield	K. Bell	Dion et al. (1995)
S-10	carbonatite	wr (2)	Sarfartoq	591	Rb-Sr	-51.250	66.500	Greenland	A. Simonetti	Bizzarro et al. (2002)
T-1	carbonatite	wr	Tupertalik	3007	Rb-Sr	-51.750	65.417	Greenland	A. Simonetti	Bizzarro et al. (2002)

Fraction abbreviations: ap - apatite, am - hornblende phenocryst, ank - ankerite, bd - baddeleyite, cc - calcite, dol - dolomite, kz - kimzeyite, sid - siderite, zr - zircon, wr - whole rock. Number in parentheses refers to number of analyzed fractions.

Methods: Rb-Sr - Rb/Sr by isotope dilution and unpsiked Sr isotopic composition by TIMS, Sr - unspiked Sr isotopic composition by TIMS, Sm-Nd - Sm/Nd by isotope dilution and unspiked Nd isotopic composition by TIMS, Lu-Hf ID - Lu/Hf by isotope dilution and Hf isotopic composition by solution MC-ICP-MS and Lu by TIMS, LA - Lu/Hf and Hf isotopic composition by laser ablation MC-ICP-MS, Hf - unspiked Hf isotopic composition by solution MC-ICP-MS, U-Th-Pb - U/Pb and Th/Pb by isotope dilution and Pb isotopic composition by TIMS.

R.O.M. - Royal Ontario Museum.

Table 2. Isotopic compositions of mantle components (after Hart et al., 1992; Stracke et al., 2005; Stracke, 2012).

Component	$^{87}Sr/^{86}Sr$	$^{143}Nd/^{144}Nd$	$^{176}Hf/^{177}Hf$	$^{206}Pb/^{204}Pb$	$^{207}Pb/^{204}Pb$	$^{208}Pb/^{204}Pb$	$\varepsilon_{Sr}(0)$	$\varepsilon_{Nd}(0)$	$\varepsilon_{Hf}(0)$	$\gamma_{Pb}(0)$
DMM	0.7022	0.51335	0.28350	17.5	15.35	36.8	-32.6	13.9	25.0	-4.6
EM1	0.7053	0.51234	0.28263	17.4	15.47	39.0	11.4	-5.8	-5.8	-5.1
EM2	0.7078	0.51258	0.28288	19.3	15.64	39.8	46.8	-1.1	3.1	5.2
FOZO minimum	0.7030	0.51288	0.28295	19.4	15.57	39.2	-21.3	4.7	5.6	5.8
FOZO maximum	0.7033	0.51305	0.28315	20.5	15.70	39.8	-17.0	8.0	12.6	11.8
HIMU	0.7028	0.51290	0.28296	21.8	15.85	40.8	-24.1	5.1	5.9	18.9

$\varepsilon_{Sr}(0) = [(^{87}Sr/^{86}Sr_{sample}/^{87}Sr/^{86}Sr_{BE}) - 1]*10^4$, where $^{87}Sr/^{86}Sr_{sample}$ is the present-day ratio in the sample and $^{87}Sr/^{86}Sr_{BE}$ is the present-day ratio in the bulk Earth (after DePaolo and Wasserburg, 1976).

$\varepsilon_{Nd}(0) = [(^{143}Nd/^{144}Nd_{sample}/^{143}Nd/^{144}Nd_{CHUR}) - 1]*10^4$, where $^{143}Nd/^{144}Nd_{sample}$ is the present-day ratio in the sample and $^{143}Nd/^{144}Nd_{CHUR}$ is the present-day ratio in the chondritic uniform reservoir (CHUR; after Jacobsen and Wasserburg, 1980; Hamilton et al., 1983).

$\varepsilon_{Hf}(0) = [(^{176}Hf/^{177}Hf_{sample}/^{176}Hf/^{177}Hf_{CHUR}) - 1]*10^4$, where $^{176}Hf/^{177}Hf_{sample}$ is the present-day ratio in the sample and $^{176}Hf/^{177}Hf_{CHUR}$ is the present-day ratio in CHUR (after Iizuka et al., 2015).

$\gamma_{Pb}(0) = [(^{206}Pb/^{204}Pb_{sample}/^{206}Pb/^{204}Pb_{BSE}) - 1]*10^2$, where $^{206}Pb/^{204}Pb_{sample}$ is the present-day ratio in the sample and $^{206}Pb/^{204}Pb_{BSE}$ is the present-day ratio in the bulk silicate Earth (BSE; after Allègre and Lewin, 1989).

DMM = depleted MORB mantle, EM1 = enriched mantle 1, EM2 = enriched mantle 2, FOZO = 'FOcus ZOne', HIMU = high-$^{238}U/^{204}Pb$ or μ.

that indicate a depleted mantle source, and using the bulk Earth reservoir (DePaolo and Wasserburg, 1976), determined a model age of ~3 Ga for depletion. This model age corresponds to the age of a depleted, closed-system reservoir formed by either the extraction of a significant volume of continental crust in the Neoarchean or a major change in the mode of heat transfer in the upper mantle at that time (Bell et al., 1982; Bell and Blenkinsop, 1987a). Close agreement between the data from the Baltic and Canadian shields suggests similar differentiation histories for mantle sources below both of these regions (e.g., Tilton and Kwon, 1990; Kramm, 1993; Tilton and Bell, 1994; Rukhlov et al., 2001; Bell and Rukhlov, 2004). Nelson et al. (1988) also noted similar evolution for mantle sources of global carbonatites. An alternative model proposed by Tichomirowa et al. (2006) involves a continuous decrease in Rb/Sr for the depleted mantle reservoir beneath the Baltic Shield.

Figure 2 shows initial $^{87}Sr/^{86}Sr$ ratios for global carbonatites as a function of age. Two important features emerge from Figure 2. First, the spread of the isotopic data suggests involvement of at least two distinct mantle sources, one depleted and one enriched, with intermittent mixing between the two over a period of 3 Ga. This is particularly well seen in the range of values from the Kola carbonatites (ca. 380 Ma; e.g., Kramm, 1993; Zaitsev and Bell, 1995; Beard et al., 1996; Arzamastsev et al., 1998; Rukhlov, 1999; Verhulst et al., 2000; Dunworth and Bell, 2001; Zaitsev et al., 2002; Bell and Rukhlov, 2004; Sindern et al., 2004; Lee et al., 2006; Balaganskaya et al., 2007; Kogarko et al., 2010; Mitchell et al., 2011; Wu et al., 2013; Zartman and Kogarko, 2014) and young carbonatites from elsewhere (e.g., Bell and Blenkinsop, 1987b; Gerlach et al., 1988; Nelson et al., 1988; Kogarko, 1993; Simonetti and Bell, 1994a, b; Bell and Dawson, 1995; Simonetti et al., 1995, 1998; Bell and Simonetti, 1996; Bell and Tilton, 2001; Hoernle et al., 2002). Second, the lowest $^{87}Sr/^{86}Sr$ values fall along a single development line that corresponds to a Rb/Sr ratio of 0.02, which is quite different from that of BSE (0.03) and consistent with the findings of Bell et al. (1982). This widespread depleted source appears to have behaved as a relatively closed system that retained its Rb/Sr ratio over long time periods, either by preservation in the lithosphere or at deeper levels in the mantle, isolated from mantle convection. Lithospheric residence seems unlikely because it implies synchronous metasomatism of the lithosphere on a global scale by an unknown mantle process. A continuous transport-depletion model (e.g., Hart and Brooks, 1970; Ben Othman et al., 1984) based on the data from MORB, ophiolites, komatiites, and meteorites implies much lower Rb/Sr ratio than that of the depleted carbonatite source. This depleted reservoir, indicated by the lowest $^{87}Sr/^{86}Sr$ values in carbonatites, has a present-day value that is quite different in its isotopic composition to that of DMM (see Bell and Tilton, 2001, 2002) and similar to FOZO, an end-member identified in OIBs, oceanic plateaus, flood basalts, and several young (<0.2 Ga) carbonatites. FOZO is considered to be relatively primitive and of deep mantle origin (Hart et al., 1992; Hauri et al., 1994; Bell and Tilton, 2002; Campbell and O'Neill, 2012) and appears to be a common source component for the 380 Ma, plume-related Kola carbonatites based on the Sr-Pb-Nd isotopic evidence (Fig. 3; e.g., Kramm, 1993; Dunworth and Bell, 2001; Bell and Rukhlov, 2004; this study).

The initial isotopic ratios from Kola cannot be directly compared with the present-day mantle components because the isotopic compositions of the latter 380 Ma ago are unknown. However, because the Sr isotopic composition of the depleted source appears to have changed little over the last 380 Ma (Fig. 2), we assume that the Kola and young carbonatites share the same reference reservoir in Sr-Pb-Nd isotope space. In addition, overlapping of the mixing patterns of the Kola and young carbonatites in $\varepsilon_{Sr}(T)$ vs. $\varepsilon_{Nd}(T)$, $\varepsilon_{Sr}(T)$ vs. $\gamma_{Pb}(T)$, and $\gamma_{Pb}(T)$ vs. $\varepsilon_{Nd}(T)$ diagrams (Fig. 3) indicates involvement of the same mantle components, one depleted (FOZO) and the other enriched (EM1). The Sr-Pb-Nd isotopic compositions of some young (<200 Ma) carbonatites also indicate involvement of HIMU and EM1 (Fig. 3; e.g., Simonetti and Bell, 1994a; Bell and Dawson, 1995; Bell and Simonetti, 1996; Bell and Tilton, 2001). In Figure 3, DMM is spatially isolated from the mixing patterns in all of the diagrams and thus played little, if any, role in generating the carbonated melts (Hoernle and Tilton, 1991; Bell and Simonetti, 1996; Bell and Tilton, 2001, 2002; Ignacio et al., 2006). An enriched end-member, 'ITEM' (Italian enriched mantle), marks the most radiogenic compositions of Cenozoic carbonatites from Italy ($^{87}Sr/^{86}Sr$ up to 0.71077; Bell et al., 2013) and, on the basis of our data, seems to have also been tapped intermittently over a period of 3 Ga. It could represent either old recycled crust and/or sediment entrained in the upwelling FOZO mantle, or C–H–O–K-rich fluids released from the core-mantle boundary during plume activity, triggered by core-mantle perturbations (Vidale and Hedlin, 1998; Bell et al., 2013; Herzberg et al., 2013). Very radiogenic $^{87}Sr/^{86}Sr$ ratios (>0.708) in separated carbonate fractions, coupled with much lower $^{87}Sr/^{86}Sr$ ratios (<0.705) in whole rock fractions from some late-stage carbonatites at Kandaguba complex, Kola Alkaline Province (Fig. 3), indicate isotopic disequilibrium resulting from complex petrogenetic processes (Bulakh et al., 2000; Pilipiuk et al., 2001).

4.2. Pb isotopic evolution

Tilton (1983) reported a major Neoarchean depletion event for both the Canadian and Baltic shields based on Pb isotopic data from granitic rocks, sulphide ores, komatiites, and carbonatites. Subsequent work by Kwon et al. (1989) and Tilton and Kwon (1990) determined a model age of ~3 Ga relative to BSE using initial Pb isotopic ratios from carbonatites and alkaline-silicate rocks with ages between 2.7 and 0.1 Ga from the Canadian Shield. These ratios converge with BSE at ~3 Ga, supporting the widespread Neoarchean differentiation event recorded by the Sr data (Tilton and Kwon, 1990).

Figure 4 shows initial $^{206}Pb/^{204}Pb$ and $^{208}Pb/^{204}Pb$ ratios for carbonatites worldwide and some 2.7 Ga syenites from the Canadian Shield plotted as a function of time. Evolution curves show the different BSE models after Galer and Goldstein

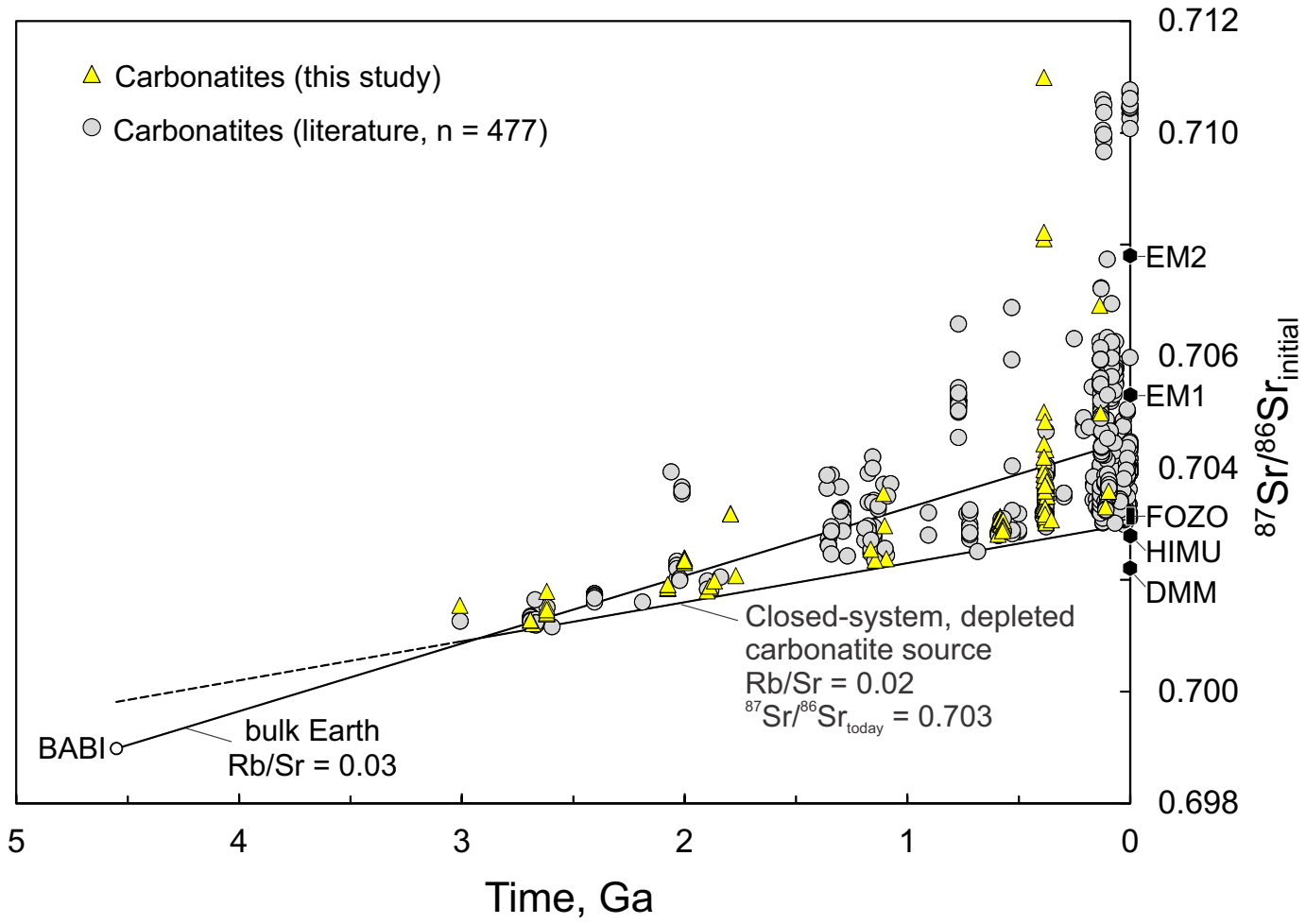

Fig. 2. Initial $^{87}Sr/^{86}Sr$ versus time for carbonatites worldwide and late Archean syenitic complexes from the Canadian Shield. Evolution curve for bulk Earth (after DePaolo and Wasserburg, 1976) assuming primordial $^{87}Sr/^{86}Sr = 0.6990$ of basaltic achondrite best initial (BABI). Depleted MORB mantle (DMM), enriched mantle 1 and 2 (EM1 and EM2), 'FOcus ZOne' (FOZO), and high-$^{238}U/^{204}Pb$ or μ (HIMU) mantle components after Hart et al. (1992), Stracke et al. (2005), and Stracke (2012). The development line indicates the presence of an ancient, depleted mantle reservoir at least 3.0 Ga old. Data from Alberti et al. (1999), Andersen (1987, 1997), Baksi (1997), Balaganskaya et al. (2000), Barreiro and Cooper (1987), Beard et al. (1996), Bell and Blenkinsop (1987a, b), Bell and Peterson (1991), Bell and Tilton (2001), Bell et al. (1987, 2013), Bernard-Griffiths et al. (1991), Bizimis et al. (2003), Bizzarro et al. (2001, 2002, 2003), Blaxland et al. (1978), Castorina et al. (1996), Cavell and Baadsgaard (1986), Comin-Chiaramonti et al. (2002), Conticelli et al. (1995, 2002), Cooper and Mellish (2001), Cooper and Reid (1998), Corfu and Noble (1992), Coulson et al. (2003), Dawson et al. (1995), Dunai et al. (1989), Dunworth and Bell (2001), Eby et al. (1995), Eriksson (1989), Grüenenfelder et al. (1986), Hansen (1981), Harmer (1985, 1999), Harmer et al. (1998), Hoernle and Tilton (1991), Hoernle et al. (2002), Huang et al. (1995), Kalt et al. (1997), Kampunzu et al. (1998), Keller and Krafft (1990), Kramm (1993), Kramm and Kogarko (1994), Kramm et al. (1997), Kumar et al. (1998), Kwon et al. (1989), Lancelot and Allègre (1974), le Roex and Lanyon (1998), Liegeois et al. (1991), Melluso et al. (2004), Middlemost (1990), Mitchell et al. (1994), Morisset (1992), Mourtada et al. (1997), Natarajan et al. (1994), Nelson et al. (1988), Nielsen and Buchardt (1985), Pandit et al. (2002), Paslick et al. (1995), Pearce and Leng (1996), Pollock (1987), Ray et al. (2000), Reischmann (1995), Ruberti et al. (1997, 2002), Savatenkov et al. (1999), Schleicher et al. (1990, 1991, 1998), Schultz et al. (2004), Silva et al. (1988), Simonetti and Bell (1994a, b), Simonetti et al. (1995, 1998), Smithies and Marsh (1998), Srivastava et al. (2005), Sun et al. (1986), Taubald et al. (2004), Thompson et al. (2002), Tilton and Bell (1994), Tilton et al. (1987, 1998), Toyoda et al. (1994), Veena et al. (1998), Verhulst et al. (2000), Verwoerd et al. (1993), Villeneuve and Relf (1998), Wagner et al. (2003), Waight et al. (2002), Walter et al. (1995), Wen et al. (1987), Ying et al. (2004), Zaitsev and Bell (1995), Zaitsev et al. (2002), Ziegler (1992), and references in Table 1.

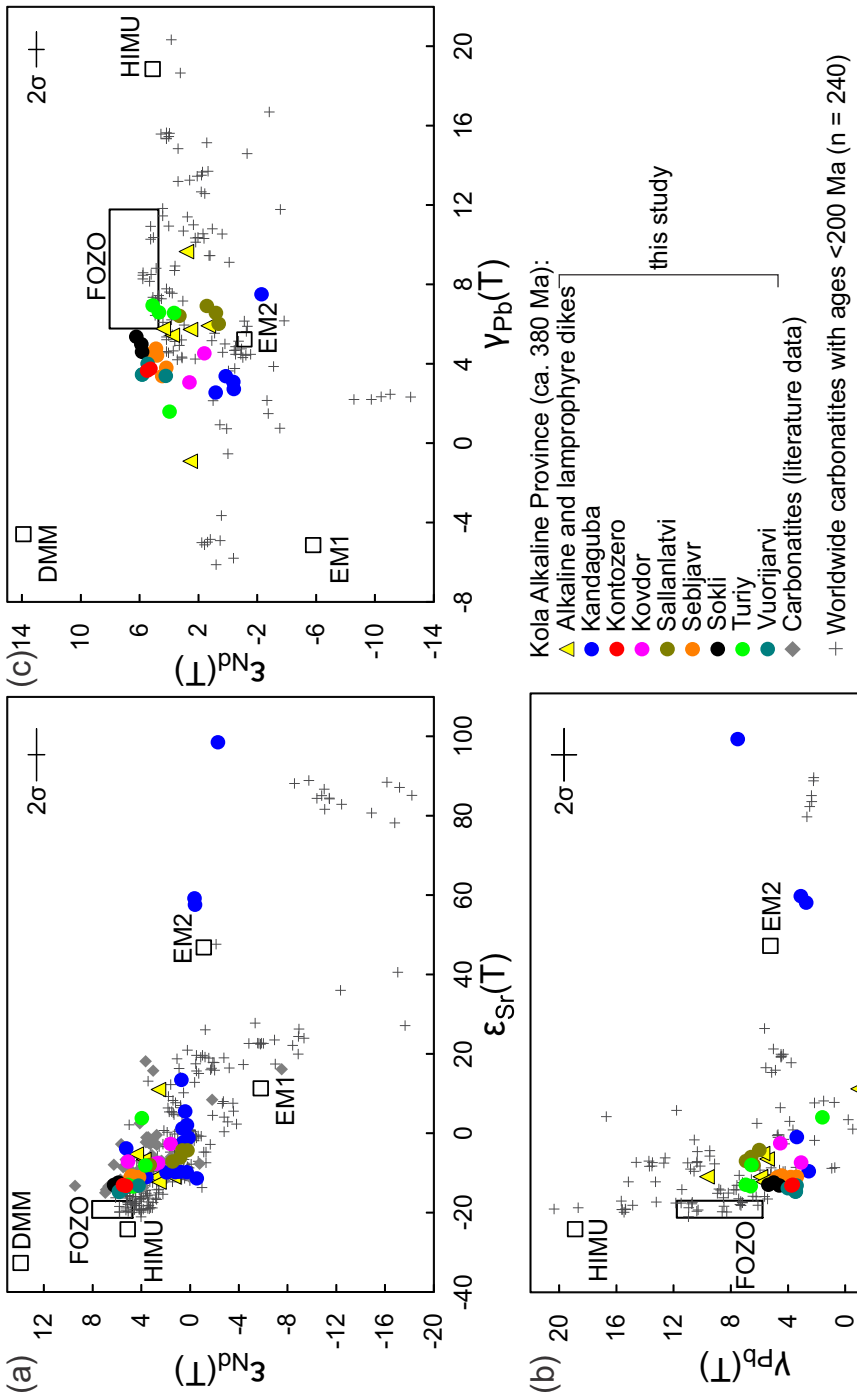

Fig. 3. Sr-Pb-Nd isotope correlation diagrams for carbonatite and alkaline complexes of the Kola alkaline province (380 Ma) in the Baltic Shield. **a)** $\varepsilon_{Sr}(T)$ versus $\varepsilon_{Nd}(T)$. **b)** $\varepsilon_{Sr}(T)$ versus $\gamma_{Pb}(T)$. **c)** $\gamma_{Pb}(T)$ versus $\varepsilon_{Nd}(T)$. $\varepsilon_{Sr}(T) = [(^{87}Sr/^{86}Sr_{sample}/^{87}Sr/^{86}Sr_{BE}) - 1]*10^4$, where $^{87}Sr/^{86}Sr_{sample}$ is the initial ratio in the sample and $^{87}Sr/^{86}Sr_{BE}$ is the ratio in the bulk Earth (after DePaolo and Wasserburg, 1976) at that time; $\gamma_{Pb}(T)= [(^{206}Pb/^{204}Pb_{sample}/^{206}Pb/^{204}Pb_{BSE}) - 1]*10^2$, where $^{206}Pb/^{204}Pb_{sample}$ is the initial ratio in the sample and $^{206}Pb/^{204}Pb_{BSE}$ is the ratio in the bulk silicate Earth (BSE; after Allègre and Lewin, 1989) at that time; $\varepsilon_{Nd}(T) = [(^{143}Nd/^{144}Nd_{sample}/^{143}Nd/^{144}Nd_{(CHUR)}) - 1]*10^4$, where $^{143}Nd/^{144}Nd_{sample}$ is the initial ratio in the sample and $^{143}Nd/^{144}Nd_{CHUR}$ is the ratio in the chondritic uniform reservoir (CHUR; after Jacobsen and Wasserburg, 1980; Hamilton et al., 1983) at that time. Depleted MORB mantle (DMM), enriched mantle 1 and 2 (EM1 and EM2), 'FOcus ZOne' (FOZO), and high-$^{238}U/^{204}Pb$ or μ (HIMU) mantle components after Hart et al. (1992), Stracke et al. (2005), and Stracke (2012). Data from Beard et al. (1996), Dunworth and Bell (2001), Kramm (1993), Rukhlov (1999), Verhulst et al. (2000), Zaitsev and Bell (1995), and Zaitsev et al. (2002). Also shown are data from the <200 Ma carbonatites worldwide (after Alberti et al., 1999; Barreiro and Cooper, 1987; Bell and Blenkinsop, 1987b; Bell and Peterson, 1991; Bell and Tilton, 2001; Bell et al., 2013; Bernard-Griffiths et al., 1991; Bizimis et al., 2003; Bizzarro et al., 2001; Castorina et al., 1996; Comin-Chiaramonti et al., 2002; Conticelli et al., 1995; Cooper and Reid, 1998; Hoernle and Tilton, 1991; Hoernle et al., 2002; Huang et al., 1995; Kalt et al., 1997; Keller and Krafft, 1990; Kwon et al., 1989; le Roex and Lanyon, 1998; Melluso et al., 2004; Mitchell et al., 1994; Morisset, 1992; Nelson et al., 1988; Paslick et al., 1995; Ruberti et al., 1997, 2002; Schleicher et al., 1991; Schultz et al., 2004; Simonetti and Bell, 1994a, b; Simonetti et al., 1995, 1998; Srivastava et al., 2005; Tilton et al., 1987, 1998; Toyoda et al., 1994; Veena et al., 1998; Wagner et al., 2003; Walter et al., 1995; Wen et al., 1987; Ying et al., 2004; Ziegler, 1992).

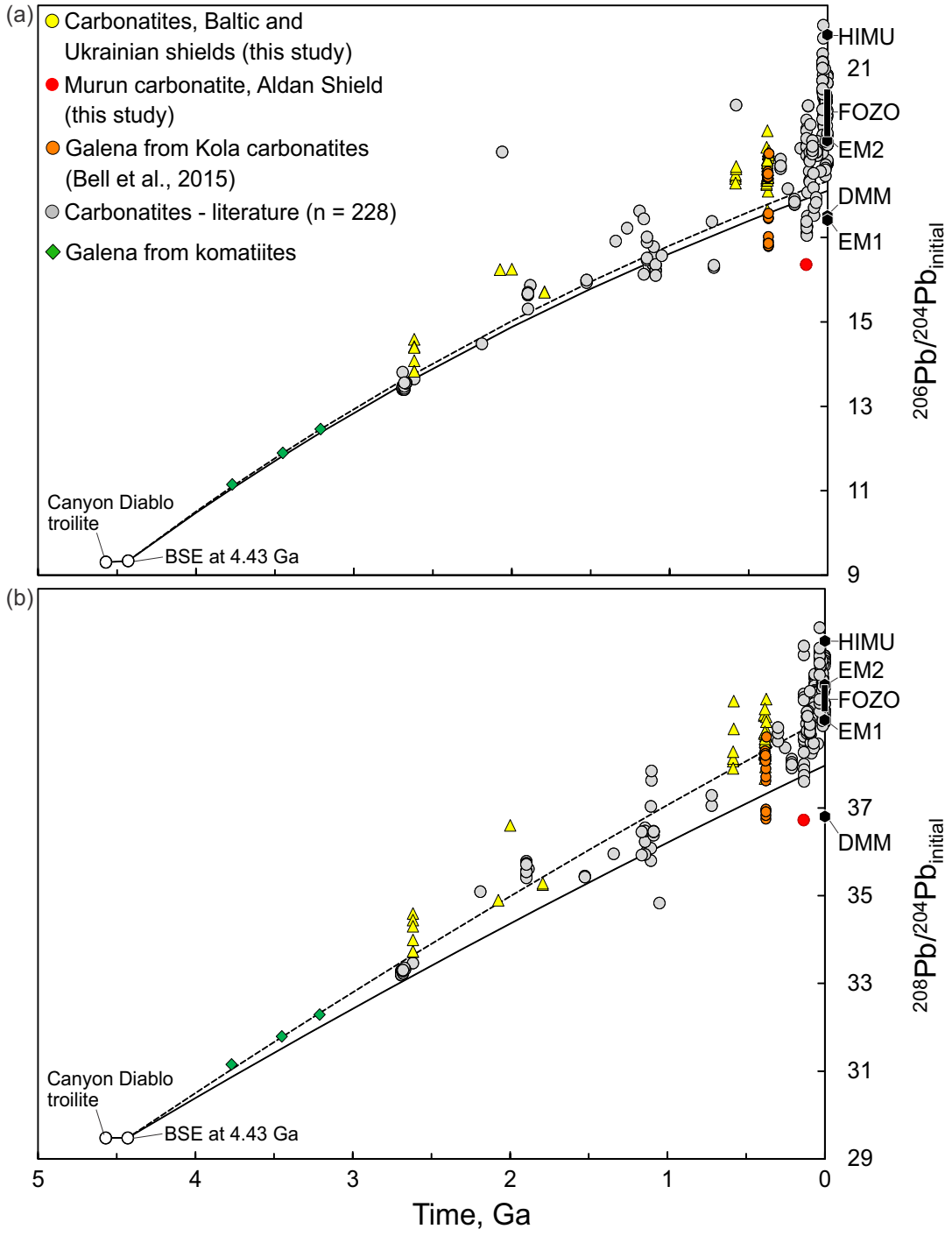

Fig. 4. Pb isotope development diagrams for carbonatites and alkaline complexes worldwide. **a)** Initial $^{206}Pb/^{204}Pb$ versus time. **b)** Initial $^{208}Pb/^{204}Pb$ versus time. BSE = bulk silicate Earth models (solid line after Galer and Goldstein, 1996; dashed line, Allègre and Lewin, 1989) assuming closed-system evolution from 4.43 Ga (Doe and Stacey, 1974; Wood et al., 2008). Depleted MORB mantle (DMM), enriched mantle 1 and 2 (EM1 and EM2), 'FOcus ZOne' (FOZO), and high-$^{238}U/^{204}Pb$ or μ (HIMU) mantle components after Hart et al. (1992), Stracke et al. (2005), and Stracke (2012). Initial Earth $^{206}Pb/^{204}Pb$ and $^{208}Pb/^{204}Pb$ ratios taken from Canyon Diablo troilite values (Tatsumoto et al., 1973) and $^{238}U/^{204}Pb$ = 0.7 at 4.57 Ga (after Allègre et al., 1995). Data from Barreiro and Cooper (1987), Bell and Tilton (2001), Bell et al. (1987, 2013), Bizimis et al. (2003), Cavell and Baadsgaard (1986), Corfu and Noble (1992), Dawson et al. (1995), Eby et al. (1995), Eriksson (1989), Grüenenfelder et al. (1986), Harmer et al. (1998), Hoernle and Tilton (1991), Hoernle et al. (2002), Huang et al. (1995), Kalt et al. (1997), Kramm and Koark (1988), Kramm and Kogarko (1994), Kwon et al. (1989), Lancelot and Allègre (1974), le Roex and Lanyon (1998), Nelson et al. (1988), Paslick et al. (1995), Ray et al. (2000), Reischmann (1995), Rukhlov and Bell (2010), Schleicher et al. (1991), Simonetti and Bell (1994a, b), Simonetti et al. (1995, 1998), Stendal et al. (2004), Thompson et al. (2002), Tilton and Bell (1994), Tilton et al. (1987, 1998), Toyoda et al. (1994), Veena et al. (1998), Verwoerd et al. (1993), and references in Table 1. Also shown are galena data from Isua, Pilbara and Barberton komatiites (after Appel et al., 1978; Richards et al., 1981; Stacey and Kramers, 1975).

(1996) and Allègre and Lewin (1989) assuming closed-system evolution from 4.43 Ga to the present (Doe and Stacey, 1974; Wood et al., 2008). Although the interpretation of the Pb isotope data is model-dependent, several important features are apparent. First, because most carbonatite data plot above BSE estimates (Fig. 4), their Pb isotopic data record higher time-integrated U/Pb and Th/Pb ratios of their sources than those of BSE, consistent with the models of increasing μ for the residual in the mantle partial melting processes (Hofmann, 1988; Kwon et al., 1989; Meijer et al., 1990; Collerson et al., 2010). Second, both the findings from U-Pb and Th-Pb in carbonatites worldwide are similar to those from Sr, lacking evidence for depleted mantle before ~3 Ga. Isotopic data for galena from Isua, and Pilbara and Barberton komatiites (Appel et al., 1978; Richards et al., 1981; Stacey and Kramers, 1975), as well as data from 2.7 Ga carbonatites and syenites from the Canadian Shield, plot close to values proposed for BSE (e.g., Allègre and Lewin, 1989; Kwon et al., 1989; Galer and Goldstein, 1996). However, the new calcite data from the Siilinjarvi carbonatite (2.6 Ga) lie about BSE towards slightly more radiogenic $^{206}Pb/^{204}Pb$ and $^{208}Pb/^{204}Pb$ ratios (Fig. 3), indicating higher U/Pb and Th/Pb ratios in their source than those in BSE, consistent with the findings of Tichomirowa et al. (2006). Third, the Pb isotope ratios from young (<0.2 Ga) carbonatites (Figs. 3 and 4) cover the range of data from OIBs involving HIMU, EM1, and FOZO (e.g., Simonetti et al., 1995, 1998; Bell and Simonetti, 1996; Bell and Tilton, 2001, 2002). Kwon et al. (1989) noted that the data from Canadian carbonatites younger than 2.7 Ga form negative slopes when plotted in $^{87}Sr/^{86}Sr$ vs. $^{206}Pb/^{204}Pb$ diagrams, similar to the mixing trends found between HIMU and EM1 end-members ('LoNd' array of Hart et al., 1986). Kwon et al. (1989) and Tilton and Kwon (1990) suggested that the carbonatite arrays resemble the slope of the OIB field, implying that both end members might have existed for at least 2.2 Ga. With the addition of new data from the Kola carbonatites (Fig. 3), it also appears that both FOZO and EM1 contributed to the 380 Ma plume.

Lead isotope data for galena from several of the Kola carbonatites show a considerable range of values that form a near-linear Pb-Pb isotope trend, a feature consistent with binary mixing (Bell et al., 2015). The more radiogenic end member, with values similar to FOZO and marked by a cluster of data from Kovdor, Sallanlatvi, Sokli and Vuoriyarvi, is interpreted to represent a closed-system, deep-seated, mantle reservoir (Fig. 4; Bell et al., 2015). The other, less radiogenic end member is represented by data from the Khibiny REE carbonatites and is similar to the very low $^{206}Pb/^{204}Pb$ and $^{208}Pb/^{204}Pb$ ratios for calcite from a Sr-Ba carbonatite from the Murun potassic complex (134 Ma) from the Aldan Shield (Mitchell et al., 1994). Both seem to have tapped the same source.

4.3. Nd isotopic evolution

Bell and Blenkinsop (1987a), Kwon et al. (1989), and Tilton and Bell (1994) presented Nd isotopic data for the same Canadian Shield complexes analyzed for Sr and Pb. In contrast to the Sr and Pb isotopic data, most Archean carbonatites and syenitic rocks are characterized by positive $\varepsilon_{Nd}(T)$ values relative to CHUR (after Jacobsen and Wasserburg, 1980; Hamilton et al., 1983) indicating that depleted mantle existed long before 3 Ga (Tilton and Kwon, 1990). The widespread nature of this depleted source is shown by the close agreement between Nd isotopic data for Archean carbonatites from the Baltic Shield, Greenland, and Canada (Karhu et al., 2001; Rukhlov et al., 2001; Bizzarro et al., 2002; Bell and Rukhlov, 2004; Tichomirowa et al., 2006, Zozulya et al., 2007).

The new Sm-Nd data shown in Figure 5a (n = 86) are similar to previously published values. Two important features are revealed in a compilation of $\varepsilon_{Nd}(T)$ values from worldwide carbonatites and from the oldest basalts, komatiites, and crustal rocks from northwestern Canada, South Africa, and West Greenland (Fig. 5a; Bowring and Housh, 1995; Blichert-Toft and Arndt, 1999; Blichert-Toft et al., 1999; Vervoort and Blichert-Toft, 1999). About 70% of the data have positive $\varepsilon_{Nd}(T)$ values marking the involvement of a depleted source. Furthermore, the scatter and range of $\varepsilon_{Nd}(T)$ values from carbonatites probably reflects intermittent mixing between enriched and depleted mantle sources over at least 3.0 Ga. With decreasing age, the $\varepsilon_{Nd}(T)$ values from carbonatites show much greater scatter and, although this might simply reflect the scarcity of Archean and Proterozoic carbonatites, we consider that it indicates a greater involvement of an enriched source, from either continental crust, or a deep-seated, primitive source.

Significantly, based on our new database, the present-day isotopic composition of the depleted mantle source is best represented by FOZO. The young carbonatites (<0.2 Ga) show a considerable range of $\varepsilon_{Nd}(T)$ values (from +6.1 to –23.3), while the Archean carbonatites have much more restricted range of $\varepsilon_{Nd}(T)$ values (from +4.4 to –2.6). We interpret these variations as indicating mixing between a depleted, FOZO-like source and a more enriched source such as the one reflected in the Phalaborwa (2.1 Ga), Spitskop (1.3 Ga), Tanil Nadu (0.8 Ga), and Murun and Laiwu-Zibo (0.1 Ga) complexes, and Cenozoic carbonatites in Italy (Eriksson, 1989; Mitchell et al., 1994; Kumar et al., 1998; Schleicher et al., 1998; Harmer, 1999; Pandit et al., 2002; Bizimis et al., 2003; Ying et al., 2004; Bell et al., 2013).

The main finding that emerges from the Nd data is that they point to a differentiation event much older than the 3 Ga depletion indicated by the Sr and Pb data (Tilton and Kwon, 1990; Rukhlov et al., 2001; Bell and Rukhlov, 2004). Either the Rb/Sr, U/Pb and Th/Pb ratios behaved differently than the Sm/Nd ratios during the Neoarchean event, or these apparent differences might be related to the choice of CHUR as the reference reservoir, especially if a non-chondritic model is assumed for BSE (e.g., Campbell and O'Neill, 2012). However, the convergence of terrestrial and extraterrestrial Nd-Hf isotope data (Martian, lunar, and eucrites) suggests that the CHUR estimate for BSE is probably correct (Bouvier et al., 2008). The Nd data from the Archean carbonatites show a spread similar to that from some of the Earth's oldest rocks (Fig. 5a; see Bowring

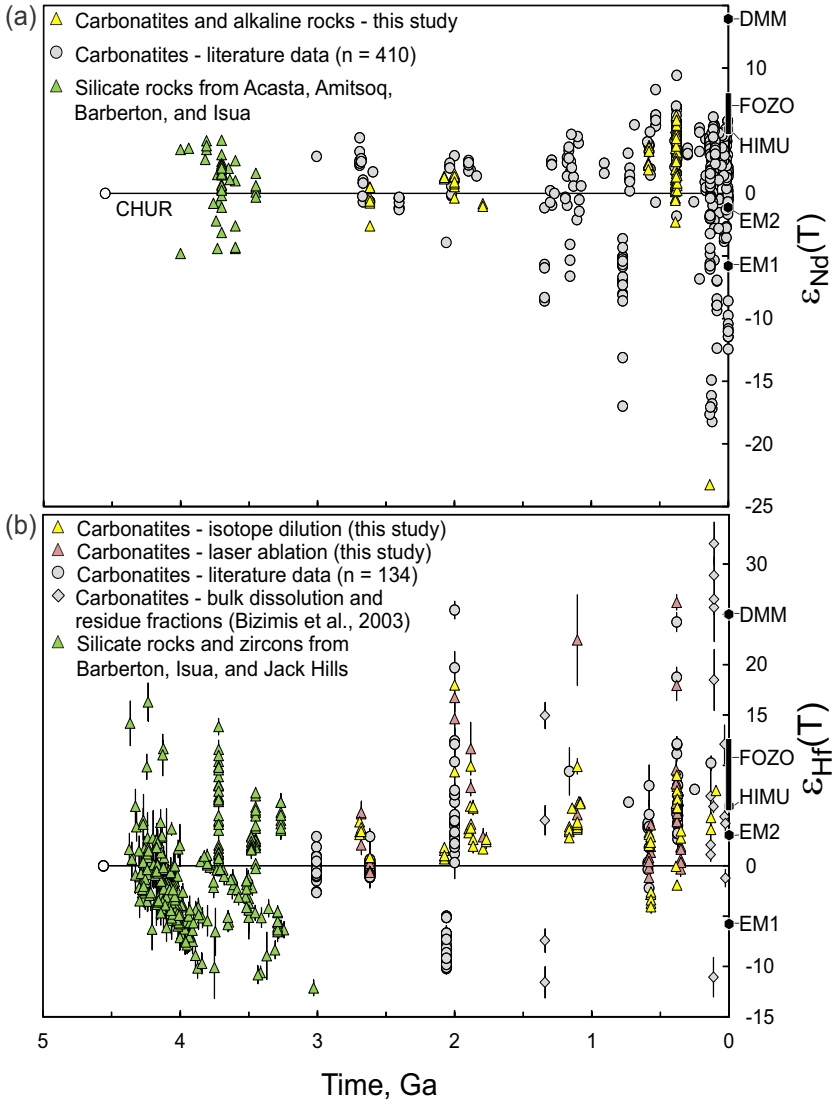

Fig. 5. Nd and Hf evolution diagrams for carbonatites worldwide and late Archean syenitic complexes from the Canadian Shield. Depleted MORB mantle (DMM), enriched mantle 1 and 2 (EM1 and EM2), 'FOcus ZOne' (FOZO), and high-$^{238}U/^{204}Pb$ or μ (HIMU) mantle components after Hart et al. (1992), Stracke et al. (2005), and Stracke (2012). **a)** $\varepsilon_{Nd}(T)$ versus time; $\varepsilon_{Nd}(T) = [(^{143}Nd/^{144}Nd_{sample}/^{143}Nd/^{144}Nd_{CHUR}) - 1]*10^4$, where $^{143}Nd/^{144}Nd_{sample}$ is the initial ratio in the sample and $^{143}Nd/^{144}Nd_{CHUR}$ is the ratio in the chondritic uniform reservoir (CHUR; after Jacobsen and Wasserburg, 1980; Hamilton et al., 1983) at that time. Data from Alberti et al. (1999), Andersen (1987, 1997), Baksi (1997), Balaganskaya et al. (2000), Barreiro and Cooper (1987), Beard et al. (1996), Bell and Blenkinsop (1987a, b), Bell and Peterson (1991), Bell and Tilton (2001), Bell et al. (1987, 2013), Bernard-Griffiths et al. (1991), Bizimis et al. (2003), Bizzarro et al. (2002), Castorina et al. (1996), Comin-Chiaramonti et al. (2002), Conticelli et al. (1995, 2002), Cooper and Mellish (2001), Cooper and Reid (1998), Corfu and Noble (1992), Coulson et al. (2003), Dunworth and Bell (2001), Eby et al. (1995), Eriksson (1989), Graham et al. (2004), Halama et al. (2005); Harmer (1999), Harmer et al. (1998), Hoernle and Tilton (1991), Hoernle et al. (2002), Huang et al. (1995), Kalt et al. (1997), Karhu et al. (2001), Keller and Krafft (1990), Kramm (1993), Kramm and Kogarko (1994), Kramm et al. (1997), Kumar et al. (1998), Kwon et al. (1989), le Roex and Lanyon (1998), Melluso et al. (2004), Middlemost (1990), Mitchell et al. (1994), Morisset (1992), Nelson et al. (1988), Pandit et al. (2002), Paslick et al. (1995), Pearce and Leng (1996), Pollock (1987), Ray et al. (2000), Reischmann (1995), Ruberti et al. (1997, 2002), Savatenkov et al. (1999), Schleicher et al. (1998), Schultz et al. (2004), Simonetti and Bell (1994a, b), Simonetti et al. (1995, 1998), Smithies and Marsh (1998), Srivastava et al. (2005), Sun et al. (1986), Thompson et al. (2002), Tilton and Bell (1994), Tilton et al. (1987, 1998), Toyoda et al. (1994), Veena et al. (1998), Verhulst et al. (2000), Verwoerd et al. (1993), Villeneuve and Relf (1998), Wagner et al. (2003), Walter et al. (1995), Wen et al. (1987), Yang et al. (2003), Ying et al. (2004), Zaitsev and Bell (1995), Zaitsev et al. (2002), Ziegler (1992), and references in Table 1. Also shown are data from the oldest silicate rocks from northwestern Canada, South Africa, and West Greenland (after Bowring and Housh, 1995; Blichert-Toft and Arndt, 1999; Blichert-Toft et al., 1999; Vervoort and Blichert-Toft, 1999). **b)** $\varepsilon_{Hf}(T)$ versus time; $\varepsilon_{Hf}(T) = [(^{176}Hf/^{177}Hf_{sample}/^{176}Hf/^{177}Hf_{CHUR}) - 1]*10^4$, where $^{176}Hf/^{177}Hf_{sample}$ is the initial ratio in the sample and $^{176}Hf/^{177}Hf_{CHUR}$ is the ratio in CHUR (after Iizuka et al., 2015) at that time. Data from Patchet et al. (1981), Bizzaro et al. (2002), Bizimis et al. (2003), Woodhead and Hergt (2005), Wu et al. (2006, 2010, 2011), Tappe et al. (2007, 2008), Kogarko et al. (2010), Ghobadi et al. (2012), Tichomoriwa et al. (2013), and references in Table 1. Also shown are data from the oldest silicate rocks and detrital zircons from South Africa, Western Australia, and West Greenland (Blichert-Toft and Arndt, 1999; Blichert-Toft et al., 2004; Harrison et al., 2005; Hoffmann et al., 2010; Kemp et al., 2010; Amelin et al., 2011; Puchtel et al., 2013). Error bars are 2σ uncertainties that include propagated errors associated with age, measured $^{167}Lu/^{177}Hf$ and $^{176}Hf/^{177}Hf$ ratios, ^{176}Lu decay constant, and CHUR parameters.

and Housh, 1995; Blichert-Toft and Arndt, 1999; Blichert-Toft et al., 1999; Vervoort and Blichert-Toft, 1999; Hoffmann et al., 2010; Caro, 2011), indicating a major differentiation event in the mantle before 3.0 Ga, perhaps within the first few hundred million years of Earth history.

4.4. Hf isotopic evolution

Although relatively scarce compared to Sr and Nd, the available Hf isotopic data from carbonatites worldwide show a huge range of initial $^{176}Hf/^{177}Hf$ ratios (Fig. 5b). Bizimis et al. (2003) reported Hf isotopic compositions for whole-rock, carbonate, and non-carbonate (leached residue) fractions from several carbonatites with different ages, which account for much of the scattering of $\varepsilon_{Hf}(T)$ values in Figure 5b (from +32 to –12). Because Hf in carbonatites resides mainly in non-carbonate minerals (see Chakhmouradian, 2006), unlike Nd, other REEs, and Sr, it is difficult to obtain a complete suite of Sr-Nd-Pb-Hf isotopic data from the same mineral or whole-rock sample. Even though carbonatites typically contain <1 ppm Lu, they still have very high Lu/Hf ratios (averaging ~1.2; Woolley and Kempe, 1989; Bizimis et al., 2003) so that their initial $^{176}Hf/^{177}Hf$ ratios cannot be measured directly. Therefore, initial $^{176}Hf/^{177}Hf$ ratios are best measured using primary magmatic minerals with low Lu/Hf ratios such as zircon or baddeleyite (Patchett et al., 1981) both of which are common in many carbonatites. Both of these minerals have very low $^{176}Lu/^{177}Hf$ ratios (<0.0047; e.g., Tichomirowa et al., 2013; this study) and very high Hf content (~1 wt.%).

Lu-Hf data from zircons and baddeleyites from sixteen carbonatite complexes with ages ranging from 2.6 to 0.4 Ga from the Baltic and Canadian shields and the Canadian Cordillera have positive $\varepsilon_{Hf}(T)$ values as high as +26, reflecting depleted mantle (Rukhlov and Bell, 2003). However, Bizzarro et al. (2002) did note enriched, negative $\varepsilon_{Hf}(T)$ values from the 3.0 Ga Tupertalik carbonatite from Greenland, the oldest known carbonatite, and attributed them to an enriched, sub-chondritic source isolated in the deep mantle for at least 3 Ga. Similar values have also been reported from the Phalaborwa carbonatite (2.1 Ga) in South Africa (Scherer et al., 2001, Wu et al., 2006, 2010, 2011). Carbonatites and kimberlites of different age from Greenland show $\varepsilon_{Hf}(T)$ values of between +7.9 to –5.1, indicating both depleted and enriched sources (Bizzarro et al., 2002).

Figure 5b shows $\varepsilon_{Hf}(T)$ values for carbonatites worldwide, along with data from the oldest terrestrial rocks and detrital zircons from South Africa, western Australia, and West Greenland (Blichert-Toft and Arndt, 1999; Blichert-Toft et al., 2004; Harrison et al., 2005; Hoffmann et al., 2010; Kemp et al., 2010; Amelin et al., 2011; Puchtel et al., 2013), plotted as a function of time. Our new Lu-Hf data obtained by solution MC-ICPMS with isotope dilution are in close agreement with the data obtained by laser ablation (Rukhlov and Bell, 2003) for Zr-minerals (Table 1) and with our database for carbonatites worldwide (Patchet et al., 1981; Bizzaro et al., 2002; Bizimis et al., 2003; Woodhead and Hergt, 2005; Wu et al., 2006, 2010, 2011; Tappe et al., 2007, 2008; Kogarko et al., 2010; Ghobadi et al., 2012; Tichomirowa et al., 2013).

Most of the carbonatite data shown in Figure 5b reflect depleted mantle. The late Archean carbonatites have $\varepsilon_{Hf}(T)$ values between +5.3 and –2.7, whereas the younger carbonatites have values between +26.2 and –10.2. The extremely radiogenic values for some of the young carbonatites are well beyond the range of the $\varepsilon_{Hf}(T)$ values from modern oceanic basalts (FOZO, HIMU, EM1 and EM2 shown in Fig. 5b) and such anomalous values are thus unlikely to reflect the isotopic composition of their mantle sources. Insights into the Hf data come from analyses of individual mineral grains.

Large variations of $\varepsilon_{Hf}(T)$ values (up to 20 units) within single zircon grains, documented by Tichomirowa et al. (2013) from the Tikseozero carbonatite complex (2.0 Ga) in the Baltic Shield, are accompanied by enrichment in Ca and other 'impurities', variable $\delta^{18}O$ values, and U/Pb disturbances. Tichomirowa et al. (2013) attributed these wide variations of Hf isotope compositions to a dissolution-reprecipitation of zircon and incorporation of radiogenic Hf from co-existing high-Lu/Hf phases such as carbonate and apatite during melt evolution. Because of their very high Lu/Hf ratios, these phases can rapidly develop very high $^{176}Hf/^{177}Hf$ ratios over a time interval of a few million years (Bizimis et al., 2003). Considering the protracted magmatic evolution proposed for the Oka carbonatite complex (0.1 Ga) in Canada of a few Ma (Chen and Simonetti, 2013), and the extremely radiogenic $\varepsilon_{Hf}(T)$ values from Oka (Bizimis et al., 2003) and other carbonatite complexes (e.g., Wu et al., 2010; Tichomirowa et al., 2013), the data may thus reflect incorporation of radiogenic Hf during mineral growth. The wide range of $\varepsilon_{Hf}(T)$ values for some of our data, especially from the Tiksheozero (2.0 Ga), Nemegosenda Lake (1.1 Ga), and Afrikanda (0.38 Ga) complexes could be consistent with these findings. If we consider some of these highly radiogenic values to be anomalous, then the present-day $\varepsilon_{Hf}(T)$ value for one of the end members could still be considered similar to FOZO.

In spite of the wide variation in $\varepsilon_{Hf}(T)$ values, the Hf isotopic data from carbonatites, along with those from the older silicate rocks and the Nd isotope data, suggest that the depleted mantle was formed by a major differentiation event before 3.0 Ga, perhaps during the Hadean (>4.0 Ga).

5. Conclusions

The Sr-Pb-Nd-Hf isotopic data from globally distributed carbonatites record the evolution of a primitive mantle source that has behaved as a relatively closed-system, at least during the last 3 Ga of Earth history, with the present-day, isotopic attributes similar to FOZO. Solar-like noble gas (He, Ne, Ar, Kr, and Xe) and N isotopic signatures in carbonatites further suggest that this widespread source may represent the deep, undegassed mantle. The Nd and Hf data from carbonatites and the oldest silicate rocks indicate a major depletion of chondritic Earth >3.0 Ga, perhaps during the Hadean (>4.0 Ga), and possibly a second, much later event at ~3 Ga, marked

by a depleted mantle with low Rb/Sr and high U/Pb ratios. The ~3 Ga event could reflect a major change in the Earth's thermal regime marked by the onset of modern-style plate tectonics accompanied by the production of voluminous and more sialic, juvenile, continental crust (Tilton and Kwon, 1990; Dhuime et al., 2015). It appears that over the last 3 Ga, HIMU- and EM-like mantle end-members, and rarely, a more exotic, high-$^{87}Sr/^{86}Sr$ component (Bell et al., 2013) have been mixed in variable proportions with a depleted source (FOZO) accounting for the isotopic heterogeneity of the carbonatitic melt. The interpretation that we favour is one in which these enriched mantle end-members represent complementary partial melt (EM1) and residual (HIMU) of the FOZO protolith (Collerson et al., 2010) or, alternatively, primordial materials, perhaps including recycled Hadean crust, sampled by deep-mantle plumes originating from the D" layer (e.g., Tolstikhin and Hofmann, 2005; Campbell and O'Neill, 2012).

Acknowledgments

Alexei S. Rukhlov visited Carleton University under the Carleton University-St. Petersburg University international exchange programme and later held a NATO post-doctoral fellowship at the same institution. This work was also supported by St. Petersburg State University, Carleton University, and the Natural Sciences and Engineering Research Council of Canada (A7813). We thank the Geological Survey of Canada, and Antonio Simonetti (formerly of the Geotop Laboratory at the Université du Québec à Montréal), for help with the Lu-Hf isotopic analyses, as well as the Royal Ontario Museum, and the many colleagues for providing rock specimens for this study. We are also grateful to Andreas Stracke (Westfälische Wilhelms Universität, Institut für Mineralogie), Lawrence Aspler (British Columbia Geological Survey), and George Simandl (British Columbia Geological Survey) for their comments.

References cited

Alberti, A., Castorina, F., Censi, P., Comin-Chiaramonti, P., and Gomes, C.B., 1999. Geochemical characteristics of Cretaceous carbonatites from Angola. Journal of African Earth Sciences, 29, 735–759.

Allègre, C.J., and Lewin, E., 1989. Chemical structure and history of the Earth: evidence from global non-linear inversion of isotopic data in a three-□ model. Earth and Planetary Science Letters, 96, 61–88.

Allègre, C.J., Manhes, G., and Gopel, C., 1995. The age of the Earth. Geochimica et Cosmochimica Acta, 59, 1445–1456.

Amelin, Y., and Zaitsev, A.N., 2002. Precise geochronology of phoscorites and carbonatites: the critical role of U-series disequilibrium in age interpretations. Geochimica et Cosmochimica Acta, 66, 2399–2419.

Amelin, Y., Lee, D.-C., Halliday, A.N., and Pidgeon, R.T., 1999. Nature of the Earth's earliest crust from hafnium isotopes in single detrital zircons. Nature, 399, 252–255.

Amelin, Y., Lee, D.C., and Halliday, A.N., 2000. Early-middle Archaean crustal evolution deduced from Lu–Hf and U–Pb isotopic studies of single zircon grains. Geochimica et Cosmochimica Acta, 64, 4205–4225.

Amelin, Y., Kamo, S.L., and Lee, D.C., 2011. Evolution of early crust in chondritic or non-chondritic Earth inferred from U–Pb and Lu–Hf data for chemically abraded zircon from the Itsaq Gneiss Complex, West Greenland. Canadian Journal of Earth Sciences, 48, 141–160.

Andersen, T., 1987. Mantle and crustal components in a carbonatite complex, and the evolution of carbonatite magma; REE and isotopic evidence from the Fen Complex, Southeast Norway. Chemical Geology, 65, 147–166.

Andersen, T., 1997. Age and petrogenesis of the Qassiarsuk carbonatite-alkaline silicate volcanic complex in the Gardar rift, South Greenland. Mineralogical Magazine, 61, 499–513.

Appel, P.W.U., Moorbath, S., and Taylor, P.N., 1978. Least radiogenic terrestrial lead from Isua, West Greenland. Nature, 272, 524–526.

Arzamastsev, A.A., and Belyatsky, B.V., 2000. Palaeozoic activation in the Northeastern Fennoscandian shield: Rb–Sr and Sm–Nd isochron dating of initial volcanics and final dyke pulses of magmatism. In: Abstracts of the 5th SVEKALAPKO Workshop, Lammi, Finland, 2–5 November 2000, Report 23. Department of Geophysics, University of Oulu, Oulu, Finland, p. 6.

Arzamastsev, A.A., Arzamastseva, L.V., and Belyatsky, B.V., 1998. Initial alkaline volcanism of the Palaeozoic tectonic and magmatic activation in the North-Eastern Fennoscandia: geochemical features and petrological consequences. Petrology, 6, 316–336 (in Russian).

Bailey, D.K., and Woolley, A.R., 1995. Magnetic quiet periods and stable continental magmatism: can there be a plume dimension? In: Anderson, D.L., Hart, S.R., and Hofmann, A.W., (Eds.), Plume 2: Alfred-Wegener conference. Terra Nostra, 3/1995, Bonn, Rottach-Egern, Federeal Republic of Germany, pp. 15–19.

Baksi, A.K., 1997. The timing of Late Cretaceous alkalic igneous activity in the northern Gulf of Mexico basin, southeastern USA. Journal of Geology, 105, 629–643.

Balaganskaya, E., Verhulst, A., Downes, H., Liferovich, R., Demaiffe, D., and Laajoki, K., 2000. Geochemistry, petrography and mineralogy of clinopyroxenite, phoscorites and carbonatites of the Seblyavr Massif, Kola Alkaline Carbonatite Province, Russia. In: Abstracts of the 5th SVEKALAPKO Workshop, Lammi, Finland, 2–5 November 2000, Report 23. Department of Geophysics, University of Oulu, Oulu, Finland, p. 8.

Balaganskaya, E.G., Downes, H., and Demaiffe, D., 2007. REE and Sr-Nd isotope compositions of clinopyroxenites, phoscorites and carbonatites of the Seblyavr massif, Kola peninsula, Russia. Mineralogia Polonica, 38, 29–45.

Barreiro, B.A., and Cooper, A.F., 1987. A Sr, Nd, and Pb isotope study of alkaline lamprophyres and related rocks from Westland and Otago, South Island, New Zealand. In: Morris, E. M., and Pasteris, J.D., (Ed.), Mantle Metasomatism and Alkaline Magmatism. Geological Society of America Special Paper 215, pp. 115–125.

Bayanova, T.B., 2006. Baddeleyite: a promising geochronometer for alkaline and basic magmatism. Petrology, 14, 187–200.

Beard, A.D., Downes, H., Vetrin, V., Kempton, P.D., and Maluski, H., 1996. Petrogenesis of Devonian lamprophyre and carbonatite minor intrusions, Kandalaksha Gulf (Kola Peninsula). Lithos, 39, 93–119.

Bell, K., (Ed.), 1989. Carbonatites: Genesis and Evolution. Unwin Hyman, London, United Kingdom, 618 p.

Bell, K., 2001. Carbonatites: relationships to mantle-plume activity. In: Ernst, R.E. and Buchan, K.L. (Eds.), Mantle Plumes: Their Identification through Time. Geological Society of America Special Paper 352, pp. 267–290.

Bell, K., and Blenkinsop, J., 1987a. Archean depleted mantle - evidence from Nd and Sr initial isotope ratios of carbonatites. Geochimica et Cosmochim Acta, 51, 291–298.

Bell, K., and Blenkinsop, J., 1987b. Nd and Sr isotopic compositions of East African carbonatites: implications for mantle heterogeneity. Geology, 15, 99–102.

Bell, K., and Dawson, J.B., 1995. Nd and Sr isotope systematics of the active carbonatite volcano, Oldoinyo Lengai. In: Bell, K., and Keller, J., (Eds.), Carbonatite Volcanism. IAVCEI Proceedings in Volcanology, 4, Springer-Verlag, Berlin, pp. 100–112.

Bell, K., and Peterson, T., 1991. Nd and Sr isotope systematics of Shombole Volcano, East Africa, and the links between nephelinites, phonolites, and carbonatites. Geology, 19, 582–585.

Bell, K., and Rukhlov, A.S., 2004. Carbonatites from the Kola Alkaline Province: origin, evolution and source characteristics. In: Wall, F., and Zaitsev, A.N., (Eds.), Phoscorites and Carbonatites from Mantle to Mine: The Key Example of the Kola Alkaline Province. Mineralogical Society Series, 10, The Mineralogical Society, London, United Kingdom, pp. 433–468.

Bell, K., and Simonetti, A., 1996. Carbonatite magmatism and plume activity: implications from the Nd, Pb and Sr isotope systematics of Oldoinyo Lengai. Journal of Petrology, 37, 1321–1339.

Bell, K., and Tilton, G.R., 2001. Nd, Pb and Sr isotopic compositions of east African carbonatites: evidence for mantle mixing and plume inhomogeneity. Journal of Petrology, 42, 1927–1945.

Bell, K., and Tilton, G.R., 2002. Probing the mantle: the story from carbonatites. American Geophysical Union, Eos Transactions, 83, 273, 276–277.

Bell, K., Blenkinsop, J., Cole, T.J.S., Menagh, D.P., 1982. Evidence from Sr isotopes for long-lived heterogeneities in the upper mantle. Nature, 298, 251–253.

Bell, K., Blenkinsop, J., Kwon, S.T., Tilton, G.R., and Sage, R.P., 1987. Age and radiogenic isotopic systematics of the Borden carbonatite complex, Ontario, Canada. Canadian Journal of Earth Sciences, 24, 24–30.

Bell, K., Lavecchia, G., and Rosatelli, G., 2013. Cenozoic Italian magmatism: isotope constraints for possible plume-related activity. In: Gwalani, L.G., Comin-Chiaramonti, P., and Downes, P.J., (Eds.), Alkaline Magmatism and the Lithospheric Mantle: a Special Issue in Honour of the Work of Celso de Barros Gomes on the Occasion of His 77th Birthday. Journal of South American Earth Sciences, 41, pp. 22–40.

Bell, K., Zaitsev, A.N., Spratt, J., Fröjdo, S., and Rukhlov, A.S., 2015. Elemental, lead and sulfur isotopic compositions of galena from Kola carbonatites, Russia: implications for melt and mantle evolution. Mineralogical Magazine, 79, 219–241.

Ben Othman, D., Polve, M., and Allègre, C.J., 1984. Nd-Sr isotopic composition of granulites and constraints on the evolution of the lower continental crust. Nature, 307, 510–515.

Bernard-Griffiths, J., Fourcade, S., and Dupuy, C., 1991. Isotopic study (Sr, Nd, O and C) of lamprophyres and associated dykes from Tamazert (Morocco): crustal contamination processes and source characteristics. Earth and Planetary Science Letters, 103, 190–199.

Bizimis, M., Salters, V.J.M., and Dawson, J.B., 2003. The brevity of carbonatite sources in the mantle: evidence from Hf isotopes. Contributions to Mineralogy and Petrology, 145, 281–300.

Bizzarro, M., Simonetti, A., Stevenson, R.K., and Kurszlaukis, S., 2001. Evidence for plume-lithosphere interaction from Nd-Sr systematics of carbonatites and kimberlite-hosted peridotite xenoliths, southwestern Greenland. In: Jones, A., Wall, F., Keller, J., and Gilmour, I., (Convenors), The Role of Mantle Carbon in the Global Carbon Cycle (A Session of the EuroCarb ESF Network). Kaiserstuhl Workshop, 6-8 April 2001, Breisach, Germany and EUG XI Conference, 8-12 April 2001, Strasbourg, France, Symposium MS10, Abstracts, p. 490.

Bizzarro, M., Simonetti, A., Stevenson, R.K., and David, J., 2002. Hf isotope evidence for a hidden mantle reservoir. Geology, 30, 771–774.

Bizzarro, M., Simonetti, A., Stevenson, R.K., and Kurszlaukis, S., 2003. In situ $^{87}Sr/^{86}Sr$ investigation of igneous apatites and carbonates using laser-ablation MC-ICP-MS. Geochimica et Cosmochimica Acta, 67, 289–302.

Blaxland, A.B., van Breemen, O., Emeleus, C.H., and Anderson, J.G., 1978. Age and origin of the major syenite centers in the Gardar Province of South Greenland: Rb-Sr studies. Geological Society of America Bulletin 89, 231–244.

Blichert-Toft, J. and Arndt, N.T., 1999. Hf isotope compositions of komatiites. Earth and Planetary Science Letters, 171, 439–451.

Blichert-Toft, J., Arndt, N.T., and Ludden, J.N., 1996. Precambrian alkaline magmatism. In: Ludden, J.N., Arndt, N.T., and Francis, D., (Eds.), Mafic Magmatism Through Time. Lithos, 37, pp. 97–111.

Blichert-Toft, J., Albarède, F., Rosing, M., Frei, R., and Bridgwater, D., 1999. The Nd and Hf isotopic evolution of the mantle through the Archean. Results from the Isua supracrustals, West Greenland, and from the Birimian terranes of West Africa. Geochimica et Cosmochimica Acta, 63, 3901–3914.

Blichert-Toft, J., Arndt, N.T., and Gruau, G., 2004. Hf isotopic measurements on Barberton komatiites: effects of incomplete sample dissolution and importance for primary and secondary magmatic signatures. Chemical Geology, 207, 261–275.

Bouvier, A., Vervoort, J.D., and Patchett, P.J., 2008. The Lu–Hf and Sm–Nd isotopic composition of CHUR: constraints from unequilibrated chondrites and implications for the bulk composition of terrestrial planets. Earth and Planetary Science Letters, 273, 48–57.

Bowring, S.A., and Housh, T.B, 1995. The Earth's early evolution. Science, 269, 1535–1540.

Campbell, I.H., and O'Neill, H.St.C., 2012. Evidence against a chondritic Earth. Nature, 483, 553–558.

Caro, G., 2011. Early silicate Earth differentiation. Annual Review of Earth and Planetary Sciences, 39, 31–58.

Bulakh, A.G., Nesterov, A.R., Zaitsev, A.N., Pilipiuk, A.N., Wall, F., and Kirillov, A.S., 2000. Sulfur-containing monazite–(Ce) from late-stage mineral assemblages at the Kandaguba and Vuoriyarvi carbonatite complexes, Kola peninsula, Russia. Neues Jahrbuch für Mineralogie-Monatshefte, 2000 (5), 217–233.

Castorina, F., Censi, P., Barbieri, M., Comin-Chiaramonti, P., Cundari, A., Gomes, C.B., and Pardini, G., 1996. Carbonatites from Eastern Paraguay: a comparison with the coeval carbonatites from Brazil and Angola. In: Comin-Chiaramonti, P., and Gomes, C.B., (Eds.), Alkaline Magmatism in Central-Eastern Paraguay. Relationships with Coeval Magmatism in Brazil. EDUSP/FAPESP, São Paulo, Brazil, pp. 231–248.

Cavell, P.A., and Baadsgaard, H., 1986. Geochronology of the Big Spruce Lake alkaline intrusion. Canadian Journal of Earth Sciences, 23, 1–10.

Chakhmouradian, A.R., 2006. High-field-strength elements in carbonatitic rocks: geochemistry, crystal chemistry and significance for constraining the sources of carbonatites. Chemical Geology, 235, 138–160.

Chen, W., and Simonetti, A., 2013. In-situ determination of major and trace elements in calcite and apatite, and U-Pb ages of apatite from the Oka carbonatite complex: insights into a complex crystallization history. In: Tappe, S., Pearson, D.G., and Prelević, D., (Eds.), Kimberlite, Carbonatite, and Potassic Magmatism as Part of the Geochemical Cycle. Chemical Geology, 353, pp. 151–172.

Chorlton, L.B., 2007. Generalized geology of the world: bedrock domains and major faults in GIS format. Geological Survey of Canada, Open File 5529, CD-ROM.

Claesson, S., Vetrin, V., Bayanova, T., and Downes, H., 2000. U-Pb zircon ages from a Devonian carbonatite dyke, Kola peninsula, Russia: a record of geological evolution from the Archaean to the Palaeozoic. Lithos, 51, 95–108.

Collerson, K.D., Williams, Q., Ewart, A.E., and Murphy, D.T., 2010. Origin of HIMU and EM-1 domains sampled by ocean island basalts, kimberlites and carbonatites: The role of CO_2-fluxed lower mantle melting in thermochemical upwellings. Physics of the Earth

and Planetary Interiors, 181, 112–131.
Comin-Chiaramonti, P., Gomes, C.B., Castorina, F., Di Censi, P., Antonini, P., Furtado, S., Ruberti, E., and Scheibe, L.F., 2002. Geochemistry and geodynamic implications of the Anitápolis and Lages alkaline carbonatite complexes, Santa Catarina State, Brazil. Revista Brasileira de Geociencias, 32, 43–58.
Conticelli, S., Manetti, P., Capaldi, G., and Poli, G.,1995. Petrology, mineralogy and isotopes in olivine mela-nephelinites, basanites and carbonatites from Uwaynat region, southeast Libya: inferences on their genesis. Africa Geoscience Review, 2, 227–235.
Conticelli, S., D'Antonio, M., Pinarelli, L., and Civetta, L., 2002. Source contamination and mantle heterogeneity in the genesis of Italian potassic and ultrapotassic volcanic rocks: Sr-Nd-Pb isotope data from Roman Province and southern Tuscany. In: Thibault, Y. and Conticelli, S., (Eds.), Alkaline Igneous Rocks: A. D. Edgar Memorial Volume. Mineralogy and Petrology, 74, pp. 189–222.
Cooper, A.F., and Mellish, S.D., 2001. Nepheline syenite and carbonatite from the Transantarctic Mountains of southern Victoria Land. In: Gehör, S., Wall, F., and Liferovich, R., (Eds.), Formation, Exploration and Exploitation of Economic Deposits Associated with Mantle Carbon, EuroCarb Finland–Kola, Russia Workshop, 14-20 September 2001. Programme and Abstracts, RES TERRAE, A20, Department of Geology, University of Oulu, Oulu, Finland, p. 7.
Cooper, A.F., and Reid, D.L., 1998. Nepheline sövites as parental magmas in carbonatite complexes; evidence from Dicker Willem, Southwest Namibia. Journal of Petrology, 39, 2123-2136.
Corfu, F., and Noble, S.R., 1992. Genesis of the southern Abitibi greenstone belt, Superior Province, Canada: evidence from zircon Hf isotope analyses using a single filament technique. Geochimica et Cosmochimica Acta, 56, 2081–2097.
Corfu, F., Bayanova, T.B., Shchiptsov, V.V., and Frantz, N., 2011. U–Pb ID-TIMS age of the Tiksheozero carbonatite: expression of 2.0 Ga alkaline magmatism in Karelia, Russia. Central European Journal of Geosciences, 3, 302–308.
Coulson, I.M., Goodenough, K.M., Pearce, N.J.G., and Leng, M.J., 2003. Carbonatites and lamprophyres of the Gardar Province: a 'window' to the sub-Gardar mantle? In: Goodenough, K.M., Coulson, I.M., and Wall, F., (Eds.), Intraplate Alkaline Magmatism: Mineralogy and Petrogenesis. Mineralogical Magazine, 67, pp. 855–872.
Dahlgren, S., 1994. Late Proterozoic and Carboniferous ultramafic magmatism of carbonatitic affinity in Southern Norway. Lithos, 31, 141–154.
Dauphas, N., and Marty, B., 1999. Heavy nitrogen in carbonatites of the Kola Peninsula: a possible signature of the deep mantle. Science, 286, 2488–2490.
Dawson, J.B., Smith, J.V., and Steele, I.M., 1995. Petrology and mineral chemistry of plutonic igneous xenoliths from the carbonatite volcano, Oldoinyo Lengai, Tanzania. Journal of Petrology, 36, 797–826.
de Ignacio, C., Muñoz, M., Sagredo, J., Fernández-Santín, S., and Johansson, Å., 2006. Isotope geochemistry and FOZO mantle component of the alkaline–carbonatitic association of Fuerteventura, Canary Islands, Spain. Chemical Geology, 232, 99–113.
DePaolo, D.J., and Wasserburg, G.J., 1976. Inferences about magma sources and mantle structure from variations of $^{143}Nd/^{144}Nd$. Geophysical Research Letters, 3, 743–746.
Dhuime, B., Wuestefeld, A., and Hawkesworth, C.J., 2015. Emergence of modern continental crust about 3 billion years ago. Nature Geoscience, 8, 552–555.
Dion, C., Machado, N., and Joanisse, A., 1995. Géochronologie préliminaire des intrusions felsiques et alcalines associées au minéralisations aurifères du segment de Caopatina, région de Chibougamau. In: Dompierre, F., (Ed.), La science au service de l'exploration: Séminaire d'information sur la recherche géologique, programme et résumés. Ministère de l'Énergie et des Ressources du Québec, Direction Générale de l'Exploration Géologique et Minérale, DV 95-04, 45 p.
Doe, B.R., and Stacey, J.S., 1974. The application of lead isotopes to the problems of ore genesis and ore prospect evaluation: a review. Economic Geology, 69, 757–776.
Dunai, T., Stoessel, G.F.U., and Ziegler, U.R.F., 1989. A Sr isotope study of the Eureka Carbonatite, Damaraland, Namibia. Communications of the Geological Survey of South West Africa/ Namibia, 5, 89–90.
Dunworth, E.A., and Bell, K., 2001. The Turiy Massif, Kola Peninsula, Russia: isotopic and geochemical evidence for multi-source evolution. Journal of Petrology, 42, 377– 405.
Eby, G.N., Roden-Tice, M., Krueger, H.L., Ewing, W., Faxon, E.H., and Woolley, A.R., 1995. Geochronology and cooling history of the northern part of the Chilwa alkaline province, Malawi. Journal of African Earth Sciences, 20, 275–288.
Eriksson, S.C., 1989. Phalaborwa: a saga of magmatism, metasomatism and miscibility. In: Bell, K. (ed.), Carbonatites: Genesis and Evolution. Unwin Hyman, London, United Kingdom, pp. 221–254.
Ernst, R.E., and Bell, K., 2010. Large igneous provinces (LIPs) and carbonatites. Mineralogy and Petrology, 98, 55–76.
Galer, S.J.G., and Goldstein, S.L., 1996. Influence of accretion on lead in the Earth. In: Basu, A.R., and Hart, S.R., (Eds.), Earth Processes: Reading the Isotopic Code. American Geophysical Union, Geophysical Monograph, 95, pp. 75–98.
Gerlach, D.C., Cliff, R.A., Davies, G.R., Norry, M., and Hodgson, N., 1988. Magma sources of the Cape Verdes archipelago: isotopic and trace element constraints. Geochimica et Cosmochimica Acta, 52, 2979–2992.
Ghobadi, M., Gerdes, A., Kogarko, L.N., and Brey, G., 2012. New data on the composition and hafnium isotopes of zircons from carbonatites of the Khibiny Massif. Doklady Earth Sciences, 446, 1083–1085.
Graham, S., Lambert, D., and Shee, S., 2004. The petrogenesis of carbonatite, melnoite and kimberlite from the Eastern Goldfields Province, Yilgarn Craton. In: Mitchell, R.H., Gruetter, H.S., Heaman, L.M., Scott Smith, B.H., and Stachel, T., (Eds.), Selected Papers from the Eighth International Kimberlite Conference: Volume 1, The C. Roger Clement Volume. Lithos, 76, pp. 519–533.
Grüenenfelder, M.H., Tilton, G.R., Bell, K., and Blenkinsop, J., 1986. Lead and strontium isotope relationships in the Oka carbonatite complex, Quebec. Geochimica et Cosmochimica Acta, 50, 461–468.
Halama, R., Vennemann, T., Siebel, W., and Markl, G., 2005. The Grønnedal-Ika carbonatite-syenite complex, South Greenland: carbonatite formation by liquid immiscibility. Journal of Petrology, 46, 191–217.
Hamilton, P.J., O'Nions, R.K., Bridgwater, D., and Nutman, A., 1983. Sm–Nd studies of Archaean metasediments and metavolcanics from West Greenland and their implications for the Earth's early history. Earth and Planetary Science Letters, 62, 263–272.
Hansen, K., 1981. Systematic Sr-isotopic variation in alkaline rocks from West Greenland. Lithos, 14, 183–188.
Harmer, R.E., 1985. A Sr isotope study of Transvaal carbonatites. Verhandelinge van die Geologiese Vereniging van Suid Afrika, 88, 471–472.
Harmer, R.E., 1999. The petrogenetic association of carbonatite and alkaline magmatism: constraints from the Spitskop Complex, South Africa. Journal of Petrology, 40, 525–548.
Harmer, R.E., Lee, C.A., and Eglington, B.M., 1998. A deep mantle source for carbonatite magmatism: evidence from the nephelinites and carbonatites of the Buhera District, SE Zimbabwe. Earth and Planetary Science Letters, 158, 131–142.

Harrison, T.M., Blichert-Toft, J., Muller, W., Albarède, F., Holden, P., and Mojzsis, S.J., 2005. Heterogeneous Hadean hafnium: evidence for continental crust at 4.4 to 4.5 Ga. Science 310, 1947–1950.

Hart, S.R., 1988. Heterogeneous mantle domains: signatures, genesis and mixing chronologies. Earth and Planetary Science Letters, 90, 273–296.

Hart, S.R., and Brooks, C., 1970. Rb-Sr mantle evolution models. In: Carnegie Institution of Washington Year Book, 68, Carnegie Institution of Washington, Washington, DC, United States, pp. 426–429.

Hart, S.R., Gerlach, D.C., and White, W.M., 1986. A possible new Sr–Nd–Pb mantle array and consequences for mantle mixing. Geochimica et Cosmochimica Acta, 50, 1551–1557.

Hart, S.R., Hauri, E.H., Oschmann, L.A., and Whitehead, J.A., 1992. Mantle plumes and entrainment: isotopic evidence. Science, 256, 517–520.

Hauri, E.H., Whitehead, J.A., and Hart, S.R., 1994. Fluid dynamic and geochemical aspects of entrainment in mantle plumes. Journal of Geophysical Research, 99(B12), 24275–24300.

Heaman, L.M., and Machado, N., 1992. Timing and origin of Midcontinent Rift alkaline magmatism, North America: evidence from the Coldwell Complex. Contributions to Mineralogy and Petrology, 110, 289–303.

Herzberg, C., Asimow, P.D., Ionov, D.A., Vidito, C., Jackson, M.G., and Geist, D., 2013. Nickel and helium evidence for melt above the core–mantle boundary. Nature, 493, 393–397.

Hoernle, K.A., and Tilton, G.R., 1991. Sr-Nd-Pb isotope data for Fuerteventura (Canary Islands) basal complex and subaerial volcanics: applications to magma genesis and evolution. Schweizerische Mineralogische und Petrographische Mitteilungen, 71, 3–18.

Hoernle, K.A., Tilton, G.R., Le Bas, M.J., Duggen, S., and Garbe-Schonberg, D., 2002. Geochemistry of oceanic carbonatites compared with continental carbonatites: mantle recycling of oceanic crustal carbonate. Contributions to Mineralogy and Petrology, 142, 520–542.

Hoffmann, J.E., Münker, C., Polat, A., König, S., Mezger, K., and Rosing, M.T., 2010. Highly depleted Hadean mantle reservoirs in the sources of early Archean arc-like rocks, Isua supracrustal belt, southern West Greenland. Geochimica et Cosmochimica Acta, 74, 7236–7260.

Hofmann, A.W., 1988. Chemical differentiation of the Earth: the relationship between mantle, continental crust, and oceanic crust. Earth and Planetary Science Letters, 90, 297–314.

Hofmann, A.W., 2014. Sampling mantle heterogeneity through oceanic basalts: isotopes and trace elements. In: Carlson, R.W., (Ed.), Treatise on Geochemistry (Second Edition), Volume 3: The Mantle and Core. Elsevier, Oxford, United Kingdom, pp. 67–101.

Huang, Y.M., Hawkesworth, C.J., van Calsteren, P., and McDermott, F., 1995. Geochemical characteristics and origin of the Jacupiranga carbonatites, Brazil. Chemical Geology, 119, 79–99.

Ickert, R.B., 2013. Algorithms for estimating uncertainties in initial radiogenic isotope ratios and model ages. Chemical Geology, 340, 131–138.

Iizuka, T., Yamaguchi, T., Hibiya, Y., and Amelin, Y., 2015. Meteorite zircon constraints on the bulk Lu-Hf isotope composition and early differentiation of the Earth. Proceedings of the National Academy of Sciences of the United States of America, 112, 5331–5336.

Jacobsen, S.B., and Wasserburg, G.J., 1980. Sm-Nd isotopic evolution of chondrites. Earth and Planetary Science Letters, 50, 139–155.

Jaffey, A.H., Flynn, K.F., Glendenin, L.E., Bentley, W.C., and Essling, A.M., 1971. Precision measurement of half-lives and specific activities of ^{235}U and ^{238}U. Physical Review, C 4, 1889–1906.

Kalt, A., Hegner, E., and Satir, M., 1997. Nd, Sr, and Pb isotopic evidence for diverse lithospheric mantle sources of East African Rift carbonatites. In: Fuchs, K., Altherr, R., Mueller, B., and Prodehl, C., (Eds.), Structure and Dynamic Processes in the Lithosphere of the Afro-Arabian Rift System. Tectonophysics, 278, pp. 31–45.

Kampunzu, A.B., Kramers, J.D., and Makutu, M.N., 1998. Rb-Sr whole rock ages of the Lueshe, Kirumba and Numbi igneous complexes (Kivu, Democratic Republic of Congo) and the break-up of the Rodinia supercontinent. In: Kinnaird, J.A., (Ed.), Aspects of Tensional Magmatism. Journal of African Earth Sciences, 26, pp. 29–36.

Karhu, J.A., Mänttäri, I., and Huhma, H., 2001. Radiometric ages and isotope systematics of some Finnish carbonatites. In: Gehör, S., Wall F., and Liferovich, R., (Eds.), Formation, Exploration and Exploitation of Economic Deposits Associated with Mantle Carbon, EuroCarb Finland–Kola, Russia Workshop, 14-20 September 2001. Programme and Abstracts, RES TERRAE, A20, Department of Geology, University of Oulu, Oulu, Finland, p. 8.

Keller, J., and Krafft, M., 1990. Effusive natrocarbonatite activity of Oldoinyo Lengai, June 1988. Bulletin of Volcanology, 52, 629–645.

Kemp, A.I.S., Wilde, S.A., Hawkesworth, C.J., Coath, C.D., Nemchin, A., Pidgeon, R.T., Vervoort, J.D., and DuFrane, S.A., 2010. Hadean crustal evolution revisited: new constraints from Pb-Hf isotope systematics of the Jack Hills zircons. Earth and Planetary Science Letters, 296, 45–56.

Kogarko, L.N., 1993. Geochemical characteristics of oceanic carbonatites from the Cape Verde Islands. In: Verwoerd, W.J., (Ed.), Special Issue on Carbonatites. South African Journal of Geology, 96, pp. 119–125.

Kogarko, L.N., Lahaye, Y., and Brey, G.P., 2010. Plume-related mantle source of super-large rare metal deposits from the Lovezero and Khibina massifs on the Kola Peninsula, eastern part of the Baltic Shield: Sr, Nd and Hf isotope systematics. Mineralogy and Petrology, 98, 197–208.

Kramm, U., 1993. Mantle component of carbonatites from the Kola Alkaline province, Russia and Finland: a Nd-Sr study. European Journal of Mineralogy, 5, 985–989.

Kramm, U., and Koark, H.J., 1988. Isotopic composition of galena lead from the Norra Karr peralkaline complex, Sweden. Geologiska Foreningens i Stockholm Forhandlingar, 110, 311–316.

Kramm, U., and Kogarko, L.N., 1994. Nd and Sr isotope signatures of the Khibina and Lovozero agpaitic centres, Kola Alkaline Province, Russia. Lithos, 32, 225–242.

Kramm, U., Maravic, H.V., and Morteani, G., 1997. Neodymium and Sr isotopic constraints on the petrogenetic relationships between carbonatites and cancrinite syenites from the Lueshe alkaline complex, East Zaire. In: Harmer, R.E., (Ed.), Carbonatites from Source to Surface. Journal of African Earth Sciences, 25, pp. 55–76.

Kumar, A., Nirmal Charan, S., Gopalan, K., and MacDonald, J.D., 1998. A long-lived enriched mantle source for two Proterozoic carbonatite complexes from Tamil Nadu, southern India. Geochimica et Cosmochimica Acta, 62, 515–523.

Kwon, S.-T., Tilton, G.R., and Grüenenfelder, M.H., 1989. Lead isotope relationships in carbonatites and alkalic complexes: an overview. In: Bell, K., (ed.), Carbonatites: Genesis and Evolution. Unwin Hyman, London, United Kingdom, pp. 360–387.

Lancelot, J.R., and Allègre, C.J., 1974. Origin of carbonatitic magma in the light of the Pb-U-Th isotope system. Earth and Planetary Science Letters, 22, 233–238.

Larsen, L.M., and Rex, D.C., 1992. A review of the 2500 Ma span of alkaline-ultramafic, potassic and carbonatitic magmatism in West Greenland. In: Foley, S., and Peccerillo, A., (Eds.), Potassic and Ultrapotassic Magmas and Their Origin, Sixth Meeting of the European Union of Geosciences (EUG VI). Lithos, 28, pp. 367–402.

Lee, M.J., Lee, J.I., Hur, S.D., Kim, Y., Moutte, J., and Balaganskaya,

E., 2006. Sr-Nd-Pb isotopic compositions of the Kovdor phoscorite-carbonatite complex, Kola Peninsula, NW Russia. In: Markl, G., (Ed.), Peralkaline Rocks: A Special Issue Dedicated to Henning Sørensen, PERALK2005 Workshop. Lithos, 91, pp. 250–261.

le Roex, A.P. and Lanyon, R., 1998. Isotope and trace element geochemistry of Cretaceous Damaraland lamprophyres and carbonatites, northwestern Namibia: evidence for plume-lithosphere interactions. Journal of Petrology, 39, 1117–1146.

Le Roux, L.J., and Glendenin, L.E., 1963. Half-life of thorium-232. In: Proceedings of the National Conference on Nuclear Energy, Pretoria, South Africa, pp. 83–94.

Liegeois, J.P., Sauvage, J.F., and Black, R., 1991. The Permo-Jurassic alkaline province of Tadhak, Mali: geology, geochronology and tectonic significance. Lithos, 27, 95–105.

Lugmair, G.W., and Marti, K., 1978. Lunar initial $^{143}Nd/^{144}Nd$: differential evolution of lunar crust and mantle. Earth and Planetary Science Letters, 39, 349–357.

Machado, N., and Simonetti, A., 2001. U-Pb dating and Hf isotopic composition of zircon by laser ablation-MC-ICP-MS. In: Sylvester, P.J., (Ed.), Laser-Ablation-ICPMS in the Earth Sciences: Principles and Applications. Mineralogical Association of Canada, Short Course Handbook, 29, pp. 121–146.

Makhotkin, I.L., 1991. Lamproites from the Aldan Province. In: Bogatikov, O.A. and Kononova, V.A., (Eds.), Lamproites. Nauka, Moscow, USSR, pp. 46–113 (in Russian).

Marty, B., Tolstikhin, I., Kamensky, I.L., Nivin, V., Balaganskaya, E., and Zimmermann, J.-L., 1998. Plume-derived rare gases in 380 Ma carbonatites from the Kola region (Russia) and the argon isotopic composition in the deep mantle. Earth and Planetary Science Letters, 164, 179–192.

McCausland, P.J., Pisarevsky, S.A., Jourdan, F., and Higgins, M.D., 2009. Laurentia at 571 Ma: preliminary paleomagnetism and Ar-Ar age of the Ediacaran St. Honore alkali intrusion, Quebec. In: 2009 AGU Joint Assembly: the Meeting of the Americas, 24-27 May 2009, Toronto, Ontario, Canada. American Geophysical Union, Eos Transactions, 90 (22), Jt. Assem. Suppl, Abstract GA12A-01.

Meijer, A., Kwon, T.-T., and Tilton, G.R., 1990. U-Th-Pb partitioning behavior during partial melting in the upper mantle: implications for the origin of high Mu components and the "Pb paradox". Journal of Geophysical Research, 95, 433–448.

Melluso, L., Censi, P., Perini, G., Vasconcelos, L., Morra, V., Guerreiro, F., and Bennio, L., 2004. Chemical and isotopic (C, O, Sr, Nd) characteristics of the Xiluvo carbonatite (central-western Mozambique). Mineralogy and Petrology, 80, 201–213.

Middlemost, E., 1990. Mineralogy and petrology of the rauhaugites of the Mt Weld carbonatite complex of Western Australia. Mineralogy and Petrology, 41, 145–161.

Mitchell, R.H., Smith, C.B., and Vladykin, N.V., 1994. Isotopic composition of strontium and neodymium in potassic rocks of the Little Murun Complex, Aldan Shield, Siberia. Lithos, 32, 243–248.

Mitchell, R.H., Wu, F., and Yang, Y., 2011. In situ U/Pb, Sr and Nd isotopic analysis of loparite by LA-(MC)-ICP-MS. Chemical Geology, 280, 191–199.

Morisset, N., 1992. Stable isotope and radioisotope geochemistry of the Panda Hill carbonatite, Tanzania. Unpublished M.Sc. thesis, Carleton University, Ottawa, Canada, 91 p.

Mourtada, S., Le Bas, M.J., and Pin, C., 1997. Pétrogenèse des magnésio-carbonatites du complexe de Tamazert (Haut Atlas marocain). Comptes Rendus de l'Académie des Sciences, Série IIA – Sciences de la Terre et des planètes, 325, 559–564.

Natarajan, M., Bhaskar Rao, B., Parthasarathy, R., Kumar, A., and Gopalan, K., 1994. 2.0 Ga old pyroxenite-carbonatite complex of Hogenakal, Tamil Nadu, South India. Precambrian Research, 65, 167–181.

Nelson, D.R., Chivas, A.R., Chappell, B.W., and McCulloch, M.T., 1988. Geochemical and isotopic systematics in carbonatites and implications for the evolution of ocean-island sources. Geochimica et Cosmochimica Acta, 52, 1–17.

Nielsen, T.F.D., and Buchardt, B., 1985. Sr-C-O isotopes in nephelinitic rocks and carbonatites, Gardiner Complex, Tertiary of East Greenland. Chemical Geology, 53, 207–217.

Pandit, M.K., Sial, A.N., Sukumaran, G.B., Pimentel, M.M., Ramasamy, A.K., and Ferreira, V.P., 2002. Depleted and enriched mantle sources for Paleo- and Neoproterozoic carbonatites of southern India: Sr, Nd, C–O isotopic and geochemical constraints. Chemical Geology, 189, 69–89.

Paslick, C., Halliday, A., James, D., and Dawson, J.B., 1995. Enrichment of the continental lithosphere by OIB melts: isotopic evidence from the volcanic province of northern Tanzania. Earth and Planetary Science Letters, 130, 109–126.

Patchett, P.W., Kouvo, O., Hedge, C.E., and Tatsumoto, M., 1981. Evolution of the continental crust and mantle heterogeneity: evidence from Hf isotopes. Contributions to Mineralogy and Petrology, 78, 279–297.

Pearce, N.J.G. and Leng, M.J., 1996. The origin of carbonatites and related rocks from the Igaliko dyke swarm, Gardar Province, South Greenland: field, geochemical and C-O-Sr-Nd isotope evidence. Lithos, 39, 21–40.

Pell, J., 1994. Carbonatites, nepheline syenites, kimberlites and related rocks in British Columbia. Province of British Columbia. British Columbia Ministry of Energy, Mines and Petroleum Resources, British Columbia Geological Survey Bulletin 88, 136 p.

Pilipiuk, A.N., Ivanikov, V.V., and Bulakh, A.G., 2001. Unusual rocks and mineralisation in a new carbonatite complex at Kandaguba, Kola Peninsula, Russia. Lithos, 56, 333–347.

Pollock, S.P., 1987. The isotopic geochemistry of the Prairie Lake carbonatite complex, Ontario. Unpublished M.Sc. thesis, Carleton University, Ottawa, Canada, 71 p.

Puchtel, I.S., Blichert-Toft, J., Touboul, M., Walker, R.J., Byerly, G.R., Nisbet, E.G., and Anhaeusser, C.R., 2013. Insights into early Earth from Barberton komatiites: evidence from lithophile isotope and trace element systematics. Geochimica et Cosmochimica Acta, 108, 63–90.

Ray, J.S., Trivedi, J.R., and Dayal, A.M., 2000. Strontium isotope systematics of Amba Dongar and Sung Valley carbonatite-alkaline complexes, India: evidence for liquid immiscibility, crustal contamination and long-lived Rb/Sr enriched mantle sources. Journal of Asian Earth Sciences, 18, 585–594.

Reischmann, T., 1995. Precise U/Pb age determination with baddeleyite (ZrO_2), a case study from the Phalaborwa igneous complex, South Africa. South African Journal of Geology, 98, 1–4.

Richards, J.R., Fletcher, I.R., and Blockley, J.G., 1981. Pilbara galenas: precise isotopic assay of the oldest Australian leads; model ages and growth-curve implications. Mineralium Deposita, 16, 7–30.

Roden, M.F., Murthy, V.R., and Gaspar, J.C., 1985. Sr and Nd isotopic composition of the Jacupiranga carbonatite. Journal of Geology, 93, 212–220.

Rotenberg, E., Davis, D.W., Amelin, Y., Ghosh, S., and Bergquist, B.A., 2012. Determination of the decay-constant of ^{87}Rb by laboratory accumulation of ^{87}Sr. Geochimica et Cosmochimica Acta, 85, 41–57.

Ruberti, E., Castorina, F., Censi, P., Gomes, C.B., Speziale, S., and Comin-Chiaramonti, P., 1997. REE–O–C–Sr–Nd systematics in carbonatites from Barra do Itapirapuã and Mato Preto (southern Brazil). In: South American Symposium on Isotope Geology (SSAGI), Campos de Jordão, Brazil. Extended abstracts, pp. 271–275.

Ruberti, E., Castorina, F., Censi, P., Comin-Chiaramonti, P., Gomes, C.B., Antonini, P., and Andrade, F.R.D., 2002. The geochemistry of the Barra do Itapirapuã Carbonatite (Ponta Grossa Arch, Brazil): a multiple stockwork. Journal of South American Earth Sciences,

15, 215–228.
Rukhlov, A.S., 1999. Dykes and explosive pipes of the Kandalaksha graben (Kola Alkaline Province): models of magmatic processes and evolution of the subcontinental mantle. Unpublished Ph.D. thesis, St. Petersburg State University, St. Petersburg, Russia, 287 p. (in Russian).
Rukhlov, A.S., and Bell, K., 2003. Depleted mantle: the story from Hf isotopes in zircons and baddeleyites from carbonatites. In: EGS-AGU-EUG Joint Assembly, Nice, France, 7–11 April 2003. Geophysical Research Abstracts, 5, 13944.
Rukhlov, A.S., and Bell, K., 2010. Geochronology of carbonatites from the Canadian and Baltic Shields, and the Canadian Cordillera: clues to mantle evolution. Mineralogy and Petrology, 98, 11–54.
Rukhlov, A.S., Bell, K., and Ivanikov, V.V., 2001. Archaean mantle below the Baltic Shield: isotopic evidence from intrusive carbonatites. In: Moutte, J. and Garcia, D., (Eds.), Carbonatite Workshop 2000, Abstracts of Presentations and Posters. Journal of African Earth Sciences, 32, pp. A30–A31.
Savatenkov, V.M., Pushkarev, Yu.D., Sergeyev, A.V., and Sulimov, R.B., 1999. Carbonatites as an indicator of new ore types in the Gremyakha-Vyrmes Massif, Russia. Geologiya Rudnykh Mestorozhdeniy, 41, 449–454 (in Russian).
Sasada, T., Hiyagon, H., Bell, K., and Ebihara, M., 1997. Mantle-derived noble gases in carbonatites. Geochimica et Cosmochimica Acta, 61, 4219–4228.
Scherer, E., Münker, C., and Mezger, K., 2001. Calibration of the lutetium-hafnium clock. Science, 293, 683–687.
Schleicher, H., Keller, J., and Kramm, U., 1990. Isotope studies on alkaline volcanics and carbonatites from the Kaiserstuhl, Federal Republic of Germany. In: Woolley, A.R. and Ross, M., (Eds.), Alkaline Igneous Rocks and Carbonatites. Lithos, 26, pp. 21–35.
Schleicher, H., Baumann, A., and Keller, J., 1991. Pb isotopic systematics of alkaline volcanic rocks and carbonatites from the Kaiserstuhl, upper Rhine rift valley, F.R.G. Chemical Geology, 93, 231–243.
Schleicher, H., Kramm, U., Pernicka, E., Schidlowski, M., Schmidt, F., Subramanian, V., Todt, W., and Viladkar, S., 1998. Enriched subcontinental upper mantle beneath southern India: evidence from Pb, Nd, Sr, and C–O isotopic studies on Tamil Nadu carbonatites. Journal of Petrology, 39, 1765–1785.
Schultz, F., Lehmann, B., Tawackoli, S., Roessling, R., Belyatsky, B., and Dulski, P., 2004. Carbonatite diversity in the Central Andes: the Ayopaya alkaline province, Bolivia. Contributions to Mineralogy and Petrology, 148, 391–408.
Silva, A.B., Liberal, G.S., Grossi Sad, J.H., Issa Filho, A., Rodrigues, C.S., and Riffel, B.F., 1988. Geologia e petrologia do Complexo Angico dos Dias (Bahia, Brasil), uma associação carbonatítica Precambriana. Geochimica Brasiliensis, 2, 81–108.
Simonetti, A., and Bell, K., 1994a. Nd, Pb and Sr isotopic data from the Napak carbonatite-nephelinite centre, eastern Uganda: an example of open-system crystal fractionation. Contributions to Mineralogy and Petrology, 115, 356–366.
Simonetti, A., and Bell, K., 1994b. Isotopic and geochemical investigation of the Chilwa Island carbonatite complex, Malawi: evidence for a depleted mantle source region, liquid immiscibility, and open-system behaviour. Journal of Petrology, 35, 1597–1621.
Simonetti, A., Bell, K., and Viladkar, S.G., 1995. Isotopic data from the Amba Dongar carbonatite complex, west-central India: evidence for an enriched mantle source. Chemical Geology, 122, 185–198.
Simonetti, A., Goldstein, S.L., Schmidberger, S.S., and Viladkar, S.G., 1998. Geochemical and Nd, Pb, and Sr isotope data from Deccan alkaline complexes: inferences for mantle sources and plume-lithosphere interaction. Journal of Petrology, 39, 1847–1864.
Sindern, S., Zaitsev, A.N., Demeny, A., Bell, K., Chakmouradian, A.R., Kramm, U., Moutte, J., and Rukhlov, A.S., 2004. Mineralogy and geochemistry of silicate dyke rocks associated with carbonatites from the Khibina Complex (Kola, Russia): isotope constraints on genesis and small-scale mantle sources. Mineralogy and Petrology, 80, 215–239.
Smithies, R.H., and Marsh, J.S., 1998. The Marinkas Quellen carbonatite complex, southern Namibia; carbonatite magmatism with an uncontaminated depleted mantle signature in a continental setting. Chemical Geology, 148, 201–212.
Söderlund, U., Patchett, P.J., Vervoort, J.D., and Isachsen, C.E., 2004. The ^{176}Lu decay constant determined by Lu-Hf and U-Pb isotope systematics of Precambrian mafic intrusions. Earth and Planetary Science Letters, 219, 311–324.
Srivastava, R.K., Heaman, L.M., Sinha, A.K., and Sun, S., 2005. Emplacement age and isotope geochemistry of Sung Valley alkaline-carbonatite complex, Shillong Plateau, northeastern India: implications for primary carbonate melt and genesis of the associated silicate rocks. Lithos, 81, 33–54.
Stacey, J.S., and Kramers, J.D., 1975. Approximation of terrestrial lead isotopic evolution by a two-stage model. Earth and Planetary Science Letters, 26, 207–221.
Stendal, H., Frei, R., Muhongo, S., Rasmussen, T.M., Mnali, S., Petro, F., and Temu, B.E., 2004. Gold potential of the Mpanda mineral field, SW Tanzania: evaluation based on geological, lead isotopic and aeromagnetic data. Journal of African Earth Sciences, 38, 437–447.
Stoppa, F., Rukhlov, A.S., Bell, K., Schiazza, M., and Vichi, G., 2014. Lamprophyres of Italy: Early Cretaceous alkaline lamprophyres of southern Tuscany, Italy. In: Marzoli, A., Princivalle, F., Melluso, L., and Baker, D., (Eds.), Within Plate Continental Magmatism and Its Mantle Sources. Lithos, 188, pp. 97–112.
Stracke, A., 2012. Earth's heterogeneous mantle: a product of convection-driven interaction between crust and mantle. Chemical Geology, 330-331, 274–299.
Stracke, A., Hofmann, A.W., and Hart, S.R., 2005. FOZO, HIMU, and the rest of the mantle zoo. Geochemistry, Geophysics, Geosystems, 6 (5), Q05007, DOI: 10.1029/2004GC000824.
Sun, S.S., Jaques, A.L., and McCulloch, M.T., 1986. Isotopic evolution of the Kimberley Block, Western Australia. In: Smith, C.B., (Compiler), Fourth International Kimberlite Conference, Perth, Western Australia. Geological Society of Australia, Abstracts, 16, Sydney, Australia, pp. 346–348.
Tappe, S., Foley, S.F., Kjarsgaard, B.A., Romer, R.L., Heaman, L.M., Stracke, A., and Jenner, G.A., 2008. Between carbonatite and lamproite – diamondiferous Torngat ultramafic lamprophyres formed by carbonate-fluxed melting of cratonic MARID-type metasomes. Geochimica et Cosmochimica Acta, 72, 3258–3286.
Tappe, S., Foley, S.F., Stracke, A., Romer, R.L., Kjarsgaard, B.A., Heaman, L.M., and Joyce, N., 2007. Craton reactivation on the Labrador Sea margins: ^{40}Ar/^{39}Ar age and Sr–Nd–Hf–Pb isotope constraints from alkaline and carbonatite intrusives. Earth and Planetary Science Letters, 256, 433–454.
Tatsumoto, M., Knight, R.J., and Allègre, C.J., 1973. Time differences in the formation of meteorites as determined from the ratio of lead-207 to lead-206. Science, 180, 1270–1283.
Taubald, H., Morteani, G., and Satir, M., 2004. Geochemical and isotopic (Sr, C, O) data from the alkaline complex of Grønnedal-Íka (South Greenland): evidence for unmixing and crustal contamination. International Journal of Earth Sciences, 93, 348–360.
Thompson, R.N., Smith, P.M., Gibson, S.A., Mattey, D.P., and Dickin, A.P., 2002. Ankerite carbonatite from Swartbooisdrif, Namibia: the first evidence for magmatic ferrocarbonatite. Contributions to Mineralogy and Petrology, 143, 377–395.
Tichomirowa, M., Grosche, G., Götze, J., Belyatsky, B.V., Savva, E.V., Keller, J., and Todt, W., 2006. The mineral isotope

composition of two Precambrian carbonatite complexes from the Kola Alkaline Province – alteration versus primary magmatic signatures. Lithos, 91, 229–249.

Tichomirowa, M., Whitehouse, M.J., Gerdes, A., Götze, J., Schulz, B., and Belyatsky, B.V., 2013. Different zircon recrystallization types in carbonatites caused by magma mixing: Evidence from U–Pb dating, trace element and isotope composition (Hf and O) of zircons from two Precambrian carbonatites from Fennoscandia. In: Tappe, S., Pearson, D.G., and Prelević, D., (Eds.), Kimberlite, Carbonatite, and Potassic Magmatism as Part of the Geochemical Cycle. Chemical Geology, 353, pp. 173–198.

Tilton, G.R., 1983. Evolution of depleted mantle: the lead perspective. Geochimica et Cosmochimica Acta, 47, 1191–1197.

Tilton, G.R., and Bell, K., 1994. Sr–Nd–Pb isotope relationships in Late Archean carbonatites and alkaline complexes: applications to the geochemical evolution of the Archean mantle. Geochimica et Cosmochimica Acta, 58, 3145–3154.

Tilton, G.R., and Kwon, S.-T., 1990. Isotopic evidence for crust-mantle evolution with emphasis on the Canadian Shield. In: Nelson, B.K., and Vidal, P., (Eds.), Development of Continental Crust through Geological Time. Chemical Geology, 83, pp. 149–163.

Tilton, G.R., Kwon, S.-T., and Frost, D.M., 1987. Isotopic relationships in Arkansas Cretaceous alkalic complexes. In: Mullen, E., and Pasteris, J.D., (Eds.), Mantle Metasomatism and Alkaline Magmatism. Geological Society of America Special Paper 215, pp. 241–248.

Tilton, G.R., Bryce, J.G., and Mateen, A., 1998. Pb-Sr-Nd isotope data from 30 and 300 Ma collision zone carbonatites in Northwest Pakistan. Journal of Petrology, 39, 1865–1874.

Tolstikhin, I.N., and Hofmann, A.W., 2005. Early crust on top of the Earth's core. Physics of the Earth and Planetary Interiors, 148, 109–130.

Tolstikhin, I.N., Kamensky, I.L., Marty, B., Nivin, V.A., Vetrin, V.R., Balaganskaya, E.G., Ikorsky, S.V., Gannibal, M.A., Weiss, D., Verhulst, A., and Demaiffe, D., 2002. Rare gas isotopes and parent trace elements in ultrabasic-alkaline-carbonatite complexes, Kola Peninsula: identification of lower mantle plume component. Geochimica et Cosmochimica Acta, 66, 881–901.

Toyoda, K., Horiuchi, H., and Tokonami, M., 1994. Dupal anomaly of Brazilian carbonatites: geochemical correlations with hotspots in the South Atlantic and implications for the mantle source. Earth and Planetary Science Letters, 126, 315–331.

Veena, K., Pandey, B.K., Krishnamurthy, P., and Gupta, J.N., 1998. Pb, Sr and Nd isotopic systematics of the carbonatites of Sung Valley, Meghalaya, Northeast India: implications for contemporary plume-related mantle source characteristics. Journal of Petrology, 39, 1875–1884.

Veizer, J., Bell, K., and Jansen, S.L., 1992. Temporal distribution of carbonatites. Geology, 20, 1147–1149.

Verhulst, A., Balaganskaya, E., Kirnarsky, Y., and Demaiffe, D., 2000. Petrological and geochemical (trace elements and Sr-Nd isotopes) characteristics of the Paleozoic Kovdor ultramafic, alkaline and carbonatite intrusion (Kola Peninsula, NW Russia). In: Downes, H., Demaiffe, D., and Kramm, U., (Eds.), Alkaline Magmatism and Xenoliths from the Baltic Shield. Lithos, 51, pp. 1–25.

Vervoort, J.D., and Blichert-Toft, J., 1999. Evolution of the depleted mantle: Hf isotope evidence from juvenile rocks through time. Geochimica et Cosmochimica Acta, 63, 533–556.

Verwoerd, W.J., Weder, E.E.W., and Harmer, R.E., 1993. The Stukpan carbonatite in the Orange Free State goldfield. In: Verwoerd, W.J., (Ed.), Special Issue on Carbonatites. South African Journal of Geology, 96, pp. 108–118.

Vidale, J.E., and Hedlin, M.A.H., 1998. Evidence for partial melt at the core–mantle boundary north of Tonga from the strong scattering of seismic waves. Nature, 391, 682–685.

Villeneuve, M.E., and Relf, C., 1998. Tectonic setting of 2.6 Ga carbonatites in the Slave Province, NW Canada. Journal of Petrology, 39, 1975–1986.

Wagner, C., Mokhtari, A., Deloule, E., and Chabaux, F., 2003. Carbonatite and alkaline magmatism in Taourirt (Morocco): petrological, geochemical and Sr-Nd isotope characteristics. Journal of Petrology, 44, 937–965.

Waight, T., Baker, J., and Willigers, B., 2002. Rb isotope dilution analyses by MC-ICPMS using Zr to correct for mass fractionation: towards improved Rb–Sr geochronology? Chemical Geology, 186, 99–116.

Walter, A.-V., Flicoteaux, R., Parron, C., Loubet, M., and Nahon, D., 1995. Rare earth elements and isotopes (Sr, Nd, O, C) in minerals from the Juquiá carbonatite (Brazil): tracers of a multistage evolution. Chemical Geology, 120, 27–44.

Wen, J., Bell, K., and Blenkinsop, J., 1987. Nd and Sr isotope systematics of the Oka Complex, Quebec, and their bearing on the evolution of the sub-continental upper mantle. Contributions to Mineralogy and Petrology, 97, 433–437.

Wood, B.J., Nielsen, S.G., Rehkämper, M., and Halliday, A.N., 2008. The effects of core formation on the Pb- and Tl- isotopic composition of the silicate Earth. Earth and Planetary Science Letters, 269, 325–335.

Woodhead, J.D., and Hergt, J.M., 2005. A preliminary appraisal of seven natural zircon reference materials for in situ Hf isotope determination. Geostandards and Geoanalytical Research, 29, 183–195.

Woolley, A.R., 1989. The spatial and temporal distribution of carbonatites. In: Bell, K. (ed.), Carbonatites: Genesis and Evolution. Unwin Hyman, London, United Kingdom, pp. 15–37.

Woolley, A.R., 2003. Igneous silicate rocks associated with carbonatites: their diversity, relative abundances and implications for carbonatite genesis. In: Rosatelli, G. and Stoppa, F., (Eds.), European Carbonatites: Implications for the Sub-European Mantle and their Geohazard Potential. Periodico di Mineralogia, 72, pp. 9–17.

Woolley, A.R., and Bailey, D.K., 2012. The crucial role of lithospheric structure in the generation and release of carbonatites: geological evidence. In: Downes, H., Wall, F., Demény, A., and Szabo, C., (Eds.), Continuing the Carbonatite Controversy. Mineralogical Magazine, 76, pp. 259–270.

Woolley, A.R., and Kempe, D.R.C., 1989. Carbonatites: nomenclature, average chemical compositions, and element distribution. In: Bell, K., (ed.), Carbonatites: Genesis and Evolution. Unwin Hyman, London, United Kingdom, pp. 1–14.

Woolley, A.R., and Kjarsgaard, B.A., 2008. Carbonatite occurrences of the world: map and database. Geological Survey of Canada, Open File 5796, 1 CD-ROM plus 1 map.

Wu, F.-Y., Yang, Y.-H., Xie, L.-W., Yang, J.-H., and Xu, P., 2006. Hf isotopic compositions of the standard zircons and baddeleyites used in U–Pb geochronology. Chemical Geology, 234, 105–126.

Wu, F.-Y., Yang, Y.-H., Mitchell, R.H., Bellatreccia, F., Li, Q.-L., and Zhao, Z.-F., 2010. In situ U/Pb and Nd-Hf-(Sr) isotopic investigations of zirconolite and calzirtite. Chemical Geology, 277, 178–195.

Wu, F.-Y., Yang, Y.-H., Li, Q.-L., Mitchell, R., Dawson, J.B., Brandl, G., and Yuhara, M., 2011. In situ determination of U–Pb ages and Sr–Nd–Hf isotopic constraints on the petrogenesis of the Phalaborwa carbonatite complex, South Africa. Lithos, 127, 309–322.

Wu, F.-Y., Arzamastsev, A.A., Mitchell, R.H., Li, Q.-L., Sun, J., Yang, Y.-H., and Wang, R.-C., 2013. Emplacement age and Sr-Nd isotopic compositions of the Afrikanda alkaline ultramafic complex, Kola Peninsula, Russia. In: Tappe, S., Pearson, D.G., and Prelević, D., (Eds.), Kimberlite, Carbonatite, and Potassic Magmatism as Part of the Geochemical Cycle. Chemical Geology, 353, pp. 210–229.

Yang, Z., and Woolley, A.R., 2006. Carbonatites in China: A review. Journal of Asian Earth Sciences, 27, 559–575.
Yang, X.-M., Yang, X.-Y., Zheng, Y.-F., and Le Bas, M. J., 2003. A rare earth element-rich carbonatite dyke at Bayan Obo, Inner Mongolia, North China. Mineralogy and Petrology, 78, 93–110.
Ying, J., Zhou, X., and Zhang, H., 2004. Geochemical and isotopic investigation of the Laiwu-Zibo carbonatites from western Shandong Province, China, and implications for their petrogenesis and enriched mantle source. Lithos, 75, 413–426.
Zaitsev, A.N., and Bell, K., 1995. Sr and Nd isotope data of apatite, calcite and dolomite as indicators of source, and the relationships of phoscorites and carbonatites from the Kovdor Massif, Kola Peninsula, Russia. Contributions to Mineralogy and Petrology, 121, 324–335.
Zaitsev, A.N., Demény, A., Sindern, S., and Wall, F., 2002. Burbankite group minerals and their alteration in rare earth carbonatites - source of elements and fluids (evidence from C-O and Sr-Nd isotopic data). Lithos, 62, 15–33.
Zaitsev, A.N., Sitnikova, M.A., Subbotin, V.V., Fernández-Sáurez, J., and Jeffries, T.E., 2004. Sallanlatvi Complex – a rare example of magnesite and siderite carbonatites. In: Wall, F. and Zaitsev, A.N., (Eds.), Phoscorites and Carbonatites from Mantle to Mine: the Key Example of the Kola Alkaline Province. Mineralogical Society Series, 10, The Mineralogical Society, London, United Kingdom, pp. 201–245.
Zartman, R.E. and Kogarko, L.N., 2014. A Pb isotope investigation of the Lovozero agpaitic nepheline syenite, Kola Peninsula, Russia. Doklady Earth Sciences, 454, 25–28.
Ziegler, U.R.F., 1992. Preliminary results of geochemistry, Sm-Nd and Rb-Sr studies of post-Karoo carbonatite complexes in Southern Africa. Schweizerische Mineralogische und Petrographische Mitteilungen, 72, 135–142.
Zozulya, D.R., Bayanova, T.B., and Serov, P.N., 2007. Age and isotopic geochemical characteristics of Archean carbonatites and alkaline rocks of the Baltic Shield. Doklady Earth Sciences, 415A, 874–879.

Nd and Sr isotopic composition of rare earth element mineralized carbonatites

P.L. Verplanck[1, a], G.L. Farmer[2], and A.N. Mariano[3]

[1] US Geological Survey, Denver, CO, USA
[2] University of Colorado, Boulder, CO, USA
[3] 48 Page Brook Road, Carlisle, MA, USA
[a] corresponding author: plv@usgs.gov

Recommended citation: Verplanck, P.L., Farmer, G.L., and Mariano, A.N., 2015. Nd and Sr isotopic composition of rare earth element mineralized carbonatites. In: Simandl, G.J. and Neetz, M., (Eds.), Symposium on Strategic and Critical Materials Proceedings, November 13-14, 2015, Victoria, British Columbia, British Columbia Ministry of Energy and Mines, British Columbia Geological Survey Paper 2015-3, pp. 65-68.

Summary

For nearly 50 years, carbonatites have been the primary sources of niobium and rare earth elements (REEs), particularly the light REEs including La, Ce, Pr, and Nd. In addition, carbonatites may be enriched in other critical elements and have the potential to be future sources. Currently, only five of the more than 500 known carbonatites in the world are being mined for REEs: Bayan Obo (Inner Mongolia, China); Maoniuping (Sichuan, China); Dalucao (or Daluxiang, Sichuan, China); and Mountain Pass (California, USA), and the carbonatite-derived laterite at Mount Weld (Australia). To achieve ore-grade REE enrichment, initial carbonatitic magmas require an adequate endowment of REEs and need to evolve in ways for these elements to concentrate in REE-bearing mineral phases.

Radiogenic isotope studies of carbonatites clearly point to a mantle origin, but a wide range in isotopic compositions has led to contrasting views about the specific mantle reservoir(s) that sourced carbonatites. In this study we use the neodymium and strontium isotopic compositions of a suite of mineralized carbonatites to establish the nature of the source magmas. We examine samples that span a wide range in age (~23 Ma to 1385 Ma), Nd concentrations (3720 to 32,900 ppm), and Sr concentrations (2290 to 167,900 ppm). Our Nd and Sr isotopic data include multiple samples from Mountain Pass (USA; $\varepsilon_{Nd\,i}$ = -3.1 to -5.4, Sr_i = 0.70512 to 0.70594), Elk Creek (USA; ~$\varepsilon_{Nd\,i}$ = 1.7, Sr_i = 0.7035), and Maoniuping (China; $\varepsilon_{Nd\,i}$ = -4.1 and -4.2, Sr_i = 0.70627 and 0.70645), and one sample each from Bear Lodge (USA; $\varepsilon_{Nd\,i}$ = 0.1, Sr_i = 0.70441), Kangankunde (Malawi; $\varepsilon_{Nd\,i}$ = 3.3, Sr_i = 0.70310), Adiounedj (Mali; $\varepsilon_{Nd\,i}$ = -0.1, Sr_i = 0.70558), and Mushgai Khudag (Mongolia; $\varepsilon_{Nd\,i}$ = -1.3, Sr_i = 0.70636). Isotopic data from two producing carbonatite REE deposits (Mountain Pass and Maoniuping) have broadly similar isotopic compositions ($\varepsilon_{Nd\,i}$ = -3.1 to -5.4 and Sr_i = 0.7051 to 0.7065), and these compositions point to a carbonated source in the lithospheric mantle. Mineralized but unmined carbonatites have higher Nd initial isotopic compositions ($\varepsilon_{Nd\,i}$ = -1.3 to 3.3) and a wider range in Sr isotopic compositions (Sr_i = 0.70310 to 0.70637), but these data are consistent with a lithospheric mantle reservoir.

1. Introduction

Carbonatites are volumetrically rare compared to silicate igneous rocks, but they have become important exploration targets because of their enrichments in critical elements. For nearly 50 years, carbonatites have been the primary source of rare earth elements (REEs), particularly the light REEs (LREEs) that include La, Ce, Pr, and Nd. Although most carbonatites contain elevated concentrations of REEs, only a few have sufficient quantities to warrant economic exploitation. Carbonatites that are currently being mined for REEs are Bayan Obo (Inner Mongolia, China), Maoniuping (Sichuan, China), Dalucao (or Daluxiang, Sichuan, China), and Mountain Pass (California, USA), and the carbonatite-derived laterite at Mount Weld (Australia). Most of the more than 500 carbonatites known worldwide are enriched in REEs but lack economic concentrations (Woolley and Kjarsgaard, 2008). To become producers, targets need to have adequate grade and tonnage, and mineralogical characteristics that would enable economically viable processing.

Carbonatites are composed of greater than 50 vol.% primary carbonate minerals, mainly calcite and/or dolomite. They contain the highest concentrations of REEs of any igneous rocks. Although substantial petrogenetic research has focused on the origin of non-mineralized carbonatites, the origin of carbonatitic magmas remains controversial. Radiogenic and stable isotopic studies show that the parental magmas of carbonatites are derived from mantle melts (Bell and Blenkinsop, 1989), but the nature of the initial melts, the processes responsible for generating carbonatitic magmas, and how the magmas evolve to form the observed rock types are still debated. In general, carbonatite magmas evolve by fractional crystallization and the gravitational separation of early-formed crystals (Twyman and Gittins, 1987). Carbonatite magmas may contain a variety of volatile components including CO_2, H_2O, Cl, F, and S. As crystallization progresses, volatiles become enriched in the residual magma, along with various incompatible elements,

and may exolve into a separate fluid phase. Fluid inclusions and fenite alteration (alkali metasomatism) provide clear evidence for the separation of a volatile-rich fluid phase.

To achieve ore-grade REE enrichment, the initial carbonatite magma needs an adequate endowment of REEs and must evolve in ways that REEs are concentrated in REE-bearing mineral phases: fluorocarbonates (bastnäsite, parisite, and synchysite); hydrated carbonates (ancylite); and phosphates (monazite and apatite). The primary ore mineral exploited at carbonatite-hosted REE mines is bastnäsite, which contains approximately 75 wt.% RE_2O. In most economic deposits bastnäsite is coarse grained, which allows for relatively straightforward processing. Bastnäsite can crystallize both directly from magmas and from evolved fluids.

The Mountain Pass REE deposit, the world's leading source of REEs from 1965 to 1995, is hosted by the Sulphide Queen carbonatite, a composite, tabular body made up of REE-bearing sövites and beforsites. Calcite and dolomite, in varying proportions, are the primary mineral phases, with subordinate and variable amounts of barite, celestine, strontianite, cerussite, phlogopite, and fluorite (Castor, 2008; Mariano and Mariano, 2012). Bastnäsite is the primary REE mineral, along with parisite, synchysite, and monazite, and lesser allanite, ancylite, apatite, cerite, florencite, hydroxylbastnäsite, and sahamalite (Castor and Nason, 2004; Castor, 2008; Mariano and Mariano, 2012). Barite and bastnäsite are generally the second, third, or fourth most abundant mineral phases in different parts of the Sulfide Queen carbonatite. Other REE-rich phases are present generally in trace amounts, but locally can make up a few percent of the rock. Bastnäsite at Mountain Pass is commonly coarse grained and displays primary igneous textures (Fig. 1). Textural evidence shows that bastnäsite and parisite crystallized with euhedral morphology with calcite, barite, and dolomite, and thus probably formed as primary magmatic phases (Mariano and Mariano, 2012). Samples used in this study include a suite of ore carbonatite and individual bastnäsite minerals.

Two actively mined carbonatite-related REE deposits (Maoniuping and the Dalucao) are in the Mianning-Dechang REE belt, Sichuan Provence, China. Surpassed only by Bayan Obo, Maoniuping is the second largest REE deposit in China. Unlike the Mountain Pass deposit, where the REE mineralization is in the carbonatite body, the REE mineralization at Maoniuping is mainly in pegmatite and stockwork veins and minor breccias. In drill core, disseminated REE mineralization in the carbonatite has been identified (Xie et al., 2015). Medium- to coarse-grained bastnäsite is the primary ore mineral along with minor brunsite, chevkinite, and cerianite. The pegmatitic veins consist of calcite and barite with coarse-grained bastnäsite, as well as fluorite with local aegirine and augite, and minor amounts of microcline arfvedsonite, biotite, apatite, quartz, and sulfides (Xu et al., 2008, 2012). In this study individual bastnäsite minerals were separated from vein and breccia ores.

In contrast to coarse-grained bastnäsite as the primary REE mineral in REE ore deposits, many unmined but REE-enriched carbonatites contain late-stage, fine-grained fluorocarbonates (bastnäsite, parisite, and synchysite) and phosphates (monazite and apatite). The fluorocarbonates are generally described as very fine grained (1-100 μm), forming syntaxial intergrowths as bundles, clusters, or aggregates of radiating needles (Fig. 2). The crystals may line miarolitic cavities or form at the expense of primary minerals. These REE mineral phases are commonly attributed to the late-stage magmatic-hydrothermal phase of carbonatite evolution. As carbonatite magmas crystallize, the REEs may behave as incompatible elements that remain in the magma. Late in the magmatic evolution, the residual magma becomes enriched in incompatible elements (including REEs) and volatiles, and a volatile-rich fluid may exsolve. These REE-rich exsolved fluids may be responsible for late-stage REE enrichment, or the enrichment may result from late-stage fluids remobilizing REEs from earlier crystallized minerals.

Fig. 1. Plane-polarized light photomicrograph of Mountain Pass black ore bastnäsite (Bast) in ferruginous calcite carbonatite displaying primary igneous texture. Field of view is 5 mm wide.

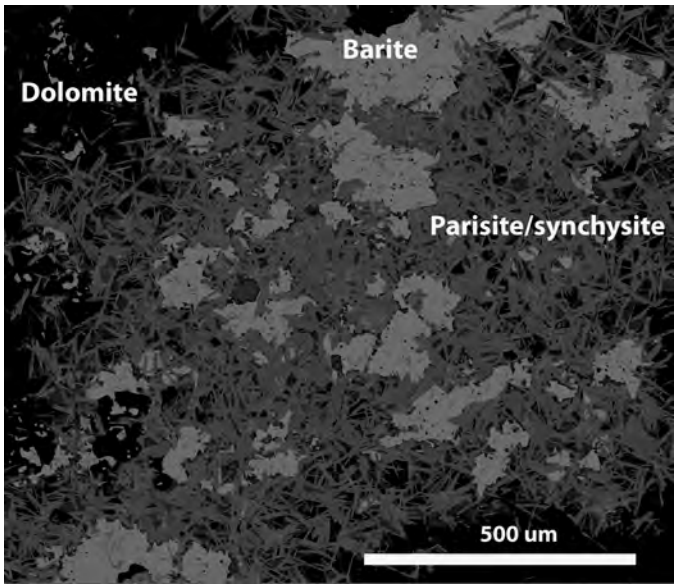

Fig. 2. SEM backscattered electron image of REE fluorocarbonates in barite beforsite unit of Elk Creek carbonatite.

For this study, we analyzed samples from unmined REE-enriched carbonatites at Elk Creek and Bear Lodge (USA), Adiounedj (Mali), Kangankunde (Malawi), and Mushgai Khudag (Mongolia). The Elk Creek samples are a representative suite of carbonatite lithologies including apatite beforsite, magnetite beforsite, and barite beforsite. A drill-core sample from Bear Lodge is from a hydrothermal vein containing ancylite-strontianite pseudomorphs and minor fluorite from the unoxidized zone. The sample analyzed from Adiounedj is a ferrocarbonatite consisting of calcite, fluorite, apatite, Fe-oxide minerals, and synchysite. The sample from Kangankunde is a ferrocarbonatite with strontianite, monazite, apatite, and barite. The sample from Mushgai Khudag, Mongolia was collected from the apatite-magnetite body and can be termed 'apatitite' because it consists of >50 vol.% apatite, with celestine, gypsum, and lesser monazite. The fine-grained monazite and celestine appear to be supergene products that crystallized during weathering.

2. Results

Most isotopic studies of carbonatites have focused on constraining the origin of carbonatitic magmas, with only a few recent studies dedicated to the nature of mineralization. Bell and Blenkinsop (1989) and Bell (1998) summarized much of the radiogenic isotopic work conducted to determine the origin of carbonatites and associated alkaline rocks. The radiogenic isotopic data document that the carbonatites are of mantle origin, but the range in isotopic data suggests that the subcontinental upper mantle is inhomogeneous (Bell and Blenkinsop, 1989).

We determined the Nd and Sr isotopic compositions of a suite of carbonatites with varying degrees of REE enrichment (Fig. 3). Mineralized carbonatite samples evaluated in this study are from four continents and span a wide range in age (~23 Ma to 1385 Ma), Nd concentrations (3720 to 32,900 ppm), and Sr concentrations (2290 to 167,900 ppm). Our new Nd and Sr isotopic data include multiple samples for Mountain Pass (USA; $\varepsilon_{Nd\,i}$ = -3.1 to -5.4, Sr_i = 0.70512 to 0.70594), Elk Creek (USA; ~$\varepsilon_{Nd\,i}$ = 1.7, Sr_i = 0.7035), and Maoniuping (China; $\varepsilon_{Nd\,i}$ = -4.1 and -4.2, Sr_i = 0.70627 and 0.70645), and one sample each from Bear Lodge (USA; $\varepsilon_{Nd\,i}$ = 0.1, Sr_i = 0.70441), Kangankunde (Malawi; $\varepsilon_{Nd\,i}$ = 3.3, Sr_i = 0.70310), Adiounedj (Mali; $\varepsilon_{Nd\,i}$ = -0.1, Sr_i = 0.70558), and Mushgai Khudag (Mongolia; $\varepsilon_{Nd\,i}$ = -1.3, Sr_i = 0.70636). In addition to the mineralized carbonatites, we analyzed the underlying carbonatite at Mount Weld (Australia; $\varepsilon_{Nd\,i}$ = 0.7, Sr_i = 0.70197) and a carbonatite sample from Kerimasi (Tanzania; $\varepsilon_{Nd\,i}$ = -0.2, Sr_i = 7.0402).

Our results are similar to previously published data from the same localities. For example, Nelson et al. (1988) report $\varepsilon_{Nd\,i}$ and Sr_i values of 3.1 and 0.7031, respectively, for a carbonatite sample from Kangankunde, Malawi, whereas we measured $\varepsilon_{Nd\,i}$ and Sr_i values of 3.3 and 0.70310 for a carbonatite sample from the same locality. Moore et al. (2015) report $\varepsilon_{Nd\,i}$ (0.5) and Sr_i (0.70462) for an ancylite-carbocernaite sample at Bear Lodge, and we report similar $\varepsilon_{Nd\,i}$ (0.1) and Sr_i (0.70441) values for a drill-core ancylite vein sample. Xu et al. (2003) published Nd and Sr isotopic data for fluorite gangue minerals from Maoniuping ($\varepsilon_{Nd\,i}$ = -3.7 to -4.3, Sri = 0.70603 to 0.70624).

Our results, together with a literature compilation, show that most unmineralized carbonatites and mineralized but unmined carbonatites have $\varepsilon_{Nd\,i}$ values >-1 and Sr_i <0.705. These two groups overlap in values and do not form individual fields on a $\varepsilon_{Nd\,i}$ - Sr_i diagram. In contrast, samples from two REE carbonatite ore deposits (Mountain Pass and Maoniuping) have distinctly different isotopic compositions, with $\varepsilon_{Nd\,i}$ values from -3.1 to -5.4 and Sr_i from 0.7051 to 0.7065. These isotopic compositions clearly point to a carbonated source in

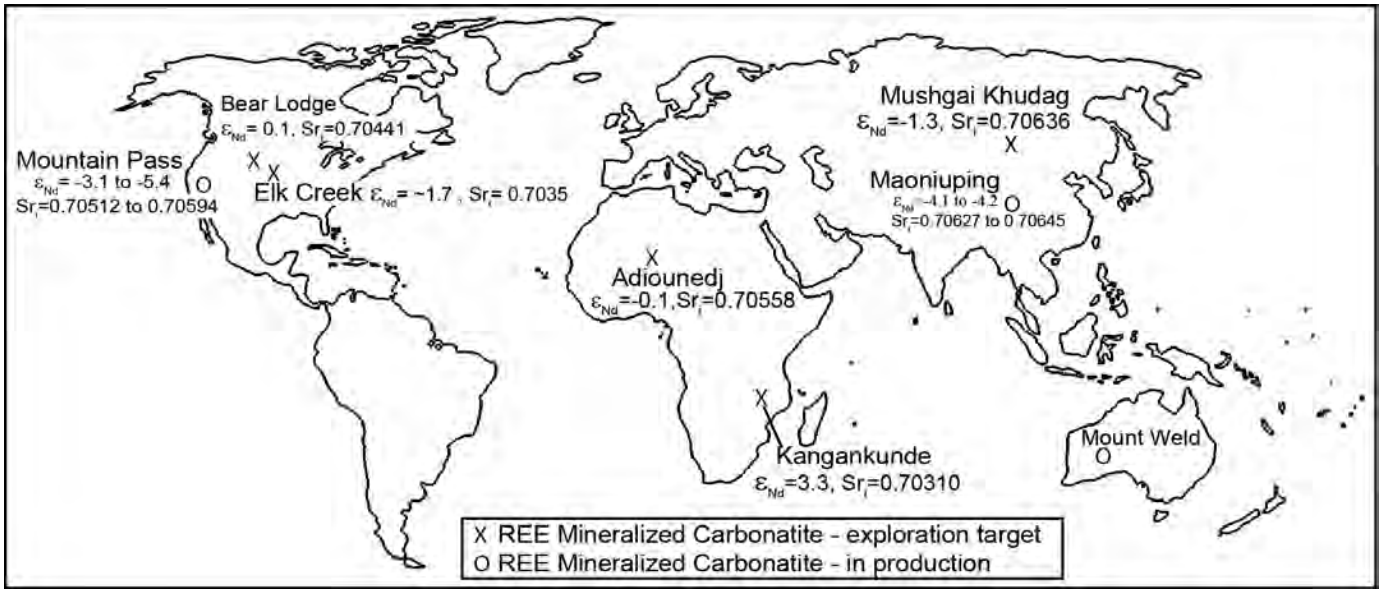

Fig. 3. Map displaying initial neodymium (ε_{Nd}) and strontium (Sr_i) isotopic compositions for samples analyzed in this study.

the lithospheric mantle. Mineralized but unmined carbonatites have higher Nd initial isotopic compositions ($\varepsilon_{Nd\,i}$ = -1.3 to 3.3) and a wider range in Sr isotopic compositions (Sr_i = 0.70310 to 0.70637), but these data are consistent with the involvement of a lithospheric mantle reservoir as well.

Acknowledgments

This work was funded by the US Geological Survey Mineral Resources Program in part through their External Research Grant Program.

References cited

Bell, K., 1998. Radiogenic Isotope Constraints on Relationships between Carbonatites and Associated Silicate Rocks—a Brief Review. Journal of Petrology, 39, 1987–1996.

Bell, K., and Blenkinsop, J., 1989. Neodymium and strontium isotope geochemistry of carbonatites. In: Bell, K. (Ed.), Carbonatites: Genesis and Evolution. Unwin Hyman, London, pp. 278-300.

Castor, S.B., 2008. The Mountain Pass rare earth carbonatite and associated ultrapotassic rocks, California. The Canadian Mineralogist, 46, 779-806.

Castor, S.B., and Nason, G.W., 2004. Mountain Pass rare earth deposit, California. In: Castor, S.B., Papke, K.G., and Meeuwig, R.O. (Eds.), Betting on industrial minerals. Proceedings of the 39th Forum on the Geology of Industrial Minerals, Reno/Sparks, Nev., May 18–24, 2003, Nevada Bureau of Mines and Geology Special Publication 33, pp. 68-81.

Mariano, A.N., and Mariano, A., 2012. Rare earth mining and exploration in North America. Elements, 8, 369–376.

Moore, M., Chakhmouradian, A.R., Mariano, A.N., and Sidhu, R., 2015. Evolution of rare earth mineralization in the Bear Lodge carbonatite, Wyoming: Mineralogical and isotopic evidence. Ore Geology Reviews, 64, 499-521.

Nelson, D.R., Chivas, A.R., Chappell, B.W., and McCulloch, M.T., 1988. Geochemical and isotopic systematics in carbonatites and implications for the evolution of ocean-island sources. Geochimica et Cosmochimica Acta, 58, 1–17.

Twyman, J.D., and Gittins, J., 1987. Alkalic carbonatite magmas: Parental or derivatives. In: Fitton, J.G., and Upton, B.G.L. (Eds.), Alkaline Igneous Rocks. Geological Society Special Publication 30, Blackwell Scientific Publications, Oxford, pp. 85-94.

Woolley, A.R., and Kjarsgaard, B.A., 2008. Global carbonatite database. Geological Survey of Canada Open File 5796, 28p.

Xie, Y.L., Li, Y., Hou, Z.Q., Cooke, D.R., Danyushevsky, L., Dominy, S.C., and Yin, S.P., 2015. A model for carbonatite hosted REE mineralization — the Mianning–Dechang REE belt, Western Sichuan Province, China. Ore Geology Review, 70, 595-612.

Xu, C., Campbell, I.H., Kynicky, J., Allen, C.M., Chen, Y.J., Huang, Z.L., and Qi, L., 2008. Comparison of the Daluxiang and Maoniuping carbonatitic REE deposits with Bayan Obo REE deposit, China. Lithos, 106, 12-24.

Xu, C., Huang, Z., Liu, C., Qi, L., Li, W., and Guan, T., 2003. Sources of ore-forming fluids in the Maoniuping REE deposit, Sichuan Province, China: Evidence from REE, radiogenic Sr, Nd, and stable-isotope studies. International Geology Review, 45, 635-645.

Xu, C., Taylor, R.E., Li W., Kynicky, J., Chakhmouradian, A.R., and Song, W., 2012. Comparison of fluorite geochemistry from REE deposits in the Panxi region and Bayan Obo, China. Journal of Asian Earth Science, 57, 76-89.

Nb-Ta-REE mineralization associated with the Crevier alkaline intrusion

Fabien Solgadi[1, a], Pierre-Arthur Groulier[2], Abdelali Moukhsil[1], Daniel Ohnenstetter[3], Anne-Sylvie André-Mayer[3], and Armin Zeh[4]

[1] Ministère de L'Énergie et des Ressources naturelles, QC
[2] Memorial University, St. John's, NL
[3] Université de Lorraine, France
[4] Goethe Universität, Frankfurt, Germany
[a] corresponding author: fabien.solgadi@mern.gouv.qc.ca

Recommended citation: Solgadi, F., Groulier, P.-A., Moukhsil, A., Ohnenstetter, D., André-Mayer, A.-S., and Zeh, A., 2015. Nb-Ta-REE mineralization associated with the Crevier alkaline intrusion. In: Simandl, G.J. and Neetz, M., (Eds.), Symposium on Strategic and Critical Materials Proceedings, November 13-14, 2015, Victoria, British Columbia. British Columbia Ministry of Energy and Mines, British Columbia Geological Survey Paper 2015-3, pp. 69-74.

1. Introduction

The Crevier alkaline intrusion is in the Grenville Province, north of the Lac Saint-Jean region of Québec (Fig. 1). It covers ~25 km^2 (Bergeron, 1980) and intrudes charnockitic suites in the allochthon belt defined by Rivers et al. (1989). This intrusion has a U-Pb zircon age of 957.5 ± 2.9 Ma (Groulier et al., 2014) and is oriented 320°, along the axis of crustal weakness known as the Waswanipi-Saguenay corridor (Bernier and Moorhead, 2000). This corridor is related to the Saguenay graben, which hosts the Saint-Honoré (Niobec) Nb-Ta-REE deposit and Montviel REE deposit. The age of the Saint-Honoré carbonatite was estimated at 584 to 650 Ma (K-Ar whole rock; Vallée and Dubuc, 1970; Boily and Gosselin, 2004). The Montviel intrusion has a U-Pb zircon age of 1894 ± 3.5 Ma (David et al., 2006; Goutier, 2006). These crystallization ages are very different and cannot be related to a single event for the injection of alkaline intrusions. As mapped by Bergeron (1980), the Crevier alkaline intrusion is broadly composed of syenite and carbonatite rocks (Fig. 2). The Nb-Ta mineralization consists of pyrochlore hosted by a nepheline syenite dike swarm in the centre of the intrusion. The highest REE concentrations, up to 729 ppm La and 1465 ppm Ce, are at the edge of the Crevier alkaline intrusion (Niotaz sud showing; Fig. 2).

2. Geology of the Crevier alkaline intrusion

Bergeron (1980) divided the Crevier alkaline intrusion into four units (Fig. 2): 1) a main unit of massive nepheline syenite with variable textures and characterized by the presence of igneous carbonates; 2) a banded syenite formed by the injection of dikes of different facies (ijolite, nepheline syenite, biotite syenite, carbonate-biotite syenite, and carbonatite); 3) a late alkaline syenite; and 4) dike swarms of pegmatitic nepheline syenite containing mineralization.

Crosscutting relationships observed in the field indicate that the second and third units were emplaced into the first, and that dike swarms cut the first two units. These dikes, which constitute the principal hosts for the Nb-Ta mineralization, are in the centre of the complex and parallel the Waswanipi-Saguenay corridor. Mineralization consists of two types: disseminated magmatic mineralization represented by small grains of pyrochlore (≤1 mm), and late magmatic mineralization that cuts the dikes (Groulier et al., 2014). The latter type is associated with networks of veins and veinlets rich in sodalite, cancrinite, zircon, sulphides and larger grains of pyrochlore (≥1 mm).

3. Geochemistry

3.1. Whole rock analysis

Based on 41 whole rock analyses, the Crevier alkaline intrusion, similar to the St Honoré complex (Currie, 1976), is miaskitic. It has an agpaitic index that ranges from 0.8 to 1 and low zirconium content (mean value 650 ppm). Baddelyite is rare and no other zirconium silicates, such as eudialyte, were observed. Two-differentiation trends are visible on total alkali silica (TAS) diagrams (LeBas et al., 1992; Fig. 3) and Harker diagrams. The first trend, which shows an increase in SiO_2 from ijolite to pegmatitic nepheline syenites, is interpreted to reflect a fractional crystallization process. The second trend represents rocks containing carbonate minerals such as calcite or ankerite. In the TAS diagram (Fig. 3), ijolite is interpreted as the starting point for both trends, and corresponds to the most mafic rock found in the Crevier alkaline intrusion. This rock is probably the best candidate for the original magma composition. The two trends that start from ijolite can be explained by an immiscibility process that may have led to the separation of silicate and carbonatitic melts. Field observations, petrographic study, and immiscibility textures between a carbonated and silicate liquids observed at macroscopic scale, support this hypothesis. Trace elements, in particular REE, are generally enriched in the carbonatite compared to the silicate phase.

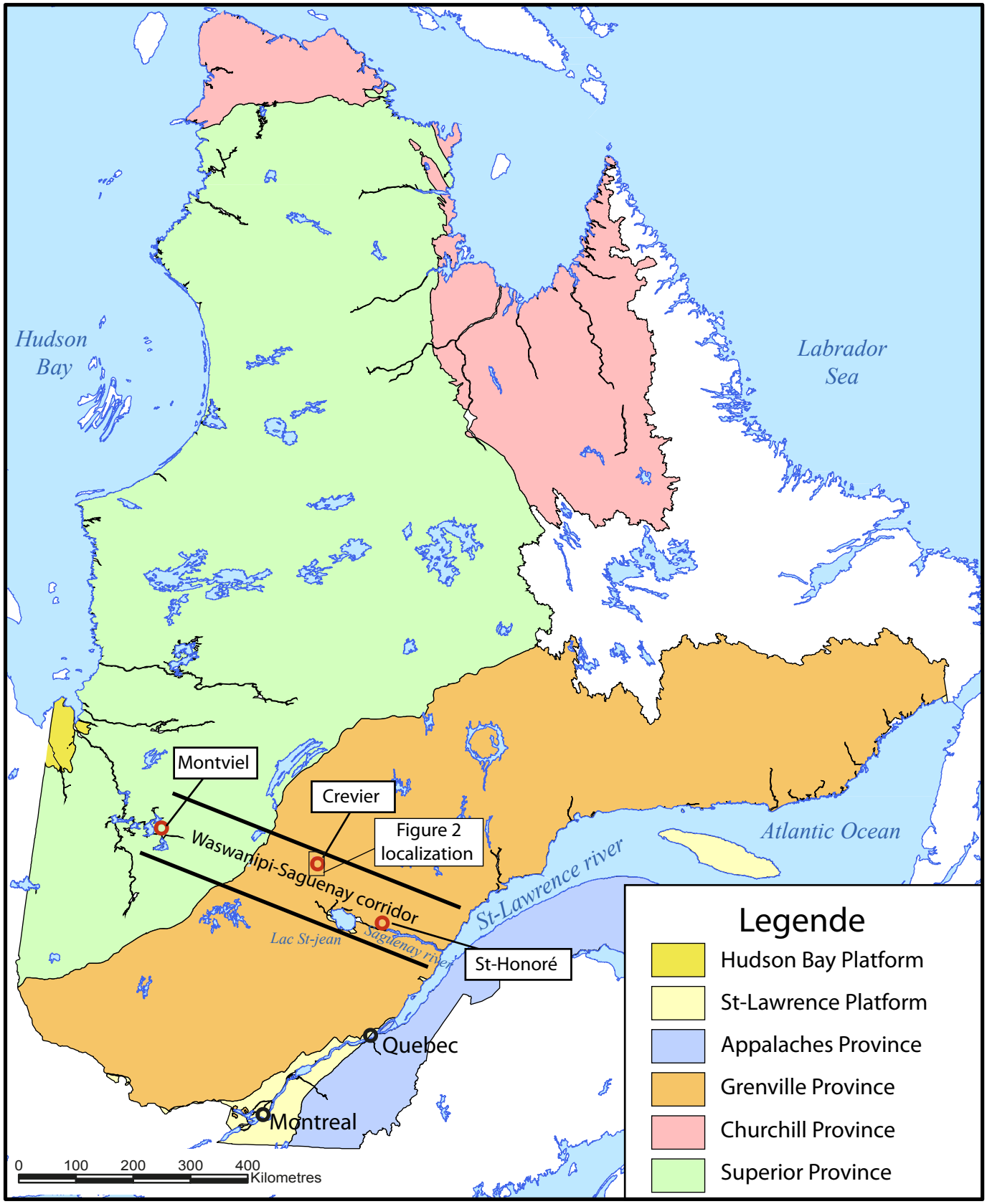

Fig. 1. Geological provinces of Quebec. Note the alignment of the principal alkaline intrusions along the Waswanipi-Saguenay corridor.

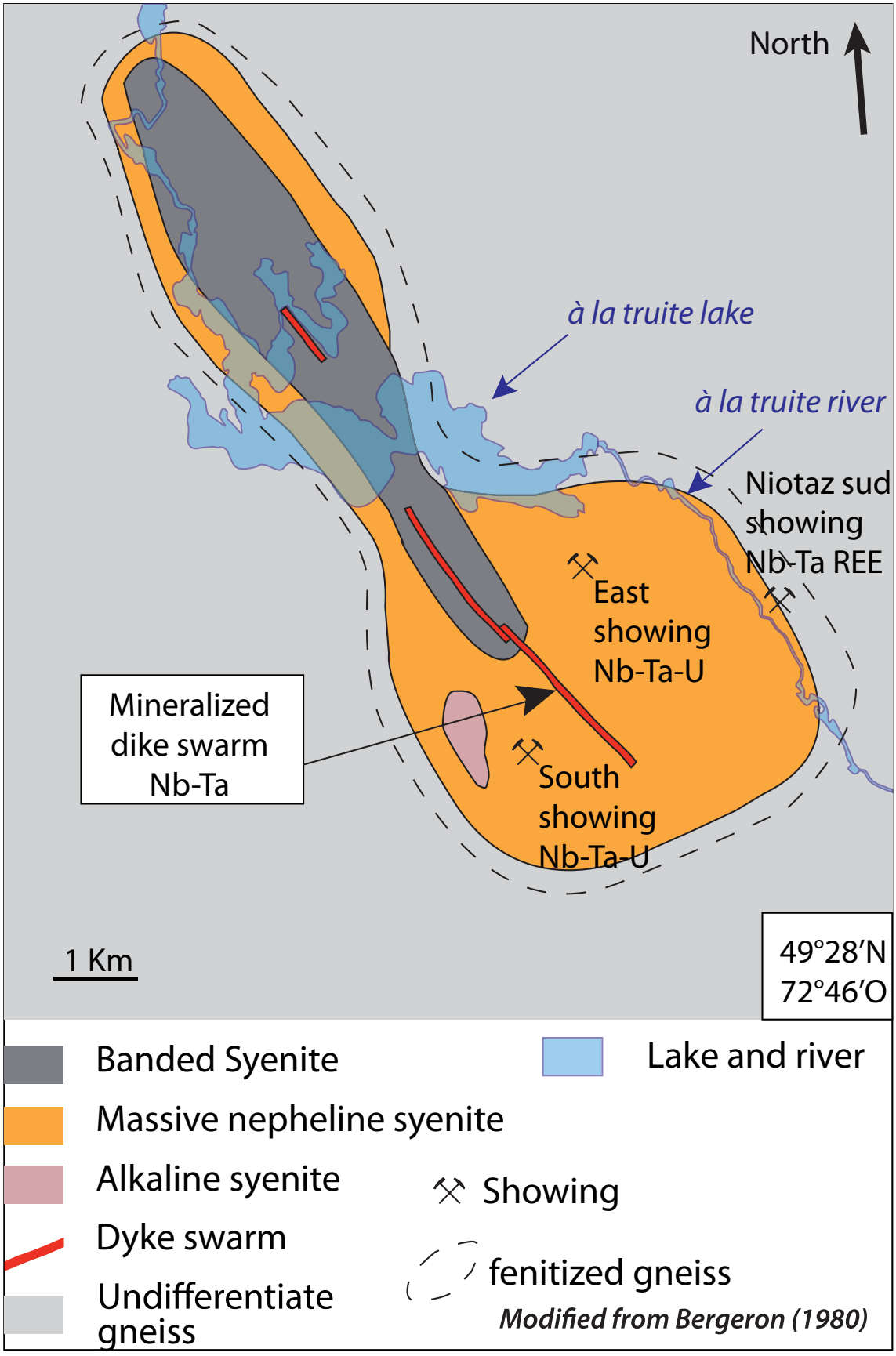

Fig. 2. Geological map of the Crevier alkaline intrusion. Modified from Bergeron (1980).

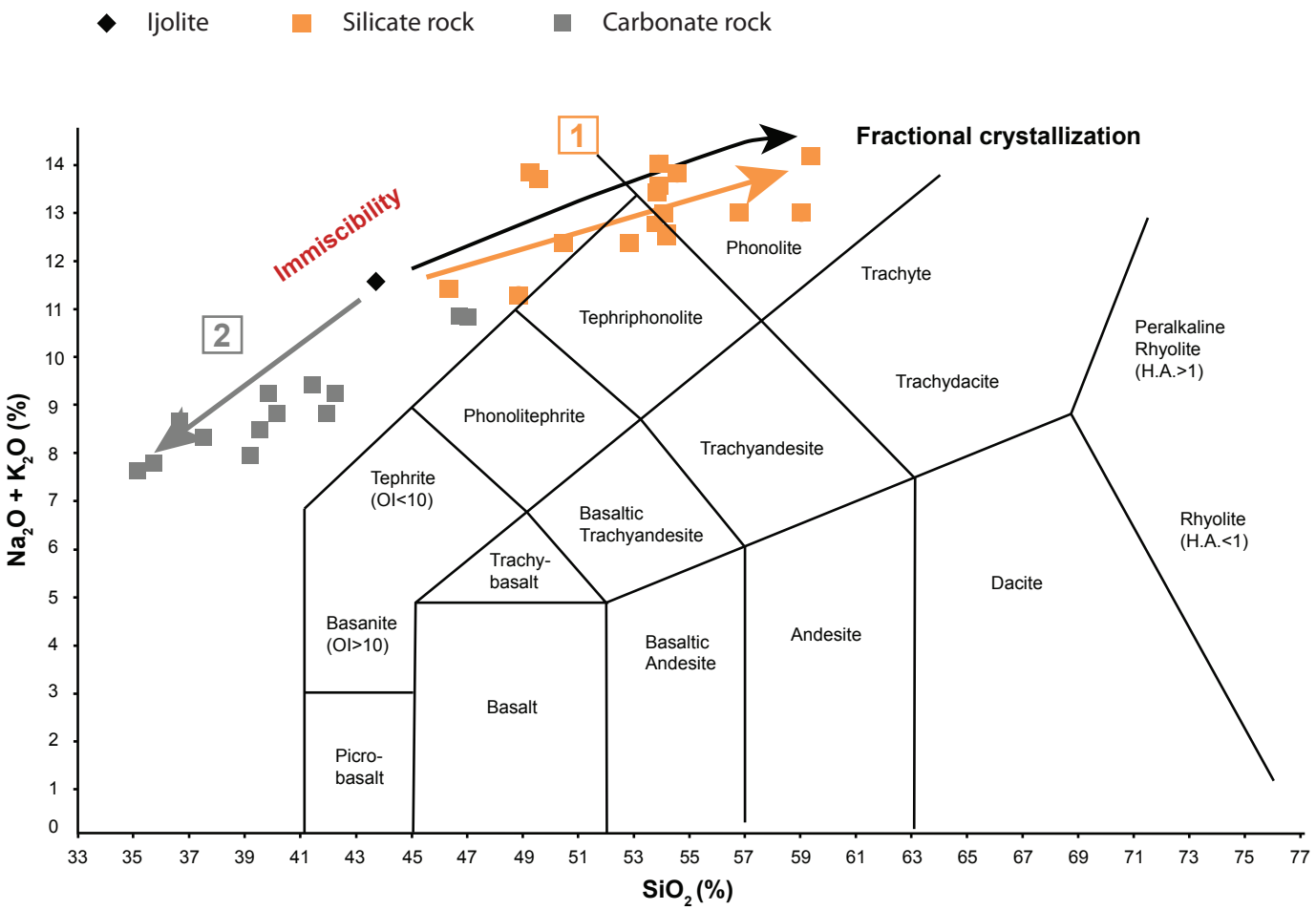

Fig. 3. TAS diagram (LeBas et al. 1992) showing composition of main rock types from the Crevier alkaline intrusion and two fractionation trends centred on ijolite.

3.2. Pyrochlore analysis

Niobium-tantalum mineralization in the Crevier alkaline intrusion is composed of oxides belonging to the pyrochlore supergroup of Atencio et al. (2010), defined by the general formula $A_{2-m}B_2X_{6-w}Y_{1-n}$. In the following, the most common elements in the formula are in bold.

The 'A' site is commonly occupied by a coordinating cation [8]; i.e. it is surrounded by eight other atoms with a large ionic radius (≈1 Å) or vacancy and, in some cases, H_2O. The A site preferably contains Na, Ca, Ag, Mn, Sr, Ba, Fe^{2+}, Pb^{2+}, Sn^{2+}, Sb^{3+}, Bi^{3+}, Y, Ce (and other lanthanides), Sc, U, Th, a vacancy or H_2O. The 'B' site is occupied by a coordinating cation [6]. This site typically contains high field strength elements (HFSE); more specifically, Ta, Nb, Ti, and Sb^{5+} and W; however, V^{5+}, Sn^{4+}, Zr, Hf, Fe^{3+}, Mg, Al and Si can also occupy this site. The 'X' site is mainly occupied by O but it may be replaced by OH or F. The 'Y' site commonly contains an anion but there may be a vacancy, H_2O or a very large (>>1 Å) monovalent cation (e.g.: OH^-, F, O, K, Cs and Rb). The parameters m, w and n in the chemical formula indicate occupancy values for the A, X and Y sites.

Minerals of the pyrochlore supergroup from the Crevier alkaline intrusion belong to the pyrochlore group sensus strico (Nb+Ta≥2Ti and Nb>Ta). Previous pyrochlore analyses are given by Laplante (1980) and Hoggarth (1989). Laplante also described an uranopyrochlore in the carbonatite from the northern portion of the Crevier alkaline intrusion in the Lac à la Truite area.

Three pyrochlore populations may be distinguished in terms of crystal-chemical data on the diagram of Nasraoui and Bilal (2000; Fig. 4).Primary euhedral pyrochlore (Pcl I) has a Na or Ca cation that occupies the A site and no vacancies in this site. It is zoned and displays dissolution and recrystallization textures. In some cases an unidentified secondary silicate phase rich in Nb surrounds this type of pyrochlore. Secondary euhedral to subhedral non-zoned pyrochlore (Pcl II) has more vacancies in the A site than Pcl I, and is interpreted as its replacement. Late xenomorphic pyrochlore (Pcl III) contains more vacancies in the A site compared to Pcl I or Pcl II and is found in fractures that were open to circulation of late-magmatic fluids.

4. Geochronology

Uranium-lead and Lu-Hf analyses on zircon grains from the massive nepheline syenite were performed by LA-ICP-

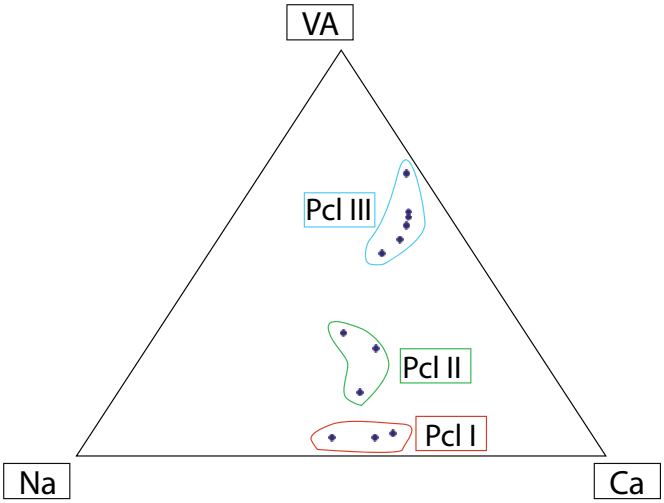

Fig. 4. Ternary (Na, vacancy (VA), Ca) plot (Nasraoui and Bilal, 2000) of three generations of pyrochlore (Pcl) from the Crevier alkaline intrusion indicating compositional differences between Pcl I, Pcl II and Pcl III.

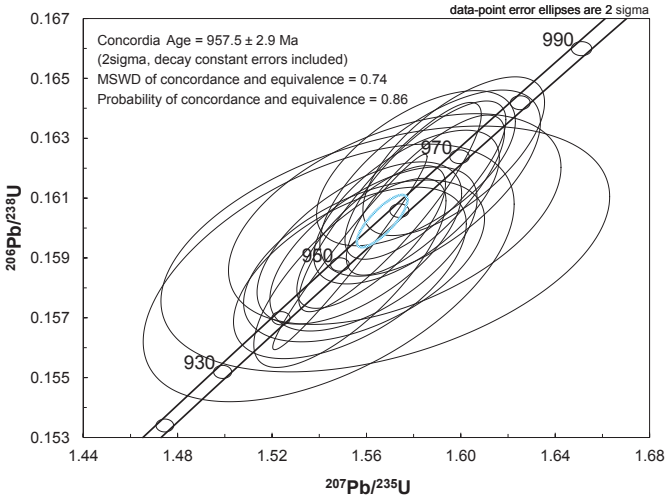

Fig. 5. Concordia diagram for U-Pb zircon data from the massive nepheline syenite.

MS in Frankfurt (University Goethe, Germany) to establish the crystallization age of the intrusion (U-Pb) and the mantle extraction age of the magma (Lu-Hf). The external shape and internal structure of zircons were imaged by combining cathodoluminescence (CL) and Scanning Electron Microscope (SEM; JEOL-6490 with Gatan MiniCL). Methods and instrumentation are described in Gerdes and Zeh (2006, 2009) and Zeh and Gerdes (2012).

4.1. U-Pb zircon analyses

Zircon observed in CL and SEM shows oscillations interpreted as magmatic zoning. Some zircons have altered edges that are white color under CL. These edges are interpreted to be a result of reaction between the zircon and a residual liquid enriched in uranium and were not analyzed. Analyses of 15 single zircons define an age of 957.5 ± 2.9 Ma, which we interpret as the age of the crystallization (Fig. 5). The mean square weighted deviation is 0.74 and the probability to find a point on the discordia is 0.86.

The 957.5 ± 2.9 Ma age corresponds to a late post-tectonic event (Gower and Krogh, 2002). Monzonitic-syenitic and granitic magmatism in the 975 to 955 Ma time interval was recognized in the eastern Grenville Province by Gower et al. (1991).

4.2. Lu/Hf zircon analyses

The model ages obtained by Lu-Hf analyses of zircon grains varies between 2.05 to 1.6 Ga. Rocks with the same model ages were also described in the central Grenville Province by Dickin and Higgins (1992) and Thomson et al. (2011) but from rocks that are generally granitic. The ages of 2.05 to 1.6 Ga are much older than the crystallization age. Two interpretations can be envisaged. In one, magma was extracted from the mantle and underplated the crust between 2.05 to 1.6 Ga, then, at the end of the Grenville orogeny, remelted to create the Crevier alkaline intrusion. Alternatively the age range may indicate magma contaminated by a heterogeneous continental crust of Archean or Paleoproterozoic age.

5. Conclusion

The Crevier alkaline intrusion is composed of rock types varying in composition from ijolite to carbonatite. The Nb-Ta mineralization is hosted in a pegmatitic nepheline syenite dike swarm. Highest REE concentrations are at the edge of the intrusion. Pyrochlore analyses indicate three types of pyrochlore and point to a possible remobilization of the primary mineralization by a late-magmatic fluid. Major and trace element geochemistry suggest that the Crevier alkaline intrusion formed by immiscibility process that resulted in silicate and carbonate phases. U-Pb geochronology on magmatic zircons from the nephelinic syenite gives a crystallization age of 957.5 ± 2.9 Ma. This age is similar to other alkaline intrusions in the eastern Grenville Province. The Lu-Hf age ranges between 2.05 to 1.6 Ga.

References cited

Atencio, D., Andrade, M.B., Christy, A.G., Giere, R., and Kartashov, P.M., 2010. The pyrochlore supergroup of minerals: nomenclature. The Canadian Mineralogist, 48, 673-698.

Boily, M., and Gosselin, C., 2004. Les principaux Types de Minéralisation en Métaux rares (Y-Zr-Nb-Ta-Be-Li-ETR) du Québec. Ministère de l'Énergie et des Ressources naturelles, Québec; ET 2004-01, 46p.

Bergeron, A., 1980. Pétrographie et géochimie du complexe igné alcalin de Crevier et de son encaissant métasomatisé. Master thesis, University of Chicoutimi, Canada, 129p.

Bernier, L., and Moorhead, J., 2000. Contrôles structuraux, caractéristiques pétrographiques et minéralogiques de la Kimberlite de d'Otish. Ministère des Ressources naturelles, Québec; MB 2000-14, 55p.

Currie, K.L., 1976. The alkaline rocks of Canada. Geological Survey of Canada Bulletin, pp. 239-228.

David, J., Dion, C., Goutier, J., Roy, P., Bandyayera, D., Legaut,

M., and Rhéaume, P., 2006. Datations U-Pb effectuées dans la Sous-province de l'Abitibi à la suite des travaux de 2004-2005. Ministère de l'Énergie et des Ressources naturelles, Québec; RP 2006-04, 22p.

Dickin, A., and Higgins, M., 1992. Sm/Nd evidence for a major 1.5 Ga crust-forming event in the central Grenville Province. Geology, 20, 137-140.

Gerdes, A., and Zeh, A., 2006. Combined U-Pb and Hf isotope LA-(MC)-ICP-MS analyses of detrital zircons: comparison with SHRIMP and new constraints for the provenance and age of an Armorican metasediment in Central Germany. Earth and Planetary Science Letters, 249, 47-61.

Gerdes, A., and Zeh, A., 2009. Zircon formation versus zircon alteration- new insights from combined U-Pb and Lu-Hf in situ LA-ICP-MS analyses and consequences for the interpretation of Archean zircon from the Central Zone of the Limpopo Belt. Chemical Geology, 261, 230-243.

Goutier, J., 2006. Géologie de la région du Lac au Goéland (32/F15) Ministère de l'Énergie et des Ressources naturelles, Québec; RG 2005-05, 39p.

Gower, C.F., Heaman, L.M., Loveridge, W.D., Schärer, U., and Tucker, R.D., 1991. Grenvillian magmatism in the eastern Grenville Province, Canada. Precambrian Research, 51, 315–336.

Gower, C.F., and Krogh T.E., 2002. A U-Pb geochronological review of the Proterozoic history of the eastern Grenville Province. Canadian Journal of Earth Sciences, 39, 795-829.

Groulier, P.A., Ohnenstetter, D., Andre-Mayer, A.S., Zeh, A., Solgadi, F., Moukhsil, A., and El Basbas, A., 2014. Étude des minéralisations en Nb-Ta de l'Intrusion alcaline de Crevier. Ministère de l'Énergie et des Ressources naturelles, Québec; MB 2014-33, 66p.

Hoggarth, D.D., 1989. Pyrochlore, apatite and amphibole: distinctive minerals in carbonatite. In: Bell, K. (Ed.), Carbonatites Genesis and Evolution. Unwin Hyman, London, pp. 105-148.

Laplante, R., 1980. Étude de la minéralisation en Nb_Ta_U du complexe igné alcalin du canton Crevier, comté Roberval, Lac St-Jean, P.Q. M. Sc. Thesis, Université de Montréal, 51p.

LeBas, M.J., Le Maitre, R.W., and Woolley, A.R., 1992. The construction of the Total alkali-Silica Chemical Classification of Volcanic Rocks. Mineralogy and Petrology, 46, 1-22.

Nasraoui, M., Bilal, E., 2000. Pyrochlores from the Lueshe carbonatite complex (Democratic Republic of Congo): a geochemical record of different alteration stages. Journal of Asian Earth Sciences, 18, 237-251.

Rivers, T., Martignole, J., Gower, C.F., and Davidson, A., 1989. New tectonics division of the Grenville Province, southeast Canadian Shield. Tectonics, 8, 63-84.

Thomson, S., Dickin, A., and Spray, J., 2011. Nd isotope mapping of Grenvillian crustal terranes in the vicinity of the Manicuagan Impact Structure. Precambrian Research, 191, 184-193.

Vallée, M., and Dubuc, F., 1970. The St-Honoré carbonatite complexe, Quebec. Transactions of the Canadian Institute of Mining and Metallurgy and of the Mining Society of Nova Scotia, 73, 346-356.

Zeh, A., and Gerdes, A., 2012. U-Pb and Hf isotope record of detrital zircons from gold bearing sediments of the Pietersburg Greenstone Belt (South Africa) – Is there a common provenance with the Witwatersrand Basin. Precambrian Research, 204-205, 46-56.

A petrographic study of Nb-bearing minerals at the Saint-Honoré niobium deposit

J. Tremblay[1, a], L.P. Bédard[1], and G. Matton[2]

[1] Sciences de la Terre, Université du Québec à Chicoutimi, Chicoutimi, QC
[2] Niobec Inc., Saint-Honoré-de-Chicoutimi, QC
[a] corresponding author: jonathan.tremblay11@uqac.ca

Recommended citation: Tremblay, J., Bédard, L.P., and Matton, G., 2015. A petrographic study of Nb-bearing minerals at the Saint-Honoré niobium deposit. In: Simandl, G.J. and Neetz, M., (Eds.), Symposium on Strategic and Critical Materials Proceedings, November 13-14, 2015, Victoria, British Columbia. British Columbia Ministry of Energy and Mines, British Columbia Geological Survey Paper 2015-3, pp. 75-81.

1. Introduction

Carbonatites are currently the focus of many studies to improve understanding of their petrogenesis and mineralization (e.g., Chen and Simonetti 2013; Chakhmouradian et al., 2015; Kamenetsky et al., 2015). Carbonatites are exploited for niobium (Nb); however they are also mined for Cu, P, and rare earth elements (REE). They tend to be enriched in Ba, F, Mn, Sr, V, Th, U, and Zr (Le Bas, 1981). Niobium is a strategic metal used in a broad range of applications, including superconducting magnets and steel alloys. Production of Nb has increased rapidly over the last decades (Roskill, 2013), driven by its use in modern equipment and for building pipelines in emerging countries such as China and India (Mackay and Simandl, 2014). However, only three mines currently produce most of the world's Nb. The Araxá and Catalão-II mines in Brazil (supergene deposits) account for more than 90% of the annual worldwide production, and the Saint-Honoré mine in Canada (magmatic-hydrothermal deposit) accounts for 8%. Other minor sources account for the remaining 2% (Papp, 2015).

This study examines mineralization at the Saint-Honoré Nb deposit. Initial studies that addressed mineralization of the Saint-Honoré carbonatite (Fortin-Bélanger, 1977; Thivierge et al., 1983) were conducted several decades ago, and recent studies that considered REE mineralization (Fournier, 1993; Grenier et al., 2012; Néron et al., 2013) did not treat the Nb-rich zone. Hence the relationships between the different Nb-bearing mineral phases remain poorly understood. Recent drilling in the deeper parts of the carbonatite offers an opportunity for new observations and improved interpretations. Herein we present the preliminary results of a petrographic study of Nb mineralization in the Saint-Honoré carbonatite.

2. Geology of the alkaline complex

The Saint-Honoré alkaline complex is in the Saguenay-Lac-Saint-Jean region, Québec (Fig. 1). It was discovered by airborne radiometric survey in 1967; exploitation began in 1976 and continues to the present. The Saint-Honoré deposit is an alkaline complex with a carbonatitic core comprising concentric zones of varying composition, with calcite in its external portion to dolomite and ankerite towards its core (Fortin-Bélanger, 1977; Thivierge et al., 1983). The carbonatite is surrounded by a nepheline syenite envelope. Syenite xenoliths are observed within the carbonatite units. The carbonatite and syenite complex was intruded into Grenvillian diorite and gneiss, which was subsequently fenitized (Fig. 1). The carbonatite is covered by Paleozoic rocks of the Trenton Group (limestone) and Utica Formation (shale). Doig and Barton (1968) reported a K/Ar age of 565 Ma for the alkaline complex; more recently, baddeleyite from lamprophyre dikes associated with the Saint-Honoré suite yielded a U-Pb age of 582.1±1.8 Ma (Michael Higgins, personal communication, 2015).

The crescent-shaped orebody is hosted entirely by dolomite and calcite units that surround the ferro-carbonatite (ankerite) core. It is currently mined to a depth of 850 metres and is open at depth. Most recent reserves estimates are 416 Mt grading 0.41% Nb (Vallières et al. 2013). Mineralization decreases gradually toward the margins of the carbonatite. The silicate rocks lack significant mineralization.

3. Objectives

Previous mineralogical studies of the Saint-Honoré alkaline complex focused primarily on the upper portion where minor interactions with surface water took place (Fortin-Bélanger 1977, Thivierge et al., 1983). Samples for this study were taken at greater depths to prevent any bias due to meteoric alteration, thus providing a clearer distinction between hydrothermal and magmatic processes. Several Nb-bearing carbonatite samples used in previous studies were degraded by weathering, and magmatic and/or hydrothermal features were only partially preserved. For example, it was recently demonstrated that the halite interpreted to be of magmatic origin is only in deep portions of the Saint-Honoré carbonatite (Kamenetsky et al., 2015).

For this study, rocks from two sub-horizontal diamond-drilled holes were considered representative of mineralization at the 490 m mine level. One hole (235 m long) plunges 6°

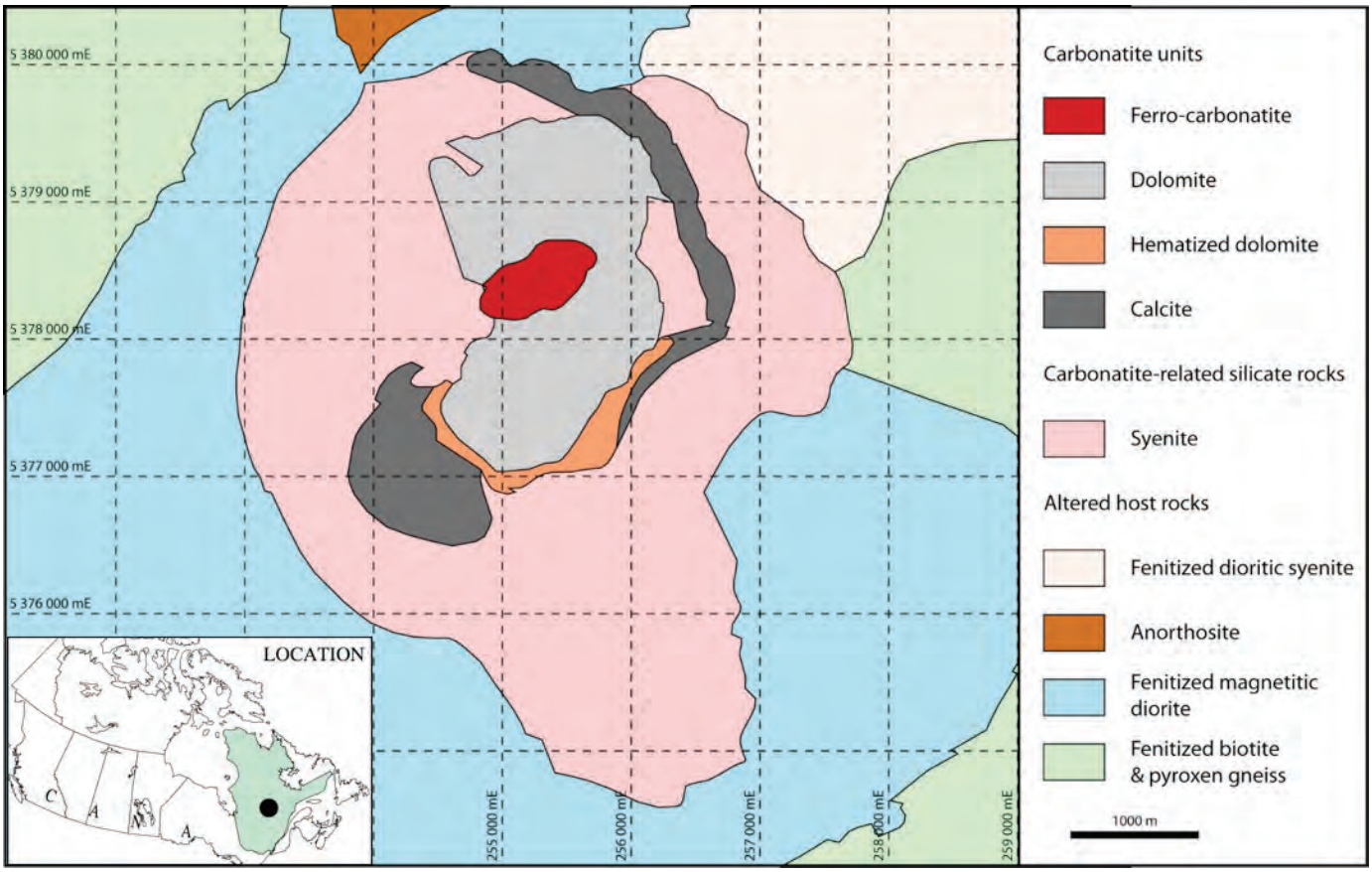

Fig. 1. Simplified geological map of the Saint-Honoré alkaline complex. Modified from Vallières et al., 2013.

north, the second (115 m long) plunges 31° south. They were selected because they provide a continuous view of mineralization from north to south in the mine. Twenty-one polished thin sections were prepared from the southern zone, 52 from the northern zone. These sections were examined using both polarized and reflected light microscopy as well as cathodoluminescence (CL) and scanning electron microscopy (SEM). Cathodoluminescence is particularly useful for detecting trace elements (activators), impurities, and growth textures (McLemore and Barker, 1987; Mariano, 1988, Götze, 2002; Götze et al., 2013). In carbonatites, magmatic zoning in apatite is clearly observed and provides critical information on geological evolution. Furthermore, zonation in pyrochlore may provide insight into the petrogenetic evolution of mineralization.

In this study we: 1) identify the Nb minerals and describe Nb mineral transformations that occurred in the carbonatite complex; 2) describe the mineralogical associations of Nb minerals to understand their evolution and petrogenesis; and 3) define variations in mineralization from north to south. Geologists at the Niobec Mine propose a north-south variation in the distribution of Nb minerals, where columbite would be predominant in the northern section and Na-Ca pyrochlore in the southern and central portions (Guillaume Matton, personal communication, 2015). Variation in Nb mineralization with increasing depth has yet to be demonstrated.

4. Ore mineralogy

The carbonatite-hosting the orebody is composed predominantly of dolomite, calcite, magnetite, pyrite, phlogopite, fluorapatite, Ca-Na pyrochlore [$(Ca,Na)_2(Nb,Ti)_2O_6(OH,F)$] and columbite [$(Fe,Mn)(Nb,Ti)_2O_6$]. Minor alkali feldspar, pyroxene, chlorite, quartz, zircon, ilmenite, rutile, hematite, pyrrhotite, sphalerite, barite, fluorite, siderite, REE minerals and other species of the pyrochlore group (e.g. uranopyrochlore [$(U,Ca,Ce)_2(Nb,Ta,Fe,Ti)_2O_6(OH,F)$]) have been observed throughout the carbonatite (Fortin-Bélanger, 1977; Thivierge et al., 1983; Grenier et al., 2013). The carbonatite units are strongly banded on scales of a few centimetres to several metres. Some band contacts are gradual whereas others are sharp. Mineral proportions are highly variable both between and within the bands. Despite a relatively homogeneous background of uneconomic Nb grades throughout the orebody, Nb-enriched zones in the form of asymmetric and elongated, steeply plunging lenses are distributed in very complex patterns.

5. Main niobium minerals

Niobium mineralization in the Saint-Honoré alkaline complex consists primarily of Ca-Na pyrochlore and columbite-(Fe) (Table 1). Both minerals are found throughout the carbonate

Table 1. Average chemical analyses, in per cent, of representative ore minerals and inclusions (calcite) determined by EDS-SEM analysis (4 analyses per mineral).

	Ca-Na pyrochlore	Columbite-(Fe)	Apatite	Inclusions in Columbite-(Fe)
TiO_2	3.47	2.25		
FeO		15.99		
MnO		2.96		
CaO	15.42	0.95	35.23	43.88
Na_2O	6.08			
P_2O_5			48.88	
Nb_2O_5	68.71	77.86		
CO_2				56.12
F	6.32		15.89	
Total	100.00	100.00	100.00	100.00

Note: Determined with an EDS-SEM system ("standardless analyses")

units. Thorium±Ta pyrochlore is uncommon. Unaltered Ca-Na pyrochlore forms euhedral 0.01-2 mm crystals that are generally beige, light brown, greyish or reddish. Altered Ca-Na pyrochlore grains are darker and difficult to distinguish from magnetite and columbite-(Fe). Under polarized light, Ca-Na pyrochlores are commonly zoned and have darker cores (Fig. 2a). Ca-Na pyrochlore is inclusion free, except for rare apatite grains. Observations under reflected light allow the distinction between pyrochlore and magnetite (Fig. 2b). Considering that this type of pyrochlore shows little heterogeneity, CL was mainly used for identifying textures, mineral inclusions, and overgrowths. Figure 2c illustrates a brown Ca-Na pyrochlore under CL with minor apatite inclusions and no overgrowth. Backscattered electron imaging (BSE) was used to identify inclusion free regions of the grain (Fig. 2d). X-ray dispersive energy (EDS) analyses (four per sample) indicate a high Ca, Na, and F content (Table 1). Calcium content varies from 12-18% CaO, sodium from 5-8% Na_2O, and fluorine from 4-9% F.

Columbite-(Fe) is the second most abundant Nb mineral at the mine, although it is considered a minor Nb-bearing phase (Vallières et al. 2013). Columbite-(Fe) is commonly anhedral and fractured. Under plane polarized light (Fig. 3a), columbite-(Fe) ranges from dark brown or dark grey to opaque. In highly altered rocks, columbite-(Fe) grains are difficult to distinguish from magnetite. However, reflected light shows textures resembling a spider web (Fig. 3b). Reflected light was therefore used to distinguish columbite from magnetite, as both are opaque in polarized light and show no internal reflections in the Saint-Honoré carbonatite. Columbite-(Fe) shows surprising peculiarities under CL (Fig. 3c). Although columbite is quenched by Fe (no luminescence; Götze et al., 2013), mineral inclusions within columbite show orange luminescence. EDS-SEM analyses (Table 1, Fig. 3d) indicate that the orange inclusions are calcite.

Thorium±Ta pyrochlore is uncommon. Complete characterization of this species of pyrochlore is outside of the scope of this study. Figure 4a illustrates one of the few grains observed in plane polarized light. It shows a characteristic pleochroism varying from translucent to pink and green. Oscillatory zoning is well developed having zones of similar thickness. Primary fractures (excluding those produced by secondary alteration) are only in the pinkish layers, suggesting radioactive damage. Reflected light analysis shows apatite inclusions (Fig. 4b). Apatite, magnetite, and pyrochlore crystals appear automorphous and moulded together suggesting a primary coeval origin. Cathodoluminescence shows multiple zonations (Fig. 4c) that are not visible under plane polarized light. The deep green suggests a strong activator. Using BSE imaging, Th±Ta pyrochlore appears brighter than Ca-Na pyrochlore (Fig. 4d). The composition of the dark halos has yet to be determined, but preliminary results show no Th or Ta values.

Calcium-Sodium pyrochlore and columbite grains are generally found in apatite bands and lenses, but rarely together. Apatite lenses in dolomitic units appear to be richer in Nb minerals than those in calcitic units. Furthermore, a few Ca-Na pyrochlore grains have a columbite-(Fe) rim, suggesting replacement. Unlike most Nb-bearing minerals, which are associated with apatite, Th±Ta pyrochlore grains occur in magnetite-rich lenses or syenite xenoliths in carbonatite.

Two types of apatite are observed in the Saint-Honoré alkaline complex. Magmatic apatite is disseminated or concentrated in flow bands and lenses throughout the carbonatite units. Grains are translucent under plane polarized light, but are orange in hand specimen. Magmatic zoning is best observed under CL. Niobium mineralization is associated with this magmatic apatite. The second form of apatite is a fine-grained red hydrothermal alteration product (Néron et al. 2013) largely confined to apatite veins. These veins could easily be misidentified as hematite. The apatite veins crosscut the Nb

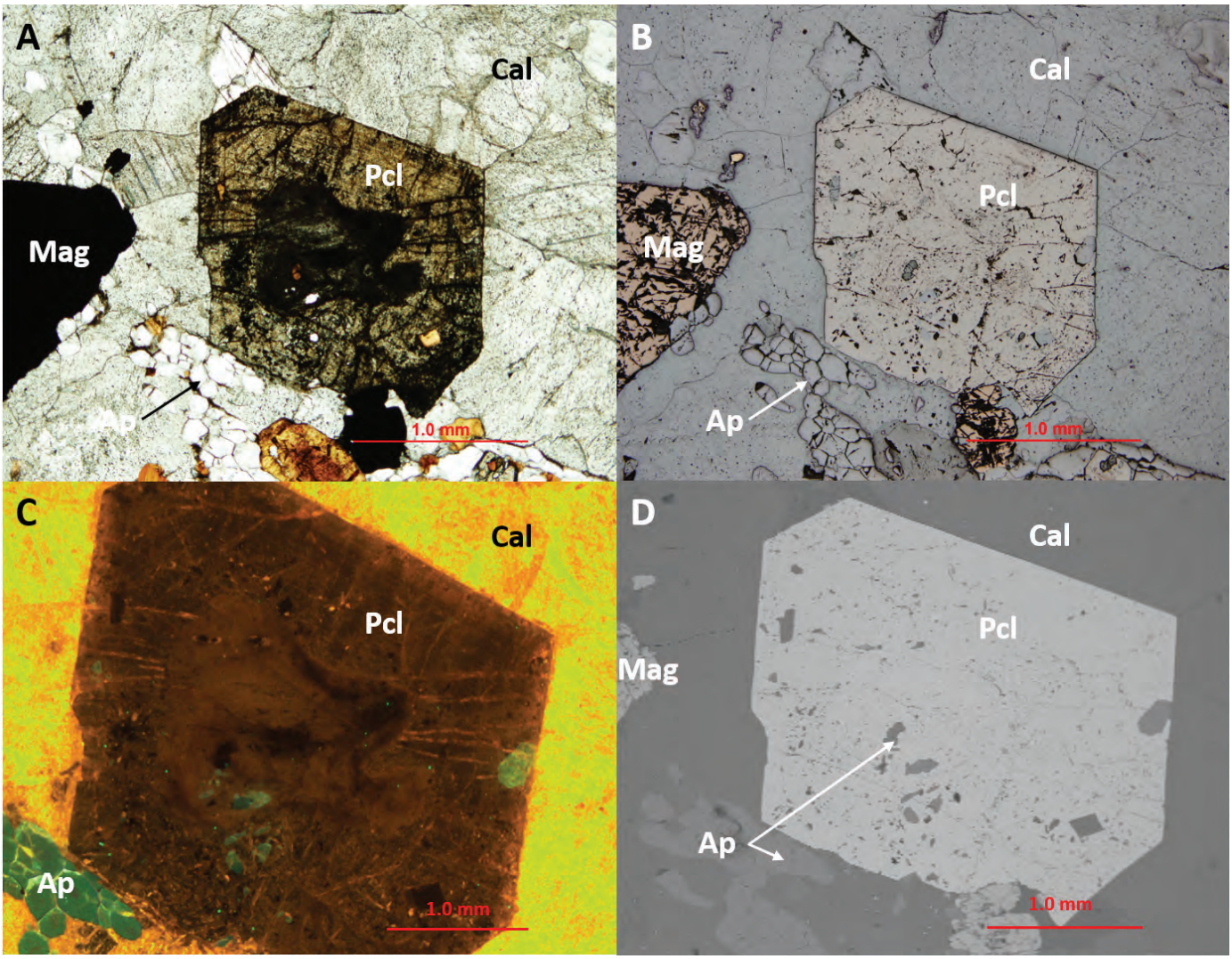

Fig. 2. Calcium-sodium pyrochlore (Pcl) morphology and mineralogical associations. **a)** Plane polarized light showing a fine zonation in a euhedral Pcl grain. **b)** Reflected polarized light showing distinction between magnetite (Mag) and Pcl. **c)** Cathodoluminescent image highlights inclusions of apatite (Ap; green) in Pcl and the calcite (Cal; orange). **d)** BSE image of apatite (Ap) inclusions in Pcl grain.

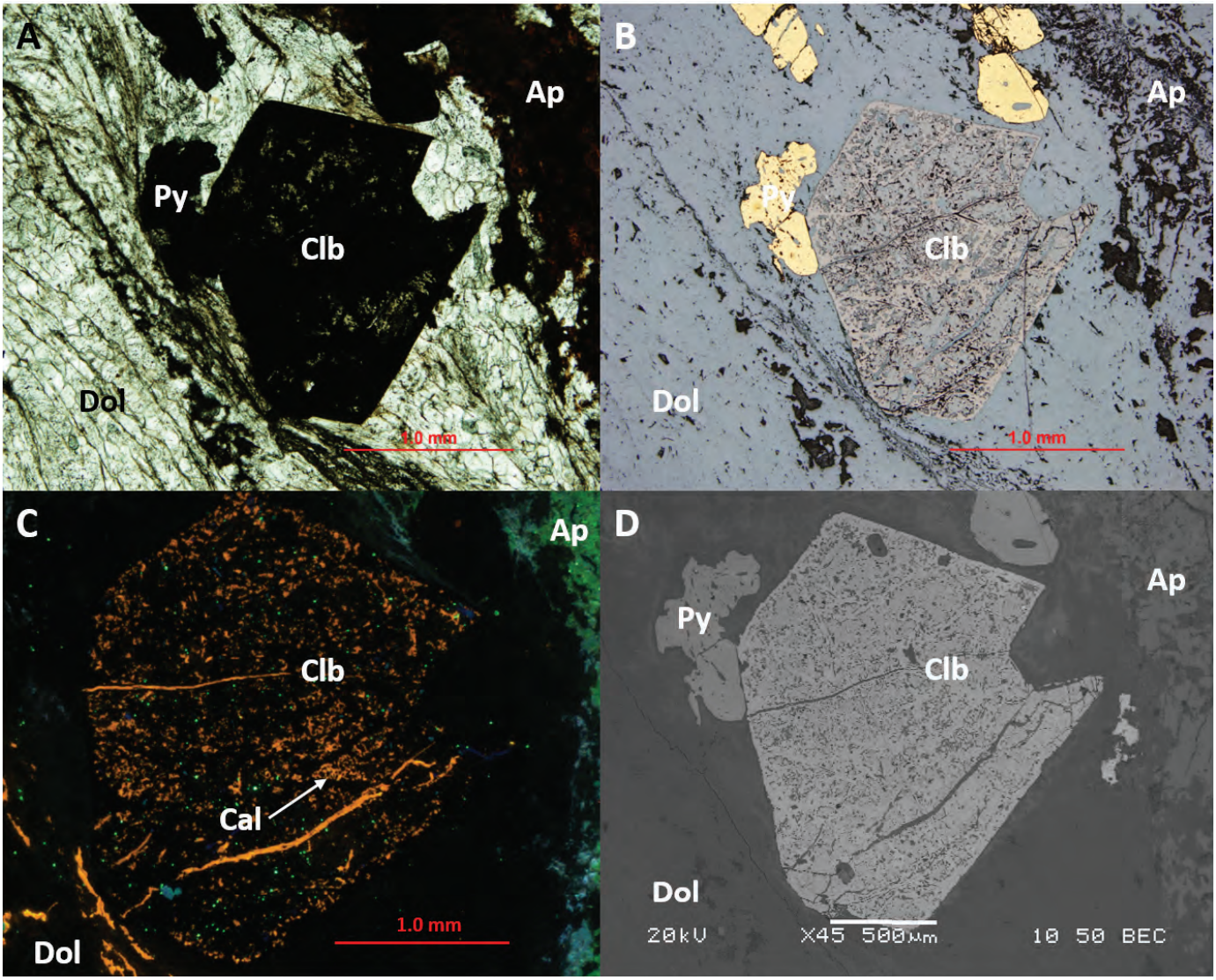

Fig. 3. Columbite-(Fe) (Clb) morphology and mineralogical associations. **a)** Dark brown to almost opaque Clb grain in contact with anhedral pyrite (Py); plane polarized light. **b**) The Clb grain contains multiple inclusions; reflected light. **c)** The cathodoluminescence activator signal (orange) suggests that inclusions in this Clb grain are composed of calcite (Cal). **d)** BSE image; SEM confirms the opaque matrix is columbite-(Fe) and the orange, under cathodoluminescence, is calcite.

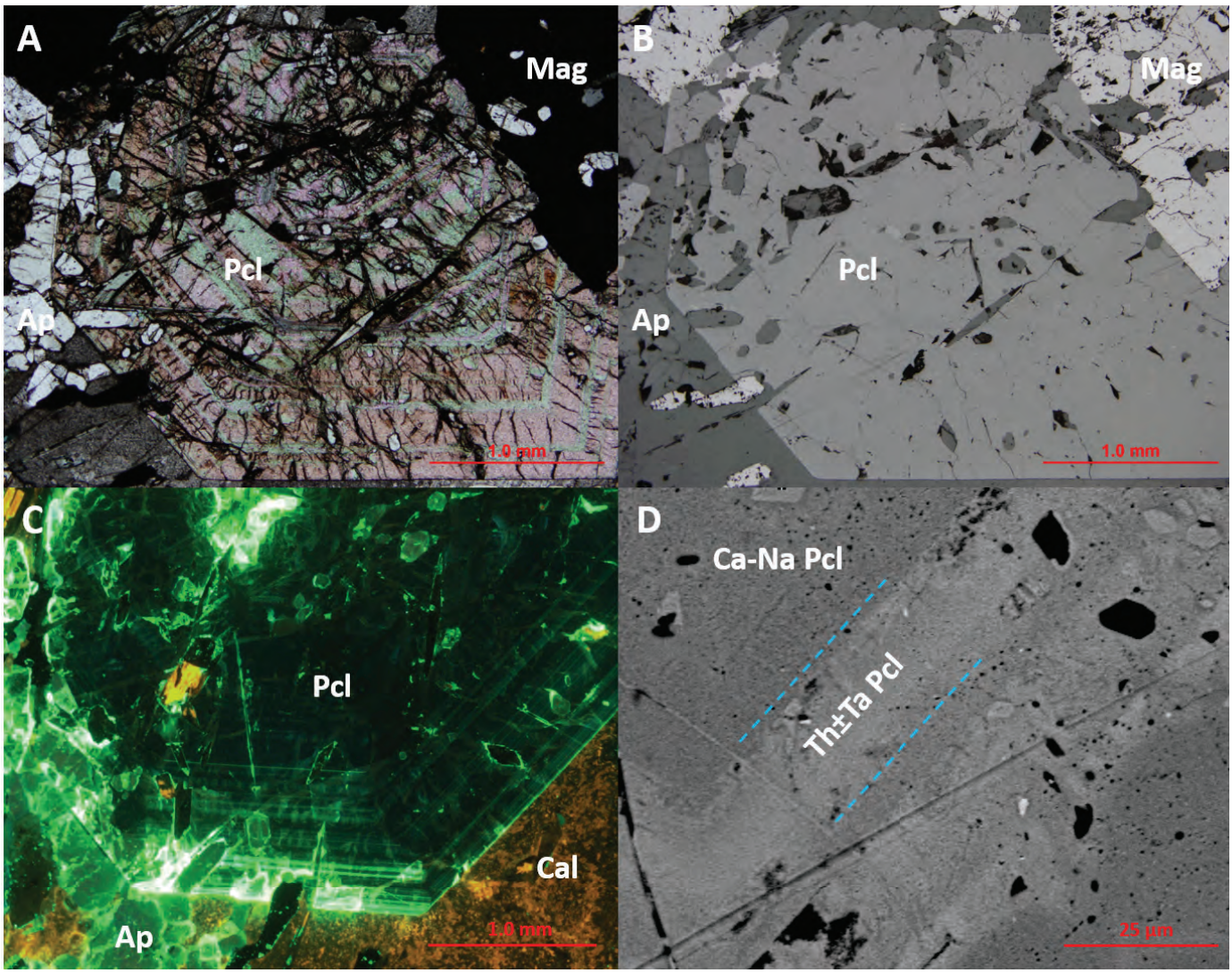

Fig. 4. Thorium±Ta pyrochlore (Pcl) morphology and mineralogical associations. **a)** Pyrochlore shows strong pleochroism and oscillatory zoning under plane polarized light. **b)** Apatite inclusions in pyrochlore displaying sharp contacts; reflected light. **c)** Unusual deep green observed in Pcl under cathodoluminescence. **d)** BSE image; SEM confirms the light halos are of Th±Ta and the dark halos refer to Ca-Na pyrochlore with trace elements (precise composition to be determined).

mineralization and are not associated with Nb mineralization.

The mineralogical observations presented in this study suggest four main forms of Nb mineralization: 1) euhedral and unaltered brown Ca-Na pyrochlore; 2) opaque columbite-(Fe); 3) replacement of pyrochlore by columbite; and 4) brown Ca-Na pyrochlore that was hydrothermally altered by red apatite-forming fluid.

6. Summary

Ca-Na pyrochlore is the main Nb ore mineral at Saint-Honoré. Columbite-(Fe), previously considered only a minor phase, was observed in a large number (30%) of our mineralized samples. Both columbite-(Fe) and Ca-Na pyrochlore are associated with apatite-rich magmatic layers in dolomite, however a few apatite lenses in calcite are also mineralized. No mineralization is related to red hydrothermal apatite veins. P- and F-complexes likely transported Nb during the early stages of carbonatite magmatism (Knudsen, 1989; Hogarth et al., 2000; Cordeiro et al., 2011). This could explain the strong relationship between the Nb minerals and apatite and the presence of F in pyrochlore in the Saint-Honoré carbonatite complex. It can be assumed that Ca-Na pyrochlore grains are of magmatic origin. Columbite-(Fe) rims around Ca-Na pyrochlore strongly suggest a chemical disequilibrium. Another important observation is that calcite inclusions are visible within the columbite-(Fe) grains. It is possible that the columbite-(Fe) expelled incompatible elements, such as Na and F, whereas Ca formed calcite suggesting a phase transformation from pyrochlore to columbite as the magma evolved.

The Th±Ta pyrochlore type needs further study using SEM to confirm absence of U. Oscillatory zoning and radial fractures in the pinkish zonations are consistent with the idea that the green zonations are relatively Th-rich; this Th is likely the cause of the radial fractures (Fig. 4a).

Both Ca-Na pyrochlore and columbite-(Fe) are visible in the northern and southern part of the orebody. Textural observations suggest that columbite is a replacement for pyrochlore. Variation in Nb mineralization with increasing depth has yet to be demonstrated.

Acknowledgments

This project is funded by Natural Sciences and Engineering Research Council of Canada (NSERC) and we thank Niobec Inc. and its team for ongoing cooperation in providing the samples and support for this study. Murray Hay (Maxafeau Editing Services) is thanked for improving the written English.

References cited

Chakhmouradian, A.R., Reguir, E.P., Kressall, R.D., Crozier, J., Pisiak, L.K., Sidhu, R., and Yang, P., 2015. Carbonatite-hosted niobium deposit at Aley, northern British Columbia (Canada): Mineralogy, geochemistry and petrogenesis. Ore Geology Reviews, 64, 642-666.

Chen, W., and Simonetti, A., 2013. In-situ determination of major and trace elements in calcite and apatite, and U-Pb ages of apatite from the Oka carbonatite complex: Insights into a complex crystallization history. Chemical Geology, 353, 151-172.

Cordeiro, P.F.O., Brod, J.A., Palmieri, M., Oliveira, C.D., Barbosa, E.S.R., Santos, R.V., Gaspar, J.C., and Assis, L.C. 2011. The Catalão I niobium deposit, central Brazil: Resources, geology and pyrochlore chemistry. Ore Geology Reviews, 41, 112–121.

Doig, R., and Barton, J.M., 1968. Ages of carbonatites and other alkaline rock in Québec. Canadian Journal of Earth Sciences, 7, 22-28.

Fortin Bélanger, M., 1977. Le complexe annulaire à carbonatites de St-Honoré (P.Q. Canada) et sa minéralisation à niobium : étude pétrographique et géochimique. Unpublished M.Sc. thesis, Université du Québec à Chicoutimi, Chicoutimi, Canada, 210p.

Fournier, A., 1993. Magmatic and hydrothermal controls of LREE mineralization of the St-Honoré Carbonatite, Québec. Unpublished M.Sc. thesis, McGill University, Montréal, Canada, 95p.

Götze, J., 2002. Potential of cathodoluminescence (CL) miscroscopy and spectroscopy for the analysis of minerals and materials. Analytical and Bioanalytical Chemistry, 374, 703-708.

Götze, J., Schertl, H.-P., Neuser, R.D., Kempe, U., and Hanchar, J.M., 2013. Optical microscope-cathodoluminescence (OM-CL) imaging as a powerful tool to reveal internal textures of minerals. Mineralogy and Petrology, 107, 373-392.

Grenier, L., Tremblay, J.F., and Sirois, R., 2013. NI 43-101 technical report, updated mineral resource estimate for rare earth elements, 2012. IAMGOLD Corporation, 166p. http://www.infomine.com/index/pr/PB/39/93/PB399305.PDF, accessed August 14th, 2015.

Hogarth, D.D., Williams, C.T., and Jones, P., 2000. Fresh rock zoning in pyrochlore group minerals from carbonatites. Mineralogical Magazine, 64, 683-697.

Kamenetsky, V.S., Mitchell, R.H., Maas, R., Giuliani, A., Gaboury, D., and Zhitova, L., 2015. Chlorine in mantle-derived carbonatite melts revealed by halite in the St.-Honoré intrusion (Québec, Canada). Geology, 43, 687-690.

Knudsen, C., 1989. Pyrochlore group minerals from the Qaqarssuk carbonatite complex. In: Möller, P., Cerny, P., and Saupé, F., (Eds.), Lanthanides, Tantalum and Niobium. Springer-Verlag, Berlin-Heidelberg, pp. 80-99.

Le Bas, M.J., 1981. Carbonatite magmas. Mineralogical Magazine, 44, 133-140.

Mackay, D.A.R., and Simandl, G.J., 2014. Geology, market and supply chain of niobium and tantalum – a review. Mineralium Deposita, 49, 1025-1047.

Mariano, A.N., 1988. Some further geological application of cathodoluminescence. In: Marshall, D.J., (Ed.), Cathodoluminescence of Geological Materials. Unwin Hyman, Boston, pp. 94-123.

McLemore, V.T., and Barker, J.M., 1987. Some geological applications of cathodoluminescence: examples from the Lemitar Mountains and Riley travertine, Socorro County, New Mexico. New Mexico Geology, 9, 37-40.

Néron, A., Bédard, L.P., Gaboury, D., and Thivierge, S., 2013. Preliminary characterization of the REE mineralization of the St-Honoré ferro-carbonatite (Québec, Canada). Mineral deposit research for a high-tech world: 12th Society for Geology Applied to Mineral Deposits (SGA) biennial meeting in Uppsala (Sweden), Program with Abstracts.

Papp, J.F., 2015. Niobium (Columbium). In: United States Geological Survey, Mineral Commodity Summaries 2015, pp. 110-111.

Roskill.com, 2013. Niobium: Markets outlook to 2017, 12th edition. http://www.roskill.com/reports/steel-alloys/niobium/leaflet, accessed August 14th, 2015.

Thivierge, S., Roy, D.-W., Chown, E.H. et Gauthier, A., 1983. Évolution du complexe alcalin de St.-Honoré (Québec) après sa mise en place. Mineralium Deposita, 18, 267-283.

Vallières, D., Ferlatte, G., Sirois, R., Tremblay, J.-F., Pelletier, P., and Gaultier, P., 2013. Technical Report NI 43-101, Update on Niobec Expansion. Feasibility Study. 305p.

Primary and secondary mineralogy of the Ilímaussaq alkaline complex, South Greenland

Henrik Friis[1, a]

[1] Natural History Museum, University of Oslo, PO 1172 Blindern, 0318 Oslo, Norway
[a] corresponding author: geofriis@yahoo.com

Recommended citation: Friis, H. 2015. Primary and secondary mineralogy of the Ilímaussaq alkaline complex, South Greenland. In: Simandl, G.J. and Neetz, M., (Eds.), Symposium on Strategic and Critical Materials Proceedings, November 13-14, 2015, Victoria, British Columbia, British Columbia Ministry of Energy and Mines, British Columbia Geological Survey Paper 2015-3, pp. 83-89.

1. Introduction

The Ilímaussaq alkaline complex is among the largest known alkaline complexes in the world and has been studied since the early 19th century, when Giesecke explored Greenland for minerals. More than 230 different mineral species occur in the complex. Ilímaussaq is the type locality for 34 minerals, including 15 that have not been reported elsewhere. Some of these are rock-forming minerals and thus, although unique to Ilímaussaq, may not be considered rare.

Among the minerals first described from Ilímaussaq are two important sources for critical materials: steenstrupine-(Ce) and eudialyte (Table 1). Steenstrupine-(Ce) is the main target mineral for the Kvanefjeld multi-element project in the northern part of Ilímaussaq, whereas eudialyte is targeted at the Tanbreez project in the southern part known as Kringlerne (Fig. 1).

The first detailed mapping and petrological studies of the complex were published by Ussing (1912), who also defined the term 'agpaitic' for rocks where the molar ratio (Na+K)/Al is greater than or equal to 1.2. Since then, the distinction between agpaitic and miaskitic has changed from being based on just rock chemistry to being based more on mineral paragenesis. Sørensen (1997) defined agpaitic as peralkaline rocks in which High Field Strength Elements (HFSE; e.g., Zr and Ti) are hosted in complex minerals such as eudialyte and rinkite. Rocks with high alkalinity, where HFSE are hosted in minerals such as zircon, are considered miaskitic. Khomyakov (1995) further developed the agpaitic classification by introducing the term hyperagpaitic for the most evolved syenites. Hyperagpaitic rocks are characterised by containing water soluble minerals (e.g., natrosilite and natrophosphate) and complex phosphosilicates (e.g., steenstrupine-(Ce) and vuonnemite; Khomyakov, 1995).

The Ilímaussaq complex is one of several alkaline complexes formed during Mesoproterozoic rifting in the southwestern part of Greenland, which collectively is called the Gardar province (Upton, 2013). With an age of ~1.6 Ga, Ilímaussaq is the youngest major intrusion of the Gardar province (Waight et al., 2002; Krumrei et al., 2006).

2. Geology

The Ilímaussaq complex consists of three main intrusive suites (Fig. 1): 1) an augite syenite, which forms the shell of the complex, cuts the Julianehåb granite in the south and a series of sedimentary rocks and volcanic flows in the north; 2) peralkaline granites and quartz syenites; and 3) alkaline nepheline syenites. The sodalite-rich nepheline syenite naujaite occurs under the roof whereas the kakortokites are in the lower part of the complex. The lujavrites are the youngest, forming a horizon between the naujaites and kakortokites. However, the lujavrite does not form a uniform unit, but rather penetrates the naujaite and appears to have flowed around the edges of the major naujaite unit, especially in the northern part of the complex (Ussing, 1912; Ferguson, 1964; Marks and Markl, 2015). Descriptions of the most important agpaitic rocks

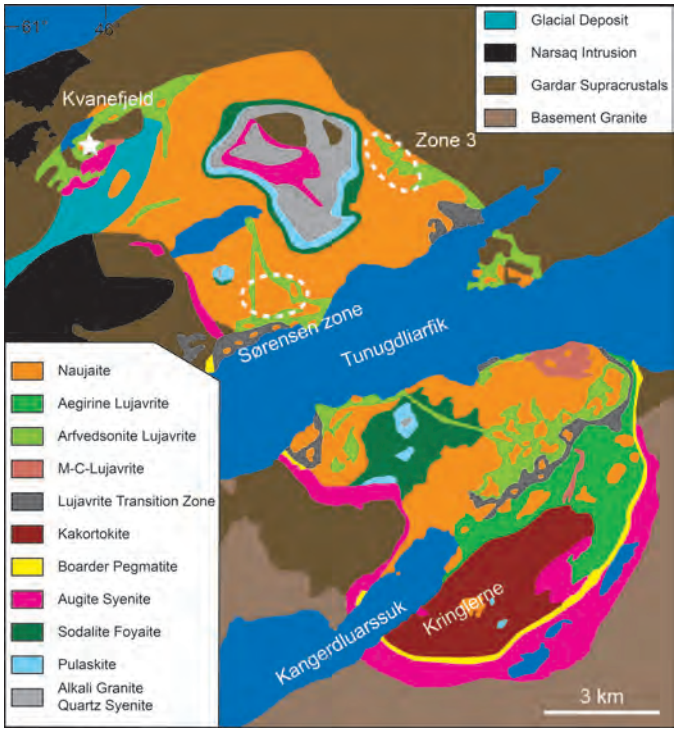

Fig. 1. Geological map of the Ilímaussaq alkaline complex. Modified after Sørensen (2001) and GME (2015).

Table 1. Simplified formulae of selected Ilímaussaq minerals.

Britholite group	$Ca_2(REE,Ca)_3(SiO_4,PO_4)_3(OH,F)$
Catapleiite	$Na_2ZrSi_3O_9•2H_2O$
Eudialyte s.s.	$Na_{15}Ca_6Fe_3Si(Si_{25}O_{73})(O,OH,H_2O)_3(Cl,OH)_2$
Gittinsite	$CaZrSi_2O_7$
Lovozerite s.s.	$Na_3□_3(Ca,□)_2Zr(Si_6O_{12})O_3(OH)_3$
Nacareniobsite-(Ce)	$Na_3Ca_3REENb(Si_2O_7)OF_3$
Natrophosphate	$Na_7(PO_4)_2F•19H_2O$
Natrosilite	$Na_2Si_2O_5$
Naujakasite	$Na_6(Fe,Mn)Al_4Si_8O_{26}$
Phosinaite-(Ce)	$Na_{13}Ca_2REE(Si_4O_{12})(PO_4)_4$
Rinkite	$(Na,Ca)_3(Ca,REE)_4Ti(Si_2O_7)OF_3$
Steenstrupine-(Ce)	$Na_{13}REE_6Mn_2(Fe^{3+},Mn^{3+})_2(Zr,Th)(Si_6O_{18})_2(PO_4)_7•3H_2O$
Townendite	$Na_8ZrSi_6O_{18}$
Ussingite	$Na_2AlSi_3O_8OH$
Villiaumite	NaF
Vitusite-(Ce)	$Na_3REE(PO_4)_2$
Vuonnemite	$Na_{11}TiNb_2(Si_2O_7)_2(PO_4)_2O_3(F,OH)$

s.s.: sensu stricto. Minerals in bold were first described from Ilímaussaq.

related to critical materials are presented below.

2.1. Kakortokite

Kakortokite is a medium- to coarse-grained nepheline syenite and forms the main magmatic layered part of the intrusion in the southern part of the complex (Fig. 2a). Most of the 29 described units consist of three layers, which are named on the basis of colour. Basal black layers of predominantly arfvedsonite are followed by red layers rich in eudialyte, then by white layers rich in nepheline and alkali-feldspar, which are generally the thickest (Bohse et al., 1971). The layers maintain a consistent thickness throughout a unit. Although most of the units contain all three layers, some do not. Black layers have abrupt lower contacts with subjacent white layers, but typically pass gradationally upwards to red layers (Fig. 2b). The units are labelled based on their position with respect to a marker unit called zero (e.g., unit +16 is the 16th unit above the marker; unit -3 is the 3rd unit below the marker). The typical thickness

Fig. 2. Rhythmic, metre-scale magmatic layering of kakortokite. **a)** Sharp-based basal black layers of predominantly arfvedsonite grade upward to red layers rich in eudialyte, which are overlain by relatively thick white layers rich in nepheline and alkali-feldspar. **b)** Close up illustrating abrupt basal contact between black layer 0 and underlying white layer -1, and gradational transition between black layer 0 and overlying red layer 0.

of the red layers is about 1 m, but red +16 is a particularly rich eudialyte zone 3.5 m thick (Bohse et al., 1971). Although eudialyte is predominant in the red layers, it is also present in the other layers.

2.2. Naujaite

Naujaite is a cumulate rock consisting of large (up to 5 mm) euhedral sodalite crystals that floated to the top of the magma chamber. Later crystallising phases are mainly nepheline, alkali-feldspar, aegirine, arfvedsonite, and eudialyte, which result in a predominantly poikilitic texture. Individual feldspars can be up to 25 cm, and both aegirine and arfvedsonite can form crystals up to 30 cm (Ussing, 1912). The amount of eudialyte in naujaite is inconsistent and it may be completely absent. Rinkite is a common accessory mineral in naujaite, which is the most exposed rock in Ilímaussaq. The naujaites are not considered potential ores for critical materials.

2.3. Lujavrite

Lujavrite is a meso- to melanocratic agpaitic to hyperagpaitic syenite with a pronounced lamination caused by the orientation of mafic minerals and, in part, felsic minerals such as feldspars. The two most abundant varieties of lujavrite in Ilímaussaq are named on the basis of colour: in green lujavrite the predominant mafic mineral is aegirine; in black lujavrite, the main mafic mineral is arfvedsonite. The felsic minerals in lujavrite are nepheline, albite, microcline, and sodalite. Lujavrites are fine grained (up to 0.6 mm), but sodalite grains can be up to 2 mm and mafic minerals up to 1 mm. A coarser type of lujavrite is called m-c-lujavrite (m-c stands for medium to coarse grained), in which the individual grains can reach sizes of more than one cm, and are locally pegmatitic. A fourth type, naujakasite lujavrite, contains naujakasite and is associated with the highly agpaitic stage of the complex. In these lujavrites, naujakasite generally occurs at the expense of nepheline (Andersen and Sørensen, 2005). Although naujakasite has been found only in Ilímaussaq, it is common; locally the lujavrite contains up to 75 % volume naujakasite. The water-soluble mineral villiaumite is abundant in most of the lujavrites but has been leached out in some near-surface rocks. Lujavrite is the rock unit containing the highest amounts of incompatible elements and is the major ore of the Kvanefjeld deposit (Bailey et al., 2001).

3. Exploration history

The first exploration activity in Ilímaussaq was initiated by The Cryolite Company in 1888 and, in 1899, K.J.V. Steenstrup mined eudialyte in the southern part of the complex. A total of 60 t of eudialyte was mined for zirconium extraction experiments (Sørensen, 1966, 1968). In 1968, the Danish company Dansk Svovlsyre- og Superphosphat-Fabrik A/S (now Superfos) extracted approximately 100 t of eudialyte ore from the kakortokites. The renewed interest in zirconium and niobium led to detailed investigations and mapping of the kakortokites. Since the work by Superfos, several minor exploration companies have held the exploration licence to this part of the complex. Tanbreez is the current licence holder and they report an inferred resource of 4.3 billion tonnes of eudialyte ore with an average grade of Zr-oxide (1.8%), Nb-oxide (0.2%), light rare earth elements (LREE) (0.5%) and heavy rare earth elements (HREE) (0.15%) (Tanbreez, 2015).

In the wake of the Second World War, demand for uranium led to a uranium-focused survey of Greenland. In the 1950s, the Kvanefjeld deposit was discovered after a radiometric survey. The ore consists of several types of lujavrite. Material with the highest radioactivity was collected to test extraction via conventional acid and carbon leach methods, but the ore was found to be refractory (Sørensen, 2001). A drilling program was started in 1958, and in 1962, 180 t of ore from a 20 m adit was extracted (Fig. 3). The ore was used to test sulphatizing roasting for extracting uranium and thorium at the Danish National laboratories (RISØ). In 1978, the 'Kvanefjeld Uranium Project' was initiated to examine the economic potential of a uranium mine at Kvanefjeld. In 1980-81, a 1 km adit was made at Kvanefjeld (Fig. 3). Each blast was checked with a scintillometer, and high-grade ore was shipped to RISØ where a 1:10-scale pilot plant had been constructed. A total of 4700 metric tons of ore were processed by pressurized carbonate leaching, which resulted in recoveries of up to 80% (Sørensen, 2001). The Kvanefjeld project was terminated in 1983 when a political decision was made for Denmark to maintain its status as a nuclear-free zone. At the end of the project, 69 holes had been drilled with a total core length of more than 10 km, and 20,000 tonnes of ore had been mined.

In 2007, Kvanefjeld received renewed interest as a multi-element deposit. Greenland Minerals and Energy Ltd. (GME) set up a drilling program and metallurgical studies. In addition to U, Th, and rare earth elements (REE), the deposit contains significant Zn in the form of sphalerite. The new drilling program at Kvanefjeld consisted of 146 holes with a total of 35.5 km of core. The feasibility report defined a measured resource of 143 Mt @ 303 ppm U_3O_8, 1.2% TREO, and 0.24% zinc (GME, 2015). Greenland Minerals and Energy Ltd. also discovered two additional lujavrite-hosted deposits (the

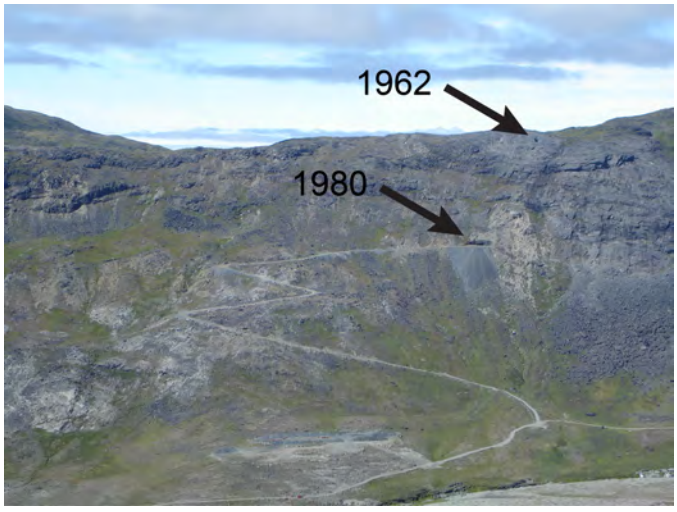

Fig. 3. View of Kvanefjeld showing the 1962 and 1980 adits.

Sørensen zone and Zone 3) north of the Tunugdliarfik (Fig. 1). The Sørensen zone has an inferred resource of 119 Mt @ 400 ppm U_3O_8, 1.2% TREO, and 0.3% zinc, and Zone 3 an inferred resource of 47 Mt @ 358 ppm U_3O_8, 1.2% TREO, and 0.3% zinc (GME, 2015).

4. Primary ore minerals

Eudialyte is concentrated in specific magmatic layers in the kakortokite. In contrast, steenstrupine-(Ce) is distributed throughout the lujavrites, making all arfvedsonite lujavrite a potential ore. Steenstrupine-(Ce) and lovozerite group minerals are the main target minerals in the lujavrites. In addition to steenstrupine-(Ce) and lovozerite group minerals, the lujavrites may contain significant amounts of other primary REE-minerals such as vitusite-(Ce) and phosinaite-like minerals (Pekov and Ekimenkova, 2001; Friis, Unpublished data). Below is a description of the three most important primary ore minerals in the Ilímaussaq complex.

4.1. Eudialyte

Eudialyte was described as a new species from Ilímaussaq by Stromeyer (1819). It occurs in all of the main agpaitic rock units, but is particularly abundant in the kakortokites, where it typically forms euhedral crystals that are generally less than 5 mm, but locally reach several cm. In pegmatites, massive eudialyte can form over several metres and be up to 50 cm thick. Pfaff et al. (2008) showed a decrease in the Fe/Mn ratio of eudialyte when moving from unit zero through the units to +16 and that the trend continued into the lower lujavrites. Pfaff et al. (2008) further showed that the Na-content in the eudialyte increases up section in the kakortokites, but that the increase in Na is more pronounced for eudialytes in the aegirine lujavrites. This is consistent with the observation that Na content in eudialyte from the aegirine lujavrites at Kvanefjeld is higher than Na in eudialyte in other lujavrites from the same locality (Friis, 2012; Andersen and Friis, 2015).

4.2. Steenstrupine-(Ce)

Steenstrupine-(Ce) was first described as a new species from Ilímaussaq by Lorenzen (1881) from material collected by Steenstrup. Steenstrupine-(Ce) is widespread in pegmatites and ussingite veins in the naujaites, and is a rock-forming mineral in many arfvedsonite-lujavrites. Steenstrupine-(Ce) has not been observed in the kakortokites and generally does not coexist with eudialyte. Steenstrupine-(Ce) is a phosphosilicate, which is a group of minerals characteristic of hyperagpaitic environments (Khomyakov, 1995). The chemical composition of steenstrupine-(Ce) is complex and can vary significantly. For example, Makovicky and Karup-Møller (1981) showed that practically all Na may be replaced by H^+ owing to large channels in the structure (Moore and Shen 1983). The structure of steenstrupine-(Ce) contains several different coordinations, which enable the incorporation of various elements or elements in different valance states (Makovicky and Karup-Møller, 1981). For example, steenstrupine-(Ce) from the Kola Peninsula has both divalent and trivalent Fe (Malczewski et al., 2005). High Th (up to 5 wt.% oxides; Makovicky and Karup-Møller, 1981; Khomyakov and Sørensen, 2001) and U (0.2-1% U_3O_8; GME, 2015) results in most steenstrupine-(Ce) being metamict and hence challenging to analyze.

The steenstrupine-(Ce) crystals in the lujavrites are typically euhedral and up to 0.6 mm. Each lujavrite may contain several types of steenstrupine-(Ce), such as inclusion-free metamict, partly altered, anisotropic rim, or poikilitic varieties (Fig. 4). A general correlation between different types of steenstrupine-(Ce) in a sample seems to be lacking, except for the poikilitic type, which is always present with at least one other type. Typical inclusions are arfvedsonite, lovozerite group minerals, and britholite group minerals. Khomyakov and Sørensen (2001) investigated steenstrupine-(Ce) with anisotropic rims and found that the rims have a lower Th and higher REE than the cores (1.22 vs. 4.37 wt.% ThO_2 and 33.15 vs. 30.00 wt.% REE_2O_3). Although steenstrupine-(Ce) is a rare mineral, only described in minor amounts at a few other alkaline complexes, it is abundant in some of the lujavrites, making it a rock-forming mineral with a modal abundance of up to 10% (Makovicky et al., 1980).

4.3. Lovozerite

Lovozerite group minerals in Ilímaussaq were first described in a few samples from the Kangerdluarssuk Fjord where they occur associated with ussingite and steenstrupine-(Ce) (Danø and Sørensen, 1959). Lovozerite was considered a rare mineral in Ilímaussaq until a new member of the lovozerite group (townendite) was discovered in flotation tails (Grey et al., 2010). Since the discovery of townendite, lovozerite group minerals have been observed in many lujavrite samples. Three types have been observed: 1) colourless (in plane polarized light) euhedral grains up to 0.1 mm, with a composition close to that of lovozerite sensu stricto; 2) pink euhedral to subhedral grains that have higher Mn, Y, and U contents than the colourless type, but still classify as lovozerite sensu stricto; and 3) brown grains that show clear evidence of alteration. The composition of the latter type is varied and probably reflects the alteration rather than a true lovozerite group composition (Friis, 2012). The lovozerite crystals typically occur on grain boundaries or partly to fully embedded in arfvedsonite and steenstrupine-(Ce). Because of the relative abundance of lovozerite in the lujavrite and its U content, it is an important ore mineral and its presence could explain the low recovery of U from ore during tests in the 1980s.

5. Alteration

Most of the rocks in Ilímaussaq show signs of alteration, which varies from thin zones along fractures and grain boundaries to complete replacement of all primary minerals. The replacements are not necessarily related to external fluids, but may have resulted from exsolution of fluids, in the final stages of crystallization, that reacted with previously formed minerals. Evidence for such an alteration has been observed

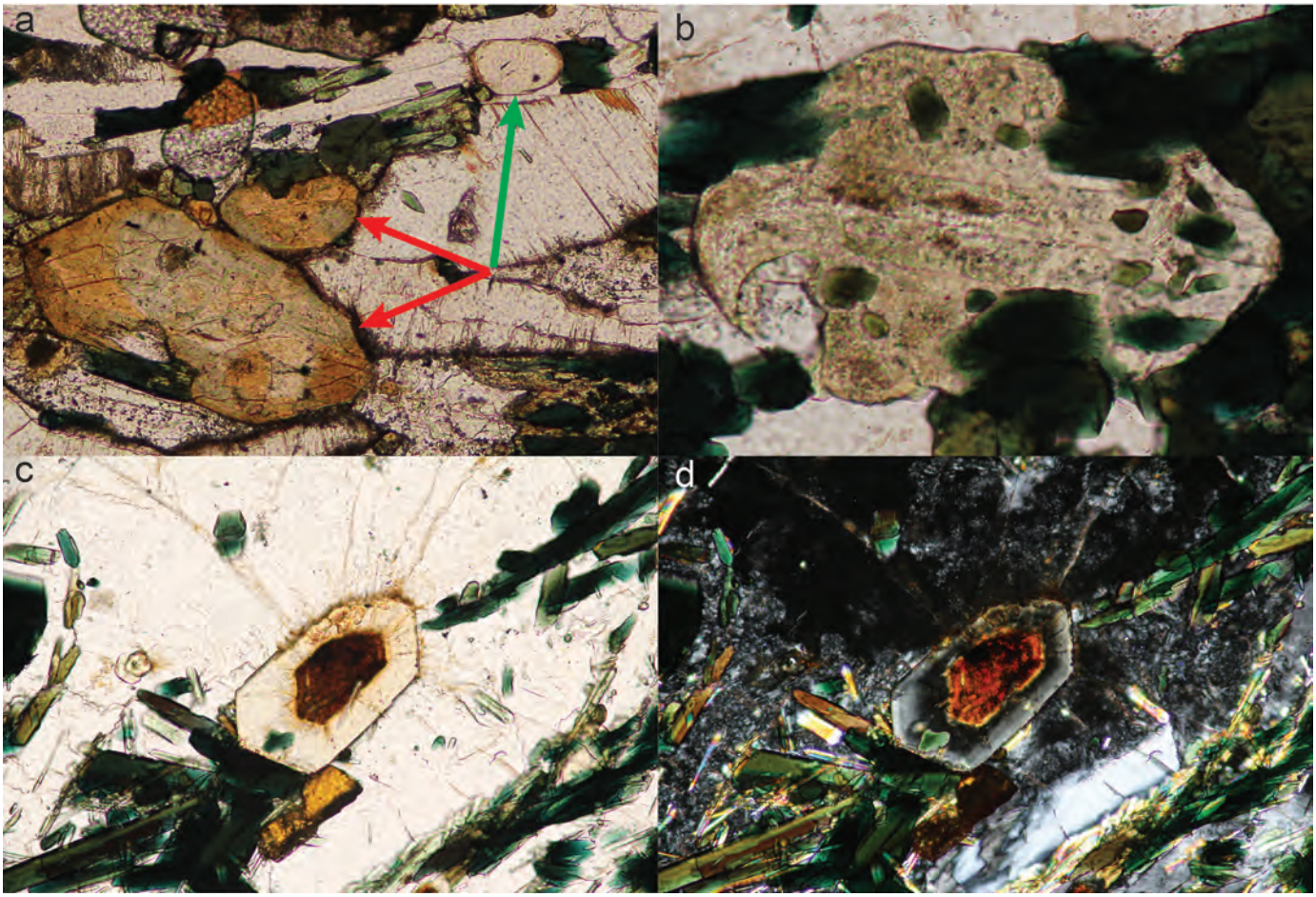

Fig. 4. Photomicrographs of steenstrupine-(Ce) in lujavrites from Kvanefjeld. **a)** Two altered crystals (red arrows) of which the larger is 0.5 mm. The smaller crystal (green arrow) is a metamict steenstrupine-(Ce). **b)** A 0.3 mm poikilitic steenstrupine-(Ce) crystal with inclusions of arfvedsonite. **c+d)** A 0.4 mm steenstrupine-(Ce) crystal with an altered core and anisotropic rim.

in many black lujavrites, which contain isolated spheroidal areas where the primary minerals have been replaced. The alteration is easily identified because the rock has patches of lighter green where the arfvedsonite is replaced by aegirine (Sørensen et al., 2003). In rocks of this type, feldspars and feldspathoids typically alter to natrolite or analcime. Secondary feldspar and sodalite may also be alteration products (Markl et al., 2001). Alteration in Ilímaussaq was produced under high pH conditions (Markl and Baumgartner, 2002) as indicated by ussingite in some zones and in late magmatic veins.

The alteration of HFSE minerals in Ilímaussaq is characterised by redistribution of the HFSE rather than by additions or removals. The most common Zr-alteration product after eudialyte is catapleiite, but locally zircon may form (Ussing, 1912; Karup-Møller et al., 2010; Borst et al., 2015). Borst et al. (2015) describe a third alteration, where late-stage fluids interacted with already formed catapleiite, which then altered to gittinsite. The REE liberated by decomposition of eudialyte typically form separate phases (e.g., nacareniobsite-(Ce) and fergusonite-(Y)) preferentially rich in either LREE or HREE (Karup-Møller et al., 2010). The same is the case for the alteration of steenstrupine-(Ce), where REE fractionate into monazite-(Ce) and xenotime-(Y), whereas thorite is the most common secondary U-Th mineral. What is characteristic for the alteration of both steenstrupine-(Ce) and eudialyte is that the REE are contained within the grain boundary of the original crystal; evidence of these elements leaving the system is lacking. The fractionation mechanism of REE into mainly LREE and Y+HREE phases was further explored by Friis (2015) who illustrated that all the known Y-minerals in Ilímaussaq are alteration products. The alteration of eudialyte releases Cl and the alteration of villiaumite-rich lujavrite releases F, elements that both can form complexes and could transport, the REE. Secondary Cl minerals are uncommon, supporting the hypothesis that Cl leaves the system during alteration. However, Migdisov and Williams-Jones (2014) showed that at high pH, fluorine and chlorine complexes with REE form solid phases. Borst et al. (2015) and Friis (2015) explain the low mobility of HFSE during alteration in Ilímaussaq as a result of the high pH (>9; Markl and Baumgartner, 2002). Therefore, fluorine and chlorine complexes are unlikely to have transported REE over large distances during alteration of the Ilímaussaq rocks.

Alteration of the Ilímaussaq rocks changes only the mineralogy, which influences the ore processing, but not

grade. This change in mineralogy poses challenges to planning a mining project. When exploring for critical materials in complex alkaline environments, detailed mineralogical studies are essential because alterations may not be easily derived from assays.

References cited

Andersen, T., and Friis, H., 2015. The transition from agpaitic to hyperagpaitic magmatic crystallization in the Ilímaussaq alkaline complex, South Greenland. Journal of Petrology, 56, 1343-1364.

Andersen, T., and Sørensen, H., 2005. Stability of naujakasite in hyperagpaitic melts, and the petrology of naujakasite lujavrite in the Ilímaussaq alkaline complex, South Greenland. Mineralogical Magazine, 69, 125-136.

Bailey, J.C., Gwozdz, R., Rose-Hansen, J., and Sørensen, H., 2001. Geochemical overview of the Ilímaussaq alkaline complex, South Greenland. In: Sørensen, H., (Ed.), The Ilímaussaq alkaline complex, South Greenland: status of mineralogical research with new results. Geology of Greenland Survey Bulletin, 190, pp. 35-53.

Bohse, H., Brooks, C.K., and Kunzendorf, H., 1971. Field observations on the kakortokites of the Ilímaussaq intrusion, South Greenland, including mapping and analyses by portable X-ray fluorescence equipment for zirconium and niobium. The Geological Survey of Greenland, 38, 43p.

Borst, A.M., Friis, H., Andersen, T., Nielsen, T.F.D., Waight, T.E., and Smit, M.A., 2015. Zirconosilicates in the kakortokites of the Ilímaussaq complex, South Greenland; implications for fluid evolution and HFSE mineralisation in agpaitic systems. Mineralogical Magazine. In Press

Danø, M., and Sørensen, H., 1959. An examination of some rare minerals from the nepheline syenites of south west Greenland. Meddelelser Om Grønland, 162, 1-35.

Ferguson, J., 1964. Geology of the Ilímaussaq alkaline intrusion, South Greenland - Description of map and structure. Meddelelser Om Grønland, 172, 1-82.

Friis, H., 2012. Zirconosilicates in the Kvanefjeld multi-element deposit, South Greenland. Unpublished report, University of British Columbia, Vancouver, Canada, 16p.

Friis, H., 2015. First occurrence of moskvinite-(Y) in the Ilímaussaq alkaline complex, South Greenland - implications for REE mobility. Mineralogical Magazine. In Press.

GME, 2015. Kvanefjeld feasibility study. http://www.ggg.gl/docs/ASX-announcements/Kvanefjeld-Feasibility.pdf. Accessed August 13, 2015.

Grey, I.E., Macrae, C.M., Mumme, W.G., and Pring, A., 2010. Townendite, $Na_8ZrSi_6O_{18}$, a new uranium-bearing lovozerite group mineral from the Ilímaussaq alkaline complex, Southern Greenland. American Mineralogist, 95, 646-650.

Karup-Møller, S., Rose-Hansen, J., and Sørensen, H., 2010. Eudialyte decomposition minerals with new hitherto undescribed phases from the Ilímaussaq complex, South Greenland. Bulletin of the Geological Society of Denmark, 58, 75-88.

Khomyakov, A.P., 1995. Mineralogy of Hyperagpaitic Alkaline Rocks. Oxford University Press, Oxford, 223p.

Khomyakov, A.P., and Sørensen, H., 2001. Zoning in steenstrupine-(Ce) from the Ilímaussaq alkaline complex, South Greenland: a review and discussion. In: Sørensen, H., (Ed.), The Ilímaussaq alkaline complex, South Greenland: status of mineralogical research with new results. Geology of Greenland Survey Bulletin, 190, pp. 109-118.

Krumrei, T.V., Villa, I.M., Marks, M.A.W., and Markl, G., 2006. A $^{40}Ar/^{39}Ar$ and U/Pb isotopic study of the Ilímaussaq complex, South Greenland: Implications for the ^{40}K decay constant and for the duration of magmatic activity in a peralkaline complex. Chemical Geology, 227, 258-273.

Lorenzen, J., 1881. Investigation of some minerals in sodalite-syenite from the Julianehaab district. Meddelelser Om Grønland, 2, 45-79. In Danish.

Makovicky, E., and Karup-Møller, S., 1981. Crystalline steenstrupine from Tunugdliarfik in the Ilímaussaq alkaline intrusion, South Greenland. Neues Jahrbuch für Mineralogie-Abhandlungen, 140, 300-330.

Makovicky, M., Makovicky, E., Nielsen, B.L., Karup-Møller, S., and Sørensen, E., 1980. Mineralogical, radiographic and uranium leaching studies on the uranium ore from Kvanefjeld, Ilímaussaq, South Greenland. RISØ, Roskilde, 186p.

Malczewski, D., Frackowiak, J.E., and Galuskin, E.V., 2005. ^{57}Fe Mössbauer spectroscopy and x-ray diffraction study of some complex metamict minerals. Hyperfine Interactions, 166, 529-536.

Markl, G., and Baumgartner, L., 2002. pH changes in peralkaline late-magmatic fluids. Contributions to Mineralogy and Petrology, 144, 331-346.

Markl, G., Marks, M., Schwinn, G., and Sommer, H., 2001. Phase equilibrium constraints on intensive crystallization parameters of the Ilímaussaq complex, South Greenland. Journal of Petrology, 42, 2231-2258.

Marks, M.A.W., and Markl, G., 2015. The Ilímaussaq alkaline complex, South Greenland. In: Charlier, B., Namur, O., Latypov, R., and Tegner, C., (Eds.), Layered Intrusions. Springer Verlag, Dordrecht, pp. 649-691.

Migdisov, A.A., and Williams-Jones, A.E., 2014. Hydrothermal transport and deposition of the rare earth elements by fluorine-bearing aqueous liquids. Mineralium Deposita, 49, 987-997.

Moore, P.B., and Shen, J., 1983. Crystal structure of steenstrupine: A rod structure of unusual complexity. Tschermaks Mineralogische und Petrographische Mitteilungen, 31, 47-67.

Pekov, I.V., and Ekimenkova, I.A., 2001. Two new rare earth-rich mineral associations in the Ilímaussaq alkaline complex, South Greenland. In: Sørensen, H., (Ed.), The Ilímaussaq alkaline complex, South Greenland: status of mineralogical research with new results. Geology of Greenland Survey Bulletin, 190, pp. 143-144.

Pfaff, K., Krumrei, T., Marks, M., Wenzel, T., Rudolf, T., and Markl, G., 2008. Chemical and physical evolution of the 'lower layered sequence' from the nepheline syenitic Ilímaussaq intrusion, South Greenland: Implications for the origin of magmatic layering in peralkaline felsic liquids. Lithos, 106, 280-296.

Stromeyer, F., 1819. Summary of meeting 16 December 1819, Göttingische Gelehrte Anzeigen, 3, 1993-2000. In German.

Sørensen, H., 1966. Tracing rare metals in South Greenland. I. Exploration history. Tidsskriftet Grønland, 14, 113-126. In Danish.

Sørensen, H., 1968. Tracing rare metals in South Greenland. VII. Zirconium - a metal for the future. Tidsskriftet Grønland, 16, 353-365. In Danish.

Sørensen, H., 1997. The agpaitic rocks - an overview. Mineralogical Magazine, 61, 485-498.

Sørensen, H., 2001. Brief introduction to the geology of the Ilímaussaq alkaline complex, South Greenland, and its exploration history. In: Sørensen, H., (Ed.), The Ilímaussaq alkaline complex, South Greenland: status of mineralogical research with new results. Geology of Greenland Survey Bulletin, 190, pp. 7-23.

Sørensen, H., Bailey, J.C., Kogarko, L.N., Rose-Hansen, J., and Karup-Møller, S., 2003. Spheroidal structures in arfvedsonite lujavrite, Ilímaussaq alkaline complex, South Greenland - an example of macro-scale liquid immiscibility. Lithos, 70, 1-20.

Tanbreez, 2015. Resource estimates. http://tanbreez.com/en/project-overview/resource-calculation/?page=1 Accessed August 20, 2015.

Upton, B.G.J., 2013. Tectono-magmatic evolution of the younger Gardar southern rift, South Greenland. Geological Survey of Denmark and Greenland Bulletin, 29, 1-124.

Ussing, N.V., 1912. Geology of the country around Julianehaab,

Greenland. Meddelelser Om Grønland, 38, 1-426.
Waight, T., Baker, J., and Willigers, B., 2002. Rb isotope dilution analyses by MC-ICPMS using Zr to correct for mass fractionation: towards improved Rb-Sr geochronology? Chemical Geology, 186, 99-116.

Fluoride-silicate melt immiscibility and the formation of the pegmatite-hosted Strange Lake REE deposit, Quebec-Labrador

A.E. Williams-Jones[1, a] and O. Vasyukova[1]

[1] Department of Earth and Planetary Sciences, McGill University, Montreal, QC, Canada
[a] corresponding author: anthony.williams-jones@mcgill.ca

Recommended citation: Williams-Jones, A.E. and Vasyukova, O., 2015. Fluoride-silicate melt immiscibility and the formation of the pegmatite-hosted Strange Lake REE deposit, Quebec-Labrador. In: Simandl, G.J. and Neetz, M., (Eds.), Symposium on Strategic and Critical Materials Proceedings, November 13-14, 2015, Victoria, British Columbia, British Columbia Ministry of Energy and Mines, British Columbia Geological Survey Paper 2015-3, pp. 91-96.

Extended Abstract

Although fluoride-silicate liquid immiscibility has been demonstrated experimentally (Veksler et al., 2005, 2012), its occurrence in nature has only been reported twice, once from a mantle xenolith (Klemme, 2004; Peretyazhko et al., 2007). Herein we provide evidence that this process was essential in concentrating rare earth elements (REE) to potentially economic levels at Strange Lake, Québec-Labrador.

The Strange Lake pluton (1240 ±2 Ma; Miller et al., 1997) is a peralkaline granite intrusion, some six kilometres in diameter, which was emplaced along the contact between an Elsonian (1.5-1.4 Ga) quartz monzonite massif and Hudsonian (2.0-1.8 Ga) banded gneisses, and is surrounded by a fluorite-cemented ring breccia (Fig. 1). Regionally, it belongs to the Nain Plutonic suite. Locally, the pluton contains potentially exploitable concentrations of the REE and other high field strength elements (HFSE). An ore-body referred to as the B-Zone has been defined recently by Quest Rare Minerals Ltd., with an indicated reserve of 278 Mt of ore, grading 0.94 wt.% REE_2O_3 (38% heavy rare earth oxides), 1.92 wt.% ZrO_2 and 0.18 wt.% Nb_2O_5. This includes a higher grade zone containing 20 million tons of ore grading 1.44 wt.% REE_2O_3 (50% heavy rare earth oxides), 2.59 wt.% ZrO_2, and 0.18 wt.% Nb_2O_5 (Gowans et al., 2014). Another potential orebody, referred to as the Main Ore Zone, with an indicated reserve of 30 Mt of ore grading 1.96 wt.% REE_2O_3, 3.25 wt.% ZrO_2, and 0.56 wt.% Nb_2O_5, was delineated in the early 1980s by the Iron Ore Company of Canada.

Igneous activity commenced with the emplacement of a hypersolvus granite distinguished by a single alkali feldspar that was later transformed to perthite. This was followed by the emplacement of transsolvus and subsolvus granite types (Salvi and Williams-Jones, 1990; Nassif, 1993; Boily and Williams-Jones, 1994). The subsolvus granite, which is strongly altered, is characterised by the occurrence of two alkali feldspars and the transsolvus granite by perthite and separate albite and orthoclase. The other major rock forming minerals are arfvedsonite and quartz. Arfvedsonite occurs interstitially to the other two minerals in the hypersolvus granite and was clearly the last major silicate phase to crystallize. By contrast, in the subsolvus granite, arfvedsonite occurs as phenocrysts and crystallized early. Alteration is evident mainly in the replacement of arfvedsonite by aegirine and also by hematisation of the latter mineral. The last rocks to be intruded were pegmatites. They occur near the roof of the intrusion, mainly in highly altered subsolvus granite, although they are also observed in the other granite types. The pegmatites form gently dipping sheets from a few tens of centimetres to 20 metres in thickness and much less common sub-vertical dikes. Typically the pegmatites are zoned in respect to their major mineralogy. The outer parts of pegmatites are composed mainly of alkali feldspars and arfvedsonite (generally altered to aegirine and also hematite) and the cores of fluorite and quartz.The rare metal mineralisation, including the Main- and B-Zone orebodies, is developed in and around pegmatite sheets in the altered subsolvus granite. The REE are concentrated in the pegmatite cores, almost exclusively as secondary minerals, whereas the high field strength elements (HFSE), notably Zr, are concentrated in the outer parts of the pegmatites (Fig. 2); Zr is mainly in secondary minerals, notably the calcium zirconosilicate, gittinsite, which is typically accompanied by hematite and quartz. Elevated concentrations of REE (mainly the light REE) and HFSE are also observed in the immediately adjacent granite. The ore mineralogy is complex and includes minerals, such as allanite-(Ce), armstrongite, bastnäsite-(Ce), elpidite, fluocerite-(Ce), gadolinite-(Y), gagarinite-(Y), gittinsite, kainosite-(Y), monazite-(Ce), narsarsukite, pyrochlore, titanite and zircon.

Previous studies of the Strange Lake pluton have attributed the rare metal mineralization to a combination of magmatic differentiation and hydrothermal remobilization (Salvi and Williams-Jones, 1990; Boily and Williams-Jones, 1994; Salvi and Williams-Jones, 1996; Gysi and Williams-Jones, 2013). According to this interpretation, the hypersolvus granite is the product of extreme fractional crystallization of a parent syenitic magma. This caused an unusual enrichment in fluorine and

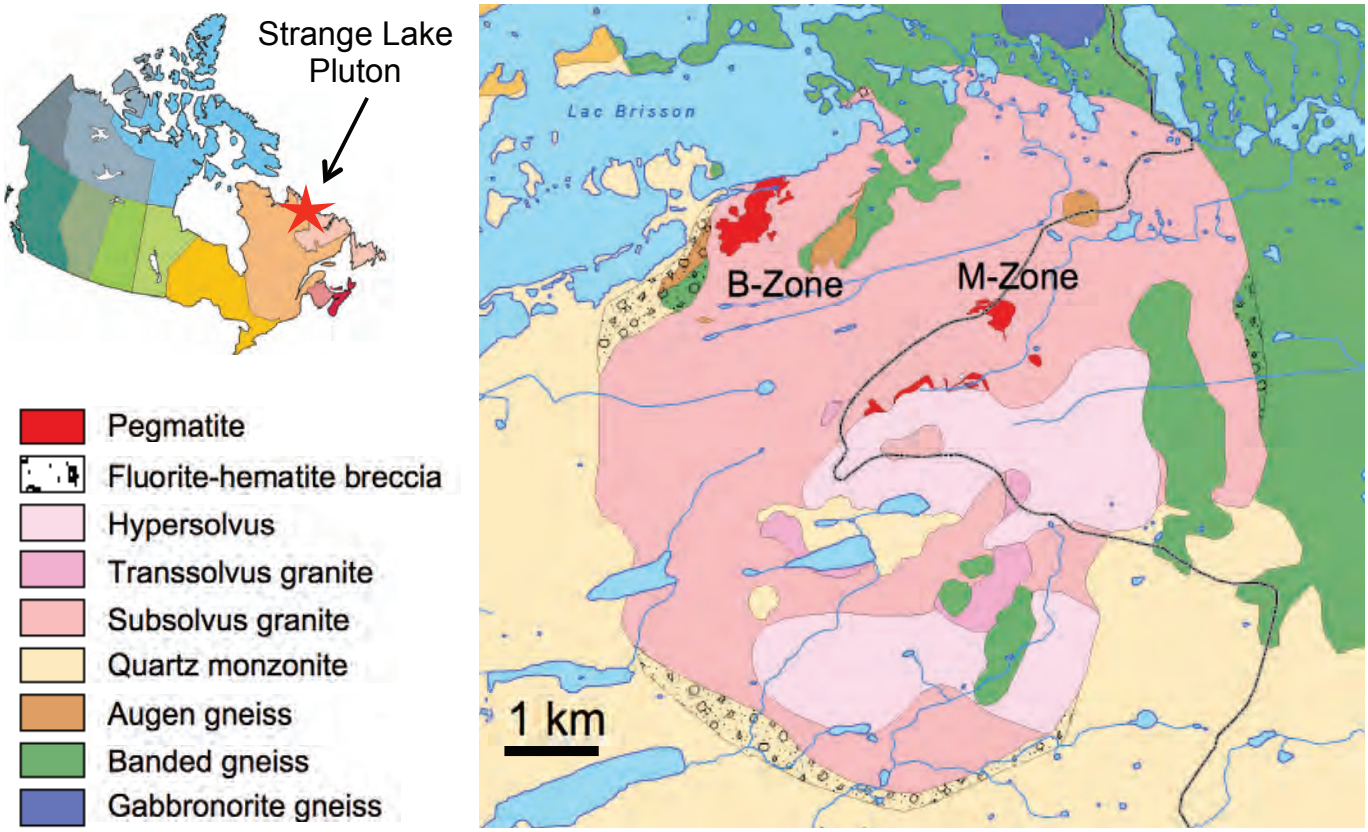

Fig. 1. Geological map of the Strange Lake Pluton showing the distribution of the principal rock types and the locations of the two pegmatite-rich zones with potential for economic REE exploitation.

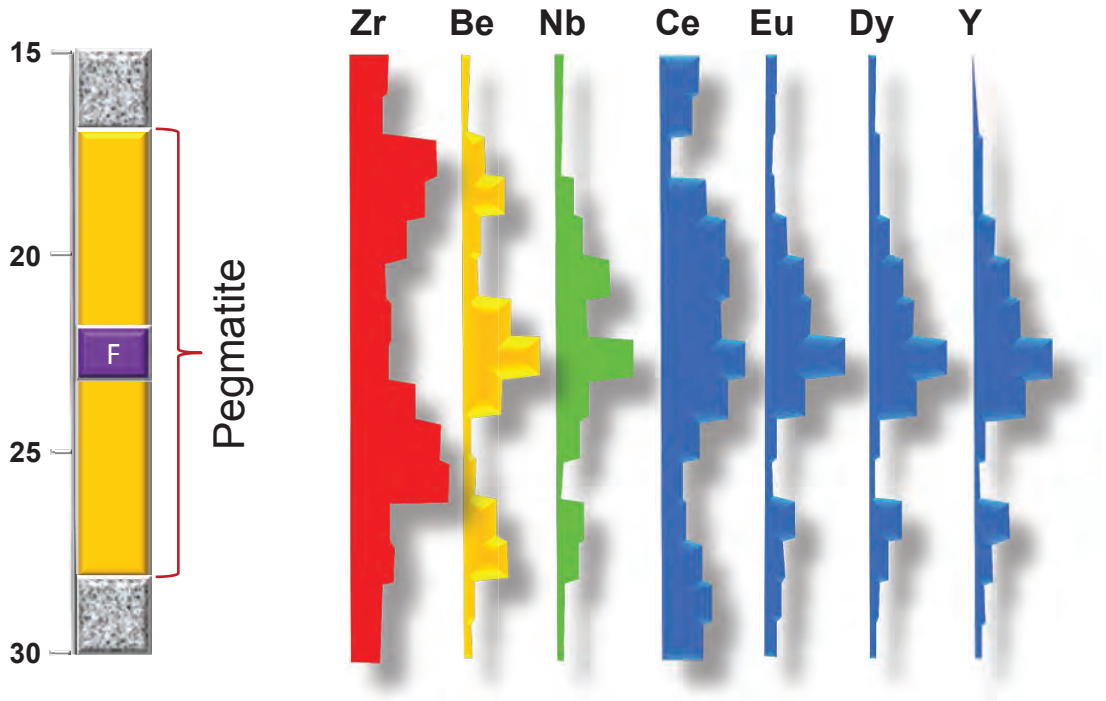

Fig. 2. A schematic drillhole through subsolvus granite and pegmatite illustrating the concentration of fluorite in the pegmatite core and the distribution of selected elements. Note that Zr is concentrated at the pegmatite margins and the heavy REE in the core. Cerium concentrations are more evenly distributed and are elevated in the adjacent granite.

other incompatible elements, including the REE and HFSE; dissolution of the REE and HFSE was facilitated by fluoride complexation. Further fractional crystallization, mainly of alkali-feldspar, lead to the formation of the transsolvus and subsolvus granites and ultimately the pegmatites. As a result there was hyper-enrichment of the REE and HFSE, particularly in the pegmatites. During this fractionation, the H_2O fugacity increased progressively, as did the concentrations of the other incompatible components. As a result, the size of the alkali feldspar immiscibility field increased, and crystallization of a single alkali feldspar was succeeded by crystallization of K-feldspar and albite to form the subsolvus granite. This increase in H_2O fugacity culminated in the exsolution of a hydrothermal phase, which auto-metasomatized the subsolvus granite and pegmatites, altering the primary mineralogy. Rare metals, including the REE, were mobilized locally by these fluids to form a variety of secondary minerals. In the apical parts of the pluton, further alteration ensued as a result of the infiltration of formational waters heated by the intrusion. Primary and secondary sodic minerals, including HFSE and REE phases, were replaced by low temperature secondary calcic minerals, and iron-bearing phases, notably arfvedsonite, were oxidised to hematite. This further concentrated the REE and HFSE. The recent discovery of melt inclusions in the granites has allowed us to build on the above model by identifying a potentially important new and powerful mechanism for concentrating the REE and HFSE in granitic rocks, namely silicate-fluoride liquid immiscibility (Vasyukova and Williams-Jones, 2014).

Melt inclusions represented by micron-scale spherical accumulations of minerals (post-entrapment crystallization) are common in the early granites (hypersolvus and transolvus, with respect to alkali feldspar); the later granites (subsolvus) and pegmatites have been strongly altered and evidence of inclusions destroyed (Fig. 3). The melt inclusions were overlooked in earlier studies because of their small size and post-entrapment crystallization. After being heated to 900 or 950°C, a significant proportion of the melt inclusions quench to immiscible fluoride and silicate glasses (Fig. 4). The relative proportions of fluoride and silicate glass, however, vary enormously. Some of the inclusions are composed only of silicate glass, others only of fluoride glass and still others of variable proportions of silicate and fluoride glass, suggesting heterogeneous entrapment of silicate and fluoride melt. Where the proportions of the two glasses are appreciable, the silicate glass forms an annulus in the outer part of the inclusion and the fluoride glass forms the core. The silicate glass contains several weight percent Zr and the fluoride glass >10 wt.% REE. In some cases, there are two fluoride glasses, an outer glass with predominantly Ca containing 10-15 wt.% REE, and an inner glass containing up to 50 wt.% REE (Fig. 4).

In addition to the melt inclusions, there are rare examples of larger fluorine- and REE-rich inclusions in the hypersolvus granite, including one ~5 cm in diameter that contains ~25 wt.% REE (Fig. 5). This latter inclusion consists of a rim composed mainly of chevkinite-(Ce) and zircon in a fluorite matrix, an intermediate zone of gagarinite-(Y), bastnäsite-(Ce) and fluorite and a core of fluorbritholite-(Ce) and fluorite. Alkali feldspar, and arfvedsonite are concentrated in the outer parts of the globule.

We propose a model (Fig. 6) in which extreme fractional crystallization caused the early hypersolvus magma to saturate with and exsolve an immiscible Ca-fluoride melt (Vasyukova and Williams-Jones, 2014). Consistent with recent experimental data (Veksler et al., 2005, 2012), the REE partitioned preferentially into this melt, leaving behind a silicate melt in which HFSE (e.g., Zr and Nb) were further enriched. With progressive fractional crystallization and evolution of the silicate melt, the proportion of immiscible fluoride melt grew, reaching 6 wt.% in the subsolvus granite magma and 12 wt.% in the pegmatite magma. Although the fluoride magma was probably denser than the silicate magma, the low viscosity of the latter and strong convection ensured that it remained in the residues of silicate magma that formed the pegmatites in the apical parts of the intrusion. Crystallization of the pegmatites proceeded with alkali feldspar, arfvedsonite, quartz and zirconosilicate minerals in the outer parts of the sheets pushing the fluoride melt and volatiles into the core, where finally the fluoride melt crystallized fluorite and a variety of REE minerals. The quartz likely crystallized from the volatile phase. The timing of exsolution of the second, REE-rich fluoride melt phase is unclear but its exsolution likely occurred after the bulk of the fluoride melt in the pegmatites. A very small proportion of the fluoride melt remained trapped in the earlier granites documented by the 5 cm diameter fluoride melt inclusion. Based on observations of this inclusion, primary chevkinite-(Ce) crystallized in the fluoride melt along its boundary with the silicate melt taking Ti from the latter and the REE from the fluoride melt; the accompanying zircon took its components from the silicate melt. Within the body of the fluoride melt, fluorbritholite-(Ce) and gagarinite-(Y) were the main REE phases to crystallize. During or after crystallization of fluoride melt, the crystallized or partly crystallized pegmatite core 'stewed in its own juices' altering the primary magmatic mineralogy and releasing REE, particularly light REE into the immediately adjacent granite (Gysi and Williams-Jones, 2013).

In summary, although fractional crystallization and hydrothermal mobilization are clearly important processes in the formation of economic and potentially economic REE deposits from peralkaline magmas, the evidence presented in this contribution shows clearly that fluoride-silicate liquid immiscibility is an additional process that needs to be considered when evaluating the genesis of REE deposits in alkaline silicate igneous rocks. Indeed, it is possible that, as is the case for sulphide-silicate liquid immiscibility in concentrating Ni, Cu and the PGE in mafic and ultramafic igneous rocks, fluoride-silicate liquid immiscibility may be the dominant process in forming REE deposits in some alkaline silicate rocks and not just in granites but also in silica-undersaturated rocks such as nepheline syenites.

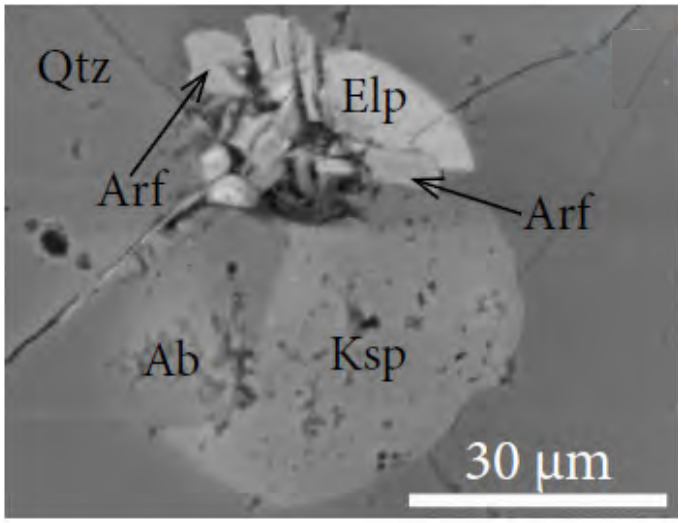

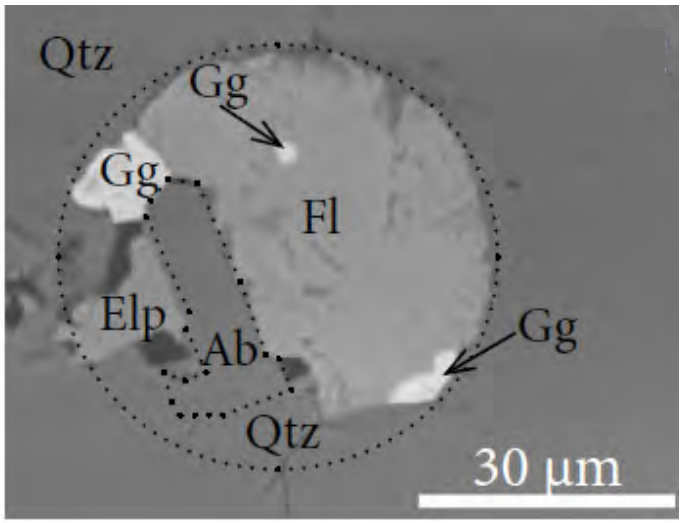

Ab – abite
Arf – arfvedsonite
Gg – gagarinite-(Y)
Fl –fluorite
Ksp – K-feldspar
Qtz – quartz
Elp – elpidite

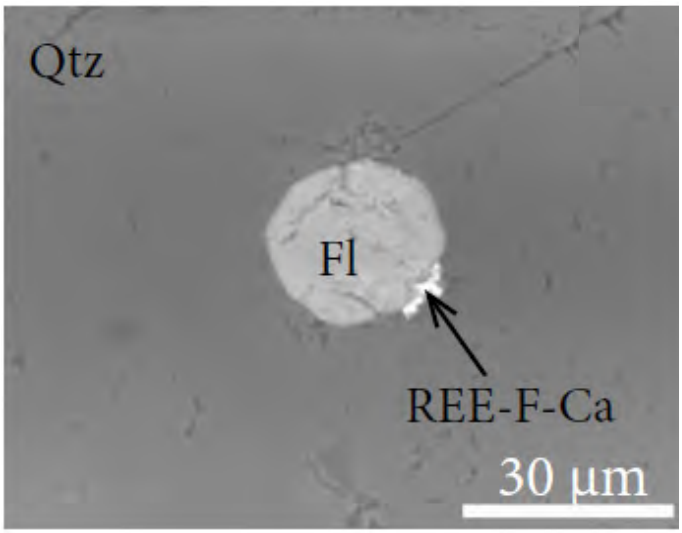

Fig. 3. Backscattered electron images of near-spherical crystallized melt inclusions before heating. The inclusions are hosted in quartz in hypersolvus granite.

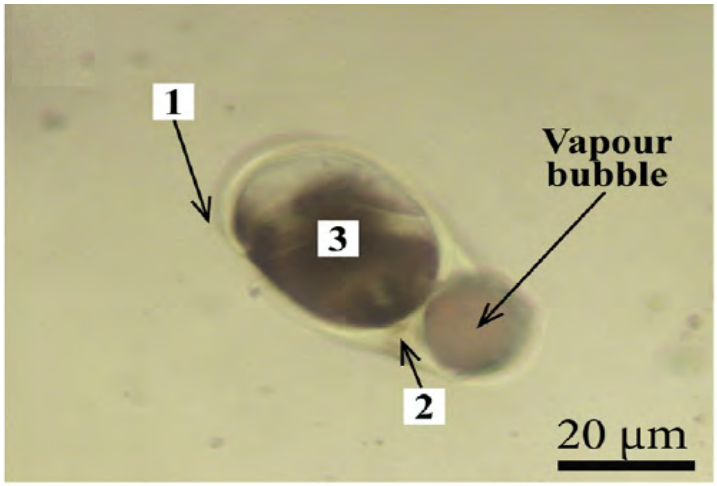

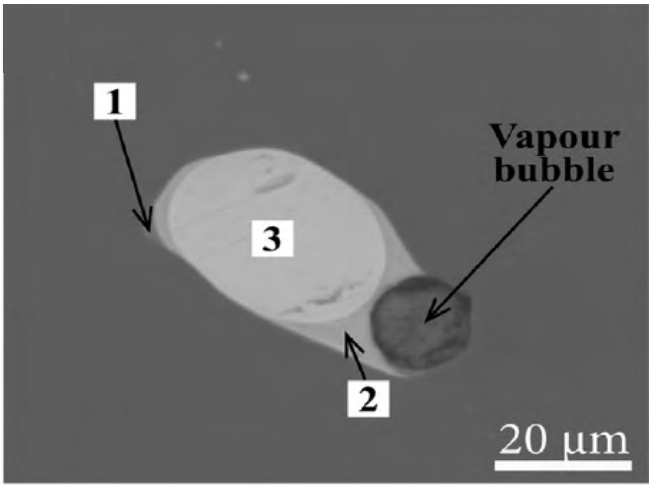

Fig. 4. Transmitted light (left) and backscattered electron (right) images of a melt inclusion with 1) silicate glass containing ~3 wt.% Zr, 2) calcium fluoride glass containing ~10 wt.% REE, 3) REE fluoride glass containing 47 wt.% REE, and a vapour bubble after being heated to 900°C and quenched.

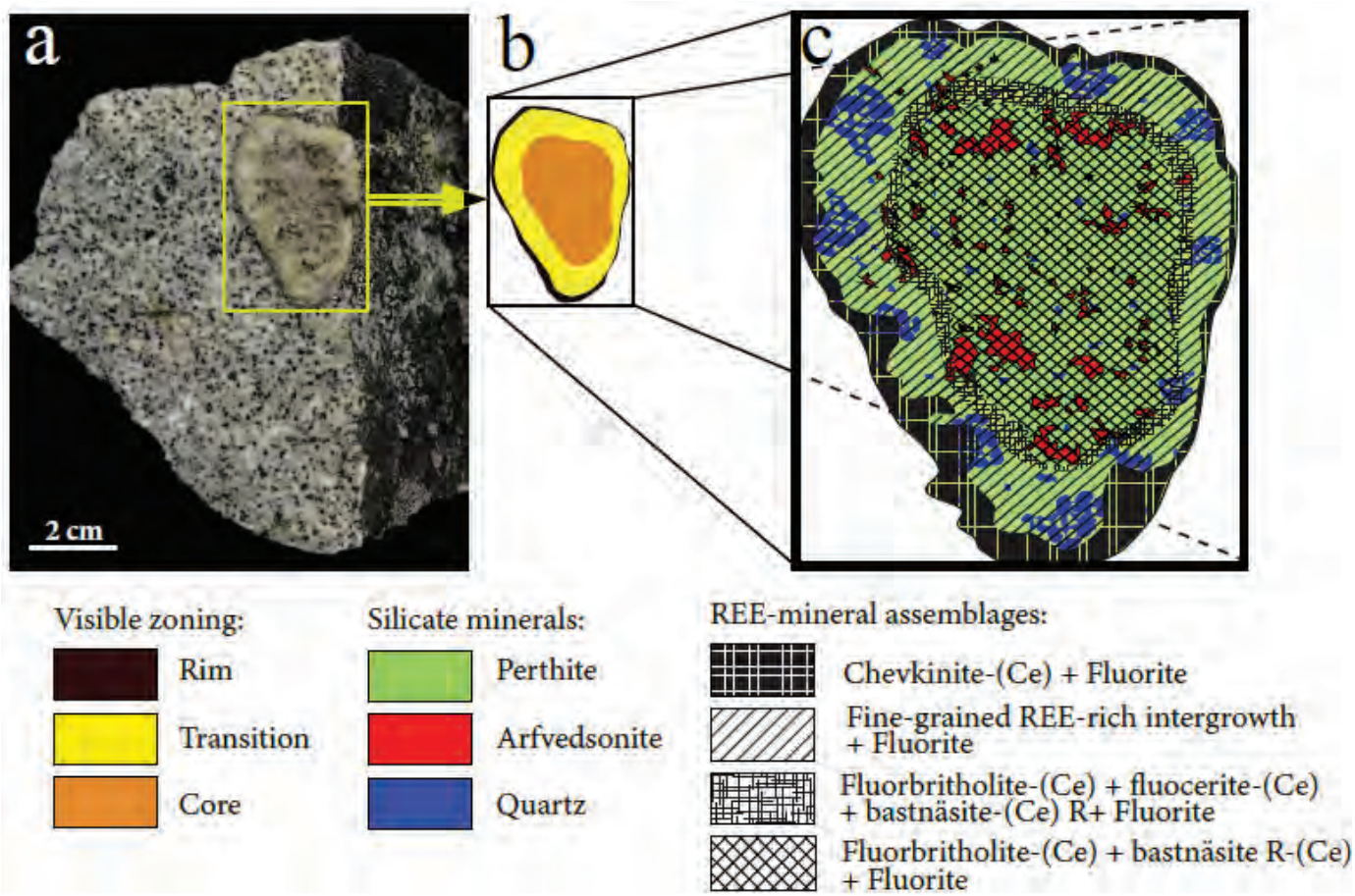

Fig. 5. An immiscible fluoride inclusion in hypersolvus granite. **a)** Photograph showing the inclusion in the host granite. **b)** Sketch identifying macroscopic zoning in the inclusion. **c)** Sketch showing the distribution of silicate minerals and REE mineral assemblages in the inclusion.

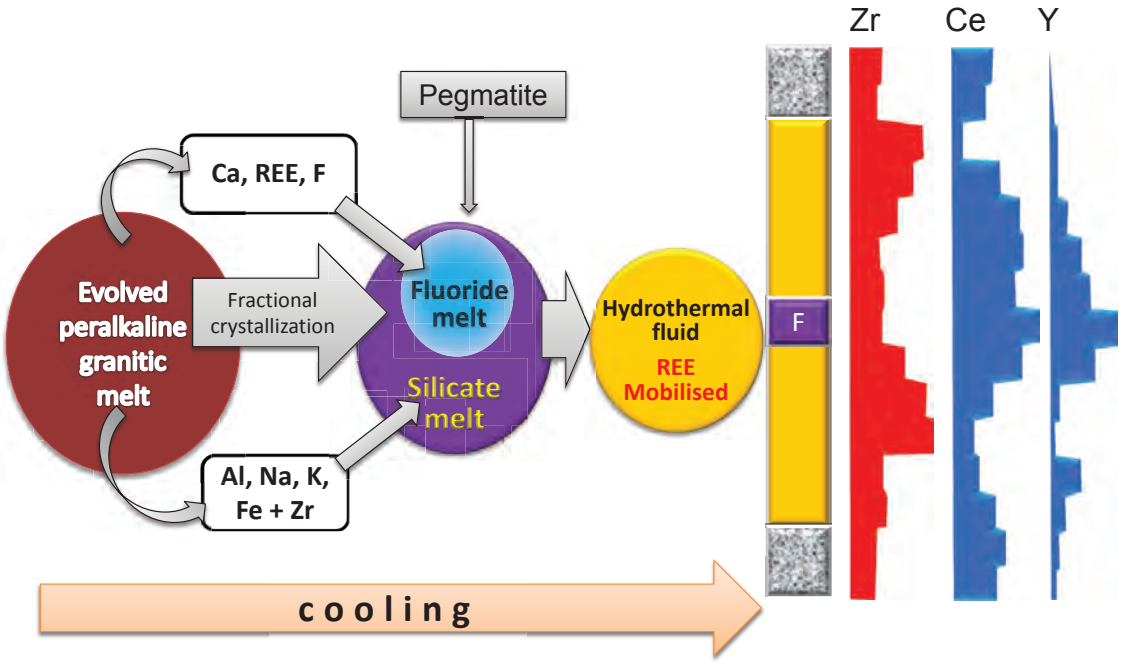

Fig. 6. A schematic model for the evolution of the Strange Lake Pluton and the concentration of the REE.

References cited

Boily, M., and Williams-Jones, A.E., 1994. The role of magmatic and hydrothermal processes in the chemical evolution of the Strange Lake plutonic complex (Quebec–Labrador). Contributions to Mineralogy and Petrology 118, 33–47.

Gowans, R.M, Lewis, W.J, Shoemaker, S., Jr., Spooner, J. and Zalnieriunas, R.V., 2014. NI 43-101 technical report on the preliminary economic assessment (PEA) for the Strange Lake property Quebec, Canada, http://www.questrareminerals.com/pdfs/Strange%20Lake%20PEA%20NI%2043-101%20Report%20FINAL%209%20April%202014%20REV%20E.pdf >accessed September 16, 2015.

Gysi, A., and Williams-Jones, A.E., 2013. Hydrothermal mobilization of pegmatite-hosted REE and Zr at Strange Lake, Canada: A reaction path model. Geochimica et Cosmochimica Acta, 122, 324-352.

Klemme, S., 2004. Evidence for fluoride melts in earth's mantle formed by liquid immiscibility. Geology, 32, 441-444.

Miller, R.R., Heaman, L.M., and Birkett, T.C., 1997. U–Pb zircon age of the Strange Lake peralkaline complex: Implications for Mesoproterozoic peralkaline magmatism in north-central Labrador. Precambrian Research, 81, 67–92.

Nassif, J.G., 1993. The Strange Lake peralkaline complex, Quebec-Labrador: The hypersolvus-subsolvus granite transition and feldspar mineralogy. M.Sc. thesis, McGill University, 104 p.

Peretyazhko, I.S., Zagorsky, V.Y., Tsareva, E.A. and Sapozhinikov, A.N., 2007. Immiscibility of calcium fluoride and aluminosilicate melts in ongonites from the Ary-Bulak intrusion, Eastern Transbaikal region. Doklady Earth Sciences, 413, 315-320.

Salvi, S., and Williams-Jones, A.E., 1990. The role of hydrothermal processes in the granite- hosted Zr, Y, REE deposit at Strange Lake, Quebec/Labrador: Evidence from fluid inclusions. Geochimica et Cosmochimica Acta, 54, 2403–2418.

Salvi, S., and Williams-Jones, A.E., 1996. The role of hydrothermal processes in concentrating HFSE in the Strange Lake peralkaline complex, northeastern Canada. Geochimica et Cosmochimica Acta, 60, 1917-1932.

Vasyukova, O., and Williams-Jones, A.E., 2014. Fluoride–silicate melt immiscibility and its role in REE ore formation: Evidence from the Strange Lake rare metal deposit, Quebec-Labrador, Canada. Geochimica et Cosmochimica Acta, 139, 110-130.

Veksler, I.V., Dorfman, A.M., Kamenetsky, M., Dulski, P. and Dingwell., D.B., 2005. Partitioning of lanthinides and yttrium between immiscible silicate and fluoride melts, fluorite and cryolite and the origin of the lanthanide tetrad effect in igneous rocks. Geochimica et Cosmochimica Acta, 60, 2847-2860.

Veksler, I.V., Dorfman, A.M., Dulski, P., Kamenetsky, V.S., Danyushevsky, L.V., Jeffries, T., and Dingwell., D.B., 2012. Partitioning of elements between silicate melt and immiscible fluoride, chloride, carbonate, phosphate and sulfate melts, with implications to the origin of natrocarbonatite. Geochimica et Cosmochimica Acta, 79, 20-40.

Geology, mineralogy, and metallurgical processing of the Norra Kärr heavy REE deposit, Sweden

Mark Saxon[1, a], Magnus Leijd[1], Kurt Forrester[2], and Johan Berg[1]

[1] Tasman Metals Ltd., Vancouver, BC, Canada, V6E 3V7
[2] GBM Minerals Engineering Consultants Limited, Twickenham, United Kingdom, TW1 3QS
[a] corresponding author: msaxon@tasmanmetals.com

Recommended citation: Saxon, M., Leijd, M., Forrester, K., and Berg, J., 2015. Geology, mineralogy, and metallurgical processing of the Norra Kärr heavy REE deposit, Sweden. In: Simandl, G.J. and Neetz, M., (Eds.), Symposium on Strategic and Critical Materials Proceedings, November 13-14, 2015, Victoria, British Columbia. British Columbia Ministry of Energy and Mines, British Columbia Geological Survey Paper 2015-3, pp. 97-107.

1. Introduction and project location

The Norra Kärr peralkaline complex is about 300 km southwest of Stockholm in southern Sweden (Fig. 1). As the only heavy REE deposit in the European Union, Norra Kärr is significant for the security of future REE, zirconium (Zr) and hafnium (Hf) supply (European Commission's European Rare Earths Competency Network; ERECON, 2015). The project is well serviced by power and other infrastructure that will allow year-round mining and processing. A four-lane highway links Scandinavia to mainland Europe and passes with 1km of Norra Kärr. The skill-rich cities of Linköping and Jönköping, lie within daily commuting distances from Norra Kärr. A rail line that passes within 30 km of the site may be used to transport feed stocks and products. If Norra Kärr is developed, European REE users will no longer require substantial material stockpiles to deal with market uncertainties.

2. Project history

The Norra Kärr peralkaline complex was discovered in the early 20th century by Dr. K.E. Norman of the Geological Survey of Sweden during bedrock mapping (Thulin, 1996), and described in detail by Törnebohm (1906), who named the intrusion after a local farm, and Adamson (1944).

Limited exploration of Norra Kärr for Zr and nepheline was conducted by the Swedish mining company Boliden AB in the 1940s and again during the 1970s. At the time, little or no value was placed on REEs and few assays were completed.

Following the global rise in REE prices and the need for secure long-term non-Chinese REE supply, Tasman Metals Ltd. claimed the project in 2009. Surface rock chip sampling and mapping showed REE and Zr-enriched mineralization, and drilling began in December 2009. Norra Kärr is now the one of the largest heavy (REE) projects in the world, with a particular enrichment of the high-value elements, dysprosium (Dy), terbium (Tb), and yttrium (Y). More than 20,000 m of drilling has been completed, with consistent resource drilling to 200 m vertical depth. Tasman has been granted a 25 year renewable Mining Lease for Norra Kärr by the Swedish Mining Inspectorate.

Mining consultants RungePincockMinarco Limited prepared a Preliminary Economic Assessment (PEA) for the Norra Kärr deposit in 2013. In January 2015, a Pre-Feasibility Study (PFS), completed by GBM Minerals Engineering Consultants Limited updated a Mineral Resource.

3. Geology

The Norra Kärr peralkaline complex is a small, Proterozoic complex of agpaitic nepheline syenite rocks. The term 'agpaitic' is restricted to peralkaline nepheline syenites containing complex silicates of zirconium, titanium, REEs, and fluorine and other volatiles, and lack simple Zr minerals like zircon and baddeleyite. Zirconium (up to 2 wt.% ZrO_2) is mainly hosted in rock-forming complex Na-Ca-Zr silicate minerals such as members of the catapleiite, eudialyte, rosenbuschite, and wöhlerite groups (Sørensen, 1997).

The Norra Kärr complex was emplaced along a north-south trending corridor of ductile shear zones in the westernmost part of the Paleoproterozoic Trans Scandinavian Igneous belt (TIB). The TIB comprises an elongate array of mainly felsic plutonic and volcanic rocks extending for about 1400 km along the Scandinavian Peninsula from southeastern Sweden to northwestern Norway. Norra Kärr intruded rocks of the TIB, specifically the Växjö Granite of the Småland-Värmland belt, with U-Pb zircon crystallization ages of 1.81 to 1.76 Ga (Andersson and Wikström, 2004). Recently, Sjöqvist et al. (2014) reported a U-Pb zircon age of 1781 ± 8 Ma from unaltered Växjö Granite country rock adjacent to the Norra Kärr intrusion. Zircon from fenitized Växjö Granite that formed during magmatism-related alkaline alteration yielded a U-Pb age of 1489 ± 8 Ma, which is considered to record when the Norra Kärr intrusion was emplaced (Sjöqvist et al., 2014). New Ar-Ar step heating gave plateau ages on sodic amphibole (1.1 Ga) from Norra Kärr and muscovite and biotite from the country rocks (0.94 Ga) which correspond to ages derived for Sveconorwegian shear zones in the area (Sjöqvist et al., 2014).

At surface, the intrusion is roughly elliptical, with a north-south long axis of about 1300 m and an east-west short axis of about 500 m (Fig. 1). Structural observations from drill

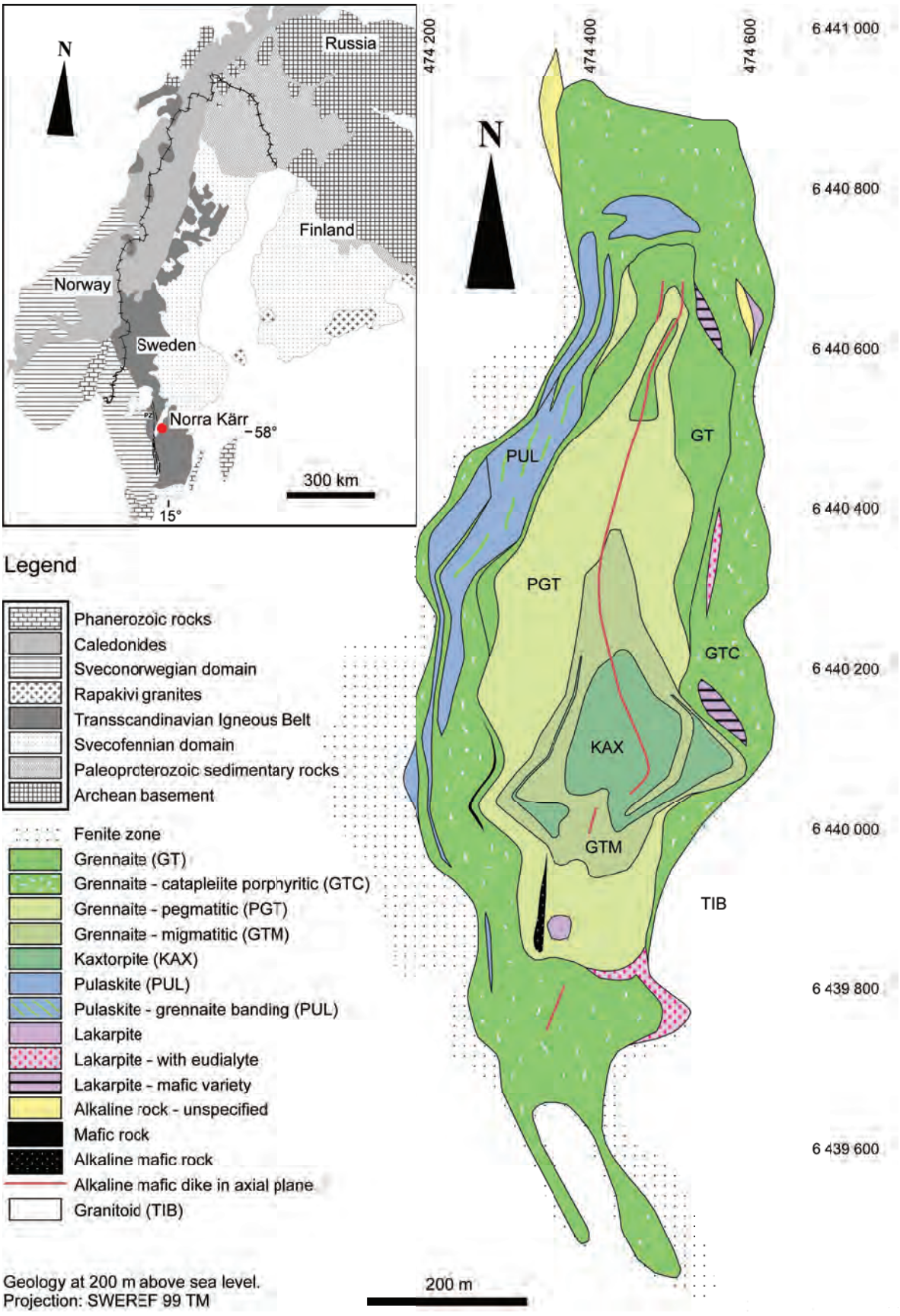

Fig. 1. Geology and location of the Norra Kärr peralkaline complex, Sweden.

core suggest that the intrusive defines a west-dipping (45-60°) doubly plunging synform (Fig. 2). Based on gross magmatic layering and orientation of early deformation fabrics, the body may have been emplaced as a sill (possibly lopolithic) into the Palaeoproterozoic granite-gneissic basement of the TIB.

At surface, the Norra Kärr intrusion exhibits a concentric layering, similar to Ilimaussaq (Sørensen et al., 2011) and Lovozero (Khomyakov, 1995). By analogy, it is probable that there was at least a degree of igneous differentiation, followed by deformation and metamorphic overprint. Layering at Norra Kärr from the synformal core out to the flanks consists of the sequence described in Table 1. Rock units are referred to by informal names derived from local features.

Approximately 80% of the intrusion consists of varieties of 'grennaite', an aegirine-rich nepheline syenite carrying the zirconosilicate minerals, eudialyte and catapleiite. The modal mineralogy of the three main varieties is shown in Table 2. The grennaite rock type may be analogous to a deformed and partly recrystallized lujavrite (Le Maitre, 2002), displaying some similarity to the Ilimaussaq Alkaline complex in south Greenland (Sørensen et al., 2011).

The remaining 20% of the complex consists of poorly Zr-REE mineralized sodic-amphibole bearing lithologic units informally named kaxtorpite and lakarpite (Table 1) and pulaskite. The average major element, REE-Zr and U-Th content of the principal rock types of Norra Kärr is shown in Table 3. Along with its high heavy REE fraction, Norra Kärr mineralized units are relatively low in thorium (Th) and uranium (U). Thorium in Norra Kärr is below the level of the regional-scale granites of the TIB.

The kaxtorpite is an REE-poor lithology, found in the centre of the synform. The rock consists mainly of eckermannite and sodic pyroxene, microcline, albite and altered nepheline (to zeolite). The kaxtorpite is folded, and infolded bands of grennaite are common towards the margins of the unit. Through the central part of the intrusion, the kaxtorpite thins out at depth, which supports the idea that a lopolithic intrusive has been deformed into a synform (Fig. 2).

The series of REE-mineralized grennaite units surrounds the kaxtorpite synform core. The grennaite is subdivided into three distinct units: fine grained grennaite (GTC); pegmatitic grennaite (PGT); and migmatitic grennaite (GTM), based mainly on textural features and spatial setting. The major element chemistry and bulk mineralogy do not vary significantly

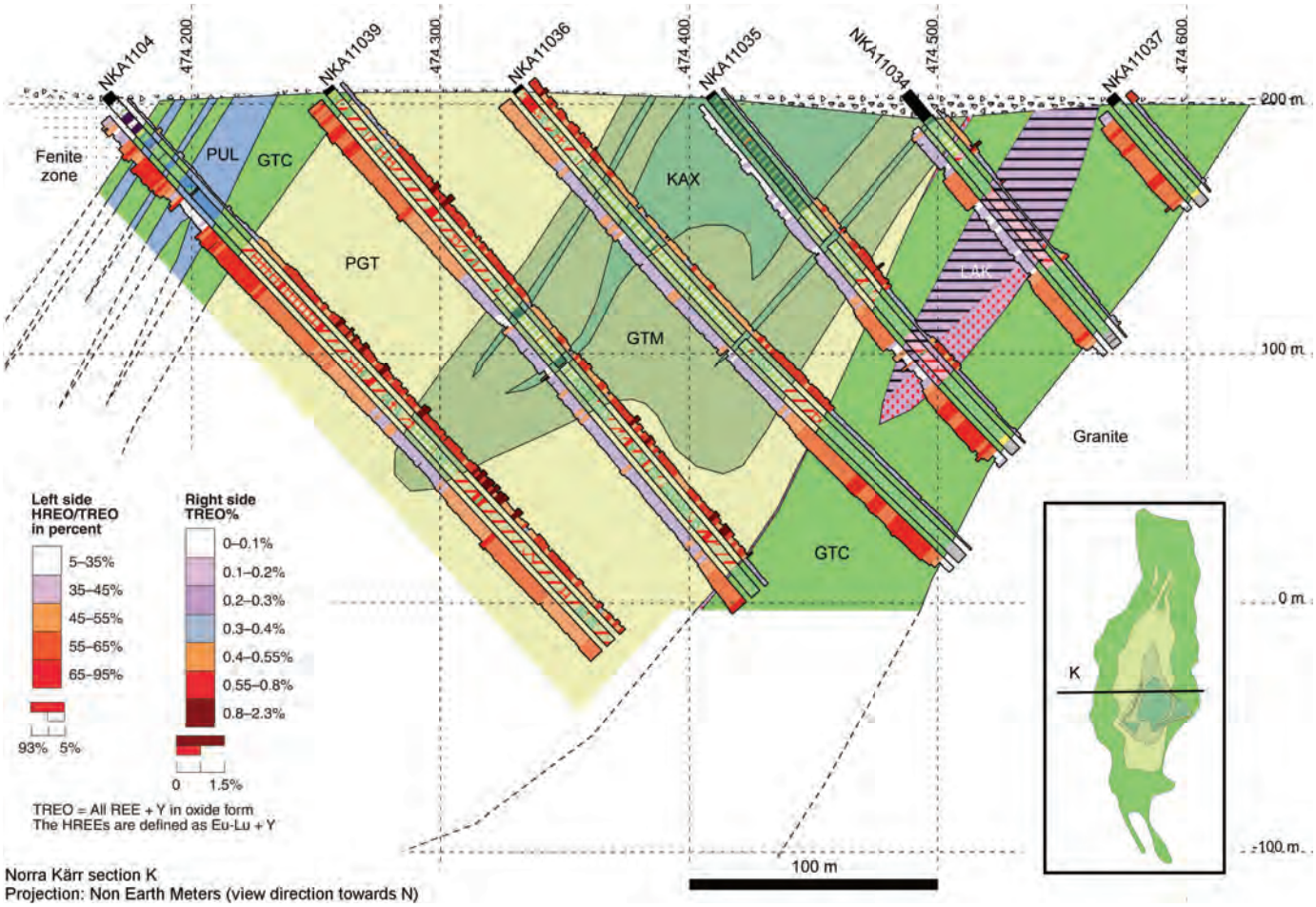

Fig. 2. Geological cross section through the central part of the complex. The distribution of TREO and percentage of HREO are shown beside the drillholes.

Table 1. Rock units comprising the Norra Kärr Peralkaline complex, Sweden.

Rock Type (Map Code)	Relative Position	Description
Kaxtorpite (KAX)	In the central part of the complex, probably as the core of a synform; offset cone-shaped body that does not persist to depth.	Relatively dark, medium grained, commonly folded rock. Alkali feldspar-eckermannite-aegirine with lesser nepheline-zeolite-pectolite. Towards margins commonly interfolded with bands of fine-grained grennaite.
GTM domain Grennaite (GTM)	Innermost grennaite unit, wrapping around the central kaxtorpite.	Medium REE-grade. Recrystallized to almost migmatitic grennaite. Commonly folded. Alkali feldspar-aegirine-nepheline-zeolite-eudialyte-catapleiite mineralogy.
PGT domain Grennaite (PGT)	More than 100 m wide zone between the GTM and GTC type grennaites. Principal mineral resource unit.	Variably recrystallized ground mass with highly varying coarser grained, leucocratic bands and zones. From just 5-10% leucocratic, thin schlieren to more than 10 m wide very coarse-grained pegmatitic zones.
GTC domain Grennaite (GTC)	Outermost grennaite zone that lies along the outer contacts of the intrusive.	Very fine-grained, foliated grennaite with 2-10%, elongated to locally band-like laths of catapleiite porphyroblasts. Eudialyte only very rarely visible by naked eye.
Lakarpite (LAK)	Elongated bodies along the eastern contact between the PGT and GTC varieties of grennaite.	Medium- to coarse-grained, albite-arfvedsonite-microcline-nepheline dominated rock. Locally carrying pink eudialyte close to its contacts with surrounding grennaite.
Pulaskite (PUL)	Elongated bodies close to the W and N contacts of the intrusive. Locally as large boudins within GTC type grennaite.	Medium- to coarse-grained alkali feldspar syenite with some amphibole-aegirine and minor nepheline. Characterized by coarse microcline augen.
Fenite Aureole (FEN)	Mainly exposed or drilled along the western contact as a 5-100 m wide zone of sodic metasomatic alteration of surrounding granite.	Characterized by albitization and by aeginine and alkali amphibole replacing biotite.

between these three varieties. The distribution of the REE varies between the grennaite units (Fig. 3), and the percentage of HREEs within TREO varies from about 40% in the more central GTM variety and gradually increases outwards to about 65% in the GTC zone (Fig. 4).

Grennaite of the GTM domain is found in the central part of the synform, immediately surrounding the barren core of kaxtorpite. GTM grennaite is recrystallized commonly bears a folded foliation. The extent of the recrystallization varies from a gneissic diffuse medium-grained texture close to the kaxtorpite to a slight coarsening of the texture farther away from the central kaxtorpite core. TREO and ZrO_2 grade of GTM is typically in the range of 0.53% and 1.49%, respectively.

Surrounding this domain, lies a wide zone of well mineralized, leucosome-rich partly pegmatitoidal textured grennaite, defined as the PGT domain. This unit is inhomogeneous, ranging from zones with 5-10% of 1 cm wide, medium-grained, leucocratic schlieren in finer grained PGT grennaite, to several metre wide zones of very coarse-grained nepheline-syenite pegmatite. The pegmatitic zones and schlieren consist of the same minerals as the fine-grained PGT grennaite, though are generally poorer in aegirine and richer in feldspar, nepheline and eudialyte.

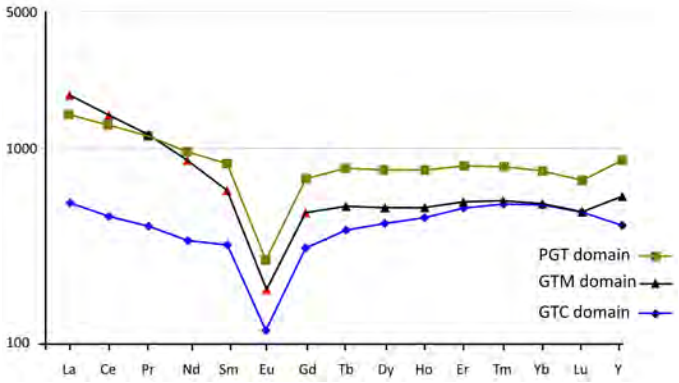

Fig. 3. Chondrite-normalized REE distribution for mineralized domains.

The grain size of the minerals in the thinner schlieren is around 5 mm. Zones up to 10 m wide of very coarse-grained nepheline syenite are also common. The eudialyte content and thus the REE grade is generally more elevated with greater pegmatitic texture. Zones with less leucocratic schlieren in

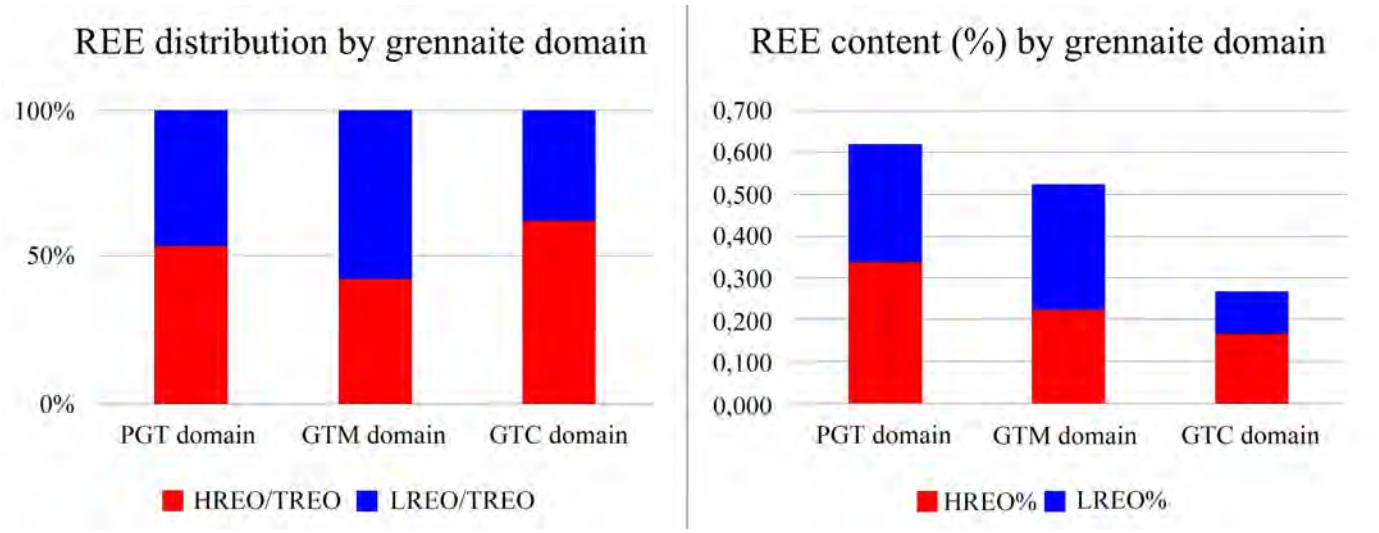

Fig. 4. Relative and absolute contribution of heavy REE (HREO) and light REE (LREO) to total REE content in each grennaite unit. PGT forms the most significant mineralized rock type by both volume and grade.

Table 2. Modal mineralogy of the three varieties of mineralized grennaite (GTM, PGT, GTC).

Mineral	**PGT**	**GTM**	**GTC**
Weight %	**domain**	**domain**	**domain**
Aegirine	21.4	21.2	16.6
Albite	17.7	20.4	28.0
Anorthoclase	1.3	1.5	1.8
Microcline	16.0	18.1	14.5
Nepheline	11.2	8.0	20.7
Zeolite (Natrolite-Analcime)	16.3	16.0	9.6
Eudialyte	8.2	7.0	4.4
Catapleiite	4.0	2.5	3.1
Mica-alteration	2.9	4.1	0.8
Fluorite	0.2	0.4	0.2
Prehnite	0.3	0.3	0.2
Britholite-Ce	0.08	0.09	0.01
Mosandrite	0.08	0.09	0.02
Galena	0.14	0.04	0.00
Calcite-Mn	0.05	0.09	0.02
Zircon	0.05	0.07	0.00

general carry REE grades well above the cut off. Typical TREO and ZrO_2 concentrations of PGT are 0.62% (Fig 4) and 2.01% respectively.

Outside of the PGT domain and closer to the granite contact, the grennaite groundmass becomes gradually finer grained to an aphanitic and schistose texture. Typically this domain, known as GTC grennaite, is porphyritic in appearance, with a few percent of 1-30 mm long, lath like, elongate to needle shaped porphyroblasts of the rare zirconosilicate mineral catapleiite. Typical TREO and ZrO_2 grades of GTC are 0.27% (Fig. 4) and

Table 3. Major element geochemistry of the principal rock types comprising the Norra Kärr complex. TREO refers to total rare earth oxides whereas %HREO corresponds to the proportion of heavy rare earth oxides within TREO in %wt.

	Kaxtorpite (KAX)	PGT domain	GTM domain	GTC domain	Lakarpite (LAK)	Pulaskite (PUL)
SiO_2%	60.2	55.6	56.7	56.5	64.7	62.0
$Al2O_3$%	13.7	16.5	17.3	18.5	15.8	15.7
Fe_2O_3%	4.3	6.4	5.3	4.6	2.9	4.2
CaO%	2.7	1.3	1.5	0.6	1.8	2.4
MgO%	1.6	0.2	0.2	0.1	0.9	1.2
Na_2O%	8.8	10.8	10.2	11.5	7.4	6.9
K_2O%	3.0	3.7	3.8	3.6	5.2	5.0
TiO_2%	0.5	0.1	0.1	0.0	0.3	0.4
MnO%	0.6	0.2	0.4	0.1	0.1	0.2
TREO%	0.20	0.62	0.53	0.27	0.23	0.13
%HREO	30.10	55.40	43.10	63.50	42.10	40.80
ZrO_2%	0.33	2.01	1.49	1.35	0.55	0.35
Th ppm	68	6	11	5	25	25
U ppm	24	12	21	5	10	8

1.35% respectively.

The lakarpite (LAK) unit is a rare and sporadic low REE grade alkaline unit, composed principally of sodic amphibole, albite, microcline with minor sodic pyroxene, nepheline and fluorite. Both mesocratic and melanocratic varieties occur. It forms an intermittent, elongated body in the eastern part of the intrusive. The lakarpite may contain abundant REE-poor, bright pink eudialyte especially close to contacts with grennaite.

Pulaskite (PUL) occurs mainly along the western and northern contacts of the intrusion. It is a medium-coarse grained rock low in REEs and typically carries large rounded microcline augen in a groundmass of albite, aegirine, amphibole, microcline and minor biotite and nepheline. Rosenbuschite, apatite, titanite and fluorite occur as accessories. Pulaskite may occur together with fine-grained grennaite as alternating zones.

The PGT type mineralization makes up about 75% of the mineral resource at Norra Kärr and the GTM type most of the remaining. The GTC and less common alkaline rocks are currently excluded due to lower grades or lower process certainty.

4. REE mineralogy and distribution

Norra Kärr is unusual for a REE deposit in that nearly all of the REE are found in the one mineral, and not distributed through multiple phases. The complex zircono-silicate mineral eudialyte ($Na_4(Ca,Ce)_2(Fe^{2+},Mn,Y)ZrSi_8O_{22}(OH,Cl)_2$) hosts greater than 95% of REE, with lesser amounts in a secondary Ca-LREE-F-silicate mineral tentatively identified as britholite, with trace mosandrite and cerite. In comparison to most other similar deposits, the eudialyte at Norra Kärr is REE rich and also contains a very high proportion of HREO (Fig. 5). The low-REE sample from Norra Kärr reported by Schilling et al. (2011) was taken from an unrepresentative outcrop of the lakarpite unit that lies outside the mineral resource.

Various mineral studies (e.g., Sjöqvist et al., 2013), have shown that, within the resource, the TREO content of the eudialyte varies between 6% and 10%. The percentage of HREO in the mineral also varies from about 30% in the more central GTM zone to above 70% in the more distal GTC zone. Electron microprobe and Laser Ablation ICP-MS analyses of eudialyte from different parts of the Norra Kärr intrusion suggest that the REE distribution in the mineral is proportional to that in the corresponding whole rock. These data have further shown that the TREO content and percentage of HREO is highest in eudialyte found in the GTC unit. However, the relatively low (4.4%) total content of eudialyte compared to 8.2% in the PGT and 7.0% in the GTM rock types result in a low total REE grade, and GTC's current exclusion from the mineral resource.

Sjöqvist et al. (2013) defined three compositional varieties of eudialyte group minerals at Norra Kärr: 1) Fe-rich, REE-poor, classical pink eudialyte; 2) Fe-Mn-bisected, HREE-rich eudialyte from pegmatitic grennaite (PGT; and 3) Mn-rich, LREE-rich eudialyte from 'migmatitic' grennaite (GTM). The pink, REE-poor eudialyte occurs locally, within the lakarpite unit in contact with grennaite and only a very small part of

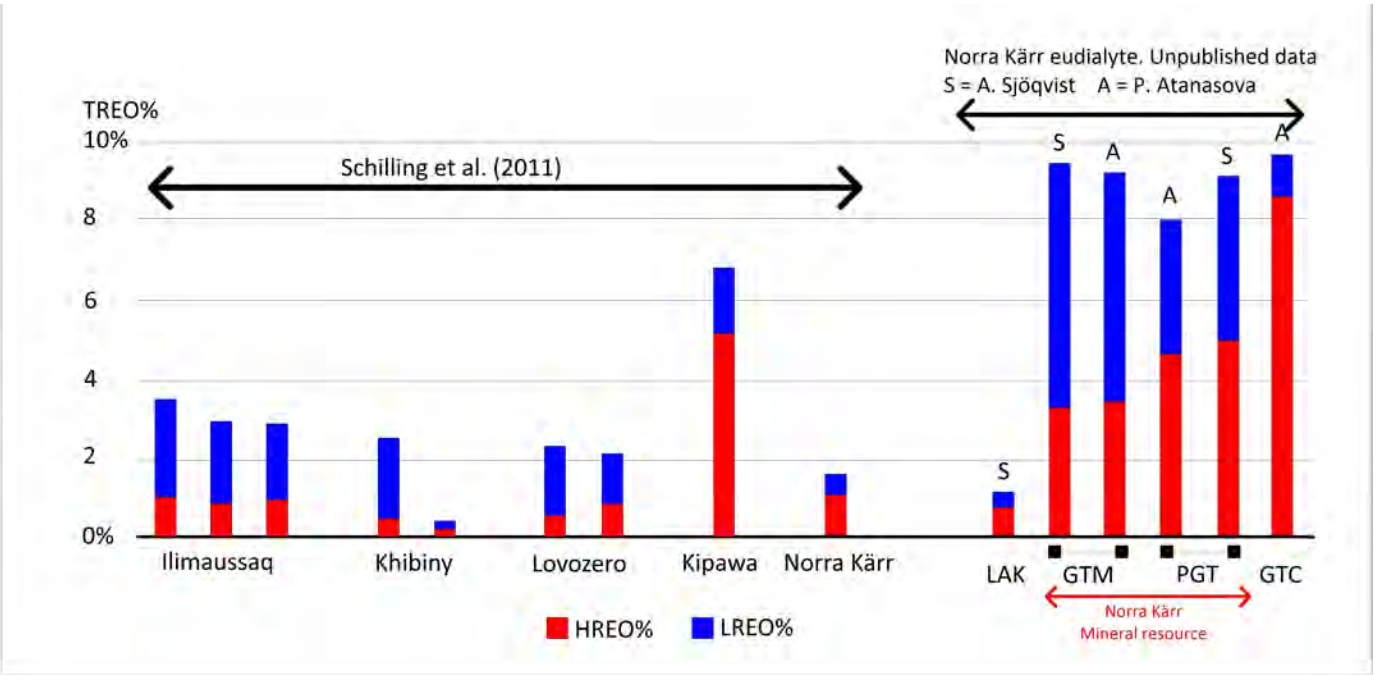

Fig. 5. Laser ablation ICP-MS analyses of eudialyte from various locations worldwide.

the mineral resource belongs to this variety. The HREE-rich eudialyte, which varies from mid to dark orange-brown to deep yellow or red, is the greatest contributor to the Norra Kärr resource.

In contrast to the REE, which are only found in significant amount in eudialyte, Zr and Hf are distributed through two minerals. Approximately 60% of the Zr is hosted by eudialyte, with the balance contained in the hydrated zirconosilicate catapleiite ($Ca/Na_2ZrSi_3O_9•2H_2O$). Current metallurgical design does not envisage recovery of these elements.

5. Mineral resources

The indicated mineral resource in a planned pit at Norra Kärr stands at 31.1 million tonnes grading 0.61% TREO (Short et al., 2015), corresponding to a 20 year mine life. Additional mineralized rock, about four times the volume of the quoted resource, is known to lie beneath and along strike from the planned pit. The indicated mineral resource is based on TREO cut-off grade of 0.4% and has a high HREO/TREO proportion (Short et al., 2015; Table 4).

6. Proposed mining

Under the model assumed by Short et al., (2015), Norra Kärr could be exploited by open pit mining. The deposit crops out or lies under only a thin soil cover, and is typically greater than 100 m wide, such that risk of dilution or loss is extremely low. Mineral extraction methods have taken account of two constraints, blasting fragmentation and the nearby E4 highway. Fragmentation has been required to meet a maximum size of 600 mm and planned blasting has been designed with a safety envelope for a nearby highway. Mined waste totals 17.3 Mt for total rock movement of 40.8 Mt.

Underground mining was also considered. It presents the potential to reduce the land use footprint, a significant consideration in ensuring project sustainability.

7. Metallurgical testing

As established above, greater than 95% of REEs at Norra Kärr are hosted by the Na-Ca zirconosilicate mineral eudialyte. The name eudialyte is taken from the Greek to mean ‘easily dissolved’, due to the mineral’s high solubility in weak acid. However, despite this solubility and simplicity of the ‘cracking’ stage of processing, to date eudialyte has not been used commercially as a source for REE or Zr.

Historically, pregnant leach solutions (PLS) from eudialyte ores have resisted purification and REE separation due to the high silica content of the PLS. The past 5 years of research by various exploration companies, applying continuous solution monitoring and 21st century chemicals and equipment have contributed to providing silica management solutions, and preventing or limiting the formation of unfilterable silica gels.

7.1. Beneficiation

In 2012, German mineral processing consultants at DORFNER Analysenzentrum und Anlagenplanungsgesellschaft mbH (ANZAPLAN) were engaged by Tasman to determine the most suitable mineral beneficiation route for the Norra Kärr mineralized material. ANZAPLAN conducted mineralogical characterization and testing on domain specific composite samples. Samples from each domain were crushed and ground, then subjected to mineralogical characterization employing automated scanning electron microscope based mineral liberation analysis (MLA) technology. The mineral characterization determined that, despite hand specimen scale

Table 4. Indicated mineral resources and reserves from Norra Kärr REE project. From Short et al., (2015).

Tonnes (M)	TREO (%)	%HREO in TREO	Dy_2O_3 (%)	Y_2O_3 (%)	Eu_2O_3 (%)	La_2O_3 (%)	Nd_2O_3 (%)	Ce_2O_3 (%)	Gd_2O_3 (%)	Tb_2O_3 (%)	Pr_2O_3 (%)	Sm_2O_3 (%)	Lu_2O_3 (%)
Indicated Mineral Resource Estimate, 0.4% cut-off													
31.1	0.61	52.6	0.027	0.218	0.002	0.057	0.067	0.128	0.020	0.004	0.017	0.018	0.003
Probable Mineral Reserve Estimate													
23.6	0.59	53.1	0.027	0.215	0.002	0.055	0.065	0.124	0.020	0.004	0.016	0.018	0.002

variations, the constituent mineralogy was indistinct between the domains and displayed only minor variability (Fig. 6). The minor variation in modal mineralogy translates into only minor differences in geochemistry. The high degree of similarity of potentially economic rock domains with regard to mineralogy and grade is viewed as promising, limiting the need for blending or selective mining.

The degree of eudialyte liberation was satisfactory for particle sizes of 60 µm to 80 µm. Several beneficiation methods were investigated to upgrade the eudialyte. The principal finding is that due to paramagnetism of the eudialyte, magnetic separation alone was sufficient for eudialyte beneficiation, and adequately rejected much of the acid consuming gangue. A follow-up study identified the Metso HGMS technology as most appropriate to recover eudialyte using a single stage magnetic separation.

7.2. Leaching

Diagnostic leach tests were conducted by ANSTO to determine the minimum acid activity required to dissolve eudialyte. It was determined that a mild acidic environment, around pH 1, was required to dissolve the eudialyte while leaving intact most of the accompanying minerals. Additionally, tests were conducted at various temperatures to determine the impact on leaching kinetics and pulp handling. The results indicated that a leach temperature of 30°C is sufficient to maintain satisfactory leach kinetics and pulp condition. Follow-up tests further examined the mineral solubility at constant acidities, around the determined range, at various pulp densities to determine the operating limits for silica in solution. When operating at higher pulp densities a threshold limit was exceeded whereby the silica would precipitate from solution causing the pulp to gel. REE extractions into solution were routinely in excess of 90%.

The PLS generated by the sulphuric acid dissolution of the eudialyte mineral concentrate has a characteristically high silica concentration that is in excess of that acceptable for metal recovery by traditional solvent extraction. To remove the silica, the pH is increased from the leach condition to a value in excess of pH 3 to destabilize the silica, causing it to precipitate. The neutralization residue, comprised largely of silica and minor contributions of Zr and aluminium (Al), is then separated from the PLS and washed to recover the entrained solution. The testing to date indicates that the neutralization process is capable of producing a clarified liquor suitable for solvent extraction (unpublished data).

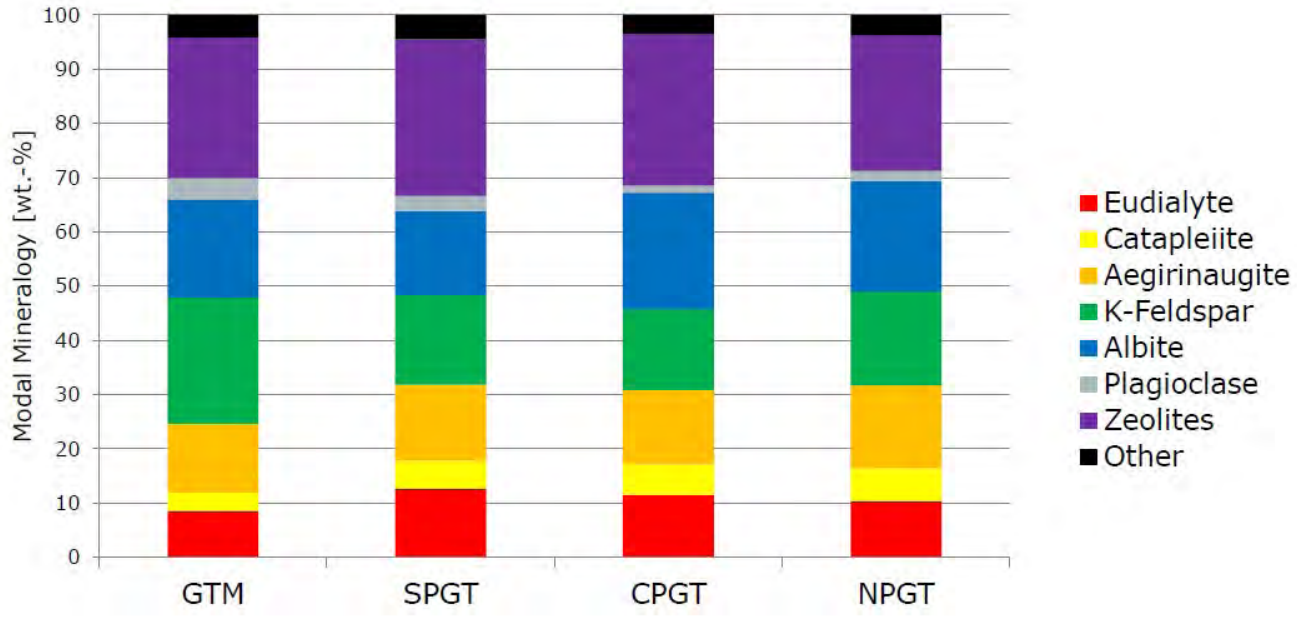

Fig. 6. Mineral distribution of Norra Kärr mineralized rock types as determined by MLA.

7.3. Solvent extraction

The principal method tested to recover the REEs from the PLS was solvent extraction. ANSTO conducted the preliminary definition work using a PLS mixture generated as part of the leaching and neutralisation definition programmes. Phase disengagement studies determined that an elevated operating temperature was required to ensure satisfactory phase disengagement within the system. Kinetic loading studies determined that the rate at which equilibrium was attained was faster than the phase separation kinetics.

Equilibrium loading isotherms were generated using a primary amine solvent in order to determine its loading capacity and the likely number of equilibrium stages required to extract the REEs from the aqueous PLS into the organic solvent. The equilibrium loading work enabled the determination of the organic to aqueous ratio as well as the number of stages to effect an acceptable level of extraction.

The REEs were strongly complexed with the solvent and resulted in excessive acid requirements to achieve satisfactory stripping efficiency. An alternative reactive stripping process was assessed, whereby oxalic acid was contacted with the loaded organic causing the formation of a rare earth oxalate precipitate at the interface of the two phases. The precipitate was then separated from the two phases by centrifugation, producing a mixed oxalate concentrate. The resulting concentrate was subjected to chemical analyses (Table 5), demonstrating high REE content with low degree of impurities. The balance of the assay mass is the oxalate anion and hydration water from the oxalate salts.

8. Process flowsheet

Metallurgical testwork has allowed the determination of a flowsheet to prepare a mixed REE oxide product with characteristics suitable for immediate sale or toll separation (Figs. 7, 8).

9. Conclusions and recommendation for future research

Norra Kärr is a peralkaline intrusion-hosted HREE deposit, where the main ore mineral is eudialyte. The project is in the advanced stage of development with established probable reserves sufficient to supply all of Europe's REE needs for several decades. More specifically, it has a potential to produce more than 250 tonnes per annum of Dy for the same period of time. Immediate targets for additional research include: the coarse removal of Ce and/or La on the mine site to reduce subsequent separation charges; the consideration of alternative acids to limit waste streams and improve reagent recyclability; and comparative test work to limit the use of the most expensive reagents and consumables.

Table 5. REE oxalate concentrate chemical analyses. Sample prepared and assayed by ANSTO. Relative % distribution indicated high proportion of HREE. LREE = Ce-Sm; HREE = Eu-Lu+Y.

Element	Overall Recovery [%]	Weight [%]	Relative % Distribution
La	77.84	4.935	10.9
Ce	78.02	10.750	23.6
Pr	78.82	1.458	3.2
Nd	79.01	6.763	14.9
Sm	79.42	1.650	3.6
Eu	79.44	0.269	0.6
Gd	79.32	1.657	3.6
Tb	79.13	0.351	0.8
Dy	78.78	2.191	4.8
Ho	78.00	0.491	1.1
Er	77.40	1.288	2.8
Tm	76.89	0.182	0.4
Yb	76.10	1.138	2.5
Lu	75.48	0.149	0.3
Y	72.92	12.210	26.8
Impurity		0.171	
TREE		45.48	100
LREE		23.91	56.2
HREE		21.58	43.8

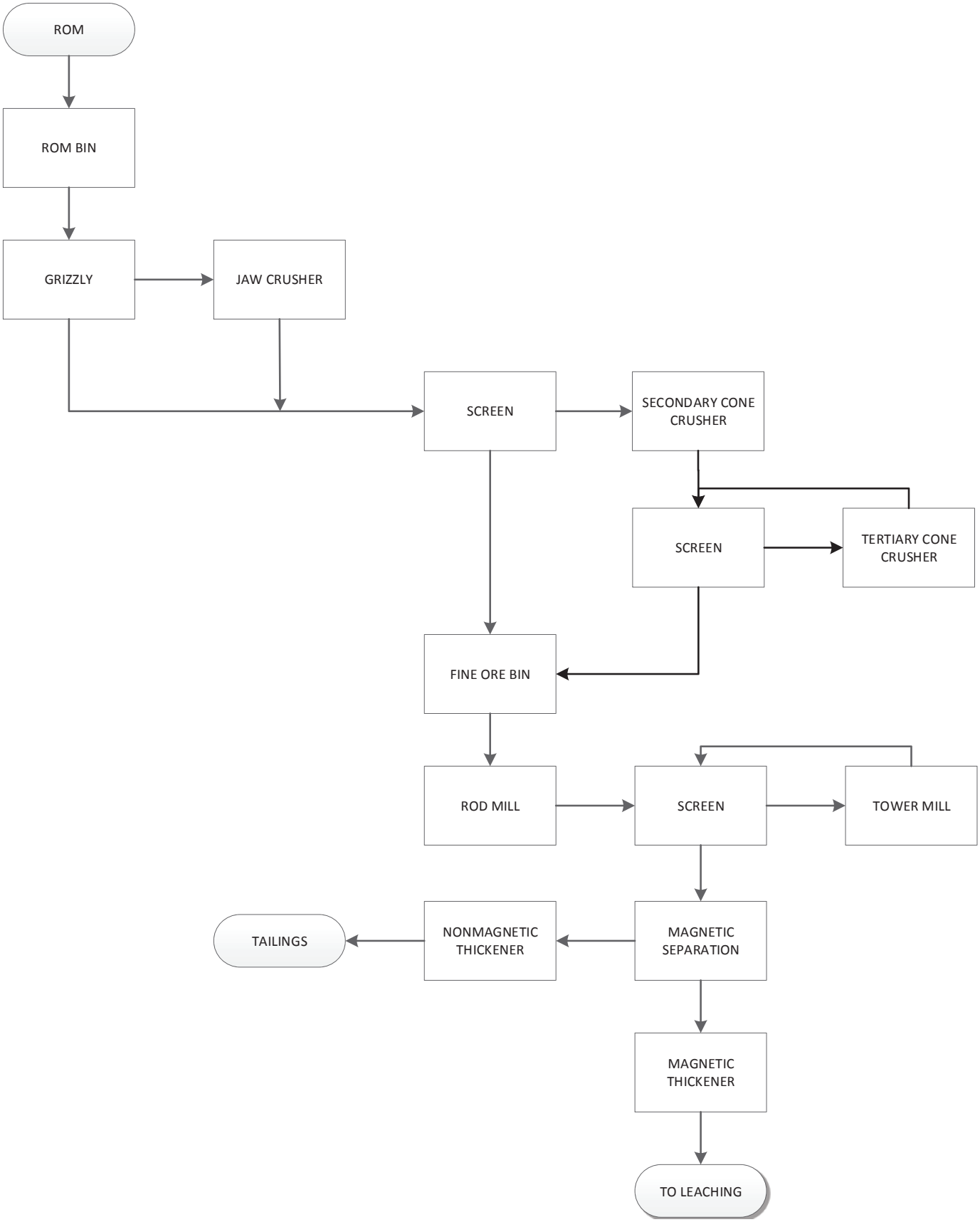

Fig. 7. Comminution and beneficiation block flow diagram.

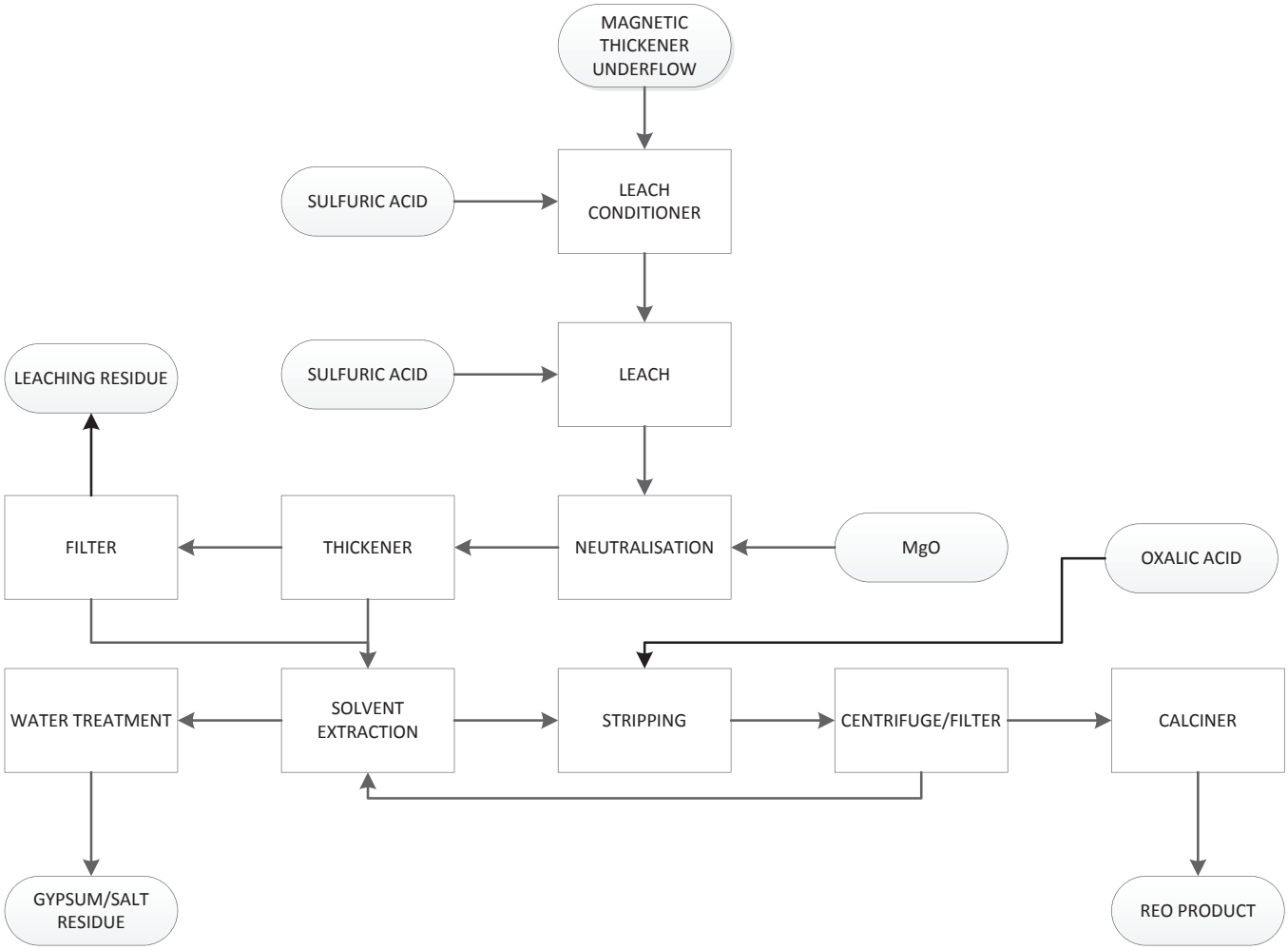

Fig. 8. Hydrometallurgical extraction and recovery block flow diagram.

References cited

Adamson, O.J., 1944. The petrology of the Norra Kärr district: An occurrence of alkaline rocks in southern Sweden. Geologiska Föreningens i Stockholm Förhandlingar, 66, 113–255.

Andersson, U.B., and Wikström, A., 2004. The Småland-Värmland Belt: Overview. In: Högdal, K., Andersson, U.B., and Eklund, O., (Eds.), The Transscandinavian Igneous Belt (TIB) in Sweden: a review of its character and evolution. Geological Survey of Finland Special paper 37, 15-20.

European Rare Earths Competency Network (ERECON), 2015. Strengthening of the European RareEarths Supply China – Challenges and policy options. European Commission, DG GROWTH, 106p.

Khomyakov, A.P., 1995. Mineralogy of hyperagpaitic alkaline rocks. Clarendon, Oxford, 223p.

LeMaitre, R.W., (Ed.), 2002. Igneous rocks: A classification and glossary of terms, 2nd ed. Cambridge University Press, 236 pp.

Schilling, J., Wu, F.-Y., McCammon, C., Wenzel, T., Marks, M.A.W., Pfaff, K., Jacob, D.E., and Markl, G., 2011. The compositional variability of eudialyte-group minerals. Mineral Magazine, 75, 87–115.

Short, M., Moseley, G., Mounde, M., and La Touche, G.D., 2015. Prefeasibility Study – NI 43-101 – Technical report for the Norra Karr Rare Earth Element Deposit. Tasman Metals Ltd., Vancouver, Canada, 384p.

Sjöqvist, A.S.L., Cornell, D.H., Andersen, T., Erambert, M., Ek, M., and Leijd, M., 2013. Three compositional varieties of rare-earth element ore: Eudialyte-group minerals from the Norra Kärr alkaline complex, southern Sweden. Minerals, 3, 94-120.

Sjöqvist, A.S.L., Cornell, D.H., Andersen, T., Andersson, U.B., Christensson, U.I., Ranjer, S.J.E., Holtstam, D., and Leijd, M., 2014. Geochronology of the Norra Kärr alkaline complex, southern Sweden. Abstract, 31st Nordic Geological Winter Meeting, Lund, Sweden, 95p.

Sørensen, H., 1997. The agpaitic rocks—An overview. Mineralogical Magazine, 61, 485–498.

Sørensen, H., Bailey, J.C., and Rose-Hansen, J., 2011. The emplacement and crystallization of the U–Th–REE-rich agpaitic and hyperagpaitic lujavrites at Kvanefjeld, Ilímaussaq alkaline complex, South Greenland. Bulletin of the Geological Society of Denmark 59, 69–92.

Thulin, H., 1996. Norra Kärr - avsnitt 1 [in Swedish]. Litofilen, 1996/1, 17–51.

Törnebohm, A.E., 1906. Katapleiit-syenit, en nyupptäckt varietet af nefelinsyenit i Sverige [in Swedish]. SGU Ser. C, 199, 1–54.

Pantellerite-hosted rare earth element mineralization in southeast Labrador: The Foxtrot deposit

Randy R. Miller[1, a]

[1] Search Minerals Inc., North Vancouver, BC, B7P 3P9
[a] corresponding author: randymiller@searchminerals.ca

Recommended citation: Miller, R.R., 2015. Pantellerite-hosted rare earth element mineralization in southeast Labrador: The Foxtrot deposit. In: Simandl, G.J. and Neetz, M., (Eds.), Symposium on Strategic and Critical Materials Proceedings, November 13-14, 2015, Victoria, British Columbia. British Columbia Ministry of Energy and Mines, British Columbia Geological Survey Paper 2015-3, pp. 109-117.

1. Introduction

The Foxtrot rare earth element (REE) deposit is hosted by peralkaline volcanic rocks, primarily pantellerite and commendite flows and ash-flow tuffs, of the Fox Harbour Volcanic belt in southeast Labrador, near the coastal community of St Lewis (Fig. 1). Search Minerals personnel discovered the deposit in 2010 as a result of a REE exploration program in southeast Labrador. Exploration diamond drilling in late 2010, 2011, and early 2012, totalling 72 diamond-drill holes and 18,855 metres, outlined a Dy-Nd-Y-Tb deposit of 9.2 million tonnes indicated resource (cut-off 130 ppm Dy), grading 189 ppm Dy, 1442 ppm Nd and 1040 ppm Y, and, 5.2 million tonnes inferred resource, grading 176 ppm Dy, 1233 ppm Nd, and 974 ppm Y (Table 1; Srivastava et al., 2012, 2013). A smaller high-grade resource (HGC) was also defined (Table 1) and was the subject of a Preliminary Economic Assessment (Srivastava et al., 2013). The Foxtrot deposit and the Fox Harbour Volcanic belt have been the target of continued REE exploration and the subject of engineering and metallurgical studies (Srivastava et al., 2012, 2013; Search Minerals 2014, 2015b) to evaluate the possibility of developing a REE mine at Foxtrot and a REE processing plant in the St. Lewis area (Fig. 1).

Herein we outline the geology and mineralization of the Foxtrot REE deposit and develop a preliminary exploration model for REE mineralization in the Fox Harbour Volcanic belt and related belts in southeast Labrador.

2. Regional geological setting

Terranes in the eastern Grenville Province (Fig. 1) are distinguished on the basis of rock types, structures, ages, and metamorphic signatures, and are separated by major fault zones (Gower et al., 1987, 1988; Hanmer and Scott, 1990; Gower, 2010, 2012). The Foxtrot deposit is in the Fox Harbour Volcanic belt, which is part of the Fox Harbour domain. Single zircon U-Pb crystallization ages indicate that the peralkaline rocks and related mineralization at Foxtrot are 1.3 Ga (Haley, 2014). The Fox Harbour domain is bounded to the north by the Lake Melville terrane, to the west and southwest by the Mealy Mountains terrane, and to the south by the Pinware terrane (Fig. 1). Compilations of U-Pb zircon crystallization age data for rocks in southeastern Labrador indicate that the Lake Melville and Mealy Mountains terranes contain rocks older than 1.6 Ga and the Pinware terrane contains rocks with ages of 1.5 Ga (Gower, 2012).

The Lake Melville terrane contains the Alexis River anorthosite, biotite-bearing granite, granodiorite, and quartz diorite to diorite gneiss (Gower et al., 1987, 1988; Hanmer and Scott, 1990; Gower, 2010;). The Fox Harbour fault zone (Gower, 2012) separates the Lake Melville Terrane from the Fox Harbour domain. Near the Foxtrot deposit, terrane boundary interpretations (Gower, 2012) indicate that a thin sliver (5-6 km wide) of Mealy Mountains terrane occurs between the Lake Melville terrane to the north and the Pinware terrane to the south. Detailed mapping indicates that the Fox Harbour domain, is in the northern half (2-3 km wide) of the sliver and that the Deer Harbour domain is in the southern half.

Near the Foxtrot deposit, the Fox Harbour domain is bordered to the south by the Deer Harbour fault zone (Fig. 1). The Fox Harbour domain has been traced for 64 km; to the northwest it is cut off by a fault, to the east it disappears beneath the Labrador Sea. REE mineralization, peralkaline felsic and mafic volcanic rocks (Fox Harbour Volcanic suite) and an associated anorthositic gabbro distinguish this domain from adjacent domains and terranes. Feldspar porphyries and deformed augen gneisses also occur in this domain.

The Mealy Mountains terrane consists of mostly biotite granitic gneiss, potassium feldspar megacrystic granite gneiss, quartz diorite to dioritic gneisses, and pelitic to semipelitic sedimentary gneisses (Gower et al., 1987, 1988; Gower, 2010).

The Pinware terrane, in the St. Lewis Inlet area, consists of metamorphosed felsic to intermediate intrusions and older intercalated quartzofeldspathic supracrustal rocks. Intrusions consist mainly of granite, k-feldspar megacrystic granite, quartz monzonite, granodiorite, and supracrustal rocks consisting mainly of felsic volcanic rocks and arenitic sedimentary rocks (Gower, 2007, 2010). The Long Harbour fault zone (Gower, 2012) is interpreted to separate the Deer Harbour domain from the Pinware terrane to the south.

Mapping and exploration south of the Long Harbour fault zone indicate that peralkaline volcanic and intrusive rocks

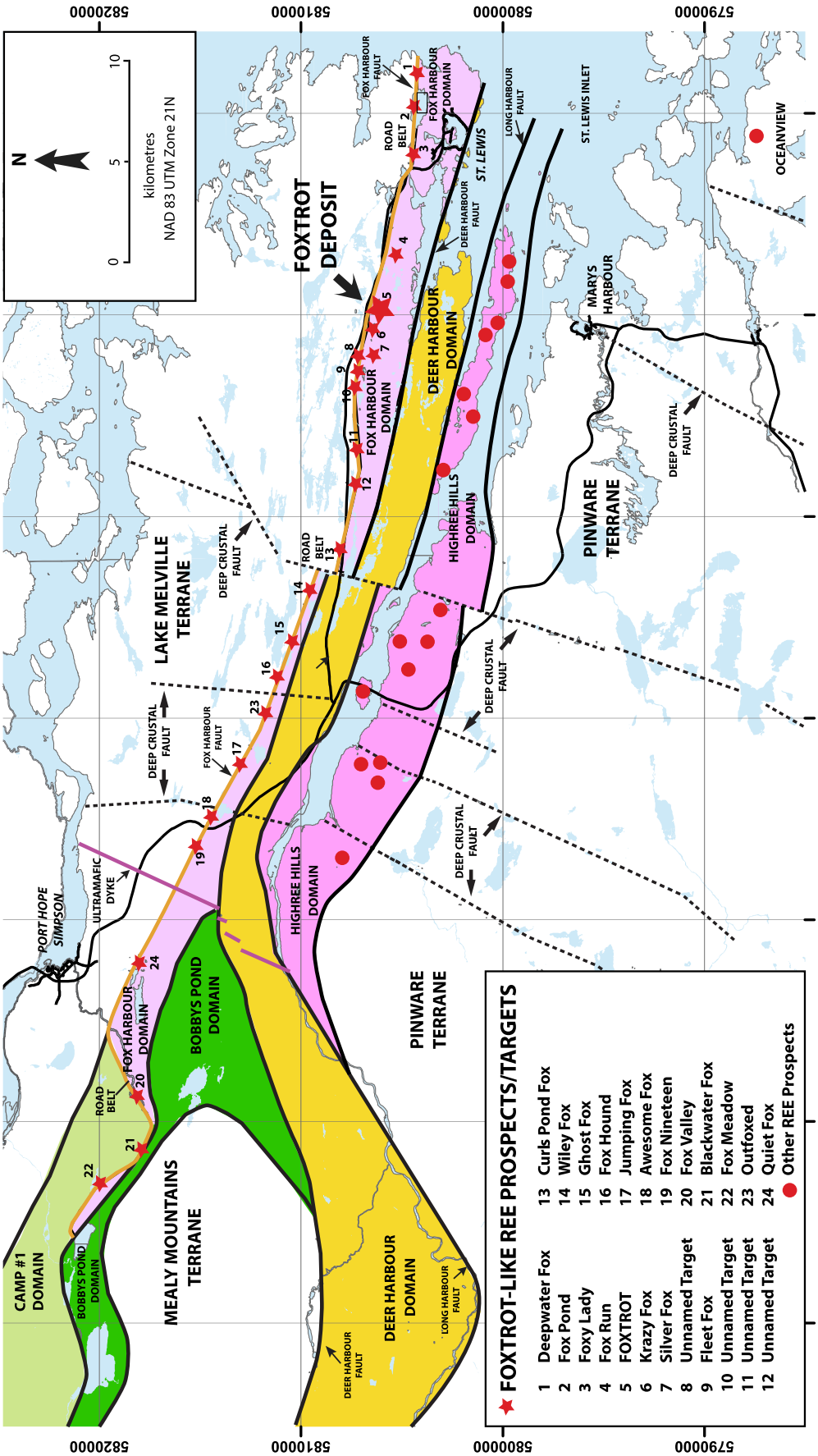

Fig. 1. Rare earth element prospects and targets in the Port Hope Simpson – St. Lewis area, southeast Labrador. Terrane boundaries are modified from Gower (2012). The Fox Harbour Volcanic belt, host to the Foxtrot REE mineralization is in the Fox Harbour domain; the pale brown line corresponds to a marker horizon and is referred to as the Road belt. The HighREE Hills domain also hosts REE mineralization. All domain names are informal.

Table 1. Foxtrot resource (September, 2012).

	Foxtrot Resource		**Foxtrot HGC**	
	Foxtrot Inferred	Foxtrot Indicated	HGC Inferred	HGC Indicated
	5,165,000 (tonnes)	9,229,000 (tonnes)	660,000 (tonnes)	3,423,000 (tonnes)
Y	974	1,040	1,199	1,238
Zr	10,064	9,619	11,716	11,779
Nb	538	626	676	691
La	1,426	1,646	1,894	1,931
Ce	2,881	3,337	3,861	3,945
Pr	330	384	443	455
Nd	1,233	1,442	1,658	1,711
Sm	228	262	302	312
Eu	11.0	13.0	15.0	16.0
Gd	183	205	238	245
Tb	30.0	33.0	38.0	39.0
Dy	176	189	219	228
Ho	34.0	37.0	43.0	44.0
Er	98	103	121	125
Tm	14.0	15.0	17.0	18.0
Yb	91	92	108	111
Lu	14.0	14.0	16.0	16.0
LREE	6,098	7,071	8,158	8,354
HREE	651	701	815	842
HREE + Y	1,625	1,741	2,014	2,080
TREE	6,749	7,772	8,973	9,196
TREE + Y	7,723	8,812	10,172	10,434
%TREE	0.67%	0.78%	0.90%	0.92%
%TREE + Y	0.77%	0.88%	1.02%	1.04%
%HREE	8.43%	9.02%	9.08%	9.16%
%HREE + Y	21.04%	19.76%	19.80%	19.93%

Note:	All amounts parts per million (ppm). 10,000 ppm = 1% = 10 kg/tonne.
REE	Rare Earth Elements: La, Ce, Pr, Nd, Sm, Eu, Gd, Tb, Dy, Ho, Er, Tm, Yb, Lu (Lanthanide Series).
TREE	Total Rare Earth Elements: Add La, Ce, Pr, Nd, Sm, Eu, Gd, Tb, Dy, Ho, Er, Tm, Yb, Lu.
LREE	Light Rare Earth Elements: Add La, Ce, Pr, Nd, Sm.
HREE	Heavy Rare Earth Elements: Add Eu, Gd, Tb, Dy, Ho, Er, Tm, Yb, Lu.
Y	Y not included in HREE due to relatively low value compared to most Lanthanide series HREE.
%HREE+Y	%(HREE+Y)/(TREE+Y).
%HREE	%(HREE/ TREE).
HGC	Subset of mineral resource within a contiguous volume; estimated inside preliminary pit shell.

and related REE mineralization (e.g., Search Minerals 2010a, 2010b) also occur in an area interpreted to be Pinware terrane (Gower, 2012). These rocks and spatially associated non-peralkaline supracrustal rocks have been grouped into the HighREE Hills domain (Fig. 1). The HighREE Hills domain contains peralkaline volcanic and subvolcanic rocks and related pegmatite- and vein-hosted REE mineralization. Several REE prospects have been discovered in the HighREE Hills (see Search Minerals 2010a, 2010b).

3. Fox Harbour Volcanic belt

The Fox Harbour Volcanic belt is about 64 km-long and ranges in width from <50 m in the northwest to 3 km in the east. Units strike westerly to northwesterly, parallel to bounding faults, and dip steeply northward. The belt contains one (in the northwest) to three (in the east) sub-belts of bimodal rocks with mainly REE-bearing felsic peralkaline flows and ash-flow tuffs and mafic to ultramafic volcanic and related subvolcanic units. Feldspar augen gneisses and porphyritic units, including crystal tuffs in the eastern portion of the belt, predominantly occur between the three sub-belts. Sedimentary supracrustal units, including quartzite and locally derived volcaniclastic rocks sourced by felsic (commonly peralkaline) and mafic units, are locally abundant.

The three bimodal sub-belts (Road belt, Magnetite belt and South belt) have been the focus of REE exploration. The Road belt, is on the northern boundary of the Fox Harbour Volcanic belt, and can be traced throughout its full length, but the Magnetite and South belts have only been observed in the eastern 30 km. The mineralized units within the sub-belts, predominantly pantellerite (a peralkaline rhyolite with high Fe and low Al contents) and commendite (similar to pantellerite but with less Fe and more Al), outcrop poorly and commonly occur in bogs or water-filled topographic lows. These units exhibit relatively high radiometric (anomalous U and Th values) and relatively high magnetic (anomalous concentrations of magnetite) signatures that, when combined, are excellent indicators of REE mineralization. Airborne and ground-based radiometric-magnetic surveys clearly outline the three mineralized belts (Srivastava et al., 2012, 2013).

High-grade mineralization, characterized by Dy from 100–300 ppm, is predominantly hosted by fine-grained, layered to massive, pantellerite. Lower grade mineralization, characterized by Dy from 20–100ppm, is predominantly hosted by fine-grained, mostly massive commendite. Mineralized units are commonly interbedded with mafic volcanic units, quartzite, and locally derived volcanogenic sedimentary rocks.

Most of the REE mineralization occurs in allanite and fergusonite; minor amounts of REE occur in chevkinite, monazite, bastnasite and zircon (Srivastava et al., 2012, 2013). Most of the light REE (i.e., La to Sm) in the mineralization occurs in allanite, whereas most of the heavy REE (i.e., Eu to Lu) and Y occurs in both fergusonite and allanite (Srivastava et al., 2012, 2013).

The Road belt commonly consists of non-peralkaline porphyritic feldspar-bearing units, mafic volcanic rocks, non-peralkaline felsic volcanic units, commendite, and pantellerite. A medium-grained anorthositic gabbro, with minor amounts of gabbro, always occurs north (i.e., within 25 m) of Road belt volcanic units on the southern side of the Fox Harbour fault zone. Mineralized units commonly range from 1 to 10 m thick. The Road belt hosts several significant REE prospects with high-grade REE mineralization including the Fox Pond, Fox Valley, Fox Meadow, and Deepwater Fox prospects (Fig. 1; Search Minerals, 2012, 2013, 2015a). High-grade plus medium-grade mineralization at some of these prospects ranges from 10 to 30 m thick.

The Magnetite belt commonly consists of pantellerite, commendite, non-peralkaline rhyolite, and mafic to ultramafic volcanic and related subvolcanic units. Mineralized units commonly range from 5 to 20 m thick. This belt hosts the Foxtrot deposit and additional REE prospects (e.g., Silver Fox and Fox Run; Fig. 1). Mineralization is up to 100m thick (commendites plus pantellerites) at the Foxtrot deposit; high-grade mineralization is up to 25 m thick but usually averages 10 to 14 m.

Lower grade REE mineralization is commonly found in the South belt. This sub-belt commonly consists predominantly of commendite, minor mafic and pantelleritic units, feldspar-bearing porphyry and locally abundant volcanogenic sedimentary rocks. Mineralization is commonly 10 to 50 m thick.

4. Foxtrot deposit

The Foxtrot deposit is about 8 km west of St. Lewis and 0.5 km south of Highway 513 in the Magnetite sub-belt of the Fox Harbour Volcanic belt (Figs. 1-3). Near the Foxtrot deposit, the Magnetite belt consists of, from north to south: 1) commendite; 2) pantellerite with interlayered non-peralkaline rhyolite; and 3) a mafic to ultramafic unit with interlayered non-peralkaline rhyolite. Minor units of locally derived volcanogenic sedimentary rocks, mafic volcanic rocks and related subvolcanic units, and pegmatites occur throughout this sequence. Augen/porphyritic gneiss borders the mineralized units to the north, and a mafic unit, forming a predominant ridge, occurs to the south. Table 2 lists representative REE, Nb, Y, and Zr data for the major units at the deposit.

The commenditic mineralization, which is approximately 50 m thick, consists of individual units of fine-grained, commonly <1 to 2 m thick, massive to poorly layered commendite. These commendites commonly contain trace to minor magnetite, exhibit radioactivity 3-5 times higher than background levels, and contain lower amounts of REE (e.g., 20–60 ppm Dy) and other incompatible elements (Table 2) relative to other mineralized units. Zirconium values commonly range from 800 to 5000 ppm.

The pantelleritic mineralization, up to 30 m thick, consists of individual units of fine-grained, commonly <1 to 5 m thick, poorly to well-layered pantellerite. These pantellerites contain up to 10% magnetite and local amphibole and pyroxene;

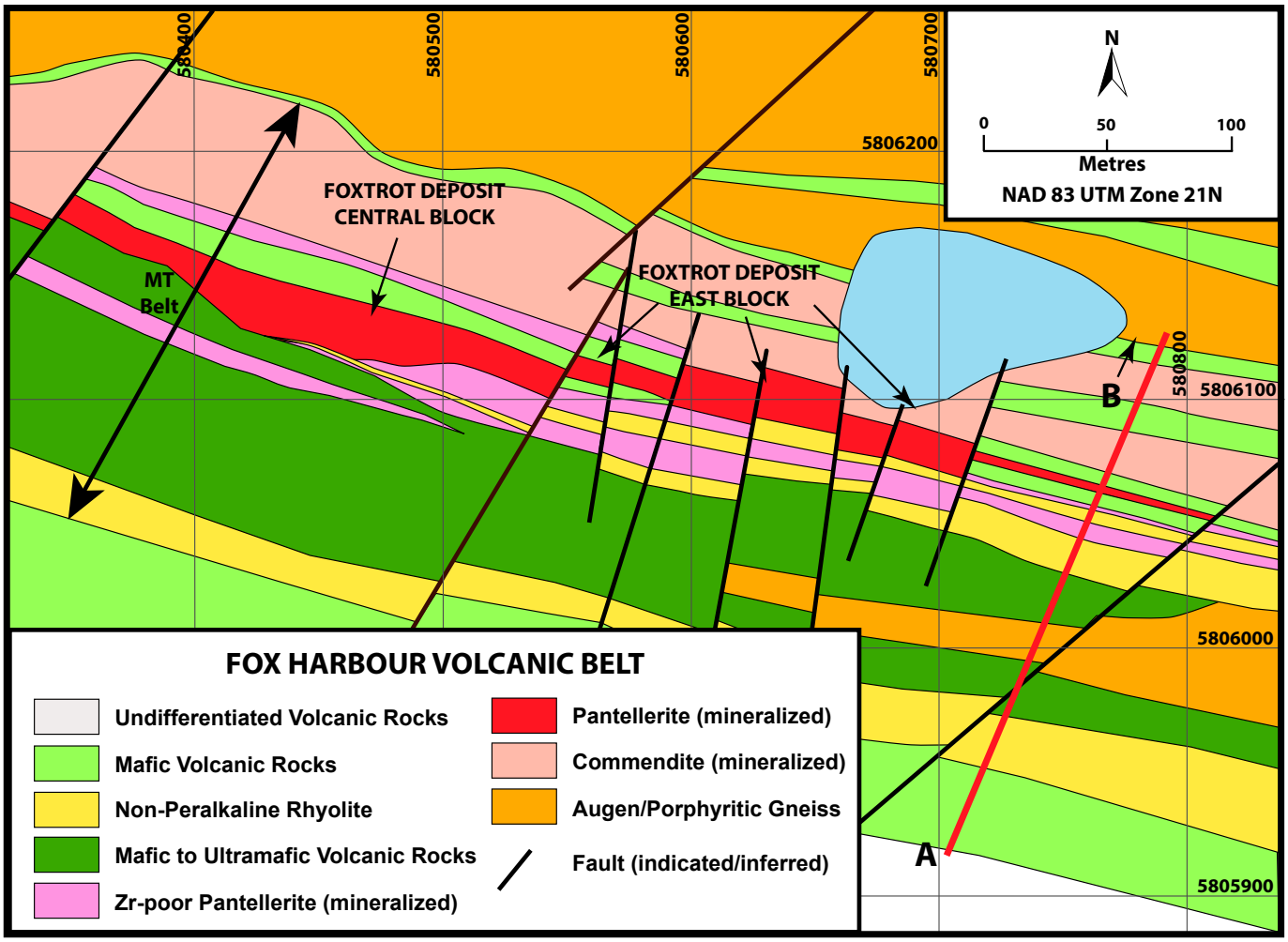

Fig. 2. Geology of the Foxtrot deposit based on 25 metre spacing ground magnetic survey, detailed mapping, channeling, core logging, and chemical analysis. Section A-B illustrated in Figure 3.

magnetite is mostly fine grained but may occur as porphyritic grains up to 4 mm across. They exhibit radioactivity from 5 to 40 times background. Layering in the units, observed as darker and lighter bands, is commonly defined by varying contents of magnetite. These units are relatively highly mineralized and contain potentially economic concentrations of REE (e.g., 60–300 ppm Dy) and other incompatible elements (Table 2). Differences in average Zr values subdivide the pantellerites into two mappable units: Zr-poor Pantellerite (5000–10,000 ppm Zr) and Pantellerite (10,000–15,000 ppm Zr); Zr-enriched pantellerite (>15,000 ppm Zr) is also observed but is commonly <1 m thick and is not depicted in Figures 2 or 3. The mineral resource at Foxtrot essentially encompasses the pantelleritic units. However, the high-grade core (Table 1), which is the main focus of development plans (Srivastava et al., 2013), includes mostly pantellerites with over 10,000 ppm Zr.

Mafic volcanic and locally derived sedimentary units, commonly <0.5 m thick, separate many mineralized units. Thicker mafic units, up to 10 m thick, occur in the commenditic unit and near the contact between the commenditic and pantelleritic units. Mafic units commonly contain <300 ppm Zr and <10 ppm Dy.

Locally derived sedimentary rocks consist of thin (<20 cm) quartzite layers interbedded with thin (<30 cm) mafic and felsic bands. Felsic bands consist of non-peralkaline rhyolite, commendite, low Zr pantellerite, or a mix of mafic and felsic volcanic rocks.

Ultramafic units up to 90 m thick contain epidote-bearing fragments and appear layered. Zirconium and Dy values are commonly <100 ppm and <4 ppm respectively. These units mostly occur to the south of the pantelleritic mineralization.

Several units of non-peralkaline rhyolite, <1 to 8 m thick, occur within the mineralized zones, particularly in the eastern part of the deposit (Figs. 2, 3). They are commonly associated with low-Zr pantellerite, mafic rocks, and locally derived sedimentary rocks. Non-peralkaline rhyolite contains low Zr values (300–600 ppm), low Dy values (<12 ppm) and low mafic mineral concentrations (commonly <5%).

Detailed geological mapping, a 25 m-spaced detailed ground magnetometer survey (Srivastava et al., 2013), radiometric prospecting, and 12 channels, cut throughout the mineralized zone, were used to compile the surface geology of the deposit

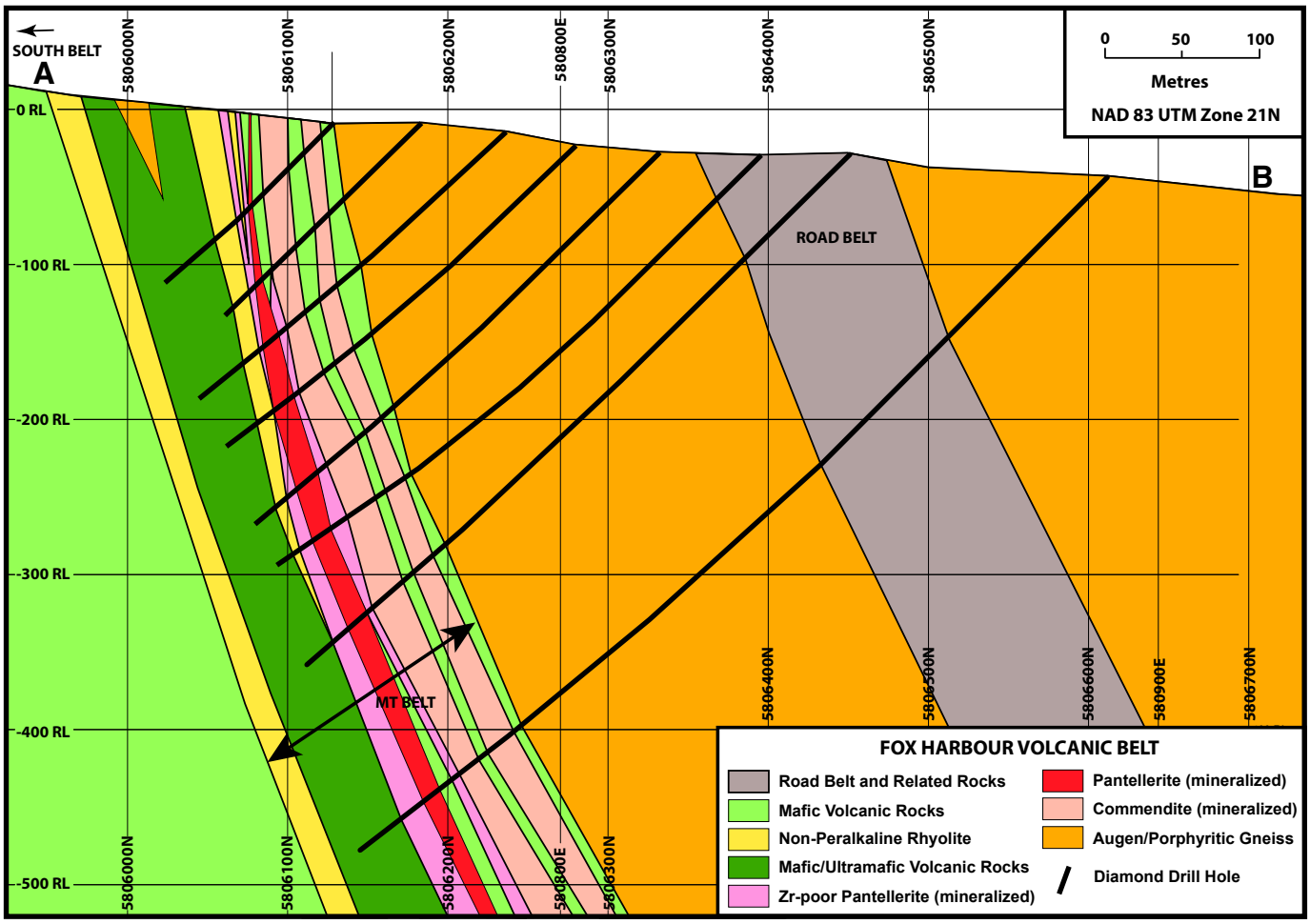

Fig. 3. Foxtrot deposit in NNE-SSW cross-section. View to the northwest along line A-B (Fig. 2); no vertical exaggeration. Drillholes are perpendicular to the general strike of the volcanic stratigraphy (Fig. 2), whereas the thickest and highest grade portion of the deposit plunges to the NE. This results in a thin zone of high-grade mineralization at surface that thickens at depth. Road belt, MT belt (Magnetite belt) and South belt (300m south of A) contain REE mineralized peralkaline volcanic rocks.

(Fig. 2). Faults, defined by the geology, magnetic survey offsets, and topographic lineaments, divide the deposit into two major blocks, the Central block and the East block. The observed faults are northerly to northeasterly striking and steeply dipping, with up to 15 m observed horizontal offset and an unknown amount of vertical offset.

The vertical movement on the faults appears to have been partly responsible for changes along strike in the thickness of units, including the mineralization, and the presence or absence of specific units. Change in the thickness of mineralization is observed across the western boundary of the Central block and across the eastern boundary of the East block (Fig. 2). Non-peralkaline rhyolite is prominent in the East block, where it commonly occurs as two units, and very minor in the Central block, where it occurs as one thinner unit or is absent. Similar changes in thicknesses and absence or presence of specific units also occurs across smaller faults in the East block and may also occur in the Central block, but corroborating data are lacking.

5. Discussion

The peralkaline mineralized units and spatially associated mafic-ultramafic, non-peralkaline rhyolite and locally derived sedimentary units of the Foxtrot deposit are interpreted to represent a subaerial bimodal sequence of volcanic and related volcanogenic sedimentary rocks and subvolcanic intrusions (e.g., Marshall et al., 2009). The probable mantle derivation of the peralkaline and mafic to ultramafic rocks, the subaerial setting, the occurrence on 1.5 to 1.6 Ga continental crust and the occurrence of these units in a narrow belt over a strike-length of at least a 64 km are consistent with a continental rift setting. Possible modern analogues would include Pantelleria (e.g., Civetta et al., 1998) and the East African Rift (e.g., Marshall et al., 2009).

Peralkaline volcanic and intrusive rocks of similar age to the Fox Harbour Volcanic belt are also found in central and northern Labrador (Miller et al., 1996; Gower, 2012). These include REE mineralized peralkaline volcanic rocks, mainly pantellerite (Nuiklavik Volcanic suite; Miller, 1993), REE mineralized peralkaline intrusive rocks, granites-syenites

Table 2. Representative content of REE, Nb, Y and Zr in major rock units, Foxtrot deposit.

	Unmineralized Units		**Mineralized Felsic Volcanic Rocks**			
	NPR	Mafic	Commendite	Low Zr	Pantellerite	High Zr
	FTC-11-08	FTC-11-12	FTC-12-02	FTC-11-12	FTC-11-12	FTC-15-07A
From (m)	16.00	19.70	5.43	0.16	6.87	5.9
To (m)	16.90	20.85	6.23	0.42	7.88	6.05
Interval (m)	0.90	1.15	0.80	0.26	1.01	0.15
Y	51	17	135	620	1260	1428
Zr	404	67	1746	7028	11560	16600
Nb	32	6	87	767	832	621
La	70	6	142	1150	2160	1770
Ce	163	13	299	2350	4260	4180
Pr	18	2	37	269	481	488
Nd	62	9	142	1020	1810	1880
Sm	11	3	27	182	329	356
Eu	0.5	0.9	4.2	10.2	16.3	17.8
Gd	9	3	24	145	245	267
Tb	1.5	0.1	4.3	21.5	38.7	44
Dy	9	4	28	116	234	268
Ho	1.7	0.1	5.8	22.5	43.3	49.9
Er	5	2	17	62	127	144
Tm	0.8	0.3	2.5	9.0	18.4	20.5
Yb	5	2	16	56	113	126
Lu	0.9	0.3	2.4	8.2	17.1	18.1
LREE	324	33	647	4971	9040	8674
HREE	34	12	104	451	853	955
HREE + Y	85	29	239	1071	2113	2383
TREE	358	45	751	5422	9893	9629
TREE + Y	409	62	886	6042	11153	11057
%TREE	0.04%	0.00%	0.08%	0.54%	0.99%	0.96%
%TREE + Y	0.04%	0.01%	0.09%	0.60%	1.12%	1.11%
% HREE	9.42%	27.24%	13.80%	8.31%	8.62%	9.92%
%HREE + Y	20.73%	47.28%	26.94%	17.72%	18.94%	21.55%

Note: All amounts parts per million (ppm). 10,000 ppm = 1% = 10 kg/tonne.
REE Rare Earth Elements: La, Ce, Pr, Nd, Sm, Eu, Gd, Tb, Dy, Ho, Er, Tm, Yb, Lu (Lanthanide Series).
TREE Total Rare Earth Elements: Add La, Ce, Pr, Nd, Sm, Eu, Gd, Tb, Dy, Ho, Er, Tm, Yb, Lu.
LREE Light Rare Earth Elements: Add La, Ce, Pr, Nd, Sm.
HREE Heavy Rare Earth Elements: Add Eu, Gd, Tb, Dy, Ho, Er, Tm, Yb, Lu.
Y Y not included in HREE due to relatively low value compared to most Lanthanide series HREE.
%HREE+Y %(HREE+Y)/(TREE+Y).
%HREE %(HREE/ TREE).
NPR Non-peralkaline Rhyolite.
Low Zr Zr-poor Pantellerite.
High Zr Zr-enriched Pantellerite.
Mafic Mafic to Ultramafic Volcanic Unit.

(Strange Lake; Miller, 1996, Miller et al., 1996; Two Tom Lake syenite; Miller, 1987, 1988), and undersaturated syenites (Red Wine suite; Miller, 1987, 1988). In all these examples, peralkaline rocks, hosting the REE mineralization represent low-volume late differentiates of high-level (crustal) magma chambers. For intrusions the mineralization occurs in late pegmatites, vein systems, or small-volume intrusions at or near the top of the source magma chamber. In the volcanic settings the mineralization occurs as vent filling or near-vent magma flows and/or ash-flow tuffs (Miller, 1993).

Mineralized pantellerites, containing extreme concentrations of REE and other incompatible elements (e.g., Zr, Nb, Y; Table 2), are very rare and must represent extreme differentiation of peralkaline or near peralkaline magma in crustal magma chambers. The 1.3 Ga (Haley, 2014) Foxtrot deposit occurs on 1.5 to 1.6 Ga continental crust (Gower, 2012). The mineralized pantellerite at Foxtrot, using a strike length of 400 m, average width of 20 m and known depth of 500 m (Figs. 2, 3) gives a volume of pantellerite of less than 0.01 km^3. Such small volumes of pantelleritic magma, occurring in a continuous unit, must occur within or near the source vent. Widespread dispersal of this volume of mineralized pantellerite from other vents would result in very thin units, perhaps represented by less than 1 m-thick units throughout the Fox Harbour Volcanic belt.

6. Conclusion

The exploration program at the Foxtrot deposit reveals the relationship between peralkaline volcanic rocks, vent or near-vent locations, and significant REE mineralization. The deposit is being used as a model for further exploration in the Fox Harbour Volcanic belt.

Acknowledgments

Search Minerals personnel and consultants collected data and descriptions used in this manuscript. Permission to publish received from Jim Clucas, Executive Chairman of the Board, and the Board of Directors of Search Minerals. Andrea MacFarlane read an earlier draft of the manuscript. Michaela Neetz and an anonymous reviewer are thanked for suggestions and comments.

References cited

Civetta, L., D'Antonio, M., Orsi, G., and Tilton, G.R., 1998. The geochemistry of volcanic rocks from Pantelleria Island, Sicily channel: petrogenesis and characteristics of the mantle source region. Journal of Petrology, 39, 1453-1491.

Gower, C.F., 2007. Protolith recognition of metamorphosed volcanic/volcaniclastic rocks, with special reference to the Grenville Province in southeast Labrador. In Current Research. Newfoundland and Labrador Department of Natural Resources, Geological Survey, Report 07-1, 11-23.

Gower, C.F., 2010. Geology of the St. Lewis River area (NTS sheets 03D/04 and 05; 13A/01, 02, 07 and 08), southeastern Labrador. Geological Survey, Mines Branch, Department of Natural Resources, Government of Newfoundland and Labrador, Map 2010-24, Open File LAB/1566.

Gower, C.F., 2012. The Grenville Province of southeast Labrador and adjacent Quebec. Geological Association of Canada – Mineralogical Association of Canada, Joint Annual Meeting, St. John's, Field Trip Guidebook – B6, 140 pp.

Gower, C.F., Neuland, S., Newman, M., and Smyth, J., 1987. Geology of the Port Hope-Simpson map region, Grenville Province, eastern Labrador. In Current Research. Newfoundland Department of Mines, Mineral Development Division, Report 87-1, 183-199.

Gower, C.F., van Nostrand, T., and Smyth, J., 1988. Geology of the St. Lewis River map region, Grenville Province, eastern Labrador. In Current Research. Newfoundland Department of Mines, Mineral Development Division, Report 88-1, 59-73.

Haley, J.T., 2014. 1.3 Ga bimodal volcanism in southeastern Labrador: Fox Harbour. Unpublished M.Sc. thesis, Memorial University of Newfoundland, St. John's, Canada, 204p.

Hanmer, S., and Scott, D.J., 1990. Structural observations in the Gilbert River Belt, Grenville Province, southeastern Labrador. In Current Research, Part C. Geologic Survey of Canada, Paper 90-1C, 1-11.

Marshall, A.S., Macdonald, R., Rogers, N.W., Fitton, J.G., Tindle, A.G., Nejbert, K., and Hinton, R.W., 2009. Fractionation of peralkaline silicic magmas: the Greater Olkaria, Volcanic Complex, Kenya Rift Valley. Journal of Petrology, 50, 323-359.

Miller, R.R., 1987. The relationship between Mann-type Nb-Be mineralization and felsic peralkaline intrusives, Letitia Lake Project, Labrador. Newfoundland and Labrador Department of Mines and Energy, Mineral Development Division, Report 87-1, 83-91.

Miller, R.R., 1988. Yttrium (Y) and other rare metals (Be, Nb, REE, Ta, Zr) in Labrador. Newfoundland and Labrador Department of Mines and Energy, Mineral Development Division, Report 88-1, 229-245.

Miller, R.R., 1993. Rare-metal mineralization in the Nuiklavik volcanic rocks of the Flowers River Igneous Suite. Newfoundland and Labrador Department of Mines and Energy, Mineral Development Division, Report 89-1, 363-371.

Miller, R.R., 1996. Structural and textural evolution of the Strange Lake peralkaline rare-element (NYF) granitic pegmatite, Quebec-Labrador. Canadian Mineralogist 34, 349-371.

Miller, R.R., Heaman, L.M. and Birkett, T.C., 1996. U-Pb zircon age of the Strange Lake peralkaline complex: implications for Mesoproterozoic peralkaline magmatism in north-central Labrador. Precambrian Research, 81, 67-82.

Search Minerals Inc., 2010a. Search Minerals Inc. discovers heavy rare earth element mineralization in the Port Hope Simpson REE District, Labrador. <http://searchminerals.mediaroom.com/index.php?s=26366&item=81769>. accessed Oct. 19, 2015

Search Minerals Inc., 2010b. Search Minerals Inc. discovers four new heavy REE showings in Port Hope Simpson REE District, Labrador. <http://searchminerals.mediaroom.com/index.php?s=26366&item=81760>. accessed Oct. 19, 2015.

Search Minerals Inc., 2012. Search Minerals discovers two further REE-Zr-Y-Nb prospects in the Port Hope Simpson REE District, SE Labrador. <http://searchminerals.mediaroom.com/index.php?s=26366&item=125025>. accessed Oct. 19, 2015.

Search Minerals Inc., 2013. Search Minerals announces ten new Foxtrot-like REE prospects in 64 km-long mineralized belt in SE Labrador. <http://searchminerals.mediaroom.com/index.php?s=26366&item=137194>. accessed Oct. 19, 2015

Search Minerals Inc., 2014. Search Minerals announces metallurgical breakthrough for rare earth recovery. <http://searchminerals.mediaroom.com/index.php?s=26366&item=137204>. accessed Oct. 19, 2015.

Search Minerals Inc., 2015a. Search Minerals announces "Critical REE" discovery in the Port Hope Simpson REE District. <http://searchminerals.mediaroom.com/index.php?s=26366&item=137243>. accessed Oct. 19, 2015.

Search Minerals Inc., 2015b. Search Minerals announces successful scale up of proprietary metallurgical process to produce 98.9% purity rare earth oxide product. <http://searchminerals.mediaroom.com/index.php?s=26366&item=137244>. accessed Oct. 19, 2015.

Srivastava, R.M., Gauthier, J., Cox, J.J., and Krutzelmann, H., 2012. Technical report on the Foxtrot Project in Labrador, Newfoundland and Labrador, Canada. Technical Report NI 43-101, Search Minerals Inc., Vancouver, Canada, 174p. <http://www.searchminerals.ca/i/pdf/reports/RPA-Foxtrot-July2012.pdf>. accessed Sept. 25, 2015.

Srivastava, R.M., Gauthier, J., Cox, J.J., and Krutzelmann, H., 2013. Technical report on the Foxtrot Project in Labrador, Newfoundland and Labrador, Canada. Technical Report NI 43-101, Search Minerals Inc., Toronto, Canada, 203p. <http://www.searchminerals.ca/i/pdf/reports/RPA-Foxtrot-May2013.PDF>. accessed Sept. 25, 2015.

The hydrothermal mobility of the rare earth elements

A.E. Williams-Jones[1]

[1] Department of Earth and Planetary Sciences, McGill University, Montreal, QC, Canada
[a] corresponding author: anthony.williams-jones@mcgill.ca

Recommended citation: Williams-Jones, A.E., 2015. The hydrothermal mobility of the rare earth elements. In: Simandl, G.J. and Neetz, M., (Eds.), Symposium on Strategic and Critical Materials Proceedings, November 13-14, 2015, Victoria, British Columbia, British Columbia Ministry of Energy and Mines, British Columbia Geological Survey Paper 2015-3, pp. 119-123.

Extended Abstract

Although magmatic processes commonly control the formation of REE ores, in many deposits the REE have been remobilized by hydrothermal fluids, and some are almost exclusively hydrothermal in origin. Genetic models for the hydrothermal transport and deposition of the REE generally assume that the REE are transported mainly as fluoride complexes. This is partly because of a common association of hydrothermal REE mineralization with fluorite and partly because aqueous REE-fluoride complexes are more stable than REE species involving most other plausible ligands. As a result, the potential role of these other ligands in transporting the REE to sites of ore formation has largely been ignored. This contribution evaluates the nature of hydrothermal REE transport, and the processes of REE mineral deposition in chlorine-, fluorine-, and sulphate-bearing hydrothermal fluids.

Hydrothermal fluids appear to have concentrated the REE in numerous deposits. For example, the Gallinas Mountains deposit, New Mexico, USA, is an exclusively hydrothermal light REE deposit of marginal economic interest in which a fluorite-bastnäsite-(Ce)-barite assemblage cemented quartz-syenite, rhyolite porphyry and sandstone breccias (Fig. 1). Based on a detailed study of fluid inclusions, the deposit is interpreted to have formed between 300 and 400ºC from brines containing 12 to 18 wt.% NaCl equivalent (Williams-Jones et al., 2000). Although the source of the mineralizing fluids is uncertain, it is inferred to be the magma that crystallized the quartz syenite or rhyolite porphyry. However, some researchers (e.g., Schreiner, 1993) have speculated that the fluids may have originated from a hidden carbonatite. In contrast, the Browns Range deposit, Australia, is a predominantly heavy REE hydrothermal deposit that hosts a potentially economic resource containing 8.98 million tonnes of ore grading 0.63 wt.% total REE oxide, of which the heavy REE make up 85%. The REE mineralization is hosted by hematite-altered meta-sandstones in veins and breccias or as disseminations, and takes the form of xenotime-(Y) and minor florencite-(Ce). The geological context is poorly known because of poor outcrop, but the presently accepted interpretation is that the mineralizing system was emplaced along a failed continental rift, and that the source of the fluids was a granitic magma (Cook et al., 2013). The Wicheeda deposit, British Columbia, Canada, is an example of a carbonatite-hosted light REE deposit (LREE) containing 11.3 million tons, grading 1.95 wt.% total REE oxide (Trofanenko et al., in press). The REE mineralization, mainly bastnäsite-(Ce), occurs with dolomite mostly in vugs and veins in dolomite-carbonatite that forms the core of a small intrusion with a marginal calcite carbonatite facies. Proximal potassic and distal sodic fenites surround the intrusion; the potassic fenites host very minor REE mineralization in the form of monazite-(Ce). On the basis of its mode of occurrence, the REE mineralization is interpreted to be hydrothermal or carbo-hydrothermal, an interpretation that is supported by carbon and oxygen isotopic data (Trofanenko et al., in press). The latter suggest that the fluids originated from a carbonatite magma, which 'stewed in its own juices' and deposited the ores at a temperature between 300 and 400°C.

Fig. 1. Bastnäsite (beige rectangular crystals) cemented by fluorite in a sample of sandstone-hosted breccia (numerous small irregularly shaped fragments) from the Gallinas Mountains deposit, New Mexico.

At several important deposits, hydrothermal fluids remobilized magmatically concentrated REE. An example is the Nechalacho deposit in the Northwest Territories, which is hosted by a layered, silica-undersaturated alkaline complex (varieties of nepheline syenite), and contains a resource of 62 million tonnes grading 1.65 wt.% total REE oxide (22% HREE) and 0.4 wt.% Nb oxide (Sheard et al., 2012; Ciuculescu et al., 2013). There, the primary magmatic REE mineralization formed as a result of gravity settling of eudialyte (a complex

zirconosilicate containing ~7 wt.% REE_2O_3) and zircon (containing ~3 wt.% REE_2O_3) in the upper parts of the layered suite during the end stages of crystallization (Sheard et al., 2012). This crystallization culminated with the exsolution of orthomagmatic hydrothermal fluids that altered the mineralized horizon and overlying rocks to a biotite-magnetite assemblage. These fluids dissolved the primary ore minerals and re-precipitated the REE as fergusonite-(Y), secondary zircon, allanite-(Ce), bastnäsite-(Ce) and monazite-(Ce) together with fluorite. The HREE were deposited proximal to the precursor minerals, whereas the LREE were mobilized upwards on a scales of metres and perhaps 10s of metres.

Experimental studies have shown that the REE form very stable fluoride complexes in hydrothermal fluids, that REE-sulphate complexes have lower stability, and that REE complexes with chloride ions are less stable than with the other two ligands (Migdisov and Williams-Jones, 2008; Migdisov et al., 2009). Experimental data on the stability of other potentially important REE complexes, such as those involving carbonate, are lacking. However, theoretical calculations suggest that the stability of REE-carbonate complexes is comparable to that of REE-fluoride complexes. The experimental studies have shown that the stability of the REE fluoride and chloride complexes decreases with increasing atomic number of the lanthanides, implying that the light REE are likely to be more mobile than the heavy REE (Fig. 2). This effect, however, is not observed with sulphate complexes.

In some cases, such as the Gallinas Mountains deposit, the fluids were chloride-bearing brines which, from the association of the ores with fluorite and in some cases barite, also may have contained significant fluorine and sulphate ions. Unfortunately, the only reliable measurements of the fluorine and sulphate concentrations of fluids known to have precipitated REE minerals are those of Banks et al. (1994). These fluids contained ~500 ppm F and ~2 wt.% $SO4^{2-}$. We have modelled the transport of the REE for a fluid containing these concentrations of fluoride and sulphate and a concentration of chloride equivalent to 10 wt.% NaCl, and temperatures up to 400°C. From this modelling, it is evident that significant concentrations of REE (>10 ppm) can only be transported as chloride complexes and at low pH, or as sulphate complexes at mildly acidic pH and high temperature (Fig. 3). There are no conditions at which fluoride complexes can transport significant REE, and the reason for this is that at low pH, fluoride activity is low because HF is a weak acid and at higher pH, saturation of the fluid with fluocerite buffers fluoride activity to very low values. The modelling also showed that REE ore deposition is promoted by a decrease in temperature (Fig. 4) and an increase in pH. Although the REE form very stable complexes with carbonate ions, we do not consider that carbonate complexes are significant in REE transport. On the contrary, because of the very low solubility of bastnäsite-(Ce) (Williams-Jones, et al., 2012; Migdisov and Williams-Jones, 2014; Gysi and Williams-Jones, 2015), the main role of carbonate ions is to promote REE ore deposition. The same is also true of fluoride

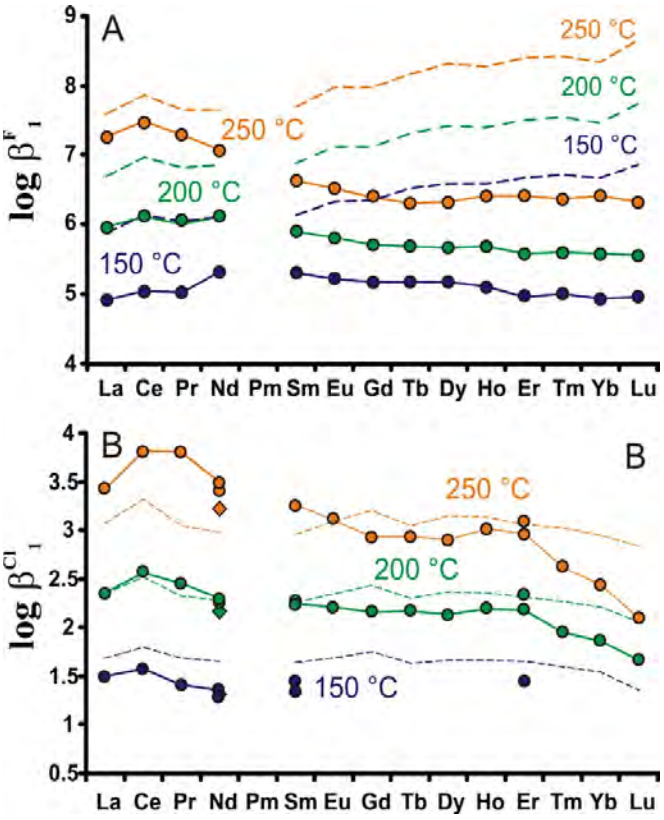

Fig. 2. Stability constants for **a)** $REEF^{2+}$ and **b)** $REECl^{2+}$ at elevated temperature. The solid lines represent experimentally derived values from Migdisov et al., (2009) and the dashed lines, theoretical estimates from Haas et al. (1995). The experimental data show that the REE are more stable as REE-fluoride complexes than REE chloride complexes, and that overall their stability decreases with increasing atomic number, i.e., from light REE to heavy REE. The comparison with the theoretical estimates emphasizes the danger inherent in extrapolating to higher temperature based on experimental determinations made at ambient temperature.

ions as inferred above. In principle, the REE should form strong complexes with phosphate ions because the REE are hard cations and phosphate is a hard anionic species (Williams-Jones and Migdisov, 2014). However, both monazite-(Ce) and xenotime-(Y), the main REE phosphate ore minerals, are extremely insoluble (Migdisov and Williams-Jones, 2014; Gysi et al., 2015). It therefore follows that the main role of phosphate ions in hydrothermal ore formation, like that of fluoride and carbonate ions, is not to transport the REE but rather to facilitate their deposition.

Because the light REE form much more stable complexes in chloride-bearing solutions, they will be more mobile than the heavy REE, as shown for the Nechalacho REE deposit. Modelling of the solubility of various end-members of monazite in an environment of decreasing temperature and increasing fluid-rock interaction confirms this observation. The modelling shows that the heavier REE-bearing monazite end members will be deposited at high temperature close to the point of fluid input, whereas monazite-(La) will deposit at locations

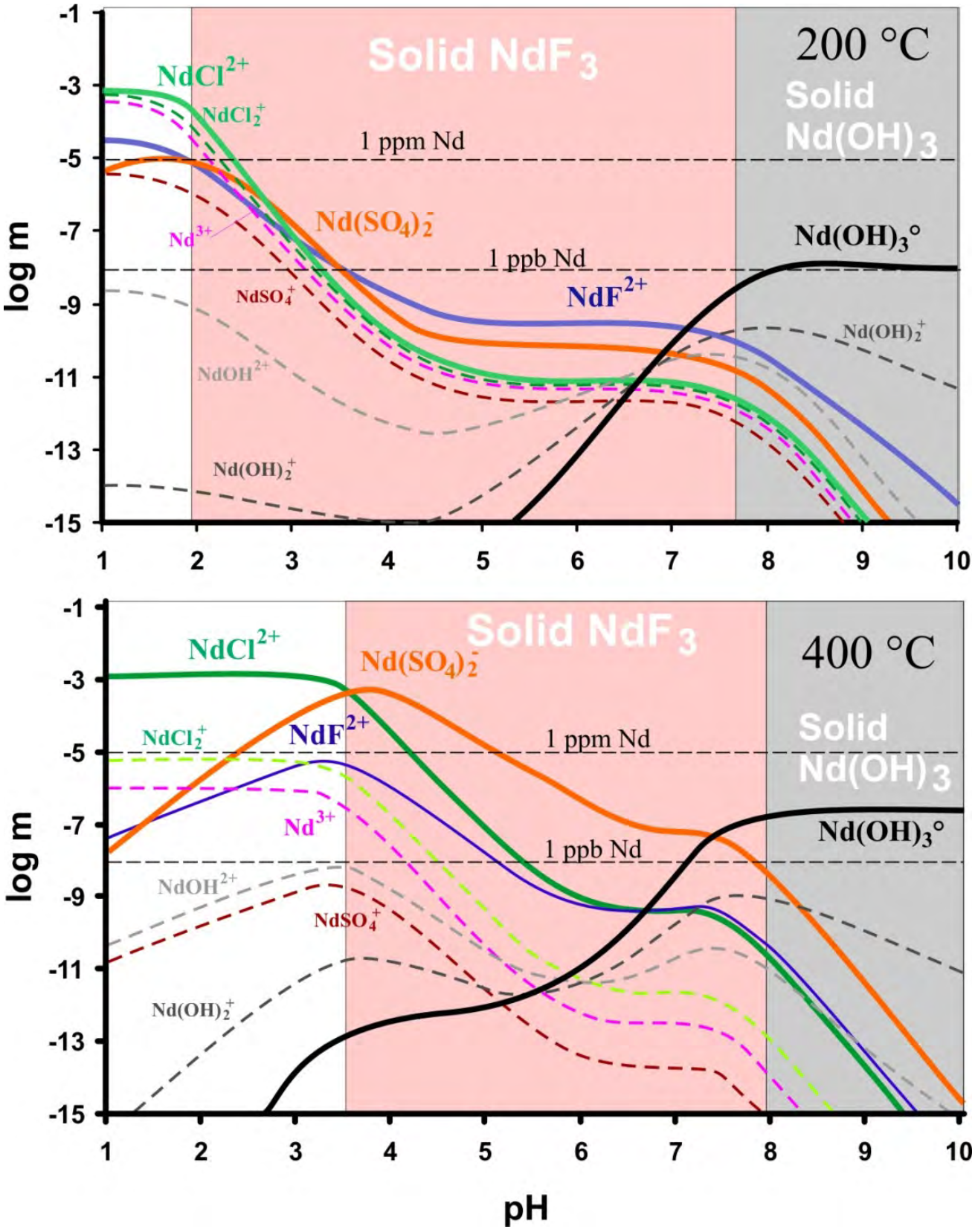

Fig. 3. The speciation of Nd as a function of pH, assuming that the fluid contains 10 wt.% NaCl, 2 wt.% Na_2SO_4, 500 ppm F, 200 ppm Nd (See Banks et al., 1994). The pink region shows conditions for which Nd-solubility is buffered by the precipitation of NdF_3 and the blue region for which it is buffered by precipitation of $Nd(OH)_3$.

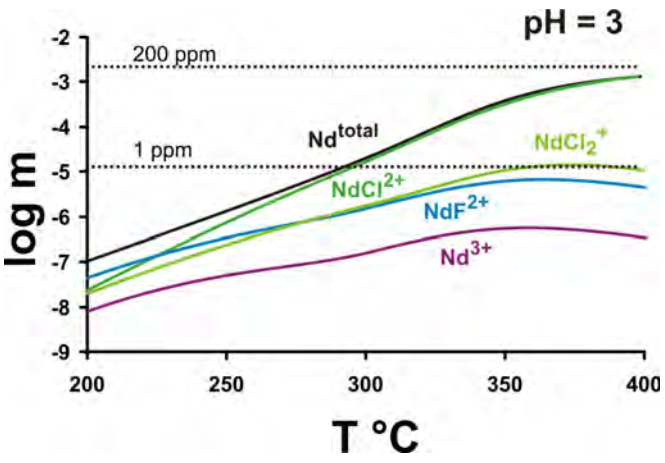

Fig. 4. The solubility of Nd as a function of temperature, assuming that the fluid contains 10 wt.% NaCl, 500 ppm F, 200 ppm Nd (See Banks et al., 1994).

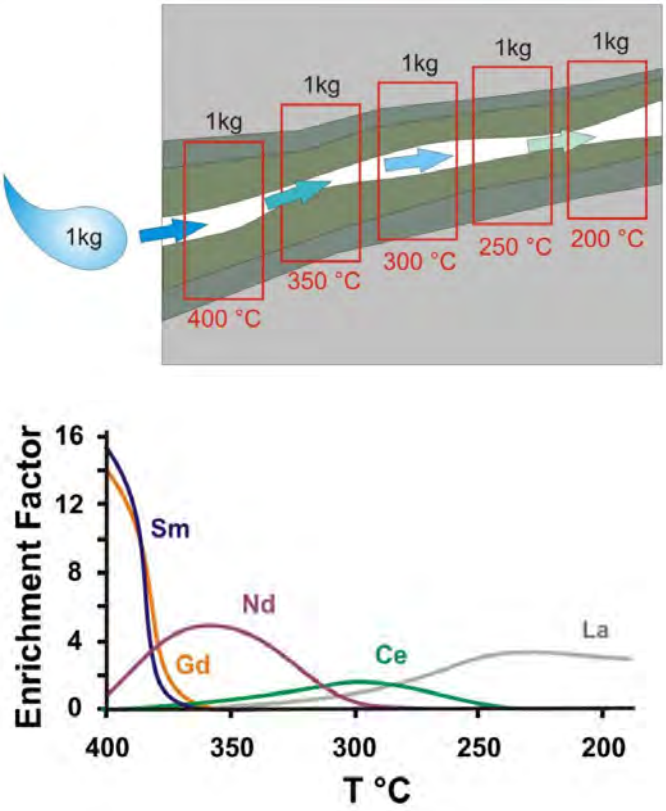

Fig. 5. A model of the fractionation of the REE as a result of fluid-rock interaction. Consecutive 1 Kg aliquots of a fluid containing 10 wt.% NaCl, 500 ppm F, and 50 ppm are introduced along a thermal gradient into 1 Kg of nepheline syenite containing 100 ppm P (illustrated by the cartoon). This results in the deposition of monazite in decreasing proportions away from the fracture due to the increasing pH (bands coloured by shades of green). Each red box defines a region at constant temperature. The binary diagram illustrates the enrichment of the rock in each of the REE after the introduction of five aliquots of fluid. As is evident, La is most enriched at low temperature, i.e., distal from the source, whereas Sm and Gd are most enriched at the source. Thus the light REE are more mobile than the heavy REE. The enrichment factor is $(REE/\Sigma REE)_{Rock}/(REE/\Sigma REE)_{Initial\ solution}$.

distal from the point of fluid input and at lower temperature (Fig. 5). An important question concerning the Browns Range REE deposit is why its mineralization is so rich in heavy REE, particularly given that almost any conceivable ore fluid will be enriched in the light REE relative to the heavy REE; the light REE have much greater crustal abundance than the heavy REE. A possible answer to this question is that the deposit formed relatively close to the source of fluid input and that the host-rocks (sandstones) had limited capacity to buffer the pH of the fluid to higher pH. In such a scenario, the light REE would have been transported to crustal levels above the current level of erosion, whereas the heavy REE would have been deposited in the rocks immediately above the granite, which is inferred to have been the source of the fluids.

To conclude, in many environments where hydrothermal processes play a role in ore formation, the REE are transported predominantly as REE-chloride complexes. In these cases, ore deposition will be promoted by processes that increase pH and decrease temperature such as interaction with cold rocks having high pH buffering capacity (e.g., marbles and limestones), boiling (which decreases temperature and increases the pH of the ore fluid) and fluid mixing (e.g., with a lower temperature external fluid of higher pH). Finally, fluids transporting the REE as chloride complexes will fractionate the REE to varying degrees depending on the pH buffering capacity of the host rocks. This could explain why deposits such as Browns Range (hosted by rocks with low pH buffering capacity) are enriched in the heavy REE, whereas others are light REE-enriched (hosted by rocks with higher pH buffering capacity).

References cited

Banks, D.A., Yardley, B.W.D., Campbell, A.R., and Jarvis, K.E., 1994. REE composition of an aqueous magmatic fluid: A fluid inclusion study from the Capitan Pluton, New Mexico, U.S.A.. Chemical Geology, 113, 259-272.

Ciuculescu, T., Foo, B., Gowans, R., Jacobs, C., and Spooner, J., 2013. Technical report disclosing the results of the feasibility study of the Nechalacho rare earth element project, 291 p. http://www.avalonraremetals.com/_resources/projects/may_2013_ni43_report.pdf> accessed October 1, 2015.

Cook, N.J., Ciobanu, C.L., O'Reilly, D., Wilson, R., Das, K., and Wade, B., 2013. Mineral chemistry of rare earth element (REE) mineralization, Browns Range, Western Australia. Lithos, 172-173, 192-213.

Gysi, A.P., and Williams-Jones, A.E., 2015. The thermodynamic properties of bastnäsite-(Ce) and parisite-(Ce). Chemical Geology, 392, 87-101.

Gysi, A.P., Williams-Jones, A.E. and Harlov, D., 2015. The solubility of xenotime-(Y) and other HREE phosphates ($DyPO_4$, $ErPO_4$ and $YbPO_4$) in aqueous solutions from 100 to 250°C and psat. Chemical Geology, 41, 83-95.

Migdisov, A.A., and Williams-Jones, A.E., 2008. A spectrophotometric study of Nd(III), Sm(III) and Er(III) complexation in sulphate-bearing solutions at elevated temperatures. Geochimica et Cosmochimica Acta, 72, 5291-5303

Migdisov, A.A., Williams-Jones, A.E., and Wagner, T., 2009. An experimental study of the solubility and speciation of the rare earth elements (III) in fluoride- and chloride-bearing aqueous solutions at temperatures up to 300ºC. Geochimica et Cosmochimica Acta, 73, 7087-7109.

Migdisov, A.A., and Williams-Jones, A.E., 2014. Hydrothermal transport and deposition of the rare earth elements by fluiorine-bearing aqueous liquids. Mineralium Deposita, 49, 987-997.
Schreiner, R.A., 1993. Mineral investigation of the rare earth-element-dearing deposits, Red Cloud mining district, Gallinas Mountains, Lincoln County, New Mexico. United States Bureau of Mines, Open File Report, 99-93, 189 p.
Sheard, E.R., Williams-Jones, A.E., Heiligmann, M., Pederson, C., and Trueman, D.L., 2012. Controls on the concentration of zirconium, niobium and the rare earth elements in the Thor Lake rare metal deposit, Northwest Territories, Canada. Economic Geology, 107, 81-104.
Trofanenko, J., Williams-Jones, A.E., Simandl, G., and Migdisov, A.A., in press. The nature and origin of the REE mineralization in the Wicheeda carbonatite, British Columbia, Canada. Economic Geology.
Williams-Jones, A.E., Samson I.M, and Olivo, G.R., 2000. The genesis of hydrothermal fluorite-REE deposits in the Gallinas Mountains, New Mexico. Economic Geology, 95, 327-342.
Williams-Jones, A.E., Migdisov, A.A., and Samson, I.M., 2012. Hydrothermal mobilization of the rare earth elements – a tale of “Ceria” and “Yttria”. Elements, 8, 355-360.
Williams-Jones, A.E., and Migdisov, A.A., 2014. Experimental constraints on the transport and deposition of metals in hydrothermal ore-forming systems. Society of Economic Geologists, Special Publication 18, 77-95.

Hydrothermal fractionation of the rare earth elements and the genesis of the Lofdal REE deposit, Namibia

A.E. Williams-Jones[1, a], R. Wollenberg[1], and S. Bodeving[1]

[1] Department of Earth and Planetary Sciences, McGill University, Montreal, QC, Canada
[a] corresponding author: anthony.williams-jones@mcgill.ca

Recommended citation: Williams-Jones, A.E., Wollenberg, R., and Bodeving, S., 2015. Hydrothermal fractionation of the rare earth elements and the genesis of the Lofdal REE deposit, Namibia. In: Simandl, G.J. and Neetz, M., (Eds.), Symposium on Strategic and Critical Materials Proceedings, November 13-14, 2015, Victoria, British Columbia, British Columbia Ministry of Energy and Mines, British Columbia Geological Survey Paper 2015-3, pp. 125-130.

Extended Abstract

The Lofdal rare earth element (REE) deposit in northern Namibia, which is currently being explored by Namibia Rare Earths Inc., is of particular interest because of its unusually high proportion of heavy REE (more than 85%) and because previous research concluded that it was carbonatite-hosted (Wall et al., 2008). This would make the deposit highly unusual because, almost invariably, carbonatite-hosted deposits contain mainly light-REE (Castor, 2008; Moore et al., 2014; and Trofanenko et al., in press). However, as we show below, the Lofdal REE mineralization is not carbonatite-hosted. Instead, it occurs in narrow veinlets in albitite that has been subjected to later carbonate alteration, and thus the host rocks and their REE mineralization are hydrothermal in origin.

The Lofdal deposit, in the Damara Orogen of northern Namibia, is spatially associated with the Lofdal Intrusive suite, a group of alkaline silicate rocks and carbonatites that were emplaced at ~750 Ma during an episode of continental rifting, which preceded the orogeny (de Kock et al., 2000). The suite intrudes Paleoproterozoic schists, gneisses, and amphibolites of the Welwitschia inlier which, together with the Kamenjab and Braklaagte inliers, forms the southern edge of the Archean Congo Craton (Miller, 2008). Several plutons and numerous NW-SE trending dikes follow the regional foliation (Fig. 1). The largest of the plutons is the Main Intrusion (~2 km in diameter), which is composed of an early nepheline syenite facies and a later but subordinate calcio-carbonatite facies. The contact between the two facies is invariably marked by a zone of fenitised nepheline syenite. The dikes form a swarm ~5 km wide that extends ~10 km along strike. They comprise phono-tephrite, phonolite and carbonatite. However, the carbonatite dikes, are largely restricted to within ~1 km of the Main Intrusion. In addition to the carbonatites, many faults follow the regional foliation and are sites where basement gneisses and schists were albitized. Subsequent intense carbonate alteration (both calcite and dolomite) replaced much of the albitite. Weathering of these rocks, which also contain pyrite, produced brown, grey, and red zones that form ridges up to two metres wide and a metre high (Fig. 2). It is these rocks that have been misinterpreted by previous researchers as ferrocarbonatite dikes, and host the REE mineralization.

The Lofdal REE deposit is one of a number of zones in the area with elevated concentrations of REE, but the only one currently deemed to have economic potential. This zone, which is referred to as Area 4 by Namibia Rare Earths Ltd. (Fig. 3), has measured and indicated reserves of 1.65 million tons of ore grading 0.60 wt.% total rare earth oxide with 85.4% heavy REE (Dodd et al., 2014) and is second only to Browns Range, Australia, in having the highest proportion of heavy REE among 50 deposits worldwide currently at an advanced stage of exploration. The heavy REE mineralization occurs as xenotime-(Y), which is mainly concentrated in discontinuous millimetre-wide veinlets that cut albitite and also contain biotite, calcite and, in some cases, pyrite and zircon (Fig. 4). Some of this mineralization is in biotite-rich shear zones in albitite, some is disseminated in albitite, and some is in fluorapatite veinlets, where it occurs at triple junctions of apatite crystals that have incorporated REE at their rims. As mentioned above, the albitites and their REE mineralization have been subjected to carbonate alteration. The intensity of this alteration increases upwards and, at the erosional surface, has largely obliterated the textures of the precursor rocks, creating an impression that the xenotime-(Y) occurs mainly as disseminations in calcite or dolomite. In addition to the heavy REE mineralization, there is also light REE mineralization in the form of monazite-(Ce). This mineralization is concentrated mainly in biotite-calcite±pyrite veinlets that cut amphibolites and mafic dikes immediately outside the confines of the albitized Area 4 fault, although some is seen along the fault beyond the limits of the potentially economic mineralization. The latter also occurs in biotite-calcite±pyrite veinlets, but instead of the veinlets being hosted by albitite, they occur in thin carbonatite dikelets or mafic rocks in the fault zone.

The occurrence of the REE mineralization in biotite-calcite veinlets (with or without pyrite) provides clear evidence for a hydrothermal origin. The source of the mineralizing fluids, however, is much less clear. Given the close global spatial association of REE-mineralized rocks to continental rift-related alkaline silicate and carbonatite intrusions, and the observation that such rocks are commonly enriched in REE (e.g., Sørensen,

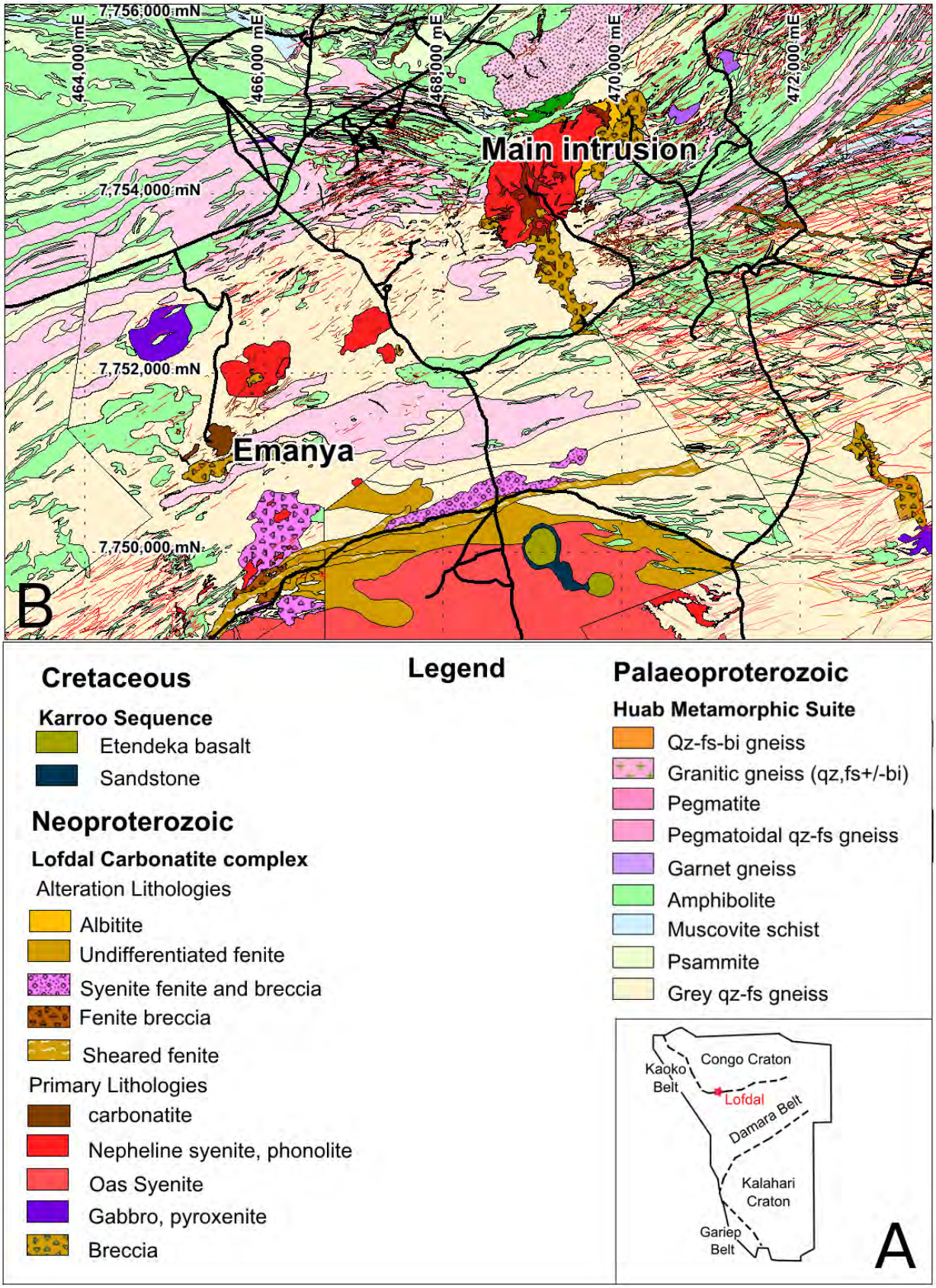

Fig. 1. a) Location of the Lofdal intrusive suite in an outlier of the Congo Craton. **b)** Geological map of the Lofdal field area showing the distribution of alkaline rocks and carbonatites, which intrude upper amphibolite to granulite facies gneisses of the Huab metamorphic complex. The map was prepared by Namibia Rare Earths Inc.

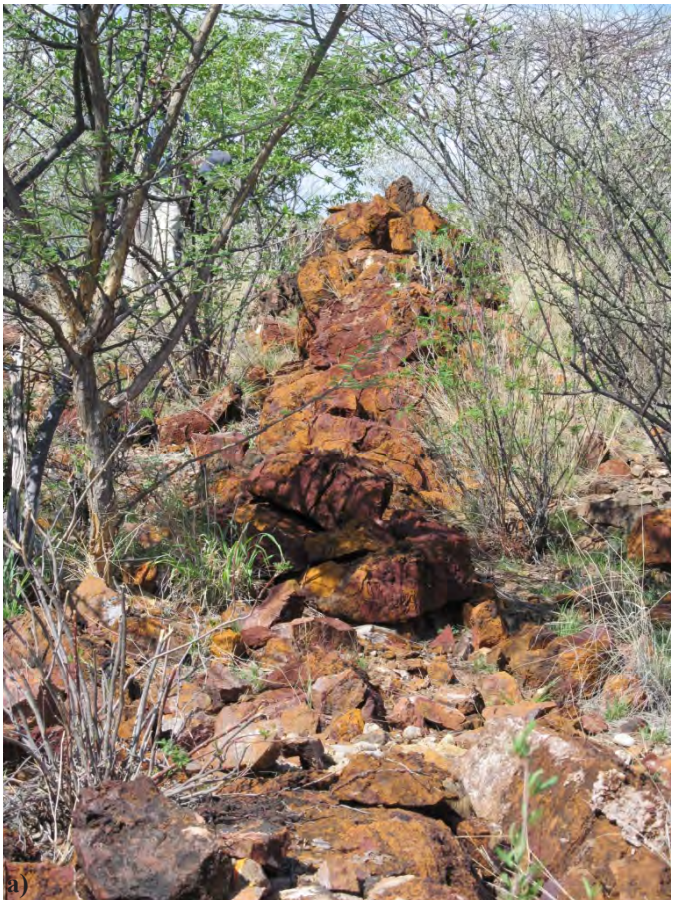

Fig. 2. a) A REE-mineralized fault breccia previously interpreted to be a ferrocarbonatite dike is instead a fault-controlled sodic fenite (albitite) that has been altered to calcite. The red colour reflects the oxidation of pyrite.

Fig. 2. b) A thin, carbonate altered fault breccia surrounded by albitite.

1992; Sheard et al., 2012), it seems likely that magmas generated during Neoproterozoic rifting sourced the Lofdal REE fluids. On the basis of trace element and isotopic data, we consider that these rocks are of mantle origin. Significantly, the data show that they are also cogenetic. Indeed, their geochemistry is best explained by a model in which small degrees of partial melting of a carbonate-metasomatised mantle produced a phono-tephrite parent magma that evolved by fractional crystallization to phonolite and their plutonic equivalent, nepheline syenite, and ultimately calcio-carbonatite. This genesis is particularly evident from chondrite-normalized REE profiles that have the same shape for the three rock types, and a weak trend of increasing La/Lu ratios from phono-tephrite through phonolite to calcio-carbonatite (La, with a much larger charge/radius ratio than Lu, is the more incompatible element and thus is predicted to be most enriched in the most fractionated magma, i.e., the calcio-carbonatite magma); the calcio-carbonatites are the most enriched in the REE of the three rock-types. However, all three rock types are preferentially enriched in the light REE and thus any fluid exsolved from them would be expected to be light REE-enriched. By contrast, the Lofdal REE deposit, as noted above, is extremely rich in the heavy REE. The alternative would be to call upon a magma that is not represented by the igneous rock-types observed at surface, but this just transfers the problem. Furthermore, to our knowledge, no igneous rocks on the planet contain heavy REE in proportions even approaching those at Lofdal. It therefore seems more reasonable to attribute the source of the REE to a magma corresponding to one of the three igneous rock-types referred to above. As the calcio-carbonatites contain the highest proportions of the REE and their chondrite-normalized REE profiles have the same shapes as the other two rock-types, we consider that the calcio-carbonatite magma is the most plausible source for the REE-bearing fluids. Normally, such a choice would be unreasonable, as most carbonatites display strong depletions in the heavy REE. In marked contrast, the Lofdal calcio-carbonatites have chondrite-normalized REE profiles that are effectively flat from gadolinium to lutetium, and therefore the corresponding magmas could have contributed significant heavy REE to an orthomagmatic mineralizing fluid (Fig. 5). Assuming that a calcio-carbonatite magma was the source of the mineralizing fluid, it therefore follows that the reason for the hyper-enrichment of the potential ores must lie in the hydrothermal process that gave rise to the deposit.

Recent experimental data and thermodynamic modelling have shown convincingly that, in most geological settings, the

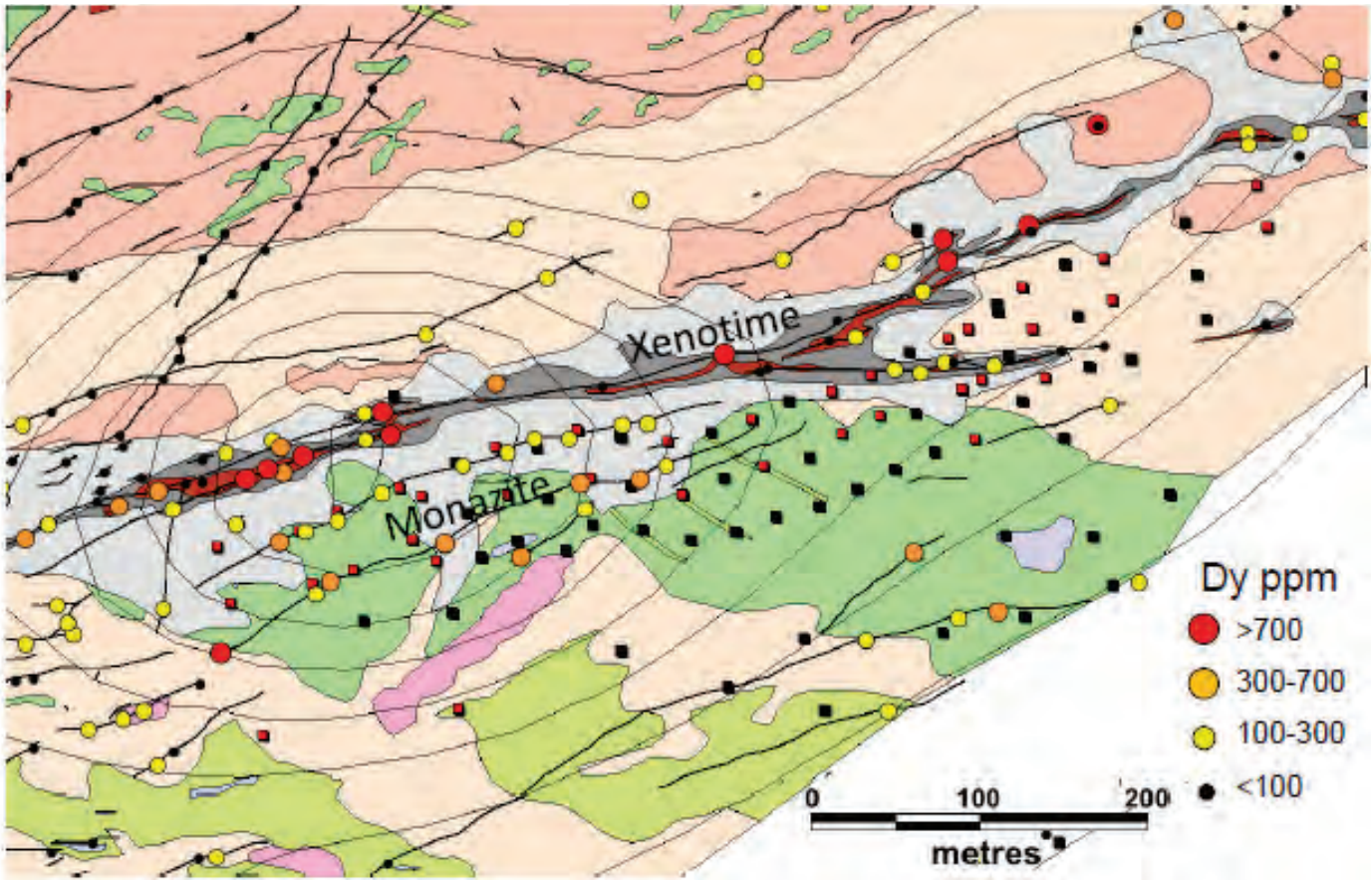

Fig. 3. Distribution of dysprosium in surface samples of the potential ore zone on the Lofdal property. The dark grey denotes a zone of intensely fenitised Huab gneisses adjacent to a fault; the surrounding light grey area is a zone of weaker fenitization. The other lithological units are: amphibolite (green); calc-silicate gneiss (apple green); granitic gneiss (light pink); quartzofeldspathic gneiss (tan) and pegmatite (pink).

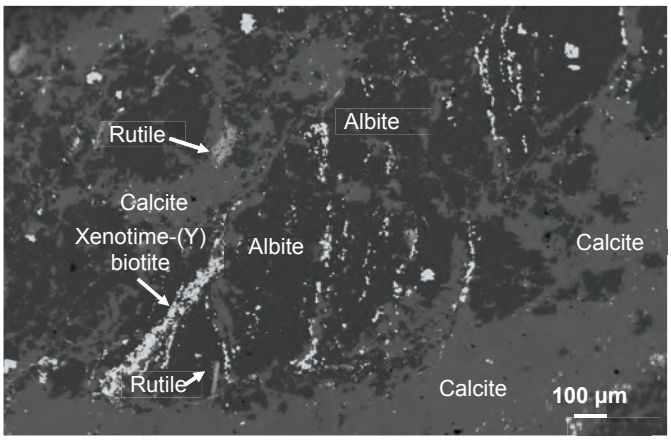

Fig. 4. Albitite cut by xenotime-(Y)-biotite veins and, in turn, replaced by calcite.

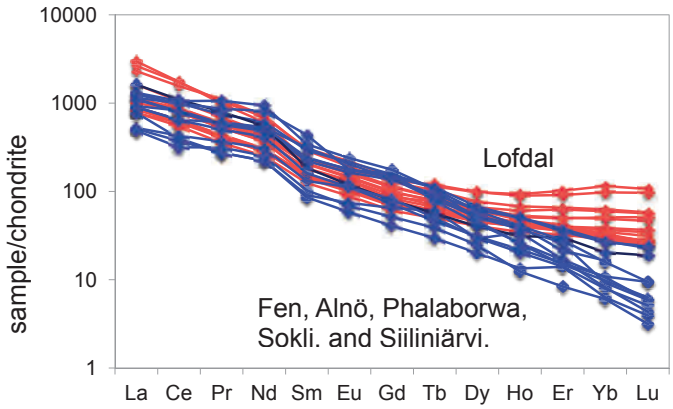

Fig. 5. Chondrite-normalised REE profiles for Lofdal calcio-carbonatites compared with those of other carbonatites.

REE are transported mainly as chloride complexes (Migdisov et al., 2009; Williams-Jones et al., 2012; and Migdisov and Williams-Jones 2014). Furthermore, the experimental data show that chloride complexes of the light REE are considerably more stable than those of the heavy REE, and that this difference in stability increases with increasing temperature. Thus, hydrothermal fluids in which the REE are transported as chloride complexes have the capacity to strongly fractionate the REE by preferentially mobilizing the light REE to locations that are considerably more distal from their source than those in which the heavy REE are concentrated. The main factors controlling the deposition of REE minerals are decreasing temperature, increasing pH, and the activities of the transporting and depositional ligands (Williams-Jones et al., 2012; and Migdisov and Williams-Jones 2014).

A model for the genesis of the Lofdal REE deposit must explain both the albitization and the occurrence of the REE in biotite-calcite veinlets, mainly as xenotime-(Y) but in places as monazite-(Ce). An important feature of carbonatite magmas is that they exsolve carbo-hydrothermal fluids, which are responsible for fenititisation of the host rocks. Indeed, the Lofdal carbonatites that intruded the nepheline syenites in the Main Intrusion are surrounded by haloes of fenitised nepheline syenite. Depending on the temperature, fenites may be sodic or potassic and, in the case of felsic host rocks, the fenitisation may involve albitization or K-feldspathization (Kresten, 1988; Williams-Jones and Palmer, 2002; Le Bas, 2008). Commonly but not universally, the sodic fenitisation is early and occurs at higher temperature than the potassic fenitisation; the same is true of sodic and potassic alteration in porphyry systems (Le Bas, 2008; Sillitoe, 2010).

In view of the above, we propose that albitization at Lofdal, which was focussed along faults, was produced by early high-temperature carbo-hydrothermal fluids exsolved from a carbonatite magma emplaced below these structures, and that the biotite-calcite veins and biotite-filled shear zones, which host the REE mineralization and cut the albitites, formed from the same fluids as temperature decreased. Late carbonate alteration was the product of relatively cold orthomagmatic carbo-hydrothermal fluids. According to this model, REE mineral deposition was due in large part to the decrease in temperature. This, however, does not explain the REE fractionation, namely why the core of the deposit is so rich in heavy REE and the distal parts in light REE. For this, we turn to pH. As was noted earlier, REE-mineral deposition is favoured by increasing pH, and as was also noted, the heavy REE mineralization (xenotime-(Y)) is hosted exclusively by albitite, whereas the light REE mineralization (monazite-(Ce)) is hosted by carbonatite dikes, amphibolites and mafic dikes, which have much higher capacity to buffer pH than albitite. We therefore propose that in the albitites, where the capacity to buffer pH was very low, the fluids transported the light REE above the present erosional surface, precipitating only the less mobile heavy REE, whereas in rocks with much higher pH buffer capacity, both light and heavy REE were deposited in the proportions in which they were present in the fluid, thereby ensuring light-REE dominated mineralization (Fig. 6).

In summary, contrary to previously reported research, the heavy REE mineralization at Lofdal, Namibia, is not hosted by carbonatites but by albitites developed along faults. However, the source of fluids responsible for albitization and REE mineralization was a carbonatite magma. We propose a model in which early carbo-hydrothermal fluids albitized quartzofeldspathic gneisses and, on cooling, deposited xenotime-(Y)-bearing biotite-calcite±pyrite veins. The poor pH buffering capacity of the albitite ensured that that only the heavy REE deposited. Outside the the main faults or along strike from the main REE mineralization, where the fluids encountered carbonatites, amphibolites and mafic dikes, the higher pH buffering capacity of these rocks caused the fluids

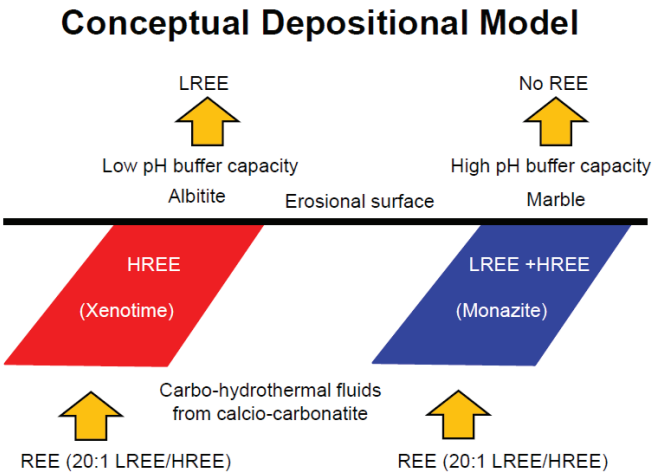

Fig. 6. Conceptual model for the formation of the Lofdal HREE deposit from carbonatite-derived carbo-hydrothermal fluids.

to deposit both light and heavy REE (monazite-(Ce)) in the proportions that they were originally present. This model likely explains the genesis of other heavy REE deposits where hydrothermal processes were predominant.

References cited

Castor, S.B., 2008a. Rare earth deposits of North America. Resource Geology, 58, 337-347.

Castor, S.B., 2008b. The Mountain Pass rare-earth carbonatite and associated ultrapotassic rocks, California. The Canadian Mineralogist 46, 779-806.

de Kock, G.S., Eglington, B., Armstrong, R.A., Harmer, R.E., Walraven, F., 2000. U-Pb and Pb-Pb ages of the Naauwpoort rhyolite, Kawakeup leptite and Okongava Diorite: implications for the onset of rifting and of orogenesis in the Damara belt, Namibia. Communications of the Geological Survey of Namibia, 12, 89-97.

Dodd, D.S., Siegfried, P.R., Hall, M.R., Hannon, P., Roy, W.D., 2014. Preliminary economic assessment of the Lofdal Rare Earths Project Namibia. http://www.namibiarareearths.com/upload/5. November_14_2014_NREI_Files_43-101_PEA_Report_for_ Heavy_Rare_Earth_Mine_at_Lofdal.pdf> accessed October 1, 2015.

Kresten, P., 1988. The chemistry of fenitization: Examples from Fen, Norway. Chemical Geology, 68, 329-349.

Le Bas, M.J., 2008. Fenites associated with carbonatites. The Canadian Mineralogist, 46, 915-932.

Migdisov, A.A., and Williams-Jones, A.E., 2014. Hydrothermal transport and deposition of the rare earth elements by fluorine-bearing aqueous liquids. Mineralium Deposita 49, 987-997.

Migdisov, A.A., Williams-Jones, A.E., Wagner, T., 2009. An experimental study of the solubility and speciation of the rare earth elements (III) in fluoride- and chloride-bearing aqueous solutions at temperatures up to 300ºC. Geochimica et Cosmochimica Acta 73, 7087-7109.

Miller, R.McG., 2008. The Geology of Namibia. Ministry of Mines and Energy, Geological Survey, Windhoek, Volumes 1-3.

Moore, M., Chakhmouradian, A.R., Mariano, A.N., and Sidhu, R., 2014. Evolution of rare earth mineralization in the Bear Lodge carbonatite, Wyoming: Mineralogical and isotopic evidence. Ore Geology Reviews, 64, 499-521.

Sheard, E. R., Williams-Jones, A. E., Heiligmann, M., Penderson, C., and Trueman, D. L., 2012. Controls on the concentration of zirconium, niobium, and the rare earth elements in the Thor Lake

rare metal deposit, Northwest Territories, Canada. Economic Geology, 107, 81–104.
Sillitoe, R.H., 2010. Porphyry copper systems. Economic Geology, 105, 3-41.
Sørensen, H., 1992. Agpaiitic nepheline syenites: A potential source of rare elements. Applied Geochemistry, 7, 417-427.
Trofanenko, J., Williams-Jones, A.E., Simandl, G.J. Migdisov, A.A., in press. The nature and origin of the REE mineralization in the Wicheeda carbonatite, British Columbia, Canada. Economic Geology.
Wall, F., Niku-Paavola, V.N., Storey, C., Müller, A., and Jeffries, T., 2008. Xenotime-(y) from carbonatite dykes at Lofdal, Namibia: Unusually low LREE:HREE ratio in carbonatite, and the first dating of xenotime overgrowths on zircon. The Canadian Mineralogist, 46, 861-877.
Williams-Jones, A.E., and Palmer, D., 2002.The evolution of aqueous–carbonic fluids in the Amba Dongar carbonatite, India: implications for fenitisation. Chemical Geology, 185, 283-301.
Williams-Jones, A.E., Migdisov, A.A., and Samson, I.M., 2012. Hydrothermal mobilization of the rare earth elements – a tale of “Ceria” and “Yttria”. Elements, 8, 355-360.

REE enrichment in granite-derived regolith deposits of the Southeastern United States: Prospective source rocks and accumulation processes

Nora Foley[1, a] and Robert Ayuso[1]

[1] United States Geological Survey, Reston, VA, 20192, USA
[a] corresponding author: nfoley@usgs.gov

Recommended citation: Foley, N. and Ayuso, R., 2015. REE enrichment in granite-derived regolith deposits of the Southeastern United States: Prospective source rocks and accumulation processes. In: Simandl, G.J. and Neetz, M., (Eds.), Symposium on Strategic and Critical Materials Proceedings, November 13-14, 2015, Victoria, British Columbia, British Columbia Ministry of Energy and Mines, British Columbia Geological Survey Paper 2015-3, pp. 131-138.

Summary

The Southeastern United States contains numerous anorogenic, or A-type, granites, which constitute promising source rocks for REE-enriched ion adsorption clay deposits due to their inherently high concentrations of REE. These granites have undergone a long history of chemical weathering, resulting in thick granite-derived regoliths, akin to those of South China, which supply virtually all heavy REE and Y, and a significant portion of light REE to global markets. Detailed comparisons of granite regolith profiles formed on the Stewartsville and Striped Rock plutons, and the Robertson River batholith (Virginia) indicate that REE are mobile and can attain grades comparable to those of deposits currently mined in China. A REE-enriched parent, either A-type or I-type (highly fractionated igneous type) granite, is thought to be critical for generating the high concentrations of REE in regolith profiles. One prominent feature we recognize in many granites and mineralized regoliths is the tetrad behaviour displayed in REE chondrite-normalized patterns. Tetrad patterns in granite and regolith result from processes that promote the redistribution, enrichment, and fractionation of REE, such as late- to post-magmatic alteration of granite and silicate hydrolysis in the regolith. Thus, REE patterns showing tetrad effects may be a key for discriminating highly prospective source rocks and regoliths with potential for REE ion adsorption clay deposits.

1. Introduction

Currently mined only in South China (Kynicky et al., 2013), rare earth element (REE) ion-adsorption clay deposits are of global economic importance because they supply virtually all heavy (Gd-Lu) REE and a significant portion of light (La-Eu) REE to global markets. Nonetheless, considerable ambiguity remains about the source rocks, genesis, and global distribution of this deposit type. Herein we present the results of ongoing studies to investigate the role of parent rock in the formation of REE ion adsorption deposits in the southeast United States. Our objective is to understand the genesis of REE-enriched regolith profiles and establish the potential for economic REE ion-adsorption clay deposits. Although all weathered materials may contain some exchangeable REE, one of our aims is to identify the role of source rock composition and mineralogy in generating high concentrations of REE in a regolith. Our initial work (e.g., Foley, et al., 2013, 2014, 2015) focused on anorogenic granite as a promising source rock for ion adsorption type REE deposits because they contain inherently high concentrations of REE (e.g., Whalen et al., 1987).

The main features of the deposit type (Bao and Zhou, 2008) include: the presence of igneous suites, generally granitic rocks; long periods of intense weathering with little subsequent erosion; and evidence for enrichment of REE in the regolith. REE mobilization processes are thought to include late-magmatic-to-deuteric (hydrothermal) alteration and deep lateritic weathering (Bao and Zhou, 2008, Ishihara et al., 2008). Ore consists of REE ions or hydroxides attached to interlayer and edge sites in clay minerals, and forms when REE are released from host igneous phases and adsorbed to newly formed clay minerals generated by weathering of aluminosilicate minerals. Mined deposits in China reportedly have grades in the range of 500 to over 3000 ppm REE, contain 3-5 times the REE concentration of the source rock and contain mainly either light REE or heavy REE (Bao and Zhou, 2008). Differential mobility of REE within soil profiles is thought to contribute to formation of heavy-REE- vs. light-REE-enriched deposits (Bao and Zhou, 2008). Protoliths for the Chinese deposits were originally considered as calc-alkaline to alkaline granites, with peralkaline syenite and granite as likely parents for ore with mainly heavy-REE and Y (Wu et al., 1996, and references therein). More recent work by Wang et al. (2015) indicates that both REE-enriched anorogenic (A-type) granites and highly fractionated igneous (I-type) granites are prospective source rocks in South China.

2. Granites and granite-derived regoliths, Southeastern United States

The Southeastern United States contains three major belts of weathered igneous rocks. The westernmost belt consists of

Neoproterozoic anorogenic plutons and related rocks that have highly silicic compositions, high contents of Ga, F, Nb, Sn, Ta, Y, and Zr, and high total REE (Tollo et al., 2004). Granite discrimination diagrams classify these rocks as high-K calc-alkaline granites, having compositions that range from slightly metaluminous to peraluminous and peralkaline. These granites were emplaced along the eastern flank of the Blue Ridge province during regional crustal extension related to opening of the Iapetus Ocean and breakup of the supercontinent Rodinia (Tollo et al., 2004). In Virginia, the plutons formed mainly during an early period of extension, between 765 and 680 Ma (Tollo et al., 2004). Plutons and prospective regolith sites (Fig. 1) were selected based on geologic attributes, such as rock type, whole-rock chemistry, topographic setting, and accessibility. Studies were conducted on the Stewartsville (SHRIMP U-Pb zircon age of 680±5.7 Ma, unpublished data) and Striped Rock (SHRIMP U-Pb zircon age of 735.4±5.2 Ma, unpublished data) plutons, and two younger plutons (SHRIMP U-Pb zircon ages of 703.6±13.4 Ma for the Amissville granite, and 697.2±6.8 Ma for the Battle Mountain granite, unpublished data) of the Robertson River batholith (Tollo and Aleinikoff, 1996).

The Stewartsville pluton (Fig. 1) is a medium- to coarse-grained biotite granite that forms a narrow lobate to irregular belt southeast of Roanoke, Virginia (Henika, 2011). It is one of a number of medium-grey, poorly foliated to massive, biotite granitoid bodies of similar age that occur throughout central Virginia (Henika, 2011). The granite is equigranular and contains quartz, sericitized and albitized, perthitic, pale red and white feldspars, sodic plagioclase, and mafic clots and stringers. Feldspars contain inclusions of synchysite-(Nd) and fergusonite. Mafic clots are primarily composed of biotite and stilpnomelane and, less typically, include magnetite, remnant cores of green and green-brown hornblende, and accessory minerals including apatite, epidote, garnet, Nb-rutile, fergusonite, monazite, titanite, xenotime, gadolinite, and zircon. Abundant allanite and fluorite are diagnostic of the Stewartsville granite (Henika, 2011).

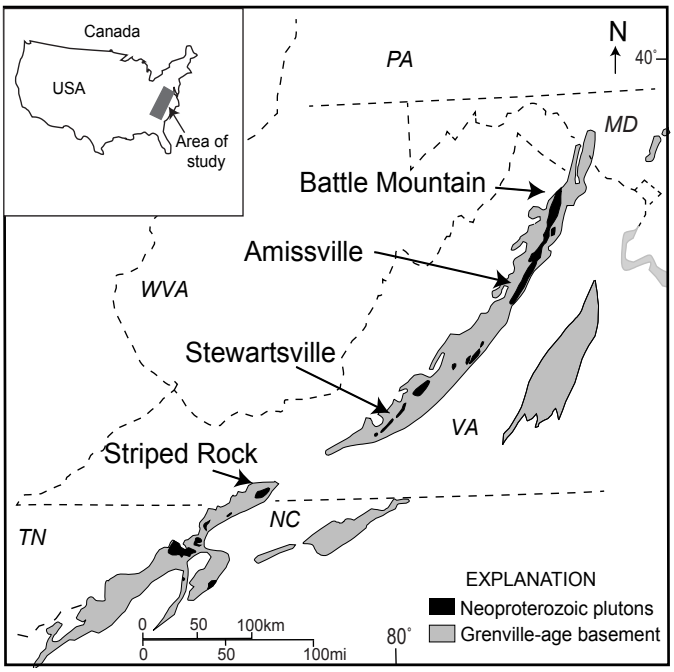

Fig. 1. General location of the granitic plutons and granite-derived regoliths reported on here. Modified from Tollo et al. (2004).

The Striped Rock pluton (Fig. 1) is slightly foliated to equigranular and composed of medium- to coarse-grained hornblende-biotite granite, with minor amounts of fine-grained aplite and dikes (Essex, 1993). The main body of the pluton is lens-shaped and is exposed over an area of approximately 65 km^2, with small outliers to the northeast making it one of the largest single Neoproterozoic granite bodies in Virginia. The granite is composed mainly of white, grey, and pink alkali feldspar, anhedral and interstitial quartz, and plagioclase. Alkali feldspar commonly has rapikivi textures and albitized rims. Anhedral clots of green biotite are the most common mafic phase and, in the centre of the pluton, the green biotite is intergrown with sodic amphibole (ferro-pargasite; Essex, 1993). Aplites contain porphyritic quartz, alkali feldspar, and plagioclase and, as a late-stage alteration product, muscovite. Accessory phases in all rock types include allanite and fluorite, zircon, epidote, ilmenite, fine-grained apatite, and rare anhedral to subhedral titanite. Fine-grained biotite and epidote also form fracture fillings in and around quartz and feldspar. Allanite is typically metamict and zoned, with epidote rims. Purple fluorite occurs mainly as fracture fillings in the medium- to coarse-grained granite, and as anhedral grains and inclusions in plagioclase and biotite in the aplite.

The Roberson River batholith (Tollo and Aleinikoff, 1996) was emplaced in two pulses, at 735–722 Ma and 706–702 Ma. Most of the batholith is composed of metaluminous granite, with peralkaline rocks of the Battle Mountain complex (Fig. 1) making up the younger magmatic phase (Tollo and Aleinikoff, 1996). Granite of the Battle Mountain complex contains mainly feldspar and quartz with mafic clots of biotite, sodic clinopyroxene (aegirine) and amphibole (riebeckite), stilpnomelane, and abundant fluorite (Tollo et al., 2004). The rocks have high concentrations of Zr (~1000 ppm), contained in zircon and chevkinite (Belkin, 2015), and high concentrations of REE plus yttrium (>1000 ppm; Tollo and Aleinikoff, 1996). Other REE-bearing phases include fluorocarbonate minerals, mainly bastnäsite-(Ce), with minor parisite-(Ce), and synchysite-(Ce); chevkinite-(Ce), allanite-(Ce), gadolinite-(Y), and a variety of Nb phases (aeschynite-euxenite, fergusonite, and samarskite) (Belkin, 2015).

3. Regolith formation

Many naturally exposed granite outcrops in the Piedmont region of Virginia are intensely weathered, with overlying regolith consisting of saprolite extending to depths of tens of metres overlain by B-horizon type soils, and the region is highly vegetated. The regoliths may be thin and discontinuous or metres thick and laterally extensive. Regolith is sparsely distributed across the Battle Mountain pluton, whereas the

Striped Rock pluton is one of the most deeply weathered of the anorogenic plutons. Regolith formed by weathering of the Stewartsville pluton is well developed in near-vertical exposures that crop out near the Roanoke River in southwest Virginia. The Stewartsville exposures consist of >30 metre high by >60 metre long weathered sections that extend from bedrock up through regolith materials (Fig. 2). The sections include units of nearly fresh rock, highly weathered saprolite, indurated gravels and sands, and poorly delineated layers of subsoil and topsoil. Granite at the base of the profile is iron stained and weathered on exposed surfaces and along cracks. Partially weathered sections of the profiles display a range of rock textures throughout rather than systematic changes from base to surface. In the lower parts, cobble- and boulder-sized relics of spheroidally weathered granite retaining distinctive primary textures are surrounded by nearly disaggregated granite that crumbles to sand- and gravel-sized fragments when sampled. Soil layers overlying the saprolite are mainly of B-horizon-type and contain a higher proportion of clay (mixed chlorite and kaolinite) than the saprolite. A thin veneer of A-horizon-type soil overlies the Stewartsville profile.

4. REE and Pb-Nd isotope geochemistry

Whole rock REE patterns for the granites (Fig. 3a) show steep chondrite-normalized patterns that are light-REE-enriched at 200 to 800x chondrite and with heavy-REE at ~20 to 100x chondrite. The range in REE patterns shows a wide variability in total REE concentrations among plutons within the batholith (compare Amissville and Battle Mountain) and within a single pluton (e.g., Stewartsville). All the granites show a negative Eu anomaly and most lack a Ce anomaly. REE data for bedrock, saprolite, and soils at the Stewartsville site (Fig. 3c) show an increase from 300-650 ppm REE in bedrock at the base of the profile to over 2880 ppm REE in clay-rich soils. A negative Eu anomaly in the granite is retained in weathered alluvium, and the uppermost soil samples show a pronounced negative Ce anomaly, likely due to downward migration of Ce and cerianite precipitation elsewhere in the weathering profile. Normalized to average values for bedrock at the base of the profile, the soils and saprolite show increases in light and middle-REE (La-Dy) relative to bedrock (Fig. 3d). The heavy REE (Dy-Lu) show a subtle expression of tetrad behaviour in the M-type rounding seen in third and fourth tetrads (Fig. 3d). These results compare favourably with light REE-enriched deposits at Heling (Figs. 3e-f), in contrast to heavy REE-enriched deposits such as those at Xinzui (Figs. 3g-h). Sequential leaching of regolith samples from Stewartsville included a weak acid-ion exchange process (Na-acetate at pH~5) to extract ions adsorbed to clay (Fig. 3b), and aqua regia and four-acid leaches to assess the proportion of refractory REE-bearing minerals (e.g., monazite, zircon) remaining in the regolith. The fraction of readily extractable REE in the bedrock-soil profile varied from 30 to 70%, with an average yield of 900 ppm REE from saprolite and soils.

Fig. 2. Granite-derived regolith field site, Stewartsville pluton, Virginia, showing a profile with bedrock at base, which is overlain by a 30-metre high exposure of partly weathered granite knobs, saprolite, disaggregated granite gravels and sands, and soils. The uppermost metre is mainly B-horizon type soil.

Characterization of Pb and Nd isotopes of parent rocks, soils, and potential anthropogenic inputs can provide critical data for quantifying in-situ vs. transported REE in soils (Harlavan et al., 2009; Ohlander et al., 2000). Nd isotopes in igneous rocks are commonly distributed in rock-forming minerals and accessory minerals, and in alteration products that differ in Sm/Nd ratios. At the Stewartsville site, values of $^{143}Nd/^{144}Nd$ for regolith samples vary from 0.512037 to 0.512415, compared to a bedrock value of 0.512424. Nd isotope compositions show limited correlation with Nd, Sm, and Sm/Nd ratios (soils: 0.242-0.260; bedrock: 0.180-0.271). The moderate scatter in Nd isotope ratios and Sm/Nd values in the surficial materials, compared to bedrock, is consistent with mineral weathering. In comparison, Sm/Nd values of mild acid leachates range from 0.233 to 0.261. This suggests that one or more weathering minerals have bulk Sm/Nd comparable to bedrock. Such minerals would be important hosts of REE in the profile. Pb in regoliths results from a combination of Pb from feldspar and other igneous minerals and Pb from anthropogenic sources such as fertilizers, other clay-based agricultural amendments, and past use of leaded gas. Pb isotope signatures can be used to discriminate natural versus anthropogenic Pb in soils (Ayuso et al., 2008) and, by inference, indicate local anthropogenic addition of REE to a profile from clay-based agricultural amendments. In the Stewartsville profile, changes in Pb isotopes from bedrock to surface soils correlate with total REE and reflect progressive and sequential weathering of igneous

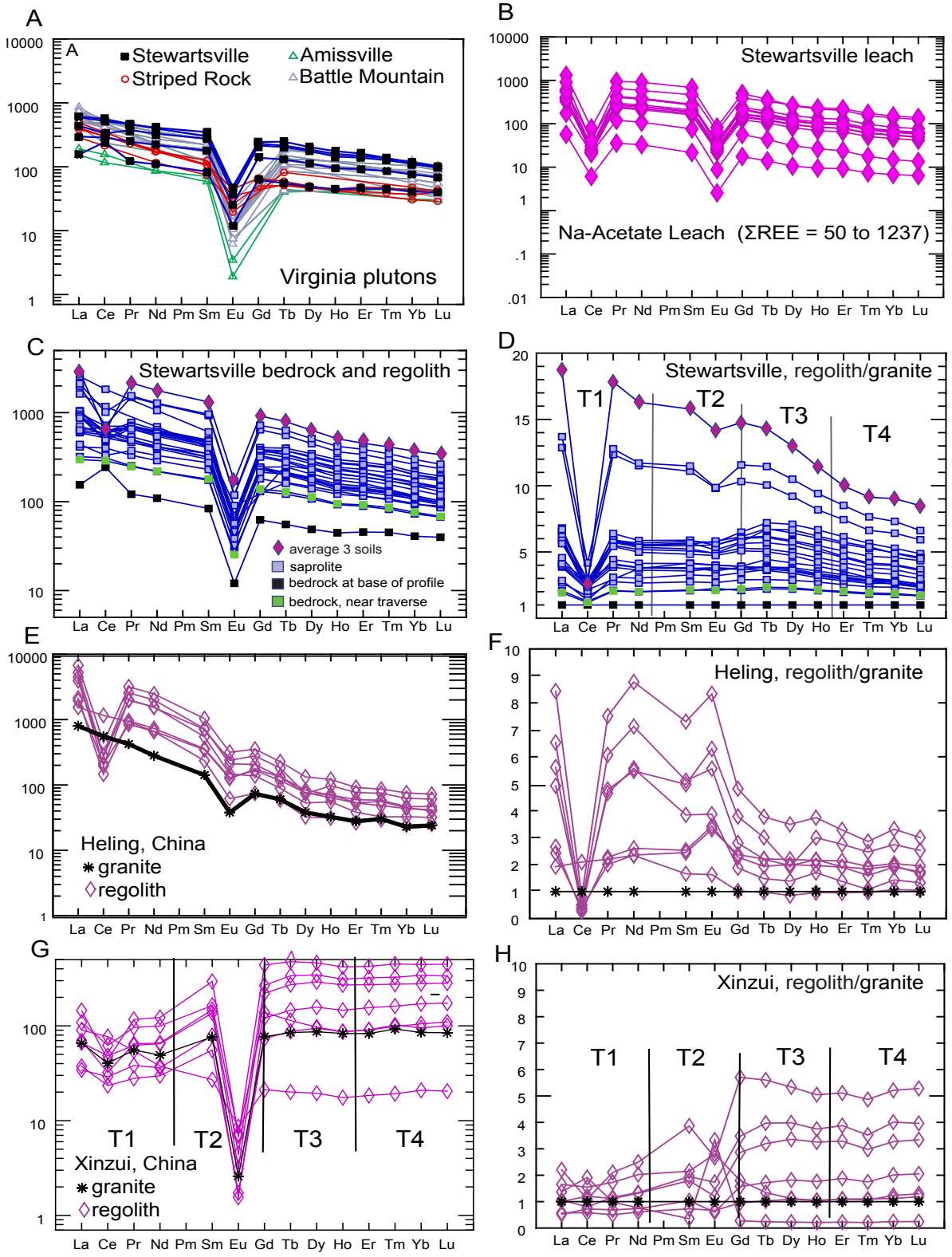

Fig. 3. a) REE patterns for four Neoproterozoic anorogenic granites showing whole rock concentrations ranging from ~200 to nearly 1000 ppm REE. **b)** Selected sequential leach results for regolith samples from a Stewartsville profile. REE patterns for **c)** Stewartsville granite and granite-derived regolith showing increases in REE concentrations in saprolite and overlying soils, and **d)** regolith samples from a bedrock-soil profile over the Stewartsville granite, normalized to average REE values for 2 bedrock samples near the site. Vertical lines show tetrad subdivisions (T1, T2, T3, T4). See text for details. Analyses from ActLabs, Canada. **e)** and **f)** Granite-regolith patterns for light REE enriched deposits at Heling, China ion adsorption clay deposit; **g)** and **h)** patterns for heavy REE deposit at Xinxui, China (data from Bao and Zhou, 2008). Chondrite-normalization values from Sun and McDonough (1989). Note scale change for pattern pairs c) - d), versus g) - h).

allanite, biotite, and feldspars, thus establishing that the profiles likely contain no anthropogenic addition of REE.

5. Mineral residence and REE enrichment in regolith

Allanite is the predominant source mineral for light-middle-REE in most of these granites; zircon is the most abundant mineral that selectively incorporates heavy-REE. Apatite, garnet, titanite, and fluorite in the rocks generally have REE contents that are less than 0.5 weight percent or below limits of detection (0.1-0.2 wt.% by element: electron microprobe analysis). Monazite, xenotime, fergusonite, chevkinite, gadolinite, and other phosphate and niobate minerals are volumetrically minor. REE-fluorocarbonate minerals are unevenly distributed and volumetrically minor in all plutons, except where they occur as late phases in peralkaline rocks, such as at Battle Mountain. The granite-derived regolith studied in detail at Stewartsville contains a diverse suite of REE-bearing minerals, including refractory igneous minerals (e.g. zircon, xenotime, monazite) and remnants of relatively soluble igneous phases (e.g. allanite, titanate, apatite), a wide variety of secondary and authigenic REE-bearing minerals (e.g., cerianite, monazite-(Ce), Ca-REE fluorocarbonate minerals) as replacements and cements, and REE adsorbed to neoformed clay minerals.

Allanite is generally abundant in all the granites and forms euhedral to subhedral, brown crystals that commonly attain lengths of up to 3 mm, contain greater than 18 wt.% REE, and are zoned in Th contents. For example, unweathered allanite from Stewartsville has Sm/Nd values of 0.140 to 0.160, 23-27 wt.% REE, and up to 2 wt.% Th. Allanite weathers readily in granites on exposed surfaces and is typically completely altered to orange and white clays and iron-oxide (Fig. 4a). In the Stewartsville profile, REE released from allanite are distributed within clay mineral sheets (Fig. 4b) and as oxide and fluorocarbonate fill in veins and fractures that cut altered grains. Secondary REE minerals are also found at grain boundaries, in crosscutting stringers and anastamosing veinlets, and as cements in weathered saprolite. Cements typically consist of varying mixtures of Mn-oxide or Mn-clays, kaolinite, and goethite intermixed with spheroidal cerianite and a monazite-(Ce).

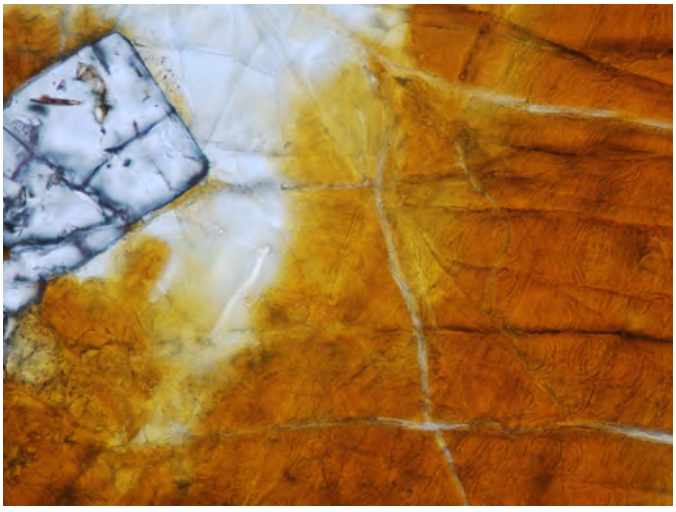

Fig. 4. a) Altered core of deeply weathered allanite from Stewartsville regolith profile showing white kaolinite, yellow-orange Fe-clay, and zircon. Field of view is 500 µm.

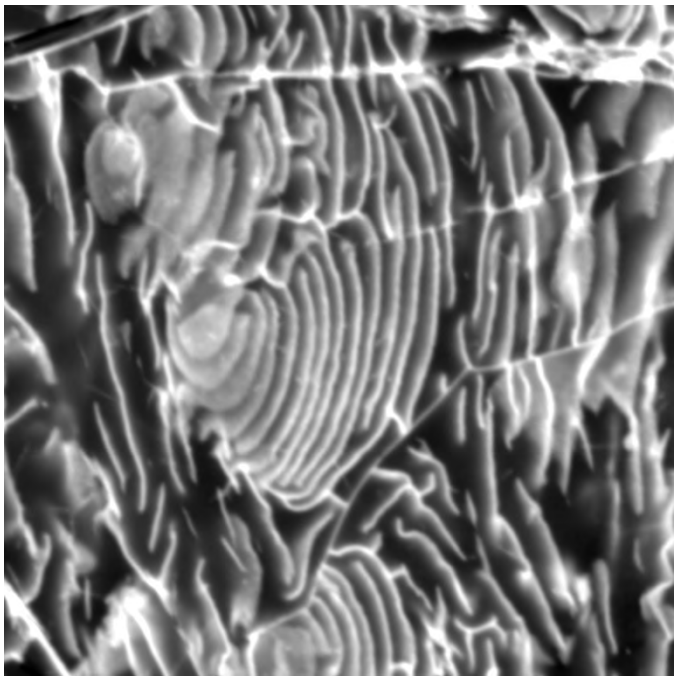

Fig. 4. b) SEM back-scatter electron image showing area of Fe-Al clays (dark layers) defined by REE oxide edges (bright areas are REE: La, Nd, Sm, Gd, Dy) in weathered allanite from saprolite; Stewartsville pluton. Field of view is 20 µm.

Zircon in most of these plutons shows complex and highly variable features, including variations in color, size, and compositional zoning. For example, in the Stewartsville and Striped Rock plutons, some zircon populations have features typical of magmatic zircon, such as Hf-zonation, low Th and U, REE contents of less than 2500 ppm, and patterns with La at 1x-100x chondrite and Lu at ~10,000x chondrite. Another population has complex interiors with dark cores enriched in REE up to 1.8% REE (light REE at 10,000x chondrite, 2800 ppm Th, and 4800 ppm U). Zircon rims from peralkaline rocks of the Battle Mountain complex form amoeboid and altered masses that have mean values of ~1.3 wt.% REE plus Y (Belkin, 2015); in contrast, Hf-zoned cores have patterns typical of magmatic zircon with La at 0.1-100x chondrite and Lu at 1000-10,000x chondrite. Zircon from the Amissville pluton is spongy and fragmented with up to 1.6 wt.% REE. The patterns show La at 1-1000x chondrite and Lu at 1000-10,000x chondrite. Zircon is the most abundant residual igneous accessory phase in most of the saprolites and soils. Zircon separates from weathered profiles at Stewartsville show removal of light-middle REE from the dark cores, likely due to metamictization.

At Stewartsville and many other granite-derived regoliths of the central Appalachians, we consider that enrichment of REE in the regolith is predominantly a result of hydrolysis of igneous

minerals (feldspars, allanite, apatite, biotite) and removal of the alkali elements. Progressive weathering of allanite, biotite, feldspars, hornblende, apatite, and titanite results in the occurrence of secondary Fe-oxides (goethite, hematite) and Al-clays (illites, kaolinite, halloysite) throughout the regolith. The redistribution of REE as either adsorbed ions or secondary minerals is likely controlled by local microchemical domains in the regolith defined by solubility factors inherent in the aqueous phase, such as pH, redox state, and available complexing agents. Silicate weathering is acid-consuming and if it proceeds unbuffered (for example, by acidic meteoric waters), pH will move to neutral values where the relative stability of REE-carbonate or phosphate complexes may result in formation of monazite or fluorocarbonate minerals (Wood, 1990, and references therein). At Stewartsville, the enrichment of REE in the regolith is predominantly a result of light-middle-enriched allanite weathering, with subsequent fixing of released REE as ions or hydroxyl ions on clays, or as poorly crystalline secondary oxide, niobate, fluorocarbonate, and phosphate minerals.

6. Comparison with granite source rocks of China

Large igneous suites of the Southeastern United States generally match the compositional range of granitic rocks associated with the South China REE deposits. Chinese granites that host REE ion adsorption deposits also include both highly fractionated and anorogenic granites; for example, at Zhaibei and Xihuashan, Jiangxi Province, South China. Weathering of the highly peraluminous A-type Zhaibei granite led to formation of light-middle REE ion adsorption deposits (Wang et al., 2015). The Zhaibei granite has chondrite-normalized REE patterns exhibiting strong enrichment in light-REE with steep positive slopes (average La_N/Yb_N = 32), negative Eu anomalies, and whole rock REE concentrations of <600 ppm REE. REE are distributed among a variety of minerals, including titanite (~7500 ppm REE), allanite, thorite (~4.5 % by wt. Y), zircon, monazite, apatite, and REE fluorocarbonate minerals. In contrast, the Xihuashan granite has light REE at 40x chondrite and heavy REE at ~100x chondrite, a strong negative Eu anomaly, whole rock concentrations of ~100 ppm REE, and La_N/Yb_N <1. The rare earth minerals include xenotime, monazite, fergusonite, samarskite, gadolinite, aeschynite, euxenite and parisite-(Y). Weathering of the high-silica A-type granite at Xihuashan resulted in regolith containing ion adsorption deposits enriched in heavy REE (Xiao et al., 2009). Regoliths formed on the metaluminous-peraluminous granites of the southeastern US share many of the attributes of the Zhaibei granite and regolith, whereas peralkaline granites of the southeastern US (e.g., Battle Mountain, Amissville) share mineralogical similarities that are more comparable to the Xihuashan granite.

Petrographic and mineralogical evidence from a number of studies (e.g., Whalen et al., 1987) indicates an important role for late dueteric to hydrothermal processes in REE enrichment in A-type granites. The common development of a fluid phase rich in F, CO_2 and H_2O late in the evolution of A-type and highly fractionated granites can lead to hydrolysis-type reactions capable of converting, for example, monazite to bastnäsite and xenotime to synchysite-(Y) (Johan and Johan, 2005). Furthermore, the low concentrations of phosphate in most A-type granite melts (e.g., Bonin, 2007) may limit initial monazite formation, leaving light-to-middle REE available for incorporation in less refractory minerals such as allanite and soluble REE fluorocarbonates. Thus, hydrothermal alteration and mineralization have a significant influence on the diverse character of ion adsorption type REE deposits because they catalyse conversion of more refractory igneous phases to less refractory REE-rich minerals and provide possible pathways for generating granites with high concentrations of REE in minerals that weather readily in surface environments.

We suggest that the notable development of tetrad behaviour in REE patterns of granites and granite-derived regoliths, such as those at Zudong and Guanxi, China (Fig. 5), represent an important attribute of highly prospective source rocks for ion adsorption clay deposits, particularly those of the heavy REE type. Tetrad behaviour controls REE distributions in geological samples such that REE representing quarter, half, three-quarter, and completely filled 4f shells have increased stability (e.g., McLennan, 1994). Tetrad effects in REE patterns may highlight the occurrence of processes such as high degrees of fractional crystallization, hydrothermal alteration, and mineralization (Jahn et al., 2001). Expressions of tetrad behaviour are well documented for granite-related rare metal deposits (see, for example, Monecke et al., 2002) and in rare metal granites of South China (e.g., Zhao et al., 2002). We note that tetrad expressions are retained in regoliths associated with many South China REE ion adsorption deposits (Fig. 5). The tetrad effect is especially pronounced for heavy REE ion adsorption deposits at Zudong and Xinzui (Figs. 3e, 5) and light-middle REE deposits at Guanxi and Heling (Figs. 3g, 5). The concave-down M-type patterns in the third (T3) and fourth (T4) tetrads (Figs. 3, 5), suggest mobility in the middle and heavy REE. The Zhaibei granites, which host light REE ion adsorption deposits, lack the tetrad behaviour exhibited by many Chinese source granites. In contrast, subtle tetrad effects in T3 and T4 do appear in the granite and regolith that host the heavy REE ion adsorption deposits at Xihuanshan (data from Xiao et al., 2009). REE patterns for most anorogenic granites of the Southeastern United States also lack obvious tetrad behaviour. However, some regolith samples from Battle Mountain and Stewartsville display subtle expressions of T3 and T4 (for example, Fig. 3d). Belkin (2015) noted that many accessory phases in the peralkaline rocks of Battle Mountain and Amissville are altered and show complex zoning, overgrowths, and multiple generations, leading him to suggest that late-stage, Na, Fe, and F-rich fluids carrying REE, Y, Nb, and Zr moved through the rock during early cooling. Likewise, garnet, fluorite, zircon, allanite, and niobate minerals in much of the Stewartsville granite show embayments, altered cores, overgrowths, and veining, suggesting multiple generations of hydrothermal and

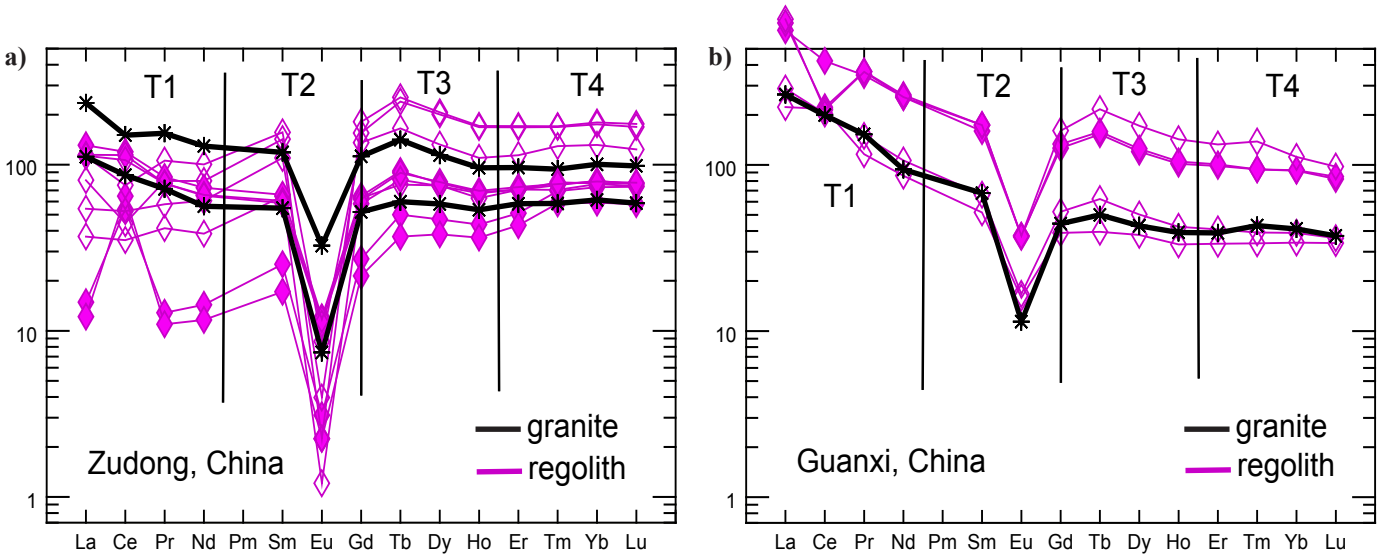

Fig. 5. Chondrite-normalized REE patterns for 2 Chinese granites (black) and associated regolith materials (pink) showing subtle tetrad behavior in T3, T4. **a)** Zudong heavy REE ion adsorption clay deposits (Longnan, China) and **b)** Gaunxi regolith deposits enriched in light and light-middle REE. Data from Ishihara et al. (2008), Bao and Zhao (2008), and Murakami and Ishihara (2008).

deuteric alteration, both early and late in the petrogenesis.

7. Conclusions

Our studies demonstrate significant potential in the Southeastern United States for REE ion adsorption clay deposits of a type containing light-middle REE and yttrium, and an-as-yet unknown potential for high-value heavy REE deposits.

- Large igneous suites of the Southeastern United States generally match the compositional ranges of granitic rocks associated with South China REE ion adsorption clay deposits. Source rocks that result in regolith deposits highly enriched in REE in the Southeastern United States include high-silica anorogenic granitic suites with high total REE and low P. Granites that show tetrad behaviour in REE patterns may be highly prospective source rocks for REE ion adsorption clay deposits.
- The importance of weathering of a REE-enriched parent (A-type or highly fractionated I-type granite) is in the potential for generating high concentrations of mobile REE in the developing regolith. The Stewartsville example highlights the importance of allanite weathering in generating a light-middle-REE-enriched regolith. However, weathering of other REE-bearing minerals, such as garnet, metamict zircon, REE-fluorcarbonates (for example, bastnäsite, parisite, synchysite), chevkinite, gadolinite, and niobates (aeschynite-euxenite, fergusonite, and samarskite) may be key to generating a heavy REE enriched regolith.
- It remains to be fully established if regoliths containing high enough concentrations of readily extractable and high-value REE occur in adequate volumes to be considered a future resource in the US. Further studies are underway to refine the full range of potential source rocks for REE-bearing clay deposits and to determine, in particular, the most prospective source rocks for high-value REE-bearing clay deposits.

Acknowledgments

We thank M. Carter, A. Merschat, and C.S. Southworth for valuable discussions on geology field sites. Excellent laboratory support was provided by J. Jackson (XRD, mineral separations), R. Indela and S. Robinson (USGS Reston-Radiogenic Isotope Lab), J. Vazquez (USGS-Stanford SHRIMP), H. Belkin (USGS-Reston Microprobe) and L. Hayden (USGS-Menlo Park Microprobe). Constructive reviews of an early version by reviewers and the Editors resulted in a much improved paper.

References cited

Ayuso, R., Foley, N., and Lipfert, G., 2008. Lead isotopes as monitors of anthropogenic and natural sources affecting the surficial environment. In: DeVivo, B., Belkin, H., and Lima, A., (Eds.), Environmental Geochemistry: Site Characterization, Data Analysis and Case Histories. Elsevier, Chapter 12, 291-318.

Bao, Z.W., and Zhao, Z.H., 2008. Geochemistry of mineralization with exchangeable REY in the weathering crusts of granitic rocks in South China. Ore Geology Reviews, 33, 519-535.

Belkin, H.E., 2015. REE, Y, Zr, and Nb mineralogy of the Neoproterozoic rift-related Robertson River igneous suite, Northern Virginia, USA [abs]. AGU-GAC-MAC-CGU Joint Assembly, Abstracts volume, p. 297.

Bonin, B., 2007. A-type granites and related rocks: Evolution of the concept, problems, and prospects. Lithos, 97, 1-29.

Essex, R.M., 1993. Age and petrogenesis of the Striped Rock pluton, Virginia. Unpublished M.S. thesis, Virginia Tech, Blacksburg, Virginia, 98 p.

Foley, N. K., and Ayuso, R.A., 2013. REE mobility in high-alumina altered metavolcanic deposits, South Carolina, USA. Journal of Geochemical Exploration, 133, 50-67.

Foley, N.K., Ayuso, R.A., Bern, C.R., Hubbard, B., and Vazquez, J., 2014. REE distribution and mobility in regolith formed on granite bedrock, Southeast United States. Acta Geologica Sinica, 88(supp. 2), 428-430.

Foley, N.K., Ayuso, R.A., Hubbard, B., Bern, C., and Shah, A ., 2015. Geochemical and mineralogical characteristics of REE in

granite-derived regolith of the Southeastern United States. 13th SGA Biennial Meeting, Mineral Resources in a Sustainable World. Proceedings, 2, 725-728.

Harlavan, Y., Erel, Y., and Blum, J.D., 2009. The coupled release of REE and Pb to the soil labile pool with time by weathering of accessory phases, Wind River, WY. Geochimica et Cosmochimica Acta, 73, 320-336.

Henika, W.S., 2011. Geologic map of the Hardy quadrangle, Virginia. Virginia Division of Geology and Mineral Resources Open File Report 2011-3, 1:24,000 scale.

Ishihara, S., Renmin, H., Hoshino, M., and Murakami, H., 2008. REE abundance and REE minerals in granitic rocks in the Nanling Range, Jiangxi Province, Southern China, and generation of the REE-rich weathered crust deposits. Resource Geology, 58, 355–372.

Jahn, B.M., Wu, F.Y., Capdevila, R., Martineau, F., Zhao, Z.H., and Wang, Y.X., 2001. Highly evolved juvenile granites with tetrad REE patterns: the Woduhe and Baerzhe granites from the Great Xing'an Mountain in NE China. Lithos, 59, 171–198.

Johan, Z., and Johan, V., 2005. Accessory minerals of the Cínovec (Zinnwald) granite cupola, Czech Republic: indicators of petrogenetic evolution. Mineralogy and Petrology, 83, 113-150.

Kynicky, J., Smith, M.P., and Xu, Cheng, 2013. Diversity of rare earth deposits: The key example of China. Elements, 8, 361–367.

McLennan, S.M., 1994. Rare earth element geochemistry and the "tetrad" effect. Geochimica et Cosmochimica Acta, 58, 2025-2033.

Monecke, T., Kempe, U., Monecke, J., Sala, M., and Wolf, D., 2002. Tetrad effects in rare earth distribution patterns: A method of quantification with application to rock and mineral samples from granite-related rare metal deposits. Geochimica et Cosmochimica Acta, 66, 1185-1196.

Murakami, H., and Ishihara, S., 2008. REE Mineralization of weathered crust and clay sediment on granitic rocks in the Sanyo Belt, SW Japan and the Southern Jiangxi Province, China. Resource Geology, 58, 373–401.

Ohlander, B., Ingri, J., Land, M., and Schoberg, H., 2000. Change of Sm/Nd isotope composition during weathering of till. Geochimica et Cosmochimica Acta, 64, 813-820.

Sun, S., and McDonough,W.F., 1989. Chemical and isotopic systematics of oceanic basalts: implications for mantle composition and processes. In: Saunders, A.D., and Norry, M.J. (Eds.), Magmatism in the Ocean Basins. Special Publication, Geological Society of London 42, 313-345.

Tollo, R.P., and Aleinikoff, J.N., 1996. Petrology and U–Pb geochronology of the Robertson River Igneous Suite, Blue Ridge province, Virginia: evidence for multistage magmatism associated with an early episode of Laurentian rifting. American Journal of Science, 296, 1045-1090.

Tollo, R.P., Aleinikoff, J.N., Bartholomew, M.J., and Rankin, D.W. 2004. Neoproterozoic A-type granitoids of the central and southern Appalachians. Precambrian Research, 128, 3-38.

Wang, L., Xu, C., Zhao, Z., Song, W., and Kynicky, J., 2015. Petrological and geochemical characteristics of Zhaibei granites in Nanling region, Southeast China: Implications for REE mineralization. Ore Geology Reviews, 64, 569-582.

Whalen, J.B., Currie, K.L., and Chappell, B.W., 1987. A-type granites: geochemical characteristics, distribution and petrogenesis. Contributions to Mineralogy and Petrology, 95, 407-419.

Wood, Scott, 1990. The aqueous geochemistry of the rare earth elements and yttrium, 1. Review of available low-temperature data for inorganic complexes and the inorganic REE speciation of natural waters. Chemical Geology, 82, 159-186.

Wu, C., Yuan, Z., and Bai, G., 1996. Rare earth deposits in China. In: Jones, A.P., Wall, F., and Williams, C.T., (Eds.), Rare Earth Minerals, Chemistry, Origin, and Ore Deposits. Mineralogical Society Series 7, 281-310.

Xiao, J., Wang, Y., Hong, Y.L., and Zhou, Y.Z., 2009. Geochemical characteristics of Xihuashan tungsten granite and its relationship to tungsten metallogenesis. Journal of the East China Institute of Technology, 32, 23-31.

Zhao, Z.H., Xiong, X., Han, X.D., Wang, Y., Wang, Q., Bao, Z.W., and Jahn, B.M., 2002. Controls on the REE tetrad effect in granites: Evidence from the Qianlishan and Baerzhe Granites, China. Geochemical Journal, 36, 527-543.

Kwyjibo, a REE-enriched iron oxides-copper-gold (IOCG) deposit, Grenville Province, Québec

Serge Perreault[1, a] and Benoit Lafrance[2]

[1] SOQUEM Inc., 600 avenue Centrale, Val-d'Or, QC, J9P 8P1
[2] Focus Graphite Inc., 138 Rue Price ouest, bureau 205, Chicoutimi, QC, G7J 1G8
[a] corresponding author: serge.perreault@soquem.qc.ca

Recommended citation: Perreault, S. and Lafrance, B., 2015. Kwyjibo, a REE-enriched iron oxides-copper-gold (IOCG) deposit, Grenville Province, Québec. In: Simandl, G.J. and Neetz, M., (Eds.), Symposium on Strategic and Critical Materials Proceedings, November 13-14, 2015, Victoria, British Columbia. British Columbia Ministry of Energy and Mines, British Columbia Geological Survey Paper 2015-3, pp. 139-145.

1. Introduction

Iron oxide-copper-gold (IOCG) refers to a group of ore deposits that contain more than 10% low-Ti Fe oxides (mainly magnetite and hematite) and have elevated Cu, Au, REE, P, U, Ag or Co (Barton, 2014). This term excludes sedimentary iron deposits, magmatic iron-titanium oxide deposits, and members of the porphyry copper clan. They tend to be structurally or stratigraphically controlled and are temporally and spatially associated with intense and pervasive Na-Ca-K metasomatism. They are usually magmatic-hydrothermal deposits, commonly associated with large-scale continental A- to I-type granitic suites, and are found in late-or post-orogenic, extensional, shallow- to mid-crustal intracratonic, intra-arc, or back-arc settings (Barton, 2014), although metamorphic-affiliated deposits appear to be related to compressional settings (Corriveau, 2007; Groves et al., 2010; Barton, 2014). Some qualify as giant deposits such as the Olympic Dam Cu-Au-U deposit in Australia (Groves et al., 2010 and Barton, 2014). Total REE content in IOCG is commonly in the range of 0.2 to 3%, mostly enriched in light REEs (Barton, 2014). In magnetite-rich deposits, such as Kiruna (Sweden), the Fe-oxides – apatite end-member of the IOCG group, the main REE-bearing minerals are apatite, titanite and allanite. In the Kiruna district, the average REE-content of iron ore-type deposits ranges from 3275 ppm to 6560 ppm, and most of the REEs are associated with apatite (Parak, 1973). In hematite-rich deposits, such as Olympic Dam, REE occur in apatite and a variety of minor phases of REE-bearing phosphates (monazite, xenotime, britholite), REE-bearing flourocarbonates (bastnasite, synchysite) and silicates (allanite) (Barton, 2014).

Kwyjibo is a Mesoproterozoic Fe-Cu-REE-(Au) deposit of IOCG type in the northeastern part of the Grenville Province, on the north shore of St-Lawrence Gulf, in the Province of Québec (Fig. 1). It consists of 10 known polymetallic mineralized zones over a strike length of 4 kilometres. The main mineralized zones (Malachite, Josette, Andradite, Fluorine, Grabuge and Gabriel) were discovered between 1993 and 1995 during regional follow-up of regional geochemical lake-bottom sediment anomalies spatially associated with a

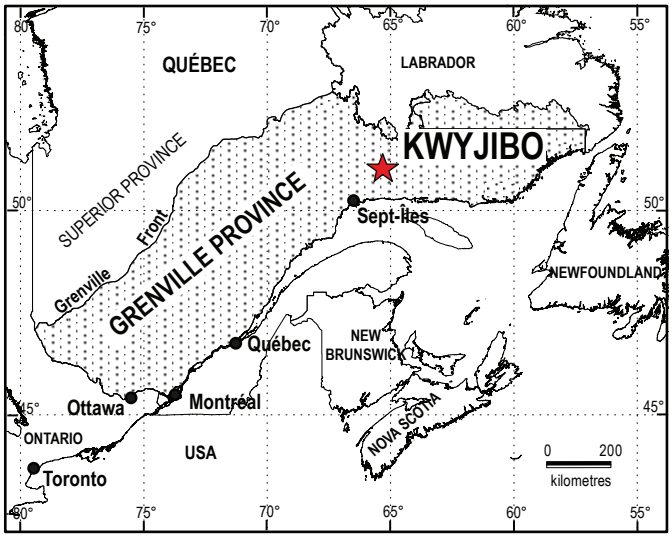

Fig. 1. Location of the Kwyjibo deposit.

regional curvilinear magnetic anomaly. Most of the zones consist of low-grade copper and REEs, except in the Josette horizon, a deformed hydrothermal iron formation (referred to as a magnetitite) metamorphosed to upper amphibolite metamorphic grade that extends for more than 1.2 kilometres (Fig. 2). High grade REE-mineralization, mainly of Nd, Y, Dy and Tb, has been delineated by both surface work at the Josette showing (2.95% total rare earth oxide [TREO] and 1.44% Cu over 10 m) and by close-spaced diamond drilling along the Josette horizon (reported weighted average intervals from 0.84% TREO over 65 m to 3.64% TREO over 33 m).

In the early 1990s, SOQUEM recognized that rocks of the Kwyjibo area share many similarities with IOCG type deposits (Perry and Raymond, 1996), including a regional linear magnetic anomaly and alteration patterns such as: iron enrichment, calcic and sodic-calcic alteration, potassic alteration with associated sodium depletion, anomalous content in F, P, REE,Y, Cu, Mo, Th, and locally U, silicification and quartz veins, hematization (specular hematite) and sodic-calcic alteration (Clark et al., 2005, 2010). Mineralized zones at Kwyjibo display a complex

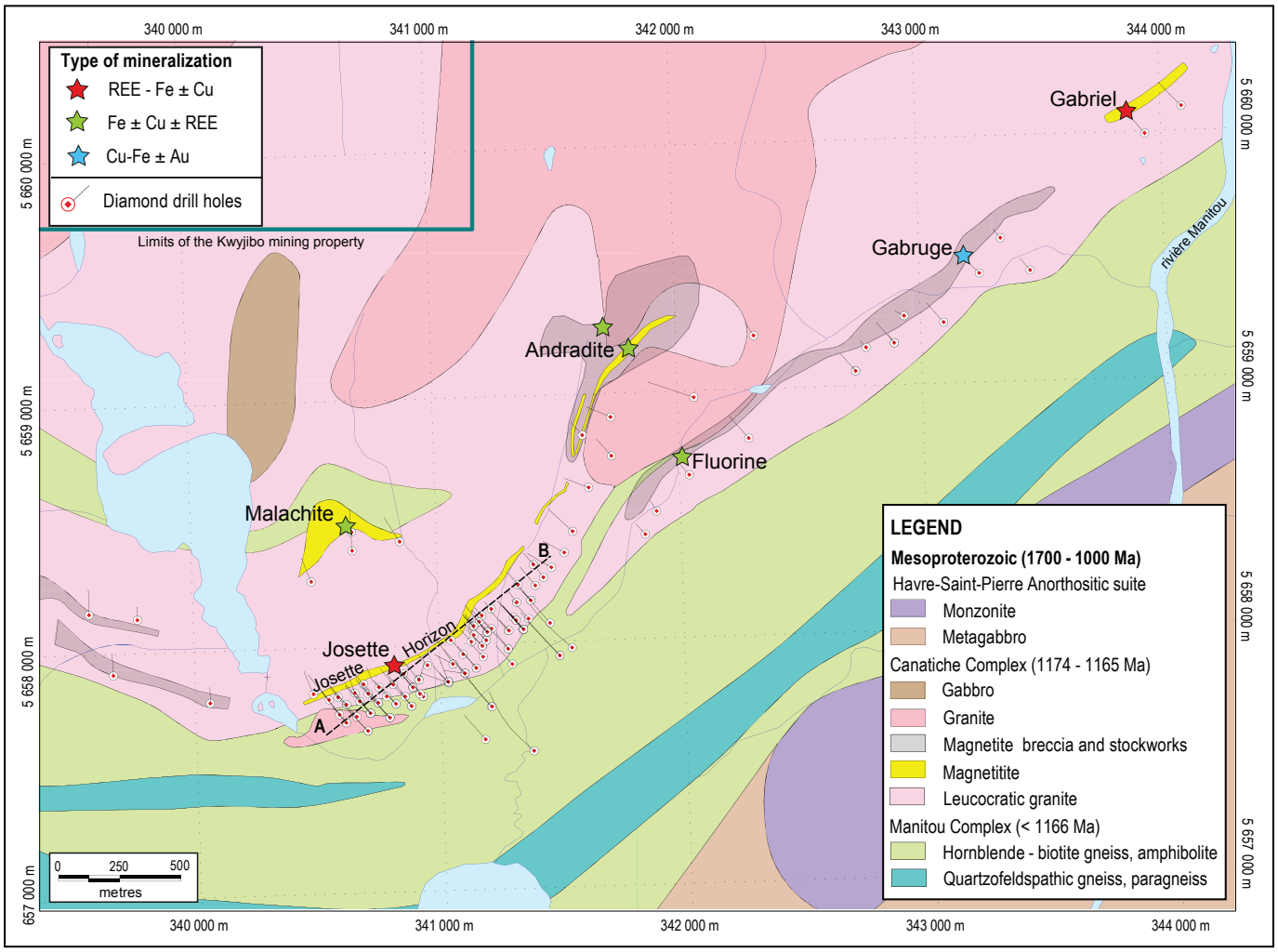

Fig. 2. Geological map of the Kwyjibo deposit showing the mineralized prospects, Josette horizon and the location of the diamond-drill holes. Coordinates are in UTM Zone 20 (NAD 83).

alteration history, resulting from mixed hydrothermal and meteoric fluids, and are strongly controlled by structures (Clark et al., 2005 and 2010). The mineralizing event forming the hydrothermal iron formation began during shortening related to the Grenville orogen, but most of the REE and Fe-Cu sulphide minerals were remobilized and deposited during the later extensional stages (Gauthier et al., 2004, Clark et al., 2005 and 2010). High-grade REE mineralization is found in the late apatite- allanite- britholite- kainosite-bearing calcsilicate (andradite-titanite-hornblende) veins and stockworks (with and without fluorite, biotite, and magnetite), with or without magnetite, that brecciated the magnetitite and its host gneissic leucogranite.

2. Geological setting

The property straddles two lithotectonic complexes separated by a major thrust fault: the Manitou complex, with mainly supracrustal rocks, in the south and the Canatiche complex, with mainly granitic rocks to the north (Fig. 2). The Canatiche complex, comprises undated orthogneiss, slivers of paragneiss, undeformed to weakly-deformed biotite ± hornblende granite (1181 ± 2Ma, U-Pb zircon, Clark et al., 2005) and leucogranites (1175 ± 5 Ma, U-Pb zircon, Clark et al., 2005, and 1165+4/-2 Ma, U-Pb zircon, David, 2014, personal communication) that host most of the mineralized zones, gabbros and pegmatite. All units have been metamorphosed to amphibolite facies. The biotite ± hornblende granites are magnetite-bearing, metaluminous to peraluminous, anorogenic (A-type) intraplate granites (Clark et al., 2005). Both the Canatiche and Manitou complexes were affected by thrusting during the metamorphic peak at 1083-1076 Ma attributed to the Ottawan phase of the Grenville orogeny (Clark et al., 2005 and references therein). All these units are intruded by late-orogenic granite and pegmatite associated with the Rigolet event of the Grenville Orogeny (Gauthier et al., 2004 and Clark et al., 2005).

Field and diamond drill core observations indicate that the southern limit of the Canatiche complex corresponds to a major fault zone (Clark et al., 2005, and references therein). At mineralized outcrops, the leucogranite hosting the Josette horizon is well foliated to gneissic. Metasomatized

leucogranite with mylonitic bands are observed in drill core close to the thrust contact with the hornblende-biotite gneiss of the Manitou complex. Close to the mineralized zones, quartz phenocrysts in the leucogranite are commonly elongated. At the Malachite mineralized zone and in drill core of the Josette horizon, a breccia unit mapped and logged as fragmental granitic gneiss represents a marker lying structurally above the mineralized magnetitite. The significance of this breccia is unclear. It might indicate that the leucogranite is part of a felsic volcanic complex (Gauthier et al., 2004) and this unit represents a volcaniclastic rock; alternatively it may have originated by tectonic or hydraulic fracturing (Clark et al., 2005).

Folding and boudinage in the magnetitites and associated magnetite-rich breccias, are observed at all scales in most of the mineralized zones.

3. Age of the REE mineralization

The 1165+4/-2 Ma (U-Pb zircon; David, 2014, personal communication) age of the quartz-phyric and magnetite-bearing leucogranite of the Canatiche complex that hosts the Josette horizon provides a maximum age for the Josette Horizon and other mineralized zones.

An age of 983 ± 6 Ma (David, 2014, personal communication) from REE-bearing titanites in the calcsilicate minerals veins that brecciated the magnetitite suggest a late Grenvillian age for REE enrichment at the Josette horizon. This age is in agreement with the 972 ± 5 Ma age on titanites reported by Gauthier et al. (2004) from magnetitite at the Josette mineralized zone. This late Grenvillian age for REE enrichment is supported by the minimal deformation observed in the apatite-allanite-britholite veins and veinlets and in the calcsilicate minerals veins, which commonly contain centimetre-scale euhedral crystals of apatite, allanite, andradite and hornblende.

An age of 947 ± 4 Ma (U-Pb zircon; David, 2014, personal communication) from a pegmatite cutting the mineralized zone in the Josette horizon and a similar age of 951 Ma (U-Pb titanite, perovskite and allanite; Gauthier et al., 2004) from a pegmatite cutting a Cu-bearing magnetite vein in a ductile shear zone at the Grabuge mineralized zone suggest that the late granitic magmatism is associated with the unroofing and cooling of both Canatiche and Manitou complexes during the Rigolet event of the Grenville Orogeny (Gauthier et al., 2004 and Clark et al., 2005).

4. Mineralized zones

The main mineralized zones are Malachite, Josette, Andradite, Fluorine, Grabuge and Gabriel (Fig. 2), and have been described by Gauthier et al. (2004) and Clark et al. (2005 and 2010). Magnetite is omnipresent as an accessory mineral in the Canatiche granitoids, occurring as finely disseminated grains and clots locally associated with fluorite. However, significant magnetite accumulation (magnetitite) is generally restricted to individual mineralized zones, where it forms: 1) massive magnetitite and brecciated magnetitite, 1-30 m thick; 2) magnetite-rich breccias and pseudobreccias; 3) stockworks of magnetite and calcsilicate veins; and 4) networks of anastomosing, centimetre- to decimetre-scale magnetite veins and veinlets, commonly containing apatite and allanite-bearing calcsilicate veins in the leucogranite.

The mineralized zones occur in three en-echelon zones that are concordant with the local structural grain. They consist of semi-massive to massive magnetite-bearing hydrothermal iron formation, or magnetitite, mineralized with copper and REE. Major differences between the Josette, Malachite, Andradite, Fluorine, Grabuge, and Gabriel mineralized zones involve the thickness and lateral extent of the magnetitite and its associated calcsilicate-bearing minerals veins and stockworks. Below we focus on Josette mineralization, which displays the highest grade in REE and Cu.

4.1. Josette mineralization

The mineralized zone at the Josette horizon is composed of massive and brecciated magnetitite and breccias and stockworks of magnetite, and calcsilicate veins hosted by a gneissic leucogranite. The mineralization outcropping in the central part of the horizon consists of massive and brecciated magnetitite, with stockworks of REE-bearing (apatite-britholite-allanite) calcsilicate minerals (with andradite, fluorite, blue-green hornblende) and late sulphides veins and veinlets (pyrite, chalcopyrite and pyrrhotite), hosted by a gneissic, quartz–phenocrysts bearing leucogranite. This central part displays a copper enrichment and higher U and Th content relative to the deep or lateral mineralized extensions of the Josette horizon. Analytical results of the channel samples assayed 2.95% TREO and 1.44% Cu over 10 m, including a high-grade sub-zone of: 4.59% TREO and 2.62% Cu over 2 m. The mineralized rocks are composed of magnetite, chalcopyrite, pyrite, pyrrhotite, bornite, molybdenite, apatite, and fluorite (Gauthier et al., 2004, Clark et al., 2005). The predominant REE-bearing minerals are allanite, apatite, britholite and kainosite. The mineralized zone is intruded by mafic rocks (gabbros and possibly lamprophyres), which are deformed and metamorphosed to amphibolite facies, and cut by late Grenvillian granite and pegmatite dikes.

Diamond drilling, indicates that REE mineralization is not only in the magnetitite but also in stockworks of magnetite and calcsilicate veins. The REEs and Cu mineralization in the Josette horizon occurs in three zones: upper breccia, magnetitite, and lower breccia.

The upper breccia zone is composed of magnetite veins with variable content of fluorite veinlets, locally associated with centimetre- to decimetre-scale veins of specular hematite, and centimetre- to decimetre-scale muscovite-rich bands replacing the leucogranite or the fragmental gneiss. The upper breccia zone is well developed in the fragmental gneiss (interpreted as a metamorphosed lapilli-block tuff). The thickness of the upper breccia zone varies from 1 metre to 10 metres. It generally contains very low grades in REEs.

The central magnetitite zone is a hydrothermal iron formation with more than 50% magnetite, and contains high-grade REEs, Cu, P and F. The magnetitite is a heterogeneous brecciated

rock with centimetre- to decimetre-thick lenses of fine-grained massive magnetite (>70%), and disseminated apatite, hornblende, quartz and chalcopyrite. The massive magnetitite is brecciated by stockworks of decimetre-sized metasomatic veins of secondary magnetite and veins of usually coarse apatite-britholite-allanite±kainosite with andradite, blue-green hornblende, and titanite, and locally with clinopyroxene, scapolite, plagioclase, siderite, calcite and quartz (Fig. 3). Large euhedral crystals of andradite and allanite have been observed in some veins. Veins of apatite with crystals up to 5 cm, along with intergrown britholite are characteristically red and usually indicate high-grade REE. Locally, veins can totally replace the massive magnetitite. The thickness of the magnetitite zone varies from 1 metre to more than 40 metres due to large-scale boudinage and fold limb attenuation. Most of the REEs are found in the apatite, britholite allanite and kainosite in the calcsilicates veins. The massive magnetitite contains lower grades.

The lower breccia zone, 1 metre to more than 40 metres thick, consists of centimetre- to decimetre-thick stratabound, lenticular, fine-grained magnetitite veins and boudins aligned along the regional gneissosity in the leucogranite. These rocks are cut, and locally replaced, by REE-bearing calcsilicate stockworks and veins, with or without magnetite (Fig. 4). The calcsilicate veins straddle the boundary between the massive magnetitite and the host leucogranite and their mineralogy is the same as in the magnetitite zone. The size of the stockworks and the number of veins decrease away from the magnetitite. Typically, the leucogranite shows intense potassic alteration and late hematization. At depth in the northeastern part of the Josette horizon, the REE-mineralization becomes more important in the lower breccia zone than in the magnetitite zone.

4.2. Results of 2012 and 2013 drilling

Drilling in 2012 and 2013 was designed to evaluate the thickness, continuity, and REE content of the Josette horizon (Fig. 5). The Josette horizon was subdivided into two sectors: Josette Northeast and Josette Southwest. In the central part of the Josette horizon, the magnetitite and the lower breccias are less than 5 metres thick; in some holes the magnetitite is absent. Although similar in terms of rock types and mineralogy, the mineralized zone in the southwest sector shows greater thickness (locally up to 60 metres) but lower REE grades. Locally, copper reaches as much as 3% over a metre but continuity between holes is lacking.

The best REE mineralized intervals are in the northeastern sector of the Josette horizon as shown Figure 5 with higher REO factor (equivalent of the metal factor except this is the total rare earth oxides value multiplied by the length of the mineralized section of core). Some of the best weighted average intervals are 2.38% TREO over 48.8 metres (hole 11-58) in the upper part of Josette Northeast, predominantly the magnetitite zone, and 2.12% TREO over 60 m (hole 13-112), including 12% TREO over 3 m, in the deeper lower breccia zone (Fig. 5). Neodymium-Eu-Tb-Dy and Y, the most sought

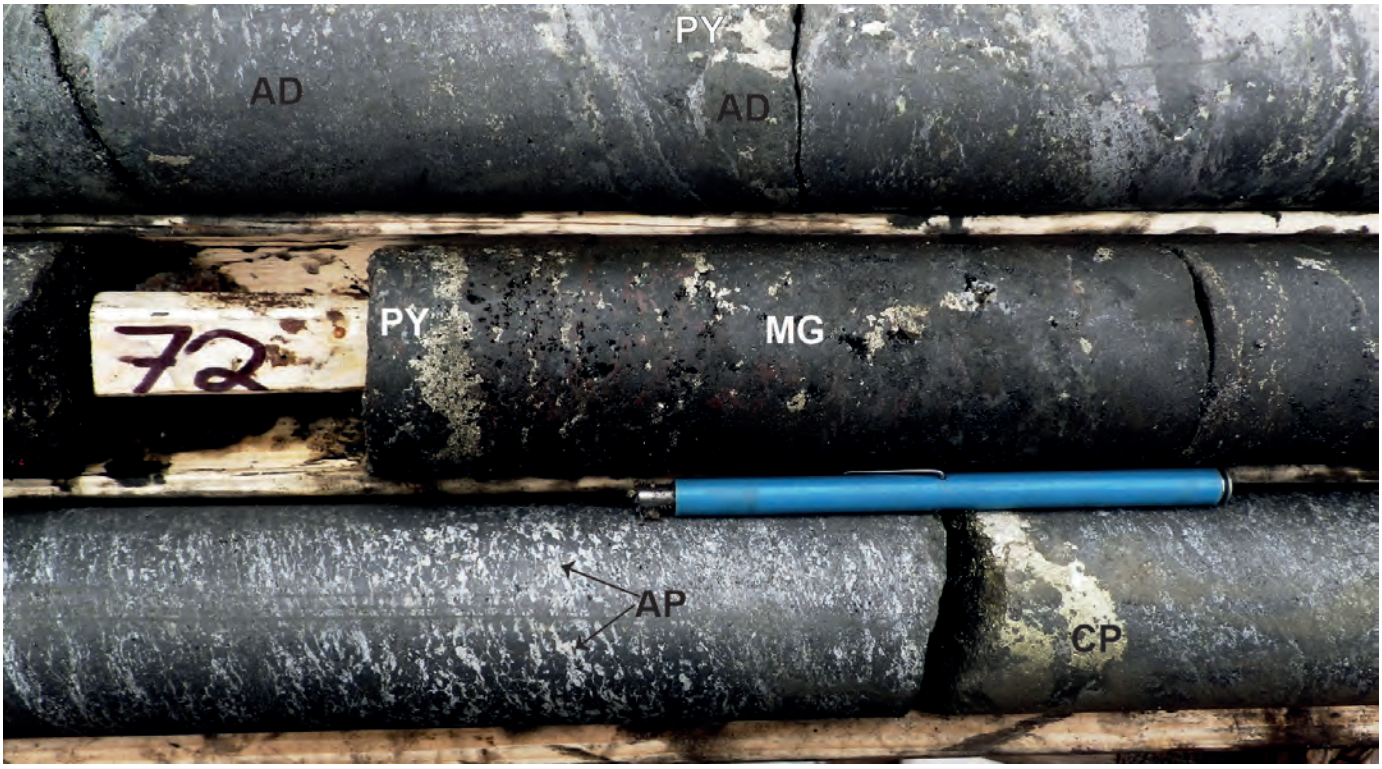

Fig. 3. Magnetitite zone with massive fine-grained magnetite, locally porous, cut by apatite (AP)-britholite-andradite (AD) veins and veinlets (upper and lower part of the photo) and by pyrite (PY) –chalcopyrite (CP) veins, from hole 10885-12-63. The magnet is 15 cm long.

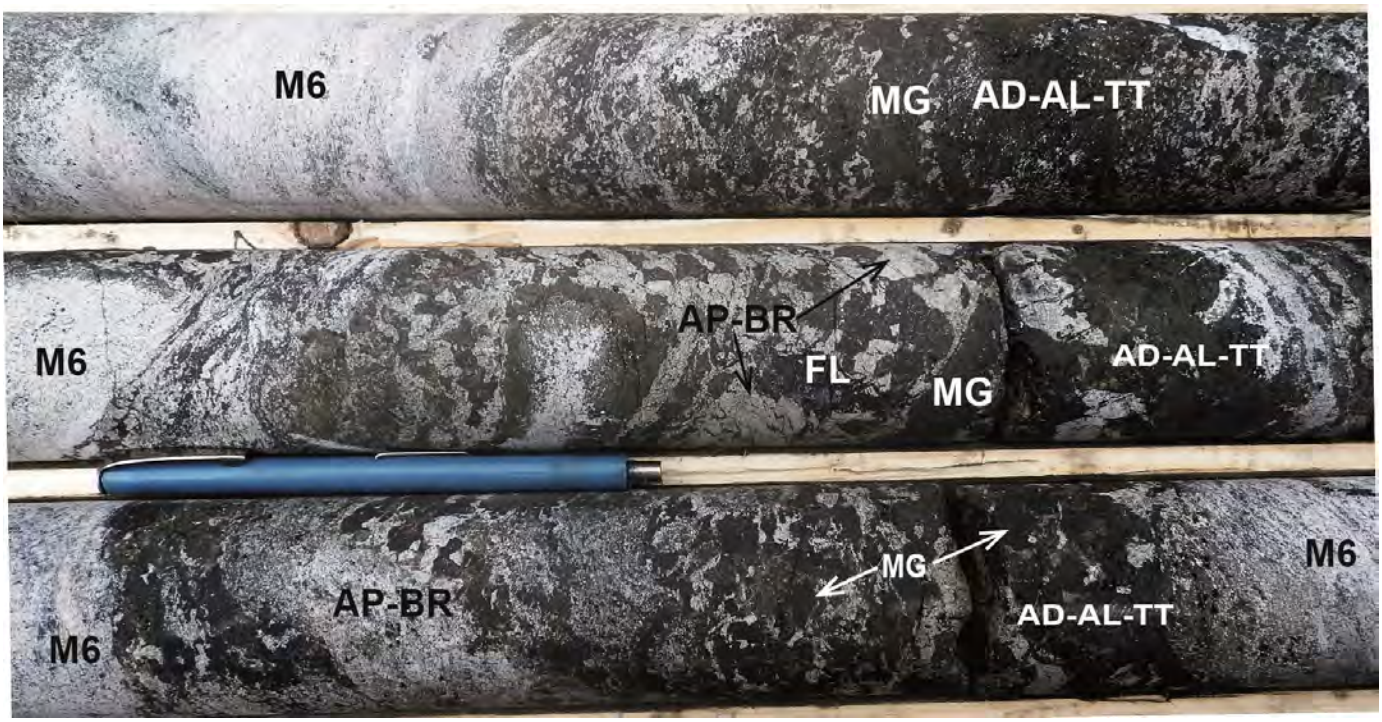

Fig. 4. Apatite (AP), britholite (BR)- and allanite (AL)-andradite (AD)-titanite (TT)-magnetite (MG) bearing calcsilicate minerals zones (in greenish grey tint with large green-black andradite crystals), locally with fluorite (FL) (blue-violet crystals in the central part of the photo) that brecciated older magnetite veins (MG); black fine-grained magnetite fragments) and the host metasomatized gneissic leucogranite (M6; in white pink).

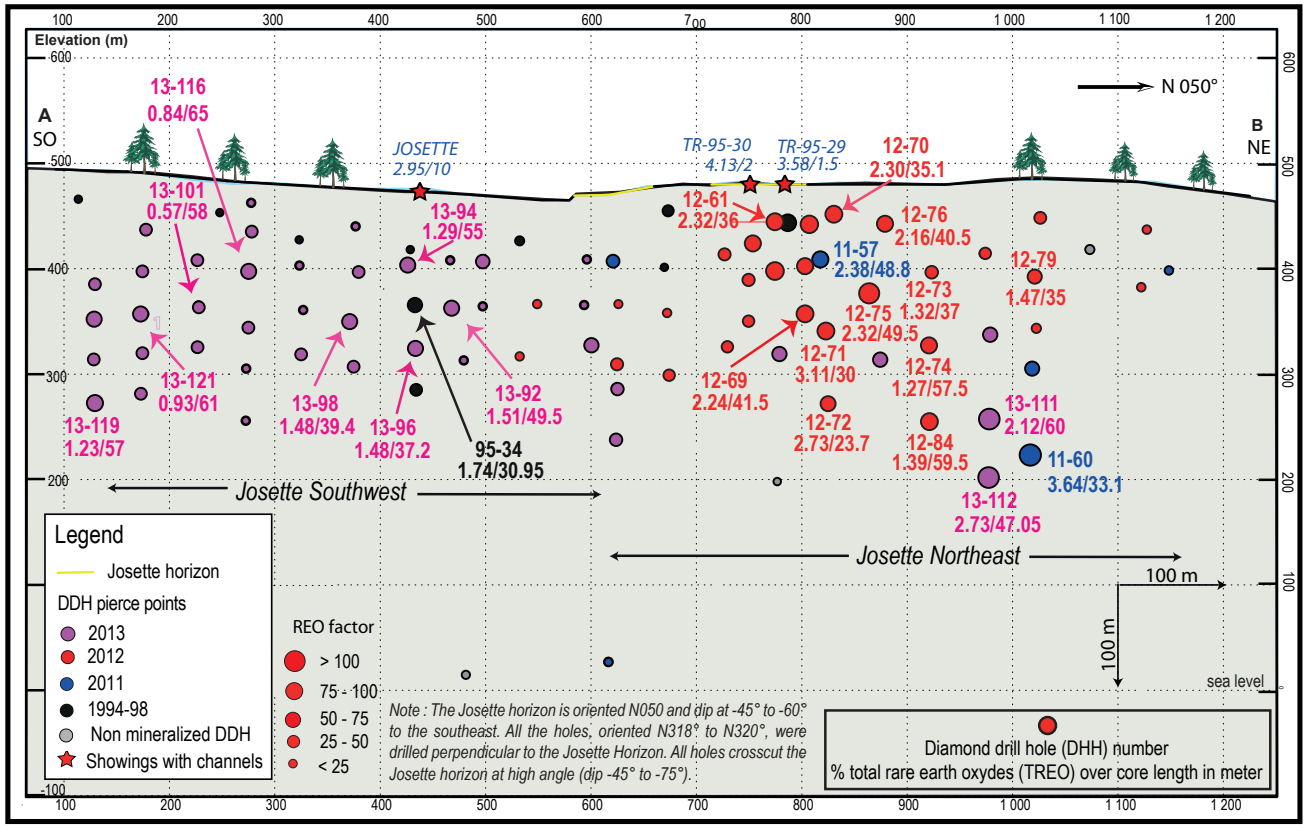

Fig. 5. Vertical longitudinal section of the Josette horizon, looking northeast with pierce points for the 1994 to 2013 diamond-drill holes. The size of the circles shows the range of the REO factor. The REO factor = % TREO multiplied by the core length (not the true thickness) in metres. Circle colours represent drilling year.

REE under current market conditions, represent 35 to 45% of the total REO's.

4.3. Mineralogy and distribution of REE

Apatite, britholite, and allanite are the main sites for REE in the Josette horizon (Wilhelmy, 2014; Laflamme, 2015). Kainosite ($Ca_2(Y,Ce)\ SiO_4O_{12}(CO_3)\bullet(H_2O)$), monazite ($(Ce, La, Nd, Th)PO_4$), bastnaesite ($((Ce,La,Y)CO_3F$), gadolinite ($Y_2Fe^{2+}Be_2Si_2O_{10}$), synchysite ($(Ca(Ce,La)(CO_3)2F)$ and keilhauite ($((Ca,Ti)(Al_2,Fe_2,Y_2)SiO_5)$ have been locally identified but are rare. Chemical analyses of apatite have shown an average REE and Y of more than 2.5%, with Y, Ce, Nd and Gd as the main REE. It was selected as an attractive economic target for REE, Y and phosphate.

Two types of apatite have been observed. A fine-grained primary apatite, that forms small anhedral grains in contact with, and included in, magnetite, and a secondary coarse-grained apatite variably replaced by britholite. Britholite appears as fine inclusions in apatite, as crystals along the boundaries of apatite grains, and as veinlets that replace apatite. Due to complex textural relations with apatite, britholite contents may have been underestimated during mineralogical study. Allanite forms irregular clusters of anhedral grains or centimetre-scale euhedral crystals in the calcsilicate veins.

The modal apatite content varies between 8 and 12% in the mineralized zone. The average content of REE in the apatite is 7.9 wt.%, with a maximum of 12.5 wt.% REE in a breccia zone sample. The Y content varies from 37 to 45% of the total REE of the apatite. Varieties of Y-britholite, Ce-britholite and Ce-Nd-britholite have been detected by chemical analyses of a mixture of apatite and britholite during thin section studies of the magnetitite and breccia zones. Britholite is the main carrier of Y in the mineralized zone of the Josette horizon. Its Y content is variable depending of the subspecies of britholite. The average Y_2O_3 content is 10.7 wt.% and ranges from 9 to 19 wt.%. Britholite hosts a significant Nd_2O_3, with an average of 8.5 wt.%. Allanite averages 28 wt.% REE and hosts most of the light REE (La, Ce, Nd). It is the main carrier of Nd_2O_3, with an average of 5.1 wt.%. Kainosite is a source of Y but it is a minor component. In the mineralized zone, andradite averages 4.26 wt.% REE (with 70% of Y) and titanite 5.49 wt.% REE (with 35% of Y). In the breccia zone, andradite is an important component, comprising up to 15% of the mineral proportion of the head grade of the metallurgical samples.

5. Metallurgical tests

Two phases of metallurgical tests were done at COREM's facilities in Quebec City in 2013 and 2014. The second phase was more extensive and included physical separation tests of the iron concentrate, grindability and abrasion tests, and flotation and leaching tests. The final flow sheet includes magnetic separation, sulphide flotation, flotation of REE-bearing phosphates and silicates to ultimately produce one or two concentrates (one of REE-bearing phosphates and a second one of REE-bearing silicates), and subsequent lixiviation of the concentrates to produce solutions that contains the rare earth elements (Laflamme, 2015). Results of Low Intensity Magnetic Separation (LIMS) show that the magnetic iron concentrate contains a high concentration of deleterious elements (phosphate, silica or sulphide) that do not meet steel industry requirements. On the other hand, the magnetic separation is essential in the ore treatment as it eliminates up to 50% of the total mass that has to be processed by flotation with a very low loss of REE (less than 10%) for the ore from the magnetitite. Flotation results show that 84% to 90% of the REE-bearing minerals are recovered in the concentrates, the traditional phosphate flotation with a fatty acid collector returning the highest recoveries. Acid (HCL) lixiviation of the different concentrates allows recovery of 80% to 94% of REE

6. Conclusion

Zones of the Kwyjibo deposit are examples of IOCG-type mineralization enriched in REE. Nedymium, Tb, Dy and Y, and the extent of mineralization are of economic interest. The best mineralized section lies in the northeastern part of the Josette horizon, where high REE content is found in the magnetitite and the lower breccia zone. In the southwestern part, the magnetitite and the lower breccia zones are thicker but the REE content is lower. Most of the REE are contained in apatite, allanite, and britholite. Light REE are mostly concentrated in allanite and, to a lesser extent, in Ce-britholite and Ce-Nd britholite. Heavy REEs are concentrated in apatite and britholite and, to a lesser extent, in kainosite, andradite and titanite. Metallurgical tests show that most of the REE-bearing minerals can be recovered by traditional phosphate flotation. Lixiviation (with HCl) of the concentrates allows high recoveries by dissolving most of the REE-bearing minerals. Further tests are mandatory to optimize the flow sheet, maximize the recovery of REE-bearing minerals during the flotation process, and to evaluate the best methods of lixiviation and recovery of Nd-Eu-Dy-Tb-Y after the lixiviation.

References cited

Barton, MD., 2014. Iron Oxide (-Cu-Au-REE-P-Ag-U-Co) Systems. In: Holland, H. and Turkian, K., (Eds.), Treatise in Geochemistry, 2nd Edition, Volume 13, Geochemistry of Mineral Deposits, pp. 515-541.

Clark, T., Gobeil, A., and David, J., 2005. Iron Oxide-Copper-Gold-type and related deposits in the Manitou Lake area, eastern Grenville Province, Quebec: variations in setting, composition, and style. Canadian Journal of Earth Sciences, 42, 1829-1845.

Clark, T., Gobeil, A., Chevé, S., 2010. Alteration in IOCG-type and Related Deposits in the Manitou Lake Area, Eastern Grenville Province, Quebec. In: Corriveau, L. and Mumin, H., (Eds.), Exploring for Iron Oxide Copper-Gold Deposits: Canada and Global Analogues. Geological Association of Canada, Short Course Notes 20, pp. 127-146.

Corriveau, L., 2007. Iron oxide copper-gold deposits: A Canadian perspective. In: Goodfellow, W.D., (Ed.), Mineral Deposits of Canada: A Synthesis of Major Deposit-Types, District Metallogeny, the Evolution of Geological Provinces, and Exploration Methods. Geological Association of Canada, Mineral Deposits Division, Special Publication 5, pp. 307-328.

Gauthier, M., Chartrand, F., Cayer, A. and David, J., 2004.

The Kwyjibo Cu-REE-U-Au-Mo-F Property, Quebec: A Mesoproterozoic Polymetallic Iron Oxide Deposit in the Northeastern Grenville Province. Economic Geology, 99, 1177-1196.

Groves, D.I., Bierlin, F.P., Meinert, L.D. and Hitzman, M.W., 2010. Iron Oxide Copper-Gold (IOCG) Deposit through Earth History: Implications for Origin, Lithospheric Setting, and Distinction from Other Epigenetic Iron Oxide Deposits. Economic Geology, 105, 641-654.

Laflamme, P., 2015. Production de concentrés et lixiviation d'apatites/terres rares, phase 2. Unpublished internal report for SOQUEM. COREM, Quebec, Canada, rapport final T1544, révision 2, 377p.

Long, K.R., Van Gosen, B.S., Foley, N.K., and Cordier, D., 2010. The principal rare earth elements deposits of the United States-A summary of domestic deposits and a global perspective. In: U.S. Geological Survey Scientific Investigations, Report 2010–5220, 96p.

Parak, T., 1973. Rare Earths in the Apatite Iron Ores of Lapland Together With Some Data About the Sr, Th, and U Content of These Ores. Economic Geology, 68, 210-221.

Perry, C., and Raymond, D., 1996. Le projet Nipissis de SOQUEM-IOC : Un nouveau type de minéralisation cuprifère sur la Côte-Nord. In : Vers de nouvelles découvertes; Séminaire d'information sur la recherche géologique, programme et résumés. Ministère des Ressources naturelles du Québec, DV 96-02, p. 16.

Wilhelmy, J.-F., 2014. Étude détaillée de cinquante (50) lames minces polies du projet Kwyjibo. Unpublished internal report for SOQUEM. COREM, Quebec, Canada, rapport T1543, 277p.

A review of hydrometallurgical flowsheets considered in current REE projects

N. Verbaan[1, a], K. Bradley[1], J. Brown[1], and S. Mackie[1]

[1] SGS Mineral Services (Lakefield Site), 185 Concession Street, PO Box 4300, Lakefield, ON, K02 2H0
[a] corresponding author: niels.verbaan@sgs.com

Recommended citation: Verbaan, N., Bradley, K., Brown, J., and Mackie, S., 2015. A review of hydrometallurgical flowsheets considered in current REE projects. In: Simandl, G.J. and Neetz, M., (Eds.), Symposium on Strategic and Critical Materials Proceedings, November 13-14, 2015, Victoria, British Columbia. British Columbia Ministry of Energy and Mines, British Columbia Geological Survey Paper 2015-3, pp. 147-162.

Summary

The last 10 years witnessed a sharp increase in the number of REE projects under development because of a surge in REE prices. Seeking to take advantage of escalating metal prices, many junior mining companies focused exploration efforts on REE. Although determining the size and nature of a REE property is a key step in project development, it was quickly discovered that the metallurgical processes required to extract REE from these deposits are dependent on ore mineralogy, which is commonly varied and complex. A wide range of extractive metallurgical processes are known for REE minerals including caustic cracking, acid baking, agitated leaching, heap leaching, and ionic desorption. Furthermore, options for recovering REE from leach liquors are also numerous. In many cases, equipment used in these processes is relatively novel, and operating experience to benchmark against is minimal. Hence extensive testing is required to minimize the risks associated with these projects.

In this paper we review the various metallurgical processes currently under consideration by mining companies pursuing REE deposits, and attempt to identify potential key challenges and risks.

1. Introduction

The boom in rare earth element (REE) prices, which peaked in mid-2011, prompted the appearance of many new junior REE mining companies on the Australian and Toronto Stock exchanges (ASX and TSX). Many of these companies claimed easy metallurgy for their projects and presented accelerated paths to production and the phrase 'race to production' was commonly used (Trumbull, 2013). Typical hurdles in the 'race' are defining the resource, developing a metallurgical flowsheet, and gaining environmental permits. REE have been mined and processed for decades, but recent processing experience is predominantly in China, and although information on processing technologies in that country are known, mineralogical differences make this knowledge of limited relevance. In the West, detailed design knowledge for the separation of REE has been largely lost.

Herein we present an overview of the processing routes used by selected REE junior mining companies and by the two current or recent operating mines in the Western world (Mount Weld mine, Western Australia; Mountain Pass mine, California). Using data from publically available preliminary economic assessments (PEA), preliminary feasibility studies (PFS), feasibility studies (FS), and other NI 43-101 compliant technical documents, as well as environmental impact statements (EIS) and press releases, we review 26 projects, including 12 from North America, 7 from Africa, 4 from Australia, and one from each of South America, Europe, and Asia (Table 1). The Mount Weld mine and concentrator is operated by Lynas Corporation with a hydrometallurgical processing plant in Malaysia (Lynas Advanced Materials Plant; LAMP). The first concentrate was fed to the kiln in November 2012. The Mountain Pass mine is operated by Molycorp Inc. A new plant started its ramp-up in January 2013, but never achieved technical, production, or economic targets, and was recently placed on Care and Maintenance (Molycorp, 2015).

2. REE project geology and mineralogy

Adopting the geological classification of REE deposits provided by Simandl (2012, 2014), we consider projects that are related to alkaline rocks and carbonatites, and vein, placers (and paleoplacers), and ionic clay deposits (Table 1).

The alkaline granite-hosted projects are typically relatively low grade (<2% TREO), but display a comparatively high relative HREO (Heavy Rare Earth Oxide; Sm to Lu+Y) distribution (HREO/TREO, %). With the exception of the Kvanefjeld project in Greenland, all alkaline rock associated projects have a HREO distribution of greater than 20%. The mainly xenotime Browns Range project has the highest relative HREO distribution (87%). The HREE-carrying minerals are typically xenotime (YPO_4), zirconium silicates (eudialyte or zircon), or fergusonite ($Y,Ln(NbO_4)$).

Both plants now operating in the Western world were designed to process carbonatite-type mineralization. Ore grades for this type of deposit vary significantly, from a low 0.1% TREO in the Lofdal project (Dodd et al., 2014) to an exceptionally high 54.3% in the Gakara deposit (Rainbow Rare Earths, 2015). The Lofdal mineralization consists predominantly of xenotime, which is highly unusual for a carbonatite-related deposit.

Table 1. REE Projects and REE mineralogy overview.

Property	Owner	Country	Development Stage	Host Rock	REE Carrying Minerals	% TREO Ore	% HREO relative	Reference
Bokan Mountain	Ucore Rare Metals Inc.	USA	PEA	Alkaline rock-associated	Thalenite, bastnasite, xenotime, monazite	0.65	40	Bentzen et al., 2013
Browns Range	Northern Minerals Ltd.	Australia	FS	Alkaline rock-associated	Xenotime	0.66	87	Northern Minerals, 2015
Dubbo	Alkane Resources	Australia	FS	Alkaline rock-associated	Eudialyte, bastnasite, zircon, natroniobite, columbite	0.9	25	Alkane Resources, 2012
Kvanefjeld	Greenland Minerals	Greenland	FS	Alkaline rock-associated	Steenstrupine (complex sodic phospho-silicate)	1.2	11.8	Greenland Minerals, 2015a
Nechalacho	Avalon Rare Metals Inc.	Canada	FS	Alkaline rock-associated	LREE in bastnasite, synchisite, monazite and allanite. HREE in zircon, fergusonite and xenotime	1.72	27.3	Ciulescu et al., 2013
Norra Karr	Tasman Metals Ltd.	Sweden	PFS	Alkaline rock-associated	Eudialyte	0.59	52	Short et al., 2015
Port Hope Simpson	Search Minerals Inc.	Canada	PEA	Alkaline rock-associated	Allanite, fergusonite, chevkinite	1.07	19.6	Dreisinger et al., 2014
Round Top	Texas Rare Earth Resources Corp.	USA	PEA	Alkaline rock-associated	Yttrofluorite	0.06	72	Hulse et al., 2014
Strange Lake	Quest Rare Minerals Ltd.	Canada	PEA	Alkaline rock-associated	Complex silicates, phosphates and zircon	0.93	39	Gowans et al., 2014
Zeus	Matamec Explorations Inc.	Canada	FS	Alkaline rock-associated	Eudialyte	0.41	37	Saucier et al., 2013
Ashram	Commerce Resources Corp.	Canada	PEA	Carbonatite	Monazite, trace bastnasite, xenotime	1.81	4.7	Gagnon et al., 2015
Bayan Obo	CN Northern Rare Earth (Grp)	China	Operating	Carbonatite	Bastnasite / monazite	6		Zhi Li and Yang, 2014
Bear Lodge	Rare Element Resources Ltd.	USA	PFS	Carbonatite	Bastnasite, synchysite, monazite, cerianite, ancylite	4.7	4.4	Dahlberg, 2014

Table 1. Continued.

Property	Owner	Country	Development Stage	Host Rock	REE Carrying Minerals	% TREO Ore	% HREO relative	Reference
Gakara	Rainbow Rare Earths Limited	Burundi	Reserves Development	Carbonatite	Monazite, bastnasite	54.3	1.1	Rainbow Rare Earths, 2015
Lofdal	Namibia Rare Earths Inc.	Namibia	PEA	Carbonatite	Xenotime	0.1	76	Dodd et al., 2014
Montviel	GeoMega Resources Inc.	Canada	PEA under development	Carbonatite	Ba-Ce carbonates and monazite	1.5	1.8	Belzille et al., 2015
Mountain Pass	Molycorp Inc.	USA	Care and Maintenance	Carbonatite	Bastnasite	8	1	Molycorp 2014 a, b, 2015
Mt Weld	Lynas Corp. Ltd.	Australia	Operating	Carbonatite	Monazite, apatite	15.4	3	Lynas, 2005
Ngualla	Peak Resources Ltd.	Tanzania	PFS	Carbonatite	Bastnasite, monazite	4.54	1.9	Peak Resources, 2014
Songwe Hill	Mkango Resources Ltd.	Malawi	PFS	Carbonatite	Synchysite, apatite	1.6	6.8	Croll et al., 2014
St-Honoré	Magris Resources Inc.	Canada	unknown	Carbonatite	Bastnasite / monazite	1.65		
Zandkopsdrift	Frontier Rare Earths Ltd.	South Africa	PFS	Carbonatite	Monazite	1.9	7.8	Harper et al., 2015
Serra Verde	Mineracao Serra Verde	Brasil	PFS (not published)	Ionic clay	N/A	0.16	25 (37 if no Ce)	Rocha et al., 2013 and 2014
Tantalus	Tantalus Rare Earths AG	Madagascar	Reserves Development	Ionic clay	N/A	0.09	19 (30 if no Ce)	Desharnais et al., 2014
Eco Ridge	Pele Mountain Resources Inc.	Canada	PEA	Vein / sedimentary	Monazite + U minerals	0.15	11.4	Cox et al., 2012
Nolans Bore	Arafura Resources Ltd.	Australia	FS	Vein / sedimentary	Apatite, allanite	2.6	4	Arafura Resources, 2014
Steenkampskraal	Great Western Minerals Grp Ltd.	South Africa	FS	Vein / sedimentary	Monazite	14.4	3.8	Clay et al., 2014

Recent studies indicate that the Lofdal deposit, consisting of narrow veinlets of albitite that have been subjected to late carbonate alteration, is hydrothermal and not carbonatite hosted (Williams-Jones et al., 2015). Mineralization at Gakara is probably carbonatite related; where exposed the mineralization consists of variably oriented veins and veinlets a few cm to tens of cm thick (Rainbow Rare Earths, 2015). No NI 43-101 compliant report is available on the company website.

The two ionic clay projects (Table 1) are a distinct category and are similar to the ionic clay projects in Southern China. Grades are typically very low (<0.2% TREO) and only REE adsorbed onto clay minerals are recovered. REE associated with competent REE-carrying minerals (e.g., monazite, xenotime) are refractory and not typically extracted during the clay desorption process. Cerium and thorium are not sorbed on clay but were precipitated during weathering as the moderately refractory mineral cerianite $(Ce^{4+},Th)O_2$, and both elements are therefore typically not extracted in the desorption process (Rocha et al., 2013, 2014). It therefore makes sense to report the relative HREO distribution expressed as HREO/(TREO-Ce), which consequently leads to HREO distributions of 30% (Tantalus) and 37% (Serra Verde).

3. Generic REE flowsheets

A generic conceptual flowsheet describing most of the processes is shown in Figure 1. The following steps are normally included.

- Mineral beneficiation to produce an upgraded mineral concentrate. Most processing costs are incurred in the hydrometallurgical plant, where REE are chemically extracted using an acid or alkaline reagent or a combination thereof. Operating costs are usually directly related to material throughput, therefore a reduction in mass recovery (or equivalent increase in concentrate grade), even at the expense of some REE recovery, is usually worth considering. Ionic clays cannot be economically upgraded and are therefore treated on a whole ore basis.
- Chemical extraction using acid to dissolve REE into a pregnant leach solution (PLS), commonly after an alkaline process to 'crack' the refractory minerals.
- Primary purification. Most flowsheets include a simple acid neutralization step using alkaline reagents such lime, limestone, MgO, $MgCO_3$, or Na_2CO_3. Care must be taken when using calcium-based reagents in sulphate media because REE co-precipitation with gypsum can lead to significant REE losses. Elements such as Th, Fe, P and Al are usually targeted at this stage.
- Crude (or primary) REE precipitation. Many flowsheets produce a partial purified intermediate REE precipitate, which is subsequently re-leached (with or without selective cerium removal). This allows further purification steps to be conducted on more concentrated solutions and therefore a much smaller plant size (and associated lower capital expenditure).
- Impurity removal. Undesirable elements such as uranium, radium, residual thorium, and base metals are removed in a secondary impurity removal step.
- Product recovery. A final purified REO product is produced by oxalic acid (followed by calcination) or carbonate precipitation.
- Reagent regeneration. The reagent could be acid (H_2SO_4, HCl or HNO_3), alkaline (NaOH), or ($(NH_4)_2SO_4$). Although this usually leads to a net reduction in reagent consumption (and associated operating expenditures), it is always at the cost of increased operational complexity.

4. REE flowsheets: beneficiation and pre-leaching

Typically, metallurgical testwork focuses on the beneficiation and chemical extraction stages. In beneficiation, direct flotation of REE minerals is the main option for the alkaline rock associated and carbonatite ore types due to the finely disseminated nature of the mineralization. Magnetic or gravity separation has also found applications to further upgrade flotation concentrate. Of the 26 projects evaluated (Table 2), 19 included a beneficiation flowsheet. Of these 19 projects, 13 included flotation as a separation technique, including 6 in combination with magnetic separation. Magnetic separation was used as a separation technology in 11 projects, including 2 as a standalone process, 1 combined with dense media separation, and 2 combined with X-ray sorting.

Ideally, low-grade ore is upgraded to a concentrate with minimal losses. In reality mineralogical analyses reveal that the REE-carrying minerals are commonly locked in gangue minerals, leading to reduced concentrate grades. Table 2 summarizes the reported or estimated mineral concentrate grades, as produced. An upgrade factor (concentrate-grade to ore-grade ratio) can be calculated, which typically ranges from 2 to 8, with outliers such as the Browns Range (Northern Minerals, 2015) and Kvanefjeld (Greenland Minerals, 2015a) properties with upgrade factors of 30 and 12.5 respectively.

The design for Ashram deposit stands out due to combined mineral and hydrometallurgical processes to produce feed for chemical cracking (acid bake). Whereas the PEA (Gagnon et al., 2015) reports on a mineral processing route based on froth flotation only, a recent press release of Feb 11, 2015 (Commerce Resources, 2015) indicates that the 10% grade flotation concentrate is pre-leached with HCl, and the leach residue further upgraded by wet high-intensity magnetic separation (WHIMS) to produce a final concentrate of 39% TREO.

The Songwe property in Malawi, which produces a 4.7% TREO concentrate, also employs an HCl-based pre-leach at moderately low acidity of pH 3 to 3.5 (Croll et al., 2014). The pre-leach (or gangue leach) dissolves the calcite while leaving the REE-carrying minerals apatite and synchysite in the residue. Beer et al. (2014) reported that the pre-leach reduced flotation concentrate mass by 39%, with minimal HREE losses of 1%. The resulting liquor– predominantly $CaCl_2$ and $SrCl_2$– is used to regenerate HCl by the addition of H_2SO_4, which leads to the formation of gypsum. Similar to the Songwe Hill project,

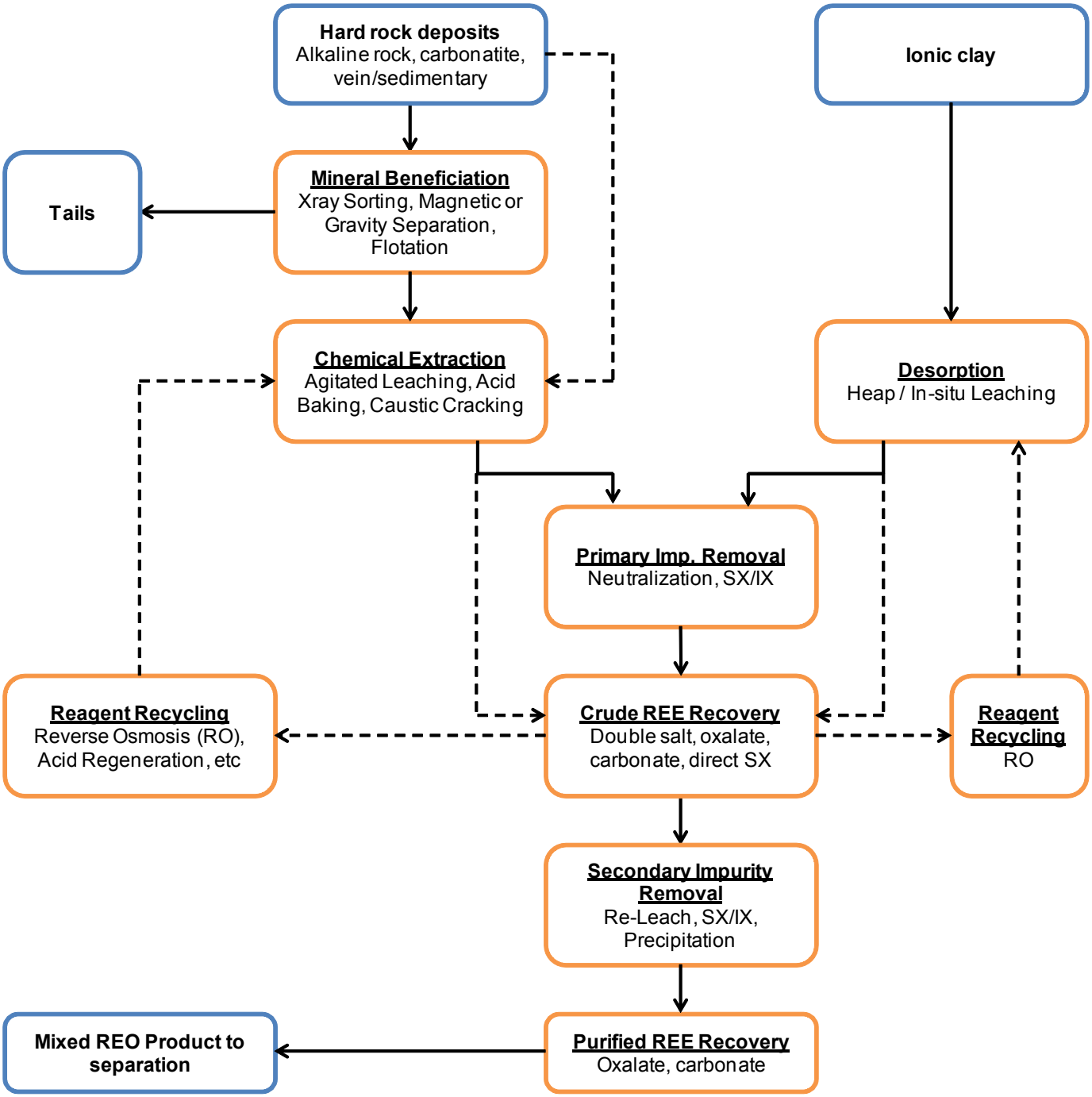

Fig. 1. Generic conceptual REE flowsheet.

the Lofdal property also uses an HCl based pre-leach to remove gangue minerals (Dodd et al., 2014).

5. Chemical treatment of concentrate

All projects require the use of hydrometallurgy (e.g., leaching, cracking, baking, sulphation) to dissolve the REE from the carrier minerals and subsequent separation of impurities (Fe, Al, PO_4, Th, U, base metals, radionuclides) from the REE.

A significant range of technologies and reagents is used in concentrate leach processes (Table 3). Of the 18 concentrate leach processes reviewed, 11 use sulphuric acid as primary lixiviant, 3 use hydrochloric acid and 1 uses nitric acid (Bokan Mountain). In addition, three projects (Songwe Hill, Mountain Pass and Lofdal) use an intermediate caustic crack step to metathesize or crack phosphate minerals into REE hydroxides, which are subsequently leached in hydrochloric acid.

Table 2. Beneficiation processes.

Property	% TREO Ore	Beneficiation Process	% TREO Concentrate	Upgrade Factor
Bokan Mountain	0.65	X-ray sorting and magnetic separation	~2	3.1
Browns Range	0.66	Magnetic separation and flotation	20	30.3
Dubbo	0.9	none - whole ore leach	N/A	N/A
Kvanefjeld	1.2	Flotation	15	12.5
Nechalacho	1.72	Magnetic separation and flotation	6-8	4.1
Norra Karr	0.59	Magnetic separation	1.6	2.8
Port Hope Simpson	1.07	none - whole ore leach	N/A	N/A
Round Top	0.06	none - whole ore leach	N/A	N/A
Strange Lake	0.93	Flotation	1.5-2	1.9
Zeus	0.41	Magnetic separation	0.75	1.8
Ashram	1.81	Flotation	10	5.5
Bayan Obo	6	Magnetic separation and flotation	50	8.3
Bear Lodge	4.7	Size and gravity separation	~10	2.1
Gakara	54.3	unknown		
Lofdal	0.1	X-ray sorting and magnetic separation	17-20 (after pre-leach)	
Montviel	1.5	Flotation	3	2.0
Mountain Pass	8	Flotation	65	8.1
Mt Weld	15.4	Flotation	40	2.6
Ngualla	4.54	Magnetic separation and flotation	17	3.7
Songwe Hill	1.6	Flotation	4.7	2.9
St-Honoré	1.65	unknown		
Zandkopsdrift	1.9	none - whole ore leach	N/A	N/A
Serra Verde	0.16	none - whole ore leach (desorption of ionic clay)	N/A	N/A
Tantalus	0.09	none - whole ore leach (desorption of ionic clay)	N/A	N/A
Eco Ridge	0.15	Magnetic separation and flotation	0.6	4.0
Nolans Bore	2.6	Magnetic separation and flotation	8	3.1
Steenkampskraal	14.4	Magnetic separation and dense media separation	30	2.1

In terms of process simplicity, one could envisage the following ranking from simple to complex: straight agitated leaching; counter current agitated leaching; acid baking; integrated caustic crack; and agitated leaching. Five projects employ straight agitated/atmospheric acid leaching: Montviel (HCl), Norra Kärr (H_2SO_4), Zeus (H_2SO_4), Ngualla (H_2SO_4), and Bear Lodge (HCl). Except for the Norra Kärr and Zeus eudialyte projects, the others are carbonatite hosted. Short et al. (2015) reported that the Norra Kärr project to suffers from high silicon dissolution, which could lead to challenging liquid solid separation (LSS) properties and challenging performance in its direct solvent extraction (SX) process route to recover REE.

Due to the high cost of hydrochloric acid, projects involving HCl need to include acid recycling and/or regeneration strategies to remain economically viable. Of the technologies available (for review, see Bedrossian and Connell, 2014), the choice depends on the effluent stream composition and local site conditions. For example, at Mountain Pass a chlor-alkali plant converts NaCl from a separation plant into HCl and NaOH (Molycorp, 2014a), Montviel and Lofdal use low-temperature reaction of soluble $CaCl_2$ with H_2SO_4 to form HCl and $CaSO_4.2H_2O$ (Yu et al., 2013), and Bear Lodge uses evaporation and distillation of excess free HCl to form 20.2% HCl for re-use (Dahlberg, 2014).

Integrating the acid regeneration circuit adds a degree of complexity and should be thoroughly tested to determine the effect of impurities on the acid regeneration circuit and, conversely, the effect of recycling gypsum-saturated liquor back to a leach circuit. A high-purity brine is essential as feed for chlor-alkali plants and therefore additional purification circuits may be required. Molycorp (2014b) reported suffering from quality issues in its feed liquor, which impacted the overall plant operation.

Counter current leaching provides the advantage of lower overall acid consumption by using excess acidity from a strong acid leach stage to leach reactive ore components in a weak acid stage. In addition, the PLS moving forwards in the flowsheet typically requires less reagent to neutralize residual acidity (Fig. 2). Possible disadvantages include an additional liquid-solid separation step and the potential to lose soluble

Table 3. Overview of concentrate leach processes.

Property	% TREO Ore Grade	% TREO Concentrate Grade	REE Carrying Minerals	Concentrate Leach Process	Leach Extraction, % TREO
Kvanefjeld	1.2	15	Steenstrupine (complex sodic phospho-silicate)	Counter current atmospheric agitated leach with H_2SO_4 to leach U. The leach residue is caustic cracked and subsequently HCl leached	70[1]
Strange Lake	0.93	1.5-2	Complex silicates, phosphates + zircon	Selective Thermal Sulphation (STS) followed by water leaching of REE sulphates	88
Ashram	1.81	10	Monazite, trace bastnasite, xenotime	Pre-leach (HCl), WHIMS to produce 39% TREO con, Acid Bake (250ºC) in rotary kiln	95
Songwe Hill	1.6	4.7	Synchysite, apatite	Gangue pre-leach (PL) with HCl. Pre-leach liquor is treated to regenerate HCl. Pre-leach residue is leached with HCl and its residue caustic converted and leached again with HCl. Both leach liquors are combined and advance to purification	90
Montviel	1.5	3	Ba-Ce carbonates and monazite	Atmospheric / agitated acid leach using regenerated and recycled HCl	99
Mt Weld	15.4	40	Monazite, apatite	Acid Bake with H_2SO_4 in rotary kiln, followed by water leach of sulphated minerals	95
Mountain Pass	8	65	Bastnasite	Atmospheric / agiated acid leach using regenerated and recycled HCl. Leach residue is cracked (NaOH) and subsequently HCl leached	
Norra Karr	0.59	1.6	Eudialyte	Atmospheric / agitated leach with H_2SO_4	90
Zeus	0.41	0.75	Eudialyte	Atmospheric / agitated leach with H_2SO_4	85
Bayan Obo	6	50	Bastnasite / monazite	Acid Bake with H_2SO_4 in rotary kiln, followed by water leach of sulphated minerals	>90
Steenkampskraal	14.4	30	Monazite	Acid Bake with H_2SO_4 in rotary kiln, followed by water leach of sulphated minerals	95
Nechalacho	1.72	6-8	LREE in bastnasite, synchisite, monazite and allanite. HREE in zircon, fergusonite and xenotime	Thermal crack followed by HCl Leach	>93
Browns Range	0.66	20	Xenotime	Dried concentrate is mixed with H_2SO_4 in pug mill type device. Acid Bake in rotary kiln, followed by water leach of sulphated minerals	95
Ngualla	4.54	17	Bastnasite, monazite	Atmospheric / agitated leach with H_2SO_4	96
Nolans Bore	2.6	8	Apatite, allanite	Pre-leach with fresh H_2SO_4, Acid bake of pre-leach residue with fresh H_2SO_4. Preleach and acid bake water leach pregnant liquors are combined.	90
Eco Ridge	0.15	0.6	Monazite + U minerals	Acid Bake with H_2SO_4 in rotary kiln, followed by water leach of sulphated minerals	97
Bear Lodge	4.7	~10	Bastnasite, synchysite, monazite, cerianite,	Atmospheric / agitated leach with fresh 35% HCl and recovered 18% HCl	87
Bokan Mountain	0.65	~ 2	Thalenite, bastnasite, xenotime, monazite	Counter current atmospheric / agitated leach with HNO_3	93
Lofdal	0.1	17-20 (after pre-leach)	Xenotime	Atmospheric / agitated gangue leach with HCl. Pre-leach residue is caustic cracked and subsequently leached with HCl	

REE due to formation of double salts or incorporation into gypsum formed in the weak acid leach stage. Two projects are considering using a counter current acid flowsheet. At the Kvanefjeld project, concentrate is counter currently leached with H_2SO_4 to dissolve uranium, while the strong acid leach residue is metathesized with NaOH and subsequently leached with HCl to solublize REE. At the Bokan Mountain project, a counter current nitric acid leach process is being considered to dissolve REE (Bentzen et al., 2013).

Seven projects currently are using or considering using acid baking of mineral concentrate as part of the flowsheet (Strange Lake, Ashram, Mt Weld, Bayan Obo, Steenkampskraal, Browns Range and Eco Ridge).

Acid baking is typically used for concentrates or ores where straight agitated leaching will not 'crack' the REE minerals and a more aggressive mineral attack (in terms of reagent dosage and operating temperature) is required (Fig. 3). Acid baking, though considered a mature technology in China on high-grade (~50% TREO) concentrates, is not a common processing technology on any material in the Western world. The challenges arise from the fact that the mixture of liquid acid and feed (wet or dry) forms a high yield strength pasty mass, which dries out as it moves through a rotary kiln or other high-temperature processing equipment. Free and/or reaction

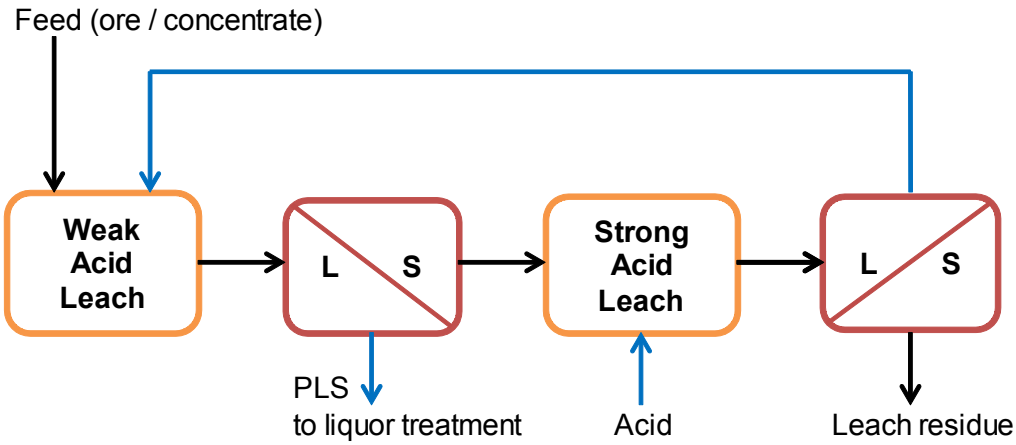

Fig. 2. Schematic counter current leach process.

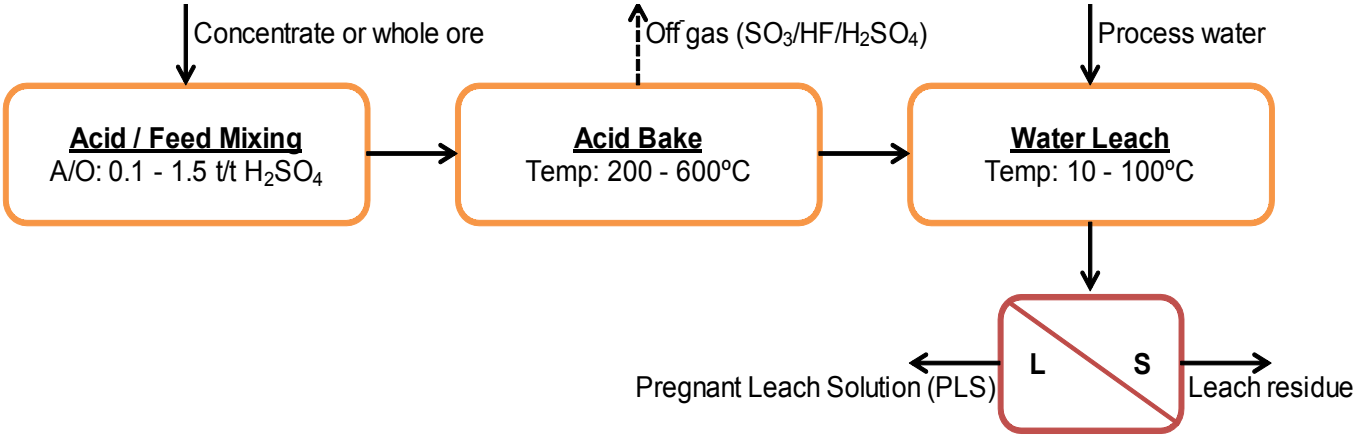

Fig. 3. Acid bake flowsheet schematic.

water and sulphuric acid are evaporated or otherwise consumed in the formation of hydrated metal sulphate salts. It is therefore commonly also referred to as a 'sulphation' step. The final kiln discharge is usually a dry, free-flowing powder or agglomerate, which is transferred into a leach circuit where sulphated salts (e.g., $Fe_2(SO_4)_3$, $Ln_2(SO_4)_3$) are dissolved in water.

Whereas the acid bake flowsheet is fairly easily tested at bench scale using crucibles in a muffle furnace or tube furnaces, it can be very challenging to test continuously for extended periods of time in a pilot plant. Primary challenges exist around the acid-feed mixing system and the associated material handling equipment. In addition, the movement of material through the kiln can be problematic and the actual properties depend on many factors, such as the concentrate/ore mineralogy and if, at the optimum (from a metal extraction point of view) acid dosage, the acid-feed mixture is amenable to agglomeration. In certain situations it is recommended to take a deliberate reduction in metal extraction to obtain more favourable material handling characteristics (Fig. 4a). Plugging of a rotary kiln (Fig. 4b) may only become apparent when a test program is advanced from extensive bench testing to continuous piloting. Selecting materials of construction for the severe and corrosive acid bake applications has also led to significant challenges during the piloting stages of various test programs. Possible solutions may include pre-bake formation of cured agglomerates (Fig. 4c), if the feed mineralogy and required acid addition are amenable.

Lynas' Mount Weld hydrometallurgical operation in Malaysia is an example of an operating project that has selected the acid bake route. The ore is mined and concentrated in Western Australia and concentrate is shipped to Lynas's Advanced Material Plant in Malaysia. The hydrometallurgical plant was commissioned in late 2012, and ramp-up commenced in January 2013. The flowsheet consists of acid baking of the flotation concentrate, followed by water leaching of the calcine, impurity removal and solvent extraction to recover REE (Lynas, 2005). Various press releases have commented on lower than design production rates (Lynas, 2014) and issues with premature wearing of "some equipment of the cracking unit" and "clogging of filters" in the leach circuit (Lynas, 2013). After nine quarter-year periods, current production (Fig. 5) seems to remain well below design capacity, and follows a McNulty Category 4 ramp-up behaviour, one that is typically observed in plants with complex metallurgy, poor understanding of feed and/or chemistry, and limited pre-operation piloting testwork

Fig. 4. Photographs of **a)** an easy flowable material, **b)** a plugged rotary kiln, and **c)** an agglomerated product.

(McNulty, 1998 and McNulty, 2004). The Lynas plant output is comparable to the ramp-up of Western Australian nickel laterite projects in the 1990s (Verbaan et al., 2014), which were also characterized by complex metallurgy and a similar 'race to production'.

Metathesis or caustic crack step has been identified at four projects. Two (Kvanefjeld, and Lofdal) include phosphate minerals, such as xenotime, which are converted or metathesized to soluble sodium phosphate and insoluble REE hydroxides. Excess sodium hydroxide and sodium phosphate is washed out, the sodium phosphate can be crystallized to produce a tri-sodium phosphate by-product. Excess NaOH can be evaporated back to the original strength (50-60%) and re-used. The washed REE hydroxides are subsequently leached in acid.

The Mountain Pass and Songwe Hill properties contain bastnasite and synchysite, which both contain fluoride. We assume that REE precipitated in the primary HCl leach as REE fluorides are metathesized into REE hydroxides and soluble sodium fluoride. REE hydroxides are then leached with more HCl (or with the primary HCl PLS).

6. Whole Ore Treatment

Despite low ore grades, six projects do not include mineral beneficiation to produce an upgraded mineral concentrate. These projects use whole ore treatment processes (Table 4). As described below, the four hard rock projects use processes that differ from the two ionic clay projects.

The low grade Round Top project is pursuing a sulphuric acid heap leach operation using crushed (1/2 inch) ore. Hulse et al. (2014) reported testwork showing that extraction of up to 80% HREE is achievable with acid consumption as low as 30 kg/t.

The Port Hope Simpson project originally considered a beneficiation flowsheet comprising gravity separation, magnetic separation, and flotation (Dreisinger et. al., 2012). However, more recent work (Dreisinger et al., 2014) revealed that a whole ore acid bake process using crushed ore (6 mesh) and an acid dosage of 100 kg/t ore feed is effective. Reported advantages of this approach include: 1) significant flowsheet simplification and improved REE recovery by removal of the beneficiation flowsheet; 2) removal of the energy-intensive grinding circuit (feed to the hydrometallurgical plant is 6 mesh material); 3) improved material handling characteristics of the acid/feed mixture and calcine in acid bake process equipment; and 4) improved filtration of the water leach pulp due to coarse particle size.

Few process details are available on the Dubbo zirconia process flowsheet. Milled ore is mixed with sulphuric acid and then roasted in a rotary kiln. Based on the environmental impact statement (Irwin, 2013), an acid consumption of 325 kg/t ore can be calculated. Calcine is subsequently leached with water, during which double salts are formed in the solid leach residue. LREE-rich double salts are re-leached and recovered, while HREE remain in solution with Zr and Nb and advance to sequential solvent extraction to recover zirconium and niobium and recover HREE by precipitation. Overall REE extractions in the Dubbo flowsheet are low and range from 32 to 61%. It is unclear from the public data (Alkane, 2013) where most of the REE losses occur.

Frontier's Zandkopsdrift deposit contains approximately 3-4 times as much manganese as REE. Though ore beneficiation was attempted, results were unsatisfactory and a whole ore leach approach was examined instead. The whole ore leach process consists of the following steps (Harper et al., 2015).

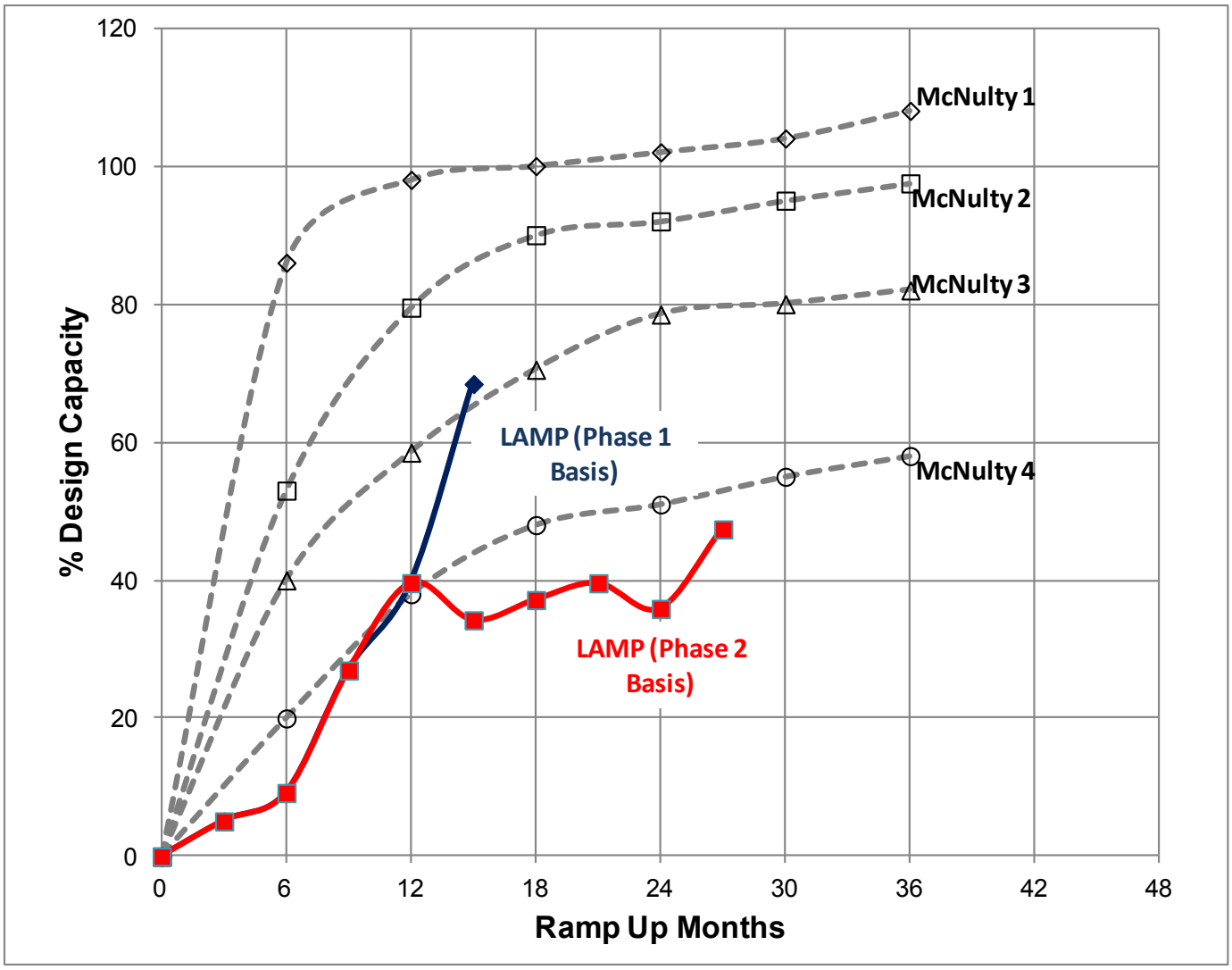

Fig. 5. Ramp-up curve Lynas LAMP (Mount Weld project).

- Reductive pre-leach to pre-extract about 90% of the Mn at an acid addition of ~100 kg/t H_2SO_4 and 70 kg/t SO_2.
- The Mn pre-leach residue is contacted with about 1 t/t sulphuric acid in a high shear mixer, which leads to the production of a dry, stable, granular, free flowing and competent material that allows the use of fluidized bed reactors rather than rotary kilns.
- The granular material is then cracked or baked at low temperature (250-350ºC), where gangue and REE minerals are sulphated.
- The low-temperature calcine is heated further in a high temperature calcination step during which ferric sulphate decomposes to hematite and gaseous SO_2 and SO_3. This needs to be done under careful temperature control to avoid the decomposition of REE sulphates.
- High-temperature calcine is leached with water, during which REE sulphates are dissolved and hematite remains in the leach residue.
- Gaseous SO_2 and SO_3 are treated in an acid plant and reconstituted to sulphuric acid. It is reported in the PFS that around 80% of the added sulphur to the Mn leach residue is regenerated to sulphuric acid. This would mean that the overall acid consumption (pre-leach + acid bake) is near 300 kg/t H_2SO_4.

The Tantalus and Serra Verde projects (Table 4) are ionic clay projects that are not amenable to mineral upgrading. Ionic clay projects do not use aggressive leach systems as outlined above for the hard-rock deposits. Instead, REE sorbed onto clays are simply desorbed using an ion-exchange-based elution process with eluants such as sodium chloride or ammonium sulphate. Current practice in China is to use in-situ or heap leaching methods (for review, see Chi and Tian, 2008). The Serra Verde and Tantalus clay properties share many similarities to the Southern China clay projects, which produce much of the global HREE. The Serra Verde project is described in detail by Rocha et al. (2013, 2014), and the Tantalus clay desorption

Table 4. Whole ore treatment processes.

Property	Host Rock Minerals	% TREO Ore Grade	Whole Ore Leach Process	Acid Consumption kg/t
Round Top	Alkaline rock-associated	0.06	Crush ore to 1/4-1/2 inch. Heap leaching with H_2SO_4.	30
Port Hope Simpson	Alkaline rock-associated	1.07	Crush ore to 6 mesh. Whole ore acid baking at low A/O of 100 kg/t H_2SO_4 and hot water leaching.	100
Dubbo	Alkaline rock-associated	0.9	Acid bake with H_2SO_4 and water leach. Double salts are formed in the WL. HREE remain in solution. DSP is re-leached.	325
Zandkopsdrift	Carbonatite	1.9	Reductive pre-leach (PL) with H_2SO_4/SO_2 to remove Mn. Agglomeration of PL residue in high shear mixer, Low temperature sulphation in fluidized bed reactor (FBR). High temperature calcination in FBR. Two stage water leach.	300
Tantalus	Ionic clay	0.09	Heap leach (i.e. desorption) with NaCl or Na_2SO_4.	N/A
Serra Verde	Ionic clay	0.16	Heap leach (i.e. desorption) with NaCl or Na_2SO_4. In situ leach is under consideration.	N/A

processes are detailed by Moldoveanu and Papangelakis (2013) and Desharnais et al. (2014). Typical REE grades are low (ranging from 0.1 to 0.4%) and consequently, the logistics of moving large quantities of ore and solution poses challenges.

Rocha et al. (2013) reported that about 50% of the total REE are adsorbed onto clay and are therefore recoverable by the desorption process, with the remainder in primary minerals or partially decomposed minerals. Testwork results indicated that about 50% La, Pr-Lu can be desorbed using either NaCl or $(NH_4)_2SO_4$ eluants. Cerium and thorium extraction is significantly limited due to their presence in cerianite minerals.

7. Pregnant leach solution (PLS) treatment options

Most processes will dissolve deleterious impurities into the leach solution along with REE during the leaching step. Hydrometallurgical methods are then used to separate the REE from impurities. Though most process routes (Table 5) differ, they can be grouped into five main categories: 1) Impurity Removal – REE Precipitation and Re-Leach (IR-RP-RL); 2) direct ion exchange or solvent extraction (IX/SX); 3) IR-direct IX/SX; 4) double salt precipitation (DSP); and 5) direct REE precipitation with oxalic acid.

7.1. IR-RP-RL process route

In this route, elements such as Fe, Al, Th, P are removed upstream of REE recovery. Impurity Removal (IR) usually uses reagents such as NaOH, $MgCO_3$, MgO, or $CaCO_3$. In addition, ion-exchange may be used to remove U. REEs are precipitated from the IR filtrate in a REE Precipitation circuit (RP) using MgO, Na_2CO_3, $MgCO_3$ or NaOH. The REE precipitate is subsequently re-leached using acid. Secondary impurity removal is likely carried out on the re-leach liquor. This flowsheet, or variations thereof, is exercised by 11 projects. These include alkaline granite projects such as Nechelacho, Port Hope Simpson, Strange Lake, Zeus, and Browns Range, and carbonatite projects such as Ashram, Lofdal, Montviel, Songwe Hill, and Zandkopsdrift.

7.2. Direct ion exchange or solvent extraction (IX or SX) process route

In this route, REEs are extracted selectively (against impurities) directly from impure leach solution without prior neutralization or impurity removal. Three projects use this approach. The Bokan Mountain project proposes using a SuperLig® resin based on Molecular Recognition Technology (MRT) to extract REE as a group first, away from other dissolved metals, in a nitric acid medium. The REE are subsequently separated into individual elements using MRT. At the Kvanefjeld project, an HCl-based leach solution is treated by direct solvent extraction (SX). REEs are subsequently separated to produce individual La, Ce, LaCe and Pr-Lu+Y product streams. The feasibility study (Greenland Minerals, 2015a) does not elaborate on impurity handling and it is unknown where impurities such as Fe, Al, Th report to or how they are dealt with. Although it is feasible, depending on mineralogy and leach conditions, that many of the impurities such as Fe, Al, and U will end up in the H_2SO_4 based uranium leach solution, elements such as thorium are expected to follow REE. A recent press release (Greenland Minerals, 2015b) indicates the presence of an impurity removal circuit upstream of SX, which would place this project into the IR-Direct IX/SX category. At the Round Top project, low-grade heap leach solutions are treated in an initial CIX (Continuous Ion Exchange) system to separate the REEs from the dilute PLS into a concentrated mixed REE

Table 5. Leach liquor Purification processes.

Property	% HREO relative	PLS Chemistry	Downstream Flowsheet Catergory	Primary Purification	Primary REE Recovery	Secondary Purification
Bokan Mountain	40	HNO_3	Direct IX/SX	-	Direct REE IX (MRT) in multiple steps	-
Browns Range	87	H_2SO_4	IR-RP-RL	Neutralization with $Ca(OH)_2$, Fe(III) and MgO to remove Fe, P and Th. U is removed by conventional IX	FS: Primary REE precipitation with Na_2CO_3. Hadley and Catovic (2014) reported on direct oxalic precip	-
Dubbo	25	H_2SO_4	DSP	Zr/NbSX from WL PLS. Various undisclosed unit ops	Double sulphate precipitation in WL. DSP is releached to form a LREE product. An HREE product is produced from Zr/Nb raffinate	-
Kvanefjeld	11.8	H_2SO_4	Direct IX/SX	-	Direct SX of REE. Production of La, Ce, LaCe and Pr-Lu	-
Nechalacho	27.3	HCl	IR-RP-RL	Impurity removal by neutralization	REE Precipitation	-
Norra Karr	52	H_2SO_4	IR-Direct IX/SX	Neutralization with MgO or $Ca(OH)_2$ to remove impurities (Si,…)	Direct SX (primary amine) of REE coupled with $H_2C_2O_4$ stripping and precipitation of REE. REE solids are separated by centrifugation and filtration	-
Port Hope Simpson	19.6	H_2SO_4	IR-RP-RL	Fe, Al, Th, removal by Na_2CO_3 / $MgCO_3$ / MgO neutralization	Bulk REE precipitation with Na_2CO_3	RP cake is re-leached in HCl and the PLS is treated for secondary Th removal prior to REE precipitation with $H_2C_2O_4$. Final REE cake is calcined to make a 98-99% REO product
Round Top	72	H_2SO_4	Direct IX/SX	-	IX to separate REE from other elements in Heap Leach PLS	-
Strange Lake	39	H_2SO_4	IR-RP-RL	Fe/Al/Th removal by MgO neutralization	Bulk REE Precipitation	REE Precip is re-leached. REE will be re-precipitated with $H_2C_2O_4$ and finally calcined
Zeus	37	H_2SO_4	IR-RP-RL	Fe/Al/Th removal by $CaCO_3$ neutralization followed by IX to (presumably remove U and residual Zr)	Primary REE precipitation with Na_2CO_3	Secondary impurity leaching with undisclosed reagent. REE are re-leached in acid, followed by SX to separate LREE from HREE
Ashram	4.7	H_2SO_4	IR-RP-RL	Impurity removal by NaOH	Na_2CO_3 precipitation	-
Bear Lodge	4.4	HCl	Direct RP with $H_2C_2O_4$	-	Direct REE Precipitation with $H_2C_2O_4$. REE oxalates are subsequently calcined at 700ºC	RP is leached with HNO_3. Th is precipitated with NH_4OH in 2 steps. REE are then precipitated with NH_4OH
Lofdal	76	HCl	IR-RP-RL	Neutralization with $Ca(OH)_2$ to remove Fe, Th	Primary REE precipitation with $Ca(OH)_2$	-
Montviel	1.8	HCl	IR-RP-RL	Fe/Al/Th removal by NaOH (from chlor alkali plant) neutralization	REE Precipitation with $NaHCO_3$	-
Mountain Pass	1	HCl	IR-Direct IX/SX	Fe and Pb removal	Direct SX	Ce redox circuit
Mt Weld	3	H_2SO_4	IR-Direct IX/SX	Fe/Al/Th removal by MgO/$FeCl_3$ neutralization	Direct SX of REE with D2EHPA. Production of La, Ce, NdPr, Sm-Lu+Y	-
Ngualla	1.9	H_2SO_4	DSP	-	Double sulphate precipitation (rejects Fe, Al, U). Conversion of DSP to hydroxide. RL with HCl and Ce rejection	Fe/Al removal from RL liquor by addition of NaOH. Final REE precip by Na_2CO_3
Songwe Hill	6.8	HCl	IR-RP-RL	Fe/Al/Th removal by $CaCO_3$ neutralization	Primary REE precipitation with NaOH. RP filtrate is treated to regenerate HCl.	RP cake is dried in air atmosphere and subsequently re-leached in HCl to reject Ce. REE are precipitated with NaOH
Zandkopsdrift	7.8	H_2SO_4	IR-RP-RL	Fe, Al, Th, U, PO_4 removal by MgO neutralization	Bulk REE Precipitation with MgO	RP is re-leached with HCl
Serra Verde	25 (37 if no Ce)	SO_4 or Cl	IR-RP-RL	Neutralization to remove Fe, Al, Th	Primary REE precipitation with $H_2C_2O_4$ or $(NH_4)_2CO_3$	-
Eco Ridge	11.4	H_2SO_4	IR-Direct IX/SX	Uranium SX (Alamine 336)	Direct REE SX with D2EHPA/TBP	-
Nolans Bore	4	H_2SO_4	DSP	-	Double sulphate precipitation (rejects Fe, Al, U). Conversion of DSP to hydroxide. RL with HCl and Ce rejection	Various, UIX
Steenkampskraal	3.8	H_2SO_4	DSP	The flowsheet allows for a split LREE (double salt) and HREE process route.	LRE route: Double sulphate precipitation (rejects Fe, Al, U). DSP is converted to REE hydroxide, which is re-leached with HCl, while rejecting Ce. HRE Route: HREE precipitation from purified DSP filtrate	IX to remove Cu and U (on LREE process route). Cu/ base metal removal by precipitation with NaHS in HREE process route

stream. Continuous Ion Chromatography (CIC) is then used to further isolate the REEs into 'lights', 'mids' and 'heavies' and reject co-extracted impurities. These solutions are then further processed to produce selected separated groups of REEs.

7.3. IR-direct IX/SX process route

This route is similar to the Direct IX/SX process route, but includes an upstream impurity removal step. Four projects are currently or considering using this type of process route. In the flowsheet for the Norra Kärr project, a sulphate based

leach solution is neutralized with MgO or $Ca(OH)_2$ to remove impurities such as silicon. A primary amine is then used in an SX step to extract REEs. Oxalic acid is used to simultaneously strip REE from organic material and precipitate the REEs. Precipitated REE oxalates are recovered through centrifugation and filtration (Short et al., 2015). It will be of interest to monitor organic losses (associated with filtered solids) in future testwork results. The Mountain Pass operation has recently been placed on care and maintenance. Few details are available, but it seems that iron and lead are removed upstream of the SX circuit. A cerium redox circuit is employed to reduce the amount of cerium advancing to the SX circuit. At Mount Weld, sulphate-based leach solutions are initially treated with a mixture of MgO and $FeCl_3$ to promote co-precipitation of Th into a $FePO_4$ compound. The $FeCl_3$ is presumably balanced to promote a Fe:P molar ratio of 1:1. REEs are subsequently extracted from the partial purified filtrate using SX (D2EHPA extractant). The LAMP produces La, Ce, NdPr and mixtures of heavy REE (Sm-Lu+Y) products. A recent quarterly report (Lynas Corporation, 2015) reveals that the production of NdPr and LaCe products was harmed by unstable SX operations. The key issue was identified to be organic degradation in the LaCe|PrNd separation circuit, which is considered the most complex part of the LAMP REE separation. The LaCe|PrNd SX circuit has 110 stages and long residence times including about three weeks for Pr. This means that any adjustments to production settings take time to resolve through the system (Lynas Corporation, 2015). At Eco Ridge, uranium is recovered from sulphate-based leach solutions through an Alamine 336 SX circuit. USX raffinates are subsequently neutralized using lime in an Impurity Removal circuit. REEs contained in the IR filtrate are then extracted in a D2EHPA SX circuit (Cox et al., 2012). This flowsheet is based on the historic Elliot Lake yttrium production flowsheets as described by Goode (2012).

7.4. Double salt precipitation (DSP) process route

The double salt ($Na_2SO_4 \cdot Ln_2(SO_4)_3 \cdot 2H_2O$) route is very common for predominantly LREE projects due to the higher preference of LREE to form double sulphate salts compared to HREE. However, the DSP route can also be applied in projects with considerable HREE, and in such projects, a crude separation between lights and heavies is accomplished. Double salts are formed by the addition of sodium sulphate to a REE leach solution. In most flowsheets, the double salt is metathesized to a hydroxide form by slurrying the DSP in caustic. The moist hydroxide cake can be subsequently oxidatively dried at 150ºC and ultimately re-leached in acid (usually HCl). The drying step leads to oxidation of Ce(III) to Ce(IV), which has limited solubility in dilute acid. Therefore, the DSP route allows for the early rejection of cerium.

Four projects are considering using the DSP route. Three predominantly LREE projects (Ngualla; Peak Resources, 2014; Nolans Bore, Arafura, 2014; and Steenkampskraal, Clay et al., 2014) apply the DSP process on dilute H_2SO_4 leach solution and also use the cerium oxidation removal step. The Steenkampskraal project also recovers HREE from the DSP filtrate and has reported using IX to remove Cu and U from the LREE stream. In addition, copper and other base metals are removed from the HREE stream by sulphide precipitation (using NaHS). At the Dubbo project, double salts appear to be formed naturally in the Dubbo project acid bake-water leach circuit, probably by operating the water leach circuit at high pulp densities and maybe because of high Na/K levels from the ore in the PLS. The leach solution (enriched in HREE) is first treated by SX to extract Zr and Nb, which are both recovered as products and then precipitated. The WL residue (enriched in LREE) appears to be re-leached and the solution treated to recover a LREE product.

7.5. Direct REE precipitation with oxalic acid process route

In this route, which is used only at the Bear Lodge project, REE are precipitated directly out of an HCl-based leach solution using oxalic acid ($H_2C_2O_4$). A significant separation of REE versus other metal occurs due to the selectivity of oxalate precipitation, though thorium is one of the main contaminants that follow the REE. REE oxalates are subsequently calcined at 700ºC and then re-leached in nitric acid. A series of consecutive precipitation steps employing ammonium hydroxide are subsequently used to separate Th from the REE.

8. REE separation

The conventional method to separate REEs is based on SX (P507) technology, as described by Liao et al. (2013) and Yan et al. (1999). Recent new developments in REE separation are being considered by some projects, although few details are publically available.

Free Flow Electrophoresis (FFE) is under consideration for the Montviel project (GeoMega, 2015). In FFE, a solution of mixed dissolved elements (REE) is passed through a separation channel, which is affected by a static perpendicular electrophoretic force, exerted by side-wall electrodes. The magnitude of this force and the charge to size ratio of each ion affects the deviation of ions from a straight trajectory along the channel. REE separation is achieved by using multiple channels and flow splitters. The FFE process is patented by Innord Inc, a wholly owned private subsidiary of GeoMega (Hajiani, 2014).

The Bokan Mountain project is considering using Molecular Recognition Technology (MRT) by IBC Advanced Technologies Inc, to produce high-purity separated REEs. MRT is a selective non-ion exchange process using custom designed organic chelating ligands (SuperLig®) and uses supramolecular 'lock and key' chemistry as the basis for its high selectivity. Elution of the loaded REE resin is accomplished by using an acidic eluent, which leads to the production of concentrated REE solutions, either as group or as individual elements.

Other methods include: Continuous Ion Chromatography (CIC) by K-technologies Inc (which is being considered for the Round Top project); micro-fluidics, membrane-supported SX, "Fast SX", and other variants on the P507 route; and Tri-n-butyl phosphate (TBP) extraction from nitrate solution, as used

by Solvay and other refiners.

9. Reagent regeneration

Due to the high costs and/or high dosages required of some reagents, reagent regeneration is a key component of some projects. Although regeneration reduces operating costs, it usually adds to process complexity. Some projects have introduced water recovery and NaOH, HCl, HNO_3 and H_2SO_4 recycling strategies (Table 6). Bedrossian and Connell (2014) review HCl regeneration by gypsum crystallization and by the chlor-alkali process. The Molycorp plant experienced significant issues in the operation of its chlor-alkali plant (Molycorp, 2014b).

10. Conclusions

It is clear that after a potential ore deposit has been found and described by geologists, much work is required by metallurgists to develop an economical and effective flowsheet suitable for the commonly complex overall ore mineralogy. Although flowsheet selections are driven primarily by ore mineralogy and specific project conditions, extractive metallurgists have many choices to make as is shown by the current wide array of metallurgical flowsheets. This applies to the beneficiation, chemical extraction (leaching), purification and separation areas of the overall treatment flowsheets. To mitigate risks, full tests of a selected flowsheet under continuous processing conditions are demanded.

Table 6. Reagent regeneration processes.

Property	PLS Chemistry	Reagent Regeneration
Bokan Mountain	HNO_3	HNO_3 recycling.
Dubbo	H_2SO_4	Reverse osmosis to treat process water for re-use.
Strange Lake	H_2SO_4	Excess H_2SO_4 and SO_2/SO_3 from decomposed $Fe_2(SO_4)_3$ from calciner.
Bear Lodge	HCl	HCl distillation from RP filtrate to form 20.2% HCl. $H_2C_2O_4$ regeneration by crystallization (cooling) from distallation bottoms.
Lofdal	HCl	HCl from the gangue leach will be regenerated by means of H_2SO_4 addition and $CaSO_4$ precipitation. NaOH regeneration is also assumed to be required.
Montviel	HCl	Chlor-Alkali plant for HCl/NaOH regeneration. Feed (RP Filtrate) is treated with Na_2CO_3 and IX to prepare for Clor-Alkali.
Mountain Pass	HCl	HCl / NaOH via Chlor-Alkali.
Songwe Hill	HCl	HCl regeneration via $CaSO_4$ precipitation with H_2SO_4.
Zandkopsdrift	H_2SO_4	Excess H_2SO_4 and SO_2/SO_3 from decomposed $Fe_2(SO_4)_3$ from calciner.
Serra Verde	SO_4 or Cl	Reverse osmosis to recycle process water and regenerate eluant ($(NH_4)_2SO_4$ or NaCl).

Acknowledgments

The authors appreciate the significant efforts and contributions made by the various reviewers of this paper. Specifically Michaela Neetz, and John Goode are hereby acknowledged.

References cited

Alkane Resources, 2012. Corporate Presentation December 2012. <http://www.alkane.com.au/pdf/presentations/20121210.pdf>. Accessed: Oct 22, 2015.

Arafura Resources, 2014. Nolans Development Report. <http://www.arultd.com/images/files/Reports/ARAFURA_Nolans-Development-Report_2014_Sept.pdf>. Accessed: Oct 1, 2015.

Bedrossian, S., and Connell, M.N.D., 2014. An overview of hydrochloric regeneration in rare earth processing. In: Conference of Metallurgists 2014 - Rare Earth Elements, Canadian Institute of Mining, Metallurgy and Petroleum.

Beer, G., Dawes, W., Brady, A. E., Bryson, M., and Sehlotho, N., 2014. Development of a metallurgical flowsheet for the Songwe Hill Rare Earth project in Malawi. In: Conference of Metallurgists 2014 - Rare Earth Elements, Canadian Institute of Mining, Metallurgy and Petroleum.

Belzille, E., Marchand, R., and Bouajila, A., 2015, NI43-101 Technical report Montviel rare earth project, Quebec, Canada, G Mining Services for GeoMegA Resources Inc., 186p.

Bentzen III, E., Ghaffari, H., Galbraith, L., Hammen, R., Robinson, R., Hafez, S., and Annavarapu, S., 2013. Preliminary Economic Assessment on the Bokan Mountain Rare Earth Element Project, near Ketchikan, Alaska. Tetra Tech, Vancouver, Canada, 244p.

Chi, R., and Tian, J., 2008. Weathered Crust Elution-Deposited Rare Earth Ores.

Nova Science Publishers Inc., New York, 288p.

Ciulescu, T., Foo, B., Gowans, R., Hawton, K., Jacobs, C., and Spooner, J., 2013. Technical Report disclosing the results of the feasibility study of the Nechalacho rare earth elements project. Micon International Limited for Avalon Rare Metals Inc. 307p.

Commerce Resources, 2015. <http://www.commerceresources.com/en/news/commerce-resources-corp-initiates-pilot-plant-for-the-ashram-rare-earth-deposit>. Accessed Oct 22, 2015.

Clay, A., Machowski, R., Jones, I., Marra, G., Duke, V., Harper, F., and de Klerk, A., 2014. NI 43-101 independent Technical Report on the Results of a Feasibility Study for the Steenkampskraal REE Project in the Western Cape, South Africa. Great Western Minerals Group, Saskatoon, Canada, 264p.

Cox, J., Ciuculescu, T., Altman, K., and Hwozdyk, L., 2012. Technical Report on the Eco Ridge Mine Project, Elliot Lake Area,

Ontario, Canada. Pele Mountain Resources Inc., Toronto, Canada, 259p.
Croll, R., Swinden, S., Hall, M., Brown, C., Beer, G., Scheepers, J., Redelinghuys, T., Wild, G., and Errol Trusler, G., 2014. NI 43-101 Pre-feasibility Report Songwe REE Deposit, Malawi. Mkango Resources Limited, Calgary, Canada, 402p.
Dahlberg, P., 2014. NI 43-101 Pre-feasibility Study Report on the Mineral Reserves and Development of the Bull Hill Mine, Wyoming. Rare Element Resources, Lakewood, U.S., 587p.
Desharnais, G., Camus, Y., and Bisaillon, C., 2014. NI 43-101 Technical Report on the Resources for the Tantalus Rare Earth Ionic Clay Project in Northern Madagascar. Tantalus Rare Earths AG, Muenchen, Germany, 165p.
Dodd, D., Hannon, P., Roy, W., Siegfried, P., and Hall, M., 2014. NI 43-101 Technical Report Preliminary Economic Assessment on the Lofdal Rare Earths Project Namibia. Namibia Rare Earths Inc., Bedford, Canada, 363p.
Dreisinger, D., Clucas, J, Verbaan, N., Grammatikopoulos, T., Aghamirian, M., and Forstner, C., 2012. The Processing of REE's from Search Minerals' Foxtrot Resource. In: J.R. Goode, G. Moldoveanu, M.S. Rayat, (Eds.), Conference of Metallurgists 2012- Rare Earth Elements, Canadian Institute of Mining, Metallurgy and Petroleum.
Dreisinger, D., Verbaan, N., and Johnson, M., 2014. The Processing of REE's from Search Minerals' Foxtrot Resource – An Update. In: Conference of Metallurgists 2014 - Rare Earth Elements, Canadian Institute of Mining, Metallurgy and Petroleum.
Gagnon, G., Rousseau, G., Camus, Y., and Gagné, J., 2015. NI 43-101 Technical Report: Preliminary Economic Assessment on the Ashram Rare Earth Deposit. SGS for Commerce Resources Corporation, Vancouver, Canada, 219p.
GeoMega, 2015. Innord Inc. – REE Seperation. <http://ressourcesgeomega.ca/innord-inc-2/>. Accessed: Oct 1, 2015.
Goode, J., 2012. Canadian rare rarth and thorium recovery operations. The first 30 years.. In: J.R. Goode, G. Moldoveanu, M.S. Rayat, (Eds.), Conference of Metallurgists 2012 - Rare Earth Elements, Canadian Institute of Mining, Metallurgy and Petroleum, pp. 31- 47.
Gowans, R., Lewis, W., Shoemaker, S., Spooner, J., and Zalnieriunas, R., 2014. NI43-101 Technical report on the preliminary economic assessment (PEA) for the strange lake property, Quebec, Canada. Micon International Limited for Quest Rare Minerals, 258p.
Greenland Minerals, 2015a. Kvanefjeld Feasibility Study Executive Summary. <http://www.ggg.gl/docs/ASX-announcements/Kvanefjeld-Feasibility.pdf>. Accessed: Oct 1, 2015.
Greenland Minerals, 2015b. Announcement. <http://www.ggg.gl/docs/ASX-announcements/Refinery-Pilot-Plant-Yields-Excellent-Initial-Results.pdf>. Accessed: Sept 29, 2015.
Hadley, T., and Catovic, E., 2014. Beneficiation and extraction of REE from Northern Minerals' Browns Range heavy rare earth project. In: Conference of Metallurgists 2014 - Rare Earth Elements, Canadian Institute of Mining, Metallurgy and Petroleum.
Harper, F., Njowa, G., Wiid, G., Vivier, J., Siegfried, P., Zietsman, R., Brown, J., Duke, V., and Hall, M., 2015. NI 43-101 Independent Technical Report on the Results of a Preliminary Feasibility Study on Zandkopsdrift REE and Manganese By-product Project in the Northern Cape Province of South Africa. Frontier Rare Earths Limited, Cape Town, South Africa, 245p.
Hajiani, P., 2014. International Patent Application No.: PCT/CA2014/050495. A system and method for separation and purification of dissolved rare earth/precious metals / compounds. Filing date: May 28, 2014.
Hulse, D., Newton, M., and Malhotra, D., 2014. Amended NI 43-101 Preliminary Economic Assessment for the Round Top Deposit. Texas Rare Earth Resources, Sierra Blanca, U.S., 206p.
Irwin, A., 2013. Dubbo Zirconia Environmental Impact Statement. Australian Zirconia Ltd, Burswood, Australia, 22p.
Liao, C., Wu, S., Cheng, F., Wang, S., Liu, Y., Zhang, B., and Yan, C., 2013. Clean separation technologies of rare earth resources in China. Journal of Rare Earths, 31, 331-336.
Lynas Corporation, 2005. Completion of the Mt Weld Rare Earths Feasibility Study. <http://www.lynascorp.com/Presentations/2005/MPJ_Feasibility_annoucement_presentation_0305.pdf>. Accessed: Oct 1, 2015.
Lynas Corporation, 2015. Quarterly Activities Report. <https://www.lynascorp.com/Quarterly%20Reports/2015/Quarterly%20Activities%20Report%201430062.pdf>. Accessed: Oct 1, 2015.
McNulty, T., 1998. Innovative Technology: Its Development and Commercialization. In: Kuhn, M.C., (Eds.), Managing Innovation in the Minerals Industry. () Society of Mining Engineers, pp. 1-14.
McNulty, T., 2004. Minimization of Delays in Plant Startups. In: Dowling, E.C., and Marsden, J.I., (Eds.), Plant Operators Forum 2004. Society of Mining Engineers, pp.113-120.
Moldoveanu, G.A., and Papengelakis, V.G., 2013. Recovery of rare earth elements adsorbed on clay minerals: I. Leaching with ammonium sulfate. Hydrometallurgy. 131-132, 158-166.
Molycorp, 2014a. Video: Mountain Pass Ramps up on Rare Earths.<http://www.molycorp.com/about-us/mountain-pass/>. Accessed: Oct 12, 2015.
Molycorp, 2014b. <http://www.molycorp.com/molycorp-announces-that-expanded-leach-system-is-in-service/>. Accessed Oct 22, 2015.
Molycorp, 2015. <http://www.molycorp.com/molycorp-to-move-its-mountain-pass-rare-earth-facility-to-care-and-maintenance-mode/>. Accessed: Sept 28, 2015.
Northern Minerals, 2015. Browns Range Project Definitive Feasibility Study. <http://northernminerals.com.au/wp-content/uploads/2015/02/1503-02-DFS-positions-Browns-Range-Project-as-next-dysprosium-supplier-.pdf>. Accessed: Oct 1, 2015.
Peak Resources, 2014. Ngualla Rare Earth Project Preliminary Feasibility Study - Executive Summary. <http://www.peakresources.com.au/irm/content/project-development.aspx?RID=310>. Accessed: Oct 1, 2015.
Rainbow Rare Earths, 2015. <http://www.rainbowrareearths.com/>. Accessed Sept 28, 2015.
Rocha, A., Schissel, D., Sprecher, A, de Tarso, P., and Goode, J.R., 2013. Process Development for the Serra Verde weathered crust elution deposited rare earth deposit in Brazil. In: London, I.M., Goode, J.R., Moldoveanu, G., and Rayat, M.S., (Eds.), Conference of Metallurgists 2013 -Rare Earth Elements, : Canadian Institute of Mining, Metallurgy and Petroleum, pp. 277-288.
Rocha, A., Coutinho, D., Soares, E., de Tarso, P., Sprecher, A., Ferreira, J., and Goode, J.R., 2014. The Serra Verde Rare Earth Deposit, Goias State, Brazil: Advancing to Production. In: Conference of Metallurgists 2014 - Rare Earth Elements, Canadian Institute of Mining, Metallurgy and Petroleum.
Saucier, G., Noreau, C., Casgrain, P., Côté, P., Larochelle, E., Bilodeau, M., Hayden, A., Poirier, E., Garon, M., Bertrand, V., Kissiova, M., Mailloux, M., Rougier, M., Camus, Y. and Gagnon, G., 2013, NI 43-101 Report: Feasibility study for the Kipawa project Temiscamingue Area, Quebec, Canada, Roche Engineering for Matamec Explorations, Inc. 768p.
Simandl, G.J., 2012. Geology and Economic Significance of Current and Future Rare Earth Element Sources. In: Goode, J.R., Moldoveanu, G., and Rayat, M.S., (Eds.), Conference of Metallurgists 2012 – Rare Earth Elements, Canadian Institute of Mining, Metallurgy and Petroleum, pp. 15-30.
Simandl, G.J., 2014. Geology and market-dependent significance of rare earth element resources. Mineralium Deposita, 49, 889-904.
Short, M., Apelt, T., Moseley, G., Mounde, M., and La Touche, G., 2015. Amended & Restated Prefeasibility Study - NI 43-101 - Technical report for the Norra Kärr Rare Earth Element Deposit prepared. Tasman Metals, Vancouver, Canada, 378p.

Trumbull, Ty., 2013. Canada makes a move in the rare earths race. <http://www.bnn.ca/News/2013/11/8/The-hunt-for-rare-earth-minerals.aspx>. Accessed: Oct 12, 2015.

Yan, C., Liao, C., Jia, J., Wang, M., and Li, B., 1999. Comparison of economical and technical indices on rare earth separation processes of bastnasite by solvent extraction. Journal of Rare Earths., 17, 58-63.

Yu, B., Verbaan, N., Pearse, G., and Britt, S., 2013. Beneficiation and extraction of REE from GeoMega Resources' Montviel deposit. In: London, I.M., Goode, J.R., Moldoveanu, G., and Rayat, M.S., (Eds.), Conference of Metallurgists 2013 - Rare Earth Elements. Canadian Institute of Mining, Metallurgy and Petroleum, pp. 215-229.

Verbaan, N., Yu, B., Brown, J., and Mezei, A., 2014. Are REE exploration companies doing enough and/or the right testwork to avoid plant failures. Conference of Metallurgists 2014 - Rare Earth Elements, Canadian Institute of Mining, Metallurgy and Petroleum.

Williams-Jones, A.E., Wollenberg, R., and Bodeving, S., 2015. Hydrothermal fractionation of the rare-earth elements and the genesis of the Lofdal REE deposit, Namibia. In: Simandl, G.J. and Neetz, M., (Eds.), Symposium on Strategic and Critical Materials Proceedings, November 13-14, 2015, Victoria, British Columbia, British Columbia Ministry of Energy and Mines, British Columbia Geological Survey Paper 2015-3, pp. 125-130.

Zhi Li, L., and Yang, X., 2014. China's rare earth ore deposits and beneficiation techniques. 1st European Rare Earth Resources Conference (ERES 2014). pp. 26-36.

Graphite deposit types, their origin, and economic significance

George J. Simandl[1, 2, a], Suzanne Paradis[3], and Carlee Akam[1]

[1] British Columbia Geological Survey, Ministry of Energy and Mines, Victoria, BC, V8W 9N3
[2] School of Earth and Ocean Sciences, University of Victoria, Victoria, BC, V8P 5C2
[3] Geological Survey of Canada, Pacific Division, Sidney, BC, V8L 4B2
[a] corresponding author: george.simandl@gov.bc.ca

Recommended citation: Simandl, G.J., Paradis, S., and Akam, C., 2015. Graphite deposit types, their origin, and economic significance. In: Simandl, G.J. and Neetz, M., (Eds.), Symposium on Strategic and Critical Materials Proceedings, November 13-14, 2015, Victoria, British Columbia, British Columbia Ministry of Energy and Mines, British Columbia Geological Survey Paper 2015-3, pp. 163-171.

1. Introduction

Graphite is an opaque, gray-black, and soft (1-2 on Mohs hardness scale) mineral with a metallic luster. It is characterized by a greasy feel, low density (2.09-2.23 g/cm^3), high resistance to thermal shock, and high electrical conductivity (Anthony et al., 2003). Inertness, compressibility, elasticity, and lubricity are other important physical properties (Wissler, 2006). The 2014 world natural graphite production was estimated at 1.17 million tonnes (Fig. 1; Olson, 2015), with most of it originating in China (67%), India (15%), Brazil (7%), Canada (3%), Turkey (3%), and North Korea (3%). Globally, most natural graphite is used in electrodes, refractories, lubricants, foundries, batteries, graphite shapes, recarburising, steelmaking, and friction products such as brake linings (Fig. 2; Shaw, 2013). Prices of selected products are shown in Table 1.

Refractory and high-technology applications make graphite a critical material in industrialized countries. High-technology uses of graphite represent a portion of the market with fastest forecasted growth.

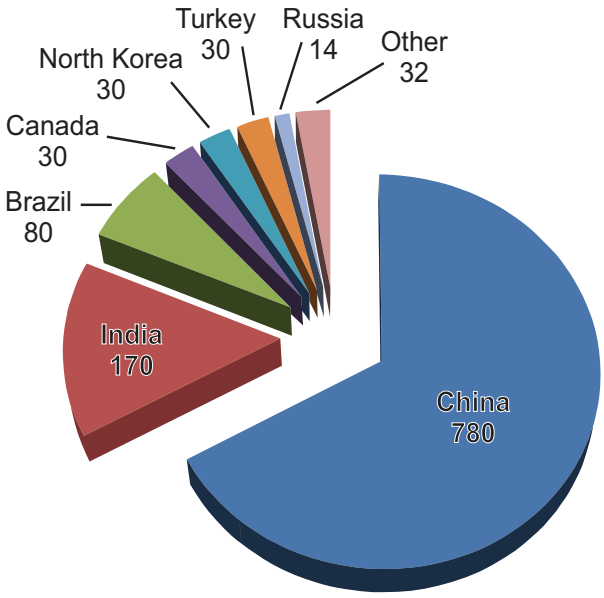

Fig. 1. Global graphite production, in thousands of tonnes, totalling 1.17 million tonnes, for 2014. Based on data from Olson (2015).

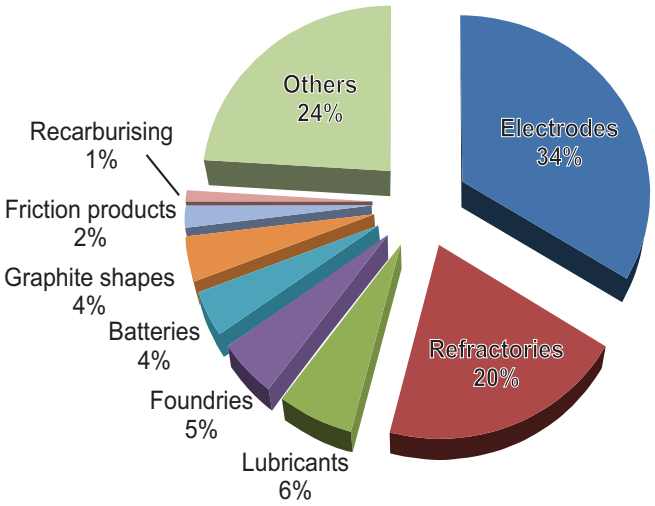

Fig. 2. Main uses of graphite for 2012. Based on data from Shaw (2013).

Examples of high-technology applications are: lithium-ion batteries for electric motor vehicles; large-scale electric energy storage devices; and graphite derivatives such as graphene (Sadasivuni et al., 2014; Dickson, 2014), spherical graphite, expanded graphite, and graphite foil. Graphene (sensu stricto) is a tightly packed layer of carbon atoms, one atom thick, bonded together in a hexagonal, honeycomb-like lattice, the stacking of which forms the graphite structure. Because of its potential uses in displays, conductive inks, composite materials, coatings and paints, electronics, energy generation, energy containers, membranes, 3D printers, sensors, photonics and optics, medicine, lubricants, and spintronics, graphene is considered to be a 'wonder material' (Mertens, 2015). Graphene-related research has received strong government financial support in many industrialized countries (Anonymous, 2015; Chiu, 2015; Hughes, 2015; Spasenovic, 2015). Spherical graphite is a product originally developed for use in lithium-ion batteries. It

Table 1. Prices of selected graphite products in US$/tonne. The purity of concentrate and, for some applications, size of crystalline flake are two key parameters. Abbreviations: FOB, free on board; CIF, Cost of Insurance and freight included; FCL, Full Container Load; ex-works, direct from the factory, excluding delivery costs, distribution costs, commission. Sources of data are: [a] Sawlan (2015), [b] Industrial Minerals (2015), and [c] Moores (2015).

	US$/tonne
Vein (lump and chip)[a]	
99.1% C, +1 mesh (>25.4mm), FOB Sri Lanka	2800
93% C, +60 mesh, FOB Sri Lanka	1550
Amorphous graphite[b]	
80-85% C, -200 mesh, China, FCL, CIF European port	430-480
Ore, 70-75% C, ex-works Austria	500-550
Flake graphite[b]	
85-87% C, +100 mesh -80mesh, FCL, CIF European port	700-800
90% C, +100 mesh -80 mesh, FCL, CIF European port	850-950
94-97% C, -100 mesh, FCL, CIF European port	900-950
90% C, +80 mesh, CIF, European port	950-1050
94-97% C, +100 mesh -80 mesh, FCL, CIF European port	1050-1150
94-97% C, +80 mesh, FCL, CIF European port	1200-1300
Spherical graphite[c]	7000-10000
Synthetic graphite[b]	
97-98%, CIF Asia	950-1450
98-99% CIF Asia	1000-1500
99.95% C, Switzerland	7000-20000

can be either synthetic or derived from crystalline flake graphite concentrate by processing that involves milling, physical rounding, purification, and surface treatment (Herstedt et al., 2003; Wu et al., 2006; Wang et al., 2008; Shaw, 2013). It takes approximately 100 kg of crystalline flake graphite concentrate (95% C) to produce 30 kg of spherical graphite assaying 99.9% C (Shaw, 2013). This is enough to produce a battery for one electric vehicle. Batteries are projected to account for approximately 5% of the global graphite production by 2016 (Shaw, 2013). In this application, spherical graphite derived from crystalline flake concentrate competes with its synthetic counterpart in terms of availability, price, and technical characteristics. Expanded graphite is another product derived from crystalline flake graphite. It is produced by intercalation with sulphuric and nitric acids (i.e., insertion of non-graphite atoms between graphite sheets) followed by expansion triggered by rapid temperature increase.

Worldwide, over 70 graphite exploration and development projects are being promoted, most of which are in Canada (see Lismore-Scott, 2014; Salwan, 2014). Barring unforeseeable political, military, or economic interference, we do not expect a natural graphite deficit before 2020.

2. Geology of graphite deposits

Natural graphite deposits of economic interest are grouped into three main categories: 1) microcrystalline; 2) vein graphite (lump and chip); and 3) crystalline flake graphite (Fig. 3). Deposit profiles by Simandl and Keenan (1998 a,b,c) provide an introduction to the main deposit types for exploration geologists and prospectors.

2.1. Microcrystalline graphite deposits

Commercially, microcrystalline graphite is referred to as ‘amorphous graphite’. This term is a misnomer because graphite has a crystal structure (readily detected by X-ray diffraction and Raman spectroscopy), which is lacking in truly

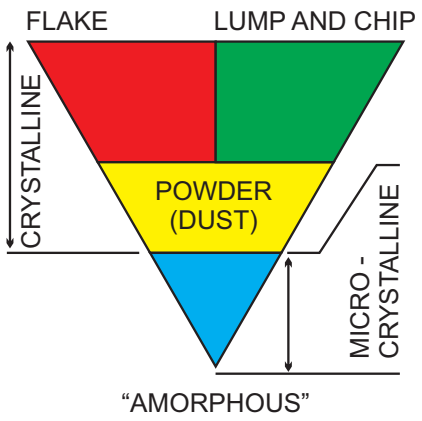

Fig. 3. Main categories of natural graphite currently available on the market. Modified from Simandl et al. (1995).

amorphous materials. In the scientific community, partially ordered graphite is referred to as 'semi-graphite' (Kwiecinska and Petersen, 2004) or, more recently, 'graphitic carbon' (Beyssac and Rumble, 2014).

Most microcrystalline graphite deposits are formed by sub-greenschist to greenschist contact metamorphism or regional metamorphism of coal seams (Taylor, 2006). Microcrystalline deposits consist mainly of small graphite particles intergrown with impurities. Typical deposits are stratiform or lens-shaped; beds may be deformed and/or repeated by folding and faulting. Pinching and swelling of beds is common. Deposits may consist of several beds, each up to a few metres thick. They may be exposed for hundreds of metres along strike. The ore contains from 30 to 95% graphite and, in many cases, more than 80%. Most mines producing microcrystalline graphite enrich ores only by hand sorting and milling. The product is sold mainly as forging lubricants and for applications where high ash content and low crystallinity is acceptable or preferred. An exception is the Kaiserberg deposit in Austria, where 92% graphite concentrate consisting of 2 micron size particles is produced (Taylor, 2006).

2.2. Vein graphite deposits

The most economically significant vein-type graphite deposits are found in the same metasedimentary belts as crystalline flake graphite deposits (see below), which are metamorphosed to upper amphibolite and granulite facies. In these belts, vein graphite deposits are found in skarn-type assemblages adjacent to igneous intrusions, in igneous intrusions, and in zones with a retrograde overprint (Simandl, 1992). Graphite veins are currently mined only in Sri Lanka, where graphite is extracted mainly by underground mining methods, routinely to depths in excess of 600 metres. The thickness of individual or anastomosing veins varies from a few millimetres to over one metre, but most are less than 0.3 metres. Other graphite-filled open spaces form pods and lenses, irregular bodies, stockworks, and saddle reefs (Simandl, 1992; Simandl and Keenan, 1998b). Rosettes, coarse flakes, fibers or needles oblique or perpendicular to wall rock and, in some cases, schistosity subparallel to the vein walls are characteristic textures. Outside of upper amphibolite to granulite facies metamorphic terrains and related intrusives (e.g., Cirkel, 1907), graphite veins, breccias, and stockworks also cut a variety of mafic and ultramafic rocks (e.g., Strens, 1965; Barrenechea et al., 1997; Crespo et al., 2006).

Vein graphite product (nearly monomineralic), graphite-rich fragments that are typically 0.5 to 0.8 cm in diameter are commercially referred to as 'lump' and 'chip' graphite, although 'lump' graphite may be much coarser (Table 1).

Pre-2009 disruptions in the supply of chip and lump graphite due to unrest in Sri Lanka forced the refractory industry to switch from vein-derived graphite to crystalline flake graphite. Once this transition was made, vein deposits lost their economic prominence as the source of graphite for refractories.

2.3. Crystalline flake graphite deposits

Disseminated graphite flakes are in a variety of rocks including marble, paragneiss, iron formation, quartzite, pegmatite, syenite (Simandl, 1992; Simandl et al., 1995) and, in extremely rare cases, serpentinized ultramafic rocks (e.g., Crespo et al., 2006). By far the most common hosts for economically significant crystalline flake deposits are paragneiss and marble that have been subjected to upper amphibolite to granulite facies metamorphism. Graphite deposits consisting of thick sequences of paragneiss are evenly mineralized and generally grade 2-3% graphite or less. A typical example is the Bissett Creek deposit in western Ontario (Fig. 4), which contains 69.8 million tonnes of measured and indicated resources grading 1.74% graphitic carbon (Cg) and 24 million tonnes of inferred resources grading 1.65% Cg (both at a 1.02% Cg cutoff grade; Northern Graphite Corporation, 2015). These resource estimates are not NI 43-101 compliant. The highest graphite grades in paragneiss-hosted deposits are along or near paragneiss-marble contacts, as exemplified by the Hartwell prospect, Quebec (Figs. 4 and 5). There, marble is separated from biotite gneiss by calcsilicate rocks (clinopyroxenites) and graphite-bearing scapolite paragneiss with graphite grades of 3-15% (Figs. 4 and 5). The contact between this graphite-rich unit and the biotite-gneiss is gradational and graphite content decreases with increasing distance from the calcsilicate rocks. Similarly, the high-grade Lac Knife deposit, in the Labrador Through (Quebec; Fig. 4), is also reported by Birkett et al. (1989), as cited by Saucier et al. (2012), to contain calcsilicate layers consisting mainly of scapolite. Measured and indicated resources at Lac Knife total 9,576,000 million tonnes grading 14.77% graphitic carbon, with inferred resources of 3,102,000 tonnes grading 13.25% carbon, using a cut-off grade of 3% graphitic carbon (Desautels et al., 2014). For some deposits (e.g., AA deposit, British Columbia; Fig. 4), the highest grade graphite is encountered in the crests of folds and is accompanied by retrograde minerals such as epidote and chlorite (Marchildon et al., 1993).

Marbles in terrains metamorphosed to granulite facies display a granoblastic texture and generally contain less than 0.5% crystalline flake graphite, although concentrations from 1 to 3% crystalline graphite are common. Graphite is regularly distributed throughout the host rock and the size of graphite flakes and calcite or dolomite crystals is directly correlated. Microscopic signs of corrosion or overgrowth on the graphite flakes that would indicate disequilibrium are lacking. Minor constituents such as diopside, magnesite, quartz, tremolite, fosterite, humite group minerals, garnets, scapolite, wollastonite, feldspar, phlogopite, muscovite, and serpentine account for less than 5% per volume of the rock.

Marbles with porphyroblastic texture are unusual. They contain from trace to 25% crystalline flake graphite. The best example is the historic Asbury graphite mine in Québec (Figs. 4 and 6). At this site, near-surface reserves were estimated to be 485,180 tonnes at 10.75% graphite (Séguin, 1974) and the mine was in production from 1980 to 1988 on seasonal basis.

Fig. 4. Location of Canadian graphite deposits discussed in the text.

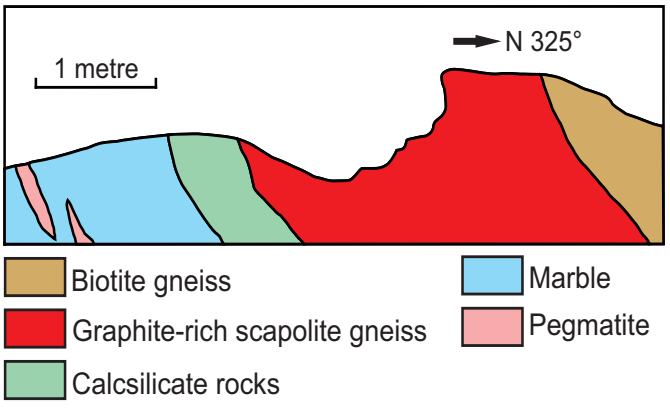

Fig. 5. Geological cross section of the Hartwell graphite prospect, Quebec. No vertical exaggeration. After Simandl et al. (1995).

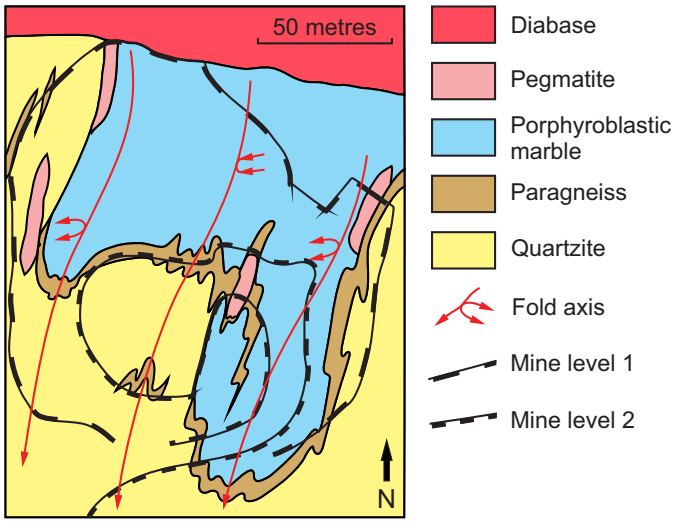

Fig. 6. Geological map of Asbury Graphite mine, Quebec. After Simandl et al. (1995).

Drilling in 1984, combined with a structural study, suggests additional resources at depth (Simandl, 1992). The graphite-rich porphyroblastic marble is calcitic and contains 2-10 mm clinopyroxene crystals. Other minerals, in concentrations less than 3%, are quartz, pyrite, garnet, titanite, magnetite, chlorite, and trace chalcopyrite, clinozoisite, and prehnite. Graphite flakes are dispersed throughout the ore, but concentrated around clinopyroxene crystals. Locally, graphite is observed as inclusions inside clinopyroxenes. Blue quartzite separates porphyroblatic graphite-rich marble from pale grey or white quartzite and indicates proximity to high-grade graphite mineralization. Obvious textural, mineralogical, or geochemical differences to explain the colour difference between the blue and white quartzites are absent. Although no primary fluid inclusions were identified in either quartzites, temperatures of homogenization and melting suggest the presence of CH_4, N_2, SO_4, or H_2S, in addition to CO_2. Limited Raman spectroscopy detected CO_2 with lesser concentrations of CH_4 and N_2 in fluid inclusions in blue quartzite (Simandl, 1992).

Most crystalline flake graphite deposits are mined in open pits. Typically, the ore is crushed, milled, processed using flotation and, depending on its physical properties and intended use, may be further processed. Crystalline flake graphite concentrate consists of flakes typically larger than 200 mesh (equivalent to 74 microns); fines produced during milling may be sold as graphite powder or dust.

Significant graphite concentrations in magnetite deposits are present in the Grenville Province (Raymond, 1978; Champigny, 1980; Gauthier and Brown, 1986; Simandl et al., 1995). Although none of these deposits are currently in production, some were mined for iron (e.g., Forsyth mine, Quebec). Several minor feldspar-rich intrusions (including pegmatites) cutting metasedimentary rocks contain up to 5%wt. graphite flakes, but are generally too restricted in size to be of economic interest (Simandl et al., 1995).

3. Origin of natural graphite deposits of economic interest

Natural graphite deposits of economic interest are most likely formed by: 1) the maturation and metamorphism of organic material; and 2) precipitation from C-O-H fluid (metamorphic or metasomatic) triggered by changes in temperature and pressure conditions, fluid buffering, or by mixing of C-O-H fluids of different compositions and probably different origins (for review, see Simandl, 1992).

3.1. Maturation and metamorphism of organic material

The transformation of immature organic material to graphite begins with carbonization and is followed by graphitization (Fig. 7). This is the generally accepted hypothesis to explain the origin of microcrystalline and low-grade crystalline flake graphite deposits. During the carbonization stage, organic substances are converted into carbon or carbon-containing residues, and oil and natural gas are released. Carbonization takes place during diagenesis, whereas graphitization takes place at higher temperatures and pressures of deeper burial and metamorphism. During both carbonization and graphitization, the atomic ratios of H/C and O/C systematically decrease (Fig. 7). Kerogens I, II, and III are derived largely from lacustrine algae (H/C > 1.25), marine microorganisms (1.1<H/C<1.5), and terrestrial plants (coal deposits; H/C<1), respectively. During the carbonization process, kerogens go from immature to oil and gas forming stages. The carbon-enriched residue stays in place, while liberated hydrocarbons are expelled. Further burial accompanied or followed by regional or contact metamorphism may result in graphitization of residual material (development of a well-ordered graphite crystal structure). Various stages and aspects of the kerogene-graphite transition are addressed by Grew (1974), Diessel and Offler (1976), Jones and Edison (1979), Oberlin et al. (1980), North (1985), Wopenka and Pasteris (1993), and Buseck and Beysasak (2014).

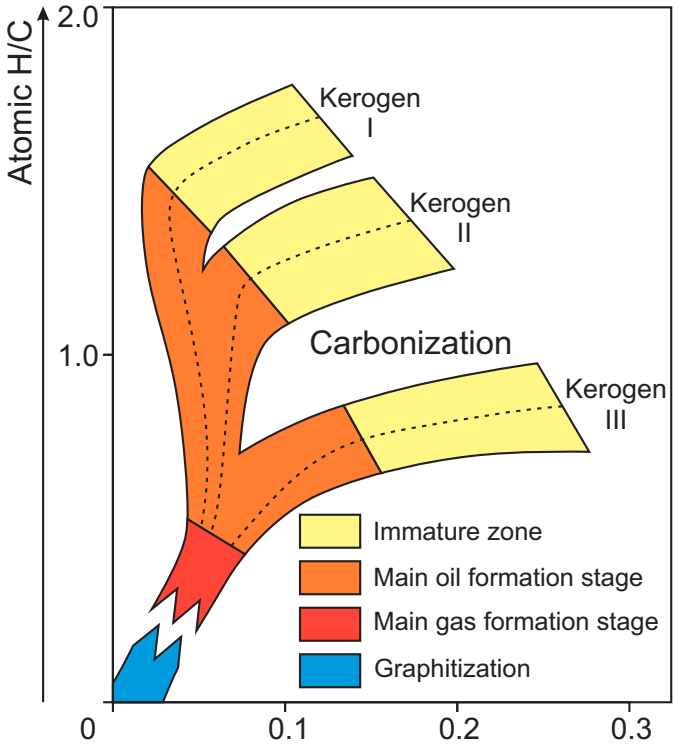

Fig. 7. Kerogen maturation in terms of H/C and O/C atomic ratios. Modified from Buseck and Beyssac (2014); based on data of Grew (1974), and Vandenbroucke and Largeau (2007).

3.2. Precipitation of graphite from C-O-H fluids

In contrast to the origin of microcrystalline and low-grade crystalline flake graphite deposits, the origin of graphite veins is still widely debated and the genesis of enrichment zones within crystalline flake graphite deposits (e.g., Hartwell prospect and Asbury Graphite deposit) remains largely overlooked. Ternary C-O-H diagrams (Figs. 8-10) offer a simple approach to explain the origin of high-grade graphite deposits that show open space features and textures such as breccia zones and veins, or enrichment zones in crystalline flake graphite deposits.

Graphite saturation curves on C-O-H ternary diagrams are temperature and pressure dependent (e.g., Holloway, 1984;

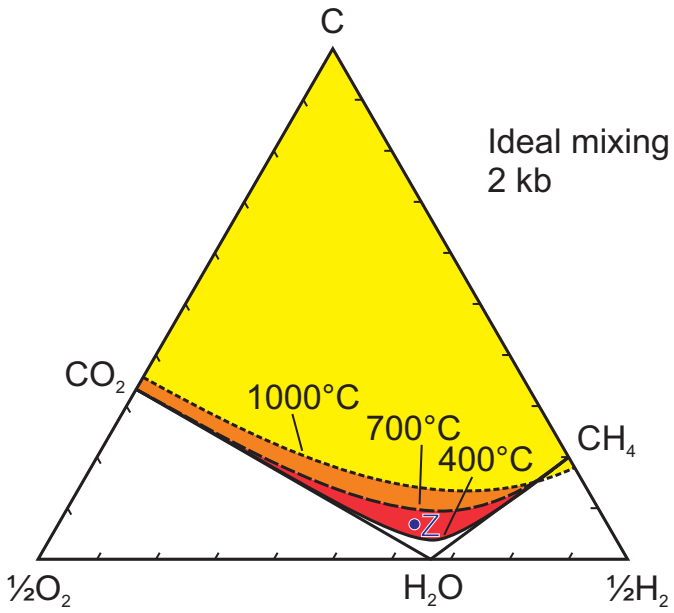

Fig. 8. Ternary C-O-H diagram showing increasing size of graphite stability field with decreasing temperatures from 1000º to 400°C for constant pressure of 2 kb, assuming ideal mixing according to Lewis and Randall Rule. Modified from Ferry and Baumgartner (1987).

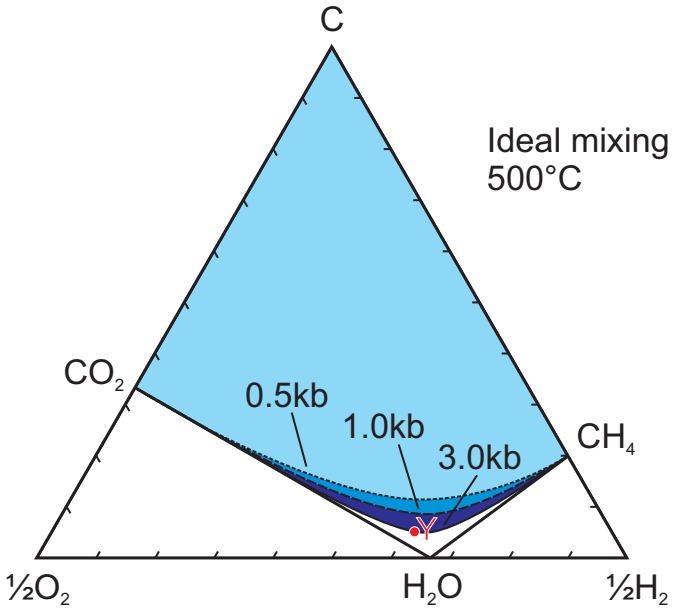

Fig. 9. Ternary C-O-H diagram showing increasing size of graphite stability field with increasing pressure from 0.5 to 3.0 kb for constant temperature of 500°C, assuming ideal mixing (Lewis and Randall Rule). Modified from Ferry and Baumgartner (1987).

Ferry and Baumgartner, 1987; Pasteris, 1999; Luque and Rodas, 1999; Huizenga, 2011; Huizenga and Touret, 2012). At constant pressure, the graphite stability field increases with decreasing temperature. For example, assuming a constant pressure of 2 kb, graphite can't precipitate from cooling of a C-O-H fluid of the composition Z at 1000ºC or 700°C, but will start to precipitate before the fluid cools below 400°C (Fig. 8). At constant temperature, the stability field of graphite increases with increasing pressure (Ferry and Baumgartner, 1987). For example, at 500°C graphite will not precipitate from a fluid of composition Y at pressures of 0.5 and 1.0 kb, but will precipitate at pressures of 3 kb or greater (Fig. 9).

Figure 10 shows part of the C-O-H ternary diagram at 600°C and pressure of 3.5 kb. A fluid of composition A plots within the graphite stability field. As graphite precipitates, the composition of the fluid evolves along the corresponding tie-line, as shown by the green arrow, towards the graphite saturation curve. Figure 10 also shows fluids of compositions B and F, both of which lie outside the graphite stability field. It would be impossible to precipitate graphite from either of these fluids alone. However, if we mix these two fluids, the composition of the resulting mixture will lie somewhere along the mixing line B-F. If a small quantity of fluid F is added to fluid B, then the composition of the resulting fluid will shift slightly to the right (e.g., point C). As more fluid F is added to the system, the composition of the resulting fluid will keep shifting to the right until point D is reached and the first crystal of graphite precipitates. As more fluid of composition F enters the system, the composition of the fluid follows the graphite saturation curve, passing through point E, and graphite keeps precipitating.

4. Discussion and summary

Microcrystalline graphite deposits form by maturation of organic material in sedimentary rocks (coal seams) followed by regional or contact metamorphism attaining sub-greenschist to greenschist facies. It is used mainly in greases and forging lubricants and has no known use in high-technology applications.

Economically minable graphite veins are typically hosted by sedimentary successions that have been subjected to granulite facies metamorphism and intruded by minor igneous bodies. Mining of graphite veins similar to those that are mined in Sri Lanka involves underground methods and is labor intensive. Graphite morphology, open-space filling textures, and thermodynamic models indicate that these veins originate by precipitation from C-H-O fluids.

Most exploration projects target crystalline flake deposits. Low concentrations of crystalline flake graphite in marbles and paragneisses probably result from maturation of organic material in precursor sediments, followed by graphitization at pressure and temperature conditions approaching or reaching granulite facies. Graphite-rich zones in disseminated crystalline flake deposits (e.g., Asbury Graphite mine in Quebec, AA deposit in British Columbia) are typically at or near marble-paragneiss contacts and in the crests of folds. These zones are characterized by porphyroblastic textures in marbles, skarn mineralogy at or near the contacts, and decreasing concentrations of scapolite in the paragneiss with increasing distance from the contacts. In these settings, graphite enrichment is likely the result of: a) mixing of fluids produced by decarbonation reactions in marbles and dehydration reactions in paragneiss, or fluids derived

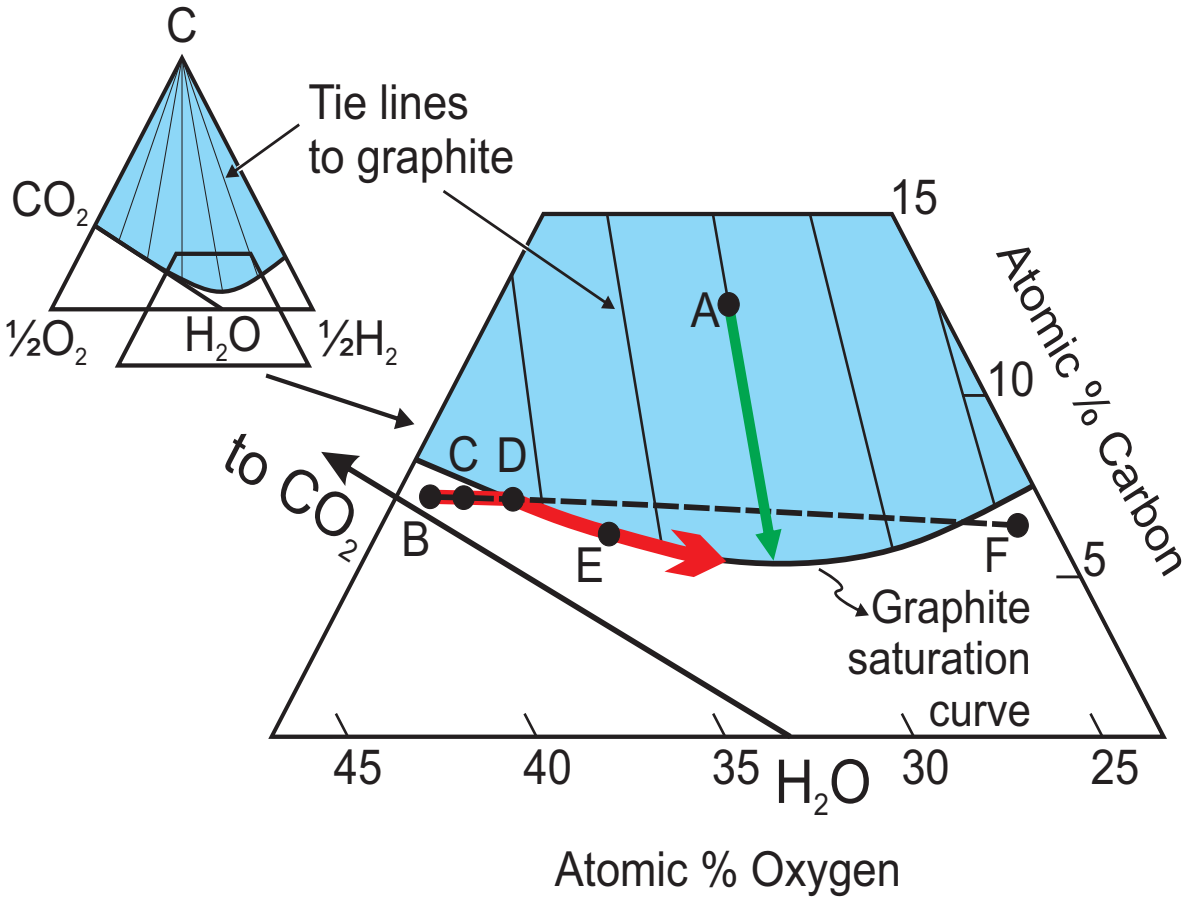

Fig. 10. Ternary C-O-H diagram at 600°C and 3.5 kb showing precipitation of graphite from the fluid of composition A (within the graphite stability field) and from mixing of fluids of composition B and F, both lying outside of the graphite stability field. Refer to detailed explanation in text. Modified from Rumble et al. (1982).

from pegmatites and other minor intrusions; or b) cooling of C-H-O fluids. Sub-granulite facies minerals (e.g., prehnite and clinozoisite) observed in some veins and high-grade portions of disseminated flake graphite deposits suggest post-metamorphic peak (retrograde) temperatures of formation.

Forecasted increase in use of natural graphite in high-technology applications turns graphite into a 'hot' commodity; however, fundamental technical and economic parameters of individual deposits have to be taken into consideration when prioritizing exploration and development targets. Enriched zones of crystalline flake graphite deposits are of particular interest to industrialized countries because they are mined by open pit methods (not labour intensive) and provide critical material for high-technology applications.

Acknowledgments

Comments and suggestions from Douglas Rumble III of the Geophysical Laboratory of the Carnegie Institution of Washington are greatly appreciated.

References cited

Anonymous, 2015. Graphene news review. Industrial Minerals, no. 571, 21-22.

Anthony, W., Bideaux, R.A., Bladh, K.W., and Nichols, M.C. (Eds.), 1990. Handbook of mineralogy, volume I: elements, sulfides, sulfosalts. Mineral Data Publishing, Tucson, Arizona, 588p.

Barrenechea, J.F., Luque, F.J., Rodas, M., Pasteris, J.D., 1997. Vein-type graphite mineralization in the Jurassic volcanic rocks of the external zone of the Betic Cordillera (southern Spain). The Canadian Mineralogist, 35, 1379-1390.

Beyssac, O., and Rumble, D., 2014. Graphitic carbon: a ubiquitous, diverse, and useful geomaterial. Elements, 10, 415-120.

Birkett, T., Godue, R., and Marchildon, N., 1989. The Knife lake graphite deposit, geology, mineralogy and mineral textures, 1989 field and laboratory investigations. Unpublished documents, Québec Géosciences Center.

Buseck, P., and Beyssac, O., 2014. From organic matter to graphite: graphitization. Elements, 10, 421-426.

Champigny, N., 1980. Stratigraphic relationship between iron formations and zinc mineralization, Mt. Laurier Basin, Quebec. Progress report to Riocanex Inc., Toronto, Ont., 15p.

Chiu, G., 2015. Perfection of the pursuit: the Canadian option for graphene's commercialisation. Industrial Minerals, no. 571, 25-26.

Cirkel, F., 1907. Graphite, its properties, occurrences, refining and uses. Canada Department of Mines, Mines Branch, Ottawa, No. 202, 263p.

Crespo, E., Luque, F.J., Rodas, M., Wada, H., and Gervilla, F., 2006. Graphite-sulfide deposits in Ronda and Beni Bouser peridotites (Spain and Morocco) and the origin of carbon in mantle-derived rocks. Gondwana Research, 9, 279-290.

Desautels, P., D'Anjou, N., Skiadas, N., Cassoff, J., Pengel, E., Bilodeau, M.L., and Buchanan, M.J., 2014. NI 43-101 technical report on the Lac Knife graphite feasibility study Quebec-Canada. Focus Graphite Inc., 293p. <http://www.focusgraphite.com/wp-content/uploads/largeReport/Lac-Knife-Feasibility-Study-Technical-Report-August-2014.pdf> Accessed July 15, 2015.

Dickson, J.S., 2014. Talga eyes graphene potential. Industrial Minerals, no. 567, 35-36.

Diessel, C.F.K., and Offler, R., 1976. The application of reflectance determination on coalified and graphitized plant fragments to metamorphic studies. Journal of the Geological Society of Australia, 23, 293-297.

Ferry, J.M., and Baumgartner, L., 1987. Thermodynamic models of molecular fluids at the elevated pressures and temperatures of crustal metamorphism. In: Carmichael, I.S.E., and Eugster, H.P., (Eds.), Thermodynamic Modeling of Geological Materials: Minerals, Fluids and Melts. Mineralogical Society of America Reviews in Mineralogy, Volume 17, pp. 323-365.

Grew, E.S., 1974. Carbonaceous material in some metamorphic rocks of New England and other areas. Journal of Geology, 82, 50-73.

Gauthier, M., and Brown, A.C., 1986. Zinc and iron metallogeny in the Maniwaki-Gracefield district, southwestern Quebec. Economic Geology, 81, 89-112.

Herstedt, M., Fransson, L., and Edström, K., 2003. Rate capability of natural Swedish graphite as anode material in Li-ion batteries. Journal of Power Sources, 124, 191-196.

Holloway, J.R., 1984. Graphite-CH_4-H_2O-CO_2 equilibria at low grade metamorphic conditions. Geology, 12, 455-458.

Hughes, E., 2015. The importance of Manchester's "Graphene City". Industrial Minerals, no. 571, 27-28.

Huizenga, J.-M., 2011. Thermodynamic modelling of a cooling C-O-H fluid-graphite system: implications for hydrothermal graphite precipitation. Mineralium Deposita, 46, 23-33.

Huizenga, J.-M., and Touret, J.L.R., 2012. Granulites, CO_2 and graphite. Gondwana Research, 22, 799-809.

Industrial Minerals, 2015. Graphite Prices. <http://www.indmin.com/Graphite.html> Accessed March 26, 2015.

Jones, R.W., and Edison, T.A., 1979. Integration of microscopic organic analysis and geochemical measurements in evaluation of source rocks. American Association of Petroleum Geologists, Bulletin 63, p.476.

Kwiecińska, B., and Petersen, H.I., 2004. Graphite, semi-graphite, natural coke, and natural char classification—ICCP system. International Journal of Coal Geology, 57, 99-116.

Lismore-Scott, S.L., 2014. Graphite projects and reserves – are we facing an oversupply situation? Industrial Minerals, no. 567, 29-32.

Luque, F.J., and Rodas, M., 1999. Constraints on graphite crystallinity in some Spanish fluid-deposited occurrences form different geologic settings. Mineralium Deposita, 34, 215-219.

Marchildon, N., Simandl, G.J., and Hancock, K.D., 1993. The AA graphite deposit, Bella Coola area, British Columbia: exploration implications for the coast plutonic complex. In: Geological Fieldwork 1992, British Columbia Ministry of Energy and Mines, British Columbia Geological Survey Paper 1993-1, 389-397.

Mertens, 2015. The graphene handbook. Lulu.com, Raleigh, North Carolina, 2nd edition, 136p. <http://www.graphene-info.com/handbook/> Accessed August 12, 2015.

Moores, S., 2015. Battery grade graphite set for record year. Mining.com <http://www.mining.com/web/battery-grade-graphite-set-for-record-year/> Accessed July 22, 2015.

North, F.K., 1985. Petroleum Geology. Allen & Unwin, Boston, 605p.

Northern Graphite Corporation, 2015. Bissett Creek Project. <http://northerngraphite.com/bissett-creek-project/> Accessed June 30, 2015.

Oberlin, A., Boulmier, J.L., and Villey, M., 1980. Electron microscopic study of kerogen microtexture. Selected criteria for determining the evolution path and evolution stage of kerogen. In: Durand, B., (Ed.), Kerogen. Editions Technip, Paris, pp. 191-241.

Olson, D.W., 2015. Graphite (Natural). U.S. Department of the Interior, U.S. Geological Survey, Mineral Commodity Summaries, January 2015, pp.68-69. <http://minerals.usgs.gov/minerals/pubs/mcs/2015/mcs2015.pdf> Accessed June 30, 2015.

Pasteris, J.D., 1999. Causes of the uniformly high crystallinity of graphite in large epigenetic deposits. Journal of Metamorphic Geology, 17, 779-787.

Raymond, D., 1978. Etude de deux indices minéralisés (magnetite) du Canton de Cameron, Comté de Gatineau, Québec. Unpublished BSc Thesis, Ecole Polytechnique de Montréal, Montréal, 65p.

Rumble, D., Ferry, J.M., Hoering, T.C., and Boucot, A.J., 1982. Fluid flow during metamorphism at the Beaver Brook fossil locality, New Hampshire. American Journal of Science, 282, 886-919.

Salwan, S., 2014. The Indian graphite industry – why we need to take notice. Industrial Minerals, no. 567, 32-34.

Salwan, S., 2015. Vein graphite prices resist market slump. Industrial Minerals. <http://www.indmin.com/Article/3471988/Graphite/Vein-graphite-prices-resist-market-slump.html> Accessed July 22, 2015.

Saucier, G., Lyons, E., and Baril, F., 2012. NI 43-101 technical report on the Lac Knife graphite project. Focus Metals Inc., 87p. <www.focusgraphite.com/french/wp-content/uploads/2012/07/43-101Report_Lac-Knife.pdf> Accessed July 10, 2015.

Séguin, E., 1974. Preliminary report on the projected operation of a graphite mine at Notre-Dame-du-Laus, Québec. Somex Ltd., 16p.

Shaw, S., 2013. Graphite demand and growth: the future of lithium-ion batteries in EVs and HEVs. Proceedings of 37th ECGA General Assembly. <http://www.saintjeancarbon.com/files/2513/7157/3343/Graphite_demand_Li-ions_April_2013.pdf> Accessed June 30, 2015.

Simandl, G.J., 1992. Gîtes de graphite de la région de la Gatineau, Québec. Unpublished Ph.D. thesis, Université de Montréal, Montréal, Canada, 383p.

Simandl, G.J., and Keenan, W.M., 1998a. Microcrystalline graphite. In: Geological Fieldwork 1997, British Columbia Ministry of Energy and Mines, British Columbia Geological Survey Paper 1998-1, 24O-1-24O-3. <http://www.empr.gov.bc.ca/Mining/Geoscience/PublicationsCatalogue/Fieldwork/Documents/1997/simandl_kenan_po3.pdf> Accessed June 30, 2015.

Simandl, G.J., and Keenan, W.M., 1998b. Vein graphite in metamorphic terrains. In: Geological Fieldwork 1997, British Columbia Ministry of Energy and Mines, British Columbia Geological Survey Paper 1998-1, 24Q-1-24Q-3. <http://www.empr.gov.bc.ca/Mining/Geoscience/PublicationsCatalogue/Fieldwork/Documents/1997/simandl_kenan.pdf> Accessed June 30, 2015.

Simandl, G.J., and Keenan, W.M., 1998c. Crystalline flake graphite. In: Geological Fieldwork 1997, British Columbia Ministry of Energy and Mines, British Columbia Geological Survey Paper 1998-1, 24P-1-24P-3. <http://www.empr.gov.bc.ca/Mining/Geoscience/PublicationsCatalogue/Fieldwork/Documents/1997/simandl_kenan_po4.pdf> Accessed June 30, 2015.

Simandl, G.J., Paradis, S., Valiquette, G., and Jacob, H.L., 1995. Crystalline graphite deposits, classification and economic potential. Proceedings of 28th Forum on the Geology of Industrial Minerals, Marinsburg, West Virginia, May 3-8, 1992, pp.168-174.

Spasenovic, M., 2015. Leavin lab status: Graphene's various routes to industrial application. Industrial Minerals, no. 571, 23-25.

Strens, R.G.T., 1965. The graphite deposits of Seathwaite in Borrowdale, Cumberland. Geological Magazine, 102, 393-406.

Sadasivuni, K.K., Ponnamma, D., Thomas, S., and Grohens, Y., 2014. Evolution from graphite to graphene elastomer composites. Progress in Polymer Science, 39, 749-780.

Taylor, H.A., Jr., 2006. Graphite. In: Kogel, J.E., Trivedi, N.C.,

Barker, J.M., and Krukowski, W.T., (Eds.), Industrial Minerals and Rocks. Society for Mining, Metallurgy, and Exploration, Inc., Littleton, Colorado, pp. 507-518.

Vandenbroucke, M., and Largeau, C., 2007. Kwerogen origin, evolution and structure. Organic Geochemistry, 38, 719-833.

Wang, X., Gai, G.-S., Yang, Y.-F., and Shen, W.-C., 2008. Preparation of natural microcrystalline graphite with high spericity and narrow size distribution. Powder Technology, 181, 51-56.

Wissler, M., 2006. Graphite and carbon powders for electrochemical applications. Journal of Power Sources, 156, 142-150.

Wopenka, B., and Pasteris, J.D., 1993. Structural characterization of kerogens to granulite-facies graphite: applicability of Raman microprobe spectroscopy. American Mineralogist, 78, 533-557.

Wu, Y.-S., Wang, Y.-H., and Lee, Y.-H., 2006. Performance enhancement of spherical natural graphite by phenol resin in lithium ion batteries. Journal of Alloys and Compounds, 426, 218-222.

Geology, ore characteristics, and origin of the Albany graphite deposit

Andrew G. Conly[1, a] and Lindsay C. Moore[1]

[1] Mineralogy and Experimental Laboratory, Department of Geology, Lakehead University, Thunder Bay, ON
[a] corresponding author: aconly@lakeheadu.ca

Recommended citation: Conly, A.G. and Moore, L.C., 2015. Geology, ore characteristics, and origin of the Albany graphite deposit. In: Simandl, G.J. and Neetz, M., (Eds.), Symposium on Strategic and Critical Materials Proceedings, November 13-14, 2015, Victoria, British Columbia. British Columbia Ministry of Energy and Mines, British Columbia Geological Survey Paper 2015-3, pp. 173-185.

1. Introduction

The Albany graphite deposit is a 24 Mt, low-grade, breccia-hosted graphite deposit currently under development by Zenyatta Ventures Ltd., near Hearst, Ontario (Fig. 1). The deposit was discovered following an airborne geophysical survey and subsequent exploration diamond drilling of nickel-copper-platinum group minerals targets. Between 2010 and 2014, Zenyatta Ventures confirmed a graphite deposit hosted in two large breccia pipes (hereafter referred to as the East Pipe and West Pipe) that intruded along the southern margin of an arcuate chain of Mesoproterozic to Neoproterozoic alkalic intrusions.

Studies of the Albany deposit have been lacking because of minimal exploration and mapping in the area, and due to extensive cover by Phanerozoic rocks and glacial overburden. Herein we integrate field, mineralogical, and isotopic data to document the origin of the deposit. We also document the physicochemical properties of the graphite, which is important to establish during early states of exploration to address questions about markets and commercial viability.We consider that Albany is an epigenetic, igneous-hosted, fluid-derived graphite deposit (see Luque et al., 2013 for a treatment of graphite deposits). Although uncommon relative to the syngenetic deposits, which are formed by the conversion of carbonaceous material by contact or regional metamorphism, fluid-derived deposits commonly account for the highest quality of natural graphite (Luque et al., 2013; e.g., Sri Lanka; Borrowdale, UK; Huelma, Spain; New York; Montana).

2. Geological setting

The Albany graphite deposit is in the southern Marmion terrane of the Superior Province (Fig. 1), along the southern margin of the Nagagami River Alkalic Rock complex (NRAC; Sage, 1988) and immediately north of the Gravel River fault, which separates the Marmion terrane and NRAC from the Quetico sub-province to the south (Figs. 1, 2; Kennedy, 1984). The Albany graphite deposit is hosted by the Albany Alkalic complex, which may be part of the NRAC (Figs. 2, 3). The Nagagami River and Albany complexes are the most southern in a series of intrusions that define a north- to northwest-trending arcuate band of inferred alkalic magmatism (Fig. 2).

The absolute ages of the Nagagami River and Albany complexes are unknown. The Nagagami River Alkali complex cuts north to northwesterly trending Paleoproterozoic Matachewan (Hearst) dike swarms (ca. 2454 Ma; Heaman, 1988; Phinney and Morrison, 1988) and the east-northeasterly Kapuskasing dike swarm (ca. 2124-2170; Stott, 2008; Fig. 2). Temporal reationships between dikes and the Albany Alkali complex are complicated, as dikes cut the complex and vice versa. However, it is possible that dikes cutting the complex are related to augite-aegirine sills that transect the Albany deposit at depth (Fig. 4b), which are mineralogically and chemically distinct from regional dike swarms.

Precambrian rocks in the region are unconformably overlain by muskeg, glacial till, and Paleozoic (Ordovician to Devonian) carbonate rocks of the Moose River basin (James Bay Lowlands; Johnson et al., 1991). The glacial overburden ranges from 28 to 55 m (average 44 m) and the Paleozoic cover ranges from 0 to 16 m (average 3.8 m) in thickness.

3. Deposit geology

3.1. Grade and tonnage

Zenyatta Ventures Ltd. discovered the Albany deposit in 2010 using VTEM airborne geophysical surveys that suggested a pipe-like structure. Subsequent ground geophysical surveys (large loop TDEM; Fig. 4a) in 2013, provided improved resolution, and led to the discovery of two adjacent breccia pipes (Legault et al., 2015). Diamond drilling by Zenyatta Ventures between 2010 and 2014 confirmed the existence of the breccia pipes (East and West pipes; Fig. 4b). Open pit indicated mineral resources are estimated to total 24.3 million tonnes (Mt) at an average grade of 3.98% graphitic carbon (C_g), containing 968,000 tonnes of C_g; inferred mineral resources (open pit and underground) are estimated to total 16.9 Mt at an average grade of 2.64% C_g, containing 445,000 tonnes of C_g (RPA Inc., 2015).

3.2. Host rocks

The graphite-hosting rocks of the Albany complex vary from quartz syenite to diorite to nepheline syenite, with quartz

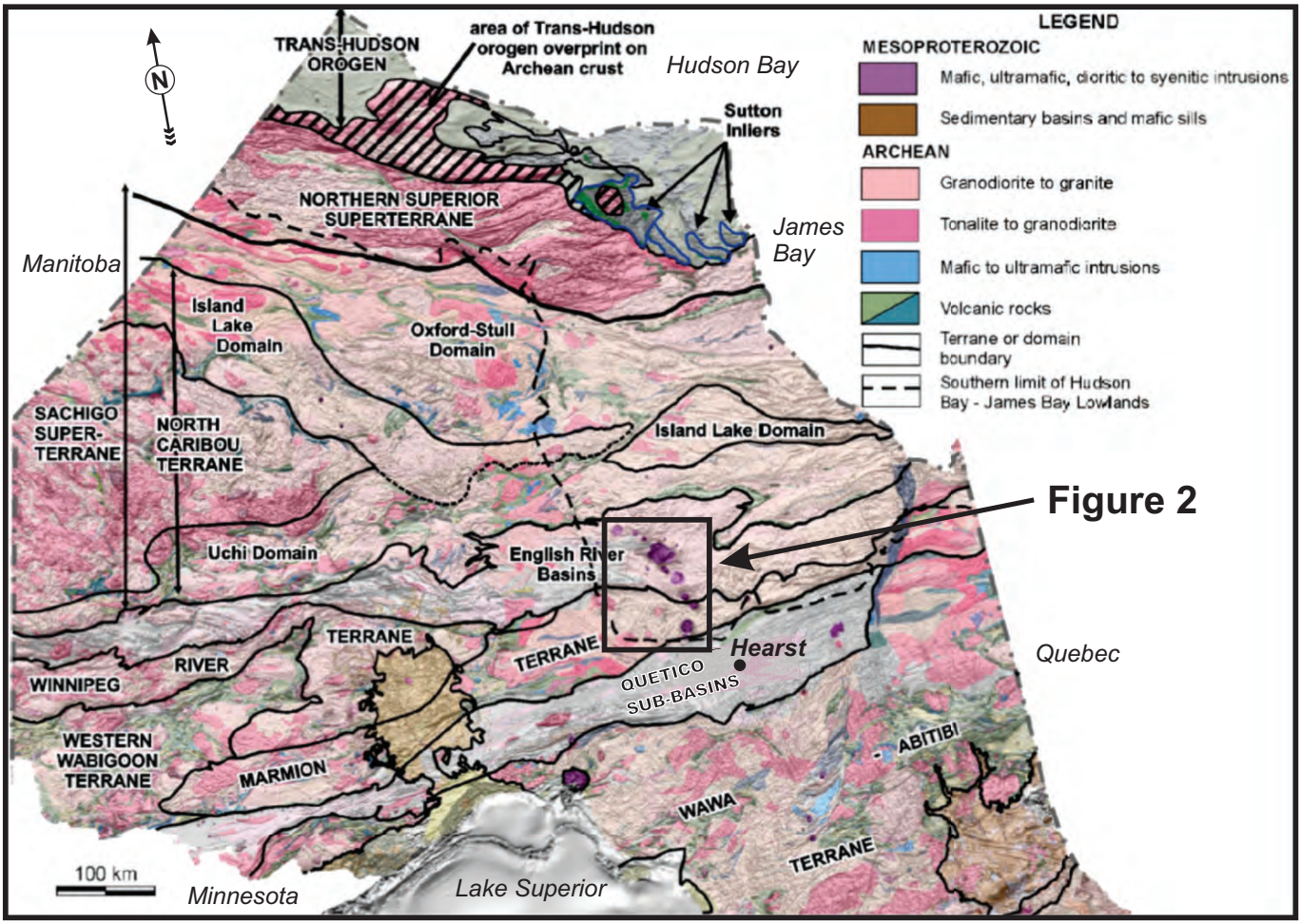

Fig. 1. Terrane boundary map of the Superior Province in Ontario (from Stott, 2011).

monzonite predominating. In contrast, the NRAC consists of fine- to coarse-grained amphibole-pyroxene syenite and lesser coarse-grained nepheline-bearing syenite and pegmatitic syenite, and minor granite (Sage, 1988).

The East (Fig. 5a) and West (Fig. 5b) pipes consist of angular to sub-rounded, millimetre- to metre-scale clasts. The clasts are mainly from the Albany complex, but fragments of amphibole-biotite schist, tourmaline-bearing granite, granite and gneiss, similar to rocks in the Marmion terrane and Quectico sub-province are common. Although sparse, brecciated fragments of semi-massive to massive graphite + silicate minerals occur in both pipes (Fig. 5c). The matrix consists of fine-grained (<0.5 mm) silicate minerals, which typically occur as discrete crystals and small monomineralic to polycrystalline aggregates intermixed with graphite (Fig. 6a). Matrix silicates tend to be angular to subangular and consist mainly of albite (30-60 modal%), perthitic feldspar (<40 modal%) and quartz (<25 modal%; Fig. 6a). Quartz crystals commonly display a polygonal fracture pattern (Fig. 6b). Finely disseminated solitary crystals and crystal aggregates of pyrite-pyrrhotite and magnetite are also observed in the matrix (Fig. 7a) and less commonly in fragments. The sulphide-oxide assemblage comprises less than 3 modal% of the rock, and typically <1 modal%. Discrete crystals of phlogopite and amphibole are rare win the matrix and local in lithic fragments. Hydrous silicate phases comprise <20 modal% of the rock.

A recently identified porphyritic monzodiorite/foid monzodiorite rock also forms breccias containing Albany complex clasts (Fig. 5d). This rock is spatially associated with, and closely, resembles, the graphite-bearing breccias but lacks graphite. Conly and Moore (2015) interpreted the rock as a hypabyssal, subvolcanic phase based on the occurrence of: 1) aphanitic groundmass consisting of albite, paragasite and minor nepheline; 2) embayed and sericitized albite xenocrysts with discontinuous, epitaxial overgrowths of sanidine; and 3) corona textured magmaclasts (consisting of a core of variably altered groundmass, an intermediate zone of subhedral to euhedral phlogopite and rimmed by anhedral to subhedal, radiating hastingsite ± phologopite). The hypabyssal phase is mainly distributed along the margins of the West pipe, but also occurs at depth (~400 m) along the outer margin of the East pipe, where it is cut by augite-aegirine syenite.

3.3. Mineralization and alteration

Graphite occurs both as intergranular (matrix) and intragranular (within lithoclasts) mineralization (Fig. 7a).

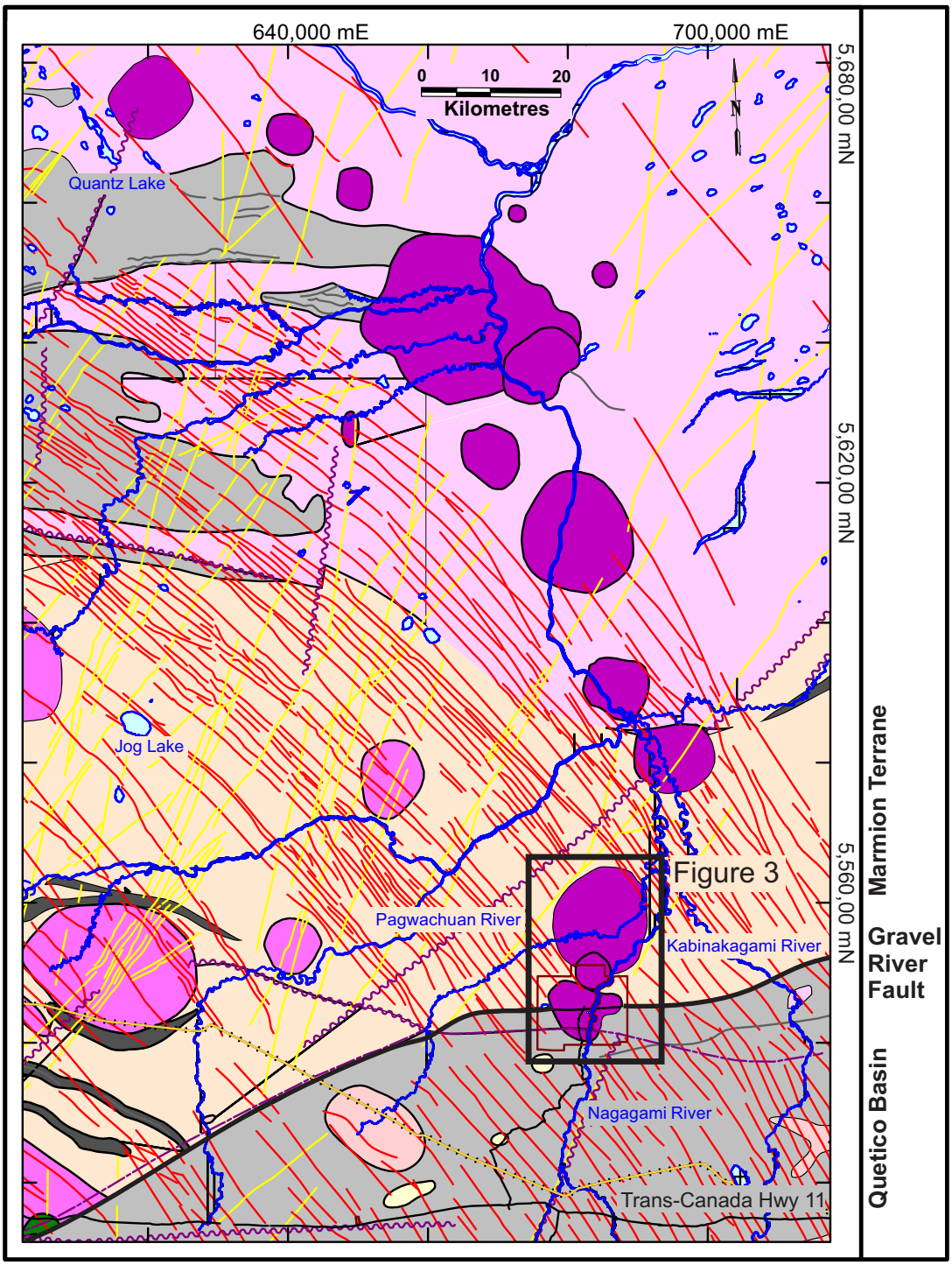

Fig. 2. Regional geology interpreted from aeromagnetic data (from Stott, 2008). UTM zone Z16, NAD 83.

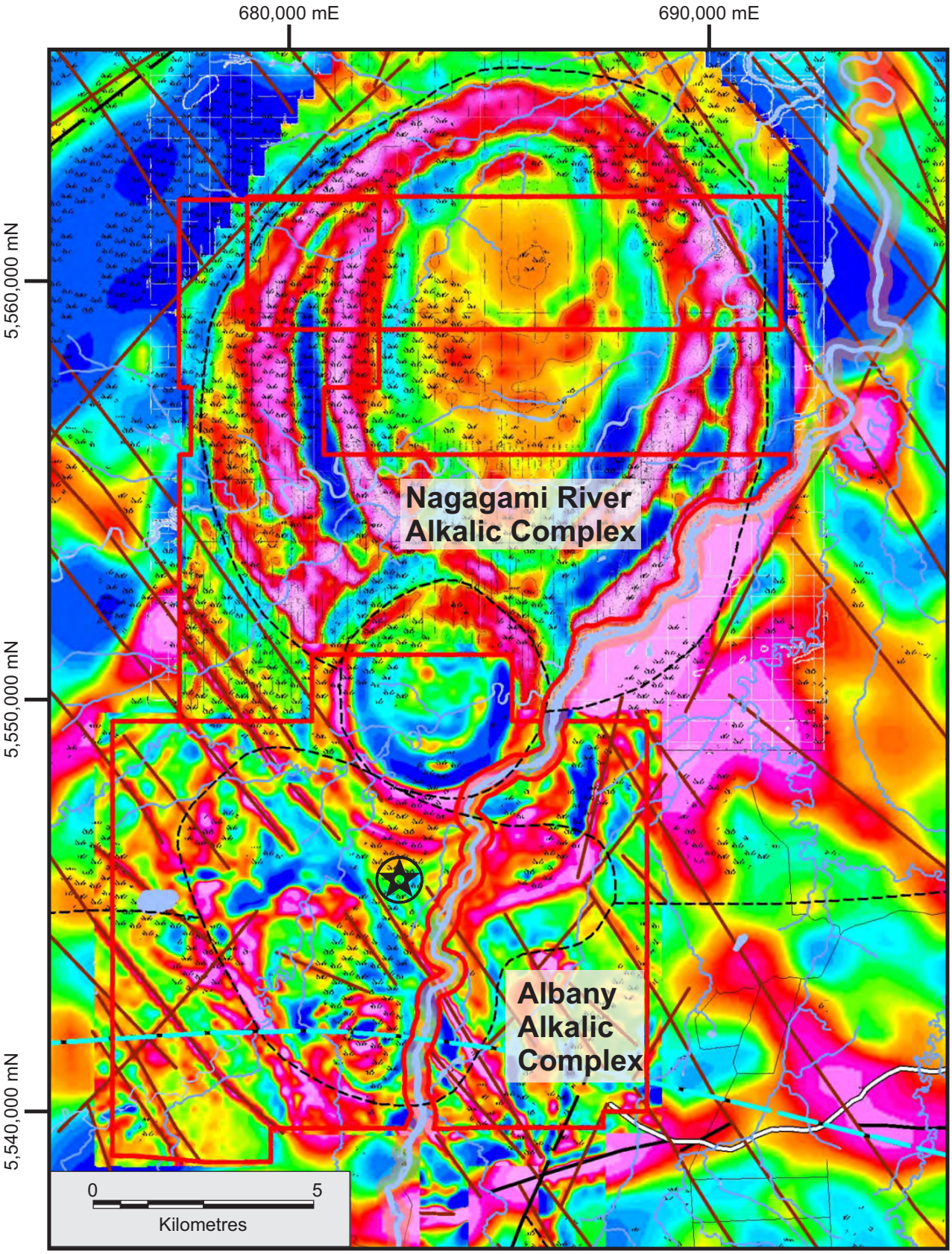

Fig. 3. Calculated vertical gradient aeromagnetic (composite) map of the Nagagami River Alkalic complex and the Albany Alkalic complex (courtesy Zenyatta Ventures Ltd.). Magnetic data are from multiple datasets that have not been merged and levelled. Location of the Albany graphite deposit is marked with the star. UTM zone Z16, NAD 83.

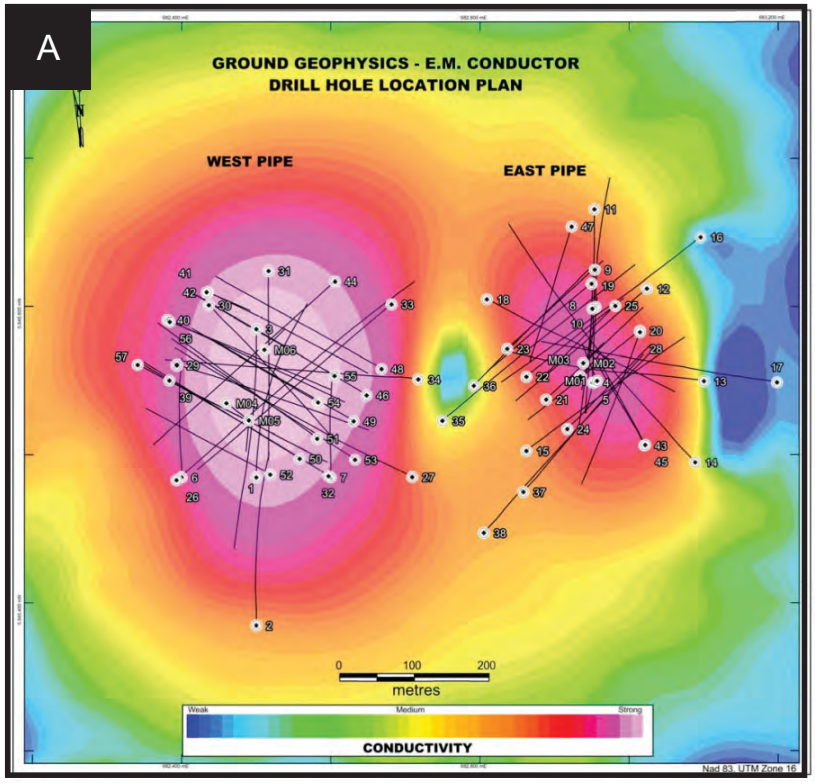

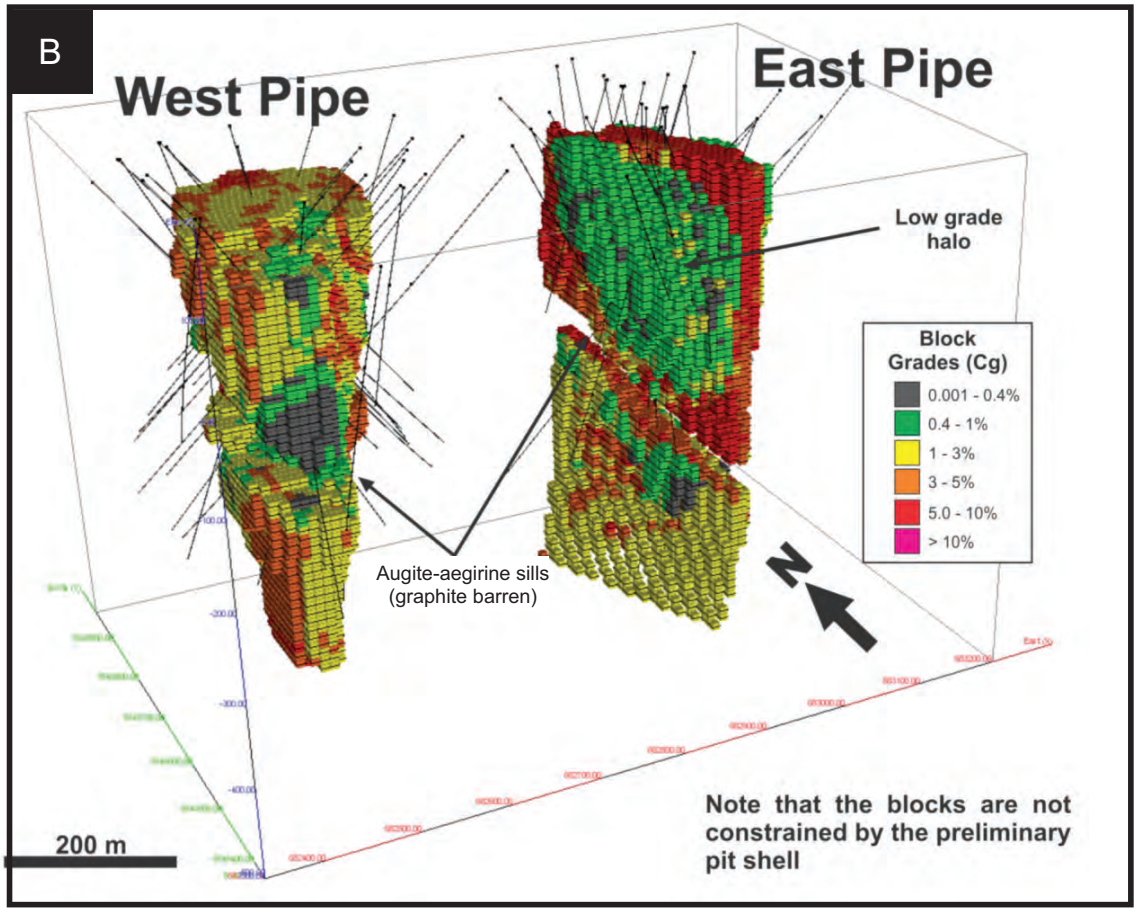

Fig. 4. a) Results of ground TDEM survey and drillhole locations and projections. **b)** 3-D block model of graphite grades, showing the pipe-like geometry of the Albany graphite deposit (both images courtesy of Zenyatta Ventures Ltd.).

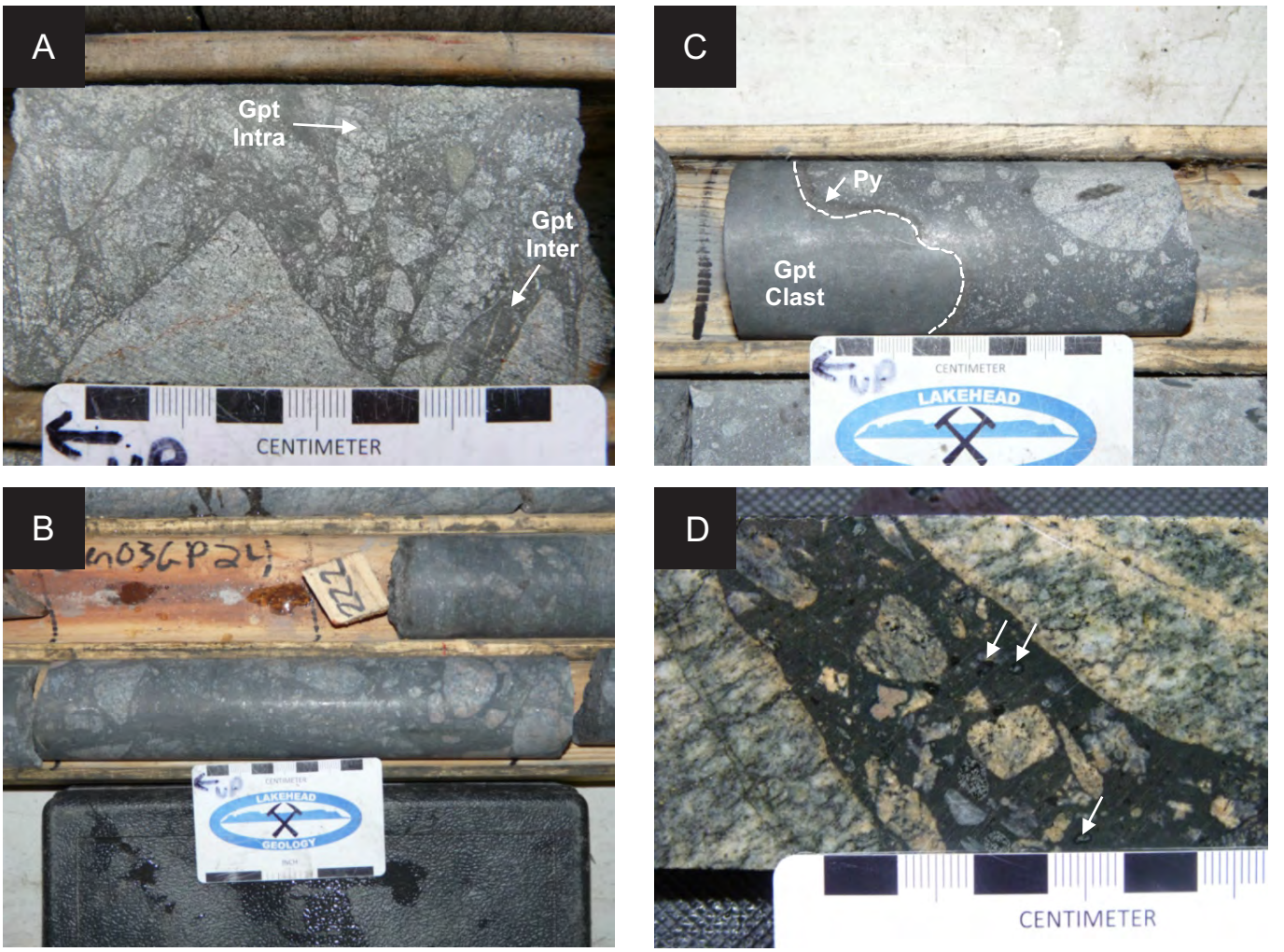

Fig. 5. Drill core photographs illustrating the typical breccia textures: **a)** East pipe with graphitic overprinting due to increased abundance of intragranular graphite in the fragments. **b)** High grade zone (~10% Cg) in the West pipe, where graphite is primarily concentrated in the breccia matrix. **c)** Graphite + silicate fragment in graphite mineralized West pipe breccia. **d)** Hypabyssal monzodiorite with fragments of potassic altered Albany complex syenite (magmaclasts are denoted by arrows). Mineral abbreviations: Gpt Intra – intragranular graphite; Gpt Inter – intergranular (matrix graphite).

Intragranular graphite represents a penetrative mineralization distributed along crystal boundaries and microfractures within lithoclasts. This style of mineralization also extends into unbrecciated to weakly veined Albany complex rock, producing a graphitic halo extending around the pipes. The higher contained graphite of the East pipe relative to the West pipe (with an indicated resource of 10.0 Mt at 5.60% C_g for the East pipe versus 14.3 Mt at 2.85% C_g for the West pipe; RPA Inc., 2015), is due to the development of a more extensive halo and a greater abundance of intragranular graphite in brecciated fragments (Fig. 5a). In the pipe halo, graphite also occurs as discrete millimetre- to centimetre-scale veins that increase in frequency towards the pipes. Matrix, graphite forms discrete laths, aggregated laths, mantles enclosing silicate crystals and lithofragments, and brecciated graphite+silicate fragments intermixed with finely fragmented silicates (Fig. 7b).

The breccias are essentially unmetamorphosed. Weak to extensive sericitization of plagioclase feldspar is the only ubiquitous alteration (Fig. 8a). Pyrite ± pyrrhotite alteration (Fig. 8b) is highly variable and consists mainly of finely disseminated crystals associated with matrix graphite and magnetite, and extends a few metres to several tens of metres beyond the graphitic halo. More discernable forms of this alteration assemblage occur as discontinuous sulphide rims along the edges of graphite+silicate fragments or encompassing graphite-rich regions of the matrix. Less common and highly localized types of alteration include phlogopite and hematite. Phlogopite alteration (Fig. 8c) is generally restricted to along matrix-clast contacts of fragments that contain a high degree of intragranular graphite mineralization ± sulphide alteration. Hematite alteration is rare and localized to the cores of sericitized feldspar crystals (Fig. 8d).

Supergene alteration is related to the development of the unconformity between the breccias and the overlying Paleozoic carbonate rocks. The supergene zone is highly variable in thickness and rarely extends into the breccias by more than

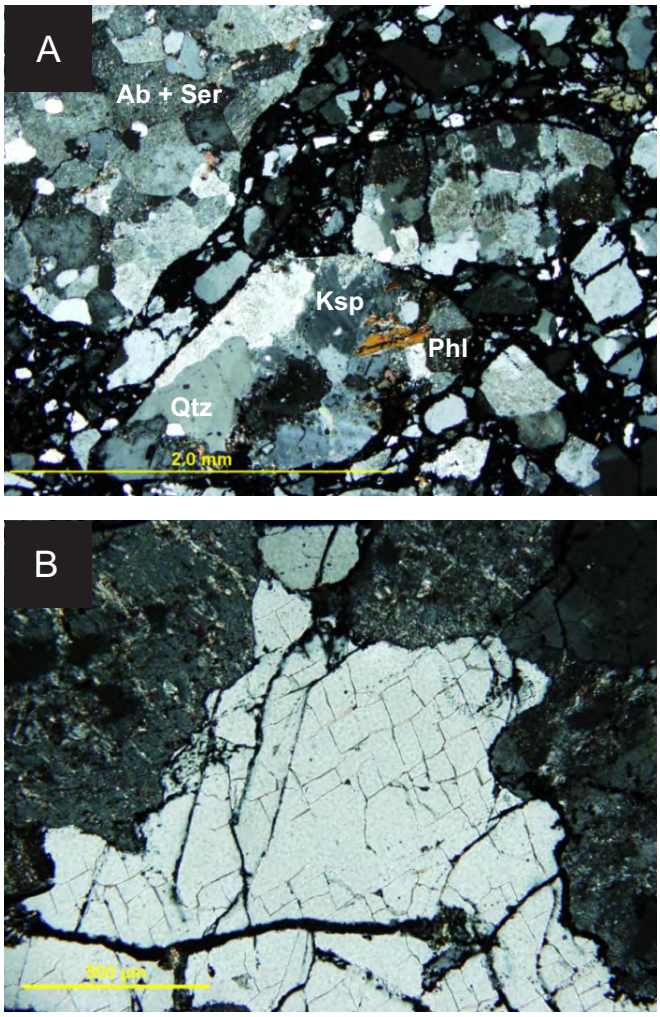

Fig. 6. a) Photomicrograph of the principle breccia mineral assemblage of plagioclase-potassium feldspar (perthitic)-quartz, with rare matrix phlogopite (cross-polarized, transmitted light). **b)** Quartz with well-developed, polygonal fracture pattern (cross-polarized, transmitted light). Mineral abbreviations: Qtz – quartz; Ab – albite; Ksp – potassium (perthitic) feldspar; Ser – sericite (muscovite) alteration; Phl – phlogopite.

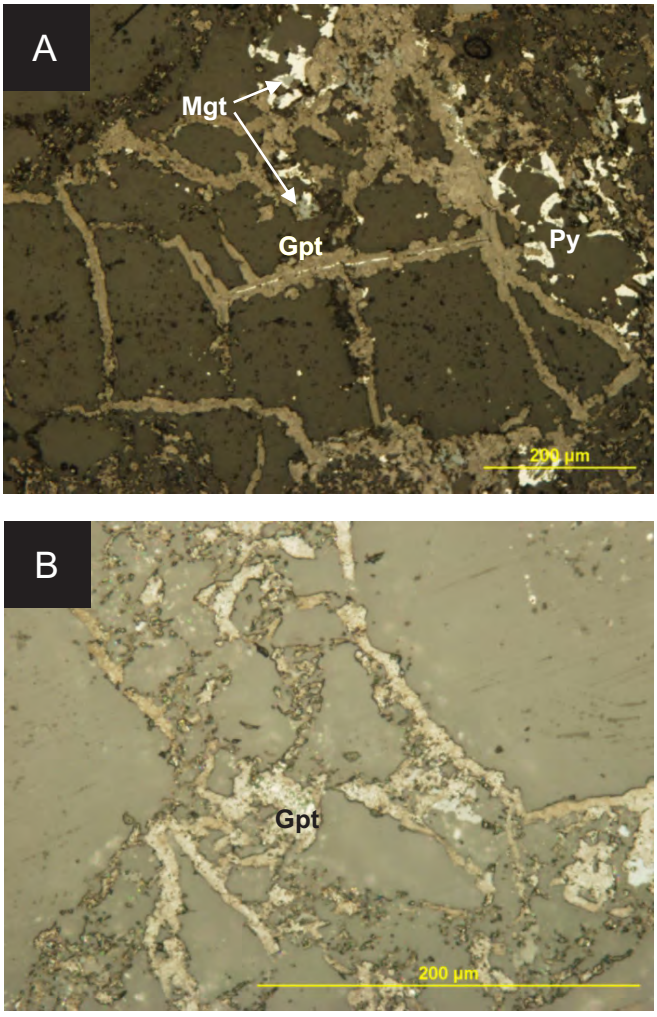

Fig. 7. Reflected light photomicrographs showing the textural differences between **a)** intragranular graphite and **b)** intergranular (matrix) graphite. Mineral abbreviations: Gpt – graphite; Mgt – magnetite; Py – pyrite.

30 m. Supergene alteration is poorly developed within non-brecciated and graphite mineralized Albany complex rocks. The supergene zone is most readily recognized by its hematite overprint and carbonate veining, but is also characterized by weak to pervasive replacement of silicate minerals in the breccias by sericite and chlorite.

4. Graphite characteristics

4.1. Morphology

Intergranular and intragranular graphite in the Albany deposit occurs as elongated lath-shaped aggregates of platy graphite crystals. Crystals and crystal aggregates are up to 300 µm long and 50 µm wide; however, the average size of individual crystals is <100 µm. Crystals are typically randomly orientated, as controlled by the orientation of breccia fragments, silicate crystal boundaries, and veins. There are, however, rare occurrences of well-foliated massive graphite in the breccias.

4.2. X-ray and Raman characteristics

X-ray diffraction of high purity concentrates (>99.9% C_g) of Albany graphite show that the graphite mineralization consists almost exclusively of hexagonal graphite (also called graphite alpha; Fig. 9a). Identification the hexagonal form is based on the position and symmetry of the peaks for (002) and (004) (planar) lattice planes. The *d*-spacing of the (002) plane of Albany graphite is 3.360 Å, with unit cell dimensions of a = 2.459 Å and c = 6.672 Å; consistent with highly ordered hexagonal graphite. The symmetry of the planar x-ray peaks and absence of discrete peaks for (101) and (012) prismatic lattice planes of rhombohedral graphite (also called graphite beta) at ~43.4 and ~46.3°2θ, respectively, indicates that Albany graphite lacks a rhombohedral phase. However, Albany graphite is characterized by a broad peak between 42.5 and 46.5°2θ, which overlaps with key prismatic peaks for hexagonal and rhombohedral forms of graphite (Fig. 9b). The peak characteristics observed for Albany graphite over this angular range are consistent with the development

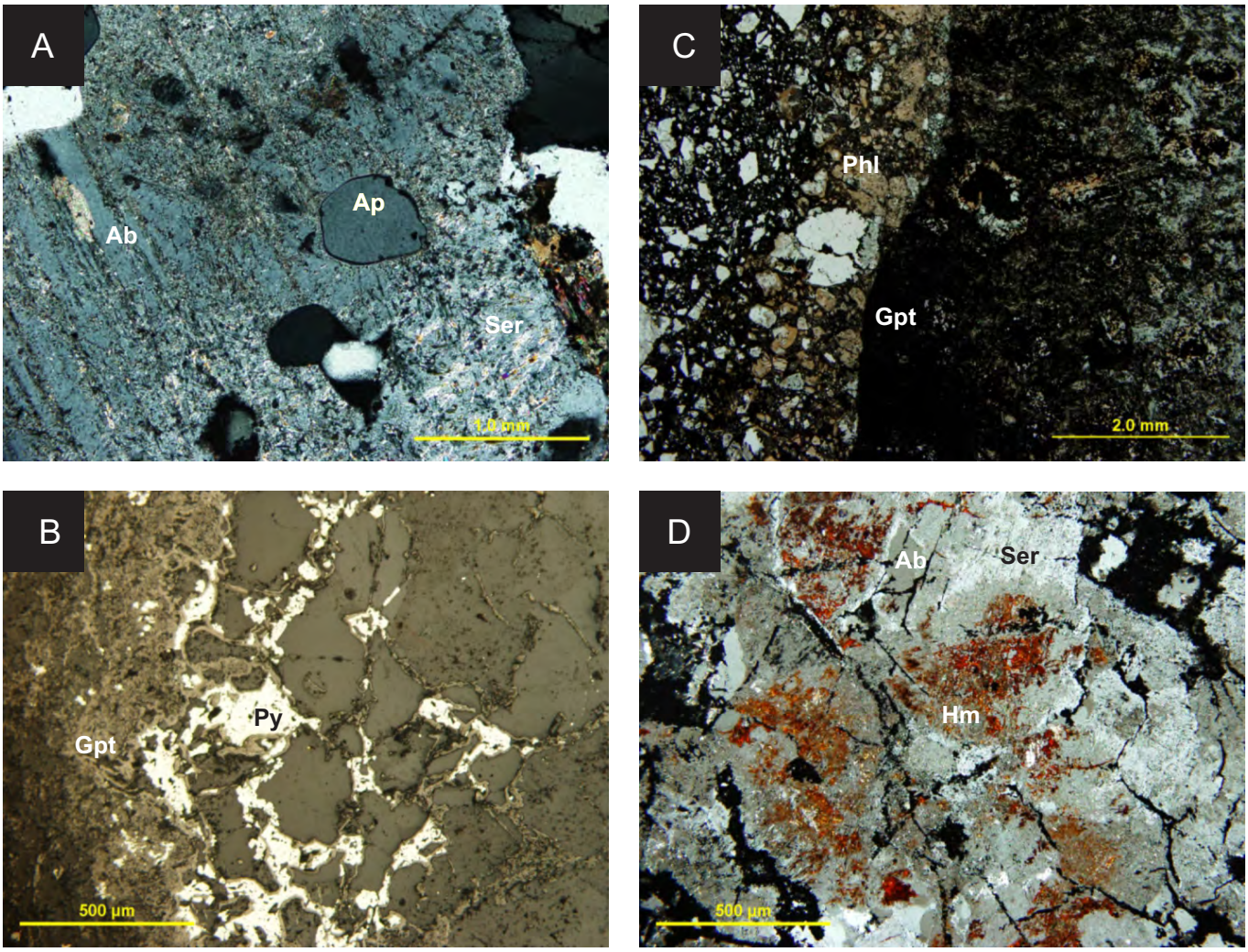

Fig. 8. Photomicrographs of the most common alteration types. **a)** Sericitization of plagioclase (cross-polarized, transmitted light). **b)** Pyrite, with graphite, forming along crystal contacts within a brecciate AAC fragment along the contact with matrix graphite (reflected light). **c)** Phlogopite rimming a graphitized Albany complex fragment (cross-polarized, transmitted light). **d)** Hematite alteration in the cores of plagioclase crystals. Mineral abbreviations: Ab – albite; Ap – apatite; Gpt – graphite; Hem – hematite; Ser – sericite (muscovite); Phl – phlogopite; Py – pyrite.

of turbostratic graphite. Similar to rhombohedral graphite, turbostratic graphite is a conversion of hexagonal graphite by mechanical modification, and results in random structural changes that may include rotation, translation, curvature and variation of interlayer spacing of graphene layers (e.g., Li et al., 2007). However, determining the specific structural changes associated with turbostratic development is not easily accomplished by XRD analysis.

Raman spectrum of graphite is composed of first-order (1100–1800 cm^{-1}) and second-order (2500–3100 cm^{-1}) regions (Tuinstra & Koenig, 1970; Nemanich & Solin, 1979). In the first-order region (Fig. 10a), the graphite band (G band) occurs at ~1580 cm^{-1} and corresponds to in-plane vibration of carbons in the graphitic structure. Bands occurring at 1350 cm^{-1} (D1 band) and 1620 cm^{-1} band (D2 band) correspond to defects in the graphitic structure and occur in poorly ordered graphite. As intensity and broadening of the D1 and D2 bands increase, the degree of ordering of the graphite crystal structure decreases. The degree of ordering can be assessed from the D1/G peak intensity ratio and D1/(D1+G+D2) peak area ratio. However, crystals must be selected with caution, as the Raman effect is dependent on crystal orientation and crystal size. For graphite, accurate Raman analyses must be performed on crystals that are orientated perpendicular to the crystallographic c-axis. Whereas loose powders can be preferentially orientated, in situ measurements from thin sections are more challenging. The D1/G ratio of Albany graphite measured in situ does vary greatly due to variances in crystal orientation. However, euhedral, hexagonal crystals with a high reflectivity are near to the ideal orientation, and yield a minimum D1/G ratio and a D1/(D1+G+D2) peak area ratio of 0.095 and 0.135, respectively, for Albany graphite. The Raman results for Albany graphite are comparable to synthetic, lithium-ion-grade graphite (D1/G = 0.102 ratio and D1/(D1+G+D2) = 0.193), and indicate a well-ordered crystal structure (Fig. 10b). The low intensity and wide band at 1500 cm^{-1} (D3 band) is also observed in some Raman

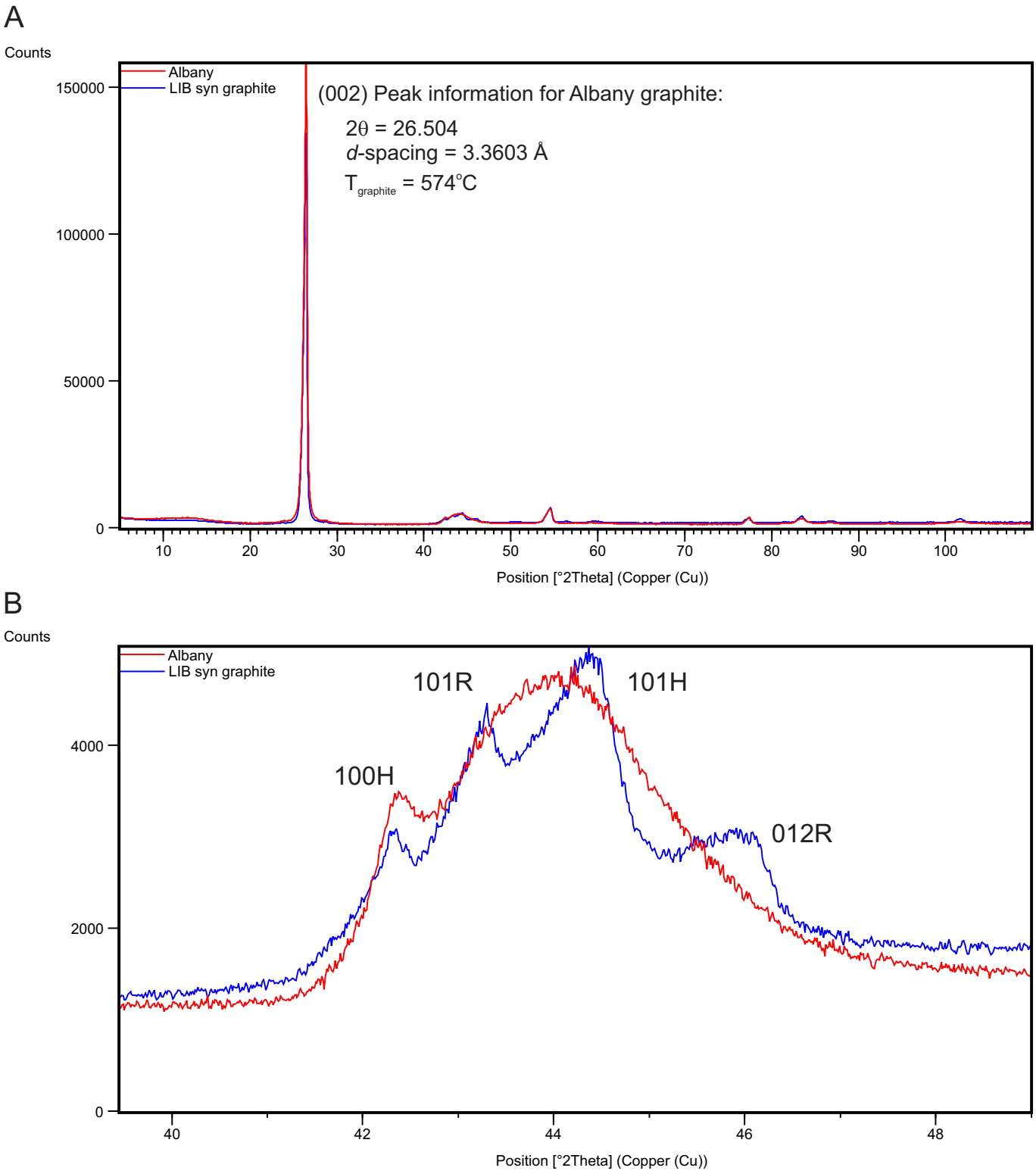

Fig. 9. X-ray diffraction patterns for Albany graphite concentrate (red) and synthetic, lithium-ion battery-grade graphite (blue). **a)** XRD patterns for the full scan range from 5 to 115º2θ. **b)** XRD patterns from the range between 40 and 48º2θ illustrating the difference in XRD profiles for turbostatic graphite (Albany) and rhombohedral graphite (synthetic graphite). Miller indices for key peaks are: H, hexagonal graphite, and R, rhombohedral graphite.

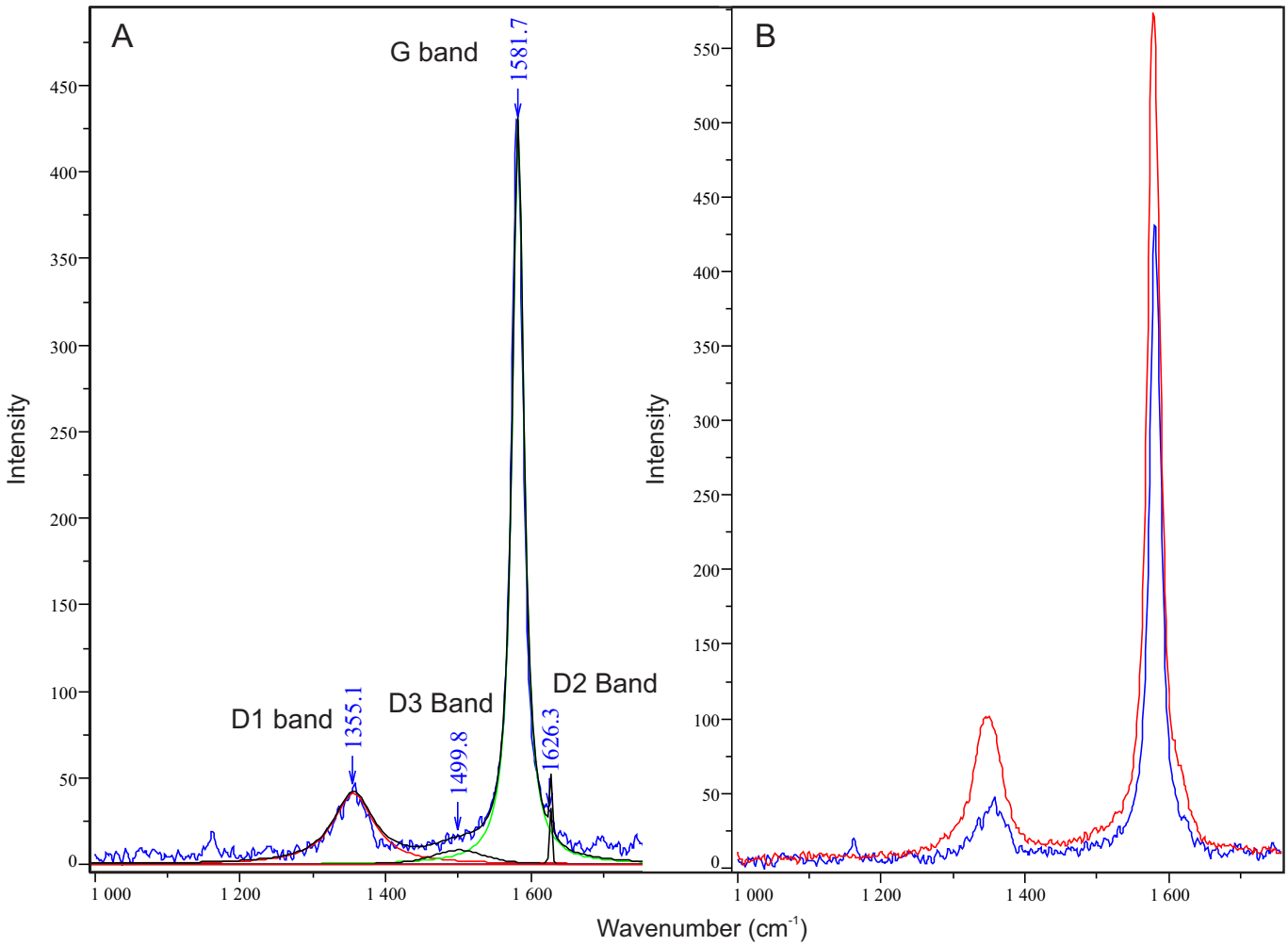

Fig. 10. a) Raman spectrum (first-order region) of an individual Albany graphite crystal aggregate aligned perpendicular to the crystallographic c-axis, yielding a D1/G peak intensity ratio of 0.95 and a Di/(D1+G+D2) peak area ratio of 0.135, corresponding to a temperature of crystallization of 581°C. **b)** Comparison of Raman spectra of Albany graphite (blue, same spectrum as in a) and synthetic, lithium-ion battery-grade graphite (red). The synthetic graphite samples yields a D1/G peak intensity of 0.102 and a Di/(D1+G+D2) peak area ratio of 0.193.

spectra of Albany graphite. The occurrence of the D3 band may reflect a poorly ordered form of carbon or it can be attributed to small crystallite sizes. This band is generally absent in graphite that has crystallized or undergone temperatures in excess of 400 to 450°C (Beyssac et al., 2002), and for this reason we attribute the manifestation of the D3 band in some Albany samples to small crystallite sizes (Nemanich and Solin, 1979).

The temperature of graphite crystallization can be estimated using XRD and Raman spectroscopy geothermometers. The graphite geothermometer of Shengelia et al. (1979) bases temperature estimates on the *d*-spacing of the (002) lattice plane. XRD-determined temperatures of high-purity Albany concentrate indicate an average crystallization temperature of 574°C. Unlike XRD, Raman spectroscopic methods have the advantage of being able to make in situ temperature estimates on individual crystals and crystal aggregates. The Raman geothermometer of Beyssac et al. (2002) uses the ratio of the peak area for first-order D and G bands to estimate crystallization temperature. Raman geothermometry of Albany samples yields a maximum crystallization temperature of 581°C. The temperature determinations are in good agreement with each other, and are within the ±20 to 50°C error for both geothermometers.

4.3. Carbon isotopic composition

Stable carbon isotope compositions for two high-purity concentrates from the East pipe are -16.9 and -16.8‰ (unpublished data). The $\delta^{13}C$ ratio of Albany graphite is intermediate between isotopically enriched sources, including mantle carbon ($\delta^{13}C \approx$ -7‰) and marine carbonates ($\delta^{13}C$ = 0 ± 2‰), and isotopically depleted organic matter ($\delta^{13}C$ = -40 to -6‰, average $\delta^{13}C$ = -25‰).

5. Genetic considerations

We interpret that the Albany graphite deposit is a rare example of crystalline graphite that formed in a shallow subvolcanic environment. Although the Albany deposit shares genetic attributes with other igneous-hosted, fluid-derived

deposits (e.g., Borrowdale, UK; Ortega et al., 2010), we consider that Albany represents a new-end member of igneous-hosted fluid-derived graphite. To the best of our knowledge the graphite-bearing conical breccia pipes are a unique attribute. We interpret the deposit to have formed during brecciation that was induced by the ascent of carbon-rich fluids that separated from alkalic magmas at depth.

5.1. Origin of the carbon and graphite precipitation mechanisms

Possible carbon sources include: 1) carbon-rich volatiles released from coeval magmas; 2) devolatilzation of carbonaceous country rock; and 3) assimilation of carbonaceous country rock. The carbon isotopic ratio of Albany graphite could readily be explained by binary mixing of a carbonaceous fluid phase that segregated from a mantle-derived melt and carbon-derived from metasedimentary country rock (such has been described from, for example, New Hampshire; Ruby Range, Montana; Black Hills, South Dakota; Huelma, Spain; Borrowdale, UK; see Luque et al., 2012, and references therein). However, Quetico sub-province rocks are relatively carbon-poor (P. Fralick, per. comm., 2014) and are, therefore, unlikely to have provided sufficient carbon.

We postulate that graphite precipitated from an orthomagmatic carbon-rich (CO_2-CH_4-H_2O ± H_2S) fluid in response to near surface magma degassing. The specific carbon species composition of the mineralizing fluid is unknown, as suitable fluid inclusions have not been identified. Nonetheless possible graphite forming reactions can be postulated using mineralogical constraints and the carbon isotope composition of Albany graphite. Direct precipitation of graphite from a CO_2-bearing orthomagmatic fluid ($CO_2 \rightarrow C + O_2$) is unlikely because reduction of CO_2 by the co-precipitation of a Fe^{3+}-bearing phase is necessary. Although magnetite co-exists with graphite, the quantity of magnetite (trace to 2 modal%) is likely insufficient to drive the required changes in the f_{O2} of the fluid to induce graphite precipitation directly from CO_2.

An alternative reaction for graphite precipitation from a fluid that is initially CO_2-bearing is:

$$CO_2 + 2H_2 \rightarrow C + 2H_2O$$

We favour that the initial fluid was CO_2-rich, in contrast to a CH_4-rich fluid, as the former species occurs in much greater pre-eruptive concentrations over a range of magma compositions (e.g., Wallace et al., 2002). The above reaction can be re-expressed as a Fischer-Tropsch reaction (e.g., Salvi and Williams-Jones, 1997) where:

$$CO_2 + 4H_2 \rightarrow CH_4 + 2H_2O$$

With the subsequent precipitation of graphite by:

$$CO_2 + CH_4 \rightarrow 2C + 2H_2O$$

or

$$CH_4 + O_2 \rightarrow C + 2H_2O$$

Fischer-Tropsch synthesis results in the precipitation of graphite with a $\delta^{13}C$ = -16.9‰, which is identical to the composition of Albany graphite concentrates, by equilibrium fractionation at 574°C (= XRD determined maximum temperature), assuming an initial $\delta^{13}C_{CO2}$ of -7.5‰ (= mantle) and $\Delta^{13}C_{CO2\text{-}CH4}$ = 13.2‰, $\Delta^{13}C_{graphite\text{-}CH4}$ = 3.4‰ and $\Delta^{13}C_{CO2\text{-}C}$ = 9.4‰ (Bottinga, 1969).

5.2. Role of hypabyssal (subvolanic magmas)

As indicated in the above reactions, Fischer-Tropsch synthesis of graphite-forming hydrocarbons requires the addition of H_2 to ultimately generate graphite. Hydrogen can be derived through various wall-rock alteration reactions involving a precursor hydrous mineral phase (e.g., Salvi and Williams-Jones, 1997). However, interaction between an orthomagmatic fluid and Albany rocks is unlikely to have generated sufficient quantities of H_2, owing to the main plagioclase-potassium feldspar-quartz assemblage and lack of metasomatic reactions involving precursor hydrogen-bearing phases (mica, amphibole). Conly and Moore (2015) proposed H_2 generation at Albany in response to hydrous crystallization (e.g., Beard et al., 2005) associated with magmaclast paragenesis of the hypabyssal, subvolcanic monzonite, via the following reactions:

Hydrous monzonite melt + Diopside + Fe-Ti oxides + Ca-plagioclase →
Hastingsite + Albite + $Melt_{(groundmass)}$ + F-bearing fluid

With subsequent replacement of hastingsite by phlogopite:

Hastingsite + F-bearing fluid →
Phlogopite + Apatite + Quartz + $Fe^{3+}_{(aq)}$ + $Na^{+}_{(aq)}$ + H_2O

And H_2 produced via:

$$Fe^{3+}_{(aq)} + H_2O \rightarrow Fe(OH)_2^{+} + H_2$$

The last two reactions also provide the fluid constituents necessary for the alteration types (sericite and hematite) observed in the graphitic breccias.

5.3. Genetic model

We propose a four-stage genetic model for the Albany deposit. The first stage corresponds to pre- and syn-mineralization events necessary to form the host rocks and generate the carbon-rich fluids from which graphite precipitated. The second and third stages include the development of the breccia pipes, segregation of a carbon-rich fluid from ascending hypabyssal magmas, and the eventual precipitation of graphite. The final stage details post-ore events.

5.3.1. Stage 1: pre- to syn-mineralization magmatic events

Emplacement of the Albany breccia pipes is estimated to be Mesoproterozoic to Neoproterozic, based on cross-cutting

relationships with the Paleoproterozoic Matachewan (Hearst) and Kapuskasing dike swarms (Fig. 2).

Emplacement of the hypabyssal monzodiorite and, possibly, the NRAC may have coincided with graphite formation. Our preliminary strontium isotope results show that present-day $^{87}Sr/^{86}Sr$ ratios for the hypabyssal monzodiorite (0.71497-0.730232) and Nagagami River complex (0.730509-0.733026) are significantly less radiogenic then the Albany complex (0.740247-0.819211). The similarity in $^{87}Sr/^{86}Sr$ ratios for the hypabyssal monzodiorite and Nagagami River complex indicate that these two may be petrogenetically related. A mantle origin is plausible considering the depleted strontium isotope composition relative to other igneous units associated with the deposit.

5.3.2. Stage 2: orthomagmatic fluid generation and breccia pipe development

Degassing of the postulated hypabyssal magma and subsequent segregation of a CO_2-bearing fluid was in response to the depressurization of the ascending magma at mid- to shallow-crustal levels, wherein CO_2 accumulated at the top of the ascending hypabyssal monzodiorite dike. Continued ascent to shallower crustal levels may have resulted in continued fracturing of the country rock and production breccia, due to decreasing overburden pressure. The co-existence of angular and rounded breccia fragments is evidence of mixing of juvenile fragments and records different amounts of mechanical abrasion.

5.3.3. Stage 3: graphite deposition

Pressure and temperature changes associated with dike accent during Stage 2 would have been insufficient to induce graphite mineralization or crystallization of the hypabyssal magma (i.e., supercritical CO_2 fluid and above liquidus temperature would have persisted). Consequently, graphite deposition is restricted to shallower crustal levels and occurred in response to decreases in pressure and temperature. We propose that graphite deposition occurred rapidly due to sudden depressurization and quenching (from supercritical to gas) of the CO_2-fluid in response to the dike head breaking the surface and venting CO_2 gas. The fine crystal size of Albany graphite and high abundances of discrete crystals and fine crystal aggregates are consistent with rapid changes in pressure-temperature conditions, which would have inhibited growth of coarser-crystalline graphite. We estimate formation within two kilometres of the paleosurface. The graphite mineralization is known to currently extend below 500 m, and underlie the two large barren sill complexes beneath the deposit (Fig. 4). The sudden pressure and temperature change would have also induced hydrous crystallization of the hypabyssal monzodiorite magma, resulting in H_2 gas generation necessary for Fischer-Tropsch synthesis. The aphanitic component of the mozondiorite is additional evidence for rapid cooling in the pipes.

5.3.4. Stage 4: post-mineralization magmatic and erosional events

Post-mineralization events include: 1) emplacement of late-stage augite-aegirine syenite; 2) intrusion of aplite and other felsic dikes; 3) erosion of upper levels of the AAC complex and supergene alteration; and 4) deposition of Paleozoic carbonate rocks and Quaternary glacial sediments.

6. Conclusions

The Albany deposit is a unique type of igneous-hosted, fluid-derived graphite mineralization. Igneous-hosted deposits are rare, as these environments do not usually provide suitable conditions for the formation of sizable deposits. The defining characteristic of the Albany deposit is the occurrence of crystalline, fine-grained graphite within two large breccia pipes. The formation of the Albany deposit required an unusual combination of geological factors, including: 1) intrusion of CO_2-rich hypabyssal monzondiorite magmas, of possible mantle origin; 2) generation of a CO_2-CH_4 orthomagmatic fluid by Fischer-Tropsch synthesis; 3) development of two vent breccia pipes due to turbulent ascent of a gas-rich orthomagmatic fluid; and 4) precipitation of graphite in response to the sudden depressurization and quenching of the orthomagmatic fluid. The rapid precipitation of graphite at temperatures up to 581°C generated fine grained, but highly crystalline graphite, with comparable crystallographic properties to synthetic graphite used in the manufacturing of lithium-ion batteries.

Acknowledgments

This study is a collaboration between Lakehead University and Zenyatta Ventures Ltd., and is funded by the Natural Sciences and Engineering Research Council of Canada (grant number CRDPJ 458909-13).

References cited

Beard, J.S., Ragland, P.C., and Crawford, M.L., 2005. Using incongruent equilibrium hydration reactions to model latter-stage crystallization in plutons: Examples from the Bell Island Tonalite, Alaska. Journal of Geology, 113, 589–599.

Beyssac, O., Goffe, B., Chopin, C., and Rouzaud, J.N., 2002. Raman spectra of carbonaceous material in metasediments: a new geothermometer Journal of Metamorphic Geology, 20, 859–871.

Bottinga, Y., 1969. Calculated fractionation factors for carbon and hydrogen isotope exchange in the system calcite-carbon dioxide-graphite-methane-hydrogen-water vapor. Geochimica et Cosmochimica Acta, 33, 49-64.

Conly, A.G., and Moore, L.C., 2015. Role of hypabyssal subvolcanic magmas in the genesis of the Albany graphite deposit: Joint Assembly (GAC-MAC-AGU) 2015 Program with Abstracts, Abstract number MD34A-0201 (web accessed May 25, 2015).

Heaman, L.M., 1988. A precise U-Pb zircon age for a Hearst dike. In Program with Abstracts, Annual Meeting Geological Association of Canada-Mineralogical Association of Canada, 13, A53.

Johnson, M.D, Armstong, D.K., Sandord, B.V., Telford, P.G. and Rutka, M.A., 1991. Paleozoic and Mesozoic Geology of Ontario. In Geology of Ontario, Ontario Geological Survey, Special Volume 4, Part 1, pp. 383-403.

Kennedy, M.C., 1984. The Quetico Fault in the Superior Province of the southern Canadian shield. Unpublished MSc thesis, Lakehead

University, Thunder Bay, Ontario, 300p.
Legault, J.M., Lymburner, J., Ralph, K., Wood, P., Orta, M. and Prikhodko, A., 2015. The Albany graphite discovery airborne and ground time-domain EM. KEGS Geophysics Symposium, Society of Economic Geophysicists Technical Program Expanded Abstracts 2015, pp. 2056-2060.
Li, Z.Q., Lu, C.J., Xia, Z.P., Zhou,Y., and Luo, Z., 2007. X-ray diffraction patterns of graphite and turbostratic carbon. Carbon, 45, 1686–1695.
Luque, F.J., Crespo-Feo, E., Barrenechea, J.F., and Ortega, L., 2012. Carbon isotopes of graphite: Implications on fluid history. Geoscience Frontiers, 3, 197-207.
Luque, F.J., Huizenga, J-M., Crespo-Feo, E., Wada, H., Ortega, L. and Barrenechea, J. F., 2013. Vein graphite deposits: geological settings, origin, and economic significance. Mineralium Deposita, 49, 261-277.
Nemanich, R.J., and Solin, S.A., 1979. First- and second-order Raman scattering from finite-size crystals of graphite. Physical Review B, 20, 392–401.
Ortega, L., Millward, D., Luque, F.J., Barrenechea, J.F., Beyssac, O., Huizenga, J.M., Rodas, M., and Clarke, S.M., 2010. The graphite deposit at Borrowdale (UK): a catastrophic mineralizing event associated with Ordovician magmatism. Geochimica et Cosmochimica Acta, 74, 2429–2449.
Phinney, W.C., and Morrison, D.A., 1988. Constraints on the environment of Matachewan dike intrusion. Abstract IGCP-257, International Symposium on Mafic Dikes and Related Magmatism, University of Lund, Sweden.
RPA Inc., 2015. Technical Report on the Preliminary economic assessment of the Albany graphite project, northern Ontario, Canada, prepared for Zenyatta Ventures Ltd., filed on SEDAR/ available at www.sedar.com (accessed August 21, 2015).
Sage, R.P., 1988. Geology of carbonatite - alkalic rock complexes in Ontario. Nagagami River Alkalic Rock Complex, District of Cochrane, Ontario Geological Survey, Study #43, 55 p.
Salvi, S., and Williams-Jones, A.E., 1997. Fischer-Tropsch synthesis of hydrocarbons during sub-solidus alteration of the Strange Lake peralkaline granite, Quebec/Labrador, Canada. Geochimica et Cosmochimica Acta, 61, 83-99.
Shengelia, D.M., Akhvlediani, R.A., and Ketskhoveli, D.N., 1979. The graphite geothermometer. Dokl. Acad. Nauk SSSR, 235, 132-134.
Stott, G.M., 2008. Precambrian geology of the Hudson Bay and James Bay lowlands region interpreted from aeromagnetic data – south sheet. Ontario Geological Survey, Preliminary Map P.3599, scale 1:500,000.
Stott, G.M., 2011. A revised terrane subdivision of the Superior Province in Ontario; Ontario Geological Survey, Miscellaneous Release—Data 278.
Tuinstra, F., and Koenig, J. L., 1970. Raman spectrum of graphite. Journal of Chemical Physics, 53, 1126–1130.
Wallace, P.J., Anderson Jr., A.T., Davis, A.M., 2002. Quantification of pre-eruptive exsolved gas contents in silicic magmas. Nature, 377, 612-616.

In-depth study on carbon speciation focussed on graphite

Jamil A. Sader[1, a], John Gravel[1], Louis Janke[2], and Lucia Hall[1]

[1] Bureau Veritas Commodities Canada Ltd., 9050 Shaughnessy Street, Vancouver, BC, V6P 6E5
[2] Quality Associates International Ltd., 6940 Mount Richardson Road, Sechelt, BC, V0N 3A4
[a] corresponding author: jamil.sader@acmelab.com

Recommended citation: Sader, J.A., Gravel, J., Janke, L., and Hall, L., 2015. In-depth study on carbon speciation focussed on graphite. In: Simandl, G.J. and Neetz, M., (Eds.), Symposium on Strategic and Critical Materials Proceedings, November 13-14, 2015, Victoria, British Columbia. British Columbia Ministry of Energy and Mines, British Columbia Geological Survey Paper 2015-3, pp. 187-191.

Summary

Quantifying and qualifying the presence and form of carbon in natural geological materials is essential to assessing value or determining potential harm to the analysis and metallurgical processing of other commodities. Early-stage resource evaluation is hampered by the lack of cost-effective, accurate tests to differentiate carbon forms and by confusion in terminology assigned to these forms.

Our study of carbon species focused on the transition zone between non-graphitic organic carbon and graphite using coal, petroleum coke, and graphite to potentially define a low-cost, accurate method for distinguishing between these forms. X-Ray diffraction (XRD) analysis established the presence of nanoscale graphite in the petroleum coke but only non-graphitic organic carbon in anthracitic coal. Graphite estimation by nitric acid extraction of organic carbon prior to Leco analysis gave correct estimation of graphite in the petroleum coke but erroneously identified graphite in the coal. Leco analysis of reference materials following pyrolysis pre-treatment at different temperatures identified a sweet-spot that minimized false positive and false negative errors in differentiating between organic carbon and graphite. It also identified an acute sensitivity in a narrow temperature range (550°C – 600°C) for the rapid oxidation of nanoscale graphite not observed with the coarser graphite tested. The contrast in oxidation rates between the nanoscale and coarser-crystalline graphite warrants further investigation to ascertain the potential for a robust, inexpensive graphite quality test.

1. Introduction

Carbon in a highly-organized aromatic arrangement as a single sheet (e.g. graphene, nanotubes) or stacked sheets (e.g., graphite) has remarkable properties. Its high electrical conductivity, tensile strength, flexibility and light weight (Geim and Novoselov, 2007) make it a strategic commodity for a growing list of applications including paper-thin Li-ion batteries (Hu et al., 2010). Conversely, carbon in gold ore can cause preg-robbing during hydrometallurgy (Helm et al., 2009) resulting in poor recoveries.

Several analytical methods can be employed to quantify graphite. X-ray diffraction analysis is a well-established method providing quantity and crystallinity (Franklin, 1951). Raman spectroscopy can quantify the degree of bulk graphitization in poor to well-ordered graphitic material (Beyssac et al., 2002a), and transmission electron microscopy (TEM) can provide detailed images of nanoscale graphite structures (Buseck and Huang, 1985). Although these methods provide accurate detailed information, they can be costly and time consuming if not conducted on a commercial lab scale, and may not provide information for non-graphitic organic carbon or inorganic carbon.

Commercial-scale carbon analysis has suffered from confusion in methodology and terminology, as noted by Girard and Klassen (2001), who examined seven published analytical methods. All methods, except for proton balance, use Leco analysis to determine total carbon, inorganic carbon (IC) and organic carbon (OC). Each method employs direct analysis of total carbon (TC) on a sample split. A second sample split is either analyzed directly to determine inorganic carbon or is pre-treated to selectively remove inorganic carbon or organic carbon. The missing component is then determined by difference using one of the following equations.

1) $OC = TC - IC$
2) $IC = TC - OC$

Girard and Klassen (2001) did not differentiate graphite from other carbon species, however they did note that, depending on the pre-treatment used, graphite would report either as organic or inorganic carbon. The transition between non-graphitic organic carbon and well-crystalized graphite is a diffuse zone of poorly to well-organized aromatically structured carbon atoms (Buseck and Beyssac, 2014) related to the degree of metamorphism (Beyssac et al., 2002b). We examined this zone to ascertain if the proportions of non-graphitic organic carbon and graphitized carbon can be accurately and precisely defined with a cost-effective Leco analysis. Carbon species are separated here into two groups: inorganic carbon (IC) comprising inorganic carbon-bearing minerals such as carbonates, and organic carbon (OC) that includes non-graphitized, partially graphitized and completely graphitized material of likely organic origin.

2. Methods

This study examined three carbon test materials comprising a medium-volatile coal from Kuzbass, Russia (Coal 2008-4), a

calcined low-volatile petroleum coke (PC-8), and a ground-up high purity graphite crucible (Graphite) with visible granularity employed in whole rock digestions and analyses and supplied by SCP Science. Both the coal and petroleum coke were analyzed by XRD at the University of British Columbia in Vancouver, British Columbia to determine graphite content. Bureau Veritas Commodities Canada laboratory in Vancouver, British Columbia analyzed all three test materials for total carbon, inorganic carbon, and organic carbon in non-graphitized and graphitized form.

2.1. XRD analysis

The samples were reduced to the optimum grain-size range for quantitative X-ray analysis (<10 μm) by grinding under ethanol in a vibratory McCrone Micronising Mill for 10 minutes. Step-scan X-ray powder-diffraction data were collected over a range 3-80°2θ with CoKα radiation on a Bruker D8 Advance Bragg-Brentano diffractometer equipped with an Fe monochromator foil, 0.6 mm (0.3°) divergence slit, incident- and diffracted beam Soller slits and a LynxEye-XE detector. The long fine-focus Co X-ray tube was operated at 35 kV and 40 mA, using a take-off angle of 6°.

2.2. Carbon species by Leco analysis

All carbon determinations were conducted on a Leco CS-230 carbon-sulphur analyser. In general, 0.1 g of sample material was combusted at 1350°C in the analyser's induction furnace. Evolved carbon was swept up by a flow of oxygen and converted to CO_2 and CO. The gases were passed through an infrared cell where the integration of the amount of infrared (IR) light absorption during sample ignition determined the quantity of total carbon in the sample. Samples reporting >40% carbon were re-analyzed using a 0.03 g sample.

2.2.1. Total carbon analysis

Analysis of total carbon entails directly combusting a 0.1 g (or 0.03 g) sample split without any pre-treatment. All carbon-bearing compounds (inorganic, non-graphitic organic and graphitic) were decomposed thus giving the total carbon content of the sample.

2.2.2. Inorganic carbon analysis

A 0.1 g (or 0.03 g) sample was reacted with perchloric acid in a closed vessel in a warm bath (70°C) for 1 hour to fully evolve CO_2 through decomposition of all carbonates. The CO_2 was swept up by a flow of oxygen into the CS230 analyser where the concentration of carbon was determined by integration of the amount of IR light absorbed.

2.2.3. Graphitic carbon determination by nitric acid leach

A 0.1 g (or 0.03 g) sample was pre-treated by leaching with concentrated nitric acid (HNO_3) at 70°C for 1 hour to oxidize and decompose the non-graphitic organic carbon fraction. The residue was then leached with hydrofluoric acid and 15% HCl to remove inorganic carbon. The residue was washed several times with de-mineralized water to remove all acid, and oven dried. The residue was analyzed by Leco CS230 analyser to determine graphitic carbon.

2.2.4. Graphitic carbon determination by pyrolysis

A 0.1 g sample was pre-treated by igniting at a specific temperature for 1 hour to remove organic carbon. The residue was leached with 15% HCl in filter crucibles at 70°C for 1 hour to remove inorganic carbon present as carbonates. The residue was then washed with de-mineralized water to remove all traces of acid, and oven dried. The residue was analyzed by Leco CS230 analyser to determine carbon present as graphite. Separate tests were conducted at 450°C, 475°C, 500°C, 525°C, 550°C, 575°C and 600°C.

2.3. Calibration and quality control

For all Leco analyses, the apparatus was calibrated using a pure calcium carbonate (calcite) and an analyte blank to establish the baseline. Analyses of the carbon reference materials were conducted on five replicate sample splits to fully evaluate precision. Accuracy was measured by inclusion of Geostats certified reference materials (CRMs) GGC-02 and GGC-06 (natural graphite from Eyre Peninsula, South Australia), and GGC-10 (flake graphite from Halls Creek, Western Australia) that were analyzed in duplicate or triplicate. Precision and accuracy of each test group is reported in the results below. Recommended values for the Geostats CRMs are listed in Table 1.

3. Results

3.1. XRD analysis

XRD analysis of the coal (Coal 2008-4) and petroleum coke (PC-8) carbon test materials are presented in Table 2. Coal 2008-4 contains abundant (95%) amorphous material comprising organic matter and 5% inorganic material consisting of carbonates (dolomite-ankerite, siderite), clay (kaolinite, illite) and quartz. Carbon reference material PC-8 is composed almost entirely of graphite (99.1%) and trace quartz, which is inferred to be a contaminant from the grinding pellets. The graphite in PC-8 is nanoscale (microcrystalline), given the extreme peak broadening.

These results correlate well with the total carbon and inorganic carbon contents reported by Leco analysis (Table 3) and the round-robin coal analyses results reported by Quality Associates International Ltd. for these materials (Table 4).

3.2. Graphitic carbon, nitric acid leach method analysis

The nitric-acid leach method reports high graphitic carbon concentrations for all three test materials. These results are acceptable for PC-8 (95% graphite) and the medium-grained graphite (101% graphite), but a graphite content of 69% reported for Coal 2008-4 is erroneous. Although the graphitic carbon results for Coal 2008-4 are inaccurate, they are nonetheless precise, with an RSD of 1.8% over the five splits tested. This suggests the presence of an organic phase readily attacked by

Table 1. Recommended values for graphite CRMs from Geostats.

Element	Units	Certified Value
GGC-02		
Graphitic Carbon	%	27.04
Total Carbon	%	28.25
Total Sulphur	%	0.04
GGC-08		
Graphitic Carbon	%	7.68
Total Carbon	%	8.16
Total Sulphur	%	0.05
GGC-10		
Graphitic Carbon	%	4.79
Total Carbon	%	5.22
Total Sulphur	%	4.40

Table 2. XRD analysis of carbon reference materials Coal 2008-4 and PC-8.

Mineral	Ideal Formula	Coal 2008-4	PC-8
Quartz	SiO_2	0.7	0.9
Kaolinite	$Al_2Si_2O_5(OH)_4$	1	
Illite	$K_{0.65}Al_{2.0}Al_{0.65}Si_{3.35}O_{10}(OH)_2$	2	
Dolomite-Ankerite	$CaMg(CO_3)_2$-$Ca(Fe^{2+},Mg,Mn)(CO_3)_2$	0.7	
Siderite	$Fe^{2+}CO_3$	0.3	
Amorphous		95	
Graphite	C		99.1
Total		100	100

Table 3. Total carbon and inorganic carbon by Leco analysis for Coal 2008-4 and PC-8.

Carbon Species (Wt%)	Coal 2008-4	PC-8
Total Carbon	84	94
Inorganic Carbon	0.1	0.0

Table 4. Constituents as reported by Quality Associates International for Coal 2008-4 and PC-8.

Constituents (wt%)	Coal 2008-4	PC-8
Carbon	84.71	96.54
Hydrogen	4.09	0.07
Nitrogen	2.22	0.81
Sulphur	0.37	2.70
Ash	4.86	0.13
Moisture	1.76	0.03

the nitric acid leach, and a nitric acid resistant, possibly poorly graphitized carbon phase. No further work was conducted using this method. However, follow-up work is warranted to determine if increasing the leaching time or temperature would improve the attack on the resistant carbon phase.

3.3. Carbon by pyrolysis

The Coal 2008-4, PC-8 and Graphite test materials define distinctly different trends (Fig. 1) in the reported graphite content following ignition pre-treatment at temperatures between at 450°C to 600°C. For Coal 2008-4, pyrolysis pre-treatment at 450°C was insufficient to remove all of the non-graphitic organic carbon, resulting in a significant residual amount of carbon (28%) reported as graphite. Successively higher temperatures removed more carbon; at 550°C essentially all the carbon was driven off leaving only a trace (0.3%) reported as graphite. The very short whiskers attest to good agreement between the five splits at each temperature. Precision was good, with RSD ranging from 2.9% at 450°C to 10.6% at 550°C where carbon concentrations were very low (15 times above the detection limit).

The nanoscale graphite in PC-8 remained relatively untouched by the ignition pre-treatment at temperatures up to 500°C, with 100% carbon reported. Minor graphite loss (4%) started to occur at 525°C. The loss accelerated with 10% loss at 550°C, 47% loss at 575°C and essentially complete destruction (97% loss) of the nanoscale graphite at 600°C. Variability between the five splits was low (RSD of 0.4% to 0.7%) from 450°C to 500°C, confirming stability in this temperature range. Variability increased in conjunction with carbon loss as seen by an RSD of 16.1% at 575°C.

The graphite test material was stable in the temperature range of 450°C to 575°C with 100% carbon reported. However, at a pre-treatment ignition temperature of 600°C, oxidation of the graphite resulted in a 15% loss of carbon. The loss is uniform among the five splits, with an RSD of 1.1%.

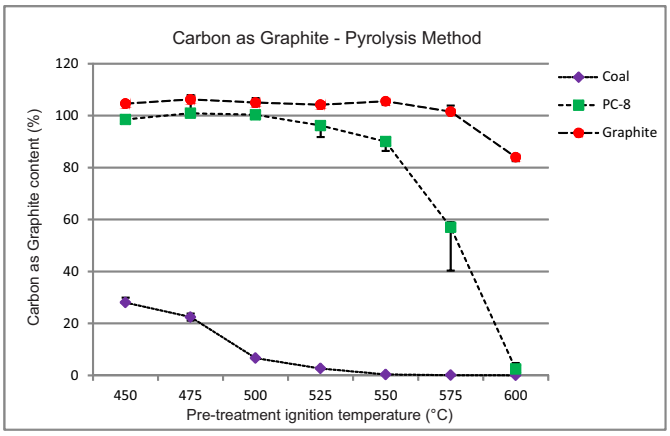

Fig. 1. Dot and whisker plot for carbon as graphite determined by pyrolysis pre-treatment followed by Leco analysis for three test materials (Coal 2008-4, PC-8 and Graphite). Dot and whiskers represent maximum value, median and minimum value of five splits analyzed for each ignition temperature.

Both GGC-06 and GGC-10 reported stable concentrations across the full temperature range (Fig. 2) coincident with their recommended values (RV). However, GGC-02 demonstrated successive losses across the entire temperature range, with accelerated loss at 575°C accompanied by greater variation among the triplicate splits.

4. Discussion

The pyrolysis method for identifying graphite in samples with mixed carbon species can minimize cases where graphite is falsely identified (false positive) and cases where graphite is present but undetected (false negative). Based on the test materials, this method appears to segregate non-graphitic organic carbon from graphite carbon. Pre-treatment by igniting the samples at a temperature between 500°C to 525°C minimizes both false negatives and false positives by preserving nanoscale and coarser graphite while driving off nearly all of the non-graphitic organic carbon. Kouketsu et al. (2014) conducted Raman analyses of carbonaceous materials to develop a geothermometer based on the degree of 'graphitization'. Temperatures from 280°C to 650°C coincide with the transition from amorphous (non-graphitized) carbon to well-crystallized graphite. The persistence of carbon in Coal 2008-4 from 450°C to 525°C may relate to graphitization that, while insufficiently crystalline to be detected by XRD, increases resistance to combustion.

The behaviour of the nanoscale graphite in PC-8 relative to the coarser-grained Graphite test material between 550°C to 600°C indicates a rate of loss that is material dependent wherein the oxidation rate may be related to crystal size and shape. The high variability between sample splits of PC-8 at 575°C indicates acute sensitivity to boundary layer conditions in the ignition crucible, possibly caused by variable oxygen availability to convert graphite to CO_2, as has been observed in experiments by Xiaowei et al. (2004), and in work by Chi and Kim (2008) and Contescu, et al. (2008). Conversely, although the Graphite test material incurred 15% loss at 600°C, the oxidation rate was low enough to avoid fully consuming oxygen in the crucible micro-environment, thus giving a uniform loss among the five sample splits.

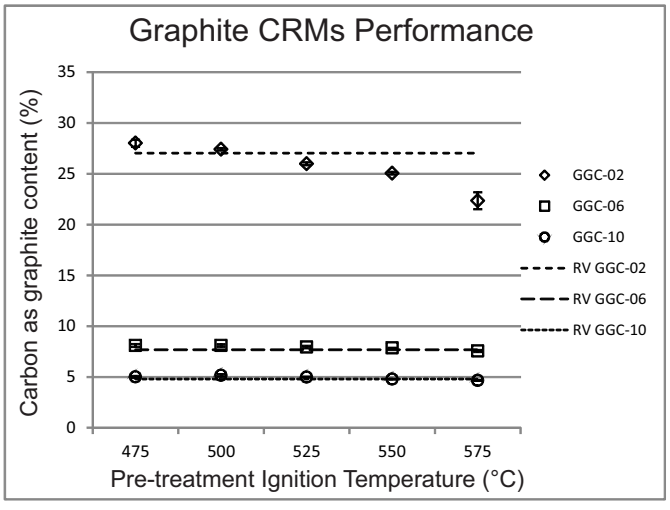

Fig. 2. Box and whisker plot for carbon as graphite by Leco analysis for Geostat CRMs. Box and whiskers represent minimum value, average and maximum value for 2 or 3 splits analyzed at each ignition temperature. Dashed lines represent recommended value (RV) for each CRM.

Behaviour of the Geostat CRMs to pre-treatment ignition temperatures may provide insight to the nature of the graphite in each CRM. GGC-06 and GGC-10 remain stable across the 475°C-575°C temperature range, much like the Graphite test material. However, GGC-02 demonstrated loss across the temperature range, with accelerated loss at 575°C much like the nanoscale graphite in PC-8. This loss suggests that GGC-02 may include a component of nanoscale graphite. The differences in behaviour between the CRMs may also be related to the presence or absence of imputities. Chi and Kim (2008) reported that cokes from different sources (pitch versus petroleum) contrasted in oxidation rates and that impurities likely have a significant influence on those rates.

5. Conclusions

Pyrolysis pre-treatment of samples at an ignition temperature between 500 and 525°C minimizes false positive and false negative errors in distinguishing between non-graphitic organic carbon and graphite. However, follow-up work is needed to define the effect of time in isothermic tests to determine if further improvement is achievable. The nature of the graphite may control the oxidation rate at different temperatures, as shown by the contrast between the nanoscale graphite in petroleum coke and the coarser grained graphite derived from the high purity graphite crucibles. Therefore, further work is also required to determine if graphite quality (crystallinity, particle size) can be quantified by quick and inexpensive Leco tests using pyrolysis pre-treatment at set temperatures and modeled against known reference materials.

References cited

Beyssac, O., Goffe, G., Chopin, C., Rouzaud, J., 2002a. Raman spectra of carbonaceous material in metasediments: a new geothermometer. Journal of Metamorphic Geology, 20, 859-871.

Beyssac, O., Rouzaud, J., Goffe, G., Brunet, F., Chopin, C., 2002b. Graphitization in a high-pressure, low-temperature metamorphic gradient: a Raman microspectroscopy and HRTEM study. Contributions to Mineral Petrology, 143, 19-31.

Buseck, P.R., and Beyssac, O., 2014. Organic Matter to Graphite: Graphitization. Elements, 10, 421-426.

Buseck, P.R., and Huang, B.-J., 1985. Conversion of carbonaceous material to graphite during metamorphism. Geochemica et Cosmochimica Acta, 49, 2003-2016.

Chi, S.H., and Kim, G.C., 2008. Comparison of the oxidation rate and degree of graphitization of selected IG and NBG nuclear graphite grades. Journal of Nuclear Materials, 381, 9-14.

Contescu, C.I., Azad, S., Miller, D., Lance, M.J., Baker, F.S., and Burchell, T.D., 2008. Practical aspect for characterizing air oxidation of graphite. Journal of Nuclear Materials, 381, 15-24.

Franklin, R.E., 1951. Crystallite growth in graphitizing and non-graphitizing carbons. Proceedings of the Royal Society of London, Series A, 209, pp. 196-218.

Geim, A.K., and Novoselov, K.S., 2007. The rise of graphene. Nature Materials, 6, 183-191.
Girard, I., and Klassen, R.A., 2001. A comparison of seven methods or analysis of carbon in soils. Geological Survey of Canada, Current Research 2001-E11, 9p.
Helm, M., Vaughan, J., Staunton, W.P., and Avraamides, J., 2009. An investigation of the carbonaceous component of preg-robbing gold ores. Proceedings of World Gold Conference 2009, The Southern African Institute of Mining and Metallurgy, pp. 139-144.
Hu, L., Wu, H., La Mantia, F., Yang, Y., and Cui, Y., 2010. Thin, Flexible Secondary Li-Ion Paper Batteries. ACS Nano, 4, 5843–5848.
Kouketsu, Y., Mizukami, T., Mori, H., Endo, S., Aoya, M., Hara, H., Nakamura, D., and Wallis, S., 2014. A new approach to develop the Raman carbonaceous material geothermometer for low-grade metamorphism using peak width, Island Arc, 23, 33-50.
Xiaowei, L., Jean-Charles, R., and Suyuan, Y., 2004. Effect of temperature on graphite oxidation behaviour. Nuclear Engineering and Design, 227, 273-280.

Exploration geochemistry: Principles and practices for the strategic commodities Nb, Ta, Zr, and rare earth elements

Peter Winterburn[1, a]

[1] Mineral Deposit Research Unit, Department of Earth, Ocean and Atmospheric Sciences, University of British Columbia, Vancouver, BC, V6T 1Z4

[a] corresponding author: pwinterburn@eos.ubc.ca

Recommended citation: Winterburn, P., 2015. Exploration geochemistry: Principles and practices for strategic commodities Nb, Ta, Zr, and rare earth elements. In: Simandl, G.J. and Neetz, M., (Eds.), Symposium on Strategic and Critical Materials Proceedings, November 13-14, 2015, Victoria, British Columbia. British Columbia Ministry of Energy and Mines, British Columbia Geological Survey Paper 2015-3, pp. 193-197.

1. Introduction: Challenges and opportunities

Geochemical exploration for Nb, Ta, Zr and rare earth element (REE) mineralization associated with carbonatite, pegmatite, and peralkaline intrusions presents unique challenges and opportunities. The challenges are mainly due to the tendency of these elements, as High Field Strength Elements (HFSE), to be relatively immobile in surface environments in addition to commonly forming minerals that are resistant to weathering. In addition, many of the host minerals are resistant to routine exploration geochemistry digestions, which are typically aimed at dissolving soluble oxides or extracting more labile ionic forms (Reimann et al., 2014).

Opportunities arise because host rocks typically represent relatively rare end products of the magmatic processes that generate peralkaline magmas including, at the far end of the spectrum, carbonatites. Hence host rocks are relatively easy to identify geochemically and commonly define classic lithological zoning (e.g., Modreski et al., 1995). In addition, many of the minerals that contain these elements are resistant to weathering, mechanically durable, have relatively high densities, and have the have the potential to form heavy mineral concentrates when released by weathering. This is particularly so for Zr, Nb, and Ta, which form primary minerals such as tantalite (Ta Nb), pyrochlore (Nb), coltan (Ta Nb), columbianite (Ta Nb), dysanalite-perovskite (Nb) and zircon (Zr). In contrast, the REE are mobile in the weathering environment and commonly re-locate from primary carbonate and phosphate minerals (e.g., synchysite, monazite, xenotime, bastnäsite, allanite) to secondary phosphate minerals such as churchite (Lottermoser, 1990) and gorceixite (Mariano, 1989).

2. Sample media

Depending on the phase and scale of exploration, diverse materials can be sampled to search for Ta, Nb, Zr, and REE. These include soils, tills, stream sediments, lake sediments, vegetation, and rock samples (Ryghaug, 1983; McConnell and Batterson, 1987; Moller et al., 1989; Galeschuk and Vanstone, 2007). Indirect detection of potential host rocks for further evaluation using host rock rather than mineralization chemistry (for example P, Ba, Zn, Be, U) should always be considered as an exploration tool, such as at Allan Lake (Ford et al., 1988).

Soils concentrate elements in amounts reflecting the resistance to weathering of individual minerals. Unless soil materials get transported physically or chemically, these elements will concentrate directly above a mineral deposit, and a broad halo is unlikely. Hence sampling design needs to consider the likely size of a target and recognize that regional-scale soil sampling densities may not directly locate mineralization.

In glaciated terrains, deposits may be buried by till. Nonetheless, evidence of mineralization may be preserved for many kilometres down the former ice-flow direction as dispersal trains comprising sediments eroded from a deposit. Geochemical sampling of soil, till, and till-derived lake and stream sediments may identify the transport paths of the commodities of interest and of ancillary pathfinder elements. Such responses have been documented at the Strange Lake deposit, Labrador (McConnell and Batterson, 1987; Batterson, 1989, McClenaghan et al., 2007), where a dispersal train in a variety of media exceeds 40 km as a narrow 4-5 km wide ribbon, and at the Allan Lake carbonatite, Ontario (Ford et al 1988)

Because of the low mobility of Ta, Nb, Zr, ions in the surface environment, dispersion of ions from a deposit buried by till via mechanisms such as proposed by Hamilton (2000) is unlikely, and partial leach techniques are unlikely to respond well.

In stream sediments, minerals with Nb, Ta, Zr and REE tend to concentrate at heavy mineral trap sites where flow deceleration causes sedimentation (e.g., sand bars; in the lee of obstacles such as logs) that can be preferentially sampled (Stendal and Theobald, 1994). In glaciated terrains, stream sediments may be sampling the till dispersal train from a deposit rather than the deposit itself (e.g., McConnell and Batterson, 1987).

Because the HFSE are generally considered insoluble in aqueous solutions, hydrogeochemistry is unlikely to generate a

significant response, and concentrations are typically in the sub-ppb to sub-ppt range (Protano and Riccobono, 2002; Gassama et al., 2012; Mason, 2013; Tepe and Bau, 2013), effectively at the detection limit of typical commercial hydrogeochemical methods. However, Y in ground water was indicated as a potential element of interest to target REE mineralization at the Strange Lake deposit, Labrador (McConnell and Batterson, 1987).

Certain plants can accumulate some of these elements as essential trace elements (Kovalevsky, 1987, Dunn, 2007; Miao et al., 2008), but owing to low element mobility, concentrations are generally low and responses subtle (Dunn, 2007). Bluemel et al., (2013) demonstrated the potential to use primitive ferns (Dryopteris Filix-mas) as a biogeochemical indicator for REE deposits, with this particular species showing LREE enrichment above mineralization.

3. Sample preparation

With the exception of preparing heavy mineral concentrates, no special treatment is required for conventional soil and stream-sediment samples beyond sieving using a mesh that ensures the minerals of interest pass through the sieve. As noted above, many elements may still reside in primary magmatic minerals that have undergone minimal grain-size reduction during weathering and transport. This physical partitioning contrasts greatly with the behaviour of more labile elements such as Cu and Zn, that are commonly bound to clays or Fe-Mn oxide particles during dispersion.

In a lithogeochemical survey, consideration must be made to the expected concentration of the elements of interest and the coarseness of the mineral grains such that a large enough sample is collected to represent the source rock. Mineral grains, particularly in pegmatite and carbonatite intrusions can achieve sizes of several centimetres, hence collecting a representative sample can be difficult. Following collection, rock samples require crushing and grinding before digestion and analysis.

4. Sample digestion and analysis

For Nb, Ta, REE and Zr, a strong multi-acid (four acid) digestion (e.g., HF, $HClO_4$, HCl and HNO_3) is required to ensure an effective dissolution of the refractory minerals and retention of elements from the mineral phase in the solution (Reimann et al., 2014). Weaker digests such as aqua-regia, although still likely to release metal into solution, are likely to produce both poor geochemical responses and contrasts. Even a four-acid digest will produce poor responses for minerals such as zircon, which is particularly resistant to HF attack (Lett and Patterson, 2011). A superior option would be to use a fusion digest with a flux such as sodium or lithium tetra/metaborate, which will effectively liberate the elements of interest. Inductively coupled plasma mass spectrometry (ICP-MS) is commonly used by commercial laboratories to measure Nb, Ta, REE, Zr, concentrations in solution following multi-acid digestion or a lithium borate fusion. The major oxide content of lithium borate fusion solutions are determined with inductively coupled plasma emission spectroscopy (ICP-OES). Total concentration of some of the elements (e.g., REE, Ta) can be accurately determined by non-destructive, instrumental neutron activation (INAA).

All of these elements, can be analyzed by X-ray fluorescence (XRF), using either a field portable (Luck and Simandl, 2014) or desk-top field or laboratory based instrument. For the latter, either a press powder or fusion disk may be appropriate. Consultation with the laboratory would be appropriate, particularly if high element concentrations outside of the calibration and dynamic range of the analytical equipment are expected.

5. Quality assurance and quality control

An established laboratory quality control scheme is an industry standard requirement. Randomly imbedding field duplicates, preparation blanks, and certified reference materials with samples for analysis, in addition to ensuring that the laboratory also has appropriate control materials to routinely monitor quality control, is key to maintaining acceptable and consistent accuracy and precision. Certified reference materials with elevated concentrations of some of these elements are available, particularly for the REE, however matrix matching the reference with that of the project samples could prove problematic. For example, at an advanced level of exploration (e.g., detailed drilling resource estimation), it may be prudent to generate project-specific certified reference materials through a commercial supplier.

6. Exploration geochemistry

Although the commodity being sought will likely be key to driving or directing the exploration program, the extreme end-member composition of many of the rock types hosting Nb, Ta, REE and Zr mineralization provides a unique suite of lithological pathfinder elements for delineating exploration targets.

In a typical soil geochemical survey, carbonatites can be clearly identified by negative Si, K, Na, and Al anomalies relative to surrounding lithologies. In particular, the Si contents over a carbonatite core can be well below 30%. Conversely, Ca, REE, Th, U, P, Cl, and F +/-Nb tend to be elevated, with distinct high La/Yb ratios, reflecting light-REE enrichment. There are also low K/Th ratios, which reflect Th enrichment and depletion in K relative to surrounding lithologies, a pattern reflected by radiometric imaging. Particular relationships such as a Ca-P-Cl association will clearly indicate the presence of Ca-phosphates (e.g., apatite), which may correlate well with REE-indicating mineral phases associated with the elements of interest, particularly in the secondary environment.

Other lithological phases in an alkaline complex, ranging from K to Na-K dominated units through to mafic units, can likewise be identified by careful major and trace element selection (Fig. 1) and simple ratios specifically selected to contrast adjacent rock types.

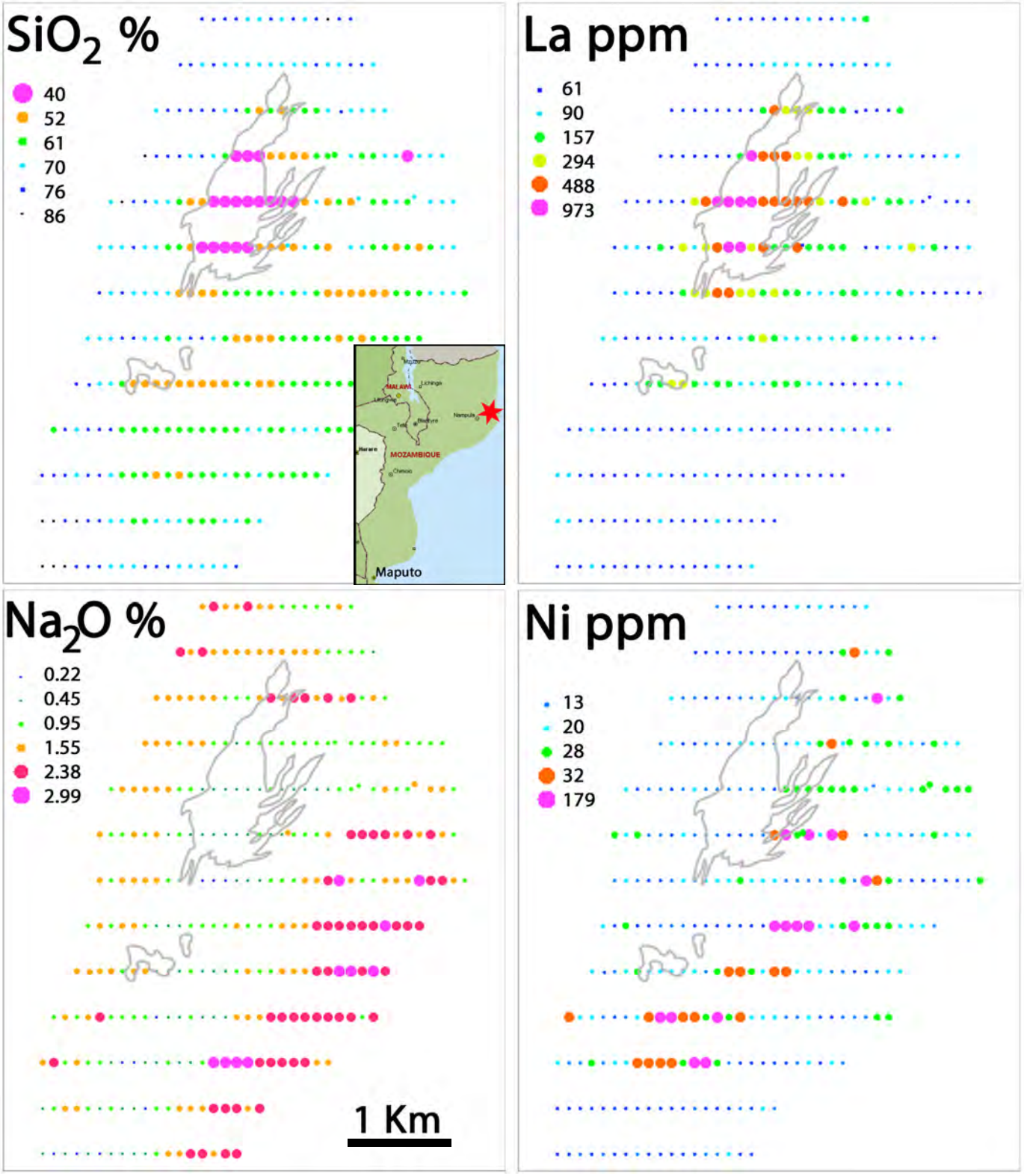

Fig. 1. La, SiO_2, Ni and Na_2O distribution in <180micron B-horizon, residual surface soils around the Evate carbonatite, Monapo complex, Mozambique. Samples analyzed by Li-Metaborate fusion ICPOES/MS. Sampling is on a 400 m by 100 m grid centred on the carbonatite phase (outlined in grey), which formed the exploration target. High La and low SiO_2 highlight the carbonatite phase. Ni highlights mafic units in the complex with Na_2O highlighting an alkali rich unit to the southeast. Inset map shows the location of the Evate carbonatite. The carbonatite itself is hosted in undifferentiated granite gneisses (Macy et al., 2013). Geochemical data published with kind permission from Vale Exploration.

7. Conclusions

Geochemical exploration for Nb, Ta, REE, and Zr mineralization in peralkaline-carbonatite and pegmatites is aided by the extreme end-member composition of the host rocks, which potentially provide a range of elements for lithological discrimination as well as resource identification. However, the resistant nature of many of the minerals that contain these elements can result in poor dispersion of the commodity signal. Because target sizes are likely to be small, relatively tight sample spacing is required for soil surveys. Heavy mineral sampling techniques are suitable for stream-sediment and till geochemical surveys because many minerals bearing Nb, Ta, REE, and Zr have high densities and are chemically stable and mechanically durable. Extensive dispersal trains can form in glaciated terrains, and tills may feed anomalous material into stream sediments and lakes. Unfortunately, due to the resistive nature of some of the minerals and low mobility of the elements of interest, partial extraction techniques are ineffective for discovering mineralization concealed beneath till or other post-mineralization units.

Geochemical analytical methods for Nb, Ta, REE, and Zr must recognize the resistant nature of the host minerals, and hence require HF, $HClO_4$, HCl and HNO_3 digestion or, preferably, lithium borate fusions followed by ICP-MS analysis or, alternatively, XRF and INAA analysis. However careful quality control is required to ensure that the required and acceptable accuracy and precision of the analyses is maintained, given the extremes of chemical composition encountered during typical geochemical surveys.

Acknowledgments

Vale are acknowledged for permission to use the unpublished surface geochemistry from Evate, Mozambique for demonstration and training purposes. George Simandl, Michaela Neetz, and an anonymous reviewer are acknowledged for reviews that greatly improved the manuscript.

References cited

Batterson, M.J., 1989. Glacial dispersal from the Strange Lake alkalic complex, northern Labrador. In: DiLabio, R.N.W., and Coker, W.B., (Eds.), Drift Prospecting: Geological Survey of Canada, Paper 89-20, pp. 31-40.

Bluemel, B., Leijd, M., Dunn, C., Hart, C.J.R., Saxon, M., and Sadeghi, M., 2013. Biogeochemical expression of rare earth element and zirconium mineralization at Norra Kärr, Southern Sweden. Journal of Geochemical Exploration, 133, 15-24.

Dunn, C.E., 2007. Biogeochemistry in Mineral Exploration, Volume 9 (Handbook of Exploration and Environmental Geochemistry), Elsevier, 480 p.

Ford, K.L., Dilabio, R.N.W., and Renez, A.N., 1988. Geological, geophysical and geochemical studies around the Allan Lake Carnonatite, Algonquin Park, Ontario. Journal of Geochemical Exploration 30, 99-121.

Galeschuk, C., and Vanstone, P., 2007. Exploration techniques for Rare Element Pegmatite in the Bird River Greenstone Belt, Manitoba. In: Milkereit (Ed) 2007, Proceedings of Exploration 07. 5th Decennial Conference on Mineral Exploration, Toronto, Canada. pp. 823-839.

Gassama, N., Kasper, H.U., Dia, A., Cocirta, C., and Bouhnik-Lecoz, M., 2012. Discrimination between different water bodies from a multilayered aquifer (Kaluvelly water- shed, India): Trace element signature. Applied Geochemistry, 27, 715-728.

Hamilton, S.M., 2000, Spontaneous potentials and electrochemical cells. In: Hale M. (Ed), Geochemical Remote Sensing of the Subsurface, Elsevier, Amsterdam, pp. 421-426.

Kovalevsky, A.L., 1987. Biogeochemical Exploration for Mineral Deposits, VNU Science Press Utrecht, The Netherlands, 255p.

Lett, R.E., and Patterson, K., 2011. A comparison of several commercially available methods for the geochemical analysis of rare earth, rare metal and High Field Strength Elements in geological samples. In: Geological Fieldwork 2010, British Columbia Ministry of Energy and Mines, British Columbia Geological Survey, Paper 2011-1, pp. 181-188.

Lottermoser, B., 1990. Rare-earth element mineralization within the Mt. Weld carbonatite laterite, Western Australia. Lithos 24 151–167.

Luck, P., and Simandl, G. J., 2014. Portable X-ray fluorescence in stream sediment chemistry and indicator mineral surveys, Lonnie carbonatite complex, British Columbia. In: Geological Fieldwork 2013, British Columbia Ministry of Energy and Mines, British Columbia Geological Survey Paper 2014-1, pp. 169-182.

Mariano, A.N., 1989. Economic geology of rare earth elements. In: Lipin, B.R., and McKay, G.A., (Eds.), Reviews in Mineralogy, Mineralogical Society of America, pp. 309-337.

Macey, P.H., Miller, J.A., Rowe, C.D., Grantham, G.H., Siegfried, P., Armstrong, R.A., Kemp, J., and Bacalau, J., 2013. Geology of the Monapo Klippe, NE Mozambique and its significance for assembly of central Gondwana. Precambrian Research, 233, 259–281.

Mason, R.P., 2013. Trace Metals in Freshwaters, in Trace Metals in Aquatic Systems, John Wiley & Sons, Ltd, Chichester, UK. pp. 310-369.

McClenaghan, M.B., Thorleifson, L.H., and DiLabio, R.N.W., 2007. Till geochemistry and indicator mineral methods in Mineral Exploration In: Gubins A.G., (Ed.), Proceedings of Exploration 97: Fourth Decennial International Conference on Mineral Exploration 1997, pp. 233–248.

McConnell, J.W., and Batterson, M.J., 1987. The Strange lake Zr-Y-Nb-Re-REE deposit, Labrador: A geochemical profile in till, lake and stream sediment and water. Journal of Geochemical Exploration, 29, 105-127.

Miao, L., Xu, R., Ma, Y., Zhu, Z., Wang, J., Cai, R., and Chen Y., 2008. Geochemistry and biogeochemistry of rare earth elements in a surface environment (soil and plant) in South China. Environmental Geology, 56, 225-235.

Modreski, P.J., Armbrustmacher, T.J., and Hoover, D.B., 1995. Chapter 6: Carbonatite deposits. In: du Brey E.A. (Ed) Preliminary Compilation of descriptive geoenvironmental mineral deposit models. USGS, Open File Report 95-831.

Moller, P., Cerny, P., and Saupe, F., 1989. Lanthanides, Tantalum and Niobium. Mineralogy, geochemistry, characteristics of primary ore deposits, prospecting, processing and applications. Special Publication of the Society for Geology applied to Mineral deposits, No. 7. Springer Verlag, Berlin. 380p.

Protano, G., and Riccibono, F., 2002. High contents of rare earth elements in stream waters of a Cu-Pb-Zn mining area. Environmental Pollution, 117, 499-514.

Reimann, C., Birke, M., Demetriades, A., Filzmoser, P., and O'Connor, P., 2014. Chemistry of Europes Agricultural soils. Part A. Methodology. Geologisches Jahrbuch Reihe B, Hannover, 521p.

Ryghaug, P., 1983. Geochemical exploration methods for niobium and rare earth elements at Saeterasen, Vestfold Volcanic area, Oslo Graben. Norsk Geologisk Tidsskrift, 63, 1-13.

Stendal, H., and Theobald, P.K., 1994. Heavy Mineral Concentrates in Geochemical Exploration. In: Hale M and Plant J., (Eds.), Handbook of Exploration Geochemistry, Vol. 6. Drainage

Geochemistry. Elsevier Science, Netherlands, pp. 185-225.
Tepe, N., and Bau, M., 2013. Controls on dissolved REE and HFSE in glacial meltwater rivers in southern Iceland. Goldschmidt Conference Abstracts, p. 2323.

Using gamma ray spectrometry to find rare metals

Robert B.K. Shives[1, a]

[1] GamX Inc., Kanata, ON, K2L 3Z8
[a] corresponding author: rob@gamx.ca

Recommended citation: Shives, R.B.K., 2015. Using gamma ray spectrometry to find rare metals. In: Simandl, G.J. and Neetz, M., (Eds.), Symposium on Strategic and Critical Materials Proceedings, November 13-14, 2015, Victoria, British Columbia. British Columbia Ministry of Energy and Mines, British Columbia Geological Survey Paper 2015-3, pp. 199-209.

Summary

For decades, gamma ray spectrometry has been used worldwide to map rocks and locate mineralization in diverse geological settings (Shives et al., 1997). The method is particularly well suited to rare metal and REE (rare earth element) exploration because primary host rocks are enriched in incompatible elements known as LILE (large-ion lithophile elements K, Rb, Cs, Sr, Ba) and HSFE (high field strength elements Zr, Nb, Hf, REEs, Th, U and Ta). As a result, the ores of REEs are commonly radioactive because host rocks, ore-bearing minerals, or associated accessory minerals may contain trace to anomalous concentrations of radioactive elements K, U and Th. These radioactive elements provide a useful and direct exploration vectors. Gamma ray data are often collected simultaneously with magnetic, electromagnetic, and gravity data in multisensor surveys.

The objective of this extended abstract is to emphasize the importance of gamma ray spectrometry as a primary exploration tool for rare metal deposits. Case histories presented herein illustrate radioactive element and magnetic signatures associated with diverse rare metal deposit types in different geological settings. Canadian examples include: Cantley, Quebec (Quinnville and Templeton carbonatites); Oka, Quebec (carbonatite); Bancroft, Ontario (pegmatites); Allan Lake, Ontario (a blind carbonatite discovery); Nechalacho, Northwest Territories (previously called Thor Lake; altered ultra-alkaline layered complex); Strange Lake, Quebec (peralkaline granite, pegmatite); and one each from British Columbia and Labrador. Also presented are examples from Greenland, Norway, and Mozambique.

1. Introduction

Gamma ray spectrometry provides quantitative measurements of radioactive elements that emit gamma rays contained in natural or man-made materials. Wide-ranging applications include geological mapping of bedrock and surficial geology, environmental concerns (mine tailings, radioactive waste, recycling and garbage disposal), detection of lost sources, emergency response, and a long list of transportation, engineering and medical uses.

Geological applications rely on measuring naturally occurring radioactive isotopes of potassium (K^{40}), uranium (Bi^{214}) and thorium (Tl^{208}), using spectrometers in properly calibrated airborne, vehicle-borne, handheld, or borehole systems. The abundance and chemical behavior of K, U and Th are quite different. Although K is abundant (%), U and Th are trace elements (ppm); U is mobile whereas Th is immobile. Thorough interpretation of gamma ray data requires consideration of these chemical attributes.

2. Radioactive elements in rare metal deposits

Rare metals and REE are most commonly found in carbonatites, peralkaline granites, silica-undersaturated rocks, peraluminous granites, and pegmatites. Associated accessory minerals may include sphene, allanite, apatite, monazite, xenotime, zircon, pyrochlore, bastnäsite, parisite, synchysite, gadolinite, wodginite, ferrocolumbite-manganotantalite, microlite, tapiolite and others. These contain the incompatible LILE and HFSE, including K, U and Th. Table 1 lists the REE and radioactive elements contained in common REE ore minerals, illustrating why the gamma ray method is so usefully applied to rare metal and REE exploration. Note that thorium is particularly common in the REE minerals.

3. Case histories

The following case histories very briefly illustrate results of airborne and ground gamma ray spectrometric surveys conducted at early exploration stages to advanced exploration and development stage deposits. The examples span various geological settings, deposit types, and ages.

3.1. Red Wine Mountain, Labrador: Peralkaline granites

This grass-roots-phase property was staked over the site of the second highest heavy-REE (HREE) value in the entire Newfoundland regional lake sediment database, containing greater than 80 ppm HREE and including europium, terbium, ytterbium and lutetium. Airborne thorium concentrations determined by a 2010 airborne gamma ray spectrometric survey (Fig. 1) show strong coincidence with TREO values in float samples (Silver Spruce, 2015). The area of host peralkaline granite (not illustrated) has no outcrop, but angular float and subcrop contained 2500 ppm La, 1520 ppm Nd and 4360 ppm Ce. Seven samples contained greater than 1% TREO; one assayed 2.58% TREO, as indicated.

Table 1. REE-bearing ore minerals commonly contain detectable concentrations of radioactive elements K, U, Th (latter is particularly common). These are pathfinder elements used in gamma ray spectrometry.The REE are shown in red, and the radioactive elements in blue.

Aeschynite	Y, Ca, Fe, Th, Ti, Nb, O, H
Allanite	Ce, La, Y, Th, U, Zr, P, Ba, Cr
Apatite	Ca, P, O, F, Cl, H, La, Ce, Pr, Nd, Sm, Eu, Gd, Dy, Er, Yb, U, Th
Bastnäsite	Y, Ce, La, C, O, F, Th
Britholite	Ce, Ca, Th, La, Nd, Si, O, P, H, F
Brockite	Ca, Th, Ce, P, O, H
Cerite	Ce, La, Ca, Mg, Fe, Si, O, (+/- uraninite inclusions)
Columbite	Nb, Ta, Y, U, Mn, Fe, Sn, W, O,
Fergusonite	Nb, Y, Ce, Nd, Ta, Ti, U, Th, O
Fluocerite	Ce, La, F, Th
Fluorite	Ca, F, Y, Yb, (+/- uraninite, thorite inclusions)
Gadolinite	Ce, La, Nd, Y, Fe, Be, Si, Th
Monazite	Ce, La, Nd, Sm, Gd, U, Th, Y, Pr, He, P, O
Parisite	Ce, La, Nd, Ca, C, O, F, Ba
Pyrochlore	Nb, Ta, La, Y, Dy, Gd, Sc, U, Th, Ru, Ca, Ti, Zr, Mo, O
Stillwellite	Ce, La, Ca, B, Si, O (+/- thorite, uranothorite, thorianite)
Synchysite	Ce, Nd, Y, Ba, La, C, O, F, Ca, Th
Titanite/Sphene	Ca, Ti, Si, O, Fe, Al, Ce, Y, U, Th
Wakefieldite	La, Ce, Nd, Y, Bi, V, O, Th
Xenotime	Y, P, O, U, Th, As, Si, Ca, Dy, Er, Tb, Yb, Gd
Zircon	Zr, Si, O, Hf, U, Th

1. There are 100s of REE-bearing minerals.
2. Elements listed are not exclusive, and may not all be present in a single mineral.
3. Radioactive elements may occur in the REE molecules, as mineral inclusions in REE-minerals, or within the same rocks.

3.2. Strange Lake, Quebec: Peralkaline granites and pegmatites

The original discovery at this advanced project (278 Mt at 0.93% TREO+Y indicated + 214 Mt at 0.85% TREO+Y inferred, (Quest, 2015) was aided by airborne gamma ray results over mineralization dispersed glacially from the host peralkaline intrusive complex (Fig. 2). The dispersal trend crosses bedrock contacts at a high angle and is defined by anomalous till concentrations of ore-related elements (Th, U, Be and others).

3.3. Oka Carbonatite, Quebec

This composite alkaline intrusion hosts a niobium resource (10.63 Mt M+I (Measured plus Indicated) at 0.68% Nb_2O_5) (Niocan, 2015) related to pyrochlore group minerals enriched in Nb, Ti, LREE (Light Rare Earth Elements), U and Th, in calciocarbonatite (sövite) phases. Airborne eU (Fig. 3) and eTh patterns accurately delineate the mineralized units and overall boundary of the intrusion. Local development regulators compared the strong airborne eU anomalies with indoor radon to assess where future housing may develop, subject to building code modifications designed to mitigate indoor radon levels and reduce radon-related health risks.

3.4. Cantley Carbonatites, Quebec

This area hosts two carbonatite-fenite fields with contrasting features (Fig. 4). The Quinnville carbonatite-fenite is non-magnetic (hematite), has K-rich bedrock (12% K due to microcline alteration), high Th (to 300 ppm), moderate U (to 50 ppm) and contains La-Ce fluorocarbonates (La >1.3%), uraninite and monazite. The Templeton carbonatite-fenite has low K, U and Th, and a positive aeromagnetic response (due

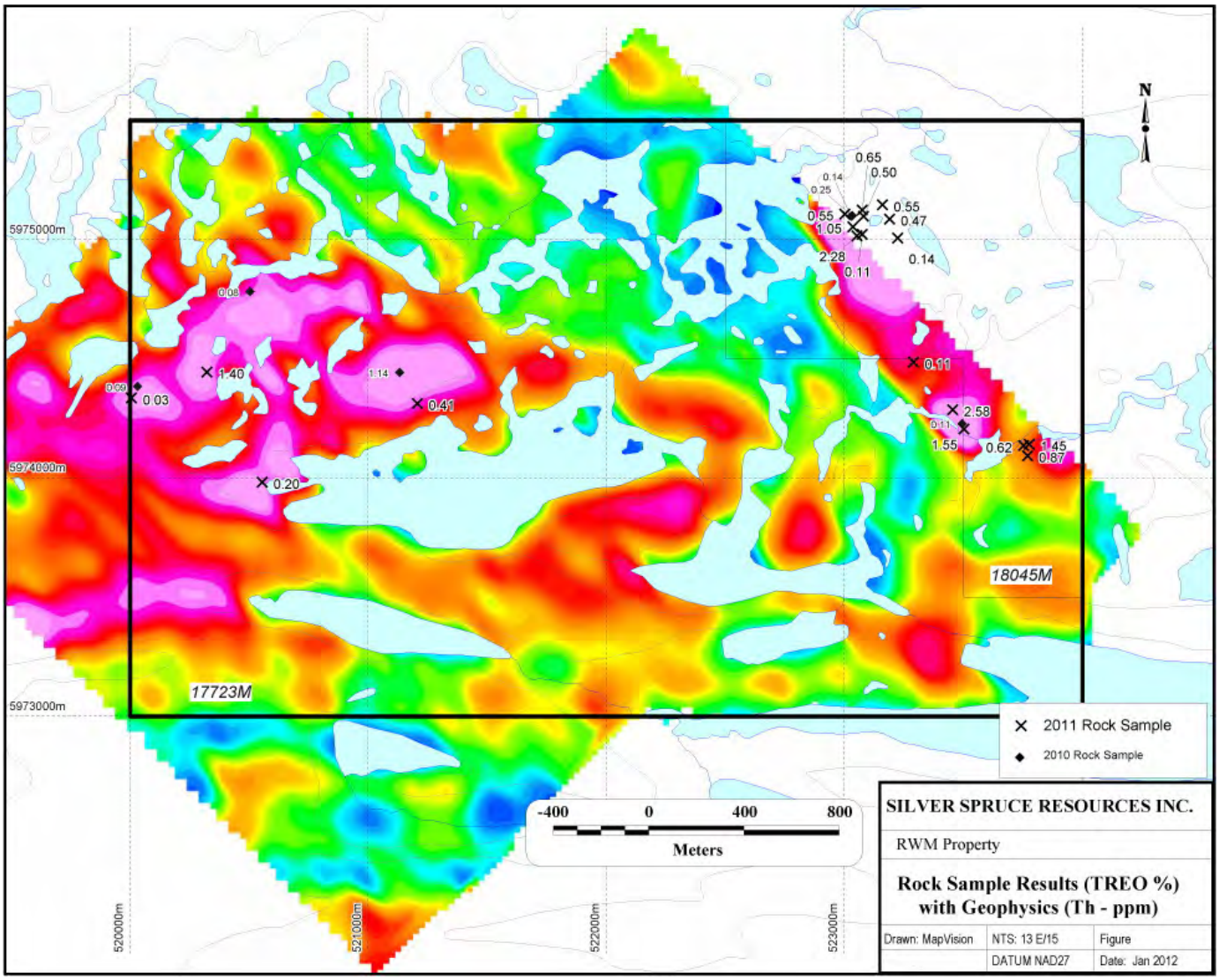

Fig. 1. Thorium concentrations estimated by airborne gamma ray spectrometry surveys over the Red Wine Mountain, Labrador property show strong correlation with TREO (Total Rare Element Oxide) values in rock samples. Pink contoured areas have relatively higher airborne Th concentrations than yellow-green areas, blue shades represent lowest airborne Th values. Map from Silver Spruce (2015).

to magnetite), but low REE concentrations (Charbonneau and Hogarth, 1988).

3.5. Bancroft, Ontario: U-pegmatites

In the Bancroft Ontario area, hundreds of uranium showings in metasedimentary rocks, granites, and pegmatites lie in well-defined U and Th anomalies at the margins of large gneissic domes (Fig. 5). Many contain uraninite, thorite and uranothorite. Associated REEs, Nb, Ta, Y, Ce, La, Nd, and Er occur in minerals such as columbite-tantalite, fergusonite, pyrochlore and gadolinite (Satterly and Hewitt, 1955). Uranium (at grades 0.05–1% U) was historically produced from four mines. Economic REE deposits are considered unlikely in this region.

3.6. Allan Lake, Ontario: Ankerite-siderite carbonatite

This unexposed, small (0.4 km^2), non-magnetic, intrusive plug was discovered in 1977 in a provincial park, through ground follow-up to a strong airborne eTh-only anomaly related to a textbook example of a glacial till dispersal train (Fig. 6). Nearest outcrops of fenitized felsic gneisses are cut by radial dikes and breccias anomalous in eTh. Drilling confirmed the presence of carbonatite containing Ce, La, Nb, Y, Zn, Th, P, Ba, Cu, Pb, Mo, Co. REEs are associated mainly with synchesite-bastnaesite and apatite (Ford et al., 1988).

3.7. British Columbia: Carbonatite sills and dikes

K, U and Th variations can commonly distinguish different carbonatite phases and REE contents. In this example, ground spectrometry refined airborne results, identifying known and new occurrences and separating them into Nb or Ta enriched sövitic (Ca) or beforsitic (Mg) types (Fig. 7; Shives, 2009).

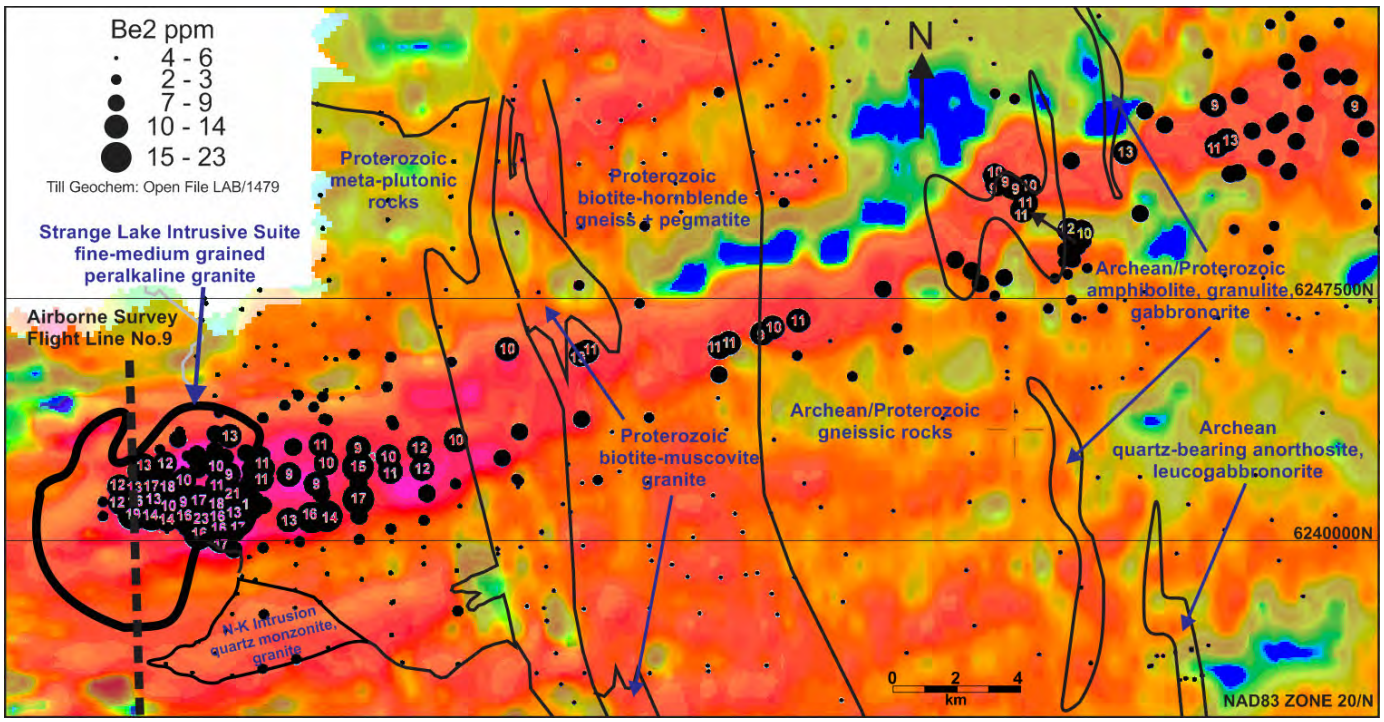

Fig. 2. Airborne survey, Strange Lake intrusive complex. Thorium patterns (relative highs are pink, lows are blue) define a 42 km-long, ENE-trending dispersal train at Strange Lake that crosses bedrock contacts (black lines) and correlates with ore-related elements in till such as Be (dots; Batterson and Taylor, 2009).

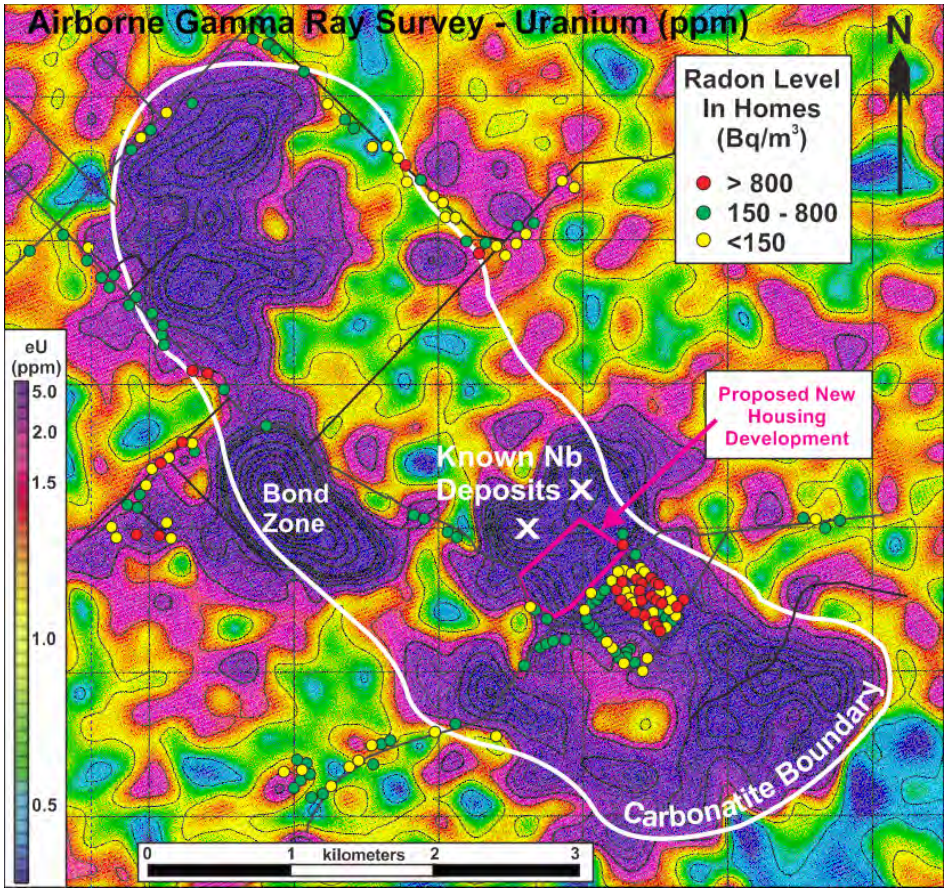

Fig. 3. Airborne eU highs (purple) outline mineralized phases of the Oka Carbonatite, Quebec, and map high indoor Rn potential (modified from Ford et al., 2001).

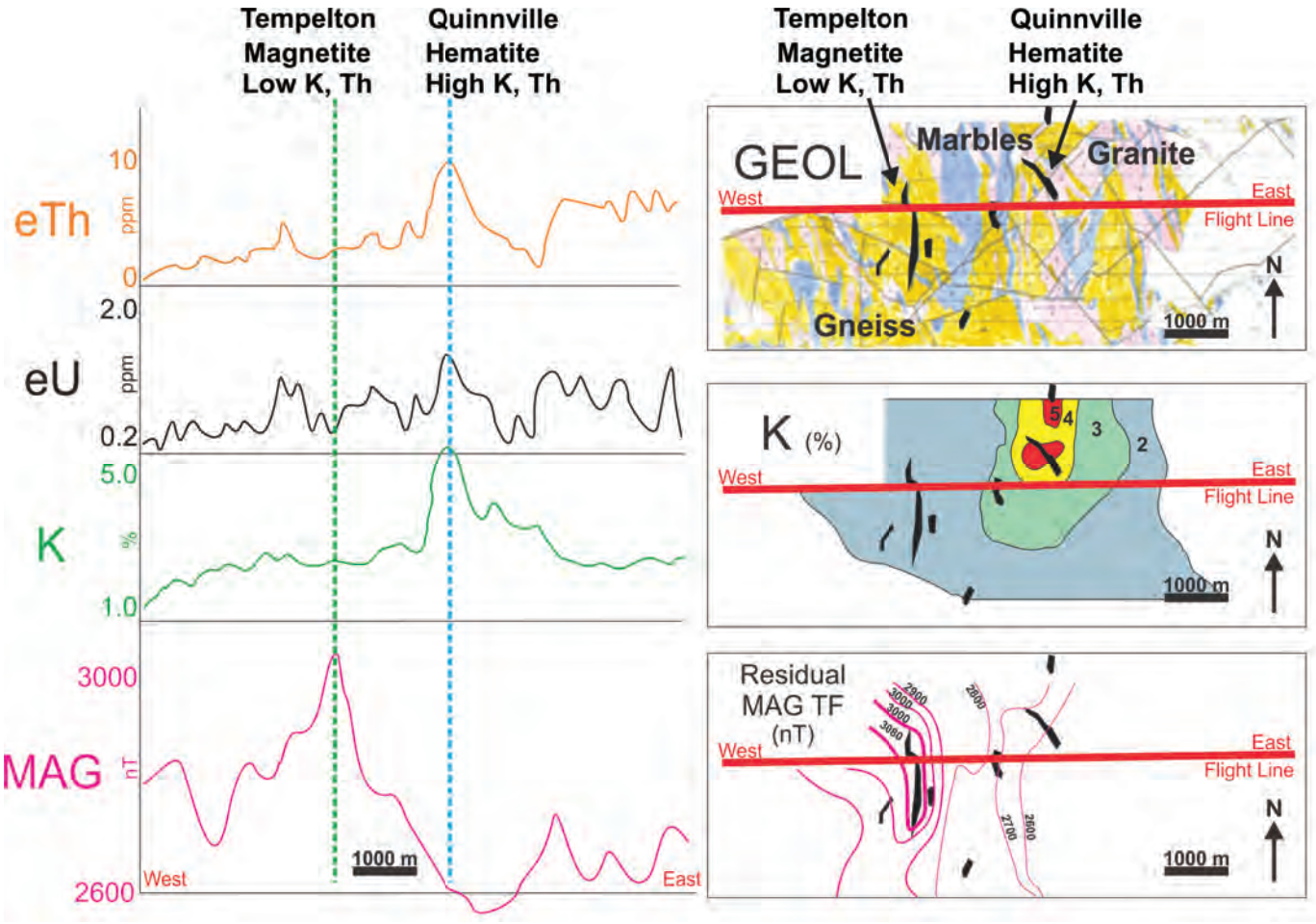

Fig. 4. Geology, airborne K and aeromagnetic maps (right) and airborne stacked profile (left) over the Templeton and Quinnville carbonatite and fenites (black on map views) at Cantley, Quebec.

3.8. Nechalacho, Northwest Territories: Alkaline complex

A 1971 airborne gamma ray spectrometric survey flown by the Geological Survey of Canada detected a strong eTh response over this deposit, which is now an advanced project (estimated measured mineral resource 12.56 million tonnes averaging 1.71% TREO, 0.38% HREO and 22.5% HREO/TREO plus Zr, Ta, Nb and total indicated mineral resource 95.54 million tonnes averaging 1.57% TREO, 0.25% HREO and 16% HREO/TREO; Avalon, 2015). Detailed gamma ray and magnetic surveys (Fig. 8) provide regional and local mapping aids.

3.9. Fen, Norway: Alkaline intrusive and carbonatite complex

Here, airborne gamma ray eTh values reflect low-Th, Nb-bearing sövite, intermediate-Th rauhaugite and high-Th, REE-rich rodberg phases (Fig. 9). REEs include La and Ce and others in monazite, bastnaesite, synchesite and parasite (Lie and Ostergaard, 2011).

3.10. Carbonatites, southwestern Greenland: Peralkaline intrusions

These two carbonatites contain low, but detectable Th, (Fig. 10) which guides to REEs and other metals of interest. Highest airborne eTh values at the Tikiusaaq (discovered in 2005) carbonatite mark the best REE grades in float (9.6% TREO; Nuna, 2015a). At the Qeqertaasaq carbonatite, eTh correlates with sövitic ring dikes cut by REE-bearing carbonatite veins. Mineralization includes Ce, La, Nb, Ta, P, Sr, Zr, and Zn (Nuna, 2015b).

3.11. Mount Muambe, Mozambique: Carbonatites and fenites

Ground gamma ray results correlate well with the location of HREO (Dy+Eu)-enriched carbonatite phases (1.22% TREO, 426 ppm Dy_2O_3, 198 ppm Eu_2O_3) within the Mount Muambe intrusion, and will guide future exploration at this grass-roots exploration project (Fig. 11). The project hosts an inferred fluorite resource of 1.63 Mt at 19% CaF_2 (fluorite) for a contained 310,000 t of CaF_2 (Globe, 2011).

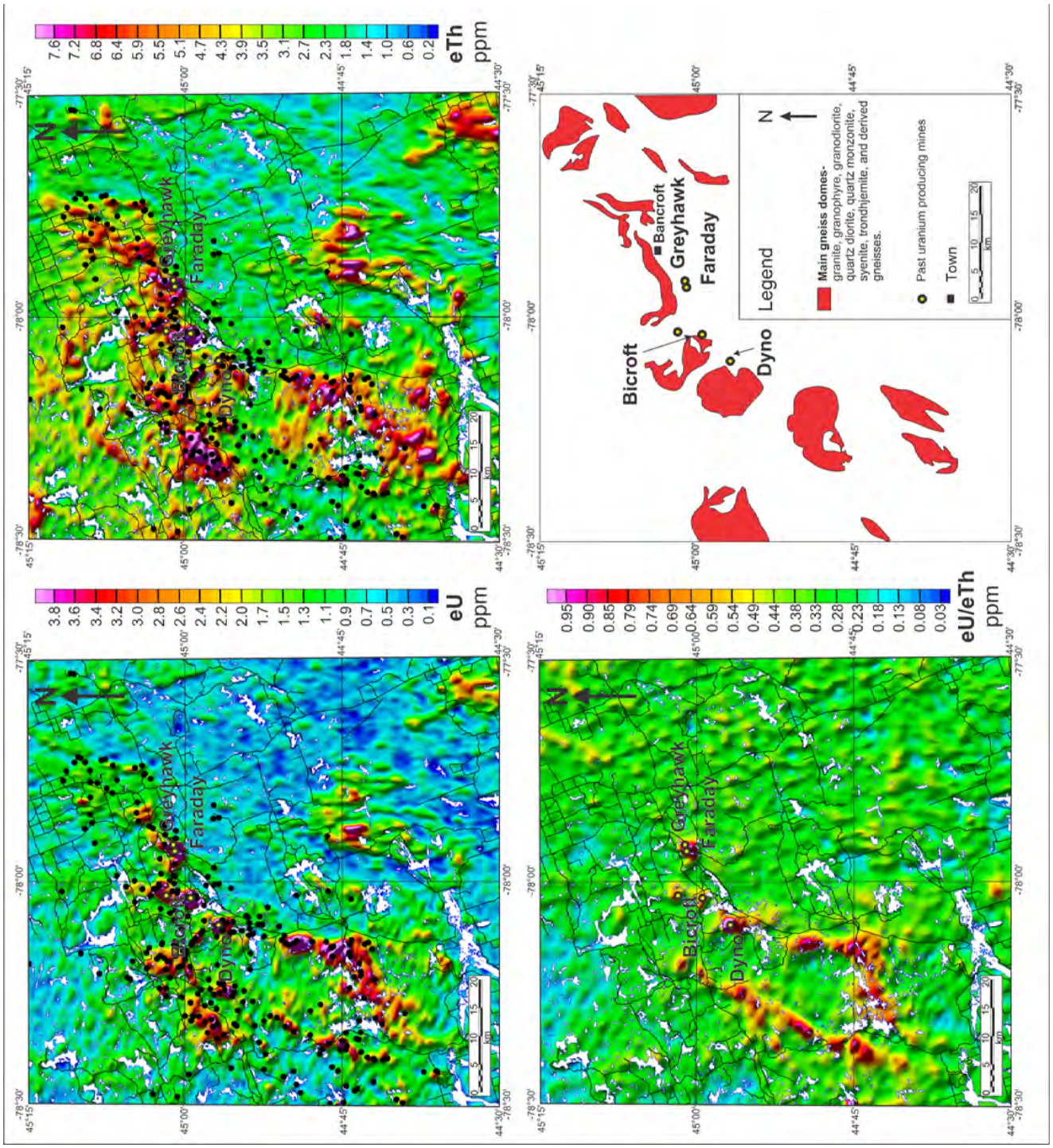

Fig. 5. Airborne eU, eTh and eU/eTh highs mimic contacts of large gneissic domes in the Bancroft area, Ontario. Black dots mark mineral occurrences. Past U mines (labeled) produce discrete anomalies on the eU/eTh map. Location of large gneissic domes from Freeman (1978).

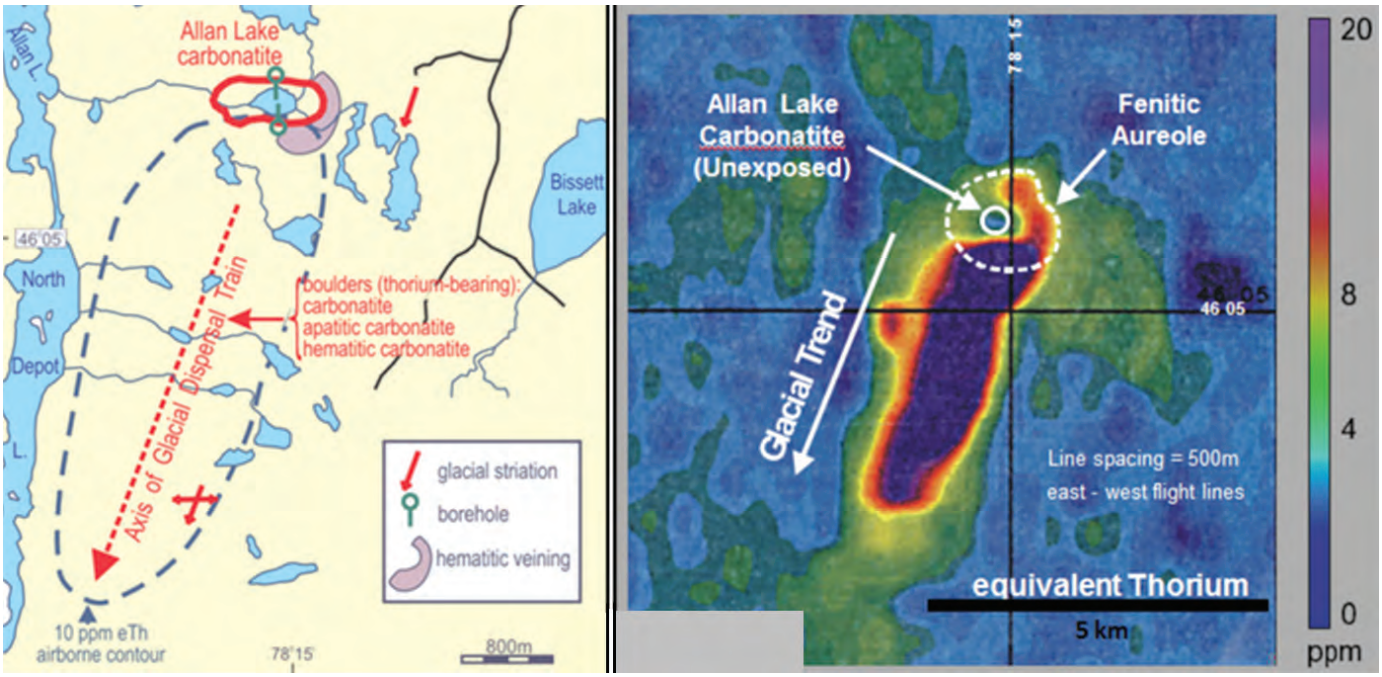

Fig. 6. Airborne eTh patterns (Geological Survey of Canada archives) map glacially dispersed Allan Lake carbonatite material versus local background till deposited on regional gneissic host rocks.

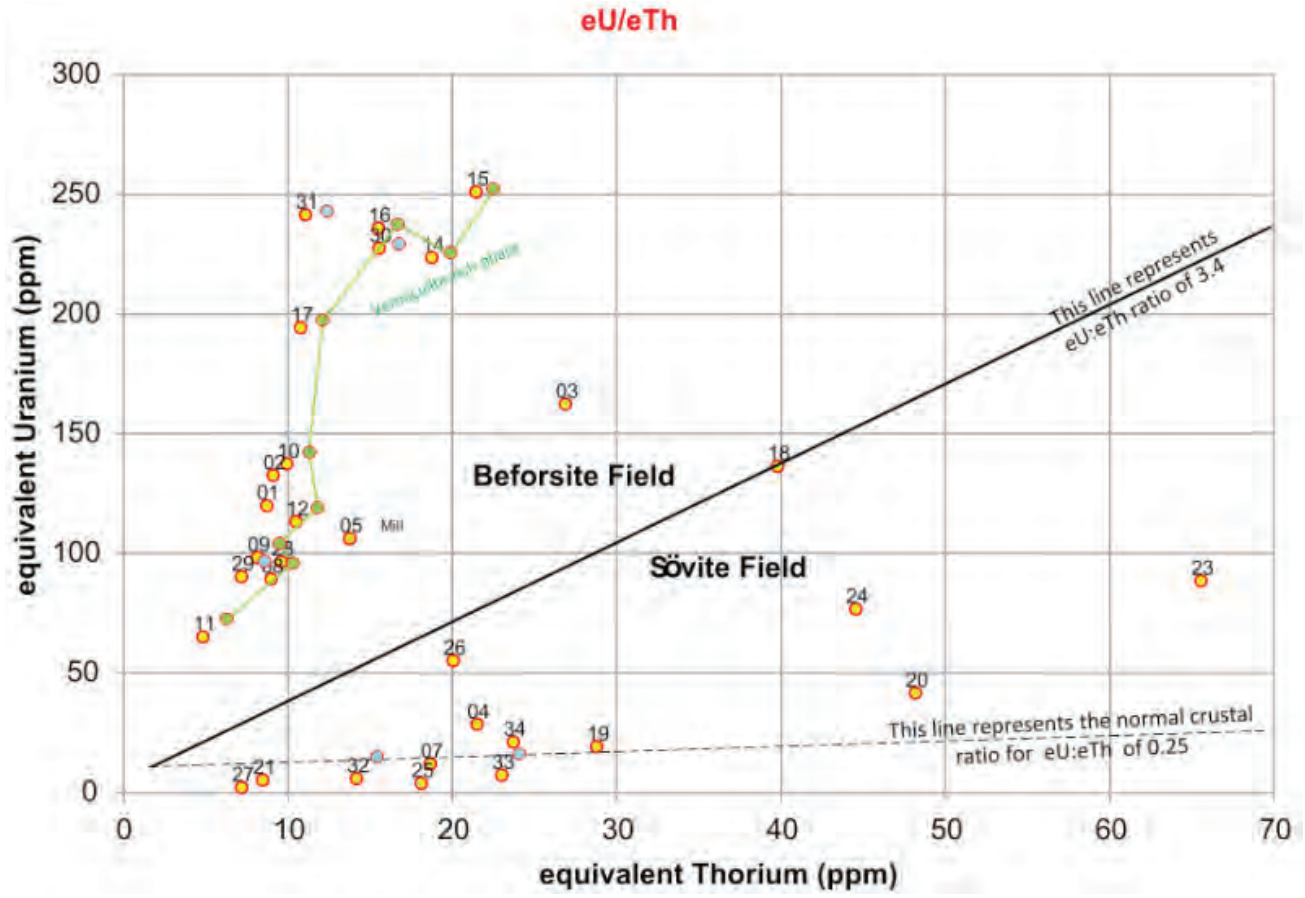

Fig. 7. Bivariate plot of ground spectrometric data (yellow dots) over unidentified carbonatites located in western Canada. Here, Ta-enriched beforsitic phases are also relatively enriched in uranium, whereas Nb-enriched sövitic phases contain relatively more thorium. Several readings taken on a vermiculite-rich phase (the smaller, green dots and trend-line) show that this phase relates to beforsitic magma, rather than sövitic (Shives, 2009).

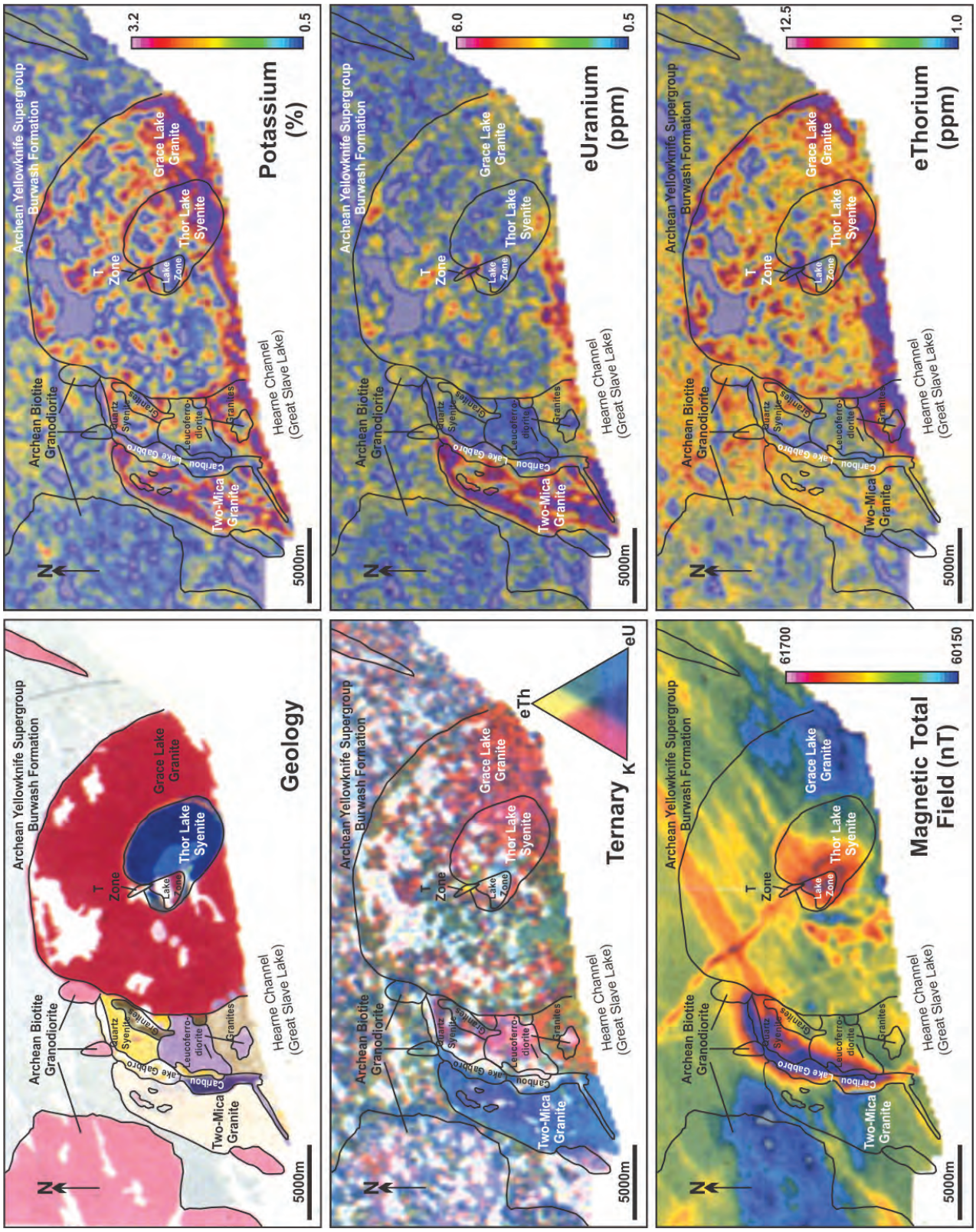

Fig. 8. Strong gamma ray and magnetic contrasts over the Nechalacho deposit in Northwest Territories, Canada, provide bedrock mapping and exploration guides. For example, the positive magnetic response over the Caribou Lake gabbro, and high equivalent uranium (eU) associated with the two-mica granite on the west side of the image, can be used to map their contacts. Note the equivalent thorium (eTh) anomaly over the T-Zone at Nechalacho. These radioactive element relative variations produce marked colour contrasts on the ternary image. Geology from Henderson et al. (1981).

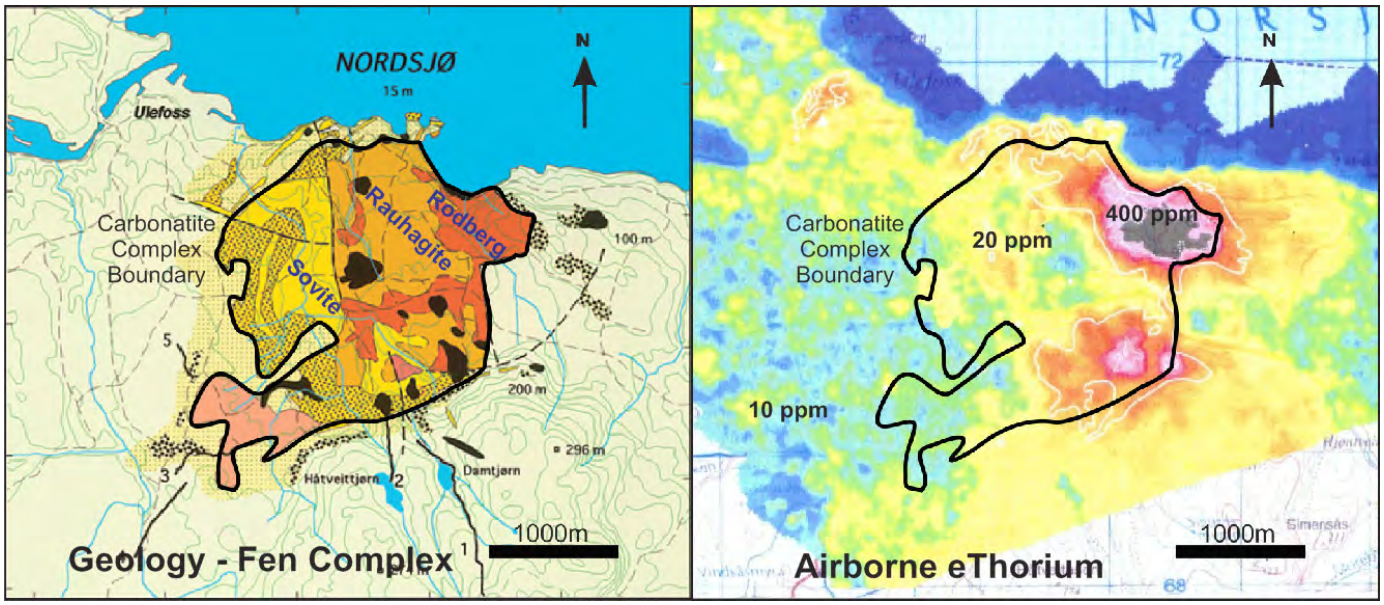

Fig. 9. The Fen Complex, Norway, hosts deposits of REEs + Y, Th and Fe (left). Airborne eTh concentrations reflect various phases (right), low-Th, Nb-bearing sövite, intermediate-Th rauhaugite and high-Th, REE-rich rodberg phases and REE, Nb, and Y mineralization (Lie and Ostergaard, 2011).

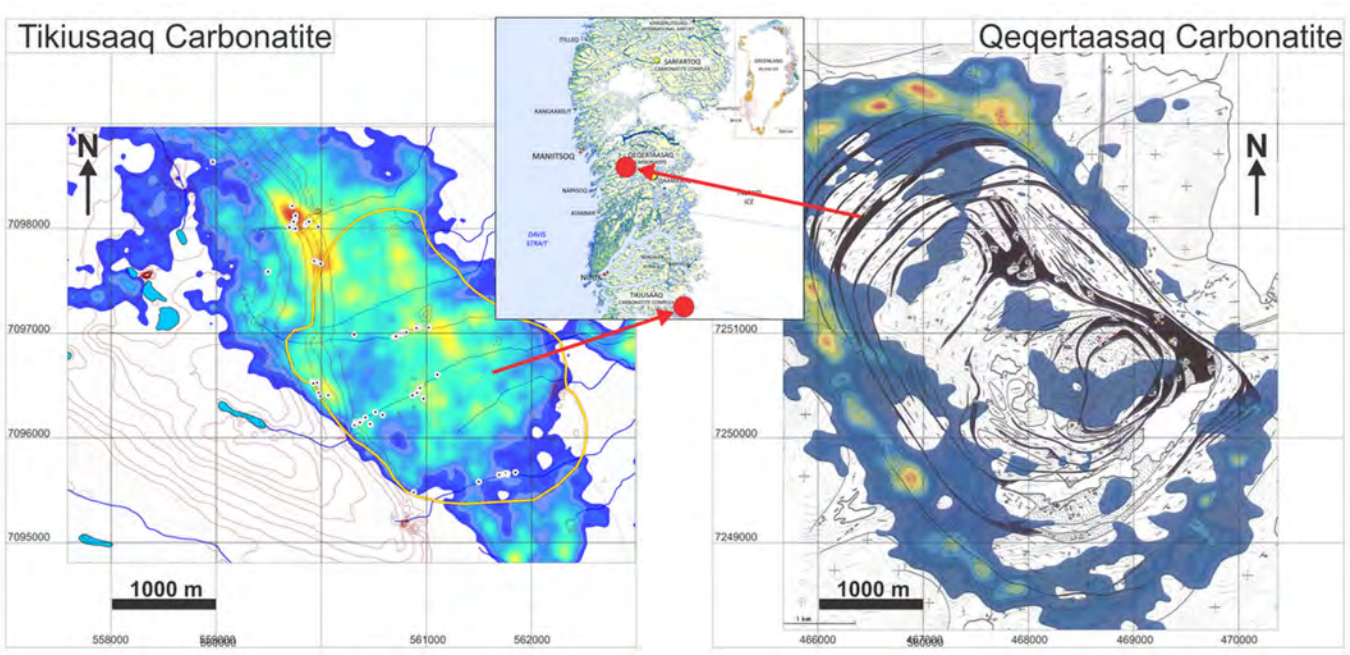

Fig. 10. Highest airborne eTh concentrations overlie Archean REE-bearing peralkaline rocks at two carbonatite complexes in southwestern Greenland. Tikiusaaq (left, outlined by yellow line) thorium values correlate with highest REE concentrations (9.6% TREO). At Qeqertaasaq (right, with eTh contours superimposed on 1987 geological map by the Geological Survey of Denmark and Greenland), thorium overlies peripheral sövitic ring dikes and veins containing Ce, La, Nb, Ta and other REEs. From Nuna (2015b).

4. Conclusion

Geological applications of gamma ray spectrometry include mapping and exploration for a wide variety of deposits, such as those containing REE, Zr, Ta, Nb, Ta, and U. The method uses absolute and relative variations of K, U, and Th to detect primary lithological signatures and subsequent alteration. Where one or more of these elements is associated with elements of economic interest, their concentrations and ratios, as determined by gamma ray spectrometry, can serve as guides to mineralization. Where political and environmental concerns exist regarding radioactivity of ores and waste products, the spectrometric data also offer important baseline information useful to all development stages from early exploration through to post-extraction reclamation.

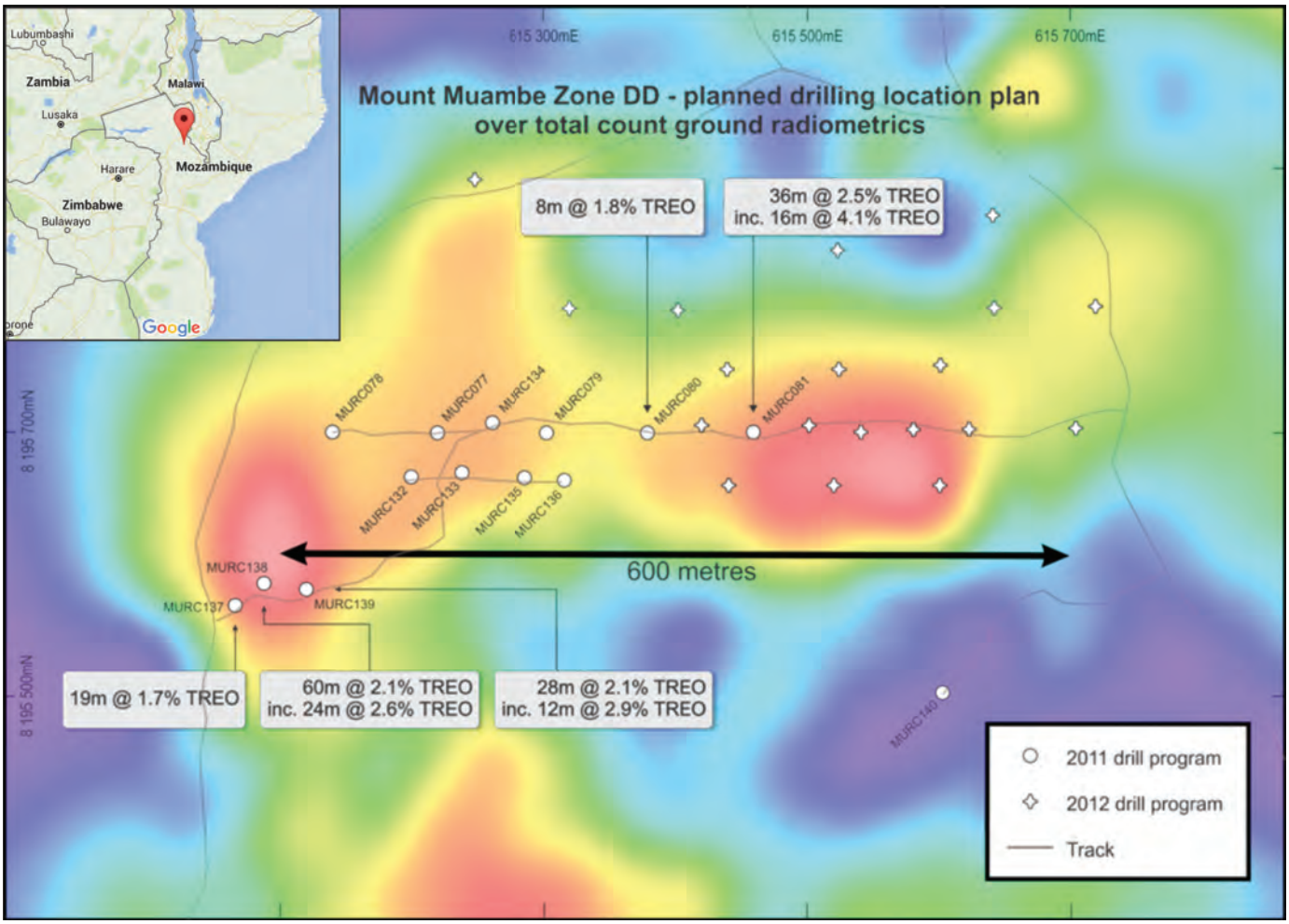

Fig. 11. At the Mount Muambe Carbonatite, Mozambique, ground gamma ray surveys have provided guides to HREO and fluorite prospects explored in 2011-2012. Higher total count values are shown in hotter pink colours, low values in blue tones. Correlation between the gamma ray results and drilling results is apparent. From Globe (2011).

References cited

Avalon, 2015. Nechalacho Project Resources and Reserves. <http://www.avalonraremetals.com/nechalacho/resources_reserves/> accessed: August 19, 2015.

Batterson, M.J., and Taylor, D.M., 2009. Geochemical re-analysis of till samples from the Strange Lake area, Labrador (NTS Sheets 14D/5 and 24A/8. Newfoundland Department of Natural Resources Open File LAB/1479.

Charbonneau, B.W., and Hogarth, D.D., 1988. Geophysical expression of the carbonatites and fenites east of Cantley, Quebec. Current Research part C: Canadian Shield, Geological Survey of Canada, Paper no. 88-1C, pp. 259-269.

Ford, K.L., Delabio, R.N.W., and Rencz, A.N., 1988. Geological, geophysical and geochemical studies around the Allan Lake carbonatite, Algonquin Park, Ontario. Journal of Geochemical Exploration, 30, 99-121.

Ford, K.L., Savard, M., Charbonneau, B.W., and Shives, B.K., 2001. The Role of Gamma-ray Spectrometry in Radon Risk Evaluation: A Case History from Oka, Quebec. Geoscience Canada, 28, 59-61.

Freeman, E. B., ed., 1978: Geological Highway Map, Southern Ontario; Ontario Geological Survey, Map 2418.

Globe, 2011. Mount Muambe REE-Fluorite Project, Mozambique. Investor Update Presentation, June 23, 2011. <http://www.globemetalsandmining.com.au/Files/Investors/Presentations/2011/Investor-Update-Mount-Muambe-June-2011_Final.aspx>. accessed: August 19, 2015.

Henderson, J.B., Davidson, A., and Hoffman, P.F., 1981. Generalized geology of the Blatchford Lake Complex. Geological Survey of Canada Open File 764, 1981.

Lie, A., and Ostergaard, C., 2011. The Fen carbonatite complex, Ulefoss, South Norway, Summary of Historic work and data. <http://www.reeminerals.no/images/Marketing/Om_oss/geologirapporter/R1%20-%2021st%20North%20-%20Fen%20Carbonatite%20complex%20-%20Summary%20of%20historic%20work%20and%20data%2013.5.11.pdf>. accessed: August 19, 2015.

Niocan, 2015. Oka Niobium Property Resource Potential. <http://www.niocan.com/ww2/index.php?option=com_content&view=article&id=20&Itemid=159&lang=en>. accessed: August 19, 2015.

Nuna, 2015a. Tikiusaaq REE Prospect. <http://nunaminerals.com/en/projects/rare-earth-element-ree-projects/tikiusaaq-ree-prospect.html>. accessed: August 19, 2015.

Nuna, 2015b. Qeqertaasaq REE prospect. <http://nunaminerals.com/en/projects/rare-earth-element-ree-projects/qeqertaasaq-ree-prospect.html>. accessed: August 19, 2015.

Quest, 2015. Strange Lake Project Preliminary Economic Assessment Highlights. <http://www.questrareminerals.com/strange_lake.php>. accessed: August 19, 2015.

Satterly, J., and Hewitt, D.F., 1955. Some radioactive mineral occurrences in the Bancroft Area; Geological Circular No.2,

Ontario Department of Mines.
Shives, 2009. GamX Inc Report. Unpublished and confidential report on results of gamma ray spectrometric measurements over carbonatite hosted REE deposits, Canada.
Shives, R.B.K., Charbonneau, B.W., and Ford, K.L., 1997. The detection of potassic alteration by gamma-ray spectrometry - recognition of alteration related to mineralization; in "Geophysics and Geochemistry at the Millenium", Proceedings of the Fourth Decennial International Conference on Mineral Exploration (Exploration 97), Toronto, September, 1997. 17p. <http://www.ing.unp.edu.ar/asignaturas/geoaplicada/Publicaciones/TP%2007%20%28Radiom%29%20K%20Alteration%20LouLake%20Canad%C3%A1,%20Shives%20et%20al.pdf>. Accessed: October 21, 2015.
Silver Spruce, 2015. Red Wine Mountain Project. <http://www.silverspruceresources.com/s/RWM.asp>. accessed: August 19, 2015.

Indicator minerals in exploration for specialty metal deposits: A QEMSCAN® approach

D.A.R. Mackay[1, 2, a], G.J. Simandl[1, 3], W. Ma[4], J. Gravel[4], and M. Redfearn[4]

[1] School of Earth and Ocean Sciences, University of Victoria, Victoria, BC
[2] De Beers Group of Companies, Yellowknife, NT
[3] British Columbia Geological Survey, Victoria, BC
[4] Bureau Veritas Commodities Canada Ltd., Inspectorate Metallurgical Division, Richmond, BC
[a] corresponding author: duncan.mackay87@gmail.com

Recommended citation: Mackay, D.A.R., Simandl, G.J., Ma, W., Gravel, J., and Redfearn, M., 2015. Indicator minerals in exploration for specialty metal deposits: A QEMSCAN® approach. In: Simandl, G.J. and Neetz, M., (Eds.), Symposium on Strategic and Critical Materials Proceedings, November 13-14, 2015, Victoria, British Columbia. British Columbia Ministry of Energy and Mines, British Columbia Geological Survey Paper 2015-3, pp. 211-217.

1. Introduction

Quantitative Evaluation of Materials by Scanning electron microscopy (QEMSCAN®) was used to assess carbonatite indicator minerals in fluvial sediments from the drainage area of the Aley carbonatite, in north-central British Columbia. QEMSCAN® is a viable method for rapid detection and characterization of carbonatite indicator minerals with minimal processing other than dry sieving. Stream sediments from directly above, and up to 11 km downstream, of the carbonatite deposit were selected for this indicator mineral study. The geology of the Aley carbonatite is described by Mäder (1986), Kressal et al. (2010), McLeish (2013), Mackay and Simandl (2014), and Chakhmouradian et al. (2015).

Traditional indicator mineral exploration methods use the 0.25–2.0 mm size fraction of unconsolidated sediments (Averill, 2001, 2014; McCurdy, 2006, 2009; McClenaghan, 2011, 2014). Indicator minerals are detectable by QEMSCAN® at particle sizes smaller than those used for hand picking (<0.25 mm). Pre-concentration (typically by shaker table) is used before heavy liquid separation, isodynamic magnetic separation, optical identification using a binocular microscope, and hand picking (McClenaghan, 2011). Following additional sieving, the 0.5-1 and 1-2 mm fractions are hand picked for indicator minerals while the 0.25-0.5 mm fraction is subjected to paramagnetic separation before hand picking (Averill, 2001; McClenaghan, 2011). Hand picking indicator minerals focuses on monomineralic grains, and composite grains may be lost during processing. Composite grains are difficult and time consuming to hand pick and characterize using optical and Scanning Electron Microscopy (SEM) methods. A single grain mount can take 6-12 hours to chemically analyse (Layton-Matthews et al., 2014).

Detailed sample analysis using the QEMSCAN® Particle Mineral Analysis routine allows for 5-6 samples to be analyzed per day. When only mineral identification and mineral concentrations and counts are required, the use of a Bulk Mineral Analysis routine reduces the analysis time from ~4 hours to ~30 minutes per sample.

2. Potential indicator minerals

Pyrochlore supergroup minerals (as defined by Atencio et al., 2010), columbite-tantalite series minerals (as defined by Černý and Ercit, 1985; Černý et al., 1992), rare earth element (REE)-bearing fluorocarbonates (such as bastnaesite and synchysite), monazite, and apatite (Bühn et al., 2001; Belousova et al., 2002) are ideal carbonatite indicator minerals because of their high density and high content of key pathfinder elements such as Nb, Ta, LREE (ΣLa, Ce, Pr, and Nd), and P.

3. Methodology

3.1. Sampling, portable XRF analysis, and processing

Sediments in streams draining the area near the Aley carbonatite contain high concentrations of Nb, LREE, and P (Mackay and Simandl, 2014). Within carbonatites, Nb is predominantly incorporated in pyrochlore and columbite-(Fe), LREE in REE-fluorocarbonates, LREE, P, Th, Y in monazite, and P in apatite.

High pathfinder element (Nb, Ta, LREE, Y, P, Ba, Sr, U, and Th) concentrations determined by pXRF in the 125-250 μm dry sieved fraction (herein referred to as 'RAW') of stream sediments (Mackay and Simandl, 2014) and extent of mineralization in the Aley deposit (Kressal et al., 2010; Jones et al., 2014) gave the expectation that indicator minerals would be detectable by QEMSCAN®.

The Mozley C800 laboratory mineral separator and Wilfley #13 shaking table were tested. Both can consistently concentrate the pathfinder elements and, by extension, targeted indicator minerals; however, the Mozley C800 is more suitable for processing smaller samples (Mackay et al., 2015a, b).

3.2. QEMSCAN® methodology

Approximately 2 g of RAW sample and/or corresponding Mozley C800 concentrate (CON) were mounted on polished smear sections (Fig. 1). Analysis was performed using an

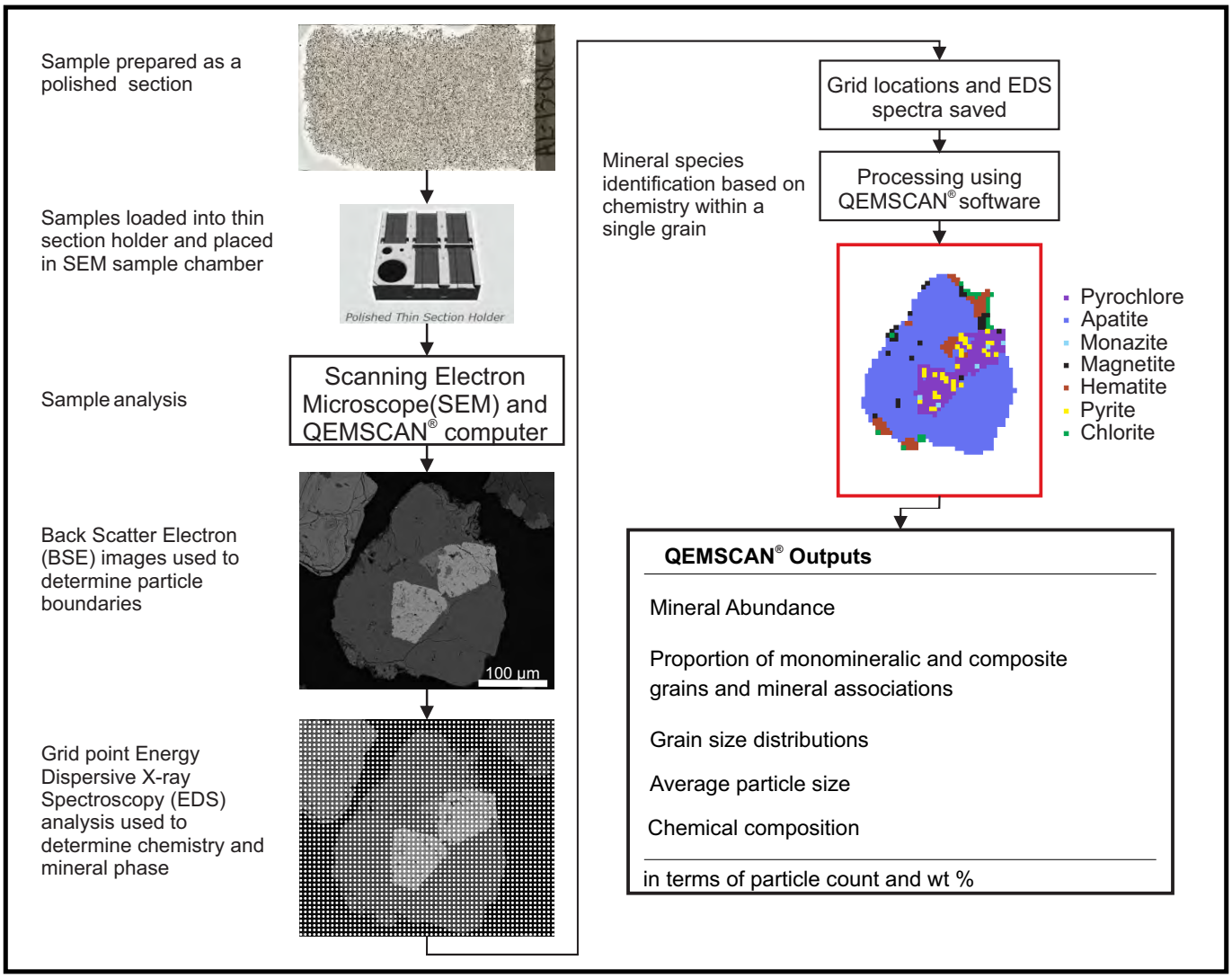

Fig. 1. Flow chart for QEMSCAN® analysis using the Particle Mineral Analysis routine. Based on QEMSCAN® software help file. Example grain is a polymineralic, or composite grain, with seven different mineral phases (identified in red box).

automated FEI Quanta Scanning Electron Microscope (SEM) with a tungsten filament operating at 10.00 nA and a maximum voltage of 25 keV.

The QEMSCAN® procedure and IDiscover® software were used to collect and process data. As part of the automated QEMSCAN® procedure (Particle Mineral Analysis routine), a Back Scatter Electron (BSE) image of each grain was acquired, with individual particle boundaries determined by contrast in brightness (Fig. 1). Energy Dispersive X-Ray Spectroscopy (EDS) analysis, performed on a grid (6.5 µm spacing in this study), provided chemical composition and identified each mineral based on a customized Species Identification Protocol. Mineral abundances in weight percent (wt.%) were calculated using particle volume (based on surface area) and density of the identified mineral. QEMSCAN® analysis output included particle count, mineral wt.%, particle size distribution(s), chemistry, and proportion of monomineralic (or liberated) and composite grains with mineral associations (Fig. 1). QEMSCAN® bulk chemical composition was derived from the chemical composition of mineral particles determined by EDS, volume measurements (which assume the polished smear section has representative mineral composition and each particle is uniform in shape), and idealized mineral densities.

3.3. Chemical analysis

A 3.5-10.5 g split of each RAW sample and corresponding Mozley concentrates was analysed using lithium metaborate fusion followed by ICP-MS for trace elements, Inductively Coupled Plasma Atomic Emission Spectroscopy (ICP-AES) for major elements, and XRF for Nb (when in concentrations >2500 ppm Nb).

4. Results

4.1. Geochemistry

The geochemical composition of the unprocessed 125-250 µm fraction of stream-sediment samples and corresponding

Mozley concentrates from the Aley carbonatite drainage were determined by ICP-MS, ICP-AES, and XRF analyses. Carbonatite pathfinder elements associated with prospective indicator minerals were detected in all samples. Concentrations of Nb in RAW samples from the Aley drainage range from 3000-10,000 ppm with an average of 5900 ppm. Concentrations in corresponding Mozley concentrates are substantially higher, ranging from 11,900-25,900 ppm Nb and averaging 17,600 ppm Nb. Similarly, concentrations of Ta, Zr, LREE, U, Th, and P_2O_5 increased following Mozley processing.

4.2. Indicator mineral abundances

Mineral abundance by wt.% and particle count for each polished smear section were determined using QEMSCAN® analysis. The main carbonatite indicator minerals were detected in RAW samples from the Aley carbonatite without additional processing (Fig. 2). However, minimal processing by Mozley C800 table effectively concentrated heavy indicator minerals (Fig. 2). Specifically, pyrochlore abundance increased on average by 12.9 x, columbite-(Fe) by 2.4 x, monazite by 3.2 x, REE-fluorocarbonates by 2.6 x, apatite by 1.7 x, magnetite by 5.8 x, and zircon by 3.2 x.

5. Discussion

5.1. Particle size distribution

QEMSCAN® provides particle size distributions for individual minerals in terms of particle count and weight percent in the 125-250 µm size fraction of RAW stream sediments and corresponding Mozley concentrates from the Aley drainage area. Particle size distributions measured by particle count for some trace minerals (eg. monazite and REE-fluorocarbonates), are skewed towards smaller (<20 µm) particle diameters. This is most likely due to the presence of small inclusions of these trace minerals in composite grains. The particle count for pyrochlore (Fig. 3a), columbite-(Fe) (Fig. 3c), monazite, and apatite show an overall decreasing trend with increasing distance downstream of source rocks in the Aley carbonatite. Abundant mineral constituents and ore minerals (e.g., pyrochlore and columbite-[Fe]) occur as larger particles with nearly normal distributions of particle diameters (Figs. 3b, d).

5.2. Mineral abundance and pathfinder element concentration

There is a good fit between the concentration of carbonatite pathfinder elements determined using laboratory geochemical analysis and abundance of carbonatite indicator minerals determined by QEMSCAN®. The highest R^2 are obtained by comparing bulk sample chemistry and indicator mineral concentration in terms of wt.%. For example, Nb content is related to pyrochlore (R^2=0.72; Fig. 4a) and columbite-(Fe) (R^2=0.78; Fig. 4b) concentrations; fersmite is a minor constituent (Fig. 2). Total niobate (sum of pyrochlore, columbite-[Fe], and fersmite) concentration shows the best fit with Nb content of samples (R^2=0.90; Fig. 4c). As fersmite is a minor Nb-bearing constituent, a low R^2 between Nb content (XRF) and fersmite concentrations (QEMSCAN®) is expected.

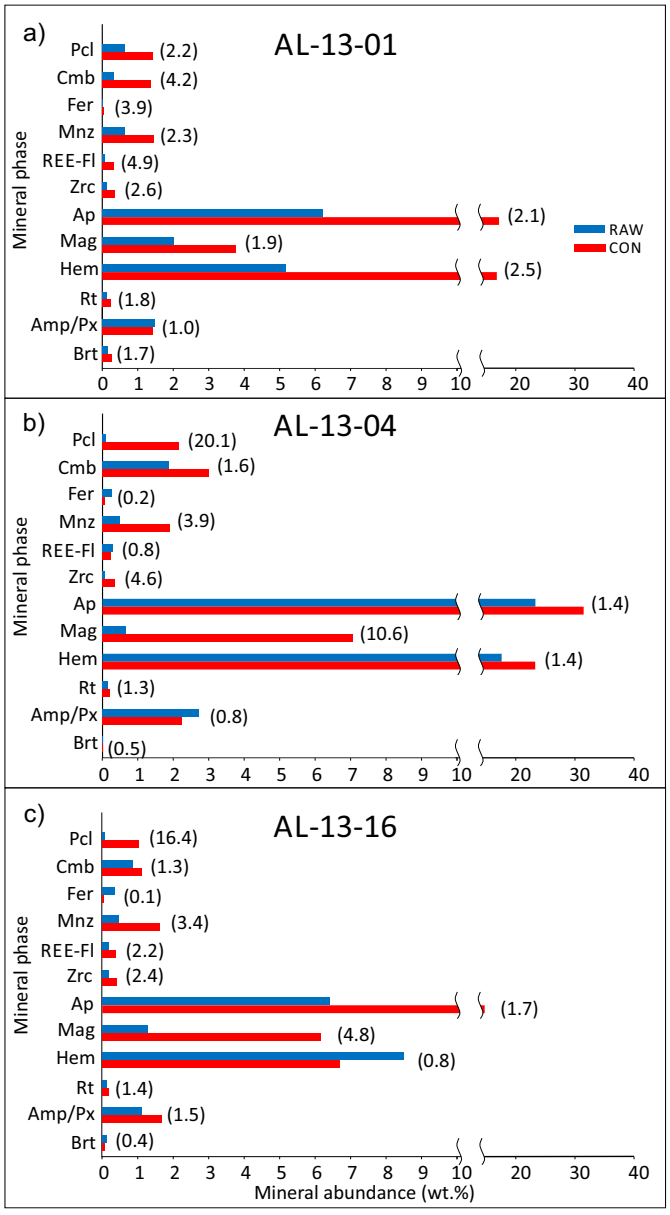

Fig. 2. Mineral abundances (wt.%; determined by QEMSCAN®) for RAW and corresponding Mozley C800 concentrates (CON) for selected samples **a)** AL-13-01, **b)** AL-13-04, and **c)** AL-13-16 from Aley (AL) carbonatite drainage. Concentration factors for CON relative to corresponding unprocessed samples (RAW) are shown in parentheses. Mineral abbreviations: pyrochlore (Pcl); columbite-(Fe) (Cmb); fersmite (Fer); REE-fluorocarbonates (REE-Fl); zircon (Zrc); apatite (Ap); magnetite (Mag); hematite (Hem); rutile (Rt); amphibole/pyroxene (Amp/Px); and barite (Brt).

Light REE content is strongly related to monazite concentration (R^2=0.91) and less strongly to REE-fluorocarbonate concentration (R^2=0.51; Fig. 4d). Concentration of P_2O_5 in RAW samples and corresponding Mozley concentrates is strongly related to apatite concentration (R^2=0.98) and weakly to monazite content (R^2=0.25). Thus, overall indicator mineral

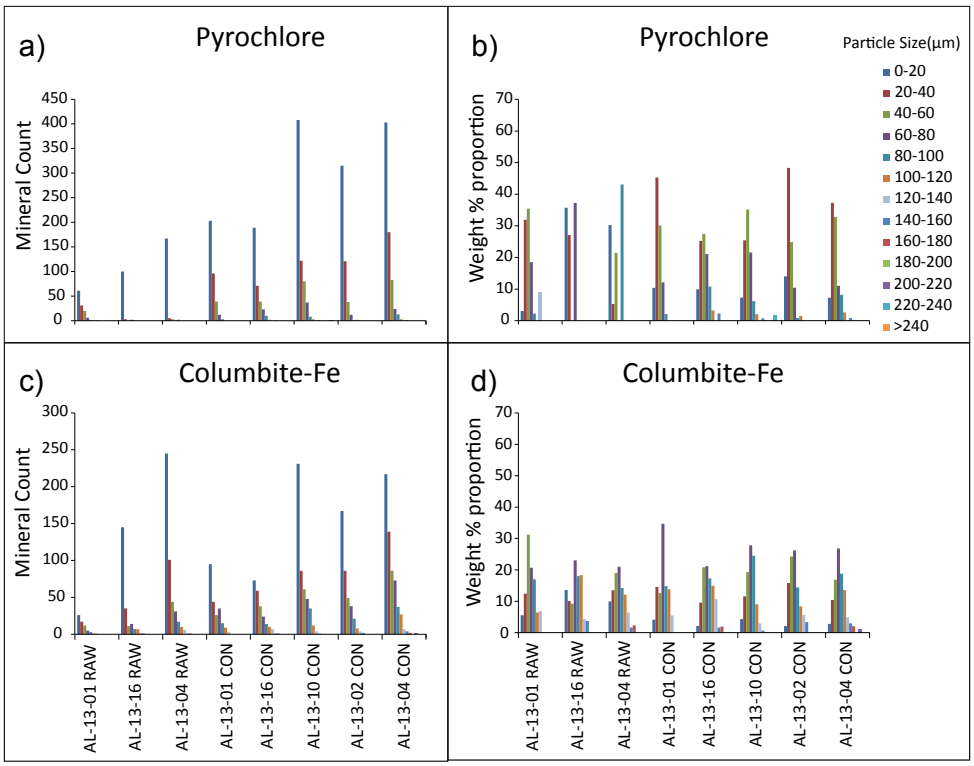

Fig. 3. Particle size distribution in terms of mineral count and wt.%. **a)** and **b)** pyrochlore; **c)** and **d),** columbite-(Fe). RAW samples and corresponding Mozley concentrates (CON) samples are each ordered from west (away from the deposit) to east (nearest the deposit). Mineral sizes are in µm.

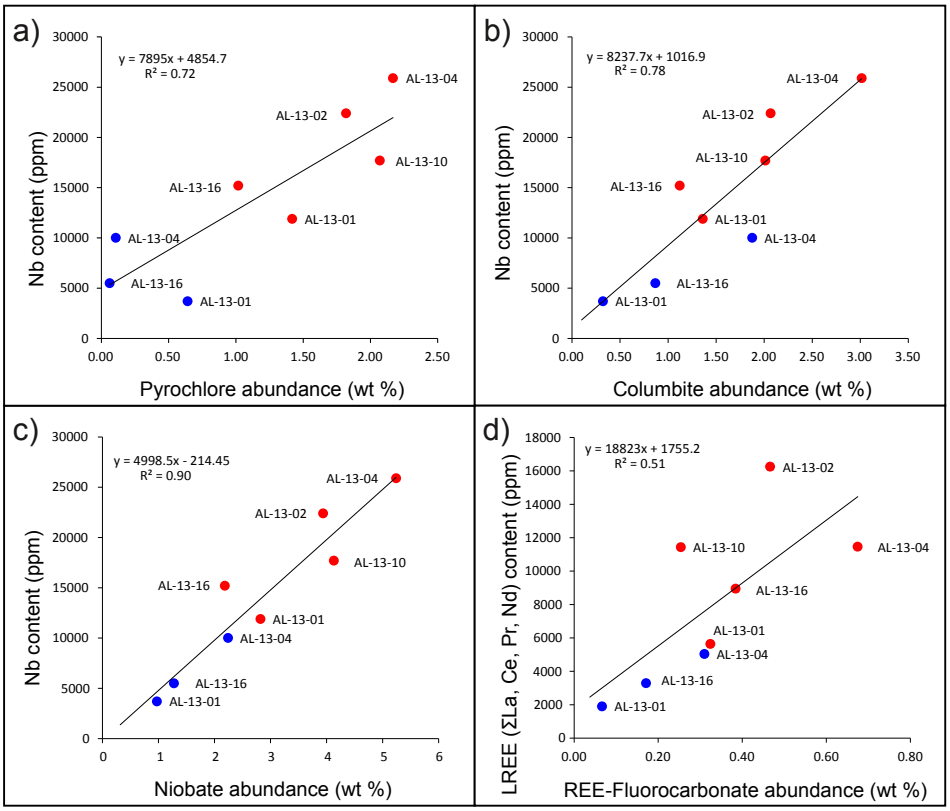

Fig. 4. Relationship between indicator mineral concentrations (determined by QEMSCAN®) and corresponding pathfinder element content for: **a)** Nb vs. pyrochlore; **b)** Nb vs. columbite(Fe); **c)** Nb vs. niobates (includes pyrochlore, columbite-(Fe), and fersmite); **d)** LREE vs. REE-fluorocarbonates. Results are for unprocessed samples (blue circles) and Mozley C800 concentrates (red circles).

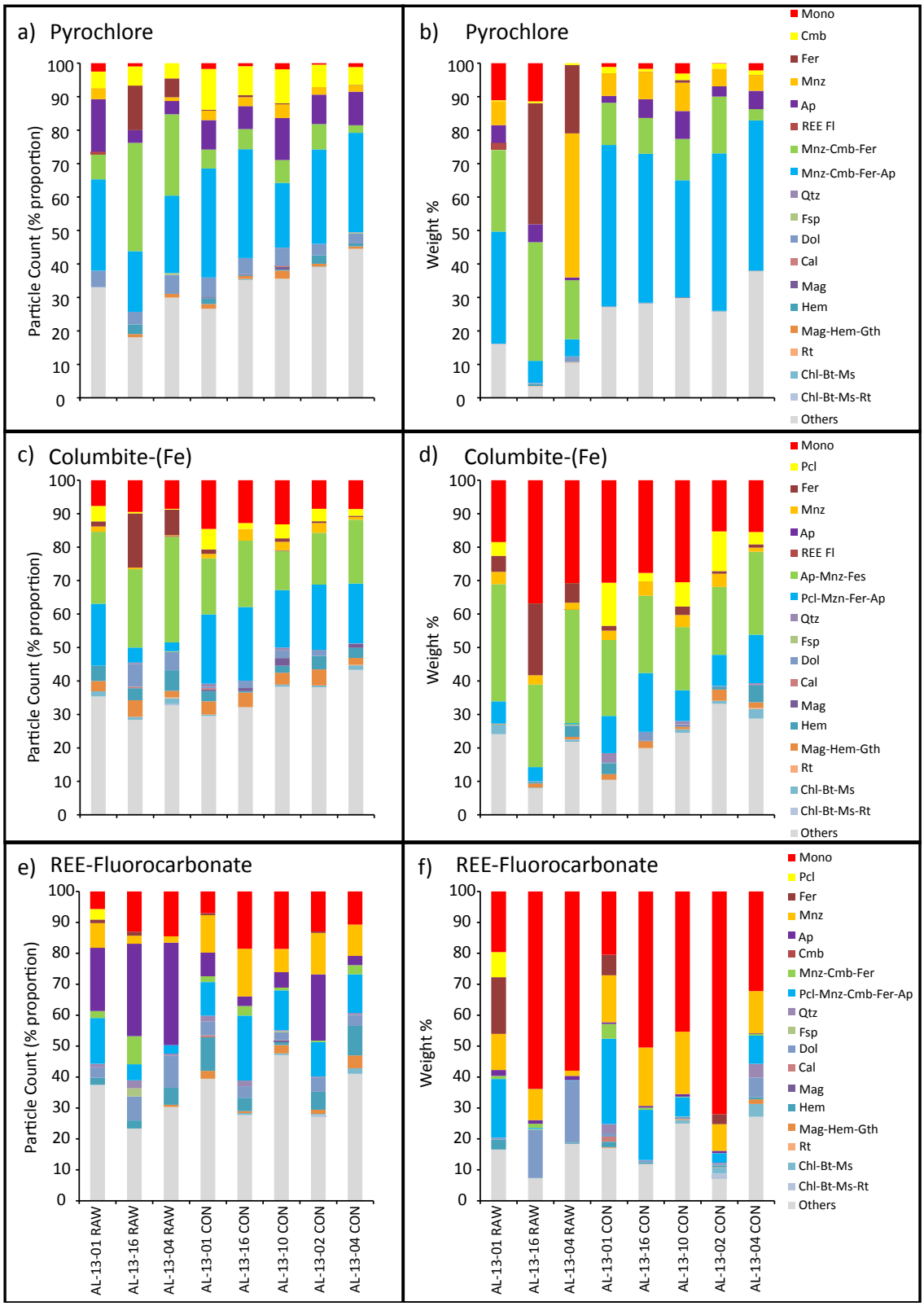

Fig. 5. Proportions of monomineralic (Mono) and composite grains with predominant mineral associations (in terms of mineral count and wt.%) for: **a)** and **b)** pyrochlore; **c)** and **d)** columbite-(Fe); **e)** and **f)** REE-fluorocarbonates. Results are for RAW samples and corresponding Mozley concentrates (CON). Sample distance increases from directly above the deposit (AL-13-04) to 11.5 km downstream (AL-13-01). 'Others' refers to complex composite grains, and those containing unidentified mineral phases. Abbreviations: pyrochlore (Pcl); columbite-(Fe) (Cmb); fersmite (Fer); REE-fluorocarbonates (REE-Fl); apatite (Ap); magnetite (Mag); hematite (Hem); rutile (Rt); quartz (Qtz); dolomite (Dol); calcite (Cal); feldspar (Fsp); hematite (Hem); goethite (Gth); chlorite (Chl); biotite (Bt); and muscovite (Ms).

abundance measured by wt.% is representative of bulk sample composition determined using ICP-MS, ICP-AES, and XRF.

5.3. Mineral association in composite grains

QEMSCAN® determines the quantitative proportions of monomineralic (or liberated) grains and minerals in composite grains. Key mineral associations in composite grains and the proportion of monomineralic grains are shown in Fig. 5. Pyrochlore (wt.%) is predominantly contained in composite grains composed of minerals associated with carbonatite magmatism and alteration (columbite-[Fe], apatite, fersmite, ±monazite; Figs. 5a, b). Apatite (wt.%) is contained predominantly in monomineralic grains. Columbite-(Fe) (Fig. 5d), REE-fluorocarbonates (Fig. 5f), and monazite fall in between these two extremes.

6. Conclusions

QEMSCAN® can detect indicator minerals in the dry sieved 125-250 µm size fraction without additional processing from stream-sediment samples taken near the Aley carbonatite. Minimal processing using a Mozley C800 mineral separator increases the concentration of indicator minerals found in low concentrations in a predictable way. QEMSCAN® can detect and characterize particle sizes too small for hand picking and provides quantifiable proportions of monomineralic grains and mineral associations in composite grains. QEMSCAN® can fully characterize a sample in 3.5-4.5 hours using the 'Particle Mineral Analysis' routine, much faster than the 6-12 hours required for traditional techniques to characterize a single sample with mineralogically complex grains.

Acknowledgments

This project was supported by the Targeted Geoscience Initiative 4 (2010–2015), a Natural Resources Canada program. The Specialty Metal component of this program was carried out collaboratively between the Geological Survey of Canada and the British Columbia Geological Survey. Bureau Veritas Commodities Canada Ltd., Inspectorate Metallurgical Division and Acme Analytical Laboratories are thanked for access to laboratory equipment and the expert advice of their staff. Helicopter and logistical support during sampling from Taseko Mines Limited and information provided by Jeremy Crozier (Hunter Dickinson Inc.) are greatly appreciated.

References cited

Atencio, D., Andrade, M.B., Christy, A.G., Gieré, R., and Kartashov, P.M., 2010. The pyrochlore supergroup of minerals: nomenclature. The Canadian Mineralogist, 48, 673-698.

Averill, S.A., 2001. The application of heavy indicator mineralogy in mineral exploration with emphasis on base metal indicators in glaciated metamorphic and plutonic terrains. In: McClenaghan, M.B., Bobrowsky, P.T., Hall, G.E.M., and Cook, S.J. (Eds.) 2001. Drift exploration in glaciated terrain. Geological Society, London, Special Publication, 185, 69-81.

Averill, S.A., 2014. Indicator mineral fingerprints in surficial sediments near Cu-Au deposits of the porphyry-epithermal-volcanogenic suite. In: McClenaghan, M.B., Plouffe, A., and Layton-Matthews, D., (Eds.) 2014. Application of indicator mineral methods to mineral exploration. Geological Survey of Canada, Open File 7553, 35-44.

Belousova, E.A., Griffin, W.L., O'Reilly, S.Y., and Fisher, N.I., 2002. Apatite as an indicator mineral for mineral exploration: trace-element compositions and their relationship to host rock type. Journal of Geochemical Exploration, 76, 45-69.

Bühn, B., Wall, F., and Le Bas, M.J., 2001. Rare-earth element systematics of carbonatitic fluorapatites, and their significance for carbonatite magma evolution. Contributions to Mineralogy and Petrology, 141, 572-591.

Černý, P., and Ercit, T.S., 1985. Some Recent Advances in the Mineralogy and Geochemistry of Nb and Ta in Rare-Element Granitic Pegmatites. Bulletin Minéralogie, 108, 499-532.

Černý, P., Ercit, T.S., and Wise, M.A., 1992. The Tantalite-Tapiolite Gap: Natural Assemblages versus Experimental Data. The Canadian Mineralogist, 30, 587-596.

Chakhmouradian, A.R., Ekaterina, P.R., Kressall, R.D., Crozier, J., Pisiak, L.K., Sidhu, R., and Yang, P., 2015. Carbonatite-Hosted Niobium Deposit at Aley, Northern British Columbia (Canada): Mineralogy, Geochemistry and Petrogenesis. Ore Geology Reviews, 64, 642-666.

Jones, S., Merriam, K., Yelland, G., Rotzinger, R., and Simpson, R.G., 2014. Technical report on mineral reserves at the Aley project, British Columbia, Canada. Taseko Mines Limited, 291 p. <www.sedar.com> accessed February 3, 2015.

Kressall, R., McLeish, D.F., and Crozier, J., 2010. The Aley carbonatite complex – Part II petrogenesis of a Cordilleran niobium deposit. In: Simandl, G.J., and Lefebure, D.V., (Eds.), International workshop on the geology of rare metals, November 9-10, 2010, Victoria, Canada. Extended Abstracts Volume. British Columbia Ministry of Energy and Mines, British Columbia Geological Survey, Open File 2010-10, pp. 25-26.

Layton-Matthews, D., Hamilton, C., and McClenaghan, M.B., 2014. Mineral chemistry: modern techniques and applications to exploration. In: McClenaghan, M.B., Plouffe, A., and Layton-Matthews, D., (Eds.) 2014. Application of indicator mineral methods to mineral exploration. Geological Survey of Canada, Open File 7553, 9-18.

Mackay, D.A.R., and Simandl, G.J., 2014. Portable X-ray fluorescence to optimize stream sediment chemistry and indicator mineral surveys, case 1: Carbonatite-hosted Nb deposits, Aley carbonatite, British Columbia, Canada. In: Geological Fieldwork 2013, British Columbia Ministry of Energy and Mines, British Columbia Geological Survey, Paper 2014-1, pp. 183-194.

Mackay, D.A.R., Simandl, G.J., Grcic, B., Li, C., Luck, P., Redfearn, M., and Gravel, J., 2015a. Evaluation of Mozley C800 laboratory mineral separator for heavy mineral concentration of stream sediments in exploration for carbonatite-related specialty metal deposits: case study at the Aley carbonatite, northeastern British Columbia (NTS 094B). In: Geoscience BC Summary of Activities 2014, Geoscience BC, Report 2015-1, pp. 111-122.

Mackay, D.A.R., Simandl, G.J., Luck, P., Grcic, B., Li, C., Redfearn, M., and Gravel, J., 2015b. Concentration of carbonatite indicator minerals using a Wilfley gravity shaking table: A case history from the Aley carbonatite, British Columbia, Canada. In: Geological Fieldwork 2014,

British Columbia Ministry of Energy and Mines, British Columbia Geological Survey, Paper 2015-1, pp. 189-195.

Mäder, U.K., 1986. The Aley carbonatite complex. Unpublished Master of Science thesis, University of British Columbia, 176 p.

McClenaghan, M.B., 2011. Overview of common processing methods for recovery of indicator minerals from sediments and bedrock in mineral exploration. Geochemistry: Exploration, Environment, Analysis, 11, 265-278.

McClenaghan, M.B., 2014. Overview of indicator mineral recovery methods for sediments and bedrock: 2013 update. In: McClenaghan, M.B., Plouffe, A., and Layton-Matthews, D., (Eds.) 2014. Application of indicator mineral methods to mineral exploration. Geological Survey of Canada, Open File 7553, 1-7.

McCurdy, M.W., Kjarsgaard, I.M., Day, S.J.A., McNeil, R.J., Friske, P.W.B., and Plouffe, A., 2009. Indicator mineral content and geochemisty of stream sediments and waters from northeast British Columbia (NTS 94A, 94B, 94G, 94H, 94I, 94K, 94N, 94O, 94P). British Columbia Ministry of Energy and Mines, Geological Survey of British Columbia, Report 2009-2 and Geological Survey of Canada, Open File 6311, 19 p.

McCurdy, M.W., Prior, G.J., Friske, P.W.B., McNeil, R.J., Day, S.J.A., and Nicholl, T.J., 2006. Geochemical, mineralogical and kimberlites indicator mineral electron microprobe data from silts, heavy mineral concentrates and water from a national geochemical reconnaissance stream sediment and water survey in northern and southwestern Buffalo Head Hills, northern Alberta (parts of 84B, 84C, 84F, and 84G): Alberta Energy and Utilities Board, Alberta Geological Survey, Special Report 76 and Geological Survey of Canada Open File 5057, 11 p.

McLeish, D.F., 2013. Structure, stratigraphy, and U-Pb zircon-titanite geochronology of the Aley carbonatite complex, northeast British Columbia: Evidence for Antler-aged orogenesis in the foreland belt of the Canadian Cordillera. Unpublished Master of Science thesis, University of Victoria, 131 p.

Visible to shortwave infrared reflectance spectroscopy of rare earth element minerals

D. Turner[1, a], B. Rivard[2], and L. Groat[1]

[1] Department of Earth, Ocean and Atmospheric Sciences, University of British Columbia, Vancouver, BC, V6T 1Z4
[2] Department of Earth and Atmospheric Sciences, University of Alberta, Edmonton, AB, T6G 2E3
[a] corresponding author: dturner@eos.ubc.ca

Recommended citation: Turner, D., Rivard, B., and Groat, L., 2015. Visible to shortwave infrared reflectance spectroscopy of rare earth element minerals. In: Simandl, G.J. and Neetz, M., (Eds.), Symposium on Strategic and Critical Materials Proceedings, November 13-14, 2015, Victoria, British Columbia. British Columbia Ministry of Energy and Mines, British Columbia Geological Survey Paper 2015-3, pp. 219-229.

1. Introduction

The mineralogy of rare earth element (REE) ore deposits is critical in understanding their petrogenesis but also has significant implications for metallurgy. Like many ore deposits, high-grade rocks do not necessarily equate to positive economic viability and this is especially true for REE deposits. Consequently, knowledge of sample mineralogy acquired early in a project's life can lead to more efficient exploration programs through confirmation of either 'good' or 'bad' mineralogy. Many REE minerals show fine grain sizes and their accumulation can be difficult to recognize in hand sample or drill core with an unaided eye. Knowledge of their distribution before sampling can ensure that the best rocks or core lengths are sampled for petrographic or detailed study.

REE minerals generally have complex yet diagnostic absorption patterns in visible to shortwave infrared (VNIR-SWIR) reflectance spectra that are driven primarily by REE-related 4*f*-4*f* intraconfigurational electronic transitions. Our recent research (Turner et al., 2014, Turner 2015) has focused on three important mineral classes: REE fluorocarbonates (bastnaesite, synchysite, and parisite), REE phosphates (monazite, xenotime, and britholite), and REE-bearing silicates (cerite, mosandrite, kainosite, zircon and eudialyte). Reflectance spectra were acquired in the visible to short wave infrared regions (500 nm to 2500 nm) and samples were characterized using scanning electron microscopy and electron microprobe analysis. The results of our work and publications from other research groups (e.g., Rowan et al., 1986, Swayze et al., 2013, Hoefen et al., 2014, Boesche et al., 2015) have shown the strong applicability of reflectance spectroscopy and hyperspectral imaging to understanding, exploring, and exploiting rare earth element ore deposits and their associated rocks.

2. Background information

2.1. The lanthanides and the rare earth elements

The lanthanides (*Ln*) are a series of 15 elements from lanthanum (La, atomic number 57) to lutetium (Lu, atomic number 71). One of these, promethium (Pm, atomic number 61) is not naturally occurring, leaving only 14 for consideration in natural systems. The lanthanides are characterized by the presence of the 4*f* orbital block in the conventional periodic table of the elements that can accommodate 14 electrons in the seven orbital configurations. Elements of the 5*f* orbital block are known as the actinides and include uranium (U) and thorium (Th). In geological environments the lanthanides are commonly found together in their trivalent state, with the exception of divalent europium (Eu) and, in some cases, tetravalent cerium (Ce) and terbium (Tb).

Rare earth elements (REE) comprise the lanthanide group of elements, commonly yttrium (Y, atomic number 39) and sometimes scandium (Sc, atomic number 21). The two latter elements show similar non-*f*-block electronic structure and are locally enriched in similar rocks. The REE are commonly inconsistently subdivided by the mineral exploration industry and geoscientists into the light rare earth elements (LREE, generally La through Gd) and heavy rare earth elements (HREE, generally Tb through Lu + Y). Uncommonly a medium rare earth element (MREE) group is defined with variable identity. The lanthanides with even atomic numbers are more geologically abundant than the odd-numbered lanthanides. This gives rise to a zig-zag pattern across the REE series, which is then commonly 'removed' through normalization of REE values to C1 Chondrite concentrations.

In general, when moving from a neutral lanthanide atom with basic electronic configuration to the Ln^{3+} cation commonly found in minerals, electrons from the 4*f*, 5*d* and 6*s* shells are stripped leaving a clean configuration of a sequentially occupied 4*f* orbital. At the start of the *Ln* series, lanthanum (La) has no unpaired 4*f* electrons (f^0), with a sequential increase of unpaired electrons (e.g., Ce and Yb as f^1 and f^{13}) towards gadolinium, which has seven unpaired electrons (f^7) available for electronic excitations. Lutetium (Lu), at the end of the *Ln* series has a filled 4*f* orbital (f^{14}) and therefore no unpaired electrons. The ionic radius of the lanthanides systematically decreases from La (largest) to Lu (smallest). The Ln^{3+} cations are generally most similar in ionic radius to U^{4+}, Th^{4+}, and Ca^{2+}. The outer radius of the 4*f* electron shells (~30 picometres, pm) for the

lanthanides is much less than that of the filled 5*s* and 5*p* shells (~200 pm, ~105 pm). Consequently, first assumptions suggest that the local electronic environment of Ln^{3+} cations interacts primarily with those outer shells, leaving the 4*f* shell relatively 'sheltered' and non-participatory in bonding.

2.2. Rare earth element minerals

In minerals, the REE predominantly populate roomy but distorted crystallographic sites with coordination numbers of eight or more. The contraction of ionic radius along the lanthanide sequence results in the heavy rare earth elements (e.g., Lu) having a greater predisposition for smaller coordination numbers (e.g., 8), whereas the larger light rare earth elements (e.g., La) prefer higher coordination numbers (e.g., 11) and longer ligand distances. This difference results in certain minerals having distinct enrichment patterns in either the light or heavy rare earths. For example, the allanite group minerals (11-coordinated, *Ln*-O to ~3.2 Å) are LREE-enriched whereas xenotime (8-coordinated, *Ln*-O ~2.3 Å) is defined by HREE+Y enrichment. The mineralogy of REE dominant phases can be largely ascribed to four broad mineral classes: carbonates, phosphates, silicates and oxides.

The REE carbonates mainly comprise the fluorocarbonate minerals bastnaesite, synchysite, parisite and rontgenite which all share a common stacking arrangement of CeF-CO_3 and Ca-CO_3 layers in variable ratios. Cordylite, burbankite and ancylite are REE-Ba-Sr-bearing carbonates whereas sahamalite is a REE-Mg-Fe species. Coordination of REE in these minerals is usually either 9 or 10, and mixed anion identities (e.g., O^{2-}, OH^- and F^-) are common. Consequently, bond lengths between cations and their coordinated anions vary considerably (from ~2.37 to 2.77 Å) and distortion of the coordination polyhedra is significant. REO contents for these minerals are generally high, with bastnaesite in particular showing up to ~75%.

The most common REE phosphates are monazite, xenotime and britholite. These minerals show a range of coordination states from 7 to 12 with bond lengths as short as 2.25 and as long as ~3.2 Å. Cation and anion substitutions in these minerals can be substantial with complex crystal chemical implications, such as in britholite. REO contents for these minerals are generally high and up to ~70%. Other REE bearing silicates other than those listed as examples of diverse coordinations include eudialyte, zircon, and kainosite.

The REE-bearing silicates are a diverse set of minerals with a wide range of coordination and overall crystal chemistry and structure. Coordination numbers for cation polyhedra range from 6 (gittinsite) to 11 (allanite), with some cases showing mixed anion coordination (cerite, 8 oxygen + 1 OH^-/F^-) and other minerals having more than one distinct REE site (mosandrite). Documented bond lengths vary accordingly, ranging from ~2.2 to ~3.2 Å. Crystal structures of many of the REE silicates are still not fully understood. Accordingly, REO contents for these minerals are variable and generally lower, but can be up to ~70%.

The oxide class comprises a number of different groupings based on how the oxide is structured, the number of distinct cation sites as well as the identity and charge of the cations. The more common REE oxide minerals include fergusonite, samarskite, aeschynite, euxenite, brannerite, and loparite (e.g., Mariano and Mariano, 2012), although the list of REE-bearing oxide species is long. These minerals are commonly Fe, U and Th bearing, and metamict samples seem to be the norm rather than the exception in the literature and in mineral museums. Like the REE silicates, REO contents for these minerals are variable and generally lower, but can be up to ~60%.

2.3. Reflectance spectroscopy and hyperspectral imaging

The aim of reflectance spectroscopy is to obtain and interpret diagnostic absorption, reflection and emission properties of a target mineral (e.g., Clark, 1999). By relying on reflected light, sample preparation is greatly reduced and the analytical environments and types of potential targets are dramatically expanded, as compared to transmitted light spectroscopy commonly used by chemists in a laboratory setting. In remote sensing, spectrometers have been mounted on satellites and aircraft and used in diverse scientific applications including forest canopy, ecosystem, urban development, geologic, environmental, and planetary investigations. Hyperspectral imaging (also known as imaging spectroscopy) can be thought of as pixel-based reflectance spectroscopy where each pixel in a scene contains a spectrum. These pixels can be built up one by one via rastering of a spot spectrometer, line by line via arrays of scanning spectrometers or, more recently, as intact 'image cubes' via snapshot imaging spectrometers.

Wavelength ranges of electromagnetic energy (light) used in reflectance spectroscopy are roughly divided into ultraviolet (UV, 1 to 400 nm), visible (VIS, 400 nm to 700 nm), near infrared (NIR, 700 to 1000 nm), short wave infrared (SWIR, 1000 to 2500 nm), mid infrared (MIR, 2.5 to 8 μm) and longwave infrared (LWIR, 8 μm to 14 μm). The term VNIR (visible to near infrared) is typically from 400 nm to 1000 nm.

The interaction between electromagnetic radiation and crystalline matter results in reflection, refraction, absorption, and emission (e.g., Clark, 1999). Together, reflection and refraction define the geometrical re-distribution of photons and can be collectively termed scattering. As light passes through crystalline material it can also be absorbed by electronic and vibrational processes. The longer the ray path interacts with the target, the greater the absorption at diagnostic wavelengths from diagnostic features. When the light returns back to the spectrometer we obtain a spectrum related primarily to the nature of the material in the field of view.

Absorption bands are local attenuations of reflected light at specific wavelengths, and are generated by the target absorbing energy. The location, intensity and shape of these features can be used qualitatively and quantitatively to discern chemical and structural information about the target material (e.g., Mustard, 1992; Salisbury, 1993; Cloutis et al., 2006). In the VNIR-SWIR range, electronic and vibrational processes are the most relevant for reflectance spectroscopy of geological materials.

Electronic processes in minerals that generate absorption features in the VNIR-SWIR include crystal field effects, intervalence and metal-oxygen charge transfers, band gaps, and colour centres. Crystal field effects deal primarily with intraorbital transitions of unpaired electrons belonging to elements of the transition, lanthanide, and actinide elements. A cation with unfilled orbitals placed into a crystal field will have the energy levels of its orbitals split into lower and higher states, which allows for excitation of relaxed 'lower' electrons into higher energy levels (Fig. 1). The relative energy levels of split orbitals depend primarily on the symmetry and coordination geometry of the locally bonding ions as well as their identity (i.e., the cation-anion polyhedron; Burns, 1993). A common example of crystal field effects is the substitution of trace amounts of $^{VI}Cr^{3+}$ for $^{VI}Al^{3+}$ in corundum, leading to absorption bands centred near 420 and 550 nm (violet and green-yellow). This results in strong transmission in the 'red' region of white light and the gemstone variety known as ruby. In the mineral beryl, $^{VI}Cr^{3+}$ substituting also for $^{VI}Al^{3+}$, but in a slightly different coordination polyhedron, leads to green transmission and the gemstone variety known as emerald.

Many vibrational modes result in absorption features in the VNIR-SWIR. These features are the result of resonance between incident electromagnetic radiation and chemical bonds in minerals. In particular, the presence of water, hydroxyl and carbonate generate absorption features in the 1000 to 2500 nm through combinations and overtones of fundamental vibrations (e.g., Metal-OH bending or OH stretching) whereas the bonds between oxygen and silicon, phosphorous, and sulfur are more prominent at longer wavelengths beyond 2500 nm.

2.4. Spectroscopy of Ln^{3+} in minerals

The spectroscopic absorptions of Ln^{3+} cations in minerals are primarily the result of intraconfigurational 4*f*-4*f* electronic transitions. The positions and intensities of energy levels (known as Stark sublevels or multiplets) for a given lanthanide ion are governed by electrostatic, spin-orbit and crystal field interactions (e.g., Binnemans, 1996). Despite the efficient shielding of the 4*f* open orbitals by the 5*s* and 5*p* closed orbitals, the energy levels defining intraconfigurational 4*f* absorption features are not static, and subtle changes do occur depending on the specific asymmetry of the coordination polyhedron. It is this last splitting factor, the crystal field, that we are most concerned with when investigating REE-bearing minerals (e.g., Turner, 2015). The magnitude of the crystal field effects can be on the order of several hundred 100 cm^{-1} (e.g., Dieke, 1968; Fig. 2). In the VNIR range (e.g., @600 nm) this translates to positional variability of absorption bands on the order of ~10 nm and in the SWIR range (e.g., @2000 nm) this translates to ~80 nm. Generally, the greater the asymmetry of the coordination polyhedron the greater the splitting of energy levels. Similarly, a greater misfit of a Ln^{3+} cation in that coordination polyhedron will generally lead to a greater absorption coefficient. Some transitions however, are more sensitive to coordination character than others (e.g., Görller -Walrand and Binnemans, 1998).

Because intraconfigurational 4*f*-4*f* transitions require unpaired electrons in the 4*f* orbitals, not all lanthanides are spectrally active (e.g., La^{3+}, Ce^{4+} and Lu^{3+}). Compilation of Ln^{3+} absorption bands was completed by the late 1960s by Dieke et al. (1968) using high symmetry halide crystals because they best approximated a free ion state without significant crystal field effects (Fig. 3). Some of the lanthanides show hundreds of potential absorptions lines before crystal field splitting (e.g., Gd^{3+} with 327 distinct levels across 119 multiplets). For the purposes of conventional VNIR-SWIR reflectance spectroscopy however, we only consider absorptions from 4000 cm^{-1} (2500 nm) to 25,000 cm^{-1} (400 nm).

2.5. Principal factors influencing reflectance spectra of REE minerals

The previous sections touched briefly on the identity of the REE, the more common minerals they form, and how REE are hosted in these minerals. Basic principles of reflectance spectroscopy were presented as well as the particular electronic transitions seen in the lanthanides. Collectively, what causes the absorption features in the reflectance spectra of these REE-bearing minerals?

The most important factor is the concentration of lanthanides in a given mineral. Minerals with higher REE content will generally show stronger absorption features. In this sense, it is important to remember that many REE plots display data normalized to CI Chondrite values, not absolute concentrations. For example, even though Tm_2O_3 is commonly equally 'enriched' as neighbouring Yb_2O_3 in normalized diagrams, Yb is usually ~4 times greater in abundance. Therefore, even in HREE-enriched minerals Tm_2O_3 is rarely above 1 wt.% and therefore Tm^{3+} will only have very weak absorptions in the spectra of REE minerals.

Next, the coordination polyhedron of the Ln^{3+} cation and the nature of the ligands affect the specific locations of absorptions and the probability of a given intraconfigurational transition (i.e., the absorption coefficient or intensity parameters; e.g., Görller -Walrand and Binnemans, 1998).

The actinide elements U and Th are common in many REE minerals and these elements host electrons in 5*f* orbitals. Uranium can show a variety of oxidation states but most commonly exhibits 4+ or 5+ valence charge. Absorptions related to $U^{4+,5+}$ are particularly noticeable in zircon. Thorium is most common as Th^{4+} and as such has no unpaired 5*f* electrons and therefore is not spectrally active in this respect.

Other factors that drive the overall reflectance spectra of REE minerals are those that affect other 'normal' minerals. These include crystal field effects of transition metals, charge transfers, colour centres, and conduction bands. Vibrational processes are also very important drivers of reflectance spectra (Fig. 4).

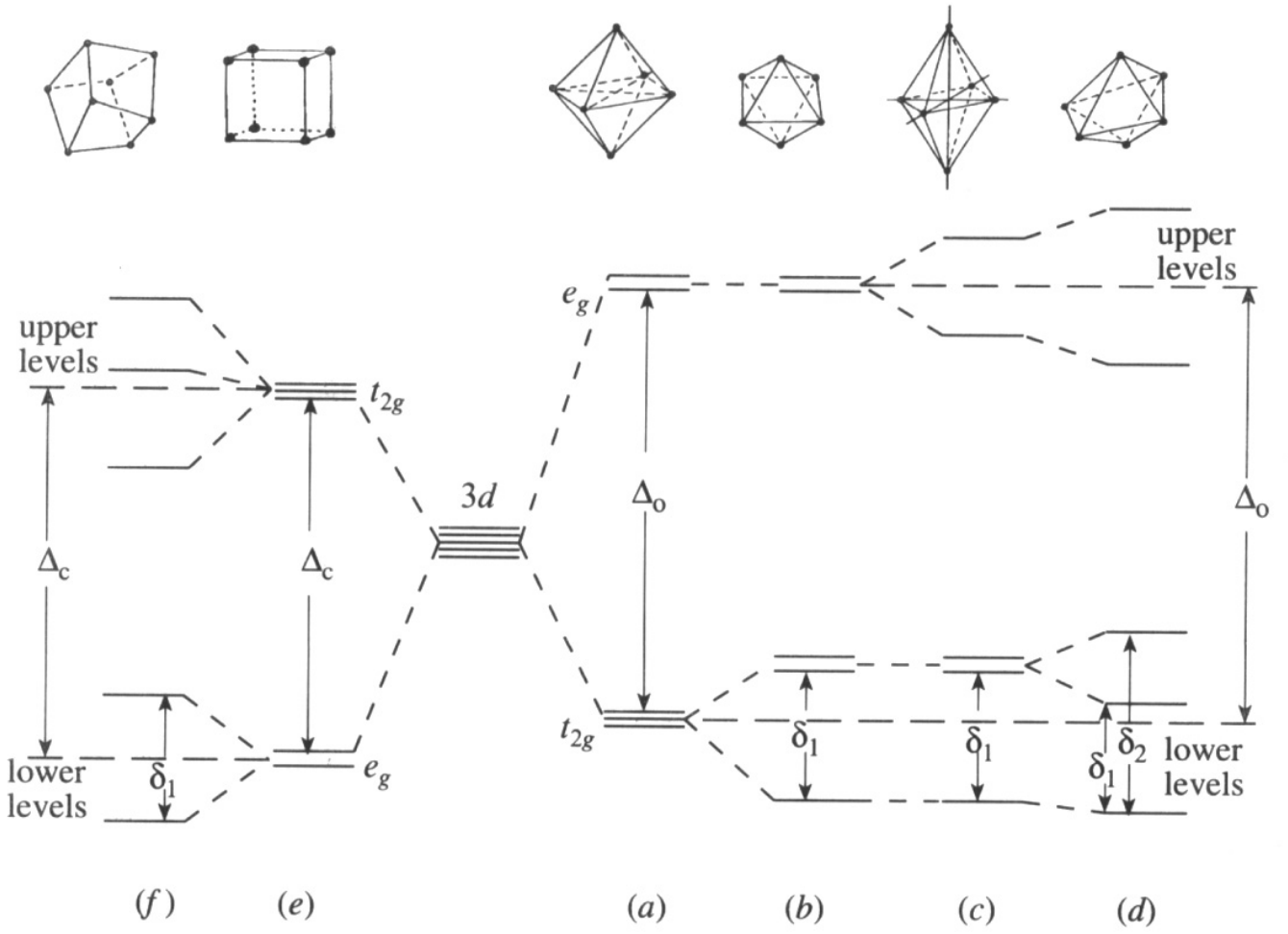

Fig. 1. Splitting of energy levels of the five *d* orbitals by cubic (**e**, **f**) and octahedral crystal fields (**a** – **d**). The Jahn Teller effect describes the subsplitting of the orbital groups by term δ, due to asymmetric distortion of a cubic environment. (From Burns 1993).

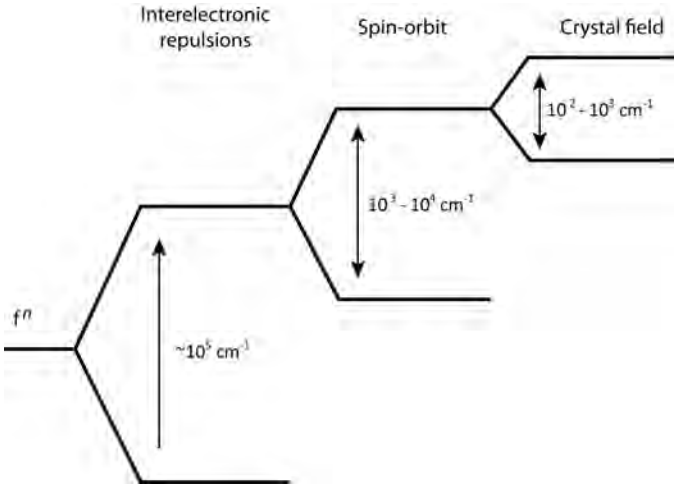

Fig. 2. Schematic representation of 4*f* energy level splitting for the lanthanides with approximate magnitudes of the splitting effects. (Modified from Malta and Carlos, 2003).

3. Examples of REE mineral reflectance spectra

3.1. The importance of REE content

The total concentration of spectrally active Ln^{3+} in a sample will impact its reflectance spectrum. Figure 5 shows 4 spectra of phosphates from the USGS Spectral Library (Speclib 06a). The pink spectrum is OH-bearing apatite lacking Ln^{3+} absorption bands whereas the red and black spectra are F- and Cl-bearing apatite with noticeable Nd^{3+} related absorptions and therefore at least trace amounts of Nd. Monazite, on the other hand, with ~60 wt.% REO, shows very strong Ln^{3+} related absorptions including Nd^{3+} at the same general location as in F and Cl bearing apatite.

Figure 6 shows reflectance spectra of four REE bearing silicates (mosandrite, cerite and 2 eudialyte samples). The plot at right shows continuum-removed spectra of the four samples and the deeper Nd^{3+} related absorptions are associated with higher Nd content. Figures 5 and 6 show that a relationship exists between the strength of at least some Ln^{3+}-related absorption bands and the concentrations of those REE in the host minerals.

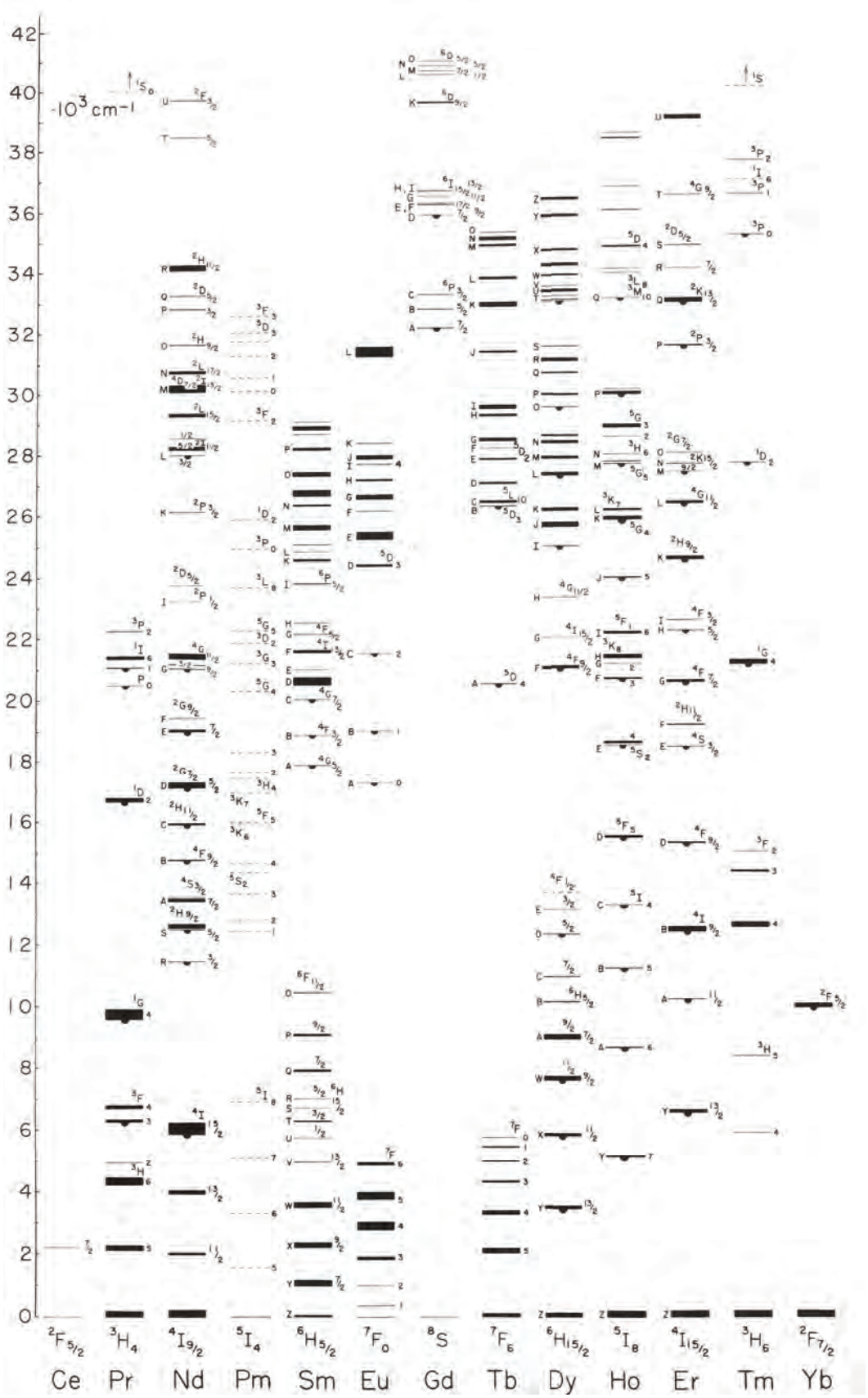

Fig. 3. 'Dieke diagram' of Ln^{3+} intraconfigurational transitions with values in X1,000 cm^{-1}. Lines represent free ion energy levels with electron repulsion and spin-orbit interactions but before effects of a crystal field. (From Dieke et al., 1968).

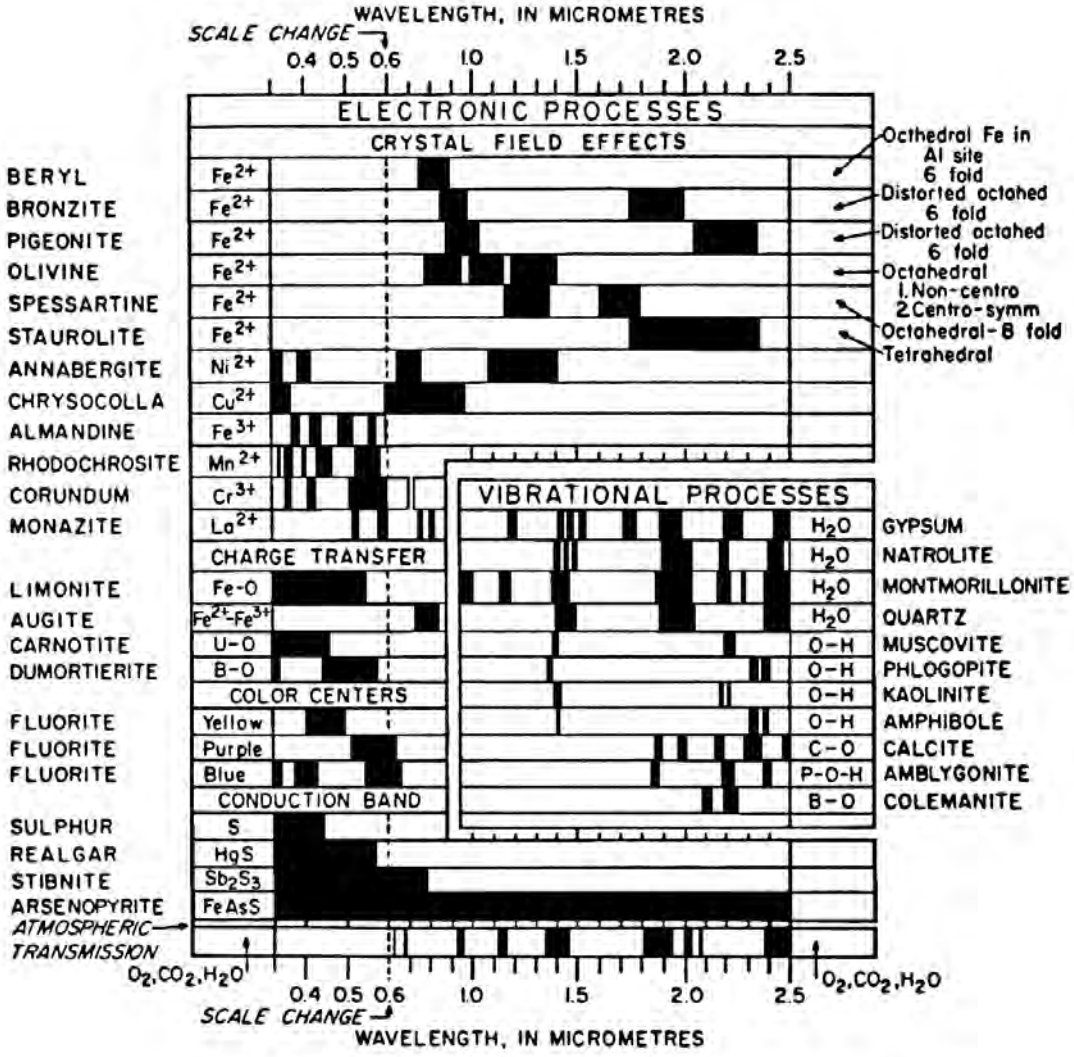

Fig. 4. Positions of diagnostic absorptions (from Hunt, 1977). Widths of black bars indicate the relative widths of absorption bands.

3.2. The importance of structure

The coordination polyhedra around Ln^{3+} can affect the positions and relative strengths of Ln^{3+} related absorptions. Figure 7 shows the coordination polyhedron of REE in parisite (a) alongside the crystal structures for bastnaesite (c, $LnCO_3F$), parisite (b, $CaLn_2(CO_3)_3F_2$) and synchysite (d, $CaLn(CO_3)_2F$). Because the site is effectively identical in each of these minerals the resulting Ln^{3+} related absorptions are also effectively identical (Figs. 8 and 9).

Conversely, coordination polyhedra that are markedly different can show significant differences in the morphology of absorptions related to the same lanthanide. For example, in Figure 6 the absorption "triplet" with bands centred near 746, 803 and 875 nm are all related to Nd^{3+} intraconfigurational electron transitions. However, it is clear that the specific locations and relative strengths of the absorption bands change depending on the coordination polyhedra of the host crystal structure. In this particular circumstance, cerite hosts three unique sites for REE that are each 9-coordinated, eudialyte hosts two unique sites for REE that are 6 and ~9-coordinated, and mosandrite hosts REE in three unique sites that are 7 and 6-coordinated.

The relative strength of an absorption feature (i.e., the absorption coefficient) can also depend on the coordination polyhedron and how well a particular Ln^{3+} 'fits' into the existing polyhedron and structure of the mineral host, both in terms of size and valence charge. Figure 10 displays reflectance spectra of kainosite (an HREE enriched silicate with 1.56 wt.% Er_2O_3 and 1.55 wt.% Yb_2O_3) and REE-enriched zircon (with 0.16 wt.% Er_2O_3 and 0.30 wt.% Yb_2O_3). The absorption features near 978 nm are predominantly related to a Yb^{3+} transition and less so to Er^{3+}. In kainosite, $^{VIII}Ln^{3+}$ can reside at only one site, and its size parameters (expected ionic radius from structure = 1.002 Å) are well suited for the HREE, like Yb^{3+} (ionic radius of 3+ cation = 0.985 Å). In zircon Ln^{3+} substitute for $^{VIII}Zr^{4+}$ in a site that is much smaller (expected ionic radius from structure = 1.002 Å) than Yb^{3+}. We postulate that this size misfit and charge imbalance in zircon drives its stronger Yb^{3+}-Er^{3+} absorption

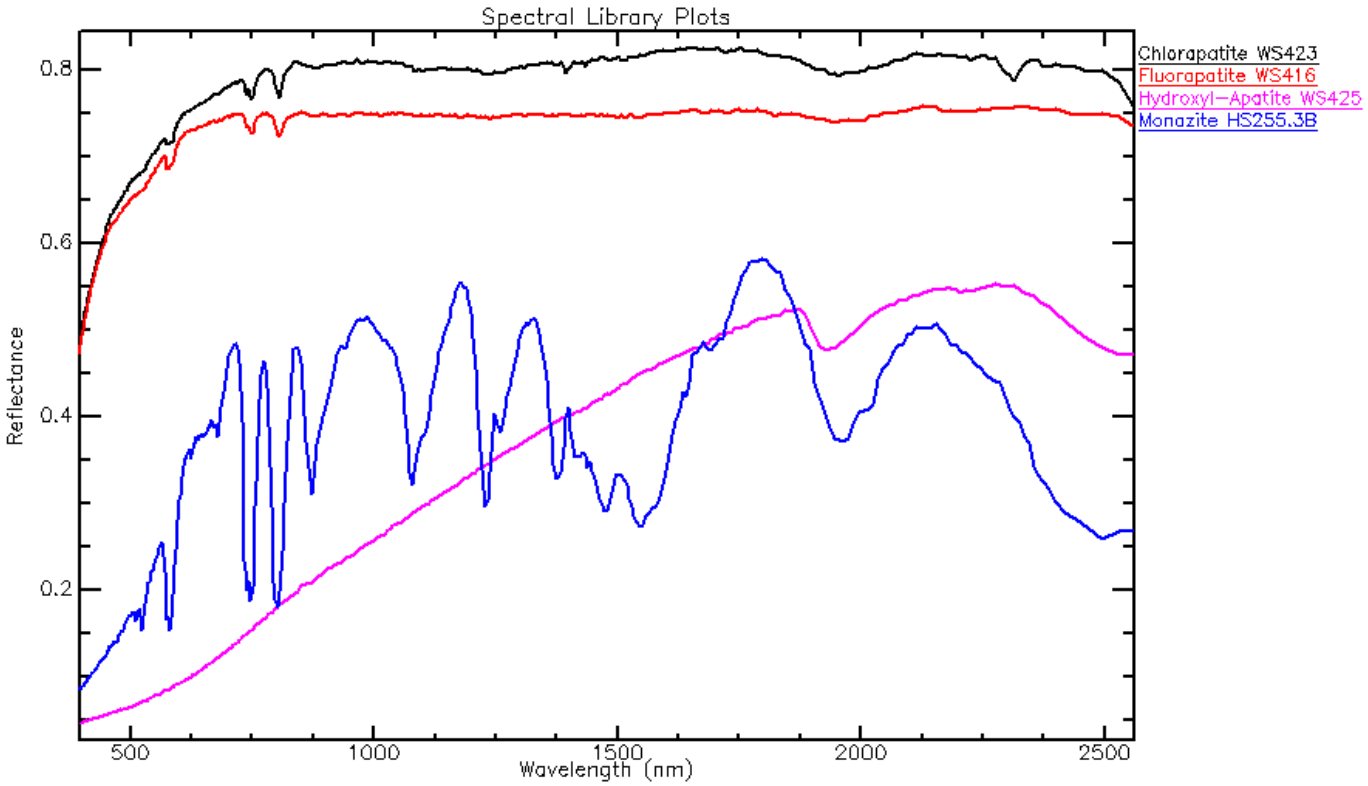

Fig. 5. Reflectance spectra from the USGS Spectral Library (Version 06a). From uppermost to lowermost near 2500 nm: Chlorapatite (black), fluorapatite (red), hydroxyl-apatite (pink) and monazite (blue). No chemical data are available.

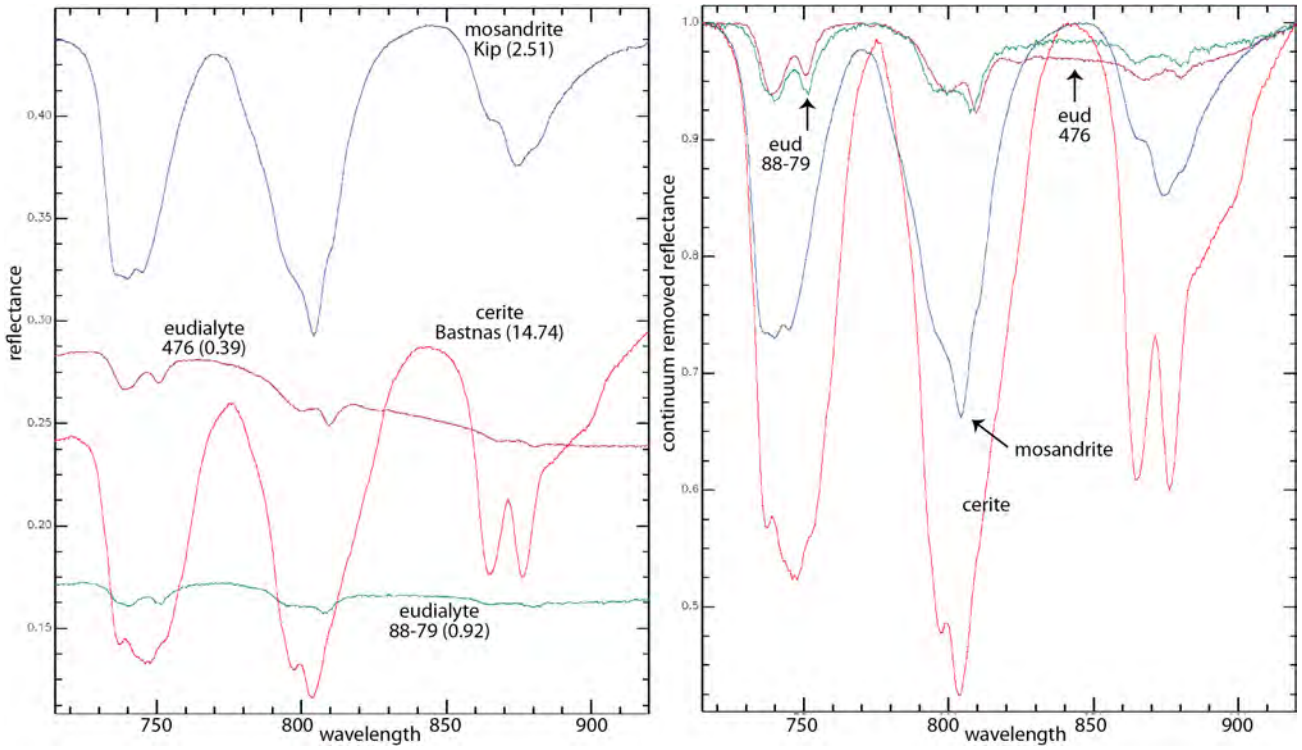

Fig. 6. Reflectance spectra (left) of selected REE bearing silicates and their continuum-removed spectra (right) displaying relative intensity and positional differences for Nd^{3+} related absorptions centred at ~746 nm, ~803 nm and 875 nm. Influence from Dy^{3+} in these samples is minimal but would be greatest in the ~803 nm cluster. Weight % of Nd_2O_3 for each sample is given in parentheses, as determined by electron microprobe analysis in Turner (2015).

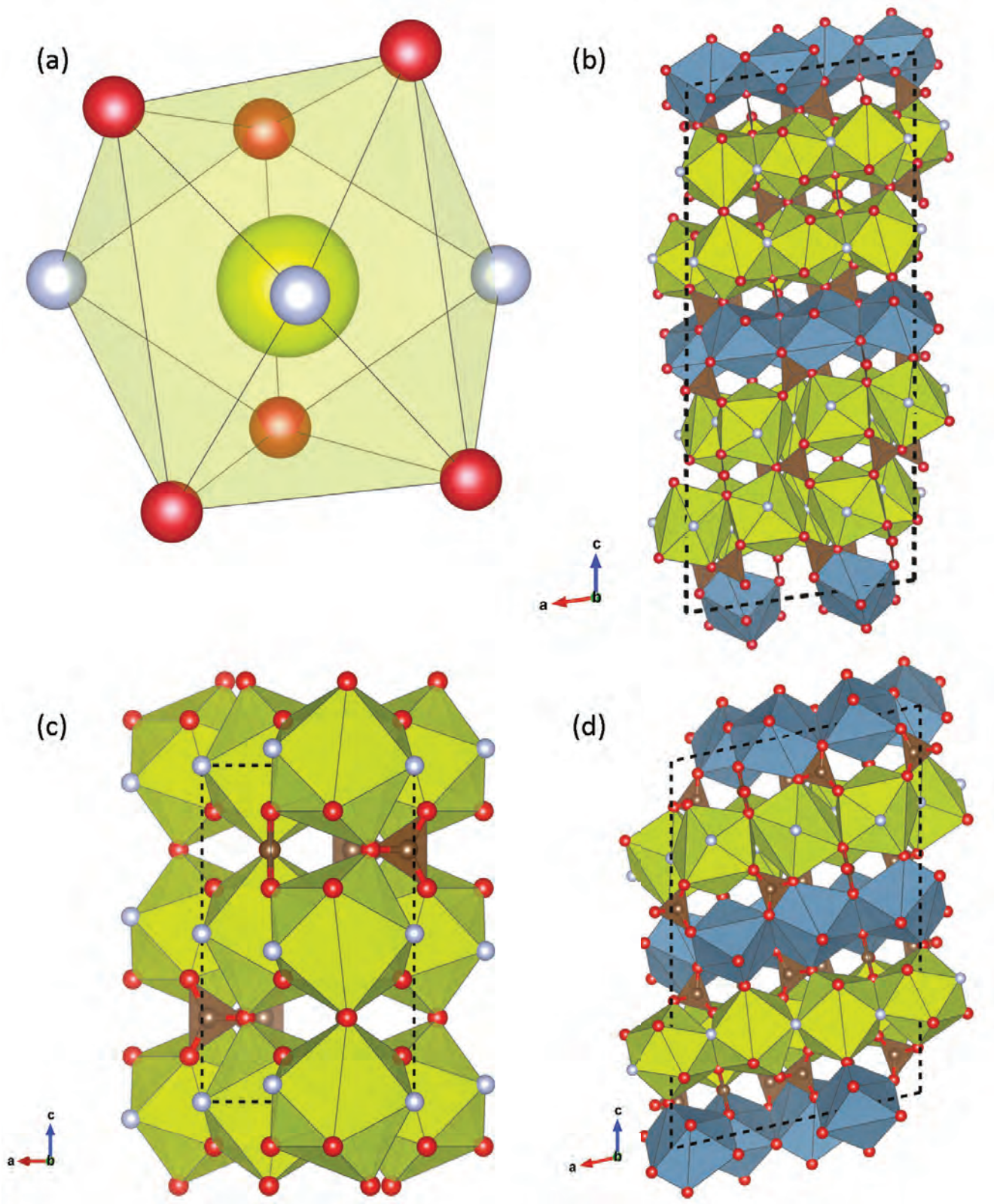

Fig. 7. a) Coordination polyhedron for the Ce1 site in parisite (Ni et al., 2000); also applicable to bastnaesite and synchysite. Ce1 (green) atom is coordinated with F1, F2 and F3 (lavender) atoms, whose plane is roughly perpendicular to c-axis, and 6 oxygen (red) atoms O11, O23, O32, O42, O53 and O61. Overall coordination number of 9 in a distorted tricapped trigonal prismatic arrangement. **b)** Parisite crystal structure from Ni et al. (2000). **c)** bastnaesite crystal structure from Ni et al. (1993). **d)** Synchysite crystal structure from Wang et al. (1994). Atom colouring: red=oxygen, green=REE, lavender=F, brown=C. Polyhedra colouring: green=$REEO_6F_3$, dark blue=CaO_8, brown=CO_3.

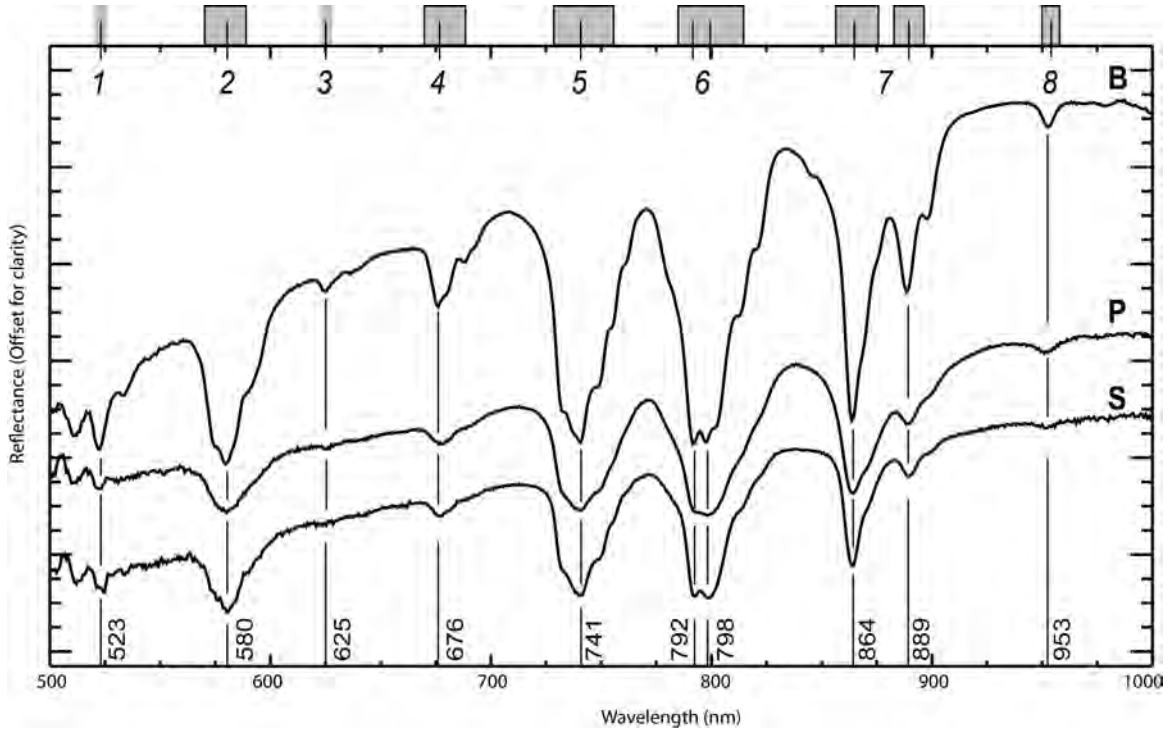

Fig. 8. VNIR (500 to 1000 nm) spectra of bastnaesite (B, top), parisite (P, middle) and synchysite (S, bottom). Italic numbers denote groups with probable origin described in Turner et al. (2014). Lines denote prominent absorption features with wavelength position, shaded boxes represent the approximate Full Width at Half Max for each absorption or absorption cluster, borderless box indicates narrow feature. Stacked spectra from sisuROCK instrument.

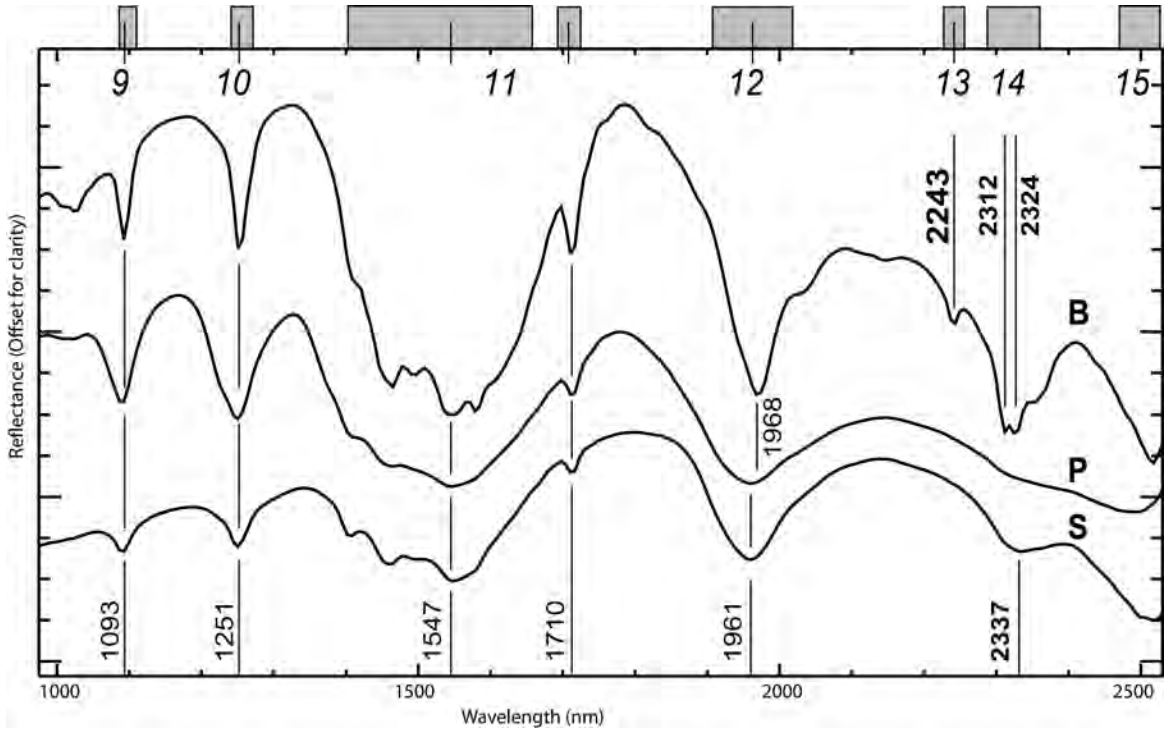

Fig. 9. SWIR (975 to 2530 nm) spectra of bastnaesite (B, top), parisite (P, middle) and synchysite (S, bottom). Italic numbers denote groups with probable origin described in Turner et al. (2014). Lines denote prominent absorption features with wavelength position, shaded boxes represent the approximate Full Width at Half Max for each absorption or absorption cluster, borderless box indicates narrow feature. Stacked spectra from sisuROCK instrument.

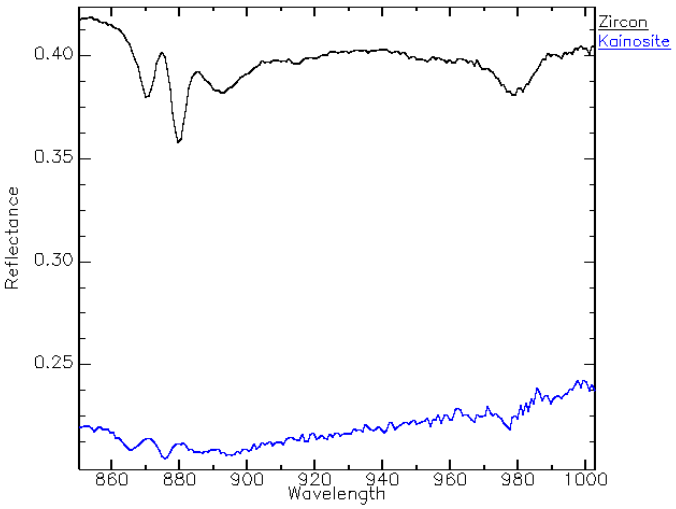

Fig. 10. Kainosite (with 1.56 wt.% Er_2O_3 and 1.55 wt.% Yb_2O_3) and REE-enriched zircon (with 0.16 wt.% Er_2O_3 and 0.30 wt.% Yb_2O_3) reflectance spectra showing the Er^{3+}-Yb^{3+} related absorption band near 978 nm.

than for kainosite, despite kainosite showing nearly an order of magnitude higher Er and Yb concentrations.

3.3. The importance of other mineral features

Despite the primary focus of this work being the Ln^{3+} related absorption bands, all other causes of absorption features are equally important to consider and can facilitate mineral identification and discrimination based on the overall spectra. Figure 7 shows the crystal structures of the common REE fluorocarbonate minerals bastnaesite, synchysite and parisite. It was noted that the REE^{3+} coordination polyhedron was effectively identical in each mineral, however, the remainder of the structures can be thought of as being built with 'layers' of CeF, Ca and CO_3 in different proportions. This leads to different characteristic bonding for the various CO_3 polyhedra amongst the minerals and therefore differences in the CO_3 related vibrational absorption features in the SWIR region (Fig. 9). Specifically, a distinct absorption at 2243 nm distinguishes bastnaesite from parisite and synchysite, neither of which have this feature. Bastnaesite also shows a well resolved doublet with absorption bands at 2312 and 2324 nm, a shoulder at 2355 nm and an additional band at 2518 nm. This is in contrast to parisite's weak absorption bands at 2324 nm and near 2499 nm, and synchysite's absorption bands at 2337 nm and 2518 nm.

Zircon ($ZrSiO_4$) is a common carrier of U^{4+} and Th^{4+} and is well known to incorporate the REE^{3+} into its structure. A suite of five zircon crystals studied in detail by Turner (2015) show a range of spectral characteristics that are driven by U^{4+}, U^{5+}, a crystalline vs amorphous matrix, Ln^{3+} content and OH/H_2O bands. Figure 11 displays their reflectance spectra in the VNIR

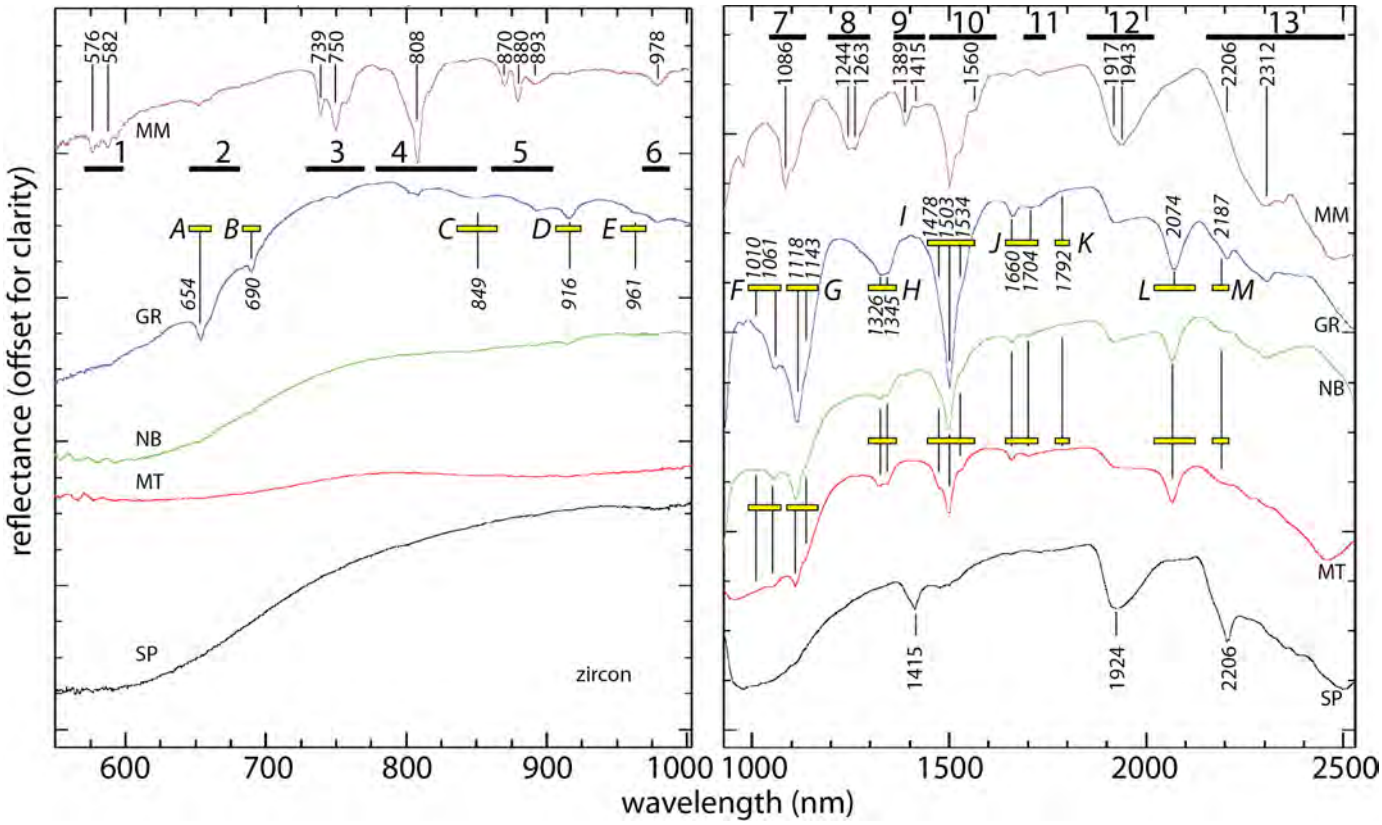

Fig. 11. Stacked reflectance spectra of zircon samples in the VNIR (550 – 1000 nm) and SWIR (975 – 2530 nm) ranges. REE–related clusters are indicated by labeled thick horizontal lines and prominent absorptions are labeled with wavelength position. Uranium related features are distinguished by lettered clusters, yellow horizontal bars and italicized wavelength labels. From top down, Mt Malosa (pink, MM) Green River (blue, GR), North Burgess (green, NB), Mudtank (red, MT), St. Peters Dome (black, SP).

and SWIR ranges, and three spectral classes of zircon exist: U bearing (North Burgess=NB, Green River=GR, Mudtank=MT), high REE with U (Mt Malosa=MM) and metamict (St Peters Dome). Many of the uranium related absorptions are fairly sharp and can overlap with regions where Ln^{3+} related absorptions are expected (e.g., the many bands near 1100 nm). This sample suite is a good example of how it is important to consider non-lanthanide variables in spectra with suspected Ln^{3+} related absorptions.

4. Conclusions and implications

Spectral features of REE minerals in the VNIR-SWIR range are primarily related to numerous 4*f*-4*f* intraconfigurational electronic transitions of trivalent lanthanides (Ln^{3+}), and 5*f*-5*f* electronic transitions of uranium and vibrational overtones and combinations of CO_3^{2-}, H_2O, and OH^- where applicable. In general, the respective spectra of the most common REE minerals are sufficiently distinct for spectral classifications. Thus, the application of reflectance spectroscopy (and especially hyperspectral imaging) can yield considerable mineralogical and geochemical information about a given REE-bearing sample. Increasing prevalence of VNIR-SWIR spectroscopy in geosciences and continuous improvement of instrumentation will no doubt benefit the understanding and exploitation of REE bearing minerals and rocks.

References cited

Binnemans, K., 1996. A comparative spectroscopic study of Eu^{3+} in crystalline host matrices. Bulletin des Sociétés Chimiques Belges, 105, 793-798.

Boesche, N. K., Rogass, C., Lubitz, C., Brell, M., Herrmann, S., Mielke, C., and Kaufmann, H., 2015. Hyperspectral REE (Rare Earth Element) Mapping of Outcrops—Applications for Neodymium Detection. Remote Sensing, 7, 5160-5186.

Burns, R., 1993. Mineralogical Applications of Crystal Field Theory, Second Edition, Cambridge University Press, Cambridge, 551p.

Clark, R. N., 1999. Chapter 1: Spectroscopy of Rocks and Minerals, and Principles of Spectroscopy. In: Rencz, A.N., and Ryerson, R.A., (Eds.), Remote Sensing for the Earth Sciences, Manual of Remote Sensing Volume 3, pp. 58.

Cloutis, E.A., Hawthorne, F.C., Mertzman, S.A., Krenn, K., Craig, M.A., Marcino, D., Methot, M., Strong, J., Mustard, J.F., Blaney, D.L., Bell III, J.F., and Vilas, F., 2006. Detection and discrimination of sulfate minerals using reflectance spectroscopy. Icarus, 184, 121-157.

Dieke, G. H., Crosswhite, H., and Crosswhite, H.M., 1968. Spectra and energy levels of the rare earth ions in crystals. Wiley Interscience, New York, 193p.

Görller-Walrand, C., and Binnemans, K., 1998. Spectral intensities of f-f transitions. In: Gschneidner, K.A., and Eyring, L., (Eds.), Handbook on the Physics and Chemistry of Rare Earths, Vol. 25, Chapter 167, North-Holland Publishers, Amsterdam, pp. 101-264.

Hoefen, T. M., Livo, K. E., Giles, S. A., Lowers, H. A., Swayze, G. A., Taylor, C. D., and Mccafferty, A. E., 2014. Characterization of REE-Bearing Minerals and Synthetic Materials Using High Resolution Ultraviolet to Near-Infrared Reflectance Spectroscopy. In AGU Fall Meeting Abstracts (Vol. 1, p. 4299).

Mariano, A.N., and Mariano, A., 2012. Rare earth mining and exploration in North America. Elements, 8, 369-376.

Mustard, J. F., 1992. Chemical composition of actinolite from reflectance spectra. American Mineralogist, 77, 345-358.

Rowan, L. C., Kingston, M. J., and Crowley, J. K., 1986. Spectral reflectance of carbonatite and related alkalic igneous rocks from four North American localities. Economic Geology, 81, 857–871.

Salisbury, J.W., 1993. Mid-infrared spectroscopy: Laboratory data. In: Pieters, C.M., and Englert, P.A.J., (Eds.), Remote Geochemical Analysis: Elemental and Mineralogical Composition, Cambridge University Press, Cambridge, pp. 79-98.

Swayze, G.A., Pearson, N., Wilson, S., Benzel, W.M., Clark, R., Hoefen, T.M., Van Gosen, B., Adams, M., and Reitman, J., 2013. Spectrally distinguishing between REE-bearing minerals based on differences in their crystal field f-f transition absorptions. In Geological Society of America Abstracts with Programs, 45, 278.

Turner, D. J., Rivard, B., and Groat, L. A., 2014. Visible and short-wave infrared reflectance spectroscopy of REE fluorocarbonates. American Mineralogist, 99, 1335-1346.

Turner, D. J., 2015. Reflectance spectroscopy and imaging spectroscopy of rare earth element-bearing mineral and rock samples. Unpublished Ph.D. Thesis, University of British Columbia, Vancouver, Canada, 310p.

Biogeochemical expressions of buried REE mineralization at Norra Kärr, southern Sweden

Britt Bluemel [1, a], Colin Dunn[2], Craig Hart[3], and Magnus Leijd[4]

[1] REFLEX Geosciences, Vancouver, BC, Canada
[2] Colin Dunn Consulting Inc., North Saanich, BC, Canada
[3] Mineral Deposit Research Unit, University of British Columbia, Vancouver, BC, Canada
[4] Tasman Metals Ltd., Boden, Sweden
[a] corresponding author: britt.bluemel@imdexlimited.com

Recommended citation: Bluemel, B., Dunn, C., Hart, C., and Leijd, M., 2015. Biogeochemical expressions of buried REE mineralization at Norra Kärr, southern Sweden. In: Simandl, G.J. and Neetz, M., (Eds.), Symposium on Strategic and Critical Materials Proceedings, November 13-14, 2015, Victoria, British Columbia. British Columbia Ministry of Energy and Mines, British Columbia Geological Survey Paper 2015-3, pp. 231-239.

Summary

Biogeochemical samples were collected from the Norra Kärr Alkaline Complex, a rare earth element (REE) and zirconium enriched mineral deposit in Southern Sweden, to determine which sample type is the most appropriate grassroots exploration medium for delineating concealed REE mineralization. We found that that the fern species *Dryopteris filix-mas* and *Athyrium filix-femina*, which are widespread in the region, are particularly efficient at concentrating high levels of REE in their leafy tissue.

Three fern species displayed distinct elemental fractionation. Each species showed enrichment in the light rare earth elements (LREE), especially *Athyrium filix-femina*. *Dryopteris filix-mas*, showed the most enrichment in heavy rare earth elements (HREE) and *Pteridium aquilinum* had lower levels of REE than the other two species.

The best contrast was observed in *Dryopteris filix-mas* samples collected over mineralization compared to samples taken over barren Växjö granites, suggesting that *Dryopteris filix-mas* is the preferred biogeochemical sample medium for REE exploration in this region.

1. Introduction

Biogeochemical exploration is an effective but underused method for delineating covered mineralization. Plants are capable of accumulating REE in their tissue, and ferns (pteridophytes) are especially adept because they are a primitive land plant. Complex plants, like trees, have developed barrier mechanisms to protect their cells from build-up of elements such as heavy metals or REE, which may be harmful to the plant at high concentrations (Kovalevskii, 1979). In contrast, less evolved plants lack these barrier mechanisms and accumulate all elements equally, therefore can absorb higher proportions of heavy elements in their tissue. Based on findings from several authors (Dunn, 1998; Wyttenbach et al., 1998; Fu et al., 1998; et. al., Zhang, 2002; Dunn, 2007) it appears that ferns are suitable sample media for REE exploration.

There is a paucity of information regarding the capacity of biogeochemical methods to explore for buried HREE (those REE with a higher mean atomic mass than ca 153) mineralization. The Norra Kärr Alkaline Complex (NKAC; Fig. 1) is well suited to evaluate the efficacy of biogeochemical sampling because the REE mineralization there is challenging to detect by conventional exploration techniques. The nepheline syenite hosting the REE has very similar density to the surrounding Växjö granites, so is indistinguishable by gravity surveys. The deposit lacks sulphide minerals, so cannot be identified by induced polarity (IP) surveys. Also, Norra Kärr has unusually low amounts of uranium and thorium for a deposit of its type, and therefore the deposit is not easily recognizable in the country-wide Swedish Geological Survey (SGU) radiometric surveys. Extensive glaciation of the study area presents an additional challenge because conventional soil surveys are not reliable exploration methods in areas of transported cover.

Biogeochemical surveys provide a viable approach to mineral exploration in most terrains because they are rapid, relatively inexpensive, and are effective in areas of disturbance or transported cover. The ferns sampled at Norra Kärr, *Athyrium filix-femina* (lady fern), *Dryopteris filix-mas* (wood fern), and *Pteridium aquilinum* (bracken) (Fig. 2), all accumulate REE in their leafy tissue and are ubiquitous in the study area, making them an ideal biogeochemical exploration media.

Recently, it has been shown that low levels of REE can benefit plant growth (Volokh et al., 1990; Welch, 1995; Guo et al., 1996) and REE have been added to agricultural fertilizers to increase crop yield. This practice has been most widely embraced in China, and as a result many researchers there have begun studying REE in soil-plant systems to better understand the distribution and accumulation of REE in the natural environment. Research has been carried out mainly on rice and corn (Li et al., 1998) as well as soybeans and wheat (Ding et al., 2006, 2007). Fu et al. (1998) undertook a comprehensive study on the distribution patterns of REE in the fern *Matteuccia* to

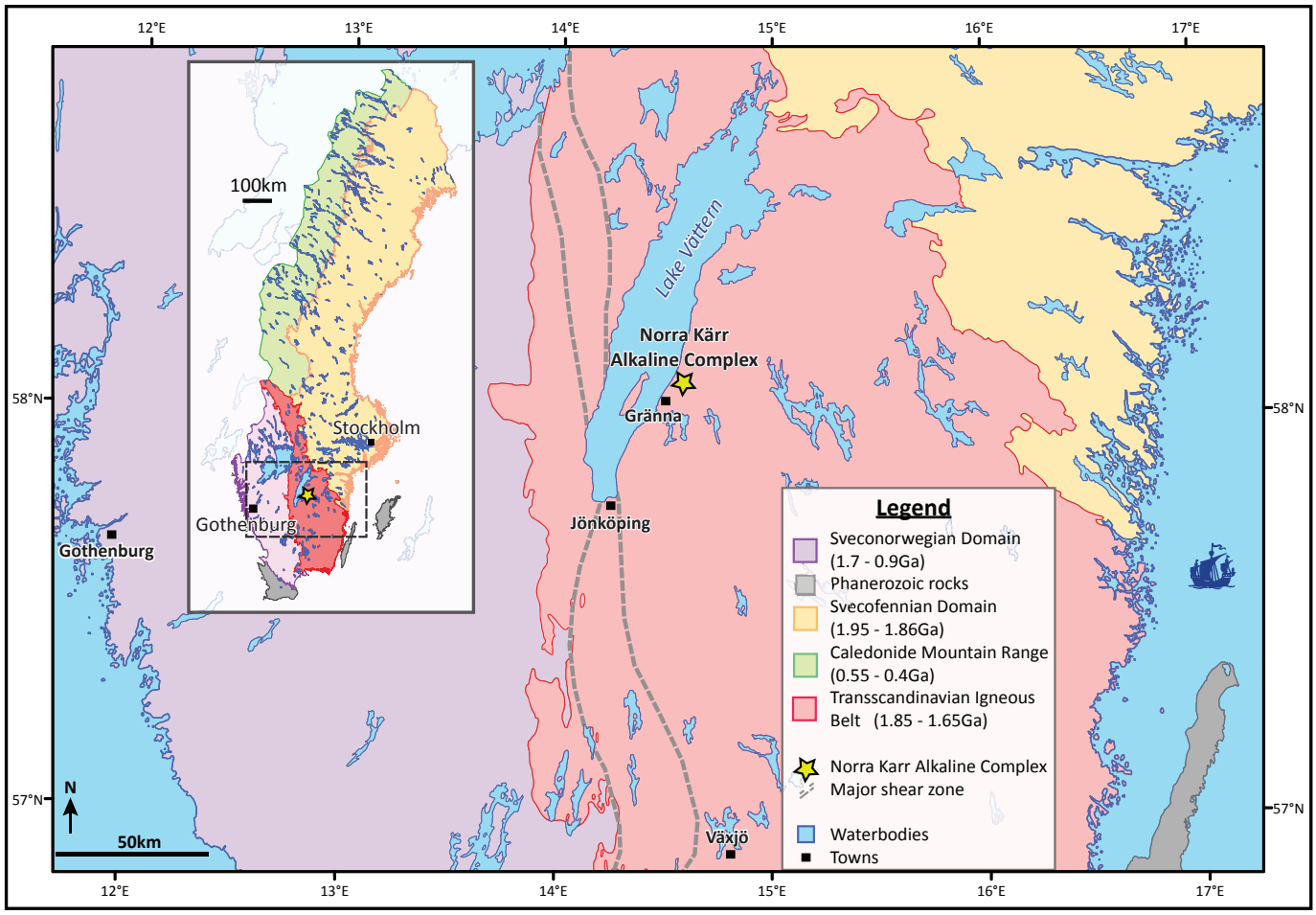

Fig. 1. Geological map of southern Sweden; Norra Kärr Alkaline Complex is indicated by the star.

Fig. 2. Fern species in the study area. **a)** *Athyrium filix-femina*, **b)** *Dryopteris filix-mas*, **c)** *Pteridium aquilinum*. Note the distinct differences in spore morphology.

investigate the implication for intake of fresh silicate particles by plants. They demonstrated that the content of REE in ferns decreased from root to leaf to stem, and hypothesized that the source of REE was from the silicate fraction of the soil.

This study evaluates the biogeochemistry of common ferns as appropriate indicators of REE enrichment and considers which species is the most effective in delineating HREE deposits.

2. Geology, physiographic setting, and land use

2.1. Geology

The Norra Kärr REE and Zr Alkaline complex is approximately 300 km southwest of Stockholm and 10 km northeast of Gränna in southern Sweden (Fig. 1). Norra Kärr, which is Swedish for "northern bog", occupies a shallow topographic low; the centre of the intrusive complex is slightly elevated. The western contact of the syenite is covered by a low-lying swampy area and, at the eastern edge of the intrusion, a small creek drains into a lake that sits directly above the eastern contact with the surrounding granites. Nepheline syenite outcrops in several places, but for the most part is overlain by 1-4 m of Quaternary sediments. The complex is approximately 1300 m long, 480 m wide, and is elongate north-south.

Mineralization is hosted within the peralkaline nepheline syenite complex and is associated with a zone of ductile deformation along a large north-south trending dip-slip fault. The deposit dips roughly 45° to the west, and is wholly

surrounded by barren Växjö granites.

The four main rock units at Norra Kärr, described in detail by Saxon et al., (2015) are locally referred to as: 1) grennaite (generally a fine-grained, grey-green rock composed of alkali feldspar, nepheline, aegerine, eudialyte, and catapleiite); 2) kaxtorpite (a coarse-grained, dark alkaline rock with microcline augen and an aegerine, alkali amphibole and nepheline groundmass); 3) lakarpite (an "often medium grained, albite–arfvedsonite–nepheline dominated rock with some microcline–rosenbuschite and minor titanite–apatite–fluorite" (Reed, 2011)); and 4) pulaskite (a rock composed of albite, microcline, aegerine, alkali amphibole, minor biotite and nepheline). The two main alkali zirconosilicates hosting the REE mineralization are eudialyte [$Na_4(Ca,REE)_2(Fe,Mn)ZrSi_8O_{22}(OH,Cl)_2$] and catapleiite [$(Na,Ca)_2ZrSi_3O_9{\cdot}2H_2O$] (Reed, 2011). Both of these minerals are relatively easily weathered, making the REE at Norra Kärr more bioavailable. The strongest REE response in the biogeochemical samples corresponds with the pegmatitic grennaite, which is the most richly endowed unit of the complex.

2.2. Quaternary geology and land use

The Quaternary cover over the NKAC was mapped by the Swedish Geological Survey as "thin or discontinuous soil cover on bedrock" (Swedish Geological Survey 2011). The bedrock has also been mapped, but is not well constrained due to the extensive cover. Regional ice-flow direction was generally north-south or slightly south-easterly. Based on field assessments it appears that that the surficial material over the NKAC is glaciofluvial outwash because it lacks the clay content and highly compact nature of typical glacial tills.

The land use around Norra Kärr is variable, changing abruptly from grassy agricultural grazing land to typical boreal Swedish forest to thickly vegetated silviculture plantations. Soil profiles above the NKAC indicate that the ground is very disturbed by agricultural practice, which has been ongoing in the region for hundreds of years, and consequently developed soil horizons are rare.

3. Results

3.1. Analytical methods

The analytical package we used was Acme Laboratories' Group 1VE-MS ultratrace package including all the REE. This involved pre-treating the sample with HNO_3 to oxidize the organic material under cool conditions before digesting in aqua regia, followed by determinations for 65 elements by ICP-MS, and ICP-ES for some of the major elements.

3.2. Background contrast and detection limits

The best contrast between anomaly and background was observed in the *Dryopteris filix-mas* samples (Fig. 3). LREE are more abundant than HREE in the Earth's crust, so they naturally accumulate in higher absolute values in the plants, and because *Athyrium filix-femina* can contain significant amounts of REE in its leaf tissue, it would seem to be a logical sample type. However, *Dryopteris filix-mas* shows a better response ratio over the NKAC, so it is a better choice of sample medium.

With the exception of Eu, the concentration of LREE in all samples exceeds the 0.02 ppm detection limit. In his comprehensive review of REE in soils and plants, Tyler (2004) included Eu with the LREE, a convention that we follow here. Of the 25 samples that reported Eu values below detection limit, only 3 were collected above the deposit. One of these was from directly over the kaxtorpite unit, which has the lowest levels of REE (less than 0.21% TREO) of any rock type in the complex; the other two samples were from parts of the complex that contain porphyritic catapleiite (0.26% TREO).

Each of the HREE reported some values below the detectable limit, but some elements, particularly Tb, Ho, Tm, and Lu, reported a larger proportion below detection limit than the other HREE. Eleven out of 88 samples showed Tm values less than 0.02 ppm, and only 5 of the 88 samples had reportable Lu. Approximately 40% of the samples had less than detection levels of Tm and Ho. The HREE Gd, Dy, and Er had the most reportable results, but still between 13% and 25% of the samples returned values below the detection limit. Only two of the below detection limit samples for Gd and Dy were located over the deposit, and these are the same samples that ran below

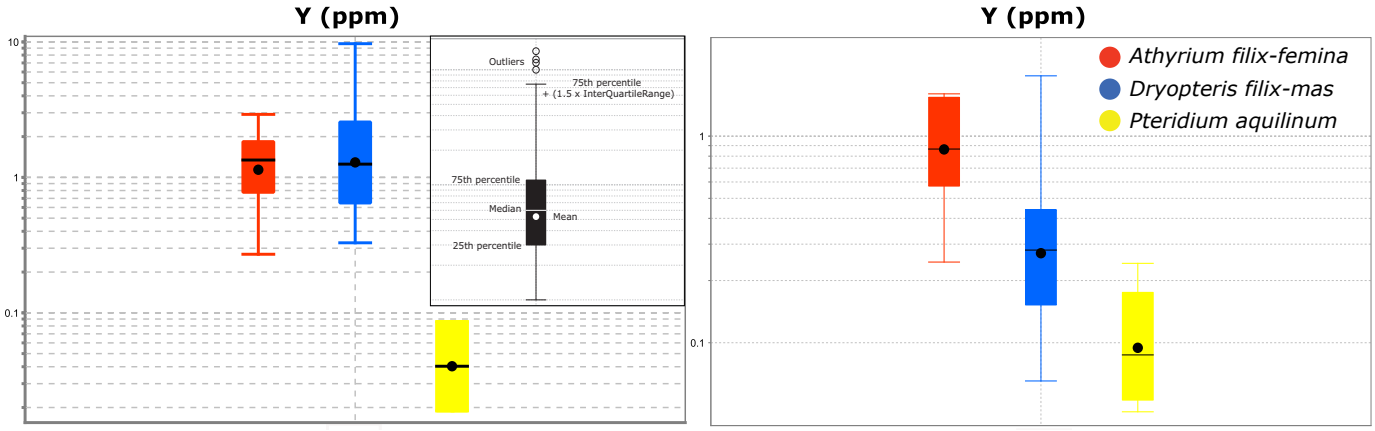

Fig. 3. Yttrium content in ferns collected over the Norra Kärr deposit (left) and in the background (right), coloured by species type.

detection limit for Eu.

The higher levels of Gd, Dy, and Er relative to the other HREE are due to the fact that lanthanides with even atomic numbers (64, 66, and 68 respectively) have greater relative crustal abundances than elements with odd atomic numbers. This pattern, inherent in the rock samples, is being preserved and displayed in the vegetation samples.

3.3. REE concentrations

The three species of ferns had significantly different trace element compositions. *Pteridium aquilinum* had the lowest levels of all REE analysed; *Athyrium filix-femina* had the highest REE values, and *Dryopteris filix-mas* had intermediate values between the other two species.

The similar behaviour and mobility within the HREE compared to the LREE is well documented (Tyler et al. 2004). There are strong correlations in this dataset, with confidence greater than the 90th percentile, among the LREE and HREE such that any one of these elements can be selected as a proxy and used to represent each group. Consequently, only Nd and Dy data are presented and graphed hereafter.

The amount of Dy ranges from below the detection limit to 0.34 ppm over the deposit, and from below the detection limit to 0.24 ppm off the deposit. The ranges of Nd are from 0.49 ppm to 20.2 ppm over the deposit, and 0.25 ppm to 15.4 ppm off the deposit.

3.4. Levelling

Different species of ferns can naturally accumulate different amounts of REE in their plant structure (Fig. 3, 4a, 4b), so to make a coherent biogeochemical response map over the deposit and surrounding area, REE values must be levelled to account for variation in sample species. The levelling method undertaken here was Z-Score, $\log_{10}$, with a power transformation ($y = ((x^{\lambda-1})/\lambda)$. Employing a $\log_{10}$ transformation recasts the trace element data into a more normal distribution, and a Z-Score transformation was used instead of a median calculation because levelling by the median does not account for the spread of the data, so any variables with a wide distribution will be predominant. The other advantage to using a Z-Score transformation is that the outliers, ranging from 1.5 to 3 standard deviations, are preserved for each variable. Outliers are classified as 1.5 x (Q3-Q1) and are represented as open circles; far outliers are classified as 3 x (Q3-Q1) and are represented as open triangles (Fig. 4).

4. Discussion

The biogeochemical samples collected above mineralization are elevated in both the heavy and light REE, particularly the LREE, compared to samples collected above the surrounding country rock (Fig. 6). Of the three fern species sampled, *Athyrium filix-femina* had the highest levels of LREE, and the highest average value for the HREE. However, *Dryopteris filix-mas* was most enriched in Gd, Tb, Dy, Ho, Er, Yb, and Y. These differences can be displayed using Tukey outlier "box and whisker" plots (Figs. 3, 4). These plots divide the data into four parts by calculating the median, 75th, and 25th percentiles, which are represented as the black line in the centre, and the upper and lower limits of the coloured box, respectively. Any values that fall outside of this range are considered outliers and will be displayed as points either above or below the vertical coloured line, which is referred to as the 'whisker'. The black circle near the centre of the coloured box is the mean of the population. Figure 3 shows the distribution of Y content above the deposit and in the background.

Figure 5 shows the fern data, coloured by species, in a chondrite-normalized plot (Boynton, 1984). No *Pteridium aquilinum* samples are plotted here because at least one HREE for each *Pteridium aquilinum* sample was below the reportable detection limit and creates a sawtooth effect, which is also visible for *Athyrium filix-femina* and *Dryopteris filix-mas* for Tm and Lu (Fig. 5). There is enrichment of LREE in *Athyrium filix-femina* (red lines). All species, with the exception of three *Dryopteris filix-mas* samples, are depleted in HREE, particularly Dy in *Pteridium aquilinum*. The three HREE-enriched *Dryopteris filix-mas* were all sampled near the most prospective rock types at Norra Kärr, the pegmatitic grennaite, strongly suggesting that this is the source of their elevated levels of Gd, Tb, Dy, Ho, Er, Tm, and Yb.

There is a slight negative Eu anomaly displayed in the *Athyrium filix-femina* and *Dryopteris filix-mas* samples (Fig. 5).

The plan maps in Figure 6 show the REE content, levelled for species type, across the deposit. Only profiles for Nd and Dy are displayed because they had the most reproducible analytical results and are good representatives for the LREE and HREE, respectively.

As shown in Figure 6a, there is a positive HREE (Dy) response directly over the grennaite in the two central lines. Also of note are the two slight elevations in the southernmost line where samples were collected over the catapleiite phyric units (displayed as purple dots in Fig. 6), as well as a positive response directly over a catapleiite phyric zone in the northeast corner of the deposit. Along the southernmost line, there is a depletion over the kaxtorpite unit because this rock type has the lowest amounts of REE in the deposit (0.2% TREO).

Very similar patterns are displayed in the LREE (Nd) profiles (Fig. 6b) but the central line, which shows a strong and uniform HREE response, has a slightly erratic LREE pattern over the same interval.

5. Conclusions

This biogeochemical orientation survey shows that

- all ferns, particularly *Athyrium filix-femina* and *Dryopteris filix-mas*, are able to uptake appreciable amounts of REE into their leafy tissueferns collected over areas of known mineralization, particularly the pegmatitic grennaite units and zones with phenocrysts of catapleiite display positive responses
- *Athyrium filix-femina* fractionates the LREE more

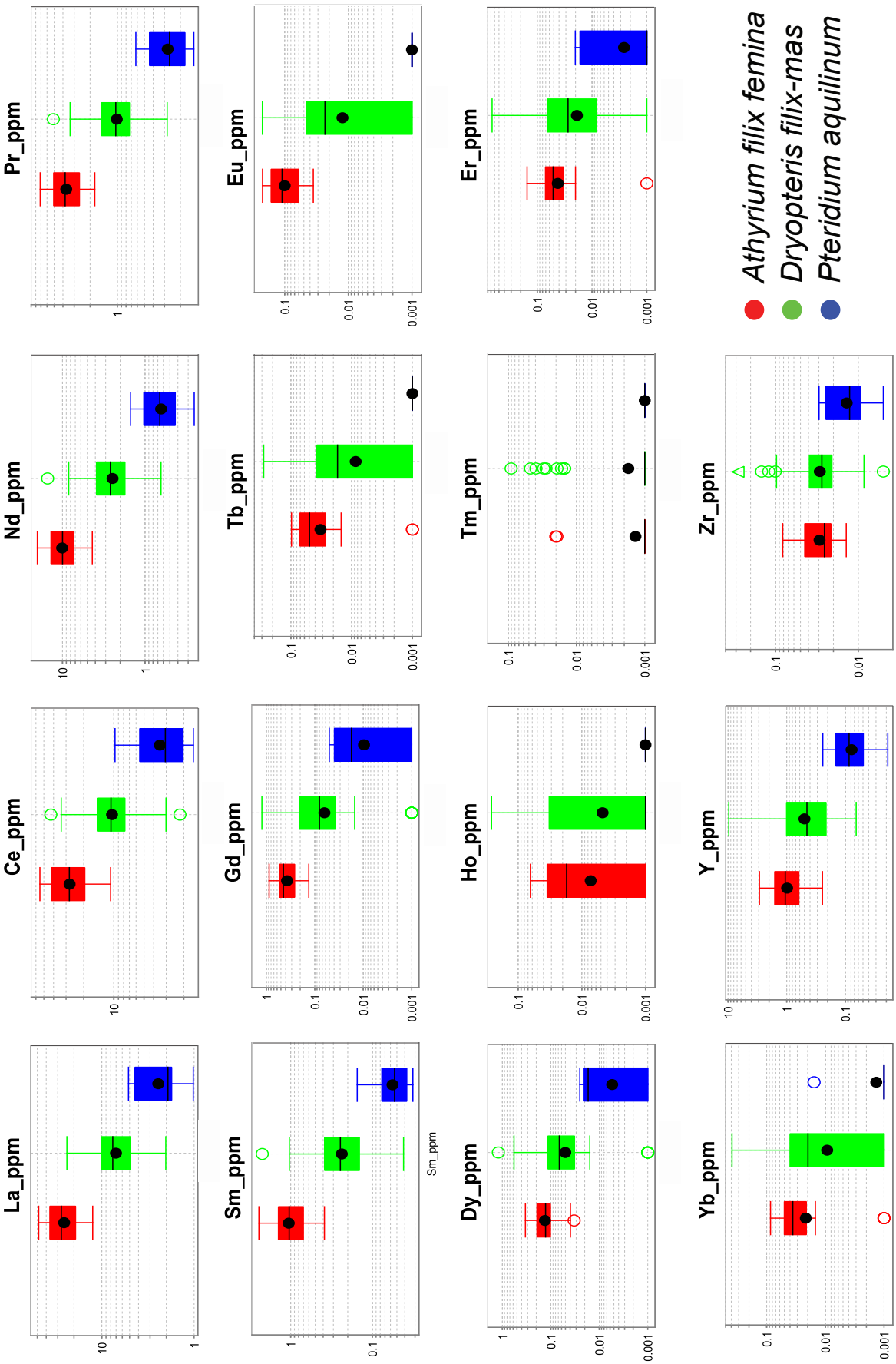

Fig. 4a. Unlevelled Tukey plots of all REE.

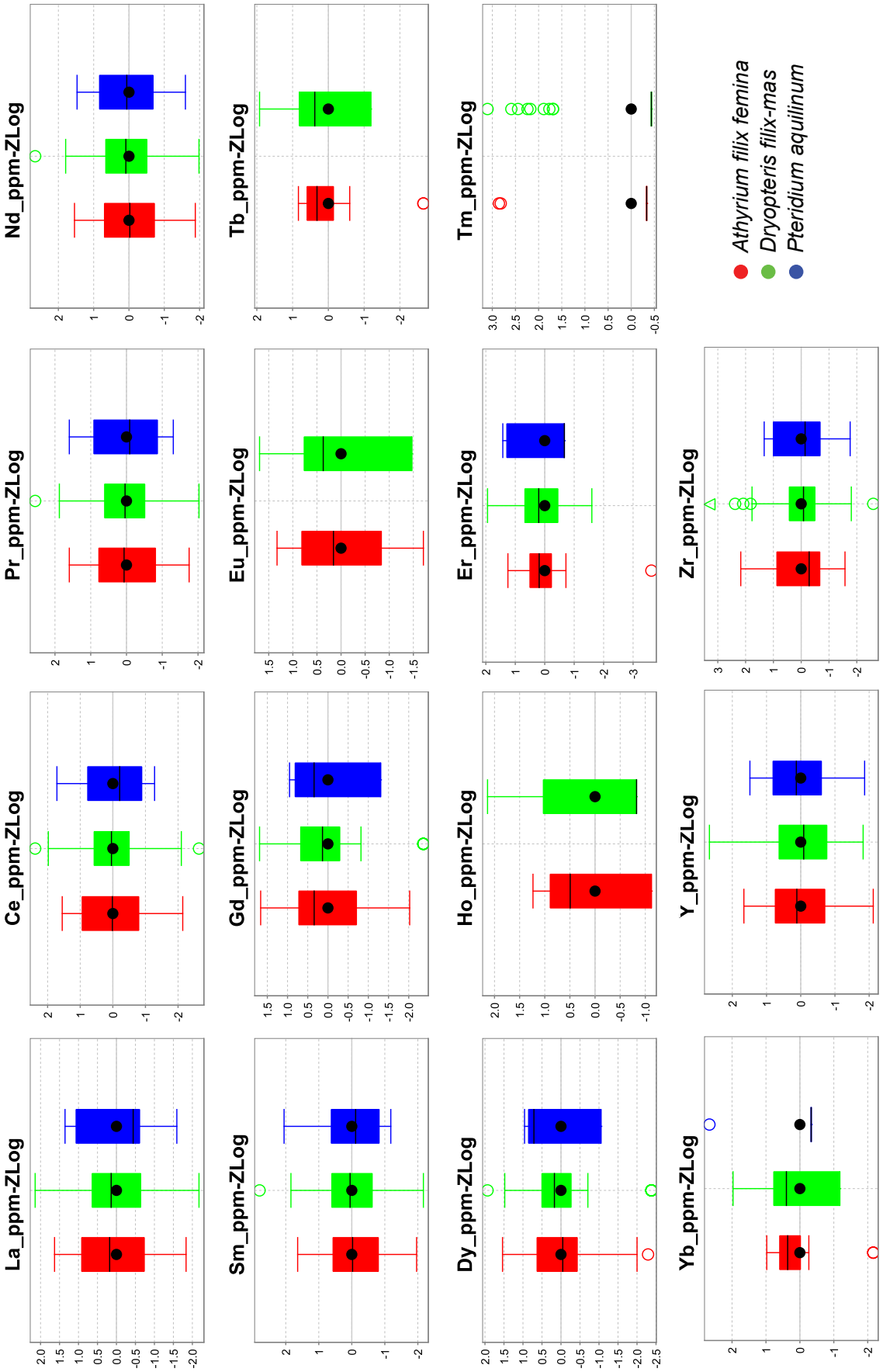

Fig. 4b. Levelled Tukey plots of all REE.

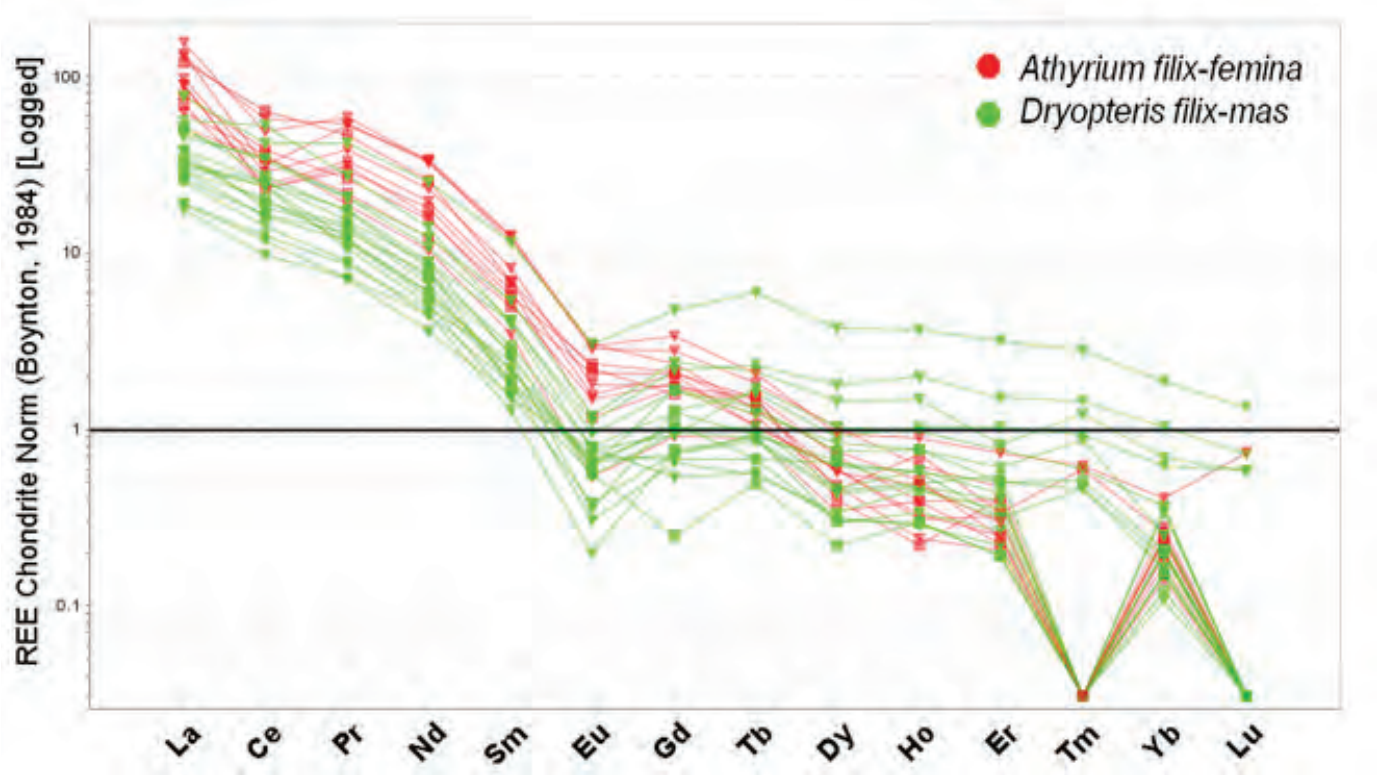

Fig. 5. Chondrite-normalized REE concentrations for *Athyrium filix-femina* and *Dryopteris filix-mas* (data above detection limit only).

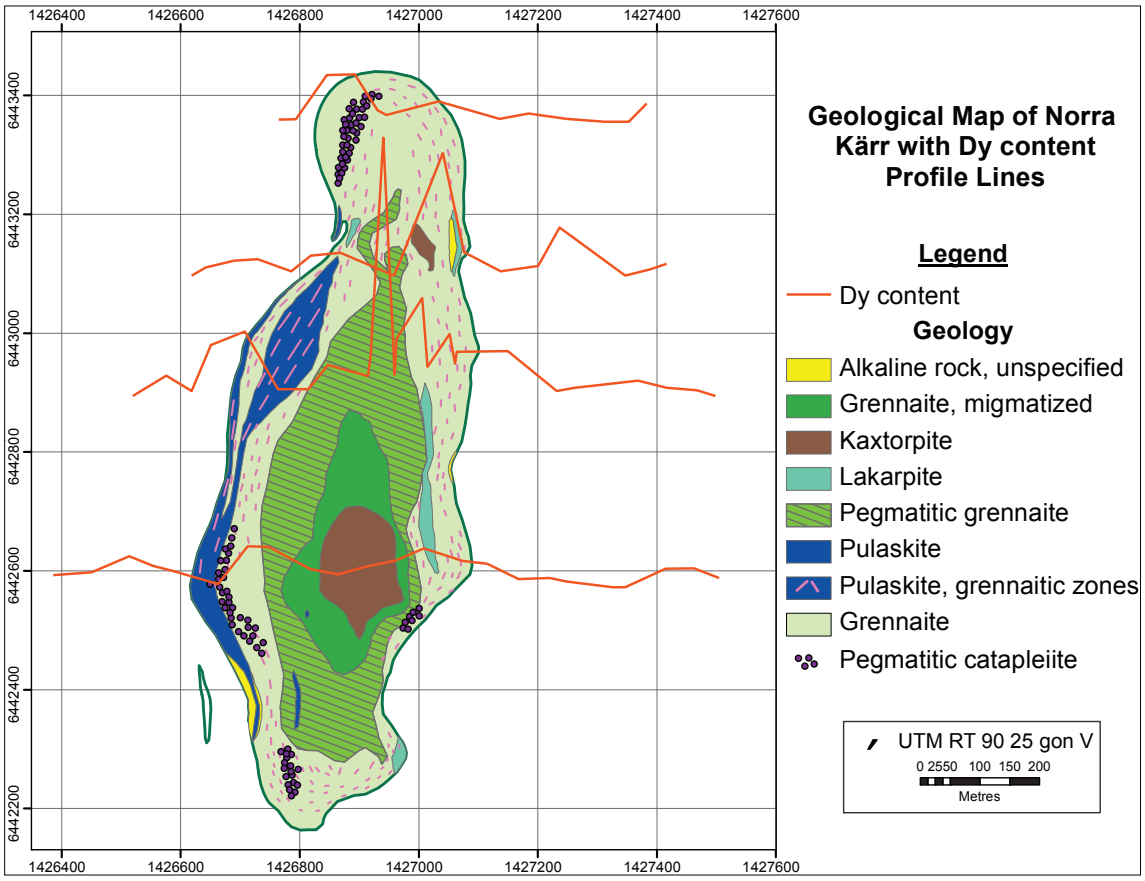

Fig. 6a. Section maps of Dy content levelled for species type, representative of HREE, over Norra Kärr.

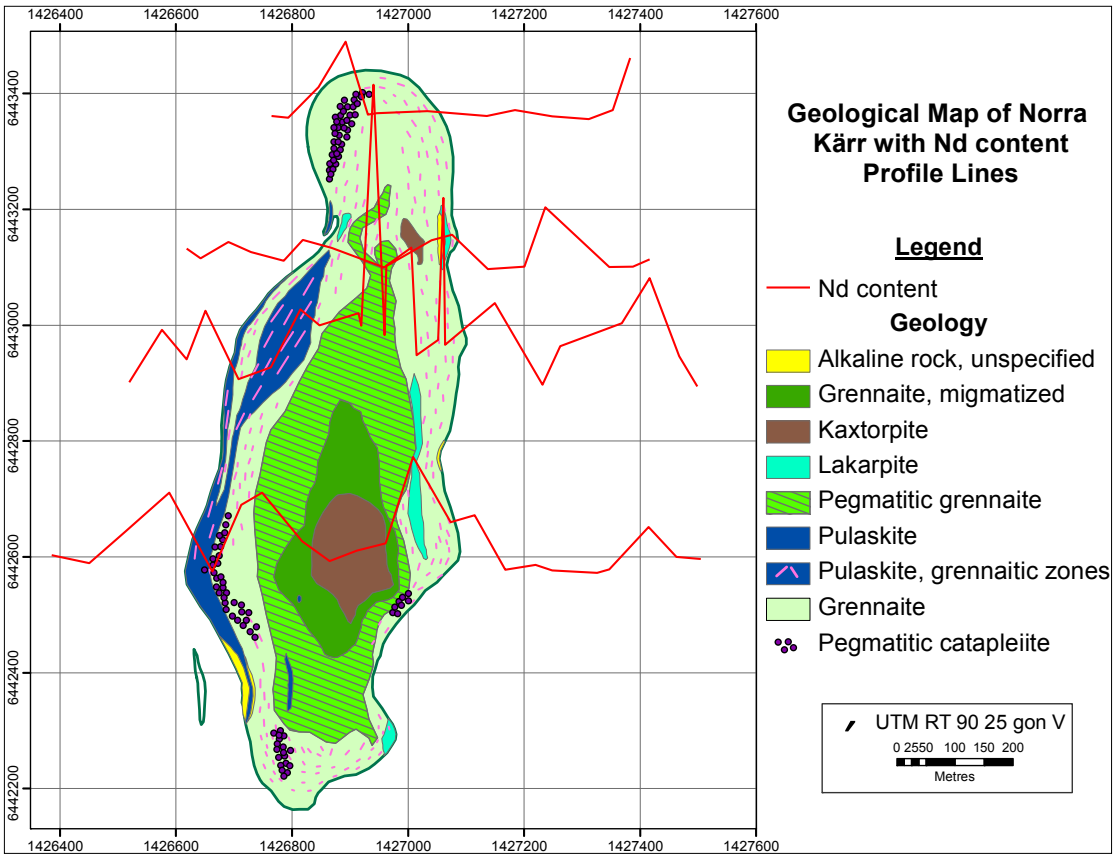

Fig. 6b. Section maps of Nd content levelled for species type, representative of LREE, over Norra Kärr.

strongly than *Dryopteris filix-mas* or *Pteridium aquilinum*

- *Athyrium filix-femina* has higher absolute contents of LREE and HREE in its leaves; however, the contrast between background and anomalous areas is more clear with *Dryopteris filix-mas*, making it the preferable biogeochemical sampling medium

Acknowledgments

We thank Tasman Metals Ltd. for their generous support and ongoing cooperation with this research.

References cited

Boynton, W.V., 1984. Cosmochemistry of the rare earth element: meteorite studies. Elsevier, Amsterdam, 63-114.

Ding, S., Liang, T., Zhang, C., Huang, Z., Xie, Y., and Chen, T., 2006. Fractionation mechanisms of Rare Earth Elements (REEs) in hydroponic wheat: An application for metal accumulation by plants. Environmental Science and Technology, 40, 2686-2691.

Ding, S., Liang, T., Yan, J., Zhang, Z., Huang, Z.,and Xie, Y., 2007. Fractionations of rare earth elements in plants and their conceptive model. Science in China Press, 50, 47-55.

Dunn, C.E., 1998. Regional and detailed biogeochemical surveys in the Nechako NATMAP area and in the Babine Porphyry Belt In: Struik, L.C., D.G.M. (Eds.), New Geological Constraints on Mesozoic to Tertiary Metallogenesis and on Mineral Exploration in Central British Columbia: Nechako NATMAP Project. Short Course Extended Abstracts, Cordilleran Section of the Geological Association of Canada, p. 17.

Dunn, C.E., 2007. Biogeochemistry in Mineral Exploration. Elsevier, Amsterdam, 231-341.

Fu, F., Akagi, T., and Shinotsuka, K., 1998. Distribution Pattern of Rare Earth Elements in Fern - Implications for intake of fresh silicate particles by plants. Biological Trace Element Research, 64, 13-26.

Guo, F., Wang, Y., Sun, J., and Chen, H., 1996. REE Bound Proteins in Natural Plant Fern Dicranopteris dichitoma by MAA. Journal of Radioactivity and Nuclear Chemistry, 209, 91-99.

Kovalevskii, A.L., 1979. Biogeochemical Exploration for Mineral Deposits. Amerind Publishing , New Delhi, India, 136p (English translation of 1974 publication in Russian).

Li, F., Shan, X., Zhang, T., and Zhang, S., 1998. Evaluation of plant availability of rare earth elements in soils by chemical fractionation and multiple regression analysis. Environmental Pollution, 102, 269-277.

Reed, G.C., 2011. NI 43–101 Technical Report, Norra Kärr REE — Zirconium Deposit. Pincock, Allen & Holt, Gränna, Sweden.

Saxon, M., Leijd, M., Forrester, K., and Berg, J., 2015. Geology, Mineralogy, and Metallurgical Processing of the Norra Kärr Heavy REE Deposit, Sweden. In: Simandl, G.J. and Neetz, M., (Eds.), Symposium on Strategic and Critical Materials Proceedings, November 13-14, 2015, Victoria, British Columbia, British Columbia Ministry of Energy and Mines, British Columbia Geological Survey Paper 2015-3, pp. 97-107.

Tyler, G., 2004. Rare earth elements in soil and plant systems - A review. Plant and Soil, 267, 15.

Volokh, A.A., Gorbunov, A.V., Gundorina, S.F., and Revich, B.A., 1990. Phosphorus fertilizer production as a source of rare-earth

elements pollution of the environment. Science of the Total Environment, 95, 141.
Welch, R.M., 1995. Micronutrient nutrition of plants. Critical Review of Plant Science, 14, 49-82.
Wyttenbach, A., Furrer, V., Schleppi, P., and Tobler, L., 1998. Rare earth elements in soil and soil-grown plants. Plant and Soil, 199, 267-273.
Zhang, Z., Wang, Y., Li, F., Xiao, H., and Chai, Z., 2002. Distribution characteristics of rare earth elements in plants from a rare earth ore area. Journal of Radioactivity and Nuclear Chemistry 252, 461–465.

Biogeochemical methods to explore for carbonatites and related mineral deposits: An orientation survey, Blue River area, British Columbia, Canada

Robert Fajber[1, 2, a], George J. Simandl[1, 3], Pearce Luck[1], and Michaela Neetz[1]

[1] British Columbia Geological Survey, Victoria, BC
[2] Present address: University of Toronto, Toronto, ON
[3] University of Victoria, Victoria, BC
[a] corresponding author: rfajber@physics.utoronto.ca

Recommended citation: Fajber, R., Simandl, G.J., Luck, P., and Neetz, M., 2015. Biogeochemical methods to explore for carbonatites and related mineral deposits: An orientation survey, Blue River area, British Columbia, Canada. In: Simandl, G.J. and Neetz, M., (Eds.), Symposium on Strategic and Critical Materials Proceedings, November 13-14, 2015, Victoria, British Columbia. British Columbia Ministry of Energy and Mines, British Columbia Geological Survey Paper 2015-3, pp. 241-243.

1. Introduction

Carbonatites host economic deposits of niobium (Nb), rare earth elements (REE), phosphate, baddeleyite (natural zirconia), vermiculite, and fluorspar, and historically, supplied copper, uranium, carbonate (for cement industries) and sodalite (Pell, 1994 and Simandl, this volume).

The Upper Fir carbonatite is in southeastern British Columbia, approximately 200 km north of Kamloops (Fig. 1). It is one of many known carbonatite occurrences in the British Columbia alkaline province, which follows the Rocky Mountain Trench and extends from the southeastern tip of British Columbia to its northern boundaries with the Yukon and Northwest Territories (Pell, 1994). The Upper Fir is a strongly deformed carbonatite with an indicated mineral resource of 48.4 million tonnes at 197 ppm of Ta_2O_5 and 1,610 ppm of Nb_2O_5, and an inferred resource of 5.4 million tonnes at 191 ppm of Ta_2O_5 and 1760 ppm of Nb_2O_5 (Kulla et al. 2013). The Nb, Ta, and vermiculite mineralization is described by Simandl et al. (2002, 2010), Chong, et al, (2012), and Chudy (2014).

In this document we present the results of an orientation survey designed to determine the biogechemical signature of a typical carbonatite in the Canadian Cordillera. This survey suggests that needles and twigs of White Spruce (Picea glauca) and Subalpine Fir (Abies lasiocarpa) are suitable sampling media to explore for carbonatites and carbonatite-related rare earth elements (REE), niobium (Nb), and tantalum (Ta) deposits.

2. Orientation Survey

2.1. Sampling and analytical procedures

All vegetation samples were collected on August 23, 2010. Sampling was completed in less than 3 hours on a single day to avoid seasonal and diurnal variations. Branch tips about 10 cm long were collected from trees 5 to 7 m tall at heights of about 1.7 m. The sample sites are a well-drained hillside. Samples were immediately placed in Kraft sample bags which were approximately 500 to 700 cm^3 in volume.

All samples were dried at 80°C for 24 hours. Needles were then separated from twigs. Twigs were milled using a Wiley mill, and a 1 g split was digested in nitric acid (HNO_3) and then in aqua regia, and analyzed using inductively coupled plasma mass spectrometry (ICP-MS) and inductively coupled plasma atomic emission spectroscopy (ICP-AES) methods to ultra-low detection limits. A 50 g quantity of dry needles was ashed using controlled ignition at 475°C for 24 hours. A 0.25 g quantity of the needle ash was then digested in HNO_3 and analyzed using the same ICP-MS/ICP-AES methods. Weights of samples before and after ashing were recorded.

Analyses were conducted at Bureau Veritas Minerals (formerly Acme Laboratories) in Vancouver, British Columbia. The same suite of elements was selected for both twig and needle samples: K, Na, Ca, Mg, Fe, Al, Mn, Cr, Ti, S, P, Ba, Mo, Cu, Pb, Zn, Cd, Ni, Co, Se, As, Sr, Zr, Au, Ag, Pd, Pt, Li, Be, B, V, Ga, Ge, Rb, In, Sn, Re, Sb, Te, Cs, Hf, W, Hg, Tl, Bi, Th, U, Nb, Ta, Sc, Y, La, Ce, Pr, Nd, Sm, Eu, Gd, Tb, Dy, Ho, Er, Tm, Yb, and Lu.

2.2. Summary of results

At Upper Fir, La, Ce, Pr, Nd, Sm, Dy, Fe, Nb, Ta, P, and Y were identified as the most promising pathfinder elements. Concentrations of Ta and heavy REE (with the exception of Dy and Y) are near or below the lower limit of detection in Spruce twigs that were not treated by ashing. In 2011, the ashing procedure concentrated most trace elements in needles to levels well above the lower limit of detection. Ashing of both twigs and needles before analysis is recommended for future surveys. All samples of twigs, with the exception of sample BR-18, in which Ta was detected in concentrations higher than 0.002 ppm are spatially related to carbonatite or related altered rocks, commonly referred to as fenites (Fig. 2; Fajber et al., 2015). Although Ta is described as an unreliable biogeochemical pathfinder by Dunn (2007), Ta concentration in sample BR-18

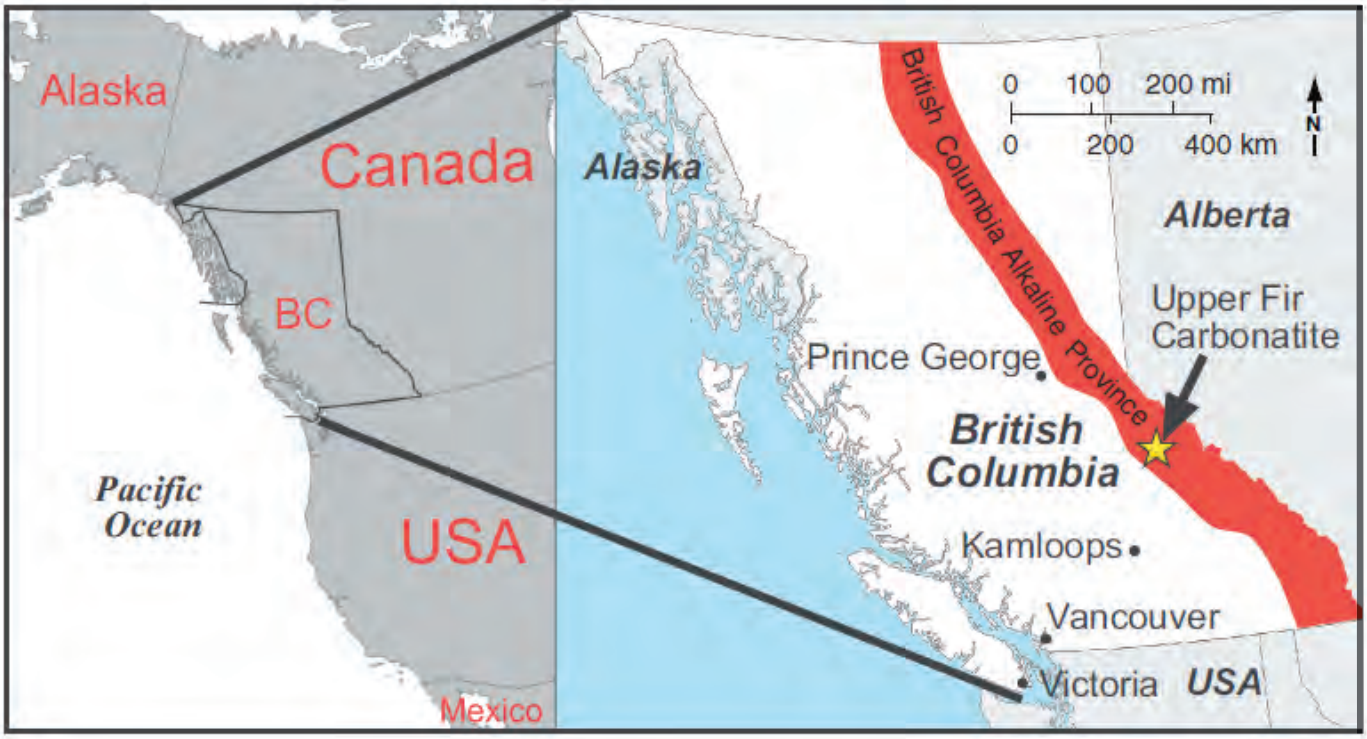

Fig. 1. Location of the Upper Fir carbonatite and British Columbia alkaline province, British Columbia, Canada.

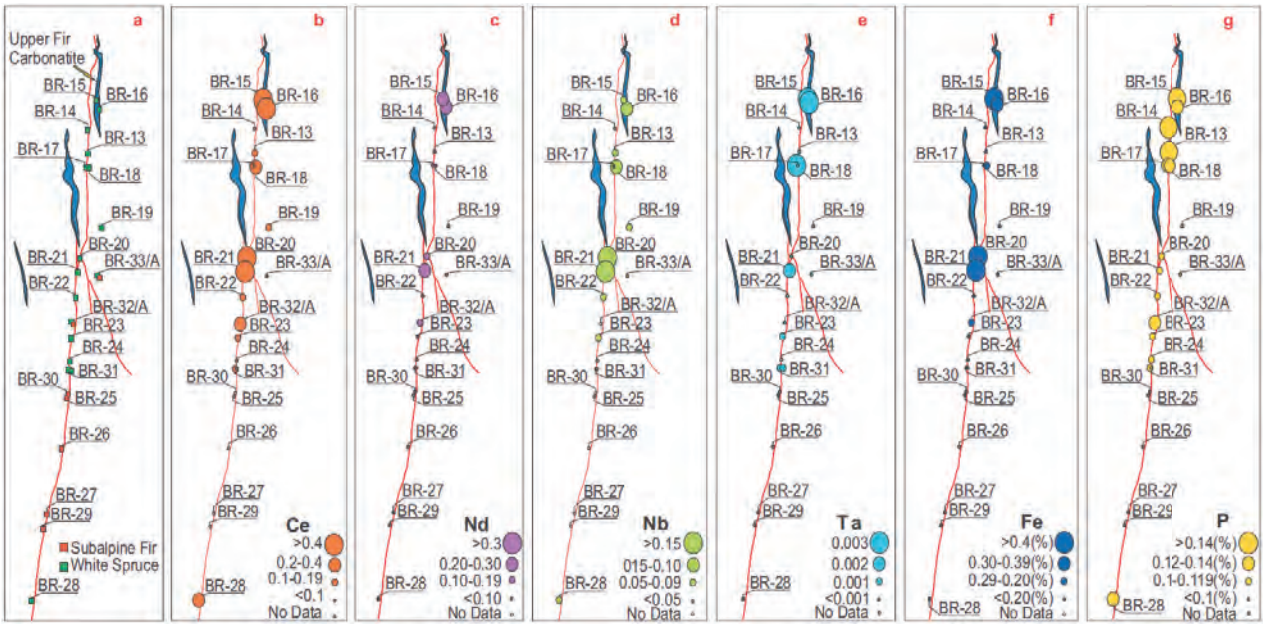

Fig. 2. Concentrations of selected carbonatite pathfinder elements in twigs (on dry weight basis), Upper Fir area. Samples BR-15 and BR-16 overlie the Upper Fir carbonatite; samples BR-20 and BR-21 overlie a zone of fenitization. **a)** sample media and concentrations of **b)** Ce, **c)** Nd, **d)** Nb, **e)** Ta, **f)** Fe, and **g)** P. All concentrations in parts per million unless otherwise indicated. From Fajber et al. (2015).

is unlikely to be spurious because it coincides with elevated concentrations of Nb, Ce and P (Fig. 2). It may correspond to a blind (near-surface, overburden-covered) extension of the carbonatite or an old drill site. Since 2011, when our samples were analyzed, the lower limit of detection for ash analysis has been reduced by half (Bureau Veritas Minerals, 2015). Because of this advancement, some of the elements we rejected in 2011 because of low concentrations may now be considered suitable pathfinders.

Twigs from a given sample contain consistently higher concentrations of pathfinder trace elements than the needles from the same sample, therefore twigs appear to be a better sampling medium. Based on our limited data (21 sample sites not counting duplicates) our survey suggests that a full-scale

survey should provide comparable results to those obtained by the soil geochemistry carried out by the Commerce Resources Corp. and described in Dahrouge and Wolbaum (2004).

Unweathered carbonatite rocks and related REE mineralization typically have steep chondrite-normalized REE patterns lacking a Eu anomaly (Fig. 3a; Fig. 6 in Simandl, 2014). Soils and vegetation samples taken above the Upper Fir carbonatite show systematic negative Eu anomalies (Fig. 3b,c). This indicates that presence or absence of a negative Eu anomaly in soil and vegetation can't be used to distinguish an anomaly caused by buried carbonatite from those caused by peralkaline intrusion, peraluminous granite, or rare metal-bearing pegmatite.

Acknowledgments

This project was supported by the Targeted Geoscience Initiative 4 (2010–2015), a Natural Resources Canada program. The Specialty Metal component of this program was carried out collaboratively between the Geological Survey of Canada and the British Columbia Geological Survey. Early comments from Colin Dunn (Consultant Geochemist, Victoria, British Columbia) and later detailed explanation regarding the laboratory procedure by John Gravel (Bureau Veritas Minerals, Vancouver) are appreciated. John Gorham, Janine Brown, and Brad Ulry from Dahrouge Geological Consulting Ltd. provided guidance in the field and constructive comments. Commerce Resources Corp. is thanked for sharing its expertise related to Upper Fir carbonatite and the Illinois Geological Survey for the permission to use figures 1, 2 and 3 that were previously published.

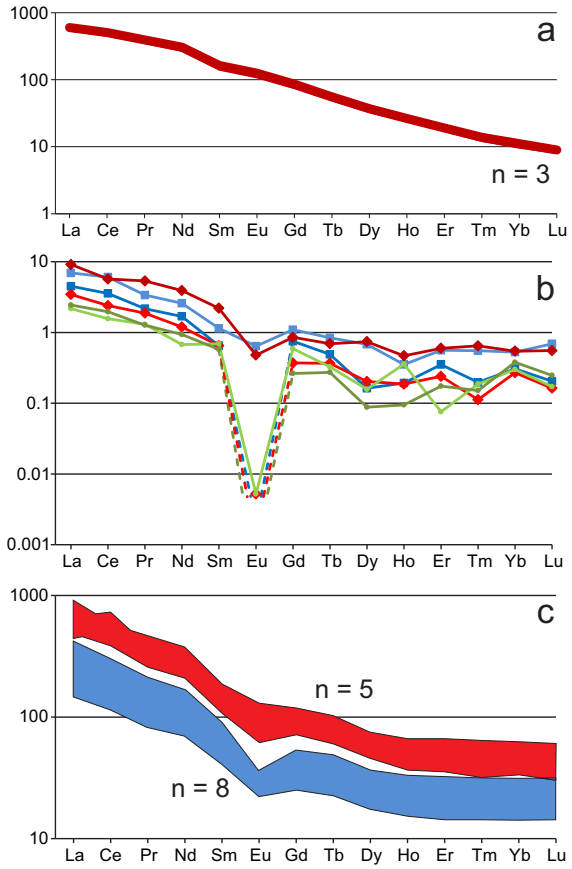

Fig. 3. Chondrite-normalized REE plots. **a)** Absence of negative Eu anomaly in Upper Fir carbonatite rocks. Envelope of three Upper Fir carbonatite analyses. **b)** Presence of negative Eu anomaly in Spruce needle ash overlying Upper Fir carbonatite (red diamonds; BR-15 and BR-16), fenite (blue squares; BR-20 and BR-21), and metasedimentary rocks (green circles; BR-13 and BR-17). Dotted lines represent projections where Eu concentrations were below the lower limit of detection. **c)** Soils overlying carbonatites (red, envelope of 5 analyses) contain higher concentrations of REE than those overlying schists and gneisses (blue, envelope of 8 analyses). All soil samples display negative Eu anomalies. Analysis of soil from Dahrouge and Wolbaum (2004). Chondrite normalization according to McDonough and Sun (1995). From Fajber et al. (2015).

References cited

Bureau Veritas Minerals, 2015. Schedule of services and fees (CDN). Bureau Veritas Minerals, 44 p., <http://acmelab.com/wp-content/uploads/2009/03/2015-Fee-Schedule.pdf>.accessed July 22, 2015.

Chong, A., Postolski, T., Mendoza, R.R., Lipiec, T., and Omidvar, B., 2012. Blue River Tantalum-Niobium Project, British Columbia. Vancouver, Canada, Commerce Resources Corp., NI 43-101 Technical Report on Mineral Resource Update, June 22, 2012, 450 p., <http://www.commerceresources.com/i/pdf/TechnicalReport-BlueRiverResourceUpdate.pdf>. accessed July 22, 2015.

Chudy, T.C., 2014. The petrogenesis of the Ta-bearing Fir carbonatite system, east-central British Columbia. Ph.D. dissertation, University of British Columbia, Vancouver, Canada, 585p.

Dahrouge, J., and Wolbaum, R., 2004. 2003 Exploration at the Blue River property, Commerce Resources Corp. Fort St. John, British Columbia Ministry of Energy and Mines, Assessment Report 27412, 11 p., <http://aris.empr.gov.bc.ca/search.asp?mode=repsum&rep_no=27412> accessed July 22, 2015.

Dunn, C., 2007. Biogeochemistry in mineral exploration. Elsevier, Amsterdam, 462p.

Fajber, R., Simandl, G.J., and Luck, P., 2015. Exploration for carbonatite-hosted niobium-tantalum deposits using biogeochemical methods (orientation survey), Blue River Area, British Columbia, Canada. In: Lasemi, Z., (ed.), Proceedings of the 47th Forum on the Geology of Industrial Minerals: Illinois State Geological Survey, Circular 587.

Kulla, G., Postolski, T., Mendoza, R.R., Lipiec, T., and Omidvar, B., 2013. Blue River Tantalum-Niobium Project, British Columbia, Canada. Vancouver, Canada, Commerce Resources Corp., NI 43-101 Technical Report on Mineral Resource Update, June 21, 2013 (Project No. 171542), 238p., <http://www.commerceresources.com/i/pdf/2013-06-21_NI43-101.pdf>. accessed July 22, 2015.

Pell, J., 1994. Carbonatites, nepheline syenites, kimberlites and related rocks in British Columbia. Victoria, British Columbia Ministry of Energy, Mines and Petroleum Resources, Bulletin 88, 133 p.

Simandl, G.J., 2014. Geology and market-dependent significance of rare earth element resources. Mineralia Deposita, 49, 889–904.

Simandl, G.J., 2015. Carbonatites and related exploration targets. In: Simandl, G.J. and Neetz, M., (Eds.), Symposium on Strategic and Critical Materials Proceedings, November 13-14, 2015, Victoria, British Columbia. British Columbia Ministry of Energy and Mines, British Columbia Geological Survey Paper 2015-3, pp. 31-37.

Simandl, G.J., Paradis, S., Simandl, L., and Dahrouge, J., 2010. Vermiculite in the Blue River area, east central British Columbia, Canada. Victoria, British Columbia Ministry of Energy and Mines, Geological Fieldwork 2009, Paper 2010-1, pp. 83–92.

Rapid and precise determination of major and trace elements in CCRMP and USGS geochemical reference samples using femtosecond laser ablation ICP-MS

Yoshiaki Kon[1, a], Daisuke Araoka[1], Terumi Ejima[1], Takafumi Hirata[2], and Tetsuichi Takagi[1]

[1] Geological Survey of Japan, National Institute of Advanced Industrial Science and Technology, 1-1-1 Higashi, Tsukuba, Ibaraki 305-8567, Japan
[2] Laboratory for Planetary Sciences, Kyoto University, Kitashirakawa Oiwakecho, Kyoto 606-8502, Japan
[a] corresponding author: yoshiaki-kon@aist.go.jp

Recommended citation: Kon, Y., Araoka, D., Ejima, T., Hirata, T., and Takagi, T., 2015. Rapid and precise determination of major and trace elements in CCRMP and USGS geochemical reference samples using femtosecond laser ablation ICP-MS. In: Simandl, G.J. and Neetz, M., (Eds.), Symposium on Strategic and Critical Materials Proceedings, November 13-14, 2015, Victoria, British Columbia, British Columbia Ministry of Energy and Mines, British Columbia Geological Survey Paper 2015-3, pp. 245-250.

Summary

We measured 10 major (SiO_2, TiO_2, Al_2O_3, total Fe_2O_3, MnO, MgO, CaO, Na_2O, K_2O, and P_2O_5) and 32 trace (Sc, V, Cr, Co, Ni, Cu, Zn, Rb, Sr, Y, Zr, Nb, Cs, Ba, La, Ce, Pr, Nd, Sm, Eu, Gd, Tb, Dy, Ho, Er, Tm, Yb, Lu, Hf, Pb, Th, and U) elements in 16 geochemical reference samples (AGV-1, AGV-2, BCR-1, BCR-2, BHVO-2, BIR-1a, DNC-1a, G-2, GSP-1, GSP-2, MAG-1, QLO-1, RGM-1, RGM-2, SGR-1b, and STM-1) distributed by United States Geological Survey (USGS) and three reference rock samples (SY-2, SY-3, and MRG-1) provided by Canadian Certified Reference Materials Project (CCRMP) using inductively coupled plasma–mass spectrometry coupled with the femtosecond laser ablation sample introduction technique (fsLA-ICP-MS). Before the elemental analysis, fused glass-beads were prepared from the mixture of sample powder and high-purity alkali flux with a mixing ratio of 1:10. The abundances of the major and trace elements were externally calibrated by using glass beads containing the major and trace elements prepared from 17 Geological Survey of Japan (GSJ) geochemical reference samples (JB-1, JB-1a, JB-2, JB-3, JA-1, JA-2, JA-3, JR-1, JR-2, JR-3, JP-1, JGb-1, JGb-2, JG-1a, JG-2, JG-3, and JSy-1). Typical analysis repeatabilities for these geochemical reference samples were better than 3% for Al_2O_3 and Na_2O; <5% for SiO_2, TiO_2, total Fe_2O_3, MnO, MgO, CaO, K_2O, P_2O_5, Zn, Rb, Sr, Zr, Nb, Ba, Nd, and U; <8% for Sc, V, Cr, Co, Y, Cs, La, Ce, Pr, Sm, Eu, Gd, Tb, Dy, Ho, Er, Tm, Yb, Lu, Hf, Pb, and Th; <11% for Ni and Cu. These data clearly demonstrate that high analytical repeatability can be achieved by the fsLA-ICP-MS technique with glass beads made from 0.5 g larger samples.

1. Introduction

Series of geochemical reference samples, such as igneous rocks, sedimentary rocks, sediments, and ores are available from institutes such as the Geological Survey of Japan (GSJ; e.g., Ando et al., 1987), the United States Geological Survey (USGS; e.g., Gladney et al., 1990) and the Canadian Certified Reference Materials Project (CCRMP; e.g., Gladney and Roelandts, 1990). These samples are widely used to evaluate the data quality of elemental analyses including critical and strategic materials.

X-ray fluorescence (XRF) spectroscopy is widely used to determine major and trace elements in rock samples. In this technique, pressed rock powder pellets (e.g., Sugisaki et al., 1981) or fused glass beads (e.g., Norrish and Hutton, 1969) are used for the analysis. A major limitation of XRF spectroscopy is that elemental sensitivity may be inadequate to obtain reliable abundance data for some trace elements, including rare earth elements (REEs). With ICP-MS, elemental sensitivity is better, and reliable abundance data for REEs can be obtained (e.g., Hirata et al., 1988). However, incomplete decomposition of refractory minerals such as chromite, monazite, and zircon may cause systematic errors in abundance data (e.g., Hirata et al., 1988; Imai, 1990). To minimize deterioration of data quality due to mass spectrometric interference or incomplete decomposition of the rock samples, the ICP-MS technique combined with a laser ablation sample introduction technique can be applied to the chemical analysis of rocks. With laser-ablation methods, possible analytical errors due to incomplete digestion can be minimized (e.g., Jarvis and Williams, 1993). Despite success in obtaining better precision in elemental determinations, a precise internal standardization procedure is still required. Abundances of the internal standardization elements (e.g., Si, Ca, or Sr) are measured separately by XRF analysis (e.g., Günther et al., 2001). Thus, the precision and accuracy of the abundance values of the analytes can be affected by the reliability of the abundance data for the internal standardization elements obtained by XRF. In this study, we employed a different internal standardization correction technique. We calibrated the abundance values of the analytes based on internal standardization with Li, obviating the use of internal standardization elements whose abundance values are

obtained separately by another analytical technique (Kon et al., 2011; Kon and Hirata, 2015).

Combination of the internal standardization protocol using Li and laser ablation using the femtosecond lasers, we then successfully determined abundances of 10 major and 32 trace elements in 18 USGS and three CCRMP geochemical reference samples. The data presented here demonstrate that combining Li normalization and the femtosecond-LA-ICP-MS (fsLA-ICP-MS) technique may be a powerful and rapid analytical tool for simultaneous measurement of major and trace elements in concentrations ranging from ppb to wt.%.

2. Analytical procedure

2.1. Sample preparation

Fused-glass beads were prepared from a mixture of 0.5 g of rock powder and 5 g of lithium tetraborate ($Li_2B_4O_7$, Spectromelt A10) flux. The weighing error in the sample-to-flux mixing ratio was not greater than 0.1%. The mixture was heated to 1200°C for 15 minutes in a 95% Pt−5% Au crucible with an inner diameter of 30 mm, using an automatic high-frequency bead sampler (TK-4100; Tokyo Kagaku Co. Ltd., Japan).

2.2. Instruments and analytical conditions of fsLA-ICP-MS

Elemental analysis was conducted by the combination of quadrupole ICP-MS system (Agilent 7500cx; Agilent Technologies Japan Ltd., Japan) and the femtosecond laser-ablation system developed in-house (Hirata and Kon, 2008) and installed at the GSJ, National Institute of Advanced Industrial Science and Technology, Japan. The femtosecond laser-ablation system incorporates a TiS femtosecond laser (IFRIT; Cyber Laser Inc., Japan) as a 260 nm UV light source (third harmonic generation from NIR fundamental wavelength). In this study, a galvanometric optical scanner was employed to move the ablation points within 10 msec without moving the samples (Yokoyama et al., 2011). Present Galvanometric optics allow laser ablation of a 20 mm x 20 mm area. The laser system was operated using a pit diameter of approximately 20 μm, and the laser ablation used a pulse energy of 10 J/cm^2, an emission repetition rate of 1000 Hz, and a pulse duration of 150 s. To minimize elemental fractionation during ablation and for effective ablation of the glass beads, the ablation spot was moved 10,000 μm/s using the galvanometric optics. Kon and Hirata (2015) present detailed analysis conditions and data processing.

2.3. Reference samples

Elemental compositions of 16 USGS and three CCRMP geochemical reference samples were determined: basalt (BCR-1, BCR-2, BHVO-2, BIR-1a), andesite (AGV-1, AGV-2), rhyolite (RGM-1, RGM-2), gabbro (MRG-1), dolerite (DNC-1a), granite (G-2, GSP-1, GSP-2), syenite (STM-1, SY-2, SY-3), quartz latite (QLO-1), shale (SGR-1b), and marine sediment (MAG-1). We used a calibration line protocol to calculate abundance values. Calibration curves for the analytes were defined using basalt (JB-1, JB-1a, JB-2, and JB-3), andesite (JA-1, JA-2, and JA-3), rhyolite (JR-1, JR-2, and JR-3), peridotite (JP-1), gabbro (JGb-1 and JGb-2), granite (JG-1a, JG-2, and JG-3), and syenite (JSy-1) geochemical reference samples provided by the GSJ. We defined calibration lines by plotting Li-normalized intensities against recent published values of the GSJ samples. The published values were selected preferentially, first using GeoReM preferred values (Jochum et al., 2005); Shimizu et al., (2011); Dulski (2001); Makishima and Nakamura (1999, 2006); Lu et al. (2007) then GSJ recommended values (Imai et al., 1995, 1999).

3. Results and discussion

3.1. Elemental compositions of the USGS and CCRMP geochemical reference samples

We determined the abundances of the major and trace elements in the 16 USGS and three CCRMP geochemical reference samples. The averaged abundance data with repeatabilities (relative standard deviation, %RSD) are listed in Table 1. The quantitative limit (QL) on each element are also listed in Table 1. Typically, the repeatabilities for the geochemical reference samples were better than 3% for Al_2O_3 and Na_2O; <5% for SiO_2, TiO_2, total Fe_2O_3, MnO, MgO, CaO, K_2O, P_2O_5, Zn, Rb, Sr, Zr, Nb, Ba, Nd, and U; <8% for Sc, V, Cr, Co, Y, Cs, La, Ce, Pr, Sm, Eu, Gd, Tb, Dy, Ho, Er, Tm, Yb, Lu, Hf, Pb, and Th; <11% for Ni and Cu.

3.2. Reliability of the analyses

We normalized the measured abundance data of major and trace elements in five USGS geochemical reference samples (AGV-1, AGV-2, BCR-1, BCR-2, and BHVO-2) by the abundance values in the GeoReM compilation (Jochum et al., 2005), and plotted the normalized values (Fig. 1).

The relative deviation ranges of the measured abundance values from the GeoReM values were as follows: Pb, –6.1% to 0.8%; Rb, –3.5% to 0.1%; Cs, –4.0% to 4.9%; Ba, 1.2% to 4.8%; Zr, –1.2% to 3.9%; Hf, 0.8% to 5.0%; Nb, –3.3% to -0.6%; and heavy REEs (HREEs), –10.5% to 4.7% (Fig. 1). For almost all trace elements, including volatile elements and zircon-favoured elements, the composition of these five reference samples were consistent with the GeoReM compilation values (Jochum et al., 2005) within the uncertainty of each, indicating good reliability of our procedure. In particular, the abundances of highly volatile (Pb) and relatively volatile (Rb, Cs, and Ba) elements were expected to be lower than the GeoReM values. This is mainly due to the evaporation loss of volatile elements during the high-temperature preparation procedures for glass bead. Abundances of zircon-favoured elements (Zr, Hf, Nb, and HREEs) might also be lower, possibly recording incomplete decomposition of the zircon grains in the rock samples. The lack of any deficiency in the abundance values of these volatile and zircon-favoured elements therefore demonstrates that reliable abundance data can be obtained by the present approach.

Table 1. Averaged regression values of the standard samples.

		AGV-1		AGV-2		BCR-1		BCR-2		BHVO-2		BIR-1a		DNC-1a		G-2		GSP-1	
(wt.%)	QL	Avg.	RSD	Avg.	RSD	Avg.	RSD	Avg.	RSD	Avg.	RSD	Avg.	RSD	Avg.	RSD	Avg.	RSD	Avg.	RSD
SiO_2	16	58.1	0.9%	59.1	0.7%	53.5	1.7%	53.1	1.2%	49.8	1.8%	48.0	2.0%	n.d.		69.4	2.7%	67.3	3.2%
TiO_2	0.029	1.04	1.4%	1.04	1.0%	2.26	3.5%	2.26	3.1%	2.78	3.3%	0.973	2.7%	0.479	3.3%	0.487	3.8%	0.672	4.0%
Al_2O_3	0.82	16.8	1.4%	16.8	0.9%	13.3	1.8%	13.3	1.5%	13.4	1.5%	15.4	2.2%	18.2	2.3%	15.4	2.7%	15.1	2.8%
tFe_2O_3	0.25	6.58	2.6%	6.65	1.9%	13.4	3.8%	13.7	2.7%	12.4	3.6%	11.5	3.4%	9.78	3.9%	2.65	3.6%	4.26	3.1%
MnO	0.012	0.0957	1.6%	0.10	0.9%	0.184	4.1%	0.198	3.5%	0.171	3.8%	0.175	3.8%	0.147	4.4%	0.034	8.6%	0.0409	7.2%
MgO	0.15	1.45	3.7%	1.74	2.7%	3.43	1.8%	3.53	1.2%	7.29	1.4%	9.67	1.4%	10.0	1.8%	0.704	7.3%	0.927	6.0%
CaO	0.13	4.73	2.9%	5.06	2.0%	6.82	3.6%	6.95	3.3%	11.4	2.8%	13.3	2.9%	11.1	3.8%	1.83	3.8%	1.90	3.9%
Na_2O	0.26	4.16	1.3%	4.12	0.9%	3.21	1.4%	3.07	1.2%	2.20	1.9%	1.81	2.9%	1.88	2.7%	4.03	1.8%	2.76	2.2%
K_2O	0.12	2.88	1.6%	2.86	0.8%	1.70	1.8%	1.76	1.8%	0.538	5.0%	n.d.		0.255	12.0%	4.44	2.9%	5.46	3.3%
P_2O_5	0.014	0.501	1.4%	0.482	2.2%	0.374	2.2%	0.364	1.3%	0.276	2.5%	0.0157	12.1%	0.0630	3.9%	0.127	3.8%	0.280	4.2%
(ppm)																			
Sc	4.6	12.1	3.1%	12.8	4.4%	32.1	3.6%	32.6	2.8%	31.4	2.8%	42.5	5.0%	30.1	3.3%	4.56	12.5%	7.21	10.6%
V	8.1	121	2.7%	121	2.7%	414	3.7%	417	3.1%	325	3.6%	332	3.9%	151	5.0%	36.6	7.5%	53.8	6.1%
Cr	25	n.d.		n.d.		n.d.		n.d.		290	3.1%	394	2.9%	283	4.1%	n.d.		n.d.	
Co	1.4	14.6	3.8%	15.1	3.6%	37.3	2.8%	37.6	2.6%	45.7	2.4%	54.2	2.8%	58.4	2.9%	n.d.		5.85	8.1%
Ni	3.3	15.0	6.5%	18.9	7.9%	10.5	14.6%	11.8	11.7%	124	2.3%	181	2.3%	274	2.8%	n.d.		n.d.	
Zn	12	93.0	5.2%	91.2	2.6%	133	3.4%	135	1.9%	106	2.6%	74.1	2.7%	67.3	5.8%	85.2	2.0%	104	2.5%
Rb	9.2	65.6	1.8%	66.3	2.1%	45.7	4.7%	45.2	4.7%	n.d.		n.d.		n.d.		166	3.7%	252	3.9%
Sr	4.9	658	3.1%	663	2.2%	335	4.7%	341	4.1%	401	3.8%	111	4.7%	144	5.4%	469	3.9%	228	2.9%
Y	5.4	18.5	5.0%	19.1	3.7%	34.3	2.6%	34.2	2.5%	25.1	3.5%	15.4	8.2%	16.8	6.4%	10.4	9.6%	25.9	3.2%
Zr	21	228	2.0%	234	1.7%	192	2.6%	191	2.3%	175	1.9%	n.d.		40.2	10.9%	347	4.0%	623	5.2%
Nb	3.9	14.1	3.3%	14.1	2.8%	12.6	4.8%	12.4	4.6%	18.0	2.7%	n.d.		n.d.		12.4	4.8%	26.2	3.0%
Cs	0.45	1.27	7.3%	1.15	6.7%	0.976	10.7%	1.14	10.0%	n.d.		n.d.		n.d.		1.33	5.2%	1.01	6.4%
Ba	20	1260	2.3%	1180	1.6%	712	3.8%	705	3.3%	133	6.1%	n.d.		102	9.0%	1920	2.9%	1320	2.5%
La	3.0	37.8	1.9%	37.8	1.8%	25.5	2.9%	25.3	2.4%	15.5	3.4%	n.d.		n.d.		86.5	4.8%	178	5.3%
Ce	5.9	68.1	2.3%	69.0	1.6%	53.3	2.9%	52.7	2.2%	37.6	2.6%	n.d.		n.d.		159	4.4%	426	5.1%
Pr	0.81	8.36	2.5%	8.19	1.5%	6.94	3.1%	6.90	2.7%	5.45	2.7%	n.d.		n.d.		16.2	4.5%	53.4	5.2%
Nd	3.1	31.3	2.4%	30.4	2.1%	28.9	2.7%	28.8	2.7%	24.6	2.1%	n.d.		n.d.		52.1	4.7%	199	5.5%
Sm	0.77	5.69	3.2%	5.43	1.8%	6.62	2.7%	6.62	2.9%	6.08	2.4%	n.d.		1.39	14.3%	6.93	4.0%	25.3	5.4%
Eu	0.016	1.61	5.5%	1.54	5.0%	2.00	6.7%	1.99	6.0%	2.11	5.6%	0.524	5.2%	0.590	8.1%	1.33	3.5%	2.19	3.9%
Gd	0.81	4.74	2.6%	4.54	4.1%	6.98	3.9%	7.07	2.7%	6.46	2.7%	1.81	12.0%	1.92	11.4%	3.99	5.5%	13.0	4.8%
Tb	0.14	0.641	3.7%	0.621	3.4%	1.05	3.1%	1.06	2.7%	0.943	1.6%	0.373	8.2%	0.393	7.4%	0.461	5.7%	1.26	3.7%
Dy	0.96	3.56	4.3%	3.48	3.5%	6.39	3.0%	6.36	3.3%	5.29	2.8%	2.55	9.5%	2.68	8.4%	2.19	7.2%	5.71	3.2%
Ho	0.22	0.666	4.6%	0.656	5.1%	1.28	3.1%	1.27	3.2%	0.978	3.6%	0.566	9.0%	0.613	6.8%	0.372	10.1%	0.931	3.8%
Er	0.55	1.82	4.7%	1.78	5.7%	3.65	3.8%	3.60	3.5%	2.50	4.9%	1.67	7.5%	1.84	7.8%	0.915	12.1%	2.29	3.2%
Tm	0.086	0.251	6.1%	0.251	6.3%	0.516	4.1%	0.521	3.3%	0.332	5.3%	0.248	7.9%	0.283	5.5%	0.123	12.5%	0.291	2.7%
Yb	0.58	1.63	6.3%	1.65	5.4%	3.37	3.4%	3.39	4.9%	2.03	5.0%	1.67	8.4%	1.92	7.6%	n.d.		1.68	6.1%
Lu	0.095	0.246	5.6%	0.245	6.7%	0.499	3.9%	0.500	3.8%	0.278	6.6%	0.244	9.8%	0.287	8.0%	n.d.		0.239	4.9%
Hf	0.76	5.14	2.1%	5.25	1.9%	5.10	3.3%	5.08	3.5%	4.58	2.3%	n.d.		1.13	13.1%	8.27	3.8%	16.0	4.7%
Pb	1.7	35.2	2.8%	13.3	1.3%	13.6	3.1%	10.3	3.7%	n.d.		3.14	12.8%	5.77	7.2%	29.8	3.9%	53.3	4.0%
Th	1.6	6.61	4.0%	6.52	2.9%	6.46	4.5%	6.39	4.3%	n.d.		n.d.		n.d.		24.4	4.6%	105	5.1%
U	0.52	2.02	2.0%	1.99	2.2%	1.82	4.0%	1.80	3.8%	n.d.		n.d.		n.d.		2.12	4.0%	2.51	3.5%

Table 1. Continued.

	GSP-2		MAG-1		QLO-1		RGM-1		RGM-2		SGR-1b		STM-1		SY-2		SY-3		MRG-1	
(wt.%)	Avg.	RSD	Avg.	RSD	Avg.	RSD	Avg.	RSD	Avg.	RSD	Avg.	RSD	Avg.	RSD	Avg.	RSD	Avg.	RSD	Avg.	RSD
SiO_2	67.0	2.2%	49.9	5.2%	n.d.		73.7	2.6%	n.d.		29.4	11%	60.0	3.2%	59.8	3.4%	59.7	4.4%	39.1	4.2%
TiO_2	0.671	3.3%	0.700	2.8%	0.594	10%	0.278	5.0%	0.271	4.6%	0.238	3.5%	0.132	5.2%	0.136	4.6%	0.150	8.3%	3.81	5.0%
Al_2O_3	14.9	2.7%	16.0	2.1%	16	9.9%	13.7	2.3%	13.7	2.5%	6.36	1.3%	18.5	2.2%	12.0	1.8%	11.5	1.7%	8.21	2.7%
tFe_2O_3	4.85	2.8%	6.71	3.2%	4.21	9.0%	1.84	3.6%	1.84	4.1%	2.59	3.4%	5.19	2.6%	6.19	2.6%	6.40	3.3%	17.9	4.4%
MnO	0.042	6.4%	0.096	2.4%	0.091	9.6%	0.036	7.8%	0.038	7.6%	0.031	9.5%	0.222	2.1%	0.319	1.8%	0.330	2.4%	0.171	5.1%
MgO	0.916	6.2%	2.95	2.2%	0.963	6.8%	n.d.		n.d.		4.48	2.2%	n.d.		2.65	2.3%	2.64	2.4%	13.5	2.0%
CaO	1.99	3.8%	1.27	4.0%	3.02	7.5%	1.13	4.6%	1.09	4.9%	8.32	2.6%	1.05	5.1%	7.90	2.5%	8.20	2.9%	14.8	3.8%
Na_2O	2.78	1.9%	3.84	1.7%	4.08	7.7%	4.11	1.9%	4.04	2.2%	2.98	1.4%	8.82	2.2%	4.26	1.5%	4.05	1.7%	0.732	9.3%
K_2O	5.37	2.7%	3.51	2.8%	3.52	8.1%	4.33	3.1%	4.31	3.0%	1.57	1.7%	4.21	2.4%	4.45	2.4%	4.14	3.1%	n.d.	
P_2O_5	0.286	2.9%	0.157	3.6%	0.251	8.2%	0.041	9.4%	0.040	9.7%	0.249	3.1%	0.154	3.2%	0.430	2.7%	0.538	3.3%	0.058	4.2%
(ppm)																				
Sc	7.39	10%	17.0	4.5%	n.d.		5.92	11%	5.76	14%	n.d.	15%	n.d.		7.72	8.3%	7.36	11%	54.3	5.6%
V	54.3	5.9%	139	2.7%	49	10%	n.d.		n.d.		121	2.6%	n.d.		51.1	4.8%	50.6	6.0%	542	4.8%
Cr	n.d.		101	5.7%	n.d.		n.d.		n.d.		36.7	15%	n.d.		n.d.		n.d.		462	3.9%
Co	6.26	9.1%	20.9	3.2%	6.21	10%	n.d.		n.d.		9.76	5.6%	n.d.		7.25	8.0%	7.48	6.1%	91.8	3.2%
Ni	16.4	8.2%	50.5	4.1%	n.d.		n.d.		n.d.		24.9	5.6%	n.d.		n.d.		n.d.		198	3.3%
Zn	113	1.9%	129	3.5%	58.9	8.0%	32.9	10%	33.7	10%	39.8	6.7%	237	3.7%	252	3.0%	247	4.1%	267	3.6%
Rb	242	3.4%	144	4.1%	68.6	8.7%	149	3.9%	149	3.8%	76.1	3.7%	112	3.3%	220	3.5%	203	5.4%	n.d.	
Sr	232	3.5%	136	3.0%	321	7.7%	105	2.5%	102	2.0%	395	4.1%	685	4.8%	273	3.1%	306	4.8%	280	5.7%
Y	25.6	4.7%	25.7	2.9%	22.6	6.6%	22.5	3.2%	22.4	3.0%	11.0	9.6%	41.9	3.8%	122	3.8%	687	7.3%	13.4	9.8%
Zr	586	4.8%	131	2.8%	186	8.8%	233	4.2%	231	4.3%	51.0	7.4%	1300	4.5%	303	3.1%	358	5.0%	111	4.6%
Nb	25.6	2.7%	15.1	4.1%	10.5	6.4%	9.59	6.6%	9.53	6.6%	6.82	11%	246	4.9%	29.0	2.3%	187	5.5%	19.2	4.0%
Cs	1.16	7.3%	8.10	4.6%	1.61	8.1%	9.72	4.3%	9.66	4.3%	4.79	3.7%	1.50	3.3%	2.68	2.2%	2.63	4.4%	n.d.	
Ba	1370	2.1%	483	3.7%	1400	10%	859	2.8%	842	2.5%	295	3.9%	587	3.4%	462	2.7%	447	5.1%	n.d.	
La	181	5.0%	40.7	4.7%	25.8	9.9%	n.d.	3.6%	22.7	3.6%	19.0	4.1%	145	4.9%	69.8	4.0%	1330	8.1%	9.4	8.2%
Ce	435	4.8%	83.5	4.7%	48.5	10%	45.3	3.2%	45.0	3.0%	34.5	3.7%	257	5.1%	161	4.3%	2270	7.6%	26.3	5.2%
Pr	54.4	4.6%	9.87	4.8%	5.77	9.5%	5.26	3.5%	5.22	3.1%	4.11	4.0%	25.2	4.9%	20.1	4.3%	224	7.5%	3.95	4.8%
Nd	202	5.0%	36.7	4.7%	22.1	9.7%	18.9	2.9%	18.9	2.7%	14.5	3.6%	78.5	4.8%	76.8	4.3%	728	7.9%	18.5	4.7%
Sm	25.5	5.6%	7.02	4.7%	4.41	9.2%	3.89	3.8%	3.86	4.8%	2.58	3.1%	11.9	5.3%	16.1	4.6%	122	7.8%	4.43	4.8%
Eu	2.21	4.5%	1.38	5.4%	1.24	7.8%	0.622	4.5%	0.607	5.1%	0.50	5.2%	3.37	5.5%	2.47	3.7%	17.7	6.0%	1.47	7.9%
Gd	13.1	4.7%	6.18	4.6%	4.28	9.8%	3.66	3.7%	3.65	4.2%	2.05	8.1%	9.39	4.5%	17.6	4.9%	125	7.5%	4.28	4.9%
Tb	1.26	5.3%	0.892	4.3%	0.642	8.5%	0.599	4.6%	0.598	3.1%	0.316	7.6%	1.37	4.5%	2.98	4.3%	19.8	7.5%	0.589	5.9%
Dy	5.65	4.1%	5.03	3.7%	3.80	7.7%	3.71	3.8%	3.67	2.9%	1.90	8.0%	7.80	4.0%	20.0	4.2%	127	7.5%	3.11	6.7%
Ho	0.930	5.0%	0.971	4.0%	0.799	8.2%	0.763	2.7%	0.765	3.7%	0.370	11%	1.47	4.8%	4.55	4.4%	27.5	7.8%	0.531	9.7%
Er	2.26	5.8%	2.68	3.6%	2.34	8.1%	2.29	4.0%	2.29	4.0%	1.04	11%	4.18	4.6%	15.0	4.5%	82.8	7.7%	1.25	11%
Tm	0.284	5.3%	0.387	3.9%	0.346	7.5%	0.356	3.6%	0.355	2.9%	0.155	11%	0.619	4.8%	2.42	4.3%	11.5	7.6%	0.156	15%
Yb	1.64	8.2%	2.54	3.3%	2.32	7.8%	2.49	4.1%	2.44	2.8%	0.994	13%	4.17	5.3%	17.7	4.9%	66.6	7.9%	n.d.	
Lu	0.228	7.7%	0.373	4.0%	0.366	7.6%	0.388	3.7%	0.390	3.7%	0.155	12%	0.614	3.9%	2.89	5.1%	8.12	8.1%	n.d.	
Hf	14.8	5.2%	3.71	4.3%	4.71	9.9%	6.15	4.4%	6.16	4.4%	1.55	7.4%	27.8	5.4%	8.61	3.8%	9.54	6.6%	4.07	4.3%
Pb	40.4	3.6%	25.2	5.0%	19.5	11%	25.8	3.9%	23.0	3.7%	10.8	3.3%	16.8	3.8%	88.6	4.6%	145	7.5%	5.08	8.2%
Th	106	5.1%	12.2	4.7%	5.00	7.7%	14.8	3.9%	14.8	3.9%	5.25	5.1%	29.9	4.7%	n.d.		n.d.		n.d.	
U	2.55	3.8%	2.82	4.4%	1.89	9.9%	5.64	3.9%	5.61	3.8%	5.31	4.4%	8.52	4.5%	n.d.		n.d.		n.d.	

QL, quantitative limit; Avg., Averaged concentration; %RSD, relative repeatability of the analyses (n = 10); n.d., not detected.

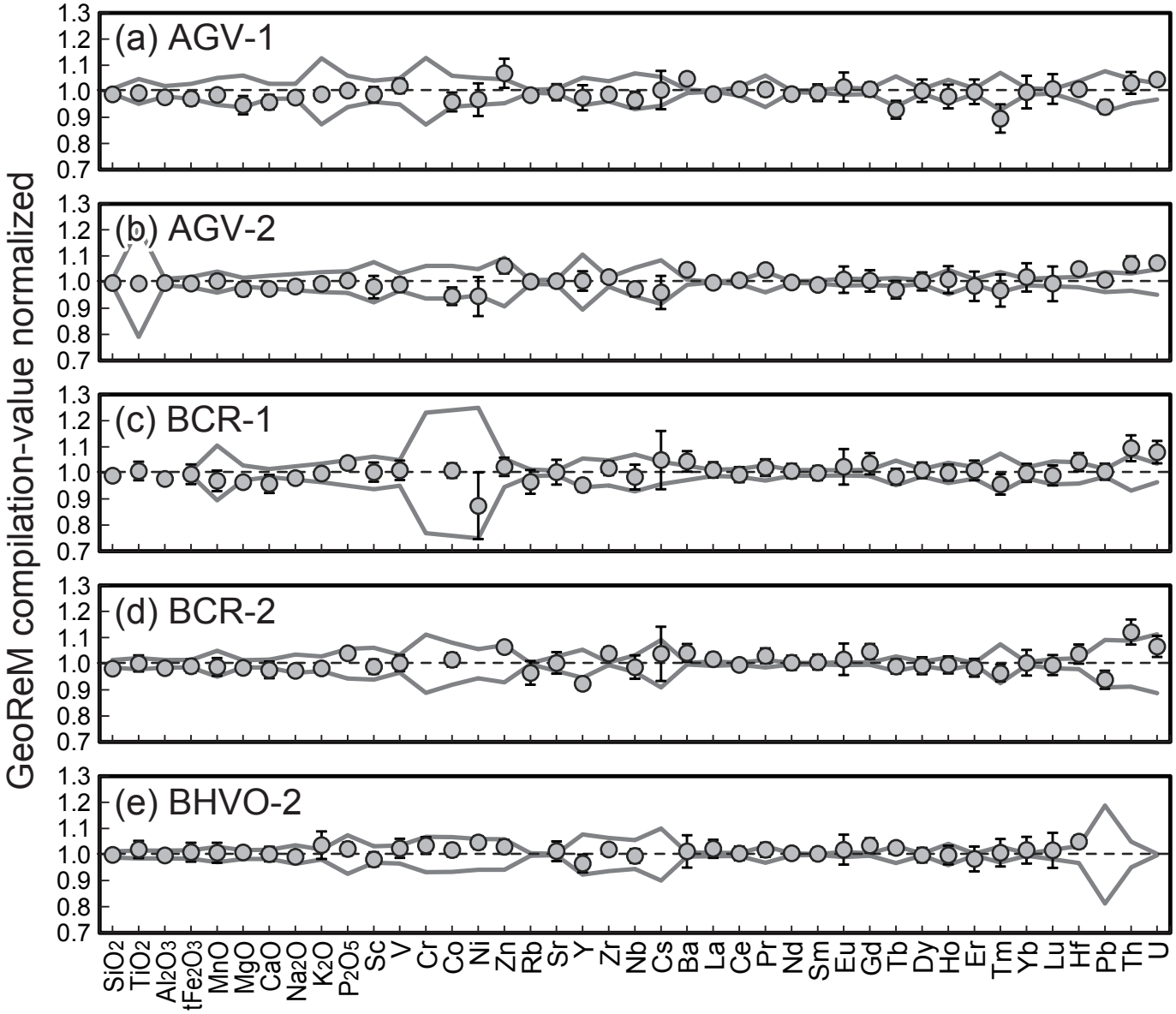

Fig. 1. Comparison of measured abundance data and recently published values for trace elements with GeoReM values (Measured/Reference). **a)** AGV-1, **b)** AGV-2, **c)** BCR-1, **d)** BCR-2, and **e)** BHVO-2. Grey lines show the uncertainties (%RSD) of the GeoReM compilation values (Jochum et al., 2005).

4. Conclusion

We measured the abundances of 10 major and 32 trace elements in 16 USGS and three CCRMP geochemical reference samples. Repeatabilities of the measurements of these samples were better than 5% for almost all major elements, and better than 8% for most trace elements. The reliability of the major and trace element measurements was evaluated by comparison of the measured abundance values with reported values for basaltic and andesitic USGS geochemical reference samples. The data obtained here showed good agreement with recently compiled values.

Acknowledgments

We thank Michaela Neetz for valuable comments. Dr. N. Imai and Dr. T. Okai helped us to obtain the reference samples. Glass beads were produced in a shared-use laboratory at GSJ, for the use of which we thank Drs. M. Ogasawara, N. Geshi, and M. Mikoshiba. This work was partly supported by a Grant-in-Aid for Scientific Research A26247094 to TH from the Ministry of Education, Culture, Sports, Science and Technology, Japan.

References cited

Ando, A., Mita, N., and Terashima, S., 1987. 1986 Values for Fifteen GSJ Rock Reference Samples, "Igneous Rock Series." Geostandards Newsletter, 11, 159–166.

Dulski, P., 2001. Reference Materials for Geochemical Studies: New Analytical Data by ICP-MS and Critical Discussion of Reference Values. Geostandards Newsletter, 25, 87–125.

Gladney, E. S., Jones, E. A., Nickell, E. J., and Roelandts, I., 1990.

1988 Compilation of Elemental Concentration Data for USGS Basalt BCR-1. Geostandards Newsletter, 14, 209–359.
Gladney, E. S., Jones, E. A., Nickell, E. J., and Roelandts, I., 1991. 1988 Compilation of Elemental Concentration Data for USGS DTS-1, G-1, PCC-1 and W-1. Geostandards Newsletter, 15, 199–396.
Günther, D., Quadt, A. v., Wirz, R., Cousin, H., and Dietrich, V. J., 2001. Elemental Analyses Using Laser Ablation-Inductively Coupled Plasma-Mass Spectrometry (LA-ICP-MS) of Geological Samples Fused with Li2B4O7 and Calibrated Without Matrix-Matched Standards. Microchimica Acta, 136, 101–107.
Hirata, T., and Kon, Y., 2008. Evaluation of the Analytical Capability of NIR Femtosecond Laser Ablation-Inductively Coupled Plasma Mass Spectrometry. Analytical Sciences, 24, 345–353.
Hirata, T., Shimizu, H., Akagi, T., Sawatari, H., and Masuda, A., 1988. Precise determination of rare earth elements in geological standard rocks by inductively coupled plasma source mass spectrometry. Analytical sciences, 4, 637–643.
Imai, N., 1990. Quantitative analysis of original and powdered rocks and mineral inclusions by laser ablation inductively coupled plasma mass spectrometry. Analytica Chimica Acta, 235, 381–391.
Imai, N., Terashima, S., Itoh, S., and Ando, A., 1995. 1994 Compilation of analytical data for minor and trace elements in seventeen GSJ geochemical reference samples, "igneous rock series." Geostandards Newsletter, 19, 135–213.
Imai, N., Terashima, S., Itoh, S., and Ando, A., 1999. 1998 Compilation of Analytical Data for Five GSJ Geochemical Reference Samples: The "Instrumental Analysis Series." Geostandards Newsletter, 23, 223–250.
Jarvis, K.E., and Williams, J.G., 1993. Laser ablation inductively coupled plasma mass spectrometry (LA-ICP-MS): a rapid technique for the direct, quantitative determination of major, trace and rare-earth elements in geological samples. Chemical Geology, 106, 251–262.
Jochum, K.P., Nohl, U., Herwig, K., Lammel, E., Stoll, B., and Hofmann, A. W., 2005. GeoReM: A New Geochemical Database for Reference Materials and Isotopic Standards. Geostandards and Geoanalytical Research, 29, 333–338.
Kon, Y., and Hirata, T., 2015. Determination of 10 major and 34 trace elements in 34 GSJ geochemical reference samples using femtosecond laser ablation ICP-MS. Geochemical Journal, 49, 351–375.
Kon, Y., Murakami, H., Takagi, T., and Watanabe, Y., 2011. The development of whole rock analysis of major and trace elements in XRF glass bead by fsLA-ICPMS in GSJ geochemical reference samples. Geochemical Journal, 45, 387–416.
Lu, Y., Makishima, A., and Nakamura, E., 2007. Coprecipitation of Ti, Mo, Sn and Sb with fluorides and application to determination of B, Ti, Zr, Nb, Mo, Sn, Sb, Hf and Ta by ICP-MS. Chemical Geology, 236, 13–26.
Makishima, A., and Nakamura, E., 1999. Determination of Molybdenum, Antimony and Tungsten at sub μg g−1 Levels in Geological Materials by ID-FI-ICP-MS. Geostandards Newsletter, 23, 137–148.
Makishima, A., and Nakamura, E., 2006. Determination of Major/Minor and Trace Elements in Silicate Samples by ICP-QMS and ICP-SFMS Applying Isotope Dilution-Internal Standardisation (ID-IS) and Multi-Stage Internal Standardisation. Geostandards and Geoanalytical Research, 30, 245–271.
Norrish, K., and Hutton, J.T., 1969. An accurate X-ray spectrographic method for the analysis of a wide range of geological samples. Geochimica et Cosmochimica Acta, 33, 431–453.
Shimizu, K., Chang, Q., and Nakamura, K., 2011. Flux-Free Fusion of Silicate Rock Preceding Acid Digestion for ICP-MS Bulk Analysis. Geostandards and Geoanalytical Research, 35, 45–55.
Sugisaki, R., Kinoshita, T., Shimomura, T., and Ando, K., 1981. An automatic X-ray fluorescence method for the trace element analyses in silicate rocks. Journal of the Geological Society of Japan, 87, 675–688.
Yokoyama, T. D., Suzuki, T., Kon, Y., and Hirata, T., 2011. Determinations of Rare Earth Element Abundance and U-Pb Age of Zircons Using Multispot Laser Ablation-Inductively Coupled Plasma Mass Spectrometry. Analytical Chemistry, 83, 8892–8899.

Fluorite trace-element chemistry and its potential as an indicator mineral: Evaluation of LA-ICP-MS method

Mao Mao[1, 2, a], George J. Simandl[1, 3], Jody Spence[3], and Daniel Marshall[2]

[1] British Columbia Geological Survey, Ministry of Energy and Mines, Victoria, BC, V8W 9N3
[2] Department of Earth Sciences, Simon Fraser University, Burnaby, BC, V5A 1S6
[3] School of Earth and Ocean Sciences, University of Victoria, Victoria, BC, V8P 5C2
[a] corresponding author: mao.mao13@outlook.com

Recommended citation: Mao, M., Simandl, G.J., Spence, J., and Marshall, D., 2015. Fluorite trace-element chemistry and its potential as an indicator mineral: Evaluation of LA-ICP-MS method. In: Simandl, G.J. and Neetz, M., (Eds.), Symposium on Strategic and Critical Materials Proceedings, November 13-14, 2015, Victoria, British Columbia. British Columbia Ministry of Energy and Mines, British Columbia Geological Survey Paper 2015-3, pp. 251-264.

1. Introduction

Fluorite (CaF_2) belongs to the isometric system, with a cubic, face-centred lattice. Fluorite commonly forms cubes or octahedrons, less commonly dodecahedrons and, rarely, tetrahexahedrons, trapezohedrons, trisoctahedrons, hexoctahedrons, and botyroidal forms. Fluorite is transparent to translucent, and has vitreous luster. It occurs in a variety of colours including purple, green, blue, or yellow, however it can also be colourless, and can exhibit colour zoning, (Staebler et al., 2006). Fluorite from many localities is fluorescent (Verbeek, 2006).

Fluorite density varies from 3.0-3.6 g/cm^3, depending to a large extent on inclusions and impurities in the crystal lattice (Staebler et al., 2006), and its hardness is 4 on Mohs scale (Berry et al., 1983). Many single fluorite crystals display sector zoning, reflecting preferential substitution and incorporation of trace elements along successive crystal surfaces (Bosce and Rakovan, 2001). The Ca^{2+} ion in the fluorite crystal structure can be substituted by Li^+, Na^+, K^+, Mg^{2+}, Mn^{2+}, $Fe^{2+,3+}$, Zn^{2+}, Sr^{2+}, Y^{3+}, Zr^{4+}, Ba^{2+}, lanthanides ions, Pb^{2+}, Th^{4+}, and U^{4+} ions (Bailey et al., 1974; Bill and Calas, 1978, Gagnon et al., 2003; Schwinn and Markl, 2005; Xu et al., 2012; Deng et al., 2014). Concentrations of these impurities do not exceed 1% (Deer, 1965) except in yttrofluorite $(Ca,Y)F_{2-2.33}$ and cerfluorite $(Ca,Ce)F_{2-2.33}$ (Sverdrup, 1968).

Fluorite occurs in a variety of rocks, as an accessory and as a gangue mineral in many metalliferous deposits and, in exceptional cases, as the main ore constituent of economic deposits (Simandl, 2009). Good examples of fluorite mines are Las Cuevas, Encantada-Buenavista (Mexico); St. Lawrence pluton-related veins and the Rock Candy Mine (Canada); El Hamman veins (Morocco) and LeBurc Montroc–Le Moulinal and Trebas deposits (France) as documented by Ruiz et al. (1980), Grogan and Montgomery (1975), González-Partida et al. (2003), Munoz et al. (2005), and Fulton III and Miller (2006).

Fluorite also commonly occurs adjacent to or within carbonatites and alkaline complexes (Kogut et al., 1998; Hagni,1999; Alvin et al., 2004; Xu et al., 2004; Salvi and Williams-Jones, 2006); Mississippi Valley-type (MVT) Pb-Zn-F-Ba deposits; F-Ba-(Pb-Zn) veins (Grogan and Bradbury, 1967 and 1968; Baxter et al., 1973; Kesler et al., 1989; Cardellach et al., 2002; Levresse et al., 2006); hydrothermal Fe (±Au, ±Cu) and rare earth element (REE) deposits (Borrok et al., 1998; Andrade et al., 1999; Fourie, 2000); precious metal concentrations (Hill et al., 2000); fluorite/metal-bearing skarns (Lu et al., 2003); Sn-polymetallic greissen-type deposits (Bettencourt et al., 2005); and zeolitic rocks and uranium deposits (Sheppard and Mumpton, 1984; Cunningham et al., 1998; Min et al., 2005).

Ore deposit studies that document the trace element distribution in fluorite are provided by Möller et al. (1976), Bau et al. (2003), Gagnon et al. (2003), Schwinn and Markl (2005), and Deng et al. (2014). The benchmark paper by Möller et al. (1976) identified variations in the chemical composition of fluorites according their origin (sedimentary, hydrothermal, or pegmatitic).

Recently, Makin et al. (2014) compiled trace-element compositions of fluorite from MVT, fluorite-barite veins, peralkaline-related, and carbonatite-related deposits. They showed that fluorite from MVT and carbonatite deposits can be distinguished through trace element concentrations, and that the REE concentration of fluorite from veins is largely independent of the composition of the host rock. Based on the physical and chemical properties of fluorite, its association with a variety of deposit types, and previous studies, it is possible that fluorite can be used as a proximal indicator mineral to explore for a variety of deposit types. Unfortunately, the compilation by Makin et al. (2014) contained chemical analyses performed at different laboratories using different analytical techniques (including laser ablation-inductively coupled plasma mass spectrometry (LA-ICP-MS), electron microprobe, neutron activation, and ICP-MS), and precision and accuracy varied accordingly.

As an orientation survey, herein we present data from five deposits, with two samples from the Rock Candy deposit (British Columbia), and one sample from each of Kootenay

Florence (British Columbia), Eaglet (British Columbia), Eldor (Quebec), and Hastie quarry (Illinois) deposits (Table 1).

The main objectives of this study are to: 1) assess variations in chemical composition of fluorite in the samples and deposit types; 2) evaluate relations between analyses made using laser ablation-inductively coupled plasma mass spectrometry on individual grains [LA-ICP-MS(IG)], and those made using laser ablation-inductively coupled plasma mass spectrometry on fused beads [LA-ICP-MS(FB)] and X-ray fluorescence (XRF); 3) test the use of stoichiometric Ca content as an internal fluorite standard, such has been done by Gagnon et al. (2003) and Schwinn and Markl, (2005); 4) select the elements that are commonly present in concentrations above the lower limit of detection of LA-ICP-MS and available for constructing discrimination diagrams; 5) consider if our results agree with the preliminary discrimination diagrams of Makin et al. (2014).

2. Laboratory methods

2.1. Sample preparation

Fluorite crystal fragments measuring 0.2-2.5 cm were broken from six fist-size rock samples. These fragments were crushed, and inclusion-free fluorite grains (0.5 to 3 mm) were selected under a binocular microscope. Grains from each inclusion-free fluorite concentrate were mounted and polished in epoxy pucks for in situ trace element analysis of individual grains by LA-ICP-MS(IG). The remaining material, approximately 25-35 fragments, was ground into powder using an agate mortar and fused into glass beads for bulk fused bead XRF and LA-ICP-MS(FB) analysis.

To determine the deviation of Ca composition of fluorite from the stoichiometry content, and to determine the accuracy of our LA-ICP-MS results, the Kootenay Florence (AHS-1) and the Rock Candy (RC-08-8) samples were duplicated to test the repeatability of fused-bead LA-ICP-MS and confirm the homogeneity of the powder.

2.2. In situ LA-ICP-MS(IG) analysis

LA-ICP-MS(IG) analyses of fluorite grains were performed on a Thermo X-Series II (X7) quadrupole ICP-MS at the School of Earth and Ocean Sciences, University of Victoria. For LA-ICP-MS(IG), a New Wave UP-213 was coupled to the X-Series II with Helium as the carrier gas.

Fluorite grains were analyzed with a 55 μm laser spot diameter, a pulse rate of 10 Hz, and measured fluence ranged from 7.69 to 12.55 $J \cdot cm^{-2}$. A pre-ablation warm-up of 5 seconds was used to avoid unstable laser energy at the beginning of each ablation. All spectra were recorded for 120 seconds including ~30 seconds gas blank before ablation started, 60 seconds during ablation, and ~30 seconds after ablation. At least 60 seconds of gas flushing occurred between analyses. The ICP-MS was optimized to maximize sensitivity and minimize oxide formation. Forward RF was 1400 watts. The dwell time was 10 ms for all elements.

A total of 114 analyses from 6 samples was obtained. For each sample, 12-42 data points were collected from different grains, and most grains contain two random analyses for examining the trace element variations due to potential zoning.

The stoichiometric Ca content (51.33 wt.%) of fluorite was used as the internal standard for LA-ICP-MS calibration. NIST glass standards (611, 613, 615) were used for external calibration (Jochum et al., 2011). Each analysis session started with NIST glasses 615, 613, and 611, followed by the Rock Candy fluorite (potential secondary matrix-matched standard), and then six to seven unknowns, and then all four standards were repeated. During the data reduction, time-resolved count rates were carefully checked and any spectra with spikes, indicating possible inclusions, were excluded. The data reduction procedure for each element was: 1) selection of the time intervals for the background and signal region of each spectrum; 2) calculation of the mean CPS (counts per second) of these intervals; 3) background correction of the signal CPS; 4) external and internal standard normalizations; 5) drift correction using a linear drifting factor determined from repeat analyses of NIST 611; and 6) calibration using sensitivities for each element determined from the initial analyses of NIST 615, 613 and 611 in each load to achieve the concentration value of each element.

Thirty-nine trace elements were analyzed by LA-ICP-MS(IG) for reconnaissance. The experimental precision was determined by repeat analyses of NIST glasses 613 and 615. Based on NIST 613, the 2σ precision for elements with concentrations ranging from dozens to several hundred ppm is <10% for Mg, Mn, Rb, Sr, Y, Ba, lanthanide, W, Pb, Th and U; and from 10% to 15% for Fe. For NIST 615, which contains lower concentrations of all elements than NIST 613, the precision is 10-15% for Rb, Nb, Ba, Pr, Eu, Tb, Ho, Tm, Lu, W, Pb, and Th; between 15-20% for Mg, Zr, Sm, Er, Yb, and U; from 20% to 25% for Dy; and >25% for other elements.

Due to instrument drifting, the limit of detection (LOD) was determined for each element per session using the following:

$$\text{LOD} = \frac{3 \text{ x (STDev background signal)}}{\text{Sensitivity (per analyte element, per session)}}$$

where 'STDev background signal' is the standard deviation of the signal for a given element collected before ablation for each sample (gas blank), and 'Sensitivity' is the calibrated sensitivity determined from NIST 615, 613 and 611 in each session.

The detection limits are typically <20 ppm for Fe; <15 ppm for Sr; <5 ppm for Mg; <3 ppm for Mn and Y; <2 ppm for Ba; <1 ppm for Rb, Ce, Nd, and Pb; <0.5 ppm for La, Pr, Sm, Gd, Dy, Th, and U; <0.2 ppm for Zr, Nb, Mo, Eu, Tb, Ho, Er, Tm, Yb, Lu, and W.

2.3. Fused bead XRF and LA-ICP-MS(FB) analysis

Milled samples (Table 2) were shipped to Bureau Veritas Mineral Laboratories (ACME) in Perth, Australia for bulk XRF and LA-ICP-MS(FB) analysis. An aliquot of sample was weighed and intimately mixed with $LiBO_2/Li_2B_4O_7$ flux into a platinum crucible and fused in an electric furnace. The

Table 1. Summary of the fluorite-bearing deposits sampled for this study.

Deposit name	Deposit type	Main host rock	Key information	Mineral assemblage
Eldor, QC	Carbonatite-related REE±fluorite±apatite	Carbonatite complex (1.88-1.87 Ga, U-Pb); Pcl and columbite in the 2nd stage carbonatite; REE±fl in the 3rd stage carbonatite. (Gagnon et al., 2012).	At the contact of SC (Proterozoic metasedimentary rocks and amphibolites) and Gerido (Le Moyne and Doublet groups, and Eldor carbonatite) zones (Gagnon et al., 2012).	3rd stage (A zone) contains 1.5-3+% TREO (mnz) +fl+breunnerite in Fe-dol matrix. Accesssory minerals are ap, py, sp, mag, xtm, qz, Nb-bearing rt, nioboaeschynite, ferrocolumbite and ilm (Wright et al., 1998; Gagnon et al., 2012).
Eaglet, BC	Fluorite-barite vein/porphyry Mo granite-syenite related	Early Mississippian granitic orthogneiss (375-335 Ma, U-Pb zircon; Mortensen et al., 1987) intruded by dikes and pods of aplite, pegmatite, lamprophyre and feldspar-porphyry dikes, adjacent to contact with the Neoproterozoic biotite-garnet metapelite (Pell, 1992).	Fl veinlets/veins/pod disseminated on mol in the proximity of the fl mineralization but not overlapping (Hora et al., 2008).	Qz, mol, fl, carbonate minerals, clt, prismatic REE-bearing carbonates, gn, sp, py, gp, dck, aln, pcl (Pell, 1992; Hora et al., 2008).
Rock Candy, BC	Fluorite-barite vein	Tertiary andesitic volcanic rocks adjacent to Coryell syenite intrusion. Subparallel veins from a few cm to 10 m wide and breccia in a silicified fracture zone (MINFILE BC, 082ESE070).	Breccia and composite veins with multiple generations of green and purple fl are exposed in a trench, containing fragments of severely-altered country rock (Pell, 1992).	Fl, brt, chalcedony, kln, py, qz, and cal (Pell, 1992; Mauthner and Melanson, 2006).
Kootenay Florence, BC	Sedimentary-related Ag-Pb-Zn/ Polymetallic Ag-Pb-Zn vein	1) veins and replacements along contact with limestone and overlaying schist; 2) fissure veins in contact with quartz and sheared greenstone (MINFILE BC, 082FNE016).	Sample cavity at the No. 7 level at the contact between vein and limestones (Fyles, 1967).	Ore minerals: coarsely crystalline gn, sp, py, pcl, and ccp. Gangue minerals: fl, qz and cal (Pell, 1992; Mauthner and Melanson, 2006).
Hastie Quarry, IL	MVT	In bedded replacement zones parallel to Mississippian host rocks, which are mainly oolitic or fossiliferous limestones underlying a sandstone unit (Pelch et al., 2015). Age of mineralization is 272 ±17 Ma (fluorite, Sm-Nd; Chesley et al., 1994).	Steeply dipping faults and fractures are spatially associated with the deposits and may have acted as feeders for mineralizing fluids (Pelch et al., 2015).	Fluorite occurs in hydrothermal Stage II and III with sp, gn, qz, and ccp. Gangue minerals: brt, qz, and cal (Richardson and Pinckney, 1984; Pelch et al., 2015).

Table 2. Summary of fluorite samples and analyses.

Sample Name	Deposit/Locality Name	Fluorite Color	No. of Analyses LA-ICPMS(IG)	No. of Analyses LA-ICPMS(FB)
ELDOR2	Eldor, QC	Purple	23	1
EAGLET9	Eaglet, BC	Light Purple	12	1
RC-08-5P	Rock Candy, BC	Purple	12	1
RC-08-8	Rock Candy, BC	Green	42	2
AHS-1	Kootenay Florence, BC	Pale green	13	2
HQ-3-12S-9EY	Hastie quarry, IL	Yellow	12	1

melt was kept at constant temperature, and poured into a glass bead. The beads were analyzed using XRF Spectroscopy, for Ca, F, and Ba, and for LA-ICP-MS(FB) using a New Wave NWR193 coupled to an Agilent 7700 for 59 trace elements (Bureau Veritas Mineral Laboratories, 2015). Each fused bead of fluorite was ablated for 60 seconds with a laser spot size of 150 μm in diameter, a pulse rate of 20 Hz, and measured fluence of minimum 5 J/cm^2. Data reduction was performed using the LIMS software (Sorby Minerals) and a proprietary internal calibration and standardization process, of Bureau Veritas Mineral Laboratories. No external standard was used.

3. Results

In total, 114 analyses from 51 individual fluorite grains were performed using LA-ICP-MS(IG). Eight equivalent samples in form fused beads were analyzed using XRF and LA-ICP-MS(FB) for major and minor elements (Table 2).

3.1. Results of XRF and LA-ICP-MS(FB)

The XRF results show that the Ca contents from 8 analyses of different fluorites range between 51.0% and 51.3% (Table 3). The F content of the samples ranges from 48.4% to 48.8% (Table 3), and the Ba concentrations are consistently below detection limit (0.01%).

The LA-ICP-MS(FB) results (Table 3) show that Sr contents are from 95.6 to 4,880 ppm; Y contents are from 15 to 337 ppm; Zn contents are from 50 to 175 ppm; Cu content varies from below the detection limit to 48 ppm; lanthanide contents are from 3.5 to 299 ppm. Elements with concentrations between 1 ppm and above the limit of detection are Be, Co, As, Rb, Nb, Mo, Ag, Cd, Sn, Te, Hf, Ta, W, Bi, and U. Elements that are almost always consistently below the detection limit are Sc, Ga, Ge, In, Se, Cs, Re, and Tl.

3.2. Results of LA-ICP-MS(IG)

Strontium concentrations across all analyzed fluorite have large variations, from 47 to 3,526 ppm. Fluorite from the Hastie Quarry (HQ-3-12s-9EY) has the lowest Sr contents (47-103 ppm). The range of Sr concentrations in Kootenay Florence (AHS-1) samples overlap with those from Hastie Quarry, but are slightly higher (83 to 142 ppm). Fluorite from Eaglet (Eaglet9) has the highest Sr contents (2,679-3,526 ppm). Fluorite from Eldor (Eldor2) has the second highest Sr contents (920-1,112 ppm). Fluorite from Rock Candy (RC-08-8 and RC-08-5p) has a variation in Sr content from 177 to 654 ppm (Table 4).

Yttrium contents range from 4 to 1,448 ppm. Hastie Quarry samples have consistently low Y concentrations, from 9 to 13 ppm. Kootenay Florence samples have a range from 6 to 31 ppm Y. The Y concentrations in Eaglet samples vary from 44 to 60 ppm; those from Eldor vary from 153 to 220 ppm. The analyses of Y concentrations from Rock Candy yield the widest variation, from 4 to 1,448 ppm (Table 4).

Total REE content is restricted to the lanthanides. The light REE (LREE) analyses include La, Ce, Pr, Nd, Sm, Eu, and Gd (it does not include Sc). The heavy REE (HREE) analyses include Tb, Dy, Ho, Er, Tm, Yb, and Lu (it does not include Y). Contents of the sum of the lanthanides of all analyzed fluorite range from 2 to 831 ppm. The lowest ΣREE contents are from Hastie Quarry (2.26-2.59 ppm). Fluorite from Kootenay Florence is also low in the ΣREE contents (4.43-6.49 ppm). The sums of LREE (ΣLREE) contents in fluorite from Hastie Quarry are the lowest, from 1.03 to 1.43 ppm. Kootenay Florence has the second lowest ΣLREE, ranging from 2.69 to 6.00 ppm. For the sum of HREE (ΣHREE), Kootenay Florence has the lowest contents from 0.72 to 1.59 ppm, and the Hastie Quarry samples are also low in ΣHREE ranging from 1.01 to 1.25 ppm. Fluorite from Rock Candy has the largest variation in ΣREE contents ranging from 10 to 831 ppm; the variations of ΣLREE and ΣHREE are also the largest, ranging from 9 to 534 ppm and from 2 to 296 ppm, respectively (Table 4).

Iron contents in the fluorite samples display a relatively limited range, from 104 to 184 ppm (Table 4), and there are no distinct differences between any of the samples. Manganese contents of most samples (92 analyses) are below detection limit (1-3 ppm typically), except for some grains from the Rock Candy and Eaglet deposits. Manganese is detectable in almost all grains from Eaglet, with contents of 3-5 ppm. Magnesium, Sc, Ti, V, Cu, Zn, Zr, Nb, Mo, Rb, Ba, W, Th, and U are rarely present at concentrations above the detection limits (Table 4).

4. Discussion

The calculated XRF average Ca content of analyzed fluorite samples is 51.18%, and the variation of Ca contents through all fluorite samples is 0.2%. This is very similar to the stoichiometric Ca content of fluorite (51.33%), which indicates that it is appropriate to use the stoichiometric Ca content (51.33%) as the internal standard for LA-ICP-MS data reduction and to construct traditional Tb/Ca–Tb/La discrimination diagrams that were popularized by Möller (1976).

4.1. Elements for constructing discrimination diagrams

Elements that may be suitable for constructing discrimination diagrams can be assessed based on the concentrations of individual elements and the relationships between elements in concentrations above detection limits.

4.1.1. Concentrations of individual elements

Based on our results, Fe, Sr, Y, and the lanthanides are consistently in concentrations above LA-ICP-MS(IG) detection limits. Strontium contents have relatively restricted, deposit-specific concentration ranges (Fig. 1a), with relatively low (~100 ppm) values from Kootenay Florence and Hastie quarry, and distinctly higher values from Rock Candy (~500 ppm), Eldor, and Eaglet fluorite (≥900 ppm). The Y contents of samples from these deposits show a comparable pattern to Sr. Both samples from Rock Candy show large variations, beyond those of all other samples (Fig. 1b). Based on similarities of elemental concentrations and distributions, the lanthanides can be divided into four groups: 1) La, Ce, Pr, Nd; 2) Sm, Eu; 3) Gd, Tb, Dy, Ho, Er; and 4) Tm, Yb, Lu. Hastie Quarry fluorite

Table 3. Comparison of LA-ICP-MS (ppm) and XRF (wt.%) results from fused beads and mean values of single-grain analyses. "m", "b", and "R^2" are parameters for the best fitted regression lines. * Sample from Eaglet deposit was not used in determination of the best-fit line. BDL: Below detection limit. NA: No analysis.

	Rock Candy					Kootenay Florence			Eaglet		Eldor		Hastie Quarry		Parameters of best fit regression line		
	RC-08-8			RC-08-5P		AHS-1			Eaglet9		Eldor2		HQ-3-12S-9EYA				
	Fused bead(FB)		Grains	FB	Grains	FB		Grains	FB	Grains	FB	Grains	FB	Grains	Slope	Intercept	
Elements	**#1**	**#2**	**Mean**	**#1**	**Mean**	**#1**	**#2**	**Mean**	**#1**	**Mean**	**#1**	**Mean**	**#1**	**Mean**	**m**	**b**	**R^2**
LA-ICPMS																	
Mn	BDL	BDL	BDL	8.00	3.07	5.00	7.00	BDL	12.00	4.60	8.00	0.66	6.00	BDL			
Cu	10.00	4.00	0.15	48.00	BDL	BDL	4.00	0.57	4.00	0.07	4.00	7.49	8.00	0.17			
Zn	175.00	160.00	BDL	95.00	BDL	75.00	65.00	0.09	50.00	BDL	105.00	2.81	95.00	BDL			
Rb	0.55	0.30	BDL	0.50	0.12	0.95	1.15	BDL	BDL	BDL	0.30	BDL	0.60	0.04			
Sr	433.00	423.00	428.13	486.00	537.88	145.00	132.00	106.59	4880	2979.34	975.00	1002.12	95.60	82.33	1.0717*	-27.2405*	0.9956*
Y	35.10	36.50	25.11	337.00	270.77	19.20	18.30	17.10	67.40	52.45	225.00	175.53	15.50	11.94	0.799	-0.890	0.999
Zr	1.00	1.00	BDL	BDL	0.02	1.00	1.00	BDL	BDL	BDL	3.50	BDL	1.50	BDL			
Nb	0.16	0.23	BDL	0.12	BDL	0.20	0.27	BDL	0.10	BDL	0.29	BDL	0.20	BDL			
Mo	0.60	0.40	BDL	2.80	0.02	0.60	0.40	BDL	0.40	0.03	0.60	BDL	BDL	BDL			
Ba	1.00	BDL	0.08	BDL	0.63	BDL	BDL	0.15	59.00	0.03	BDL	0.22	BDL	0.14			
La	12.00	12.10	5.72	21.30	14.94	0.77	0.89	0.76	2.49	1.46	1.46	0.19	BDL	BDL	0.636	-0.359	0.950
Ce	19.30	20.30	9.57	52.50	33.89	1.30	1.54	0.85	10.50	5.68	5.32	0.55	0.10	0.04	0.642	-1.270	0.982
Pr	2.31	2.54	1.30	8.63	5.27	0.22	0.21	0.18	2.04	1.32	0.75	0.13	BDL	0.02	0.612	-0.063	0.992
Nd	10.80	10.70	6.33	43.70	28.87	1.19	1.15	1.05	13.10	8.75	4.11	0.91	0.38	0.26	0.665	-0.384	0.994
Sm	2.57	2.85	1.70	20.40	13.77	0.42	0.38	0.33	4.45	2.95	1.80	0.74	0.32	0.23	0.678	-0.092	0.998
Eu	1.11	1.23	0.89	9.76	6.55	0.14	0.10	0.12	1.43	1.09	0.80	0.49	0.16	0.10	0.668	0.051	0.999
Gd	2.92	3.20	2.39	31.50	21.72	0.54	0.44	0.70	5.45	4.07	3.94	2.47	0.87	0.65	0.682	0.221	0.999
Tb	0.52	0.43	0.31	6.79	4.29	0.08	0.09	0.10	0.61	0.50	0.82	0.50	0.11	0.09	0.626	0.038	0.999
Dy	2.90	2.88	2.10	46.00	31.29	0.71	0.68	0.66	3.84	2.86	5.87	4.06	0.72	0.55	0.677	0.151	1.000
Ho	0.63	0.68	0.44	9.61	6.06	0.15	0.15	0.14	0.79	0.56	1.40	0.92	0.16	0.11	0.627	0.038	1.000
Er	1.84	1.98	1.31	24.70	16.58	0.53	0.48	0.31	1.97	1.52	4.12	2.71	0.41	0.24	0.671	0.015	1.000
Tm	0.25	0.25	0.16	3.11	1.96	0.07	0.05	0.02	0.28	0.17	0.39	0.31	0.05	0.02	0.632	0.001	0.998
Yb	1.74	1.67	1.14	19.30	11.63	0.35	0.29	0.11	1.38	1.10	2.83	2.00	0.15	0.10	0.600	0.087	0.999
Lu	0.33	0.30	0.19	2.09	1.36	0.03	0.03	BDL	0.23	0.14	0.38	0.27	0.03	BDL	0.656	-0.007	0.999
W	0.10	0.25	BDL	0.25	0.08	0.15	0.25	0.03	0.15	0.12	0.10	0.06	BDL	0.02			
Pb	3.00	1.00	BDL	2.00	BDL	BDL	BDL	0.03	BDL	0.03	11.00	0.39	BDL	BDL			
Th	0.74	1.08	0.06	0.81	0.18	0.66	0.74	0.18	0.69	BDL	1.46	0.05	0.71	0.29			
U	0.11	0.12	0.06	0.11	0.04	0.12	0.14	BDL	0.10	0.03	0.04	BDL	0.04	BDL			
Lanthanide	59.22	61.11	33.55	299.39	198.19	6.50	6.48	5.33	48.56	32.18	33.99	16.24	3.46	2.40			
XRF																	
Ca	51.0	51.1	NA	51.3	NA	51.3	51.2	NA	51.1	NA	51.2	NA	51.2	NA			
F	48.4	48.8	NA	48.7	NA	48.8	48.8	NA	48.7	NA	48.5	NA	48.8	NA			
Ba	<0.01	<0.01	NA	<0.01	NA	<0.01	<0.01	NA	<0.01	NA	<0.01	NA	<0.01	NA			

Table 4a. Trace-element contents (ppm) of fluorite grains from Rock Candy and Kootenay Florence. M.D.L.: Minimum Detection Limit. BDL: Below detection limit.* Total REE content is restricted to lanthanides.

	RC-08-8, 42 analyses					RC-08-5P, 12 analyses					AHS-1, 13 analyses					
Quartile	**Min**	**1st quartile**	**Median**	**3rd quartile**	**Max**	**Min**	**1st quartile**	**Median**	**3rd quartile**	**Max**	**Min**	**1st quartile**	**Median**	**3rd quartile**	**Max**	**M.D.L.**
Mg	BDL	BDL	BDL	BDL	0.58	BDL	BDL	BDL	BDL	0.73	BDL	BDL	BDL	BDL	1.02	0.18
Sc	BDL	BDL	BDL	BDL	BDL	BDL	BDL	BDL	BDL	0.09	BDL	BDL	BDL	BDL	BDL	0.04
Ti	BDL	0.09	0.12	0.12	0.12	BDL	0.06	0.09	0.12	0.12	0.04	0.05	0.07	0.12	0.12	0.02
V	BDL	BDL	BDL	BDL	BDL	BDL	BDL	BDL	BDL	BDL	BDL	BDL	BDL	BDL	BDL	0.01
Mn	BDL	BDL	BDL	BDL	BDL	BDL	0.96	1.52	4.01	6.47	BDL	BDL	BDL	BDL	BDL	0.09
Fe	127.31	145.94	148.76	148.76	177.00	145.50	151.08	155.15	166.63	177.76	138.37	148.05	149.22	152.25	164.27	1.40
Cu	BDL	BDL	BDL	BDL	0.24	BDL	BDL	BDL	BDL	BDL	BDL	BDL	BDL	BDL	0.57	0.05
Zn	BDL	BDL	BDL	BDL	BDL	BDL	BDL	BDL	BDL	BDL	BDL	BDL	BDL	BDL	0.09	0.06
Rb	BDL	BDL	BDL	BDL	BDL	BDL	BDL	BDL	BDL	0.12	BDL	BDL	BDL	BDL	0.02	0.01
Sr	177.86	375.02	391.25	490.16	654.74	416.93	485.16	526.61	625.86	643.73	83.67	92.69	96.75	127.03	142.18	0.15
Y	3.97	14.77	28.55	33.37	42.00	24.53	76.99	183.32	236.32	1448.55	6.04	13.62	15.98	19.91	31.46	0.05
Zr	BDL	BDL	BDL	BDL	BDL	BDL	BDL	BDL	0.03	0.05	BDL	BDL	BDL	BDL	BDL	0.01
Nb	BDL	BDL	BDL	BDL	BDL	BDL	BDL	BDL	0.02	0.02	BDL	BDL	BDL	BDL	BDL	0.01
Mo	BDL	BDL	BDL	BDL	0.03	BDL	BDL	BDL	0.02	0.04	BDL	BDL	BDL	BDL	BDL	0.01
Ba	BDL	BDL	BDL	0.07	0.14	0.35	0.51	0.57	0.77	1.02	BDL	BDL	BDL	BDL	0.51	0.01
La	BDL	2.60	3.32	7.50	11.30	2.42	8.01	11.33	15.89	52.02	BDL	0.36	0.78	0.88	1.13	0.01
Ce	BDL	5.82	6.98	12.14	19.80	6.14	18.23	25.11	36.14	123.23	BDL	0.38	0.78	1.04	1.37	0.01
Pr	BDL	BDL	1.00	1.22	2.39	0.89	2.65	3.62	5.36	20.98	BDL	0.08	0.16	0.21	0.23	0.01
Nd	BDL	2.52	5.77	6.69	11.09	4.10	11.62	18.00	26.59	134.55	BDL	0.69	0.94	1.22	1.60	0.03
Sm	0.07	0.07	1.50	1.87	2.32	2.02	4.88	8.52	12.83	65.84	0.07	0.21	0.30	0.35	0.59	0.05
Eu	BDL	BDL	0.55	1.05	1.30	1.02	2.60	4.32	6.09	29.64	BDL	BDL	0.08	0.12	0.22	0.02
Gd	BDL	BDL	2.10	2.80	3.37	2.71	7.14	13.73	19.02	108.65	BDL	0.38	0.63	0.80	1.08	0.19
Tb	0.02	0.02	0.18	0.36	0.45	0.61	1.47	2.95	3.96	19.62	0.02	0.05	0.09	0.11	0.15	0.01
Dy	0.10	0.10	1.37	2.45	3.02	4.68	11.60	22.45	29.95	135.73	0.10	0.36	0.60	0.75	1.08	0.02
Ho	BDL	BDL	0.27	0.49	0.71	0.83	2.22	4.36	5.78	26.38	BDL	0.08	0.11	0.17	0.24	0.01
Er	0.05	0.05	0.76	1.51	2.06	2.61	6.79	12.37	16.40	67.79	0.05	0.17	0.23	0.36	0.67	0.02
Tm	BDL	BDL	BDL	0.16	0.25	0.38	0.96	1.62	2.04	6.93	BDL	BDL	BDL	0.02	0.03	0.01
Yb	BDL	BDL	0.80	1.32	1.79	2.65	6.41	9.73	12.84	36.01	BDL	0.04	0.07	0.11	0.25	0.01
Lu	BDL	BDL	0.05	0.19	0.28	0.36	0.80	1.17	1.52	3.98	BDL	BDL	BDL	BDL	0.02	0.01
W	BDL	BDL	BDL	BDL	BDL	BDL	0.04	0.05	0.06	0.27	BDL	BDL	BDL	BDL	0.10	0.01
Pb	BDL	BDL	BDL	BDL	BDL	BDL	BDL	BDL	BDL	BDL	BDL	BDL	BDL	BDL	0.05	0.01
Th	BDL	BDL	BDL	0.02	0.15	BDL	BDL	BDL	BDL	0.97	BDL	BDL	0.12	0.22	0.29	0.01
U	BDL	BDL	BDL	0.01	0.43	BDL	BDL	0.02	0.07	0.10	BDL	BDL	BDL	BDL	BDL	0.01
ΣLREE	8.38	18.77	21.26	31.58	43.16	16.58	48.33	70.90	101.74	426.25	1.89	2.76	3.43	4.26	4.99	--
ΣHREE	2.99	5.35	8.36	9.91	18.78	14.83	37.39	69.10	91.44	405.10	1.10	1.41	1.68	2.17	2.67	--
ΣREE*	10.39	28.69	32.71	43.02	48.92	31.41	83.76	141.71	193.17	831.35	4.43	4.45	4.53	5.28	6.49	--

Table 4b. Trace-element contents (ppm) of fluorite grains from Eaglet, Eldor, and Hastie Quarry. M.D.L.: Minimum Detection Limit. BDL: Below detection limit.* Total REE content is restricted to lanthanides.

	Eaglet9, 12 analyses					Eldor2, 23 analyses					HQ-3-12s-9EY, 12 analyses					
Quartile	**Min**	**1st quartile**	**Median**	**3rd quartile**	**Max**	**Min**	**1st quartile**	**Median**	**3rd quartile**	**Max**	**Min**	**1st quartile**	**Median**	**3rd quartile**	**Max**	**M.D.L.**
Mg	BDL	BDL	1.21	2.50	3.29	BDL	BDL	BDL	2.58	23.21	BDL	1.01	1.61	2.05	5.93	0.18
Sc	BDL	BDL	BDL	BDL	BDL	BDL	BDL	BDL	BDL	BDL	BDL	BDL	BDL	BDL	BDL	0.04
Ti	0.04	0.08	0.12	0.12	0.13	BDL	0.12	0.12	0.12	0.17	0.03	0.12	0.12	0.12	0.50	0.02
V	BDL	BDL	BDL	BDL	0.39	BDL	BDL	BDL	BDL	2.62	BDL	BDL	BDL	BDL	BDL	0.01
Mn	BDL	3.94	4.36	4.95	5.27	BDL	BDL	BDL	BDL	0.86	BDL	BDL	BDL	BDL	BDL	0.09
Fe	119.77	130.86	137.93	140.82	184.31	104.44	115.23	127.80	131.27	159.26	133.80	143.88	147.29	149.68	157.78	1.40
Cu	BDL	BDL	BDL	BDL	0.07	BDL	BDL	BDL	BDL	9.13	BDL	BDL	BDL	BDL	0.22	0.05
Zn	BDL	BDL	BDL	BDL	BDL	BDL	BDL	BDL	BDL	2.81	BDL	BDL	BDL	BDL	BDL	0.06
Rb	BDL	BDL	BDL	BDL	BDL	BDL	BDL	BDL	BDL	BDL	BDL	BDL	BDL	BDL	0.04	0.01
Sr	2679.63	2735.74	3005.05	3115.71	3526.60	920.25	975.75	1001.14	1020.51	1112.04	47.01	82.20	85.50	91.18	103.81	0.15
Y	44.58	49.37	51.58	55.64	60.44	153.27	158.62	173.87	184.12	220.27	9.80	11.33	12.20	12.87	13.12	0.05
Zr	BDL	BDL	BDL	BDL	BDL	BDL	BDL	BDL	BDL	0.04	BDL	BDL	BDL	BDL	BDL	0.01
Nb	BDL	BDL	BDL	BDL	BDL	BDL	BDL	BDL	BDL	0.05	BDL	BDL	BDL	BDL	BDL	0.01
Mo	BDL	BDL	BDL	0.02	0.06	BDL	BDL	BDL	BDL	0.02	BDL	BDL	BDL	BDL	BDL	0.01
Ba	BDL	BDL	BDL	0.03	0.05	BDL	BDL	BDL	0.02	1.06	BDL	0.13	0.14	0.16	0.17	0.01
La	BDL	1.13	1.23	1.44	2.86	BDL	BDL	0.10	0.18	0.50	BDL	BDL	BDL	BDL	BDL	0.01
Ce	BDL	3.74	3.98	6.28	11.68	BDL	0.41	0.51	0.62	1.30	BDL	0.03	0.04	0.04	0.04	0.01
Pr	BDL	0.78	0.91	1.68	2.44	BDL	BDL	0.10	0.13	0.20	BDL	0.02	0.02	0.02	0.02	0.01
Nd	BDL	5.59	6.07	11.67	14.36	BDL	0.75	0.86	0.99	1.26	BDL	0.23	0.26	0.28	0.29	0.03
Sm	0.07	2.24	2.40	3.62	4.18	0.07	0.66	0.74	0.79	0.90	0.07	0.22	0.23	0.25	0.26	0.05
Eu	BDL	0.74	0.85	1.31	1.61	BDL	0.46	0.49	0.51	0.57	BDL	0.08	0.09	0.10	0.12	0.02
Gd	BDL	3.44	3.72	4.56	5.17	BDL	2.30	2.42	2.57	2.95	BDL	0.58	0.65	0.68	0.74	0.19
Tb	0.02	0.31	0.43	0.56	0.65	0.02	0.47	0.49	0.54	0.62	0.02	0.08	0.09	0.09	0.10	0.01
Dy	0.10	2.56	2.69	3.12	3.55	0.10	3.83	3.95	4.30	4.97	0.10	0.51	0.56	0.57	0.61	0.02
Ho	BDL	0.50	0.55	0.60	0.68	BDL	0.87	0.89	0.94	1.11	BDL	0.09	0.11	0.11	0.12	0.01
Er	0.05	1.40	1.49	1.58	1.78	0.05	2.56	2.68	2.82	3.31	0.05	0.22	0.25	0.26	0.27	0.02
Tm	BDL	0.11	0.17	0.18	0.20	BDL	0.29	0.30	0.33	0.38	BDL	0.02	0.02	0.03	0.03	0.01
Yb	BDL	1.00	1.08	1.19	1.28	BDL	1.88	2.01	2.10	2.33	BDL	0.08	0.10	0.11	0.12	0.01
Lu	BDL	0.13	0.14	0.15	0.17	BDL	0.24	0.26	0.28	0.34	BDL	BDL	BDL	BDL	0.02	0.01
W	BDL	0.07	0.10	0.13	0.17	BDL	BDL	0.04	0.07	0.11	BDL	0.02	0.02	0.03	0.03	0.01
Pb	BDL	BDL	BDL	0.03	0.04	BDL	BDL	BDL	0.02	1.53	BDL	BDL	BDL	BDL	0.02	0.01
Th	BDL	BDL	BDL	BDL	BDL	BDL	BDL	BDL	BDL	0.26	BDL	0.24	0.28	0.31	0.37	0.01
U	0.00	0.00	0.02	0.03	0.04	BDL	BDL	BDL	BDL	BDL	BDL	BDL	BDL	BDL	BDL	0.01
ΣLREE	12.54	14.87	17.46	30.42	36.63	2.33	2.66	2.97	3.31	4.59	0.54	0.63	0.64	0.69	0.69	--
ΣHREE	9.06	10.13	10.20	12.40	13.08	11.68	12.63	13.02	14.10	16.00	1.64	1.75	1.84	1.88	1.90	--
ΣREE	21.59	24.95	25.22	45.80	49.05	14.00	15.54	16.62	17.21	19.16	2.26	2.39	2.47	2.53	2.59	--

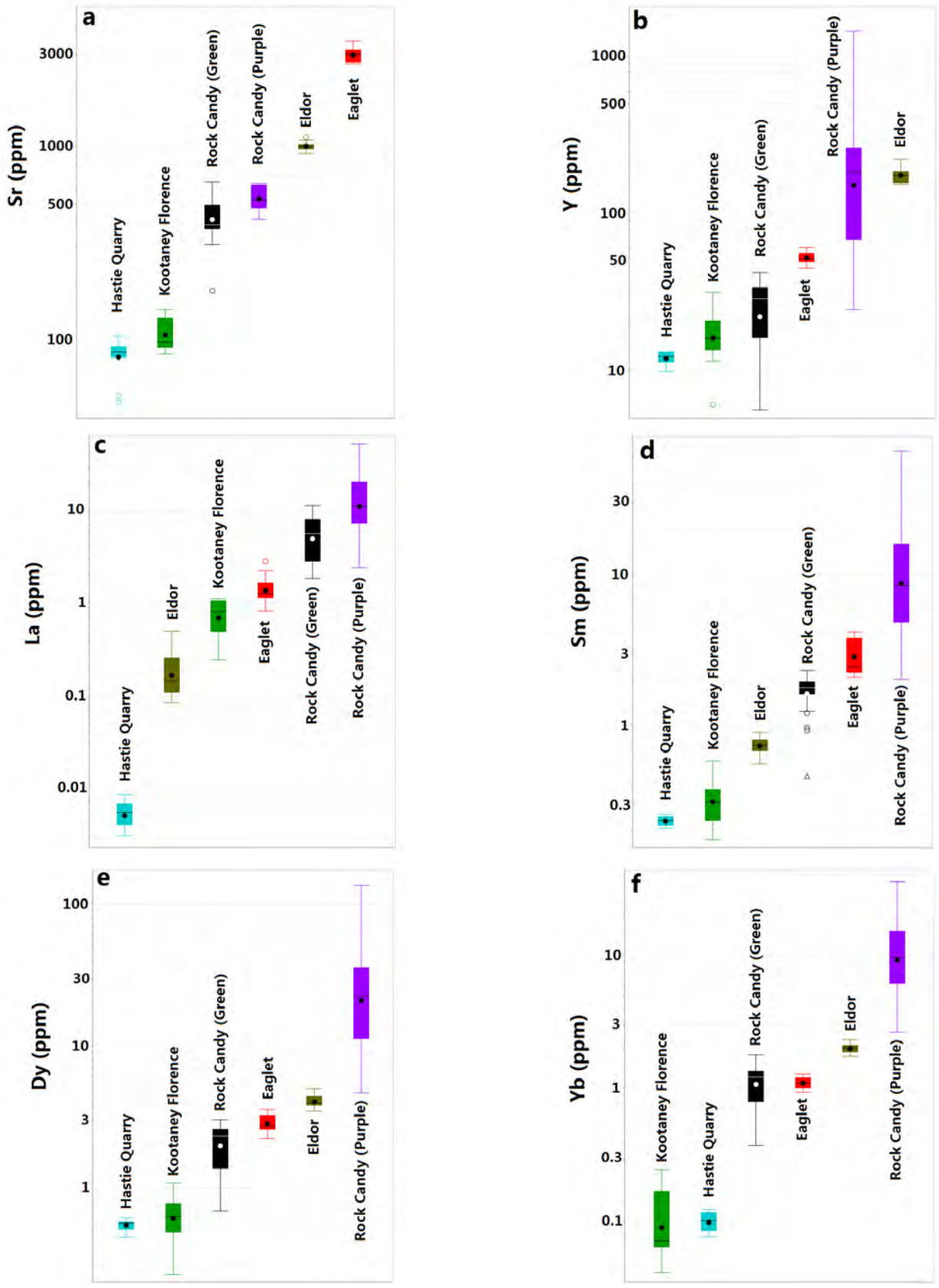

Fig. 1. Box plots of selected element contents of fluorite for each group: **a)** Sr; **b)** Y; **c)** La; **d)** Sm; **e)** Dy; **f)** Yb. Line: median value; solid dot: mean value; box: interquartile range (25th-75th percentile); open circle (outlier): further than [1.5*(75th percentile – 25th percentile)]; open triangle (outlier): further than [3*(75th percentile – 25th percentile)]; whiskers: extreme values that are not outliers.

contains the lowest La contents (<0.01 ppm), the Rock Candy fluorite has the highest La contents (2-14 ppm), and in the other three deposits La contents overlap (Fig. 1c). From La to Nd of the lanthanides, the compositions of the Eaglet samples rise to those of Rock Candy samples, and the contents of Kootenay Florence and Eldor samples become increasingly close to each other. Kootenay Florence and Hastie Quarry have the lowest Sm (~0.1-0.6 ppm) and Eu contents, whereas Eldor, Rock Candy (Green) and Eaglet all have higher Sm and Eu contents, with small ranges. The Rock Candy sample (purple) shows the highest Sm (~2-33 ppm) and Eu contents and the broadest variation (Fig. 1d). Element content patterns for Gd, Tb, Dy, Ho, and Er are almost identical, thus Dy is used as a representative for this group. Dysprosium contents range from ~0.2-1 ppm and are the lowest for Kootenay Florence and Hastie Quarry (Fig. 1e). Dysprosium contents of Rock Candy (Green) samples lie between, and partially overlap, Kootenay Florence and Eaglet samples (Fig. 1e). Eldor samples yield higher concentrations, but again, the Rock Candy sample (purple) has the highest Dy contents with the most variation (Fig. 1e). Ytterbium, together with Tm and Lu, is low in fluorite from Hastie Quarry and Kootenay Florence (around 0.1 ppm), but high in fluorite from other deposits. The Yb range is particularly well restricted in Eaglet and Eldor samples (Fig. 1f).

These results suggest that Sr, Y, and the lanthanides are strong contributors for discriminating the different deposits and rock types in simple X-Y plots. For example, plotting Nd vs. Sr concentrations (Fig. 2) displays distinct clustering for each of the different deposits. The fluorite from Rock Candy (fluorite-barite veins) and Eaglet contains higher Nd (generally greater than 4 ppm), and the fluorite from Hastie Quarry and Kootenay Florence (sedimentary-related deposits) have low Sr and Nd concentrations. The Eldor fluorite samples (carbonatite-related deposit) form a distinct group, with elevated Sr concentrations and Nd concentrations below 4 ppm.

Iron concentrations are similarly variable in all samples, and range consistently from 104 to 184 ppm, precluding its use for discriminating deposit and rock types. On the other hand, many elements such as Mn, Ba, and Th are detectable, and they may be diagnostic for specific deposit types. The project requires additional data from different samples and deposits to develop comprehensive discrimination methods; this work is ongoing.

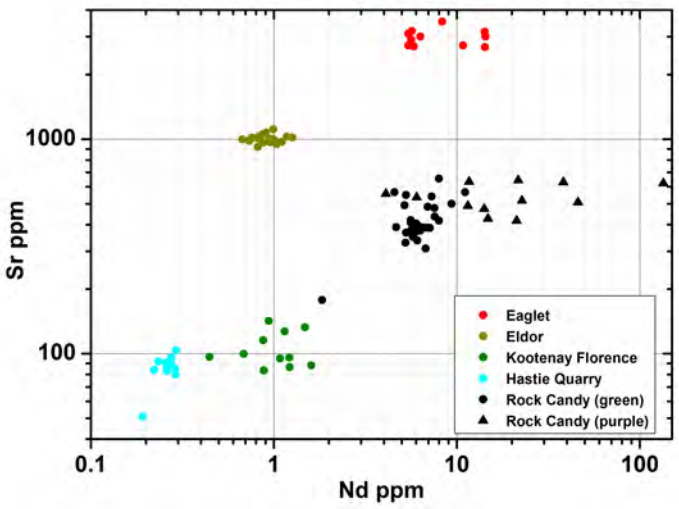

Fig. 2. Nd vs. Sr scatterplot for fluorite from different deposits.

4.1.2. Relationships between elements

Fluorite from the MVT deposit (Hastie Quarry) and a limestone-related Ag-Pb-Zn mine (Kootenay Florence) have lower concentrations of trace elements, especially Sr, Y, Sm, Eu, Gd, and HREE relative to higher temperature deposits (Figs. 1-3; Table 4). From Y-Yb (Fig. 3) and Tb/La-Tb/Ca plots (Fig. 4), the concentrations of impurities in fluorite can separate the sedimentary-related deposits from the other deposits.

Eaglet and Rock Candy fluorite lie in the hydrothermal field of the Tb/Ca vs. Tb/La diagram (Fig. 4). Rock Candy fluorite shows wide variation in concentrations of Nd (Fig. 2), Y, Yb (Fig. 3), Tb, and Tb/La ratio (Fig. 4). The variation of Tb/Ca and Tb/La from sample RC-08-8 (green Rock Candy) probably reflects the REE fractionation during mineralization (Möller, 1976).The trend from sample RC-08-5P (purple Rock Candy) is distinct from both the fractionation trend during mineralization and the remobilization trend (Fig. 4), and shows a progressive increase in Tb relative to Tb/La fractionation. We are unsure what causes this trend, but speculate that it might record a magmatic overprint. Although fluorite from the Rock Candy deposit is associated with barite, its Ba content remains below detection limits. Fluorite from the Eaglet deposit shows little concentration variations for Sr, Nd (Fig. 2), Y, Yb (Fig. 3), Tb, and Tb/La (Fig. 4). The high Sr concentration in Eaglet fluorite coincides with co-existing celestite in mineralized zones (Hora et al., 2008).

Fluorite from Eldor, a carbonatite-related deposit, plots in

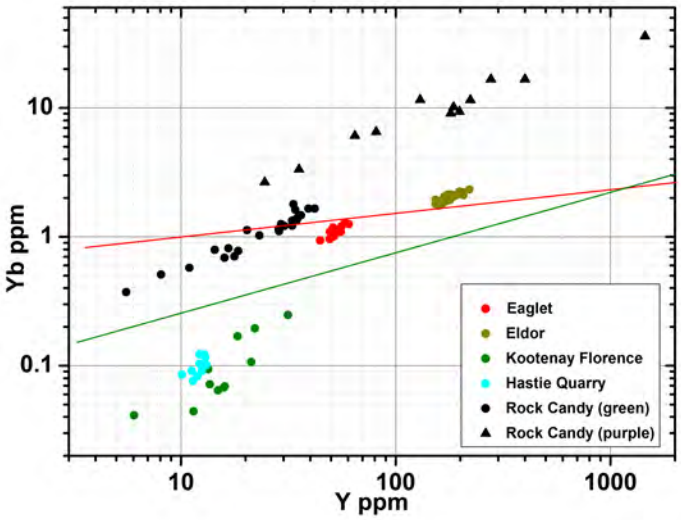

Fig. 3. Y vs. Yb scatterplot for fluorite from different deposits. The solid red line defined by Makin et al. (2014) is the boundary between MVT-related fluorite and carbonatite-related fluorite. The solid green line separates the fluorite from sedimentary-related deposits and other deposits.

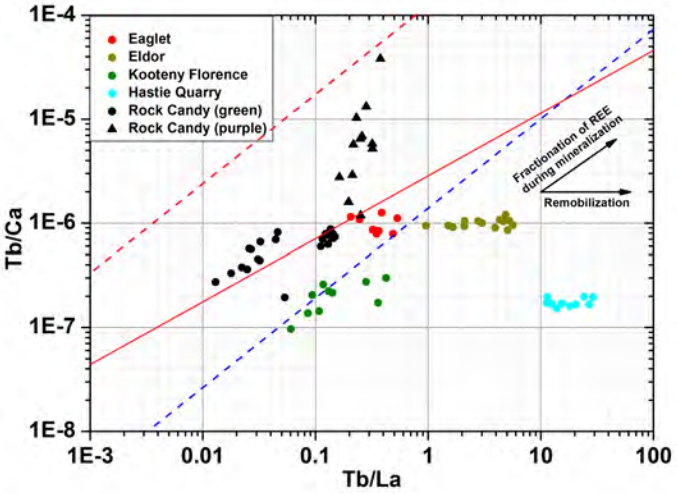

Fig. 4. Tb/La vs. Tb/Ca scatterplot of fluorite from different deposits. The Ca content for all trace-element analyses is assumed to correspond to the stoichiometric composition of ideal fluorite. The red and blue dashed lines are those from Makin et al. (2014). They were recalculated from the Möller (1976) diagram based on atomic proportions of elements rather than their concentrations in ppm. These lines represent the boundaries between fluorite of 'pegmatitic', 'hydrothermal', and 'sedimentary' origins.

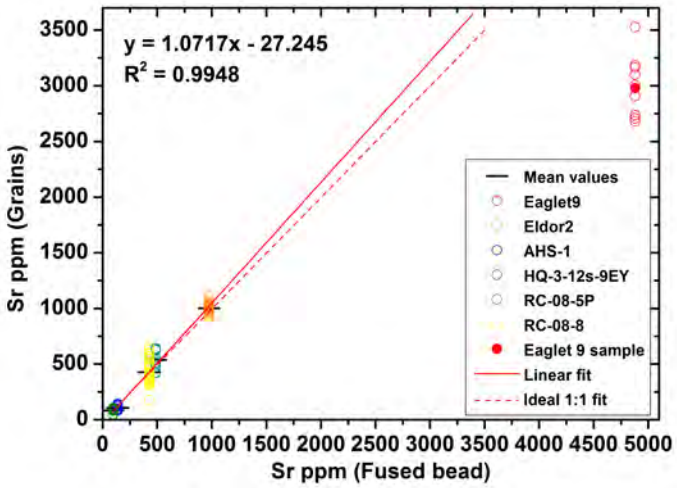

Fig. 5. Comparison of LA-ICP-MS analyses obtained from fused fluorite powder and mean values of individual grains for Sr. Red solid and dashed lines represent fitted regression lines and ideal 1:1 fit, respectively. The red point represents the data which is not used for fitting the regression line.

the sedimentary field on the Tb/Ca vs. Tb/La diagram (Fig. 4) and shows little variation in Tb/Ca, which is characteristic of a remobilization trend. This phenomenon may be related to the precipitation of LREE-rich mineral phase. At Eldor, monazite is the main ore mineral (Gagnon et al., 2012), which can incorporate most of LREE and leads to La depletion in fluorite (Bau and Dulski, 1995). To better understand the relationships between deposit types and trace element concentrations and behaviors in fluorite, more analyses from different carbonatite samples are required.

4.2. Comparison of LA-ICP-MS(IG) and LA-ICP-MS(FB)

We compare LA-ICP-MS(IG) and LA-ICP-MS(FB) using Sr, Y, and the lanthanides, which are detectable in most fluorite grains (Table 3), and evaluate the relationships between the two methods using X-Y scatter diagrams (Figs. 5-10). Linear regressions for each element were determined using the following equation (from Simandl et al., 2014):

[mean value of LA-ICP-MS(IG) result] = m [LA-ICP-MS(FB) result] + b

Fitted parameters are listed in Table 3. On an X-Y plot, a perfect match between data of the two methods will form a regression line with a slope of unity (m=1); the line will pass through the origin (intercept, b=0); and the coefficient of determination will equal 1 (R^2=1; i.e., all data points plot on the regression line).

In the case of Sr, the best-fit line between the two methods (Fig. 5) is characterized by m=1.07, and R^2=0.995. This near-perfect fit excludes sample Eaglet9, which has the mean value of Sr determined by LA-ICP-MS(IG) significantly less than the result from the fused bead (Fig. 5; Table 3). The large deviation of the Eaglet9 data from the best-fit line may be due to celestite

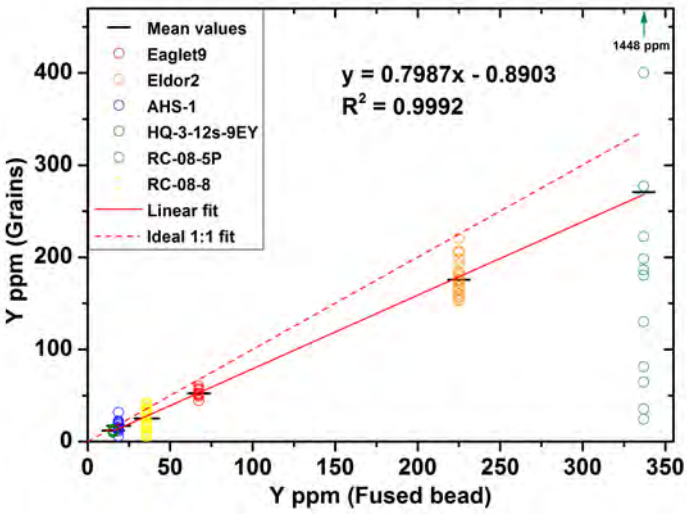

Fig. 6. Comparison of LA-ICP-MS analyses obtained from fused fluorite powder and mean values of individual grains for Y. Red solid and dashed lines represent fitted regression lines and ideal 1:1 fit, respectively.

inclusion(s) or intergrowth with fluorite. Celestite is commonly associated with fluorite at Eaglet (Pell, 1992). This explanation is further supported by the high Ba content (59 ppm) of Eaglet9 from fused bead relative to a mean of 12 analyses at 0.03 ppm from grains (Table 3). Celestite ($SrSO_4$) and barite ($BaSO_4$) are end-members of the same solid-solution series.

The sample RC-08-5P (Rock Candy, purple fluorite) shows the highest mean values of all Y and lanthanides relative to other samples (Figs. 6-10; Table 3) but it also has the largest ranges of variations in these elements (Figs. 6-10). This suggests that the fluorite in sample RC-08-5P formed from fluid(s) with highly variable concentrations of these elements (Mauthner and Melanson, 2006). Overall, the results of the

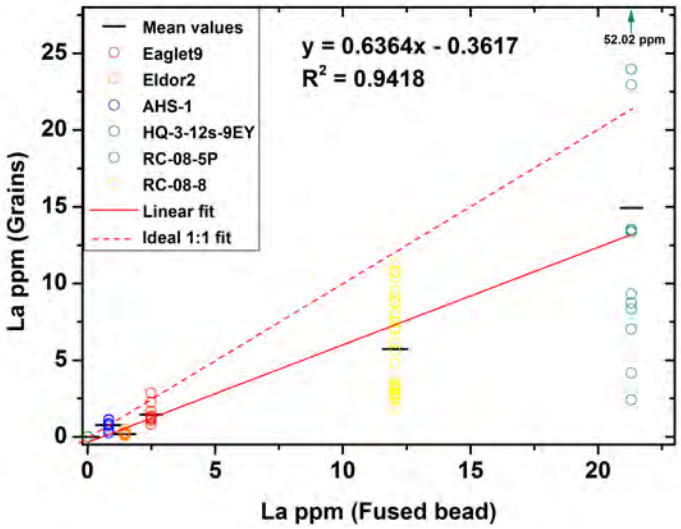

Fig. 7. Comparison of LA-ICP-MS analyses obtained from fused fluorite powder and mean values of individual grains for La. Red solid and dashed lines represent fitted regression lines and ideal 1:1 fit, respectively.

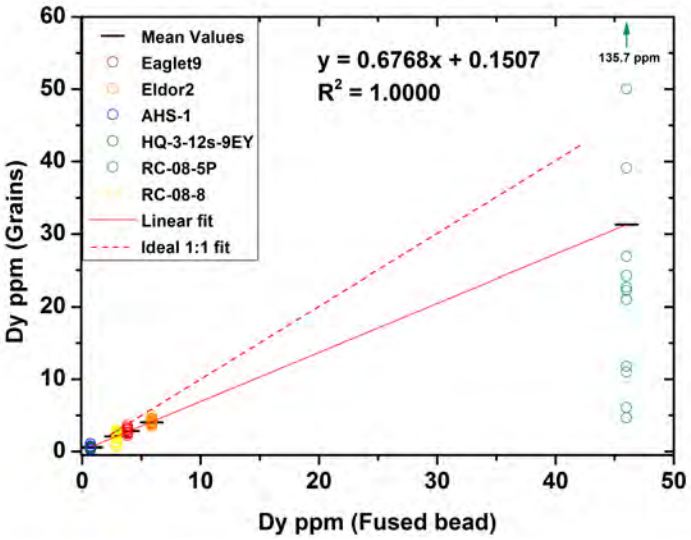

Fig. 9. Comparison of LA-ICP-MS analyses obtained from fused fluorite powder and mean values of individual grains for Dy. Red solid and dashed lines represent fitted regression lines and ideal 1:1 fit, respectively.

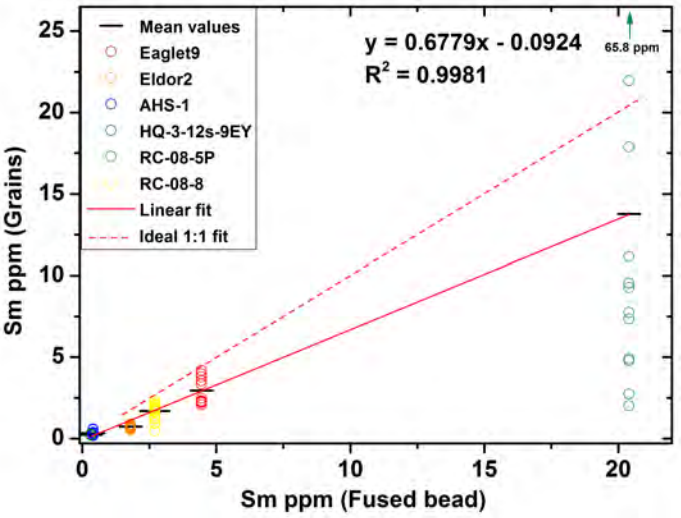

Fig. 8. Comparison of LA-ICP-MS analyses obtained from fused fluorite powder and mean values of individual grains for Sm. Red solid and dashed lines represent fitted regression lines and ideal 1:1 fit, respectively.

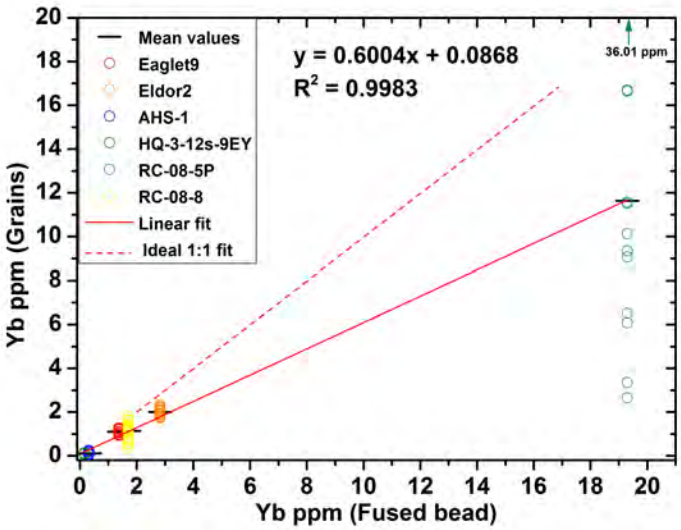

Fig. 10. Comparison of LA-ICP-MS analyses obtained from fused fluorite powder and mean values of individual grains for Yb. Red solid and dashed lines represent fitted regression lines and ideal 1:1 fit, respectively.

lanthanides and Y from fused beads are all notably higher than mean values of results from grains (Figs. 6-10; Table 3). The slope of the fitted regression lines are between 0.60 and 0.68 for the lanthanides, and 0.80 for Y, but the coefficients of determination are between 0.991 and 1.000 for all elements except La (0.94) and Ce (0.98) suggesting consistent differences of trace element contents determined from the two methods (Table 3). The difference between results from the two methods may be caused by the use of different internal standards or the presence of sub-microscopic or microscopic inclusions with elevated-REE abundances.

The differences of lanthanide and Y contents from both laboratories may be caused by the different internal standards and/or laser sources, which have different fractionation indices for the lanthanides and Y. To determine the content of any trace element, LA-ICP-MS requires that the external standard, internal standard, and sensitivity of the instrument to the detected element must be established. In practice, the selection of these standards depends on the mineral and the elements analyzed (Jackson, 2008). In the LA-ICP-MS(IG) analyses of fluorite, NIST glass was used as the external standard, Ca was the internal standard, and the sensitivities of all elements were determined from NIST glass 611, 613, and 615. However, in LA-ICP-MS(FB) analyses, an internal calibration and standardization process, developed by Bureau Veritas Mineral

Laboratories, was used without external standard. Different laser sources [Nd: YAG 213 nm for LA-ICPMS(IG) and Excimer 193 nm for LA-ICPMS(FB)] can generate distinct fractionation indeces that contribute to the difference in results from the two laboratories as previously reported by Gonzalez et al. (2002).

To avoid visible inclusions with elevated-REE, fluorite fragments were screened with a binocular microscope. Furthermore, if an unexpected signal from a potential invisible inclusion was detected during LA-ICP-MS(IG) analyses, the analysis was rejected. However, for the LA-ICP-MS(FB), fluorite and potential tiny inclusions such as monazite and allanite were ground together and incorporated into glass beads. The presence of such sub-microscopic inclusions could cause significant bias. High Zn concentrations (50-175 ppm) measured by LA-ICP-MS(FB) relative to LA-ICP-MS(IG) (<3 ppm) remain unexplained.

5. Summary

Previous studies (Möller et al., 1976; Eppinger and Closs, 1990; Gagnon et al., 2003; Schwinn and Markl, 2005; Makin et al., 2014) and preliminary data analyses in our study all show that fluorite is a potential indicator mineral for deposits such as MVT, carbonatite-related REE, fluorite-barite veins, and peralkaline-related REE deposits. This preliminary study indicates that Sr, Y, and lanthanides in fluorite are quantifiable by LA-ICP-MS(IG). Other elements, such as Mn, Ba, and Th also have potential to discriminate fluorite from different deposit types.

The differences in concentrations between LA-ICP-MS(IG) and LA-ICP-MS(FB) points to dangers of comparing results acquired using different instrumentation, methodology and data reduction. LA-ICP-MS(IG) has an advantage over LA-ICP-MS(FB) for indicator mineral studies, because smaller samples (single grain) are required, whereas many grains are required to create a single fused bead. The negative effects of mineral inclusions on data quality of LA-ICP-MS(IG) can be easily avoided by discarding data with anomalous spectra. The variations in chemical composition of fluorite grains from individual deposits suggest that ideally at least five fluorite grains per sample are required to discriminate deposit types.

Acknowledgments

This project was funded by the Targeted Geoscience Initiative 4 (TGI4), a Natural Resources Canada programme carried out under the auspices of the Geological Survey of Canada in collaboration with the British Columbia Geological Survey. Suggestions and constructive comments by John Carter of Bureau Veritas Mineral Laboratories, Perth are greatly appreciated.

References cited

Alvin, M.P., Dunphy, J.M., and Groves, D.I., 2004. Nature and genesis of a carbonatite-associated fluorite deposit at Speewah, East Kimberley region, Western Australia. Mineralogy and Petrology, 80, 127-153.

Andrade, F.R.D., Möller, P., Lüders, V., Dulski, P., and Gilg, H.A., 1999. Hydrothermal rare earth elements mineralization in the Barra do Itapirapuã carbonatite, southern Brazil: behaviour of selected trace elements and stable isotopes (C,O). Chemical Geology, 155, 91-113.

Bailey, A.D., Hunt, R.P., and Taylor, K.N.R., 1974. An ESR study of natural fluorite containing manganese impurities. Mineralogical Magazine, 39, 705-708.

Bau, M., and Dulski, P., 1995. Comparative study of yttrium and rare-earth element behaviours in fluorine-rich hydrothermal fluids. Contributions to Mineralogy and Petrology, 199, 213-223.

Bau, M., Romer, R.L., Lüders, V., and Dulski, P., 2003. Tracing element sources of hydrothermal mineral deposits: REE and Y distribution and Sr-Nd-Pb isotopes in fluorite from MVT deposits in the Pennine Orefield, England. Mineralium Deposita, 38, 992-1008.

Baxter, J.W., Bradbury, J.C., and Hester, N.C., 1973. A Geologic Excursion to Fluorspar Mines in Hardin and Pope Counties, Illinois. Illinois State Geological Survey, Guidebook Series II, 28p.

Berry, L.G., Mason, B., and Dietrich, R.V., 1983. Mineralogy, Concepts, Descriptions, Determinations. San Francisco, W.F. Freeman, 561p.

Bettencourt, J.S., Leite Jr., W.B., Goraieb, C.L., Sparrenberger, I., Bello, R.M.S., and Payolla, B.L., 2005. Sn-polymetallic greissen-type deposits associated with late-stage rapakivi granites, Brazil: fluid inclusion and stable isotope characteristics. Lithos, 80, 363-386.

Bill, H., and Calas, G., 1978. Color centers, associated rare-earth ions and the origin of coloration in natural fluorites. Physics and Chemistry of Minerals, 3, 117-131.

Borrok, D.M., Kesler, S.E., Boer, R.H., and Essene, E.J., 1998. The Vergenoeg Magnetite-Fluorite Deposit, South Africa: Support for a Hydrothermal Model for Massive Iron Oxide Deposits. Economic Geology, 93, 564-586.

Bosce, S., and Rakovan, J., 2002. Surface-structure-controlled sectoral zoning of the rare earth elements in fluorite from Long Lake, New York, and Bingham, New Mexico, U.S.A. Geochimica et Cosmochimica Acta, 66 (6), 997–1009.

British Columbia Geological Survey MINFILE: No. 082ESE070. <http://minfile.gov.bc.ca/report.aspx?f=PDF&r=Minfile_Detail.rpt&minfilno=082ESE070>. Accessed on 6th Oct. 2015.

British Columbia Geological Survey MINFILE: No. 082FNE016. <http://minfile.gov.bc.ca/report.aspx?f=PDF&r=Minfile_Detail.rpt&minfilno=082FNE016>. Accessed on 6th Oct. 2015.

Bureau Veritas Mineral Laboratories, 2015. LX001 package description. Bureau Veritas Mineral Laboratories, internal unpublished document, Perth, Australia, p.1.

Cardellach, E., Canal, A., and Grandia, F., 2002. Recurrent hydrothermal activity induced by successive extensional episodes: the case of the Berta F-(Pb-Zn) vein system (NE Spain). Ore Geology Reviews, 22, 133-144.

Cheetham, A., Fender, B., and Cooper, M., 1971. Defect structure of calcium fluoride containing excess anions: I. Bragg scattering. Journal of Physics C: Solid State Physics, 4, 3107-3121.

Chesley, J.T., Halliday, A.N., Kyser, T.K., and Spry, P.G., 1994. Direct dating of Mississippi Valley-type mineralization: Use of Sm-Nd in fluorite. Economic Geology, 89, 1192–1199.

Cunningham, C.G., Rassmussen, J.D., Steven, T.A., Rye, R.O., Rowley, P.D., Romberger, S.B., and Selverstone, J., 1998. Hydrothermal uranium deposits containing molybdenum and fluorite in the Marysvale volcanic field, west-central Utah. Mineralium Deposita, 33, 477-494.

Deer, W.A., Howie, R.A., and Zussman, J., 1965. Rock-forming minerals. Halsted Press, London, 347-353.

Deng, X., Chen, Y., Yao, J., Bagas, L., and Tang, H., 2014. Fluorite REE-Y (REY) geochemistry of the ca. 850 Ma Tumen molybdenite-fluorite deposit, eastern Qinling, China: Constraints

on ore genesis. Ore Geology Reviews, 63, 532-543.
Eppinger, R.G., and Closs, L.G., 1990. Variation of trace elements and rare earth elements in fluorite: A possible tool for exploration. Economic Geology, 85, 1896-1907.
Fourie, P.J., 2000. The Vergenoeg fayalite Fe-oxide fluorite deposit, South Africa: some new aspects. In: Porter, T.M. (Eds.), Hydrothermal Fe-oxide copper–gold and related deposits: a global perspective. Australian Mineral Foundation, Adelaide, pp. 309–320.
Fulton III, R.B., and Miller, M.M., 2006. Fluorspar. In: Kogel, J.E. et al (Eds.), Industrial Minerals and Rocks, 7th Edition. Society for Mining Metallurgy and Exploration, Inc., pp. 461-473.
Fyles, J.T., 1967. Geology of the Ainsworth-Kaslo area, British Columbia. British Columbia Geological Survey Bulletins, 53.
Gagnon, J.E., Samson, I.M., Fryer, B.J., and Williams-Jones, A.E., 2003. Compositional heterogeneity in fluorite and the genesis of fluorite deposits: Insights from LA-ICP-MS analysis. The Canadian Mineralogist, 41, 365-382.
Gagnon, G., Rousseau, G., Camus, Y., and Gagné, J., 2012. NI 43-101 Technical Report, Preliminary Economic Assessment: Ashram rare earth deposit for Commerce Resources Corporation. <http://www.commerceresources.com/assets/docs/reports/2015-01-07_GG-PEA-Report.pdf> Accessed on 12th Sep. 2015.
Gonzalez, J., Mao, X.L., Roy, J., Mao, S.S., and Russo, R.E., 2002. Comparison of 193, 213 and 266 nm laser ablation ICP-MS. Journal of Analytical Atomic Spectrometry, 17, 1108-1113.
González-Partida, E., Carrillo-Chávez, A., Grimmer, J.O.W., Pironon, J., Mutterer, J., and Levresse, G., 2003. Fluorite deposits at Encantada-Buenavista, Mexico: products of Mississippi Valley type process. Ore Geology Reviews, 23, 107-124.
Grogan, R.M., and Bradbury, J.C., 1967. Origin of the stratiform fluorite deposits of southern Illinois. Economic Geology Monograph, 3, 40-51.
Grogan, R.M., and Bradbury, J.C., 1968. Fluorite-zinc-lead deposits of the Illinois-Kentucky mining district. In: Ridge, J.D., (eds.), Ore deposits of the United States, 1933-1967: New York. American Institute of Mining, Metallurgy, and Petroleum Engineers, pp. 370-399.
Grogan, R.M., and Montgomery, G., 1975. Fluorspar and Cryolite. In: Lefond, S.J., (Eds.), Industrial Minerals and Rocks, 4th Edition, New York. American Institute of Mining, Metallurgical, and Petroleum Engineers Inc., pp. 653-677.
Hagni, R.D., 1999. Mineralogy of beneficiation problems involving fluorspar concentrates from carbonatite-related fluorspar deposits. Mineralogy and Petrology, 67, 33-44.
Hill, G.T., Campbell, A.R., and Kyle, P.R., 2000. Geochemistry of the southwestern New Mexico fluorite occurrences, implications for precious metals exploration in fluorite-bearing systems. Journal of Geochemical Exploration, 68, 1-20.
Hora, Z.D., Langrova, A., and Pivec, E., 2008. Eaglet property revisited: fluorite-molybdenite porphyry-like hydrothermal system, east-central British Columbia (NTS 093A/10W). Geological Fieldwork 2007, British Columbia Geological Survey, 17-30.
Jackson, S.E., 2008. Calibration strategies for elemental analysis by LA-ICP-MS. In: Sylvester, P. (Eds.), Laser Ablation–ICP–MS in the Earth Sciences current practices and outstanding issues. Mineralogical Association of Canada Short Course 40, Vancouver, B.C., pp. 169-188.
Jochum, K.P., Weis, U., Stoll, B., Kuzmin, D., Yang, Q., Raczek, I., Jacob, D.E., Stracke, A., Birbaum, K., Frick, D.A., Günther, D., and Enzweiler, J., 2011. Determination of Reference Values for NIST SRM 610–617 Glasses Following ISO Guidelines. Geostandards and Geoanalytical Research, 35, 397-429.
Kesler, S.E., Gesink, J.A., and Haynes, F.M., 1989. Evolution of mineralizing brines in the east Tennessee Mississippi Valley-type ore fields. Geology, 17, 466-469.
Kogut, A.I., Hagni, R.D., and Schneider, G.I.C., 1998. Geology, mineralogy, and paragenetic sequence of the Okorusu carbonatite-related fluorite ores, Namibia. In: Schweizerbart'sche, E. (Eds.), Proceedings of the Quadrennial IAGOD Symposium, 9, pp. 555-573.
Levresse, G., Trittla, J., Villareal, J., and González-Partida, E., 2006. The "El Pilote" fluorite skarn: A crucial deposit in the understanding and interpretation of the origin and mobilization of F from northern Mexico deposits. Journal of Geochemical Exploration, 89, 205-209.
Lu, H.-Z., Liu,Y., Wang, C., Xu, Y., and Li, H., 2003. Mineralization and fluid inclusion study of the Shizhuyuan W-Sn-Bi-Mo-F skarn deposit, Hunan Province, China. Economic Geology, 98, 955-974.
Makin, S.A., Simandl, G.J., and Marshall, D., 2014. Fluorite and its potential as an indicator mineral for carbonatite-related rare earth element deposits. In: Geological Fieldwork 2013, British Columbia Ministry of Energy and Mines, British Columbia Geological Survey Paper 2014-1, 207-212.
Mauthner, M., and Melanson, F., 2006. Fluorite occurrences in Canada. Rocks & Minerals, 81, 114-120.
Min, M., Fang, C., and Fayek, M., 2005. Petrography and genetic history of coffinite and uraninite from the Liueryiqi granite-hosted uranium deposit, SE China. Ore Geology Reviews, 26, 187-197.
Misra, K.C., and Lu, C., 1992. Hydrothermal calcites from the Mississippi Valley-type Elmwood-Gordonsville zinc deposits, Central Tennessee, U.S.A.: Fluid inclusion and stable isotope data. European Journal of Mineralogy, 4, 977-988.
Mortensen, J.K., Montgomery, J.R., and Fillipone, J., 1987. U-Pb zircon, monazite, and sphene ages for granitic orthogneiss of the Barkerville Terrane, east-central British Columbia. Canadian Journal of Earth Sciences, 24, 1261-1266.
Möller, P., Parekh, P.P., and Schneider, H.-J., 1976. The application of Tb/Ca-Tb/La abundance ratios to problems of fluorspar genesis. Mineralium Deposita, 11, 111-116.
Munoz, M., Preno, W.R., and Vourjault-Radé, 2005. Sm-Nd dating of the fluorite from the Montroc fluorite deposit, southern Massif Central, France. Mineralium Deposita, 39, 970-975.
Pelch, M.A., Appold, M.S., Emsbo, P., and Bodnar, R.J., 2015. Constraints from fluid inclusion compositions on the origin of Mississippi Valley-Type mineralization in the Illinois-Kentucky district. Economic Geology, 110, 787-808.
Pell, J., 1992. Fluorspar and fluorine in British Columbia. British Columbia Geological Survey, Open file 1992-16.
Richardson, C.K., and Pinckney, D.M., 1984. The chemical and thermal evolution of the fluids in the Cave-in-Rock fluorspar district, Illinois: Mineralogy, paragenesis and fluid inclusions. Economic Geology, 79, 1833-1856.
Ruiz, J., Kesler, S.E., Jones, L.M., and Sutter, J.L., 1980. Geology and geochemistry of the Las Cuevas fluorite deposit, San Luis Potosi, Mexico. Economic Geology, 75, 1200-1209.
Salvi, S., and Williams-Jones, A.E., 2006. Alteration, HFSE mineralization and hydrocarbon formation in peralkaline igneous systems: Insights from Strange Lake Pluton, Canada. Lithos, 90, 19-24.
Schwinn, G., and Markl, G., 2005. REE systematics in hydrothermal fluorite. Chemical Geology, 216, 225-248.
Sheppard, R.A., and Mumpton, F. A., 1984. Sedimentary fluorite in a lacustrine zeolitic tuff of the Gila Conglomerate Near Buckhorn, Grant County, New Mexico; Journal of Sedimentary Research, 54, 853-860.
Simandl, G.J., 2009. World fluorspar resources, market and deposit examples from British Columbia, Canada. British Columbia Geological Survey, Information Circular, 2009-4, 16 pages.
Simandl, G.J., Fajber, R., and Paradis, S., 2014. Portable X-ray fluorescence in the assessment of rare earth element-enriched sedimentary phosphate deposits. Geochemistry: Exploration, Environment, Analysis, 14, 161-169.
Staebler, G., Deville, J., Verbeek, E., Richards, R.P., and Cesbron,

F., 2006. Fluorite: From ancient treasures to modern labs and collections. In: Fisher, J., Jarnot, M., Neumeier, G., Pasto, A., Staebler, G., and Wilson, T. (Eds.), Fluorite - the collector's choice. Lithographie, LLC, Connecticut, U.S.A. pp. 4-12.

Sverdrup, T.L., 1968. Yttrofluorite-ytttrocerite-cerfluorite in Norwegian pegmatites. Contributions to the Mineralogy of Norway, 37,245-252.

Verbeek, E., 2006. Fluorite Luminescence. In: Fisher, J., Jarnot, M., Neumeier, G., Pasto, A., Staebler, G., and Wilson, T. (Eds.), Fluorite - the collector's choice. Lithographie, LLC, Connecticut, U.S.A., pp. 13-19.

Wright, W.R., Mariano, A.N., and Hagni, R.G., 1998. Pyrochlore, mineralization, and glimmerite formation in the Eldor (Lake LeMoyne) carbonatite complex, Labrador Trough, Quebec, Canada. In: Proceedings of the 33rd Forum on the Geology of Industrial Minerals. Canadian Institute of Mining, Metallurgy and Petroleum; Special Volume, 50, 205-213.

Xu, C., Taylor, R.N., Li, W., Kynicky, J., Chakhmouradian, A.R., and Song, W., 2012. Comparison of fluorite geochemistry from REE deposits in the Panxi region and Bayan Obo, China. Journal of Asian Earth Sciences, 57, 76-89.

Xu, C., Zhang, H., Huang, Z., Liu, C., Qi, L., Li, W., and Guan, T., 2004. Genesis of the carbonatite-syenite complex and REE deposit at Maoniuping, Sichuan Province, China: Evidence from Pb isotope geochemistry. Geochemical Journal, 38, 67-76.

Rare earth elements in Québec, Canada: Main deposit types and their economic potential

A.-A. Sappin[1, a] and G. Beaudoin[1]

[1] Département de géologie et de génie géologique, Université Laval, 1065 avenue de la Médecine, Québec, QC, G1V 0A6
[a] corresponding author: anne-aurelie.sappin.1@ulaval.ca

Recommended citation: Sappin, A.-A. and Beaudoin, G., 2015. Rare earth elements in Québec, Canada: Main deposit types and their economic potential. In: Simandl, G.J. and Neetz, M., (Eds.), Symposium on Strategic and Critical Materials Proceedings, November 13-14, 2015, Victoria, British Columbia. British Columbia Ministry of Energy and Mines, British Columbia Geological Survey Paper 2015-3, pp. 265-273.

1. Introduction

Rare earth elements (REE) are strategic metals vital to global economic growth because they are used in a wide range of high-technology industries (e.g., energy, transport, and telecommunications; Walters et al., 2011). The world production and reserves are mainly owned by China. In 2008, the Chinese government introduced export quotas on rare metals, which led to a global search for new sources of REE. Québec has substantial REE resources (Simandl et al., 2012), which may contribute to future production.

Gosselin et al. (2003) and Boily and Gosselin (2004) inventoried rare metals (REE, Zr, Nb, Ta, Be, and Li) occurrences and deposits in Québec and, based mainly on lithological association, subdivided them into seven types: 1) deposits associated with peraluminous granitic complexes; 2) deposits associated with carbonatite complexes; 3) deposits associated with peralkaline complexes; 4) deposits associated with placers and paleoplacers; 5) iron oxide, Cu, REE, and U deposits; 6) deposits associated with granitic pegmatites, migmatites, and peraluminous to metaluminous granites; and 7) deposits associated with calc-silicate and metasomatized rocks or skarns. Herein we review REE mineralization in the province, adopting a more genetic scheme based on the classification of Walters et al. (2011). The REE occurrences and deposits are subdivided into primary deposits, formed by magmatic and/or hydrothermal processes, and secondary deposits, formed by sedimentary processes and leaching. Primary deposits are then subdivided into four types: 1) carbonatite complex-associated; 2) peralkaline igneous rock-associated; 3) REE-bearing Iron-Oxide-Copper-Gold (IOCG) deposits; and 4) hyperaluminous/metaluminous granitic pegmatite-, granite-, and migmatite-associated deposits, and skarns. Secondary deposits are subdivided into two deposit types: 1) placers and paleoplacers and 2) REE-bearing ion-adsorption clays.

2. Definition and characteristics

According to the International Union of Pure and Applied Chemistry (IUPAC), the REE comprise of 17 metals with similar chemical properties, including the lanthanides (La, Ce, Pr, Nd, Pm, Sm, Eu, Gd, Tb, Dy, Ho, Er, Tm, Yb, and Lu), Sc, and Y. The REE are not rare in the Earth's crust. They occur in trace amounts in most rocks, some more abundant than others. The relative abundance of REE in the Earth's crust varies according to two main factors: 1) the predominance of even-numbered chemical elements relative to their odd-numbered neighbours in the solar system, because of the greater stability of their atomic nuclei (Oddo-Harkins effect); and 2) the predominance of light REE (LREE: La to Eu) compared to heavy REE (HREE: Gd to Lu) in the Earth's crust, since LREE are more incompatible than HREE (Walters et al., 2011). The REE occur in a wide range of mineral species, such as silicates, carbonates, oxides, phosphates, and clays. However, REE contents of these minerals are variable and only a few of them are of economic interest. For a REE-bearing mineral to be economically viable, it should, for example, contain easily extractable metals, form large-tonnage deposits, and have low radioactive and toxic elements content (e.g., Th, U). The REE (except Sc) belong to the list of critical raw materials defined by the European Union in 2010 (European commission, 2010) and updated in 2014 (European commission, 2014). Of the REE included in this category, Eu, Tb, Nd, Pr, and Dy are predominant in the global REE market in terms of demand and value (Lehmann, 2014).

3. World production and reserves

China is the largest producer of REE, with 85% of global REE production in 2014 (Gambogi, 2015). Chinese deposits are mostly associated, directly or indirectly, with carbonatites (e.g., Bayan Obo Fe-REE-Nb deposit; Maoniuping REE deposit) and to ion-adsorption clays (e.g., Ganzhou deposits rich in HREE). The United States is the second largest producer of REE, far behind China, with 6% of the world's REE production in 2014 (Gambogi, 2015). US production comes mainly from the carbonatite-hosted Mountain Pass deposit, which is rich in LREE. In Canada, no REE mine is currently in operation, although several projects have reached advanced stages of exploration and development (e.g., Hoidas Lake, Saskatchewan; Thor Lake, Northwest Territories; Strange Lake, Québec).

Global reserves of rare earth oxides are also predominantly

in China (44% of known world reserves), followed by Brazil (17%), Australia (3%), India (2%), and USA (1%) (Gambogi, 2015). The remaining 33% are spread across other countries, although detailed data on these are currently not available. If NI-43-101 standards were uniformly applied worldwide Canada's and Australia's proportion of global reserves would be higher (Simandl, 2014).

4. Classification of REE occurrences and deposits

4.1. Primary occurrences

4.1.1. Deposits associated with carbonatite complexes

Most carbonatite complexes are formed in intracratonic anorogenic or post-orogenic extensional settings and are commonly spatially related to major crustal structures (Woolley and Kjarsgaard, 2008). Carbonatites form composite intrusive complexes associated with alkaline rocks, sills, dikes, and isolated masses with various shapes. The carbonatite complexes display evidence of hydrothermal remobilization and metasomatism (Chakhmouradian and Zaitsev, 2012). The metasomatic alteration leads to the formation of a halo around the igneous complexes with sodic and/or potassic rocks, called fenites, and the formation of veins and veinlets rich in alteration minerals.

In carbonatite complexes, REE mineralization is particularly rich in LREE compared to HREE (Linnen et al., 2014). These igneous complexes are also rich in high field strength elements (HFSE), like Nb and Ta, except in the case of the carbonatites emplaced in post-collision settings (Hou et al., 2006; Chakhmouradian et al., 2008). The ore minerals include the main components of carbonatites (e.g., calcite, dolomite, and apatite) and numerous REE-bearing carbonates (e.g., bastnaesite-(La) and bastnaesite-(Ce)), oxides (e.g., pyrochlore-(Nb)), phosphates (e.g., monazite-(Ce)), and silicates (e.g., allanite; Chakhmouradian and Zaitsev, 2012). REE mineralization may be: 1) magmatic and formed due to fractional crystallization or magma immiscibility; 2) hydrothermal and the result of precipitation from hydrothermal fluids; 3) hydrothermal and metasomatic; and 4) residual, derived from erosion and weathering of carbonatite complexes.

Québec REE occurrences and deposits hosted by carbonatite complexes (Figs. 1, 2) are mainly located along the Waswanipi-Saguenay structural corridor (e.g., Niobec mine within the St-Honoré carbonatite complex; Crevier deposit within the Crevier alkaline intrusion, containing carbonatite dikes; Montviel deposit; Lac Shortt deposit) and the Ottawa–Bonnechère graben (e.g., St. Lawrence Columbium mine and Niocan deposit within the Oka carbonatite complex). Other mineralization is also identified farther north in the Labrador Trough (e.g., Eldor deposit). These occurrences and deposits range in age from Neoarchean to early Cretaceous (Table 1).

4.1.2. Deposits associated with peralkaline igneous rocks

Peralkaline igneous rocks crystallize in anorogenic, continental extensional settings, in close spatial association with major crustal structures (Jaireth et al., 2014). They form annular intrusive complexes, pegmatites, or subvolcanic massive bodies. The intrusions are commonly altered. The alteration includes albitization of the top of the intrusions, alteration by orthomagmatic fluids that causes F-leaching in the granitic rocks and destabilization and hematitization of amphibole and feldspar, alteration by Ca-rich low-temperature meteoric fluids that leads to the pseudomorphic replacement of Na-silicates by Ca-silicates, and silicification (Boily and Gosselin, 2004).

Rare earth deposits associated with peralkaline igneous rocks generally have large tonnages with low metal concentration. They are enriched in HREE relative to LREE, and are rich in HFSE like Nb and Zr (Castor and Hedrick, 2006). Beside rock forming minerals, the REE ore contain a range of REE-bearing silicates (e.g., eudialyte, gittinsite, mosandrite), phosphates (e.g., monazite, britholite), oxides (e.g., fergusonite, pyrochlore), carbonates (e.g., bastnaesite, synchysite), and fluoride (e.g., gagarinite). Rare earth mineralization results from magmatic and/or hydrothermal processes. However, hydrothermal remobilization appears to be essential for the formation of economic REE ore deposits (Linnen et al., 2014).

In Québec, the REE occurrences and deposits associated with peralkaline igneous rocks (Figs. 1, 3) are Mesoproterozoic and occur mainly in the Churchill and Grenville provinces (e.g., Strange Lake, Misery Lake, and Kipawa deposits; Table 1).

4.1.3. REE-bearing IOCG deposits

IOCG deposits are associated with late-orogenic and post-orogenic rifts in intracratonic, intra-arc, and back-arc extensional settings (Corriveau, 2007). These deposits form discordant masses, veins, dikes, tabular bodies, and stockworks and are emplaced along faults and other geological contacts. They are generally altered due to strong hydrothermal activity and are commonly surrounded by regional-scale sodic-calcic alteration zones and local-scale potassic and iron-oxides alteration zones (Corriveau, 2007). Alteration of the Kiruna-type (Fe±P) includes the formation of scapolite and albite, and the occurrence of actinolite and epidote in mafic wall rocks (Boily and Gosselin, 2004). Alteration of the polymetallic Olympic Dam-type (Fe±Cu±Au±U±REE) is more diverse and intense, with the formation of sericite and hematite at surface and chlorite and K-feldspar at depth (Boily and Gosselin, 2004).

Some IOCG deposits are mined for Fe, Au, and other metals but currently, REE are not recovered (Jaireth et al., 2014). Rare earths may be contained in a wide variety of REE-bearing minerals including apatite, allanite, monazite, xenotime, bastnaesite, britholite, florencite, kainosite, andradite, gadolinite, thorite, perovskite, pyrochlore, and uraninite. The formation of these deposits results from hydrothermal processes that have not yet been characterized precisely (Williams et al., 2005).

In Québec, REE mineralization in IOCG-type deposits (Figs. 1, 4) is Neoproterozoic and appears to be restricted to the Manitou area, in the Grenville Province. The most significant

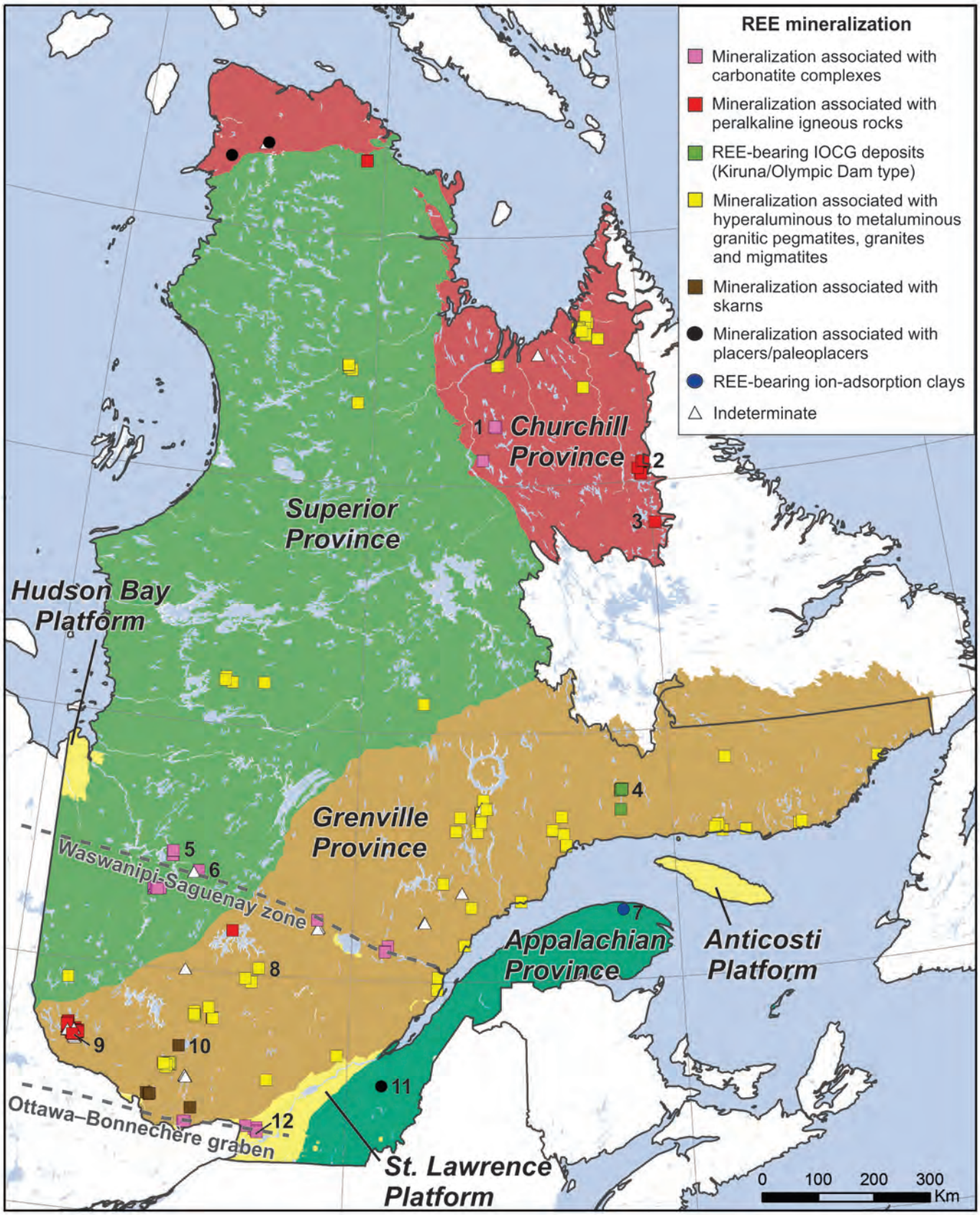

Fig. 1. Location of REE mineralization in Québec. 1- Eldor deposit, 2- Strange Lake deposit, 3- Misery Lake deposit, 4- Kwyjibo group of occurrences, 5- Montviel deposit, 6- Lac Shortt deposit, 7- Grande-Vallée deposit, 8- Haltaparche occurrence, 9- Kipawa deposit, 10- Baie-Mercier occurrence, 11- Wares occurrence, and 12- St. Lawrence Columbium mine and Niocan deposit.

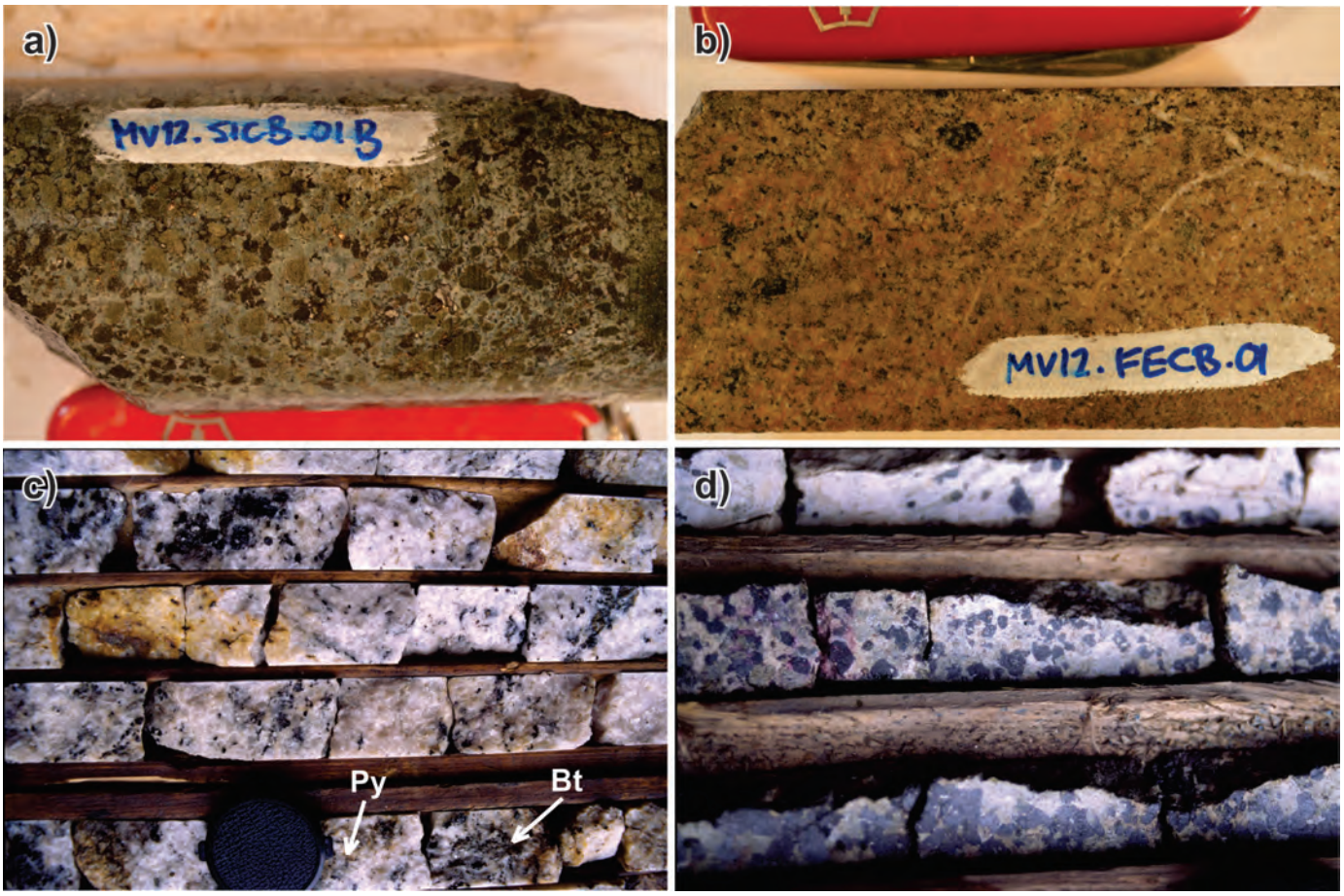

Fig. 2. Representative examples of carbonatite and skarn from carbonatite complex-related deposits. **a)** Silicocarbonatite from the Montviel carbonatite complex. The knife is ~9 cm long. Photo courtesy of O. Nadeau. **b)** Pervasively altered ferrocarbonatite hosting REE-bearing minerals (e.g., cordylite-(Ce), kukharenkoite-(Ce), and qaqarssukite-(Ce)) from the Montviel carbonatite complex. The knife is ~9 cm long. Photo courtesy of O. Nadeau. **c)** Calciocarbonatite with biotite (Bt) and, locally, disseminated pyrite (Py) from the Oka carbonatite complex. Core size is 3.6 cm in diameter. **d)** Calcic magnetite skarn in the S-60 mineralized zone from the Oka carbonatite complex. Core is 3.6 cm in diameter.

deposits are at the Kwyjibo property (Table 1).

4.1.4. Deposits associated with hyper- to metaluminous granitic pegmatite, granite, and migmatite, and skarns

The pegmatites, granites, and migmatites in this group are emplaced in continental orogenic environments during high-grade metamorphism and crustal anatexis resulting from post-collisional crustal thickening or underplating of mantle-derived mafic magmas at the base of the crust (Boily and Gosselin, 2004). Some pegmatites are derived directly from anatexis and emplaced in situ, and others are formed by magmatic differentiation of granitic melts (Boily and Gosselin, 2004). Skarns are emplaced in orogenic environments and form adjacent to felsic intrusions injected into calcareous sedimentary rocks (Jaireth et al., 2014). Granitic pegmatites form homogeneous to broadly zoned dike swarms, granites and granitic migmatites form heterogeneous masses, and skarns form irregular zones along intrusive contacts. In the pegmatites, granites, and migmatites, metasomatism results in albitization, chloritization, oxidation, and hydrous alteration of the intrusive rocks (Boily and Gosselin, 2004). In the skarns, hornfels produced by contact metamorphism are commonly replaced by anhydrous or hydrous Ca-, Fe-, and Mg-silicates (Jaireth et al., 2014).

The REE occurrences contained in hyper- to metaluminous pegmatites, granites, and migmatites, and in skarns are characterized by low tonnages and relatively low concentrations of REE-bearing minerals (Chakhmouradian and Zaitsev, 2012). Common ore minerals are monazite, xenotime, apatite, allanite, zircon, gadolinite, thorite, fergusonite, and uraninite. In granitic pegmatites, granites, and migmatites, REE mineralization is mainly magmatic in origin. However, metals are commonly remobilized and concentrated during metamorphism and hydrothermal alteration. In skarns, mineralization forms where fluids react with carbonate rocks to introduce alumina, silica, magnesium, as well as REE and Mo. Locally, mineralization may be remobilized by later fluids formed during regional metamorphism or leaching (Jaireth et al., 2014).

In Québec, these mineral occurrences (Figs. 1, 5) are mainly in the Grenville Province and include the Haltaparche occurrence hosted by a granitic pegmatite (MERN, 2014) and the Baie-Mercier occurrence primarily associated with

Table 1. Selected REE occurrences and deposits in Québec, their deposit type, age, and grade and tonnage information.

Occurrence/Deposit[a]	Type	Age	Commodity grade and tonnage
Eldor deposit [1]	Carbonatite complex	1874 Ma (Wright et al., 1998)	Inferred mineral resources of 117.3 Mt at 1.74% TREO using a 1.25% TREO cut-off grade (Laferrière, 2011)
Strange Lake deposit (B-Zone) [2]	Peralkaline igneous complex	1240 Ma (Miller et al., 1997)	Indicated mineral resources of 278.1 Mt at 1.92% ZrO_2, 0.93% TREO, and 0.18% Nb_2O_5 and inferred mineral resources of 214.4 Mt at 1.71% ZrO_2, 0.85% TREO, and 0.14% Nb_2O_5 using a 0.50% TREO cut-off grade (Gowans et al., 2014)
Misery Lake deposit [3]	Peralkaline igneous complex	1410 Ma (David et al., 2012)	Up to 8.56% TREO, 3.05% ZrO_2, and 0.72% Nb_2O_5 (Petrella, 2012)
Kwyjibo property [4]	IOCG deposit	~972 to 951 Ma (Gauthier et al., 2004)	7.0 m thick-interval with 7.04% TREO and 0.19% Cu (Focus Graphite Inc., 2013)
Montviel deposit [5]	Carbonatite complex	1894 Ma (David et al., 2006)	Indicated mineral resources of 82.4 Mt at 1.51% TREO and inferred mineral resources of 184.2 Mt at 1.43% TREO using an economic cut-off of CA$180 per tonne (Belzile et al., 2015)
Lac Shortt deposit [6]	Carbonatite complex	2652 Ma (Thorpe et al., 1984; Morasse, 1988)	Up to 2.2% REO (Quirion, 1991)
Crevier deposit[b]	Carbonatite complex	957.5 Ma (Groulier et al., 2014)	Indicated mineral resources of 12.9 Mt at 0.19% Nb_2O_5 and 234 ppm Ta_2O_5 and inferred mineral resources of 15.4 Mt at 0.17% Nb_2O_5 and 252 ppm Ta_2O_5 using a 0.10% Nb_2O_5 cut-off grade (Duplessis and Girard, 2010)
Niobec mine[b]	Carbonatite complex	565 Ma (Doig and Barton, 1968)	Total production of 1.8 Mt at 0.61% Nb_2O_5 (MRNF, 2010)
Grande-Vallée deposit [7]	Ion-adsorption clay	Cambrian (Raffle et al., 2013)	Indicated mineral resources of 1.0 Gt at 563 ppm REE and rare metals using a 18% Al_2O_3 cut-off grade (Doran et al., 2012b)
Haltaparche occurrence [8]	Granitic pegmatite	-	3950 ppm Ce, 2040 ppm La, and 1520 ppm Nd (MERN, 2015)
Kipawa deposit [9]	Peralkaline igneous complex	1033 Ma (van Breemen and Currie, 2004)	Indicated mineral resources of 13.4 Mt at 0.36% TREO and inferred mineral resources of 3.3 Mt at 0.31% TREO using a 0.20% TREO cut-off grade (Saucier et al., 2013)
Baie-Mercier occurrence [10]	Skarn	-	2800 ppm Ce, 1200 ppm La, and 810 ppm Nd (Lapointe et al., 1993)
Wares occurrence [11]	Paleoplacer	Cambrian (Gauthier et al., 1989)	1540 ppm Ce, 917 ppm La, and 568 ppm Nd (MERN, 2015)
St. Lawrence Columbium mine[c] [12]	Carbonatite complex	135 to 113 Ma (Chen, 2014)	Total production of 6.2 Mt at 0.31% Nb_2O_5 between 1961 and 1976 and mineral reserves of 25.0 Mt at 0.44% Nb_2O_5 (Trudel, 1983; Lavergne, 1985)
Niocan deposit[c] [12]	Carbonatite complex	135 to 113 Ma (Chen, 2014)	Indicated mineral resources of 6.4 Mt at 0.65% Nb_2O_5 and inferred mineral resources of 3.2 Mt at 0.61% Nb_2O_5 using a 0.40% Nb_2O_5 cut-off grade (Niocan Inc., 2015)

[a] Numbers in brackets correspond to the numbers identifying deposits in Figure 1

[b] In the Crevier deposit and Niobec mine, REE are minor substances subordinate to Nb

[c] In the St. Lawrence Columbium mine and Niocan deposit, REE are major substances, but REE resources are unknown

Abbreviation: TREO = total rare earth oxide, REO = rare earth oxide

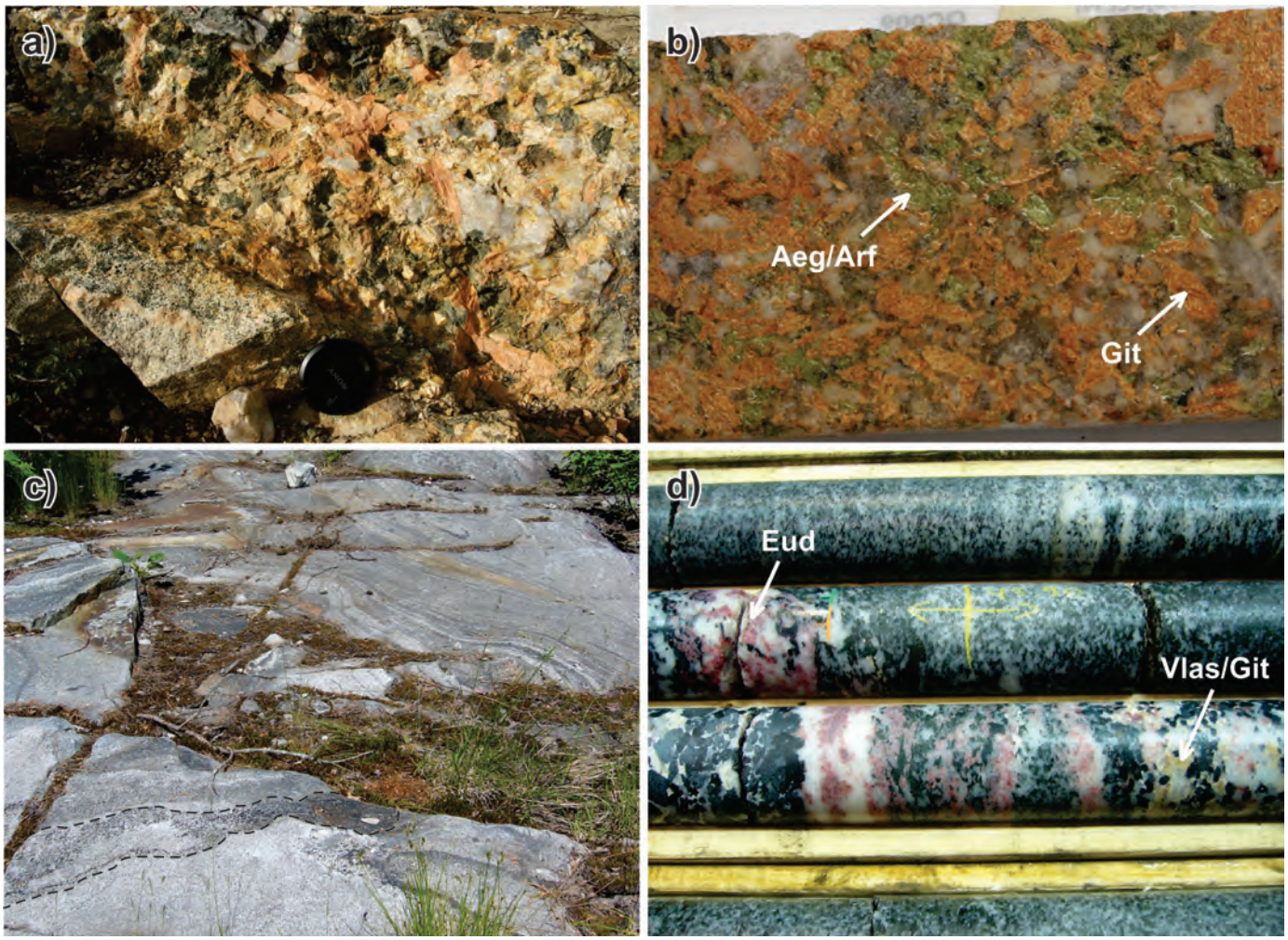

Fig. 3. Representative examples of pegmatite and syenite from peralkaline igneous rock-associated deposits. **a)** Pegmatite intruding subsolvus granite from the B-Zone of the Strange Lake intrusive complex. Lens cap is ~6 cm in diameter. Photo is courtesy of A. Williams-Jones. **b)** Pegmatite core with gittinsite (Git) and aegirine (Aeg)/arfvedsonite (Arf) from the B-Zone of the Strange Lake intrusive complex. Core is 4.7 cm in diameter. Photo courtesy of A. Williams-Jones. **c)** Syenite gneiss from the Kipawa Alkaline complex, crosscut by a 4 m-wide coarse-grained mesocratic syenite band with eudialyte and mosandrite (bottom of the picture). Photo courtesy of F. Fleury. **d)** Foliated syenite with eudialyte (Eud) and vlasovite (Vlas)/gittinsite from the Kipawa Alkaline complex. Core is 4.7 cm in diameter. Photo courtesy of F. Fleury.

a carbonatite horizon (Lapointe et al., 1993; Table 1). A few occurrences have been discovered in the Superior Province and in the Churchill Province (Labrador Trough). Pegmatites, granites, migmatites, and skarns containing REE appear to be mostly Archean to Proterozoic.

4.2. Secondary deposit-types

4.2.1. Placers and paleoplacers

Placers and paleoplacers with REE mineralization are formed near continental margins rich in reworked siliciclastic sediments, and near Mesozoic to Cenozoic volcanic arcs (Boily and Gosselin, 2004). They are found in alluvial fan, eolian, fluvial, glacial, glaciofluvial, beach, and seafloor settings. Continental deposits form thin and discontinuous lenses; coastal marine deposits form thin elongate bodies of limited lateral extent (Boily and Gosselin, 2004).

Generally, placers and paleoplacers lack major concentrations of REE-bearing minerals and contain high levels of U and Th (Castor and Hedrick, 2006). In these deposits, REE are extracted as by-products of ilmenite and zircon mining (Castor and Hedrick, 2006). The predominant REE ore minerals are monazite and xenotime. These heavy minerals are derived from erosion of a range of primary sources, including ore deposits and igneous rocks.

In Québec, the most important placer REE occurrences (Fig. 1) are in the Ungava and Appalachian orogens (e.g., Wares occurrence; Table 1). Several paleoplacers rich in Fe and Ti, which contain low concentrations of REE, have been reported in Pleistocene sands in the Basse-Côte-Nord area, along the St. Lawrence River (e.g., Natashquan deposit; Boily and Gosselin, 2004). Placers and paleoplacers containing REE mineralization are Cambrian to Holocene in age.

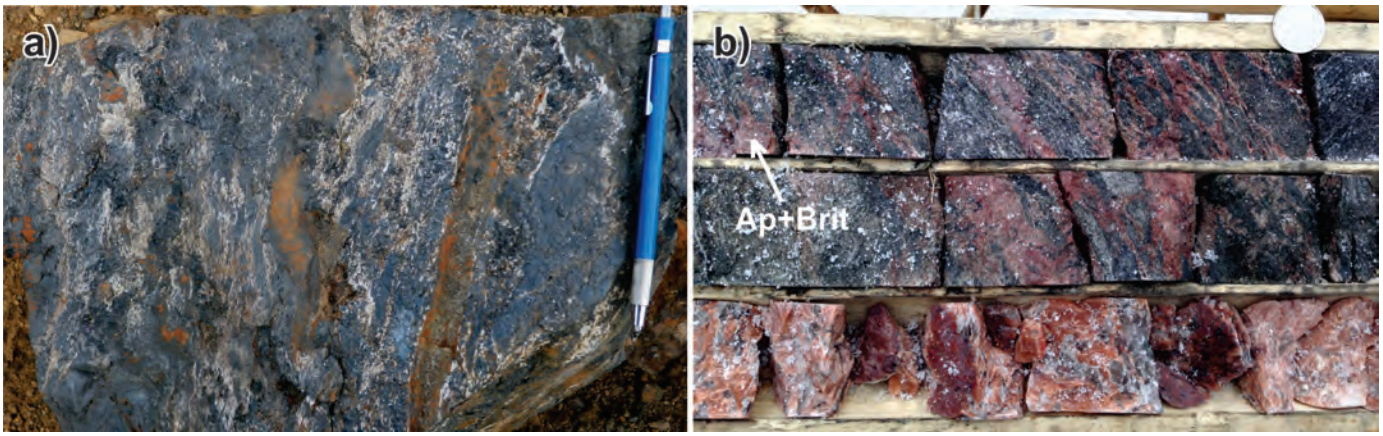

Fig. 4. Representative examples of mineralization from REE-bearing IOCG deposits. **a)** Veins with calc-silicate minerals and REE-bearing minerals (e.g., apatite, britholite, allanite), veinlets of magnetite, and fragments of massive magnetite from the Josette deposit in the Kwyjibo property. The pen is ~15 cm long. **b)** Altered biotite-hornblende-plagioclase-magnetite gneiss brecciated by veins/veinlets of apatite (Ap) and britholite (Brit) from the Josette deposit in the Kwyjibo property. The coin is 2.4 cm in diameter. Photos courtesy of S. Perreault.

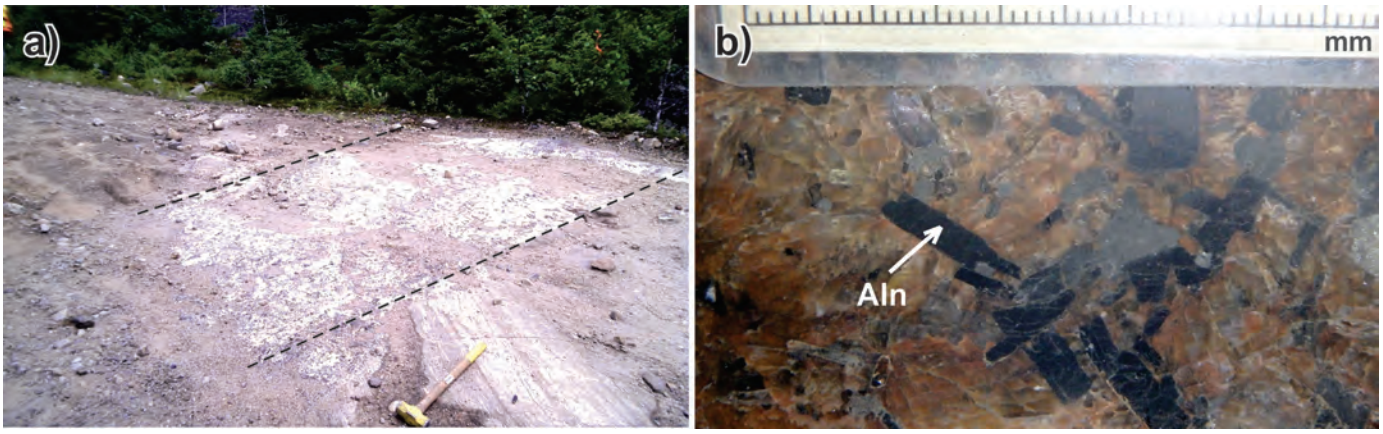

Fig. 5. Representative examples of pegmatite from hyperaluminous/metaluminous granitic pegmatite-related deposits. **a)** Dike of granitic pegmatite crosscutting the foliated charnockite of the Hibbard Plutonic suite in the Haltaparche occurrence area. The hammer is ~38 cm long. **b)** Granitic pegmatite with allanite (Aln) from the Haltaparche occurrence. Photos courtesy of F. Solgadi.

4.2.2. REE-bearing ion-adsorption clays

Rare earth element-bearing ion-adsorption clays commonly form in subtropical areas, where chemical weathering is intense, but can also be found in deep-marine settings. The clays can be unconsolidated to consolidated.

Rare earth element mineralization associated with ion-adsorption clays is characterized by low grades and large tonnages of metals and is typically rich in HREE and poor in radioactive elements. In addition, clay deposits contain REE that are easily extracted by open-pit mining and easily processed. In REE-bearing ion-adsorption clays, most of the REE are in the form of cations adsorbed on the surface of clay minerals. This REE mineralization derives from the chemical and mechanical weathering of rocks that contain a significant proportion of minerals rich in REE and sensitive to chemical alteration, like granites (Kynicky et al., 2012).

In Québec, only one REE occurrence has been identified in ion-adsorption clays (Fig. 1). This occurrence is associated with the Cambrian Grande-Vallée alumina deposit (Table 1), in the Appalachian orogen. The aluminous mudstone containing REE mineralization is composed of kaolinite and probably gibbsite or boehmite, and was deposited in a deep-marine setting on a passive continental margin (Doran et al., 2012a, 2012b). REE contents of clays in the Grande-Vallée deposit are low, but REE can be recovered as by-products of alumina (Doran et al., 2012a, 2012b).

5. Economic potential

Among all the REE occurrences in Québec, the Proterozoic deposits formed by magmatic and hydrothermal processes and associated with carbonatite complexes, peralkaline igneous rocks and, to a lesser extent, IOCG deposits have the highest economic potential. They are numerous, have locally high REE contents, and are significant sources of the most abundant REE (e.g., La, Ce) and the most critical REE (e.g., Nd, Eu, Tb). Furthermore, several of these deposits appear to have substantial REE resources (Table 1) and are currently being evaluated. Good examples are Montviel (Belzile et al., 2015; Nadeau et al., 2015), Eldor (Wright et al., 1998; Laferrière, 2011), Stange Lake (Gowans et al., 2014; Vasyukova and

Williams-Jones, 2014), Kipawa (van Breemen and Currie, 2004; Saucier et al., 2013), and Josette in the Kwyjibo property (Gauthier et al., 2004; Focus Graphite Inc., 2013).

6. Conclusion

Québec hosts numerous REE occurrences and deposits. Six main types of mineralization are recognized, according to their lithological association. Four of these types are primary and formed by igneous and/or hydrothermal processes. Two types are secondary and formed by weathering and sedimentary processes. The primary deposits are the most abundant in the province and are the main targets for exploration. They are associated with carbonatite complexes, peralkaline igneous rocks, IOCG deposits, or hyperaluminous/metaluminous igneous rocks and skarns. They vary from Archean to Mesozoic in age, and were emplaced mainly in extensional intracontinental settings near major crustal structures. In contrast, the secondary deposits are scarce. They are Paleozoic to Cenozoic in age and formed in continental and marine siliciclastic settings or in clays.

Acknowledgments

We thank Patrice Roy and Fabien Solgadi from the Ministère de l'Énergie et des Ressources naturelles du Québec (MERN) for their assistance and permission to access geoscience data from the SIGEOM databank. Thanks are also extended to George J. Simandl, Carlee Akam, and Michaela Neetz from the British Columbia Geological Survey (BCGS) for reviews that helped us improve the final version of this contribution. This study is funded by the MERN, with contributions from MITACS.

References cited

Belzile, E., Marchand, R., and Bouajila, A., 2015. NI 43-101 technical report - Montviel rare earth project, Québec, Canada. NI 43-101 technical report, 141p. <http://www.sedar.com/GetFile.do?lang=EN&docClass=24&issuerNo=00030257&fileName=/csfsprod/data151/filings/02378188/00000001/C%3A\SEDAR_docs\GeomegaResourcesInc\150730TR\150730geomegaResTR_cwm.pdf> Accessed September 8, 2015.

Boily, M., and Gosselin, C., 2004. Les principaux types de minéralisations en métaux rares (Y-Zr-Nb-Ta-Be-Li-ETR) du Québec. Ministère des Ressources naturelles et de la Faune du Québec, ET 2004-01, 46p.

Castor, S.B., and Hedrick, J.B., 2006. Rare earth elements. In: Kogel, J.E., Trivedi, N.C., and Barker, J.M., (Eds.), Industrial minerals and rocks. Society for Mining, Metallurgy and Exploration, pp. 769-792.

Chakhmouradian, A.R., and Zaitsev, A.N., 2012. Rare earth mineralization in igneous rocks: sources and processes. Elements, 8, 347-353.

Chakhmouradian, A.R., Mumin, A.H., Demény, A., and Elliott, B., 2008. Postorogenic carbonatites at Eden Lake, Trans-Hudson Orogen (northern Manitoba, Canada): geological setting, mineralogy and geochemistry. Lithos, 103, 503-526.

Corriveau, L., 2007. Iron oxide copper-gold deposits: a Canadian perspective. In: Goodfellow, W.D., (Ed.), Mineral deposits of Canada: a synthesis of major deposit-types, district metallogeny, the evolution of geological provinces, and exploration methods. Geological Association of Canada, Mineral Deposits Division, Special Publication 5, pp. 307-328.

Doran, R., Bouchard, A.-M., and Levaque, J.-G., 2012a. Preliminary economic assessment on Orbite Aluminae Inc., metallurgical grade Alumina Projet, Quebec, Canada. NI 43-101 technical report, 332p. <http://www.sedar.com/GetFile.do?lang=EN&docClass=24&issuerNo=00007619&fileName=/csfsprod/data125/filings/01848436/00000001/s%3A\ORBITE43.pdf> Accessed September 8, 2015.

Doran, R., Bouchard, A.-M., Saucier, G., Rheault, M., Ayad, A.B., Knox, A., Lafleur, P.-J., and Levaque, J.-G., 2012b. Évaluation économique préliminaire du projet d'alumine de qualité métallurgique d'Orbite Aluminae Inc., Quebec, Canada. Rapport technique révisé selon le règlement 43-101, 355p. <http://www.sedar.com/GetFile.EN&docClass=24&issuerNo=00007619&fileName=/csfsprod/data139/filings/01848436/00000007/p%3A\orbite\techrepo\TechRepf.pdf> Accessed September 8, 2015.

European commission, 2010. Critical raw materials for the EU – Report of the Ad-hoc Working Group on defining critical raw materials. 53 p. <http://ec.europa.eu/growth/sectors/raw-materials/specific-interest/critical> Accessed September 8, 2015.

European commission, 2014. Report on critical raw materials for the EU – Report of the Ad hoc Working Group on defining critical raw materials. 41p. <http://www.amg-nv.com/files/Report-on-Critical-Raw-Materials-for-the-EU-2014.pdf> Accessed September 8, 2015.

Focus Graphite Inc., 2013. Focus Graphite and SOQUEM confirm grades, thicknesses and continuity of the REE mineralization at Josette horizon, Kwyjibo property: 3.22 % TREO over 36 m in hole 10885-12-75. <http://www.marketwired.com/press-release/focus-graphite-soquem-confirm-grades-thicknesses-continuity-ree-mineralization-josette-tsx-venture-fms-1773049> Accessed September 8, 2015.

Gambogi, J., 2015. Rare earths. In: Mineral commodity summaries 2015. U.S. Geological Survey, pp. 128-129.

Gauthier, M., Chartrand, F., Cayer, A., and David, J., 2004. The Kwyjibo Cu-REE-U-Au-Mo-F property, Quebec: a Mesoproterozoic polymetallic iron oxide deposit in the northeastern Grenville Province. Economic Geology, 99, 1177-1196.

Gosselin, C., Boily, M., Beaumier, M., Leduc, M., Dion, D.-J., Garneau, C., and Thériault, R., 2003. Minéralisations en métaux rares (Y, Zr, Nb, Ta, Be, Li et ETR) au Québec. Ministère des Ressources naturelles et de la Faune du Québec, DV 2003-03, 1 poster, 1 cd-rom.

Gowans, R.M., Lewis, W.J., Shoemaker, S., Spooner, J., and Zalnieriunas, R.V., 2014. NI 43-101 technical report on the preliminary economic assessment (PEA) for the Strange Lake property, Quebec, Canada. Amended and restated NI 43-101 technical report, 241p. <http://www.sedar.com/GetFile.do?lang=EN&docClass=24&issuerNo=00026016&fileName=/csfsprod/data149/filings/02191358/00000002/i%3A\Soco\Sedar\ur2014\Quest_Amend_June27\AmendTechRep43_101.pdf> Accessed September 8, 2015.

Hou, Z., Tian, S., Yuan, Z., Xie, Y., Yin, S., Yi, L., Fei, H., and Yang, Z., 2006. The Himalayan collision zone carbonatites in western Sichuan, SW China: petrogenesis, mantle source and tectonic implication. Earth and Planetary Science Letters, 244, 234-250.

Jaireth, S., Hoatson, D.M., and Miezitis, Y., 2014. Geological setting and resources of the major rare-earth-element deposits in Australia. Ore Geology Reviews, 62, 72-128.

Kynicky, J., Smith, M.P., and Xu, C., 2012. Diversity of rare earth deposits: the key example of China. Elements, 8, 361-367.

Laferrière, A., 2011. Technical report, mineral resource estimation, Eldor property−Ashram deposit, Nunavik, Quebec, Commerce Resources Corporation. NI 43-101 technical report, 82p. <http://www.sedar.com/GetFile.do?lang=EN&docClass=24&issuerNo=00

016212&fileName=/csfsprod/data117/filings/01731026/00000001/k%3A\DATA\SEDAR\Comm_techrpt.pdf> Accessed September 8, 2015.

Lapointe, S., Gauthier, M., and Nantel, S., 1993. Étude d'indices d'uranium, de thorium et de molybdène dans la région de Maniwaki–Grand-Remous. Ministère de l'Énergie et des Ressources du Québec, MB 93-68, 102p.

Lavergne, C., 1985. Gîtes minéraux à tonnage évalué et production minérale du Québec. Ministère des Ressources naturelles, DV 85-08, 84p.

Lehmann, B., 2014. Economic geology of rare-earth elements in 2014: a global perspective. European Geologist, 37, 21-24.

Linnen, R.L., Samson, I.M., Williams-Jones, A.E., and Chakhmouradian, A.R., 2014. Geochemistry of the rare-earth element, Nb, Ta, Hf, and Zr deposits. In: Scott, S.D., (Ed.), Treatise on geochemistry — Geochemistry of mineral deposits, 13, pp. 543-568.

MERN, 2014. Nouvelles cibles pour l'exploration minérale – Travaux géoscientifiques 2014. Ministère de l'Énergie et des Ressources naturelles du Québec, PRO 2014-01, 8p. <http://www.mern.gouv.qc.ca/publications/mines/publications/Pro_2014-01_br.pdf> Accessed September 8, 2015.

Nadeau, O., Cayer, A., Pelletier, M., Stevenson, R., and Jébrak, M., 2015. The Paleoproterozoic Montviel carbonatite-hosted REE–Nb deposit, Abitibi, Canada: geology, mineralogy, geochemistry and genesis. Ore Geology Reviews, 67, 314-335.

Niocan Inc., 2015. Oka niobium property. <http://www.niocan.com/ww2/index.php?option=com _content&view=article&id=20> Accessed September 8, 2015.

Saucier, G., Noreau, C., Casgrain, P., Côté, P., Larochelle, E., Bilodeau, M., Hayden, A., Poirier, E., Garon, M., Bertrand, V., Kissiova, M., Mailloux, M., Rougier, M., Camus, Y., and Gagnon, G., 2013. Feasibility study for the Kipawa project, Temiscamingue area, Québec, Canada. NI 43-101 technical report, 429p. <http://www.sedar.com/GetFile.do?lang=EN&docClass=24&issuerNo=00010148&fileName=/csfsprod/data147/filings/02122328/00000001/y%3A\Web_Documents\RADAR\E3\MATQ\21OC13084\131017RapTechMatamec_ss.pdf> Accessed September 8, 2015.

Simandl, G.J., 2014. Geology and market-dependent significance of rare earth element resources. Mineralium Deposita, 49, 889-904.

Simandl, G.J., Prussin, E.A., and Brown, N., 2012. Specialty metals in Canada. British Columbia Geological Survey, Open File 2012-7, 48p.

van Breemen, O., and Currie, K.L., 2004. Geology and U–Pb geochronology of the Kipawa Syenite complex — a thrust related alkaline pluton — and adjacent rocks in the Grenville Province of western Quebec. Canadian Journal of Earth Sciences, 41, 431-455.

Vasyukova, O., and Williams-Jones, A.E., 2014. Fluoride–silicate melt immiscibility and its role in REE ore formation: evidence from the Strange Lake rare metal deposit, Québec-Labrador, Canada. Geochimica et Cosmochimica Acta, 139, 110-130.

Walters, A., Lusty, P., and Hill, A., 2011. Rare earth elements. British Geological Survey, Commodity Profiles Series, 54p.

Williams, P.J., Barton, M.D., Johnson, D.A., Fontboté, L., De Haller, A., Mark, G., Oliver, N.H.S., and Marschik, R., 2005. Iron oxide copper-gold deposits: geology, space-time distribution, and possible modes of origin. Economic Geology, 100th Anniversary Volume, 371-405.

Woolley, A.R., and Kjarsgaard, B.A., 2008. Carbonatite occurrences of the world: map and database. Geological Survey of Canada, Open File 5796, 28p.

Wright, W. R, Mariano, A.N., and Hagni, R.D, 1998. Pyrochlore, mineralization and glimmerite formation in the Eldor (Lake LeMoyne) carbonatite complex, Labrador Trough, Quebec, Canada. In: 33rd forum on the Geology of industrial minerals. Canadian Institute of Mining and Metallurgy, Special Volume 50, pp. 205-213.